Modélisation et optimisation du productible de centrales photovoltaïques flottantes.

Baptiste Amiot

Baptiste Amiot. Modélisation et optimisation du productible de centrales photovoltaïques flottantes.. Génie civil. Université Claude Bernard - Lyon I, 2023. Français. NNT : 2023LYO10007 . tel-04431519

HAL Id: tel-04431519
https://theses.hal.science/tel-04431519v1

Submitted on 1 Feb 2024

THESE de DOCTORAT DE

L'UNIVERSITE CLAUDE BERNARD LYON 1

Ecole Doctorale 162
(MEGA - Mécanique, Énergétique, Génie Civil et Acoustique)

Spécialité de doctorat : Énergétique

Soutenue publiquement le 06/01/2023, par :
Baptiste AMIOT

Modélisation thermique des centrales photovoltaïques flottantes

Devant le jury composé de :

Gisele Alves Dos Reis Benatto Chercheure - DTU (Danemark)	**Examinatrice**
Jean-Martial Cohard Maître de Conférence, HDR, IGE	**Examinateur**
Stéphanie Giroux–Julien Maître de conférences, HDR, UCBL - CETHIL	**Directrice de thèse**
Jean François Guillemoles Directeur de Recherche CNRS, HDR - IPVF	**Rapporteur**
Rémi Le Berre Ingénieur Chercheur, EDF R&D	**Co-directeur**
Christophe Ménézo Professeur des Universités, LOCIE	**Rapporteur**
Pietro Salizzoni Professeur des Universités, ECL - LMFA	**Président**
Ivana Vinkovic Professeur des Universités, UCBL - LMFA	**Examinatrice**
Hervé Pabiou Chargé de Recherche CNRS, HDR, INSA LYON - CETHIL	**Invité**
Martin Ferrand Maître de conférences, Ingénieur Chercheur, EDF R&D - CEREA	**Invité**

Declaration

I, undersigned, Baptiste Amiot, hereby declare that this manuscript represents my own work, under the scientific direction of Stephanie Giroux–Julien (thesis director) and the industrial supervision of Rémi Le Berre (thesis co-director), which has been done after registration for the degree of PhD at the University of Lyon 1 - UCBL, and has not been previously included in a thesis or dissertation submitted to this or any other institution for a degree, diploma or other qualifications.

Ecuelles, October 2022

ACKNOWLEDGMENT

L'écriture de ces derniers paragraphes signe la fin d'une épopée qui a commencé en 2019 et dont je n'aurais pu imaginer l'issue sans le concours de nombreux soutiens. Ces prochains paragraphes leurs sont dédiés.

Premièrement, je veux remercier les membres du jury d'avoir accepté d'évaluer ce travail de thèse. Vos commentaires et vos remarques ont permis d'améliorer le contenu du document final.

Mes remerciements vont ensuite à mes encadrants Rémi Le Berre et Stéphanie Giroux—Julien pour m'avoir permis de vivre ces trois intenses années. Je m'estime chanceux d'avoir pu bénéficier de votre savoir et savoir-faire pour forger une direction de recherche unique, merci pour votre aide durant cette parenthèse de ma vie.

Rattaché au groupe E38 *(E3V depuis peu)* au sein de la R&D d'EDF sur le site des Renardières, je souhaite dire merci aux managers que j'ai pu côtoyer, Patrick Dupeyrat et Jean-Marie Fourmigué, votre accueil et vos encouragements ont été de véritable atouts dans la réussite des travaux. Mes remerciements s'étendent également à Claire et Juliette, merci d'avoir facilité le quotidien de mes diverses missions. J'en profite également pour remercier chaleureusement les chefs successif du projet *Grandes Centrales PV*, Eric Lajoie-Mazenc et Gérald Kwiatowski, merci de m'avoir fait confiance et d'avoir appuyé les travaux à l'extérieur et à l'intérieur de la R&D.

J'aimerais ensuite exprimer ma gratitude aux ingénieurs habitants (et ex-habitants) du batiment J24 qui ont tous contribué à mon épanouissement professionnel. Merci à Gilles pour l'aide apportée sur Dymola®, Emmanuel pour son intérêt dans mes travaux et pour sa participation aux réunions de pilotage, Mike pour ses conseils sur les directions à considérer, Julien pour son aide constante sur le sujet du PV et ses relectures. Merci également à l'équipe Milanaise, Benoit, Oume et Christine; en plus de votre expertise, je retiendrai vos choix culinaires italiens parfois ... surprenants. J'en profite également pour remercier Matthieu Chioddetti, les trails du jeudi soir furent de bons exutoires, bon courage dans la ville rose.

Le bâtiment abrite également une jeune et dynamique équipe technique avec qui j'ai eu le plaisir de partager mes expériences. Merci donc à Antoine, Manuel et Florian, pour le support durant les phases fastidieuses des commandes de matériel ainsi que pour votre aide technique, j'ai apprécié partager des pauses café à 8h30 avec vous. Je n'oublie bien évidemment pas la tête pensante du laboratoire: merci à toi Frédéric pour ton humour au quotidien, cela a *fortement* contribué à mon moral durant ces trois années.

Plus globalement, j'ai apprécié pouvoir échanger avec les doctorants du département durant les évènements et autres pauses cafés communes, mention spéciale à Fanny, Hiba, Maëlle, Ana Maria et Valentin: merci pour les bons moments passés. En tant que dernier thésard du *bureau des thésards* (et des alternants) du J24, je souhaite également remercier les jeunes docteurs Nikola et Loris pour leurs accueils et conseils dès mon arrivée en 2019. Bon courage à Yann et Hugo pour la suite des opérations, je vous laisse un tableau blanc et un poster, faites-en bon usage (*pour écrire vos propres travaux de recherche ?*).

Bien que la possibilité de se déplacer fut réduite durant cette période, j'ai pu conserver de nombreux échanges avec les membres du Centre d'Energie et de Thermique de Lyon. Je souhaite donc remercier Hervé Pabiou pour son implication dans la direction expérimentale de la thèse, ainsi que Mathieu Galtier et Frédéric André pour leurs participations au pilotage des travaux. Merci également à tous les ingénieurs du laboratoire d'instrumentation du CETHIL pour avoir participé à l'élaboration des travaux sur la toiture ainsi qu'aux équipes de l'atelier pour la réalisation des structures de la Plateforme Solaire.

Mon périple m'a également mené sur le (fabuleux) site de la R&D de Chatou afin de me familiariser avec les environnements lacustres et plus globalement avec la mécanique des fluides. Au sein du Laboratoire National d'Hydraulique et d'Environnement, j'aimerai particulièrement remercier Javier pour ses conseils sur les phénomènes *évaporatif*. Dans le laboratoire de Mécanique des Fluides Energies et Environnement ainsi que dans le laboratoire commun du Centre d'Enseignement et de Recherches en Environnement Atmosphérique, je souhaite remercier chaleureusement Yannick, Aurélien et Dominique pour leur implication dans l'expérimentation des Hautes-Alpes. *Je pensais réellement que la caméra Fish-eye permettait d'observer les poissons...* J'en profite pour remercier les équipes de l'entreprise ATHOS, Gilles, Benoit et Antoine, merci d'avoir participé à cette aventure expérimentale haute en rebondissement. Je ne peux pas terminer ce paragraphe sans adresser mes plus *profonds* remerciements à Martin Ferrand pour son accompagnement scientifique et technique sur code_saturne, tu as souvent trouvé les mots justes pour me motiver, merci.

Avant de conclure ces remerciements, je ne peux oublier mon compagnon de galère, (Dr) Sylvain, merci d'avoir partagé ces trois années. Maintenant, place aux choses sérieuses (sus au Lapin seine et marnais)!

Pour finir, je souhaite remercier du fond du cœur les différents membres de mes belle-familles, David, Caroline, Xavier, Ewan, Céline et Laurent pour votre support depuis quelques années maintenant; ainsi que mon cercle familiale : Mes grands-parents, ma Sœur, Papa, Maman : merci pour tout, j'espère vous rendre fier. Enfin, Amélie, cette thèse n'aurait *jamais* eu lieu sans toi. Merci pour ton soutien indéfectible et pour la patience dont tu as fait preuve ces trois dernières années, tu es co-autrice de ce travail.

Merci à tous

RÉSUMÉ - FRANÇAIS

En 2022, plus d'un TeraWatt de module photovoltaïque (PV) a été installé à travers le monde. Ce fait d'arme, majeur pour la filière, va de pair avec une tension croissante sur l'utilisation des sols. Capter la ressource solaire, diffuse, est gourmand en espace. Ainsi une tendance de fond vise la colocalisation des usages et l'installation de ces moyens de production dans des endroits non-occupés, c'est le cas des installations photovoltaïques flottantes (FPV) sur lac et réservoirs. Les présents travaux abordent deux problématiques qui naissent dans ces applications : le refroidissement passif des modules ainsi que la réduction de l'évaporation des bassins liée à leurs couvertures.

Le concept de *cooling effect* est utilisé pour décrire la chute en température constatée dans ces applications par rapport à des installations terrestres. Ce paramètre est clef pour le producteur photovoltaïque qui voit le productible électrique amélioré. Une première étude de la littérature montre que la description du phénomène n'est cependant pas trivial. Des caractérisations thermiques plus approfondies sont nécessaires pour espérer maitriser ce refroidissement. Dans un premier temps, ces travaux s'attachent à définir la phénoménologie thermique qui anime ces installations. Des corrélations empiriques sont crées à partir de l'analyse des conditions d'opérations de système FPV développées dans le contexte de la thèse. Une nouvelle méthodologie de mesure, qui vise à déterminer le paramètre convectif avec une meilleure efficacité, est mise en oeuvre. D'abord validée sur une centrale au sol, elle est ensuite appliquée sur un système FPV.

Afin de vaincre les limitations intrinsèques de la méthodologie convective empirique, des simulations de mécanique des fluides sont mobilisées. Un modèle de simulation bi-périodique est mis en oeuvre avec le code de calcul code_saturne, et l'écoulement macroscopique de l'air dans les centrales PV est modélisé. Différentes configurations de centrales sont analysées afin de comprendre l'impact des propriétés géométriques sur les corrélations convection thermique et sur l'évaporation (espacement inter-modules, angulation et hauteur des modules). Cela se traduit par une analyse morphométrique des centrales qui permet de mettre en lumière les différences d'écoulement entre les centrales au sol et les solutions FPV.

Une dernière étape se base sur le référentiel atmosphérique et est dédiée à l'homogénisation des caractéristiques microscopiques des centrales afin d'en déduire les principaux effets sur l'écoulement macroscopique. Le modèle bi-périodique est appliqué sur une géométrie de centrale FPV industrielle. Cela se traduit par la détermination de caractéristique dynamique, thermique et évaporative, implémentée directement dans code_saturne. Dans un contexte industriel, cette stratégie permet d'étudier les propriétés de refroidissement des modules à l'échelle de la centrale, tout en réduisant drastiquement le coût de calcul nécessaire. Un taux de réduction d'évaporation est également calculée sur cette même base.

Mot clefs:*Photovoltaïque flottant, Convection, Mécanique des fluides numérique (CFD), Évaporation*

ABSTRACT - ENGLISH

In 2022, more than one Terawatt of photovoltaic modules has been installed throughout the world. This important achievement for the industry also signals the emergence of land-use issues due to the diffuse nature of the solar resource. Therefore, colocating energy production with other services is gaining momentum. This leads photovoltaics to go offshore, where human activity is less important. Therefore, new scientific questions have emerged due to unusual environmental constraints. Among the list, passive cooling of photovoltaics and evaporative rates for covered waterbodies are two elements discussed in this work.

The *cooling effect* concept describes the temperature drops observed in floating compared to land-based installations. This feature is important when designing floating plant as it is translated into a better energy yield. However, the reason of this efficient temperature is unknown; thermal characterisations are necessary so that the cooling gains can be understood and potentially controlled. The work aims to define the leading thermal phenomena in the application. New thermal correlations are proposed to describe the thermal dynamics of two floating experiments. An advanced measurement methodology is implemented on a land-based prototype so that the convective heat rates are obtained with a better accuracy. The similar method is integrated in a floating setup.

Then, the research places emphasis on convective transfers and macroscopic airflow at the array scale. A new modelling framework supported by a bi-periodic simulation is created. It is based on the computational fluid dynamics solver code_saturne. The calculation of the airflow is validated using a high-fidelity simulation and compared to wind tunnel results. The framework allows relaxing the solar array design so that airflow properties are evaluated with regard to geometrical dimensions (spacing, tilt, height). Convective and evaporative rates are calculated with regard to these dimensions. Comparison between floating and land-based configurations is performed and some conclusions are drawn on the potential *cooling effect* from wind action configuration.

In a last stage, the microclimate around floating solar is deduced by homogenising the physical quantity of interests in the bi-periodic simulation. To do so, an atmosphericist point of view is adopted. The floating array is assimilated to an effective roughness with scalar properties evolving with regard to wind direction and flow motion. Both flow and scalar fields are then resolved over a patchwork of rough surfaces related to real land-use for an industrial case study; the key advance is to keep the computational effort affordable for the scale under investigation. A new wall function for evaporative rate is created. Moreover, the module temperatures at the array-scale are obtained; a first analysis of the magnitude of temperature heterogeneity is performed so that it can illustrate how much the energy yield is uncertain due to macroscopic airflows.

Keyword: Floating photovoltaic, Convection, Computational Fluid Dynamics (CFD), Evaporation

RÉSUMÉ ÉTENDUE

Introduction

Répondre à l'augmentation de la demande en électricité à l'échelle mondiale nécessite la mise en oeuvre de moyen de production fiable et pérenne. Dans cette optique, il est nécessaire de développer des solutions techniques qui, en plus de concilier *de facto* les deux objectifs précédents, permettent de limiter la production de carbone tout en conservant le support de la société dans ces démarches. Avec l'essor des énergies renouvelables qui dépendent d'un gisement énergétique *diffus* par nature, de large espaces doivent être alloués aux installations afin de pouvoir produire des quantités suffisantes au regard de la consommation énergétique de l'humanité. La colocalisation des usages est une solution envisageable pour garantir une utilisation raisonnée des ressources. Cette thèse est principalement axée sur la colocalisation des actifs photovoltaïques au sein des environnements lacustres. Dans cette application, les centrales *photovoltaïques flottants (PVF)* sont positionnées au dessus d'un bassin d'eau douce (lac, étang, réservoir). Les actifs photovoltaïques sont donc soumis à des contraintes nouvelles du fait d'un environnement inhabituel.

Depuis 2007 et le début du déploiement de la technologie dans le monde, de nombreux acteurs du marché constatent des côtés positifs à cette installation parmi lesquels: une meilleure production électrique par rapport à des actifs au sol et une réduction de l'évaporation des bassins. Pour le premier point, il est à signaler que la production électrique est intrinsèquement liée à la température des cellules photovoltaïques qui composent les modules: une augmentation en température réduit la production électrique. Ainsi le terme anglo-saxon *cooling effect* est généralement utilisé pour décrire le *refroidissement passif* des modules dans l'application PVF. Le second point apparaît naturellement par l'expérience, la couverture des bassins permet de réduire la surface d'échange et altère les grandeurs physiques qui dirigent l'évaporation. Néanmoins, ces deux points sont sujets à controverse tant les applications PVF sont diverses et les conditions climatiques modifient les régimes de transfert thermique et massique environnementaux. Cette thèse a pour objectif de travailler sur la problématique du refroidissement passif par le spectre de la simulation thermique numérique et principalement sur la modélisation de la convection thermique à l'échelle de la centrale.

Cette thèse se compose en deux parties. Une première partie est dédiée à l'inspection de la littérature sur le sujet du photovoltaïque flottant et de sa modélisation, ce champ de littérature est étendue au système atmosphérique. Une seconde partie contributive vise à travailler sur la mesure des effets de refroidissement par l'expérimentation via différents moyens d'essais, ainsi qu'à modéliser le module photovoltaïque et ses conditions limites avec une plus grande efficacité, notamment en tenant compte de corrections des corrélations thermiques élaborées à partir des mesures sur site. La contribution principale vise à élaborer une méthode de remontée d'échelle afin de pouvoir étudier la centrale photovoltaïque et les champs aérauliques qui existent en son sein. Cette méthode est évaluée au regard d'expérience en soufflerie disponible dans la littérature puis extrapolée sur des configurations de centrales typiques dont celles qui représentent l'application PVF. Un cas d'étude est proposé pour une utilisation de la méthodologie à l'échelle de la simulation micro-climatique, tout en préservant un coût de calcul abordable. A l'issu de ces contributions, on espère pouvoir partager des corrélations thermiques et notamment convectives spécifiques à l'échelle de la centrale.

Base de l’étude

La production électrique des modules dépend du niveau d’irradiation reçu par les cellules et de leurs températures d’opérations, respectivement au premier et au second ordre. Le comportement thermique du module est déterminé par un bilan énergétique qui met en jeu, en plus du niveau de production et d’irradiation, les *conditions locales d’opérations* thermo-aérauliques et hydriques. Ces conditions dépendent naturellement du type d’intégration des modules dans leurs environnements ainsi que des types de structure qui supportent les systèmes. De manière équivalente, l’installation des systèmes photovoltaïques impact le système environnemental en réduisant les niveaux d’irradiations et en modifiant les champs physiques proches.

Les premières études liées au comportement thermique des modules ont montré que la production électrique était fortement dépendante du système de flottaison utilisé ainsi que du climat (H. Liu et al., 2018), (Dörenkämper et al., 2021). Parmi les conditions locales qui sont altérées par les flotteurs, la réduction de l’intensité des champs de vents locaux est supposé être prépondérant. Les structures agissent comme des éléments qui bloquent l’écoulement aéraulique, le phénomène convectif qui prend place au niveau des parois du module perd ainsi en efficacité du fait de la réduction du moteur advectif. La quantité de chaleur qui émane du module et qui est transportée par le vent étant réduite, la température des modules est plus importante: une dégradation de l’efficacité de production électrique est constatée. Les solutions de flotteurs sont ainsi classifiées à partir de leurs performances thermo-aérauliques (Figure 1).

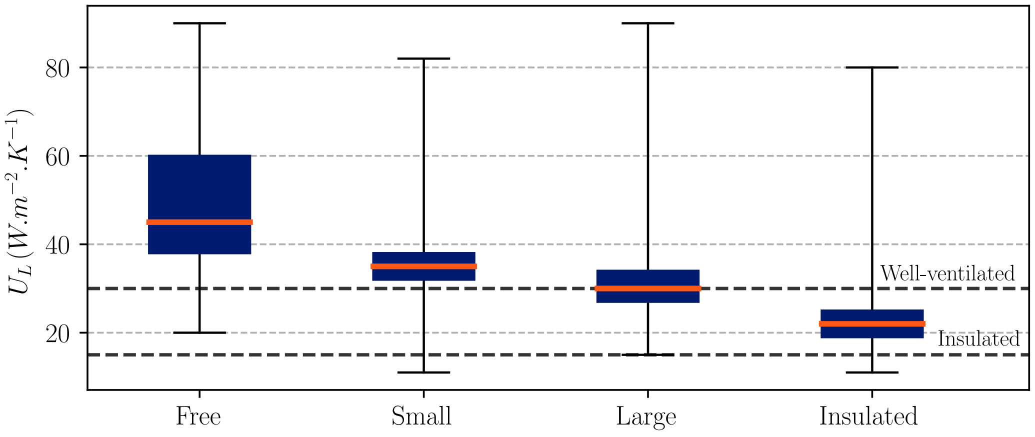

Figure 1–*Distributions des performances de refroidissement passif en fonction des types de système de flottaison obtenues dans H. Liu et al., 2018*

Les conditions aérauliques locales sont également reliées de manière complexe à l’agencement des modules entre eux. Les modules photovoltaïques flottants sont typiquement installés sous forme d’îlots dont les propriétés géométriques sont des fonctions de la course du soleil et de la bathymétrie des bassins (ancrages et amarrages). Les premières études qui s’attachent à la description des écoulement aéraulique macroscopique ont notamment montré que le niveau de refroidissement obtenu par les modules dans la centrale est plus faible que celui obtenu pour des applications isolées et indépendantes (Glick, Smith, et al., 2020). Le niveau de refroidissement apparaît être fonction des paramètres géométriques de l’installation et des paramètres du vent (vitesse, direction); ainsi déterminer l’intensité du refroidissement à l’échelle de la centrale reste un enjeu scientifique important. D’autant plus que les propriétés morphométriques sont accentués par des problèmes liés aux caractères stochastiques et chaotiques intrinsèques aux champs de vent (entrant et au sein de l’agencement d’obstacle photovoltaïque). Les premières observations différencient trois types d'écoulement dans la centrale dont les taux de transfert thermiques diffèrent du fait de la dynamique de l'écoulement dans le milieu assimilable à un agencement d'obstacles non profilés (Figure 2).

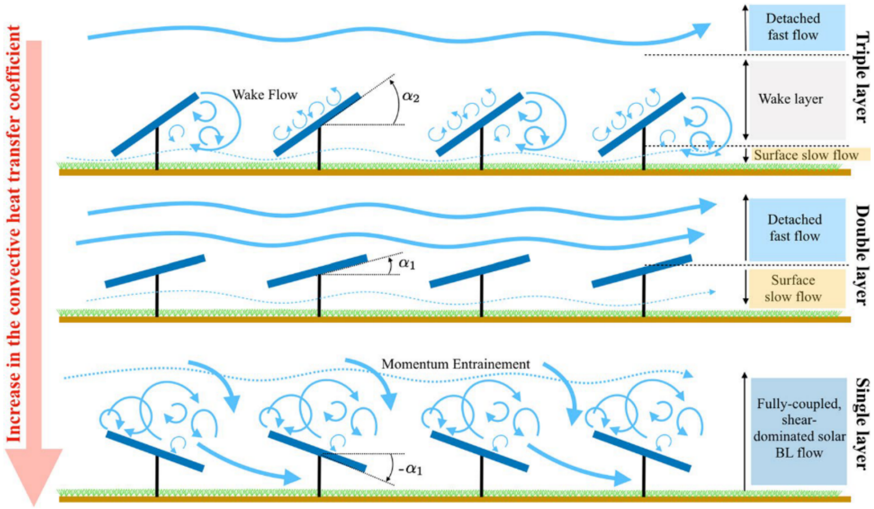

Figure 2–*Les différentes structures de l'écoulement macroscopique au sein des centrales PVF proposées dans Glick, Smith, et al., 2020.*

Le positionnement de la centrale au dessus de la surface de l'eau agit également comme un perturbateur pour le phénomène d'évaporation, que cela soit par la réduction de l'énergie radiative distribuée au milieu, ou bien par la réduction du moteur aéraulique qui transporte l'humidité de la surface vers l'atmosphère. Les études disponibles dans la littérature prennent appuis sur des concepts qui ont fait leurs preuves dans des cas de surfaces libres et découvertes (Bontempo Scavo et al., 2021). L'extrapolation à des surfaces recouvertes est néanmoins complexe et les approches adoptées diffèrent de celles disponibles dans la littérature spécialisée et qui ont reçu une attention plus forte au cour des dernières décennies (Cooley, 1970),(Assouline et al., 2010), (Assouline et al., 2011). Alliant à la fois de large portion en contact de l'eau, ainsi que d'encore plus large portion dont la vitesse du vent est perturbée, l'estimation de la réduction en évaporation reste un problème, théorique et appliqué, majeur pour la filière.

L'objectif de la thèse est d'explorer les mécanismes qui oeuvrent dans le refroidissement des modules photovoltaïques flottants, notamment lorsque ceux-ci sont intégrés dans des centrales photovoltaïques. Cette exploration porte principalement sur la problématique de la convection thermique en conciliant des méthodes empiriques et des méthodes numériques de modélisation. Les questions principales en jeu sont:

- Quels sont les champs physiques et les corrélations associées qui permettent de décrire efficacement les conditions limites thermiques des centrales photovoltaïques flottantes ?
- Quelles sont les éléments géométriques qui ont une influence sur le transfert convectif des modules à l'échelle de la centrale photovoltaïques ?

Cette dernière question est implicitement reliée à la prédiction de l'écoulement aéraulique autour des modules et par conséquent autour de la masse d'eau sous-jacente. Ainsi une extension de la seconde question touche à la quantification de la réduction en évaporation qui peut-être attribuée à l'altération de l'écoulement aéraulique.

Pour chaque question majeure posée, une méthodologie alliant expérimentation et simulation numérique est mise en oeuvre. Dans le cadre des travaux, trois expérimentations sont effectuées afin de servir de matériel de validation pour les modélisations numériques. Elles sont dénommées FPV1, FPV2 et CETHIL. Les deux premières expérimentations se positionnent sur des bassins.

Une première partie s'attache à décrire le module photovoltaïque en tant que système 1-D puis à estimer la contribution des densités de flux thermique aux limites du domaine soit par l'optimisation statistique, soit par l'intégration de conditions issus de mesures plus précises et spécifiques. Dans les deux cas de figure, les trois expérimentations sont utilisées pour supporter la simulation numérique de la dynamique en température du module. Dans la seconde partie, l'accent est mis sur la création d'une méthodologie numérique robuste qui résout le problème d'échelle d'étude lié du passage du module à la centrale. Cette méthodologie est supportée par l'utilisation d'un *solveur* de mécanique des fluides, toutes les morphométries de centrales peuvent être construites et leurs effets sur l'écoulement aéraulique sont identifiables. L'application à une géométrie de centrale existante sur le site d'étude FPV2 est produit afin de mettre en lumière l'efficacité de la méthode au regard des quantités d'intérêts définis pour les modules dans la centrale (refroidissement en face) et pour le bassin (taux d'évaporation).

Amélioration des conditions limites des modélisations thermiques 1-D FPV

L'approche numérique photovoltaïque 1-D repose sur la résolution d'un système composé de plusieurs couches de matériaux dont les propriétés sont décrites explicitement, et associé à une charge électrique. Le modèle nodal est écrit sous le langage Modelica® dans l'environnement Dymola®, et le système d'équation thermique et électrique est résolu par un schéma aux différences finies. Cette stratégie implique l'hypothèse de couche de matériaux aux propriétés homogènes, et dont l'épaisseur est petite devant les autres dimensions, ainsi que des hypothèses de conduction pure dans les matériaux, couplé à un contact thermique parfait entre les différent éléments. Le système est écrit de telle manière à tenir compte des effets capacitifs thermiques, l'accent est donc mis sur une résolution temporelle du système. Dans la suite des travaux, l'hypothèse d'une absence de conduction entre le module photovoltaïque et son environnement est formulée. L'utilisation d'un tel outil numérique est pertinent au regard de la volonté de comprendre les mécanismes qui agissent sur le module photovoltaïque flottant, les conditions limites au système décrit précédemment sont représentées par des densités de flux thermiques moyens.

Le modèle PV initial propose un découpage des conditions limites en fonction de la surface d'intérêt. Des corrélations représentatives des transferts externes pour la convection forcée et le transfert radiatif grande longueur d'onde sont appliquées dans le cadre de l'estimation des densités de flux en face avant des modules. Les même procédés sont appliqués pour la face arrière, les corrélations sont adaptées pour tenir compte de la convection naturelle et de la température du sol. Cet assemblage de modèle PV et de conditions limites est validé à partir de donnée mesurées sur site PVF (site FPV1), la température de face arrière est correctement prédite, le modèle converge. Des biais sont cependant remarqués, il est supposé que le jeu de corrélation n'est pas tout a fait adapté à la situation expérimentale.

Corrections des corrélations par optimisation statistique

Afin de construire un jeu de corrélation pertinent, une méthodologie de segmentation statistique des données théoriques et expérimentales est appliquée. La segmentation dissocie le jeu de donnée temporel en groupe de moment où la probabilité d'obtention d'un mode convectif et radiatif spécifique est importante. Le nombre de Richardson Ri et l'indice de clarté K_t sont utilisés à cette fin. Plusieurs centaines de simulations sont ensuite effectuées afin d'explorer la variabilité des prédictions en température des modules pour différentes valeurs de corrélations corrigées, et ceux pour toutes les groupes déterminés par segmentation. L'étude des statistiques de la distribution d'erreur entre les prédictions et le système expérimental met en lumière des pondérations plus importantes que les corrélations initiales de la littérature pour le site FPV1, les phénomènes convectifs sont augmentés tandis que les conditions radiatives semblent profiter d'un climat plus humide pour augmenter l'influence du milieu participatif local (Figure 3). La même procédure appliqué au site FPV2 montre des résultats différents, la convection forcée est légèrement plus importante mais surtout la convection naturelle est plutôt plus faible. Le rayonnement atmosphérique grande longueur d'onde est également plus important sur le site FPV2. Ces constats tendent à corroborer l'observation de l'effet aéraulique lié à la structure, le site FPV2 présente une géométrie dont les modules sont obstrués par des éléments bloquants au niveau de la face arrière, alors que la solution FPV1 ne possède pas ces attributs.

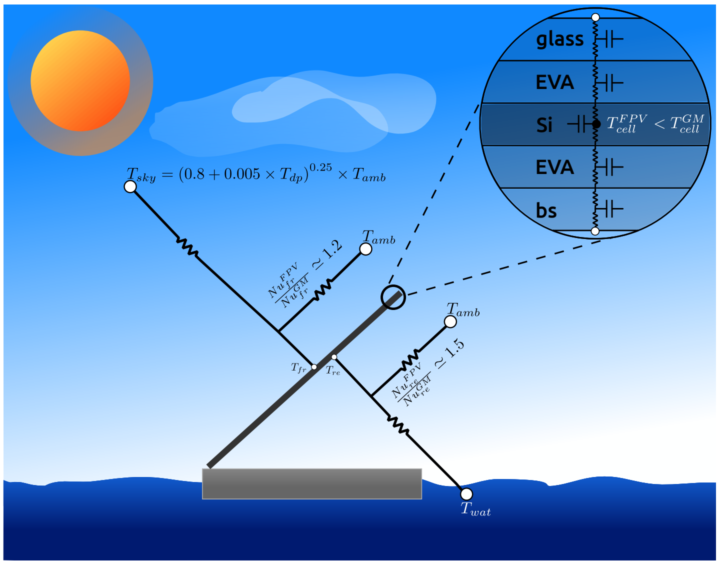

Figure 3–*Jeu de corrections des corrélations issu de l'étude exploratoire menée sur la site instrumenté FPV1.*

Preuve de concept et application d'un nouveau moyen de mesure

Pour vaincre la limitation des corrélations usuelles, une méthodologie de mesure est mise en oeuvre dans le cadre de la campagne CETHIL. Cette méthodologie permet d'acquérir la densité de flux qui traverse le module par conduction et qui sort du système photovoltaïque sous le mode de transfert convectif. Un système flux-métrique est adapté aux contraintes environnementales et est couplé à un système de mesure typique pour le suivi des conditions locales. La fréquence d'acquisition du système est de 5 secondes. Deux applications sont effectuées, la première consiste en la corrélation de la densité de flux avec la vitesse moyenne du vent de telle sorte à obtenir une corrélation linéaire fiable, la seconde consiste en l'intégration directe de la densité de flux comme condition limite convective dans le modèle 1-D.

Dans le premier cas, il est démontré que la nouvelle méthodologie améliore sensiblement la détermination d'une loi linéaire par rapport à la méthodologie usuelle et notamment pour des fréquences d'agrégation inférieures à 10min (Figure 4). Dans le second cas, la méthodologie améliore la performance de prédiction en température par rapport à la méthode optimisée par corrélation dont la forme est imposée (Figure 5). Pour ce deuxième point, la méthode de mesure est appliquée sur le site FPV2. Il en résulte que le niveau de convection forcé déterminé par la nouvelle méthodologie montre une intensité convective plus forte sur le système PVF. De plus, l'intégration directe de la mesure de taux de transfert convectif dans le modèle améliore drastiquement la qualité de la prédiction en température du module photovoltaïque. La nature stochastique du vent et son impact sur la déperdition de chaleur est considérée sans biais.

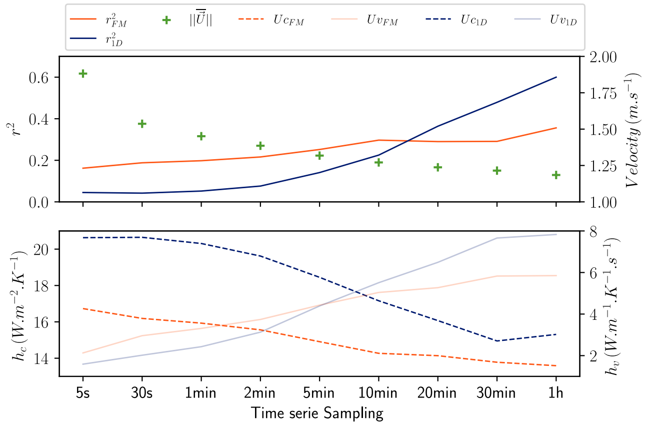

Figure 4–*Performance statistique de la mesure quasi-directe du flux convectif en face avant effectué en condition extérieure durant la campagne CETHIL en fonction de l'agrégation des données d'entrée, et comparé à la méthode classique.*

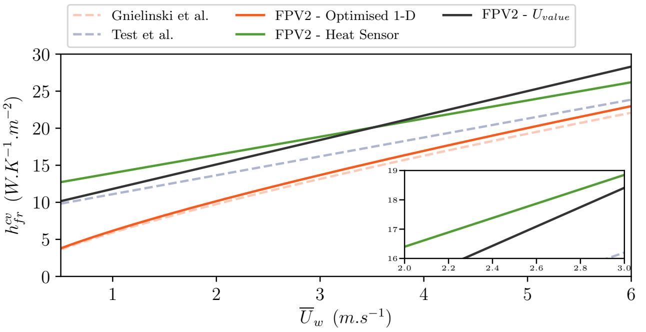

Figure 5–*Comparaison des deux méthodes de détermination du coefficient convectif au regard de la méthode classique et des corrélations pertinentes de la littérature.*

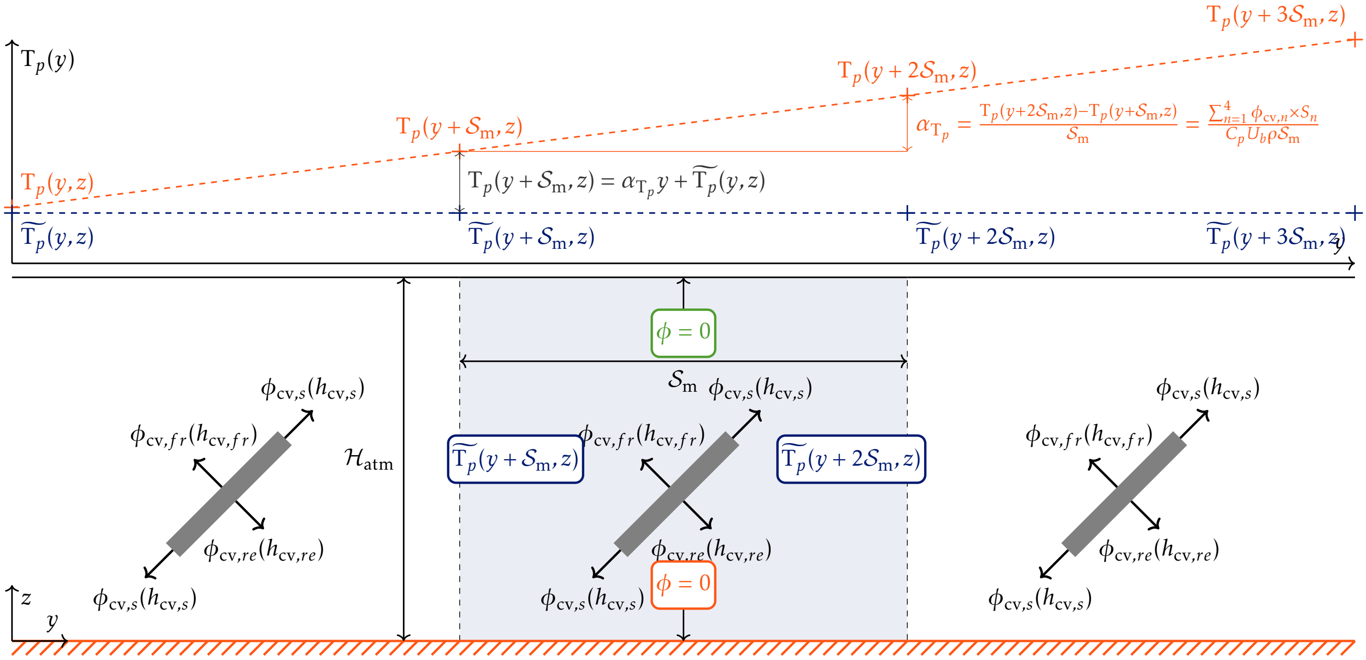

Figure 6–*Illustration de la périodicité thermique dans la centrale et mise en valeur de la zone minimale d'étude.*

Méthode de remontée d'échelle: du module à la centrale

Afin d'être en mesure de conjecturer sur les champs de vent locaux dans une centrale photovoltaïque, une chaîne de modélisation est conçue sur le logiciel SALOME® grâce aux modules SHAPER® et SMESH®. Cette dernière réalise la construction d'un maillage pour le volume d'air contenu dans un motif de centrale photovoltaïque qui est assimilé à une coupe longitudinale d'une longueur inter-module. Dans ces circonstances, le module est représenté par une absence de matière dans le domaine. La chaîne est conçue pour pouvoir modéliser la centrale dans les 3 dimensions avec l'hypothèse que cette dernière est régulière. Les équations de la dynamique des fluides sont résolues par code_saturne.

Élaboration du modèle bi-périodique

Le modèle bi-périodique consiste en la résolution d'un seul motif de la coupe longitudinale de centrale pour laquelle des conditions limites de périodicité sont appliquées aux bords du domaine. Les équations de Navier-Stokes et de conservations de l'énergie sont résolues sur les grandeurs périodiques, un terme source thermique est intégré à l'équation de l'énergie afin de satisfaire à la contribution de la surface du module par flux imposé (Figure 6). Le modèle $k-\omega\ SST$ est appliqué pour cette étude compte tenu de sa robustesse dans le calcul des distributions de vitesses pour des géométries similaires, des lois de parois sont utilisées pour modéliser les quantités pour les premières mailles au dessus des murs. Le forçage aéraulique est effectué par le haut du domaine via une condition de frottement imposé. A convergence, le profil de vitesse du vent dans le sens de l'écoulement est calculé autour du module, la distribution théorique du fluide en trois zones est obtenue (Figure 7). L'estimation de l'influence de la série d'obstacle photovoltaïque est réalisée à partir de la comparaison entre le profil aéraulique en haut du domaine et celui obtenu avec un profil atmosphérique optimisé avec une valeur spécifique de rugosité z_0. Cette valeur représente l'impact des motifs sur la dynamique de l'écoulement dans la centrale.

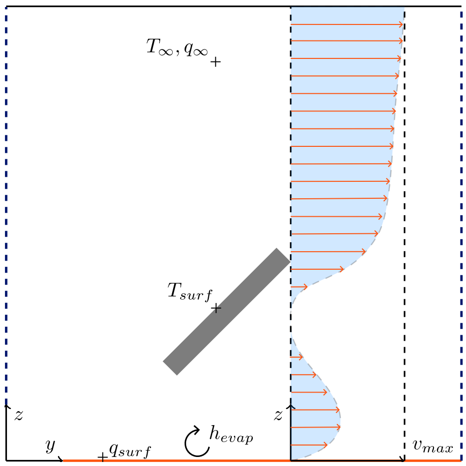

Figure 7–*Illustration du profil de vitesse moyenne du vent après un module d'une centrale.*

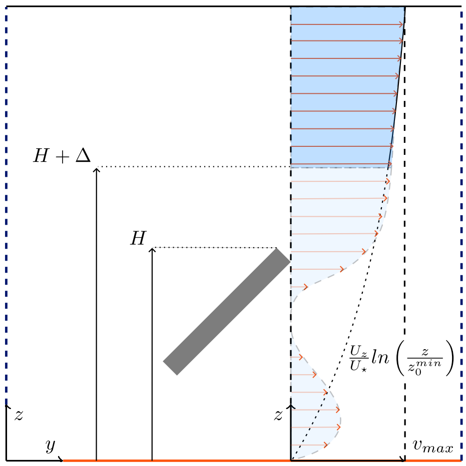

Figure 8–*Illustration de la méthodologie de calcul de l'impact sur la dynamique de l'écoulement.*

La reproduction de l'expérience en soufflerie dans Glick, Smith, et al., 2020 donne des résultats différents vis à vis du profil de vent, notamment sous les modules, où la direction du vent est trouvée contraire à celle expérimentée en soufflerie. La soufflerie est donc modélisée et un modèle de simulation aux grandes échelles (*LES*) est mis en oeuvre. Les profils de vitesse sont reproduits fidèlement tandis que les profils de turbulence sont obtenus avec des niveaux plus faibles. Les différences obtenues avec le modèle périodique sont assimilées à des effets du modèle de turbulence, la zone d'établissement estimée dans l'expérience est également questionnée.

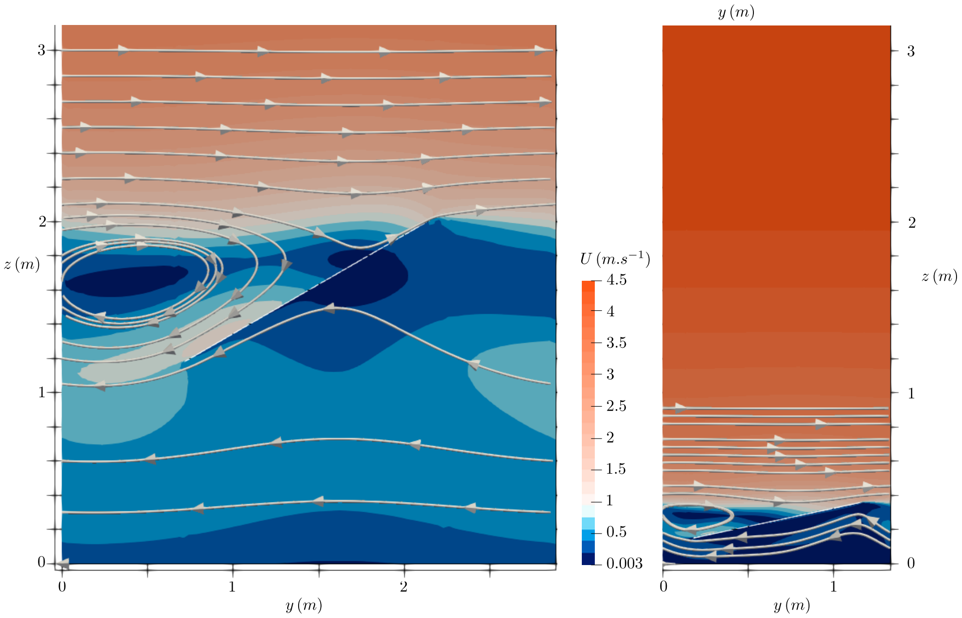

Figure 9–*Ecoulements moyens simulés pour deux géométries typiques: centrale au sol (gauche) et centrale sur l'eau (droite).*

La simulation de deux géométries représentatives des applications photovoltaïque au sol et sur l'eau met en valeur la différence des effets aérauliques liée aux propriétés d'angulation du module θ_m, la distance intermodule $\mathcal{S}_\mathrm{m}$, la hauteur des modules $\mathcal{H}_\mathrm{m}$ (Figure 6.1). Il est mis en valeur que les zones d'écoulement définis dans la centrale évoluent en fonction des paramètres, géométrique. L'intégration des propriétés thermiques des modules met également en valeur la plus faible efficacité de convection forcée pour les deux faces du module représentatives du PVF par rapport au module au sol. Ce résultat est majeur car il remet en question la source des meilleurs performances en refroidissement obtenues par l'expérience pour les modules PVF.

Evaluation des taux de transferts en fonction de la géométrie

Afin d'évaluer le rôle de la géométrie des centrales dans les performances en refroidissement, plusieurs simulations sont effectuées avec des variations d'angulations et d'espaces intermodules. L'étude des coefficients de transfert thermique moyens porte sur les deux faces du système photovoltaïque, ils sont respectivement dénommés $\langle h_{fr}^{\mathrm{cv}} \rangle$ et $\langle h_{\mathrm{bs}}^{\mathrm{cv}} \rangle$ pour la face avant et arrière. Il est démontré par la simulation que pour des vitesses de frottement atmosphérique égales, le taux de transfert convectif des deux faces est meilleur pour les vents parallèles ($\theta_{\mathrm{w}} = 90°$, Figure 10). Les vents perpendiculaires obtiennent des performances jusqu'à 50% moins bonnes (Figure 11). Il est également découvert que les centrales à faibles angulations sont plus performantes en moyenne en terme de refroidissement que les centrales à fortes angulations. Il est déduit que la mauvaise performance des centrales PVF provient principalement du taux d'occupation solaire supérieur à celui des centrales au sol. Les zones de recirculation dans les deux domaines aérauliques sont corrélées aux propriétés géométriques, ce sont elles qui altèrent le refroidissement par voie aéraulique lors de l'intégration des modules dans les centrales. La taille et la position de la zone de recirculation modifie la zone de vitesse locale maximale à proximité du module. La géométrie typique du photovoltaïque flottant permet une meilleure aération du système en haut de la paroi du fait de l'émergence d'une zone de recirculation de faible intensité. L'inverse est également démontré pour le système typique d'une centrale au sol.

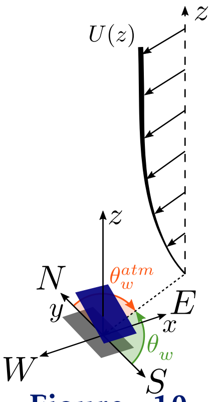

Figure 10– *Définition de l'angle d'attaque du profil atmosphérique*

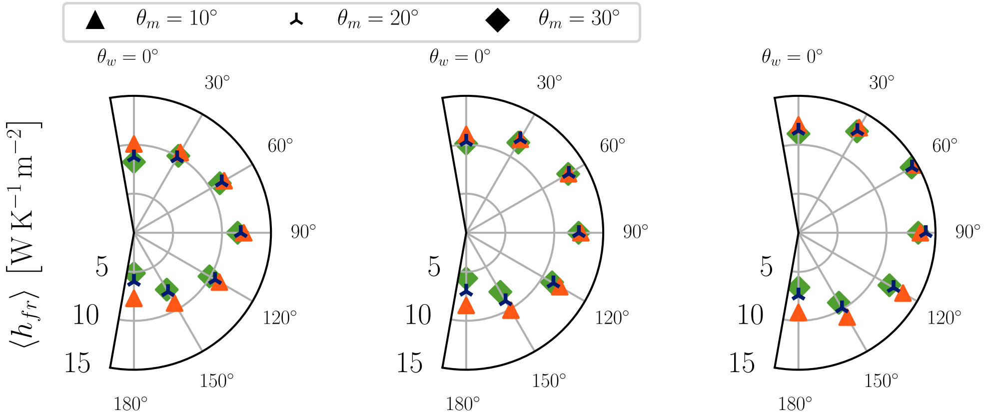

Figure 11–*Etude morphométrique des taux de transfert convectif en face avant en fonction des profils de vent.*

Modélisation des effets d'hétérogénéités thermiques et hygriques

Une modélisation 2-D à l'échelle de la centrale dans laquelle les modules sont explicitement représentés montre que l'obtention des quantités z_0, $\langle h_{fr}^{\mathrm{cv}} \rangle$ et $\langle h_{\mathrm{bs}}^{\mathrm{cv}} \rangle$ est coûteuse et peu robuste, l'établissement de l'écoulement est obtenu autour du 26ème module pour une configuration représentative. Les transferts thermiques sont réduits à partir du 3ème module qui fait face à l'écoulement ce qui justifie la nécessité de considérer l'échelle globale lors de la construction de corrélation convective.

Une variante d'utilisation du modèle bi-périodique est réalisée dans l'optique de décrire l'évolution des propriétés d'intérêts z_0, $\langle h_{fr}^{\mathrm{cv}} \rangle$ et $\langle h_E \rangle$ (taux de transfert évaporatif) tout en conservant une estimation de la zone où l'écoulement n'est pas établi. Des lois de parois sont créées, elles reproduisent l'altération des propriétés de l'écoulement (dynamique et scalaires) en conservant les dépendances des quantités calculées aux propriétés de l'atmosphère (vitesse de friction et angle du vent). Il est proposé de construire les lois de parois avec une forme polynomiale à l'ordre deux en fonction de l'angle du vent. Les limites de la méthode périodique sont atteintes pour les vents parallèles et fortement obliques, les lois de parois sont rendues continues par la mise en place de seuil (Figure 12).

L'efficacité des lois est mise en exergue par la simulation d'un cas microclimatique 3-D RANS avec un modèle de fermeture $k-\epsilon\ LP$. Le site d'étude FPV2 est numérisé par une conversion de cartographie IGN et la simulation tient compte des zones d'utilisation du sol via le couplage des surfaces de la géométrie avec les informations contenues sur la base de donnée THEIA[1]. Les propriétés de la centrale sont intégrées par le formalisme des lois de parois identifiées précédemment. La simulation d'un cas atmosphérique typique, déterminé par la mesure sur le site FPV2, montre que l'établissement de l'écoulement n'est pratiquement pas atteint sur la centrale industrielle FPV2. Ce résultat est utilisé pour calculer la distribution des températures des faces avant des modules en fonction de leurs positions dans le système. Il est démontré que le positionnement des îlots flottants agit fortement sur les températures obtenues. La hauteur de la berge apparaît comme un élément déterminant qui modifie localement les zones de recirculation atmosphérique. Cela se traduit par des modules plus chaud dans ces zones de recirculations macroscopiques. Lorsque ces effets extérieures à la centrale sont évacués, l'évolution de la température des modules suit un profil logique déjà constaté dans le système de centrale explicite (refroidissement fort des modules à l'amont et réchauffement jusqu'au régime établi dans le reste de la centrale). La méthodologie est suffisamment généralisable pour pouvoir être appliquée à de nouvelles situations à des fins de validation et d'estimation des champs physiques locaux.

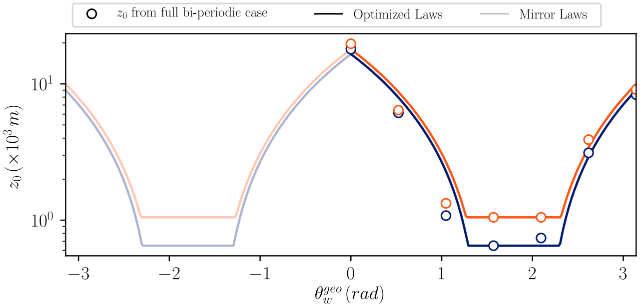

Figure 12–*Proposition de loi de paroi numérique pour la dynamique.*

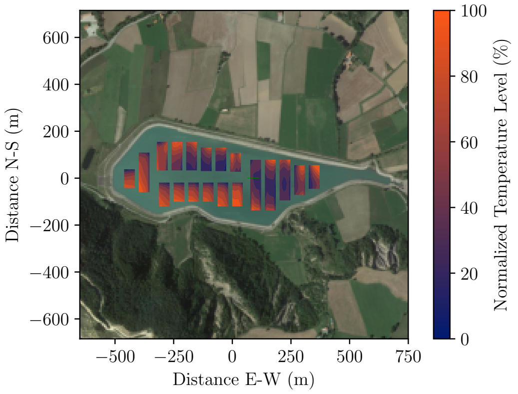

Figure 13–*Cartographie de la centrale industrielle FPV2 sur laquelle l'hétérogénéité de température des modules (faces avants) est indiquée*

---

[1] Continental surface data from national institutions

Conclusion et Perspectives

Ces travaux mettent en exergue les éléments clefs qui dirigent le comportement thermique des modules, en adoptant une approche de module isolée puis en adoptant un formalisme adapté à l'échelle de la centrale photovoltaïque. Les deux approches se focalisent majoritairement sur l'application des modules photovoltaïques flottants au dessus des réservoirs. Il est démontré dans ces travaux que les conditions particulières d'alimentation aéraulique, de température ambiante et d'humidité peuvent-être intégrées dans les modèles de prédiction thermo-électrique sous forme de corrélations spécifiques à cette application. A l'aide d'outils expérimentaux et numériques adaptés, les corrections à appliquer aux corrélations convectives et radiatives standards de la littérature ont été élaborées. Alors que la convection thermique forcée se voit être améliorée grâce à une localisation idéale pour le développement de la couche limite atmosphérique (l'augmentation est estimée autour de 4 à 20 %), les corrections déterminées pour la face arrière sont dépendantes de la structure de flottaison. Tandis que les structures dîtes *faibles empreintes* montrent une amélioration de l'intensité convective naturelle jusqu'à 50%, les structures dîtes *fortes empreintes* obtiennent des résultats dégradées de l'ordre de 25% par rapport au cas nominal. Le formalisme adopté pour obtenir ces estimations tient compte des propriétés d'inerties thermiques et d'une séparation astucieuse des conditions limites du modèle thermique photovoltaïque. Du même coup, il est démontré que le microclimat humide ambiant a une influence sur les performances de refroidissement radiatif. Un formalisme simplifié d'atmosphère équivalente à un corps gris approche correctement le comportement radiatif de l'air humide.

La généralisation de la correction convective à l'échelle globale a nécessité la mise en oeuvre d'un modèle de simulateur de centrale photovoltaïque, le solveur de mécanique des fluides code_saturne a été utilisé à cette fin. La simulation de plusieurs agencements réguliers de centrales a mis en lumière l'influence de la géométrie des modules, notamment le rôle de l'espace inter-module et de leurs angulations dans l'obtention de bonnes performances convectives. Tandis que le taux de transfert en face avant est moins influencé en moyenne par la géométrie (variations relatives de performances de l'ordre de 33%), le transfert de la face arrière se trouve être fortement dégradé dans le cas de centrales à *fortes empreintes* (la dégradation relative est estimée à 78%). Le photovoltaïque flottant et sa géométrie proche de l'eau, peu espacée et faiblement inclinée (historiquement pour réduire la charge aéraulique sur le système), s'avère être un mauvais candidat pour obtenir un important refroidissement passif.

L'utilisation de stratégie numérique d'homogénisation a finalement permis de mettre en lumière l'importance de la zone d'écoulement spatialement hétérogène dans le cas d'application d'une site FPV industriel. Le développement de lois de parois numériques dynamiques et évaporatives a permis d'estimer la distribution en température de surface des modules FPV à l'échelle de plusieurs îlots, cette distribution couvre parfois l'intégralité de l'îlot photovoltaïque tel que le régime développé n'est pas atteint sur plusieurs dizaines de mètres. Les effets de la berge sur le développement aéraulique sont également évoqués, des zones de recirculation autour des installations dégradent fortement la température des systèmes photovoltaïques dans ces zones particulières. Les premiers résultats évaporatifs ont également montré que les modules réduisent considérablement l'évaporation des bassins à cause de la réduction locale en intensité du champ aéraulique. De plus amples travaux doivent être réalisés sur cette thématique afin d'estimer le taux de rétention hydraulique des bassins couverts par des installations photovoltaïques flottantes.

Principales Contributions de la thèse

- Création de plusieurs corrélations empiriques qui permettent de décrire les conditions limites thermiques des modules photovoltaïques flottants et qui affectent le *refroidissement passif* des modules
- Preuve de concept en situation opérationnelle d'un système de mesure pour l'évaluation des taux de transfert convectif en face avant des modules (application au sol et sur l'eau)
- Construction paramétrique des géométries et des maillages de centrales photovoltaïques en 3-D
- Mise en évidence d'une stratégie de remontée d'échelle qui permet d'étudier l'écoulement macroscopique en situation de centrale photovoltaïque
- Mise en évidence des éléments géométriques clefs pour le transfert convectif des modules en centrale et identification des principaux éléments pour les cas photovoltaïques au sol et sur l'eau
- Estimation des niveaux de convections forcés pour les centrales en fonction des propriétés atmosphériques
- Développement de fonctions de paroi numérique pour la dynamique et le transfert évaporatif, tenant compte des conditions atmosphériques (direction et vitesse du vent), généralisable à toutes les géométries de centrale photovoltaïque régulière, pour les simulations 3-D microclimatique.

Contents

NOMENCLATURE

Latin Letters

T	Real Temperature,	[°C] or [K]
T_p	Potential Temperature,	[°C] or [K]
ϕ	Irradiance,	$\left[\mathrm{W\,m^{-2}}\right]$
U	Velocity vector,	$\left[\mathrm{m\,s^{-1}}\right]$
$u_x\,u_y\,u_z$	Components in x, y and z directions,	$\left[\mathrm{m\,s^{-1}}\right]$
P_m	Electrical production,	[W]
V	Voltage,	[V]
I	Current,	[A]
$\mathcal{A}$	Area,	$\left[\mathrm{m^{2}}\right]$
R	Electrical resistance,	$[\Omega]$
E_ph	Photon Energy,	[eV]
U_{values}	Global Heat Transfer,	$\left[\mathrm{W\,K^{-1}\,m^{-2}}\right]$
Cp	Specific Heat Capacity,	$\left[\mathrm{J\,K^{-1}\,kg^{-1}}\right]$
RH	Relative Humidity,	[%]
P_{vap}	Pressure Vapour,	[Pa]
K_t	Clearness Index,	[−]
P	Pressure,	[Pa]
m	Mass,	[kg]
h	Heat rate,	$\left[\mathrm{W\,K^{-1}\,m^{-2}}\right]$
θ_m	Module angulation,	[°]
$\mathcal{H}_\mathrm{m}$	Module Height,	[m]
R	Thermal resistance,	$\left[\mathrm{K\,m^{2}\,W^{-1}}\right]$
R	Evaporative resistance,	$\left[\mathrm{kg\,m^{2}}\right]$
$\mathcal{H}_\mathrm{atm}$	Atmosphere Height,	[m]
$\mathcal{L}_\mathrm{m}$	Module Length,	[m]
$\mathcal{E}_\mathrm{m}$	Module Width,	[m]
$\mathcal{S}_\mathrm{m}$	Array Pitch,	[m]
$u_\star$	Friction Velocity,	$\left[\mathrm{m\,s^{-1}}\right]$
z_0	Roughness Length,	[m]
$A\,B$	Tuning parameters	
m	Diode Ideality Factor	
$\mathrm{n}_S\,\mathrm{n}_P$	Serial & Parallel Cells	
S_{ij}	Local Strain Rate	
k	Turbulent kinetic energy,	$\left[\mathrm{m^{2}\,s^{-2}}\right]$

Greek Letters

α	Absorptivity	
ϵ	Emisivity	
τ	Transmissitivity	
$\chi\,\zeta$	Tuning parameters	
ν	Frequency of Oscillation	
η	Efficiency of photo-conversion	
τ_{ij}	Viscous Stress tensor	
δ_{ij}	Kronecker delta	
μ	Molecular viscosity	
ϵ	Dissipation rate	
ω	Specific dissipation rate	
τ_w	Wall shear stress	
θ_w	Wind direction,	[°]
Φ	Flux,	[W]
ϕ	Density of Flux,	$\left[\mathrm{W\,m^{-2}}\right]$

ρ	Density,	$\left[\mathrm{kg\,m^{-3}}\right]$
λ	Thermal Conductivity,	$\left[\mathrm{W\,m^{-1}\,K^{-1}}\right]$

Physical Constants

$k = 1.380\,649 \times 10^{-23}\,\mathrm{m^2\,kg\,s^{-2}\,K^{-1}}$ Boltzmann Constant

$\sigma = 5.67 \times 10^{-8}\,\mathrm{W/m^2/K^4}$ Stefan-Boltzmann Constant

$\mathsf{h} = 6.63 \times 10^{-34}\,\mathrm{J\,s}$ Planck Constant

$g = 9.81\,\mathrm{m\,s^{-2}}$ Gravitational acceleration

$\kappa = 0.42$ Von Karman Constant

Subscripts & Superscripts

m	Module
amb	Ambient air
$meas$	Measured Field
$pred$	Simulated Field
grd	Ground
irr	Plane of Array (Photovoltaic module)
cell	Photovoltaic cell
sky	Sky
gl	Glass
si	Silicium
eva	Ethylene Vinyl Acetate
ts	Timestep
n	Iteration
cd	Conduction Transfer
cv	Convective Transfer
ir	Thermal radiation Transfer
$free$	Free Convective Mode
$forced$	Forced Convective Mode
$mixed$	Mixed Convective Mode
ex	Explicit Representation
im	Implicit Representation
re	Module Rear Side
fr	Module Front Side
mp	Maximum Point (production)
s	Serie
sh	Shunt

Mathematical Operators

$\langle Y \rangle$	Spatial average
$\overline{Y}$	Temporal average

$\sum_{i=1}^{N} a_i b_i = a_i b_i$ Einstein summation convention

$\dfrac{\partial Y_i}{\partial x_i} = \dfrac{\partial Y_x}{\partial x} + \dfrac{\partial Y_y}{\partial y} + \dfrac{\partial Y_z}{\partial z}$ Divergence Operator

Acronyms

PV, FPV	Photovoltaics, Floating Photovoltaics
LCOE	Levelized Cost of Energy
DCO	Direct Current Output
GCR	Ground Coverage Ratio
EVA	Ethylene Vinyl Acetate
NOCT	Normal Operating Cell Temperature
STC	Standard Test Conditions
DC	Direct Current
AC	Alternative Current
HDPE	High-Density PolyEthylene
PERC	Passive Emitter and Rear Cell
Al-BSF	Aluminium- Back Surface Field
RANS	Reynolds Average Navier Stokes

Dimensionless Numbers

Re	Reynolds Number
Pr	Prandtl Number
Sc	Schmidt Number
Gr	Grashof Number
Ra	Rayleigh Number
Sh	Sherwood Number

Initial picture of energy and water saving challenges

On March 14, 2022, the world has entered the TeraWatt era JOHN FITZGERALD, 2022,Haegel et al., 2019, meaning that the installed capacity of photovoltaic modules worldwide is expressed in the same units as the global energy demand[2]. The astute eye will notice that orders of magnitude are still out of sync, thus indicating the need for a reaction from humanity to meet the challenge of climate change: turn off CO_2-based energy sources to low-carbon sources or drastically reduce energy consumption. Combining these scenarios is a good opportunity to participate in a sustainable future Pörtner and Roberts, 2022.

Although energy in the form of electricity is not primordial for humankind (after all, solar panels appeared after humans!), water and especially drinking/freshwater water[3] are infinitely more critical for the survival of the species (and many others). More than 4000 km^3 of water are consumed per year for agricultural, industrial, and municipal uses Ritchie and Roser, 2017, neglecting the water loss that occurs from *sip of the angels*[4]. Unfortunately, there is only about 50 000 km^3 of fresh water available on the surface of the earth Gleick, 1996, which is quite unevenly distributed. It remains quite likely that the inequalities will not fade away and even amplify with longer and more important droughts to be expected in several regions. **In summary, water and energy are the two main issues for humanity in the 21st century.**

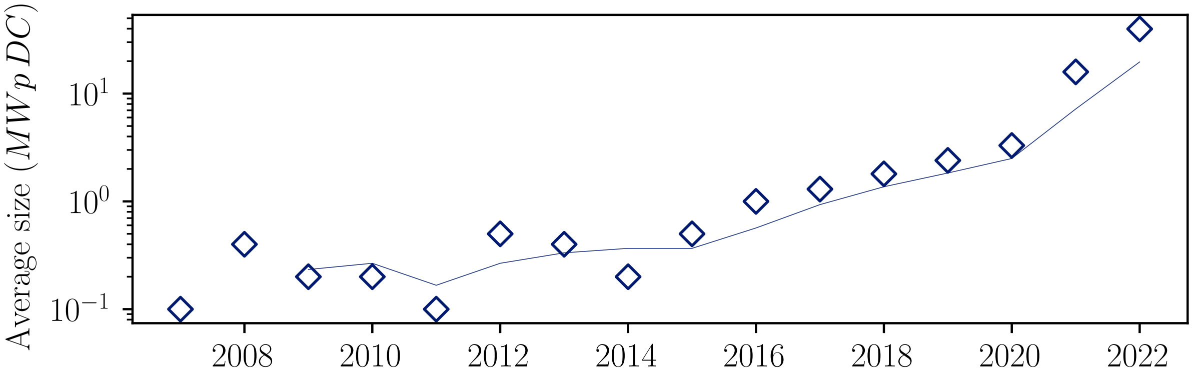

Figure 14–*Average size of Floating Photovoltaic installations since the first scientific setup. The moving average over a period of 3 years highlights the growing trend of making solar array at the utility scale.*

One way to address these issues has been developed through technology in the form of **Floating Photovoltaic** *(FPV)* installations. Initially conceived as a solution to produce decarbonised energy in territories under land tension, floating photovoltaic technology now enjoys significant support on a global scale thanks to the construction of power plants with several MWp of installed capacity (see Figure 14), especially in China after the closure and conversion of coal-fired power plants *Where Sun Meets Water: Floating Solar Market Report*, 2019. With only 2 GWp installed in 2022, forecasts indicate that this capacity will double in 4 years[5].

---

[2] Assuming an annual global primary energy consumption of $\simeq 1.7 \times 10^4$ TWh, the total power needed is estimated to $\simeq 19$ TWp

[3] Freshwater consists in water containing less than 1000 $\mathrm{mg\,l^{-1}}$ of dissolved solids

[4] Fortunately, the water loss from evaporation remains in the water cycle !

[5] https://www.woodmac.com/reports/power-markets-floating-solar-landscape-2021-476537

Motivations

Energy asset closely related to nature

Photovoltaic systems convert solar energy into electricity through a process called photoconversion. This trade-off between photons and electricity is bound to the temperature at which the material works: The warmer the material, the lower the efficiency. The elements that make up photovoltaic systems can be studied on the microscopic scale (O(μm) - ns) with p-n junctions, as well as on the mesoscopic scales (O(10 km - h) for photovoltaic power plants, passing through intermediate scales (solar cell, photovoltaic module). The biggest scale integrates the lower scale, and so fourth, their arrangements in between being versatile. **The field of photovoltaics is thus, by nature, multi-scale**. The thesis addresses most specifically the module and the utility solar array scales.

As soon as we are interested in industrial systems under operation, the environment close to the modules interferes with the photovoltaic system; its characterisation becomes necessary to be able to describe the amount of energy recovered. This characterisation can be done either by measuring the main physical fields, which are relatively well described in the literature: irradiance, ambient temperature, air humidity, average wind speed; or by numerical simulation. This time we want to simulate the physical fields by applying the fundamental laws: propagation of radiation in the atmosphere, diffusion-advection of temperature and humidity, and conservation of motion for the wind vector. Whether one chooses one method or the other, the engineer must determine the key elements that control the behaviour of the system.

Figure 15–*Prototype of floating solar array installed in Belgium by EDF.*

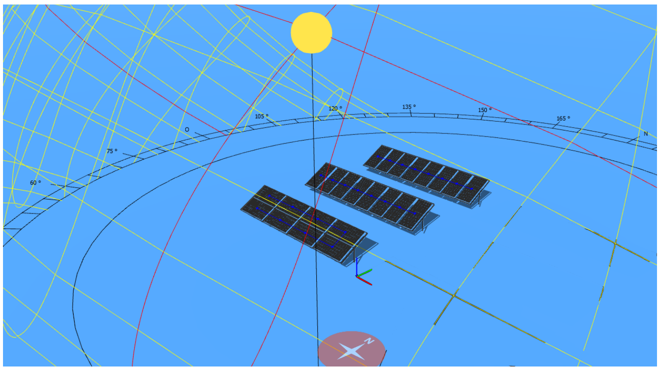

Figure 16–*Simulation of the radiative field received by the modules at the floating test site.*

Of course, installing panels on top of the tanks and basins is not a neutral operation for the two physical systems. The floating plant is subject to the atmospheric environment, whose properties are altered by the aqueous medium [6], while the tank is subject to significant variation in its energy input. Under these conditions, determining the energy yield requires a re-evaluation of key environmental elements. The use of simple numerical models is appropriate as a first step in understanding the magnitude of the induced variations. However, this strategy proves to be difficult when several phenomena are combined, for example, when one wishes to describe the thermal behaviour of photovoltaic systems. It becomes necessary to isolate one or more key elements that can be precisely modelled or measured and repeat the operation until a robust description is obtained.

---

[6] The main atmospheric variations ”near” the Earth’s surface come from the interaction between the surface and the volume of air

Thermal sciences applied in floating solar array applications

When installing photovoltaics in water, the engineer generally observes that electrical production is improved compared to a ground-based installation. Finally, it turns out that the photovoltaic system operates at a lower temperature: the precise causes of this observation are nevertheless uncertain. Early work on this subject mentions an important influence of the flotation system on the level of cooling available. In conjunction with other work specialising in atmospheric heat exchange, it is reasonable to assume that the local airflow around the modules plays a large role in the cooling effect. Although the entire role of the other mode of transfers is not totally captured, their magnitudes are reputed to have a lower influence on the photovoltaic heat budget. Therefore, the first question that the engineer must solve becomes: *How is convective transfer modified when systems are running over waterbodies?*

The question is extremely related to the characterisation of the flow properties in the atmospheric surface layer, which themselves suffer from a highly stochastic and chaotic diseases. The latter two properties are difficult for the engineer to handle because the tools at his disposal are limited to the most precise calculation and measurement capacity, compared to the cost of implementation (resources, means). In doing so, the properties of the atmospheric surface layer are partially addressed and the average field information gives a generally reliable but not very accurate indication. Therefore, more powerful tools are needed to accurately qualify the air field. From a numerical simulation point of view, tools that solve the set of conservation equations are probably the most suitable: they are adaptable to sufficiently high levels of accuracy to capture the energy spectrum of the medium.

Numerical simulation also has the advantage of versatility, as it is relatively easy to perform parametric variations to evaluate the degree of evolution of a cost function; experimental methods are much more expensive in terms of time and resources. Ideally, we would like to isolate the role of convection using a robust numerical method, while maintaining an experimental viewpoint to validate the numerical observations. Addressing the scale of the PV plant in both aspects is, however, limited by the current computational capabilities - as well as by the experimental methodology for determining the actual convective transfer rate of the modules with the atmosphere.

For the first point, a simple order-of-magnitude calculation captures most of the difficulty. Assuming that on average, large floating photovoltaic power plants house 7.2×10^5 modules [7], and assuming that only 3 points per module are sufficient to describe the average behaviour of each module: more than 200 000 operations would be necessary to describe the full-scale array. If one wants to go beyond the 3-point discretisation, for instance to improve spatial resolution and get more precise information per module, the number of operations goes quickly above the limit of available computational resources. In addition, one may consider launching new simulation for each geometric layout of array as this characteristic is largely responsible of the dynamics of the air flow. As evoked in Dauxois et al., 2021 with respect to Urban Flows: Versatile shapes of heated obstacles in external flows are challenging from the point of view of physics and the scales with respect to the spatial quality that must be obtained. Ideally, one would like to reduce the number of operation needed to capture most of the information for the modules standing in a full-scale array, for instance by not explicitly representing all the modules.

---

[7] we refer to the average size of FPV installations in 2022 according to Figure 14 (a conservative hypothesis of a capacity of 550 Wp per module is also drawn).

For the second point and in an outdoor environment, the intertwining of heat transfer modes and their implications in photoconversion make the association between the evolution of the temperature of the systems and a particular transfer mode extremely complex *ceteri paribus*. Typically, the engineer uses point measurements and a simplified thermal inverse model to determine the heat transfer rate of the system to the environment. This efficient and inexpensive strategy does not provide accurate information: in time due to the thermal inertia of the systems and in space due to the punctuality of the measurements. One may also ask the question of the principle of causality bounded to this strategy. The temperature resulting from some sorts of energy budget, modifying the set of inputs may finally average the behaviour of the system and improve/minimise the cost functions. It is then difficult to conclude on the accurate magnitude of modification for the set of inputs. Ideally, one would like to see strategies that provide clues to causal links or even overcome the intrinsic limitations of measurement in time and space.

Elements on the evaporative rates of waterbodies

When installing PV above reservoirs, the photovoltaic engineer must take into account its environment, which is sometimes hostile (flooding, drought, waves, daily tidal range) and sometimes beneficial (improved production, colocation with hydraulic tools). A claimed positive aspect is the reduction in evaporation linked to the partial coverage of water bodies. This problem is closely related to atmospheric science and hydrology. The use of numerical tools orientated towards the characterisation of the local atmosphere also allows the modelling of part of the evaporative phenomenology. In this way, one of the motivations of the present work is to advance the evaporation of semi-covered surfaces, in which the air movements direct the importance of the phenomenon. It is hoped that the work will be used on the scale of the solar power plant to determine the magnitude of the water saved in a basin due to the geometry of the plant. So far, very few authors have proposed practical solutions to this problem, and these are generally limited to small basins. Under these conditions, it can be expected that the intrinsic conditions of the lake will affect the evaporation rate (depth, water inflow and outflow, specific biology), whereas a large lake should be less affected by these biases.

Objectives

The first objective of the thesis is to explore the influence of environmental conditions in the cooling of floating photovoltaic power plants and to build a deterministic 1-D model that would allow one to describe the operating temperature of PV modules as a function of the microclimate. Under the shape of question it becomes:

What are the physical fields and the correlations that allows one to describe boundary conditions of Floating PV systems ?

The second objective of this thesis is to propose a numerical methodology that allows the quantification of aeraulic effects in situations of large photovoltaic power plants. This methodology should allow the engineer to determine the level of aeraulic cooling as a function of the geometry of the developed installation. The methodology implying a certain level of geometry versatility and an industrial use, an underlying objective is to keep the computational cost low. The focus is given to the comparison of land-based and floating photovoltaics geometries with the aim of determining the contribution of convective transfer in both installations. A question that the thesis want to address is:

What are the key geometrical elements that modify the convective transfer at the photovoltaic array scale ?

Within this scope, the evaporative rates of transfers from large waterbodies are also addressed with the purpose of helping the hydrologist estimate the aeraulic influence of floating powerplants on their main resources of study.

Ideally, we would like all strategies developed in the work to reduce the uncertainty level in the prediction of the temperature of photovoltaic modules and, moreover, floating photovoltaics. The photovoltaic plant operator will have the opportunity to better predict both electrical production and degradation related to thermal-induced failures (thermal cycling). Therefore, by referring to the industrial value chain for photovoltaics, expressed in the financial indicator of the *Levelized Cost Of Energy* (LCOE), which expresses the monetary cost of an energy production system, we hope to be able to quantify the *capacity* and *lifetime* with better efficiency (on average and in deviation). The interested reader is redirected to business-orientated publications to capture the cost of badly anticipating the installation capacity[8].

$$LCOE[\text{€}/\text{kWh}] = \underbrace{\frac{\text{€}}{\text{m}^2}}_{\textbf{Production}} \times \underbrace{\frac{\text{m}^2}{\text{Wp}}}_{\textbf{Efficiency}} \times \underbrace{\frac{\text{Wp}}{\text{W}}}_{\textbf{Capacity}} \times \underbrace{\frac{1000}{\text{h}}}_{\textbf{Lifetime}} \times \underbrace{\frac{\text{€}}{\text{€}}}_{\textbf{Capital cost}} \tag{1}$$

---

[8] knowing that a powerplant is commissioned on a 20-year period, small discrepancies are echoed over the whole life period of the installation, soaring the revenue of the project owner, see pv-magazine published in April 2022.

Manuscript organisation

The manuscript is divided into two parts.

The first part of the thesis is dedicated to the introduction of the systems and physical equations that will be dealt with in the following work. We will present elements related to the thermal model of photovoltaic modules and power plants while trying to keep the subject of the physical boundary conditions of PV systems in focus. We will see how the main authors in this field evaluate the convective heat transfer rates mainly and radiative in some extensions.

The second part of the manuscript is subdivided into two sub-sections. First, a presentation of the experimental tools and numerical models developed during the thesis will be given. The main use cases for floating and non-floating photovoltaics are identified. The models are validated against data from measurements campaigns, performed during the thesis, or available in the literature. Secondly, the results of the methodologies implemented to improve the determination of convective coefficients by empirical methodology are described. The methods are compared and their comparative advantages are discussed. The results at the scale of the photovoltaic power plant will also be introduced in this subsection with the ambition to show both the complexity of the fine aeraulic flow, but also to point out the properties of the flow in its full three-dimensional atmospheric dimension.

References

Dauxois, T., Peacock, T., Bauer, P., Caulfield, C. P., Cenedese, C., Gorlé, C., Haller, G., Ivey, G. N., Linden, P. F., Meiburg, E., Pinardi, N., Vriend, N. M., & Woods, A. W. (2021). Confronting Grand Challenges in environmental fluid mechanics. *020501*(6), 1–40. https://doi.org/10.1103/PhysRevFluids.6.020501

Gleick, P. (1996). *Water Resources* (Encycloped). Oxford University Press.

Haegel, B. N. M., Jr, H. A., Barnes, T., Breyer, C., Chiang, Y.-m., Wolf, S. D., Dimmler, B., Feldman, D., Goldschmidt, J. C., Hochschild, D., Inzunza, R., Kaizuka, I., Kroposki, B., Kurtz, S., Leu, S., Margolis, R., Matsubara, K., Metz, A., Metzger, W. K., … Bett, A. W. (2019). Terawatt-scale photovoltaics: Transform global energy. *Science*, 836. https://doi.org/10.1126/science.aaw1845

JOHN FITZGERALD, W. (2022). Humans have installed 1 terawatt of solar capacity, generated over 1 petawatt of solar electricity in 2021. *PV Magazine USA*. https://pv-magazine-usa.com/2022/03/14/humans-install-1-terawatt-of-solar-capacity-generate-over-1-petawatt-of-solar-electricity-in-2021/

Pörtner, H., & Roberts, D. (2022). *Ipcc, 2022: Climate change 2022: Impacts, adaptation, and vulnerability. contribution of working group ii to the sixth assessment report of the intergovernmental panel on climate change*. Cambridge University.

Ritchie, H., & Roser, M. (2017). Water use and stress [https://ourworldindata.org/water-use-stress]. *Our World in Data*.

Where Sun Meets Water: Floating Solar Market Report (tech. rep.). (2019). World Bank Group, ESMAP an SERIS. Washington DC. https://doi.org/10.1596/32804

Part I

Technical Basis & State-of-the-art

1 FLOATING PHOTOVOLTAIC MODULES: PRINCIPLE & MODELLING

> Get into floating solar. The ocean is the limit.
>
> *Thomas Reindl*

This chapter recalls the main industrial and physical characteristics of floating photovoltaics. State-of-the-art thermoelectric models for the photovoltaic system are described on a module scale. Modelling the convective phenomenon is also presented as a boundary condition of PV thermal models, either as lumped heat rates or through solving the thermal boundary layer at the module surfaces.

Contents

1.1/ Introduction on the Role of Temperature in PV

Solar cells are highly technical objects and contain a plurality of interrelated physical mechanisms. They are **multi-physical systems** in essence. Generally, the electrical output of the system is the objective function that needs to be qualified and ultimately controlled. Nevertheless, thermal assessment is also of great interest, as a close link between electricity generated and the temperature of the material shows up.

1.1.1/ Basics on Photovoltaic Cells

A photovoltaic cell is a complex material that is formed by joining two doped semiconductors. These materials have an electronic structure that admits an energy gap that is neither zero (conductor material) nor too large (insulator). Therefore, the current can flow through one semiconductor material on specific occasions[1]. Most of the time silicium is used as the main semiconductor component of solar cells due to two main points: availability on Earth and an appropriate 1.12 eV bandgap of energy at 300 K.

When an impurity is added to silicium, the number of electrons available in the new material is altered and called *doping impurities*. This produces a motion of the energy gap level, which results in a material which is more or less conductive[2]. For silicium, gallium doping produces a p-type semiconductor (gallium has fewer electrons than silicium); meanwhile, phosphorus produces an n-type semiconductor (phosphorus has more electrons than silicium).

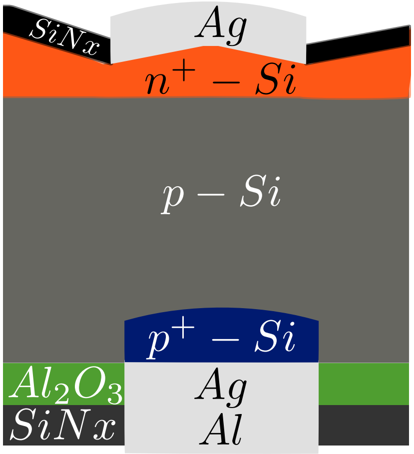

Figure 1.1–*A solar cell architecture based on the Passivated Emitter and Rear Cell (PERC).*

When two doped semiconductors n and p are physically joined, a depletion zone is formed, which induces an electric field. When photons of energy $\mathsf{E}_{\mathsf{ph}} = \mathsf{h}\nu$ pass through the junction[3], electrons and holes are ripped off, and the electric charges move. The electric field induced beforehand does not allow the torn pairs to recombine, pushing back the electrons (n-side) and holes (p-side) on both sides of the junction. In the case of photovoltaic cells, as shown in Figure 1.1, silver and aluminium contacts are located on either side of the junction to recover charges. Three options can be considered:

---

[1] electrons can leave the conduction band to reach the valence band

[2] at the human scale.

[3] $\mathsf{h} \simeq 6.63 \times 10^{-34}$ J s is the Planck constant and ν is the frequency of the electromagnetic excitation in s^{-1}

- When the silver and aluminium contacts are directly joined, the circuit is shortened, and the current flows between the two sides with the strongest intensity possible by the doping materials and the cell architecture. It is called the short-circuit current I_{SC}.
- In the case of no cabling at all, the circuit is open and no current can flow. The potential difference between silver and aluminium reaches its maximum value, the open circuit voltage V_{OC}.
- In the case of cabling resistive components at the two poles, the electrical charges can flow depending on the load properties (inverter, battery, etc.).

To get the most electrons out of the system, several cell architectures exist to improve both photon and electron capture. The passive emitter and rear cell architecture (PERC) is principally acknowledged in this work because it is now an economic option for industrial purposes. The cell layout is adapted from the older architecture Al-BSF (Aluminium- Back Surface Field). It includes texturisation and antireflection coating on the front side of the cell so that the reflectivity is reduced and as integrate a passivation role which reduces recombination processes[4]. On the rear cell, a passivation and a capping layers are manufactured. The contact is made of aluminium and silver, the aluminium and the silicon creating an aliage so that a back surface field (BSF) shows up and help reducing photon recombination in cells. These properties are fundamental in defining the electrical performance of the solar cell.

1.1.2/ Why Cell Temperature is a Key Player

An ideal representation of the solar cell is to consider a diode in parallel with a photocurrent induced by the photovoltaic effect. In this sense, the relationship between the current I and the voltage V of the cell can ideally be described as follows:

$$I = \mathrm{I}_{PH} - \mathrm{I}_0 \left[\exp\left(\frac{q \times \mathrm{V}_{\text{cell}}}{m \times k \times T_{\text{cell}}} \right) - 1 \right] \tag{1.1}$$

where I_{PH} is the photocurrent, I_0 the reverse saturation current, q is the electron charge, V the voltage at the cell level, m the diode ideality factor, k the Boltzmann constant. The exponential part refers to the limit of charge diffusion described by the Shockley equation (Shockley, 1950),(Sah et al., 1956).

It is worth mentioning that the photon conversion is not straightforward; the cell electrical behaviour has many inter-dependencies with the operating conditions; the focus is given to the link between electrical production and temperature hereafter.

In M. Green et al., 1982, Green described the link between open-circuit voltage and temperature, such as:

$$\frac{d\mathrm{V}_{oc}}{dT_{\text{cell}}} = \frac{E_{gap}^{lin} - q\mathrm{V}_{oc} + \gamma k T_{\text{cell}}}{qT_{\text{cell}}} \tag{1.2}$$

Where E_{gap}^{lin} is the semiconductor gap extrapolated to 0 K. The structure of the solar cell (either intrinsic materials such as crystalline-silicon materials or extrinsic technology factors such as PERC technology) has influence on the magnitude of the temperature effects. The efficiency of photon conversion is most of the time indicated by $\eta = \mathrm{P}_{\text{cell}}/\phi_{\text{cell}}$ and describes the relationship

---

[4] Recombination reduces the electrical charge available at the charge level.

between cell electrical production P_{cell} and received irradiance at the cell level ϕ_{cell}. Due to the temperature dependence, a current assumption for the silicium cell is to consider the evolution of η as:

$$\frac{\partial \eta}{\partial T} \simeq 0.35\,\%\,\mathrm{K}^{-1} \tag{1.3}$$

Generally amorphous silicon presents weaker thermal dependency[5] than cristalline-silicon[6] (Theristis et al., 2018).

From cells to module: Electrical aspects

A photovoltaic module gathers the photovoltaic cells and makes series or parallel connections between them to increase potential or current flow. The number of cells for one module depends on the application, and the size of the silicium wafer[7], it goes from 60 cells to 72/78 cells called *full cells*. The conventional situation consists of assuming three series of cells with bypass diodes in parallel to the cell series in order to reduce power generation losses caused by shading as well as reducing hotspots from reverse bias of shaded cells. Physically, the cells are joined by finger strips or grid fingers, metallized. They are then connected to a busbar (basically a bigger metallized path) and ultimately to the junction box which is glued to the rear surface of the module.

The $I = f(\mathrm{V})$ curve from the ideal Equation (1.1) is rewritten for modules as follows:

$$\mathrm{I}_m = \mathrm{n}_P \times \mathrm{I}_{PH} - \mathrm{n}_P \times \mathrm{I}_0 \left[\exp\left(\frac{q.(\mathrm{V}_m)}{\mathrm{m}.k.T_{cell}.\mathrm{n}_S}\right) - 1\right] \tag{1.4}$$

where n_S and n_P are the number of cell in serial and parallel, respectively. Note also that $\mathrm{V}_m = \mathrm{V}_{cell} \times \mathrm{n}_S$.

A *butterfly*[8] layout consists of positioning the bypass diodes in the centre of the three-cell series of the conventional formula. In this way, six series of cells are formed. The advantage of this technology lies in its ability to increase the availability of energy production when a shadow hides all or part of the module (Klasen et al., 2022). This electrical layout is assumed in most of the measurement campaigns in the thesis; it is now the first module layout on the PV market due to the given better performance[9].

As shown in Figure 1.2, the voltage is negatively affected by the increase in cell temperature, it is the major thermal effect. An effect on the current also happens but remains rather low. The fill factor ratio denoted FF and defined as the squareness of the $\mathrm{I} = f(\mathrm{V})$ curve[10], also presents a little dependency with temperature. Based on the fundamentals of solar cell and denoting the maximum point of production as *mp*, **the power delivered by a module** $\mathrm{P}_{mp} = \mathrm{FF} \times \mathrm{V} \times \mathrm{I}$ **is temperature bounded.**

---

[5] $\simeq 0.2\,\%\,\mathrm{K}^{-1}$, note that amorphous silicon is phased out

[6] $\simeq 0.45\,\%\,\mathrm{K}^{-1}$

[7] Wafer are related to the process of making silicium cells. It is basically the thin pieces of silicium that are cut down from silicium ingots.

[8] the denomination *half-cell* also holds

[9] Assuming a photovoltaic module is in portrait mode, half-cell technology can guarantee half of the production if all cells in the lower part are shaded. In the conventional case, this situation leads to zero power output and heating of the shaded cells.

[10] $\mathrm{FF} = \frac{\mathrm{P}_m}{\mathrm{V}_{OC} \times \mathrm{I}_{SC}}$ represents the quality of the photo-conversion processes.

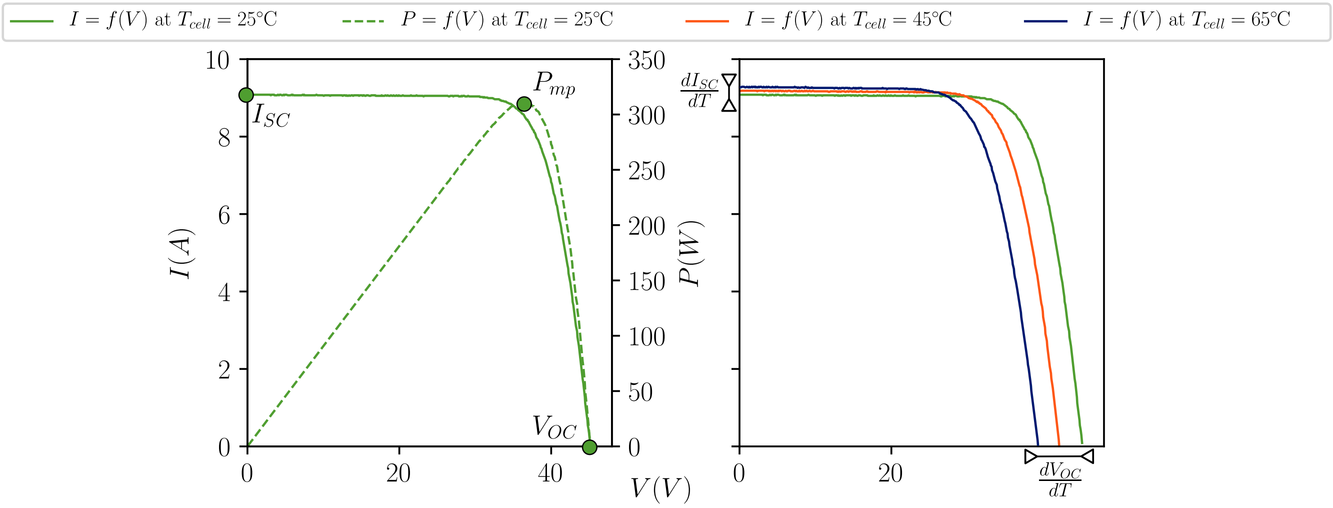

Figure 1.2–$I = f(V)$ *and* $P = f(V)$ *characteristics for a given PV module. The curves are experimentally produced by making a flash-test within a sun-simulator system which is available at the EDF R&D Laboratory.*

From cells to module: Mechanical aspects

From a mechanical viewpoint, the cells are protected against exterior agent which can cause stress and ultimately defect. Two principle mechanical layout pave the industrial market: the double glass and the glass/backsheet layouts, they are indicated in Figure 1.3. In both cases, the solar cells are encapsulated within a material like a sealing element that avoid direct contact between the cells and the humid air. Most of the time, the material is a polymer called ethylene vinyl acetate, shortly EVA. Note that the aluminium fingerprints, busbars and back contacts are also sealed in the encapsulate so that the full electrical system is insulated. The mechanical layout is therefore bound to the nature of the rear side material, either glass or backsheet. By construction, double glass modules are heavier than backsheet rear sides, on the other-hand double glass allows one to reduce mechanical stress (neutral line of module is better centred around the cell). Floating projects are mainly based on double glass layouts due to the better performance in humid environment for this solution. From a thermal prospective, the chosen material modifies the way heat is transferred from the cell/EVA system to the outside, hence it is necessary to take into account this property when one want to predict the cell temperature in real operating conditions.

1.1.3/ Floating Photovoltaics and *Cooling Effects*

In atmospheric sciences, the term *cooling effect* genuinely describes the drop in air temperature that can be observed over water bodies. The reasons for these temperature drops are a complex combination of sensible energy transfer and mass transfer between water and air; both of them are discussed in the next chapter as the *microclimate* effect.

In the context of floating photovoltaic applications, the term cooling effect is used to describe the fact that the cell temperature in these applications is lower than the equivalent cell temperature in land-based applications[11]. However, there is no consensus or standard that would allow for a rigorous definition of the cooling effect and the gain in electrical production induced by the environment. One strategy regularly adopted in the literature is to describe the cooling effect

---

[11] Sometimes the term *wind cooling effect* is used to amplify the action of air movement around the photovoltaic modules responsible for their cooling. These effects are discussed at the end of the chapter

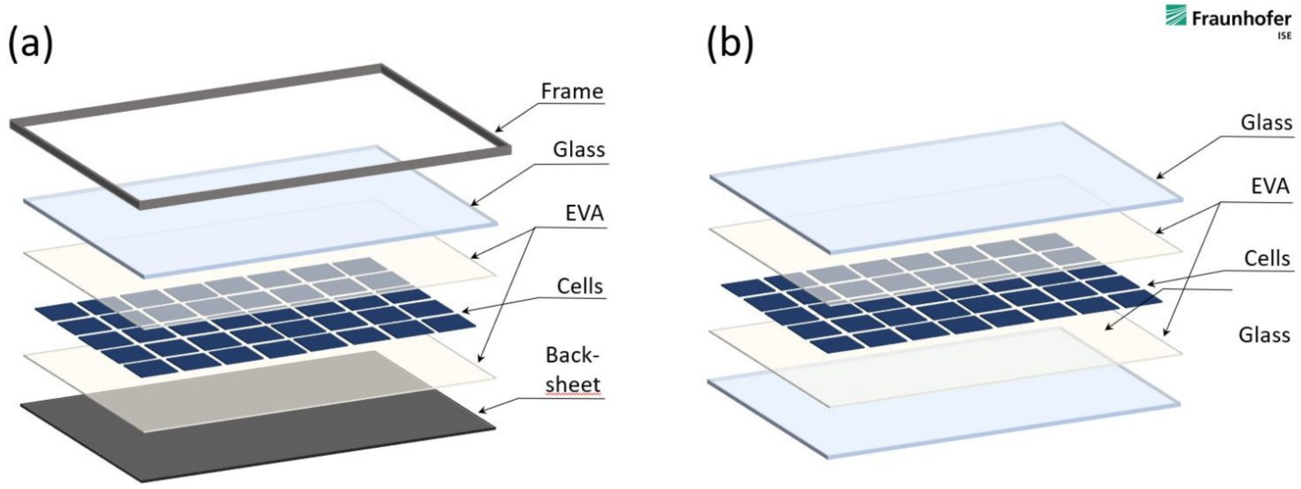

Figure 1.3–*Illustration of mechanical layout of modules for glass/backsheet (left-hand side), and double glass (right-hand side). Picture is retrieved from the Fraunhofer ISE.*

from an electrical point of view, as in Schiro et al., 2017, (Ranjbaran et al., 2019). In this situation, the thermal cooling effect ΔT_{cell} is related to an efficiency gain $\Delta\eta$ that reads:

$$\Delta\eta = \Delta T_{\text{cell}} \times \gamma_\eta \times \beta_\eta \tag{1.5}$$

Whence γ_η and β_η are thermal coefficients of the solar cell. The energy yield per module reads $\mathsf{P}_{\text{m}} = \eta\phi_{\text{cell}}\mathcal{A}$ where $\mathcal{A}$ is the total area of the cells. The difference in energy yield between two systems can be written as:

$$\Delta\mathsf{P}_{\text{m}} = \Delta\eta \times \phi_{\text{cell}} \times \mathcal{A} \tag{1.6}$$

The power difference assumes a strict similarity between the cell areas and the irradiation level ϕ_{cell} for the two systems. The temperature difference between the cooled and reference modules is directly used to deduce an electrical efficiency gain. When similar intrinsic and extrinsic properties are considered between two cells; **temperature differences are potentially produced by the shift in operating conditions**. This assumption is the main driving force of the floating photovoltaic field.

1.2/ Background of Floating PV and Challenges

Floating photovoltaics are made of elements similar to land-based systems, except that structures that maintain modules in positions are typically adapted to this special environment. This section presents the general aspects of floating photovoltaic solutions on an industrial scale. Therefore, the electrical and mechanical aspects are presented in this sense.

1.2.1/ Industrial examples

Since 2007 and the first floating photovoltaic installation for scientific purposes, identified in Japan, the photovoltaic industry has organised itself to develop increasingly large and commercially viable projects (Figure 14). It is interesting to note that the first cycle of development of FPV solutions (2014-2020) was strongly supported by the emergence of commercial solutions based on a robust technology called Monofloat (Figure 1.4). In this case, each float supports a module, and links between the floats make the whole rigid in the form of islands. For maintenance purposes, passages are provided on the sides of the module rows to allow access to the systems for the operators. From a hydrological and mechanical point of view, the installations are generally based on gravity or screw anchoring systems; sometimes tie-down lines are pulled directly from the embankment.

Figure 1.4–*An* 850 kWp *floating powerplant in Hyogo, Japan, based on the Ciel et Terre© technology.*

However, the latter practise is only possible on small lakes (a few hectares). When other activities are carried out, such as aquaculture or hydroelectric production, additional restrictions must be respected, and generally installations are much larger than one hectare. Therefore, the new generation of installations (2020-2022) is seeing the emergence of new floating technologies on stilts (Figure 1.5) or more dispersed monofloat systems (Figure 1.6) that allow for a reduction in installation cost. In both illustrative cases, the electrical constraint native to the power generation assets is integrated into the existing environment with techniques similar to those developed for marine applications (anchoring, mooring). The objective is to ensure the mechanical maintenance of the plant.

Figure 1.5–*Colocated floating project with aquaculture assets, developed by Chint Group© in China's Zhejiang province, the installed capacity reaches* 550 MWp.

Figure 1.6–*Floating project developed by Huaneng Power International© in China's Shandong province, the installed capacity reaches* 320 MWp

1.2.2/ Physics of Floating Projects

Electrical

In FPV projects, the electrical parts that allow a portion of solar irradiation to be converted into electricity and ultimately feed the utility grid are composed of: **Photovoltaic modules** electrically connected to each other by tables, **electrical cables** that distributes the direct current (DC) from the modules to the **line inverters** that converts the DC power into Alternative Current (AC). A final electrical step includes AC links between the inverters and the **general transformer** of the utility-scaled solar array. A summary of the electrical path is provided in Figure 1.7.

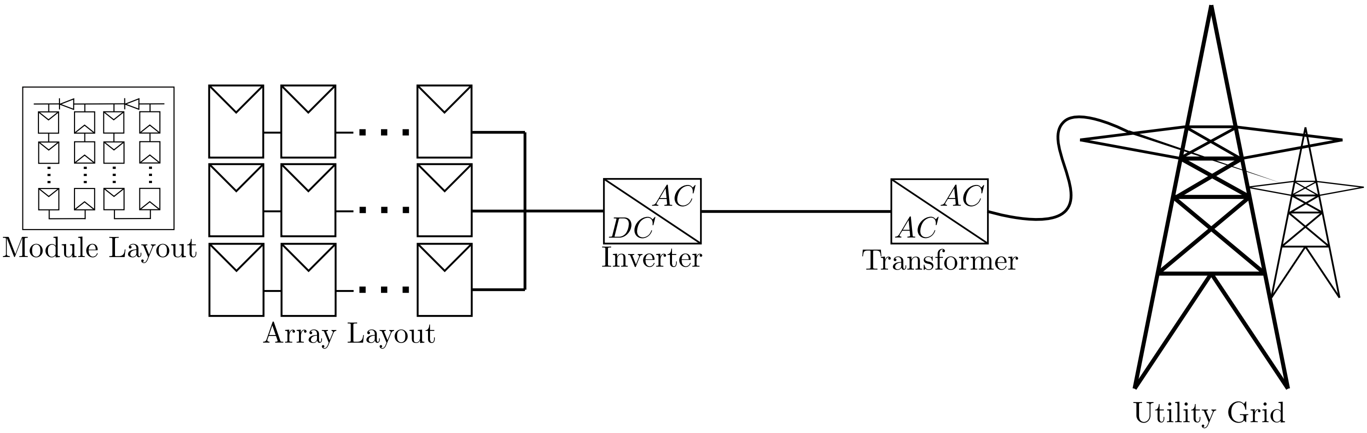

Figure 1.7–*Electrical configuration of arrays of module.* ***In this work, the focus is solely given to the DC part of the array.***

Cables and inverters are usually placed on the waterbody, as close as possible to the modules, with the aim of reducing direct contact with water to prevent system failures from insulation. The main motivation for doing so is to reduce the yield losses from the Joules effect before reaching the inverter. Reaching the high voltage for grid connection can be done at the embankment level through a step-up transformer or over an Offshore Substation (OSS). The latter is rare because of the trade-off between economic and physical constraints for the floating photovoltaics array at present.

Mechanical

The mechanical structure that supports the floating photovoltaic system is quite different from conventional land-based systems, as illustrated by Figure 1.8. Basically, it ensures that the module is properly positioned in relation to the sun so that the irradiance level is controlled. Another requirement is that the system floats and stays sufficiently stable to allow energy production and, in some cases, maintenance of the systems.

To achieve these *objective* features, several technological systems are implemented. A common grouping consists of discriminating between **float systems**, which are generally systems of buoys bound to each other, or assemblies of buoys anchored in groups that ensure the positioning of the modules, in which case they are called photovoltaic islands; **Anchoring** by deadweight or by drilling that can be carried out on the ground of the basin or directly at the bank level, which ensures the global location; **mooring lines** which make the connection between the groups of floats and the anchoring, which ensure the global positioning of the systems and the flotation of the whole.

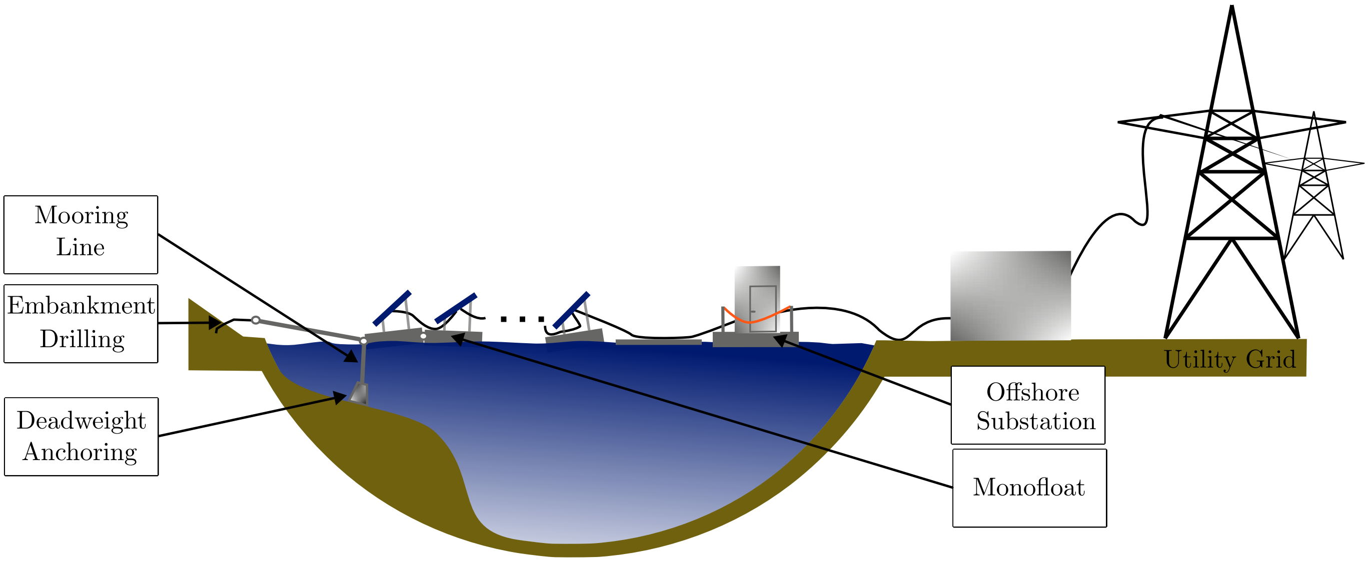

Figure 1.8–*Mechanical configuration of floating photovoltaics arrays*

Floating systems

The floating system is probably the most covered subsystem in the field of floating photovoltaics. As stated above, it is a key player in the mechanical properties of photovoltaic fields, but it also plays an important role in the economic structure of projects. Three strategies are currently paving the commercial area; they all infer specific physics that are not totally related to each other.

Monofloats

Monofloats are still the most common [12] flotation systems, the two main manufacturers being Ciel et Terre© (France) and Sungrow© (China). They are made from high-density polyethylene (HDPE) plastic. The interior of the floats is filled with air, but some technologies are designed to

---

[12] Worldwide in 2022

allow the introduction of water to reduce vibration phenomena (waves, swells)[13]. Several types of floats coexist in a power plant:

- Module-bearing floats, which are generally larger than the other floats in order to support the modules
- Secondary floats which allow the passage of maintenance operators ensure the link between the floating elements and allow the positioning of the anchoring elements.

The floating systems are joined using eyelets and fixing screws; the same eyelets are used for the anchor lines. Each module is supported by a floating board, making the system scalable but not mechanically very rigid. Once in the water, the eyelets are more susceptible to breakage due to vibration. The warranty period for the floats is from 10 to 25 years (mechanical). Floaters are generally not adaptable to many photovoltaic angulations, usually in the range of 10 to 15 °.

Pontoon based

Hybrid systems incorporate both buoyancy elements (HDPE, polystyrene foam) and structural rigidity by creating a steel or aluminium frame. The movements of the modules are reduced to the detriment of the modularity of the plant. This type of installation is also more suitable for modules with a large inclination, thanks to supports that increase the stability of the module. The main industrial solution is produced by Zimmermann© and is based on double tilt systems (east-west). A strong argument from a thermal prospective is that the opening between the two east-west rows allow the airflow to pass around the system. This should improve wind related cooling effect.

Membranes, mats and semi-submersibles

This last category concerns solutions where the contact of the modules with water is permanent or semi-permanent. While technologies based on submersible solutions are more on the scale of industrial prototypes, the membrane solution is benefiting from more significant commercial development. The company OceanSun© is the main player in marketing this system. Photovoltaic modules are installed on a tarpaulin surrounded by a flotation system, and the tarpaulin is strong enough to allow operators to move around on the system. Underneath the modules, the tarpaulin is porous and allows semi-direct contact with water. The tilt of the modules is zero due to the mechanical constraints of the system.

Project criteria

It is illusory to precisely describe the degree of application of all electrical and mechanical systems, as they are genuinely related to the structure of the project (economic, environmental, and hydraulic, in particular). However, some common elements that have a major influence on the design of power plants can be stated to position future working hypotheses.

Bathymetry is an important issue in the mechanical structure of power plants. As with offshore technologies, anchoring systems (mooring lines and anchors) become increasingly expensive as the bottom of the basin becomes deeper. This is a parameter that can have a significant influence

---

[13] This technology is mainly developed for nearshore FPV, see Heliorec©.

on the layout of the PV islands between them in order to ensure a suitable distribution of anchors (positioning, tension, number of mooring lines). The type of soil is also a key element that prevents the use of certain types of anchor (steep slopes, corrosion).

The geometry of **pond surface** is a second influencing factor that plays a major role in both themes. A small pool will require a special mechanical arrangement to ensure that the modules are consistently positioned with each other and with the Sun, and there is an indirect effect on the electrical arrangement of the modules at these points.

The **meteorological and *meteo-oceanic*** characteristics of the basin are also criteria that determine the installed potential of the electrical capacity. Wave heights, and even potential currents and tidal ranges may require the use of more robust float technology to support these particular conditions. Mooring lines can have dynamic characteristics that allow the structure to have degrees of freedom to accommodate irregular and critical weather and *meteo-oceanic* elements.

1.2.3/ Classification of Floating Photovoltaics Systems

There is obviously no universal way to classify technological solutions, whether for floating photovoltaics or any other technology. A classification can be considered appropriate if the criteria for its implementation are associated with precise and defined observables. Furthermore, a classification is expected to be robust to the selection criteria *e.g., assignment to a single class for two strictly identical individuals*.

For floating photovoltaics, some classification systems coexist to assign specific properties to projects. When referring to mechanical and thermal classifications, a non-exhaustive list of criteria would be:

- The method of **cooling** photovoltaic modules; *active or passive* technologies involved whether or not a pumping system was installed to pour water over the photovoltaic modules. It is admitted that *active class* contains solutions that reach lower module temperatures.

- The **contact** of the photovoltaic modules with the bassins; *no contact, direct partial or total contact of one of the module faces, complete submersion*. Another time, it is acknowledged that the interaction with water benefits from lower module temperatures as a result of better thermal exchange.

- The **floaters** system: *Monobuoy, Buoy and raft assembly, Concrete, Membrane*. This classification refers to the versatility of the solar array from a mechanical point of view; standalone floats are reputed to scale smoothly, whereas buoy and raft assemblies are more robust to environmentally critical situations. The classification is not well adapted to thermal properties.

- **Footprints**: *Large, Low or Free Footprint*. It merges the concept of flotation system and thermal performance; the lower the footprint, meaning the lower the module temperature could be.

The last classification will be assumed in this work because it fulfils the conditions of integrating thermal as structural aspects in the context of aerial floating systems, plus it benefits from a robust support in the literature.

The footprint ranking

The work of Liu et al. in H. Liu et al., 2018 has shown the value of classifying floating solutions according to their performance in cooling photovoltaic modules, leading to significant variations in the power generation performance from one solution to another. However, the term footprint used in the article is not defined in an absolute way but in a relative way, based on the position of the modules in relation to the water surface and the surface area occupied on the water. Thermal performances are evaluated based on PVsyst© thermal models and the contribution of the geometries to combined heat losses denoted U_{values}, see Section 1.3. The three classes of footprint can be associated with the categories of floats investigated in Bontempo Scavo et al., 2021 with respect to the retention performance of the evaporation of floating photovoltaic solutions. Therefore, the categories are as follows:

- **Free standing**: modules are placed high in relation to the water surface, and the water surface float coverage is low. In this case, the cooling coefficients of the modules are high ($40\,\mathrm{W\,K^{-1}\,m^{-2}}$) but the reduction in evaporation obtained is low, 18% for a total cover of the water surface of 30% (*suspended covers*). A good candidate for this category is shown in Figure 1.5
- **Small footprint**: The modules are placed close to the water, and the floats also cover a larger part of the surface. Thermal performance is degraded compared to the free standing solution ($30\,\mathrm{W\,K^{-1}\,m^{-2}}$). Evaporation is expected to be reduced as a result of increased water occupation. A good candidate for this category is depicted in Figure 1.6
- **Large & Insulated footprint**: The large category concerns single floating solutions with little inclination, proximity to the water surface of the modules, and high hydraulic coverage. The cooling is low under these conditions ($20\,\mathrm{W\,K^{-1}\,m^{-2}}$). Insulated solutions are based on raft systems with the same module height characteristics. While *Large* solutions benefit from high evaporation coverage, *insulated* solutions have a low evaporation rate. A good candidate for this category is depicted in Figure 1.4.

From a thermal point of view, these categories are recalled in Figure 1.9 where the standards *well-ventilated* and *insulated* are also indicated. **Floaters management appears to be a key potential in the overall performance of floating photovoltaic yield.** This ranking also involves a notion of the *absolute* cooling effect, which includes climate and local conditions, geometry configuration, and module technology.

Array-scale ranking indexes

When the footprint category is practical for constructing a single motif of the photovoltaic array, industrial indexes are usually called to get the notion of a whole island of modules and structures. Two ratios are found in the context of FPV: the standard **solar ground coverage ratio**[14] and a specific **hydraulic coverage ratio**.

Solar ground occupation ratio

This ratio is used to qualify the surface occupancy rate of photovoltaic modules in a solar power plant configuration. It is defined as the ratio between the area occupied by the modules and the

---

[14] denoted *GCR*

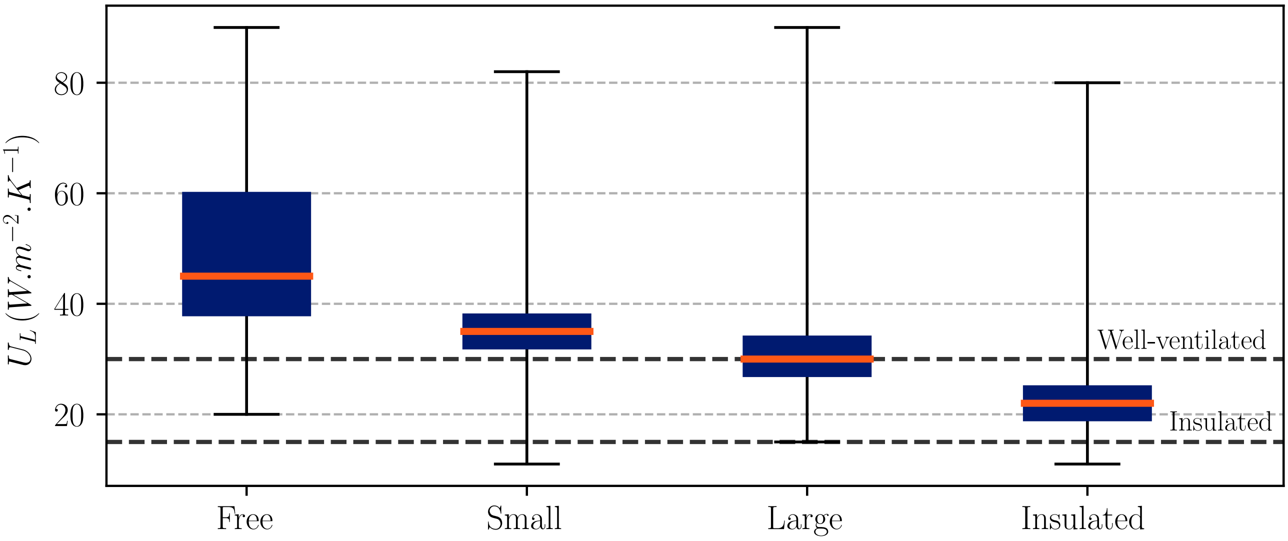

Figure 1.9–*Classification of floating structures from a footprint viewpoint, retrieved and adapted from (H. Liu et al., 2018).*

area of the surface dedicated to the activity of electricity production. Naturally, this ratio is a major variable in the establishment of solar projects, as it defines the power generation density assigned to the park. The selection of a ground occupation ratio for a power plant is difficult and must integrate economic (cost of materials [modules, structures, floats, etc.]), environmental (sun path), and technical (module type, module angulation with respect to ground) constraints. In general, it is possible to define an optimal occupancy rate with respect to the three constraints taken independently; however, the strategy of maximising solar production is rarely chosen due to degraded economic profitability.

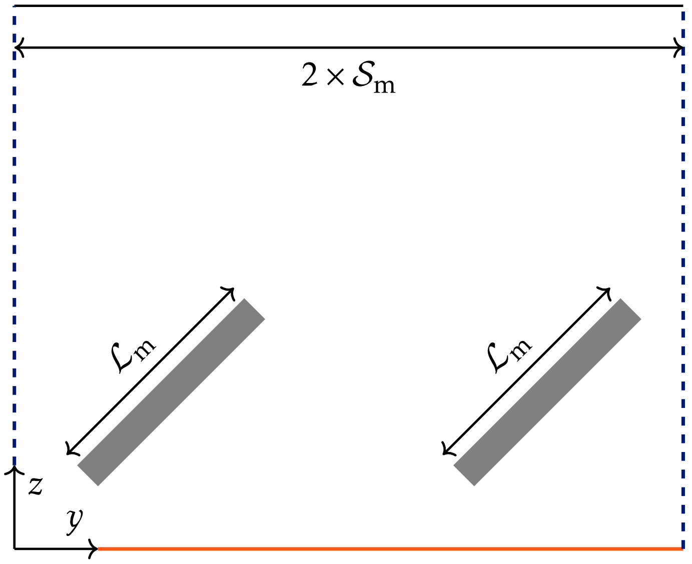

Figure 1.10–*Example of solar ground occupancy ratio using a longitudinal view, the ratio is calculated as the division of the module lengths divided by the total area occupied, here it leads to* $GCR = \frac{2\times\mathcal{S}_m}{2\times\mathcal{L}_m}$

Hydraulic coverage ratio

The hydraulic coverage ratio is defined as the relationship between the wet space of the floating elements of the plant and the total space allocated to the photovoltaic park. It is a ratio that is frequently used in the field of hydrology, particularly to quantify the rate of reduction of evaporation from covered ponds compared to an open area. In the case of technological solutions in which the modules are not in direct contact with water, the hydraulic coverage rate is evaluated from the surface *wetted*, in direct contact with the basin. These are mainly the flotation and maintenance elements.

1.2.4/ On the Reference System in *Cooling Effects* Assessments

As stated in Equation (1.6), the reference systems over which are compared floating installation are important when one wants to evaluate the enhancement in performance of floating in front of land-based solutions. In H. Liu et al., 2018, the reference is a roof system mounted in array configuration 12 km away from the lake; meanwhile, in Dörenkämper et al., 2021, free standing references are located at varying distances from the floating system 0.25 km to 110 km. In Peters and Nobre, 2022, the reference system is installed on a rooftop in the direct vicinity of the pond. Although the study by Liu et al. found better thermal cooling at the lake location, Dörenkämper et al., 2021 shows that the reference system near the lake can also get a good level of cooling effect. In Peters and Nobre, 2022, the reference system is found to be cooler than the floating system. The question that arises is thus: Why are different patterns observed? The extent of the cooling effect is not captured only by comparing a similar system (in some points) at different locations, and therefore the comparison of the values of the *absolute* cooling effect must be closely investigated.

With the role of the roof being more or less strong depending on the characteristics of the structure and the building, the strategy adopted in our work consists of defining a reference system in a *ground-mounted* situation with an open support system to correspond as closely as possible to the thermal phenomena which occur in floating modules by reducing the externalities which would emanate from buildings or equivalent structures.

1.2.5/ Elements of Literature on Evaporative Reduction

The reduction in evaporation of floating photovoltaic solutions has received little attention since the beginning of commercial development; water savings gains have been claimed by a large number of projects without having a solid scientific basis. The latter take as evidence in the direction of evaporation reduction studies carried out for other systems suspended or in direct contact with the lake surface. For example, in 1970, Cooley in Cooley, 1970 showed that the reduction in evaporation of the basins was proportional to the surface covered and that the system should preferably be in the form of a single block instead of several elements *porous*. Criteria related to the spectral properties of the liners were also indicated. However, the *proportionality* assertion is challenged for systems composed of several elements, for instance in Assouline et al., 2011 evaporation rate is found proportional to the opening available between the structures.

Down to the floating photovoltaics, Bontempo Scavo et al., 2021 extrapolates the laws of evaporation for partially covered systems; the various floating structures mentioned above are considered as elements that weight the irradiation received by the lake as well as the wind speed. Under these conditions, overwater systems are the most efficient in achieving a significant reduction in evaporation, while suspended systems have lower performance. It should be noted that the laws used are still adapted to particular diffusion-advection physics and that, for the moment, no conclusive measurements are available in the literature.

1.3/ Assessing the Energy Yield Through Model-Based Numerical Material

In the previous section, we showed that floating installations are similar to land-based installations, but mechanical and environmental constraints are factors that modify the operating conditions. In this section, we focus on the state-of-the-art modelling strategies with the objective of using a more adequate thermoelectric formalism to describe the thermal behaviour of FPV.

1.3.1/ Electrical Models

The Single Diode equivalent circuit

The power delivered under maximum operating conditions (P_{mp}) is described by the product of optimal voltage and current as

$$P_{mp} = \mathrm{V}_{mp} \times \mathrm{I}_{mp} \tag{1.7}$$

The subscript *mp* denotes the optimal operating point. In the case of large photovoltaic power plants, the maximum operating point is determined by a load impedance control system at the inverter level (MPPT, Maximum Power Point Tracker). There are several determination methods; in a review work (Reza Reisi et al., 2013), they are classified as offline, online, and hybrid methods whether the system is based on performing prediction of cell behaviour. Their performances are evaluated regarding the dynamic response of the load impedance, the efficiency of determining the MPP and their implementation costs. When Perturbation & Observation methods - probably the most current technique in the industry, reach efficiencies of around 96%, artificial intelligence methods can achieve efficiencies of 98% with respect to previous training. When choosing the ideal load on the hand of the inverter, the current intensity of the real solar cell cell, described in Equation (1.1), is reduced due to the structure of the materials. Currently, the single-diode equivalent circuit is used to describe the real cell behaviour; it reads:

$$\mathrm{I} = \mathrm{I}_{PH} - \mathrm{I}_0 \left[\exp\left(\frac{q.(\mathrm{V} + \mathrm{I} \times \mathrm{R}_s)}{\mathrm{m}.k.T_{\mathrm{cell}}} \right) - 1 \right] - \frac{\mathrm{V} + \mathrm{I} \times \mathrm{R}_s}{\mathrm{R}_{sh}} \tag{1.8}$$

in which a series resistance R_s and a shunt resistance R_{sh} describe, respectively, the losses arising from charge carrier transport within silicon to the printed channels and the losses arising from alternative paths for the free carriers. Equation (1.8) is also called *five parameters model*[15] and offers accurate results either under laboratory conditions (Shongwe & Hanif, 2015) ($\Delta\mathrm{P} \simeq 0.3\%$) or in real conditions.

The main obstacle to greater use of the model is the difficulty in obtaining the parameter with sufficient accuracy. To this end, several techniques are applied, mainly relying on laboratory measurements and numerical methods (Chatterjee et al., 2011) or analytical methods (Blas et al., 2002). The parameters are found to be functions of radiative levels and temperature (Lo et al., 2010), (Ruschel et al., 2016).

---

[15] The parameters are R_s, R_{sh}, I_{PH}, I_0, and m the diode ideality factor that describes the quality of the real diode compared to the ideal processes

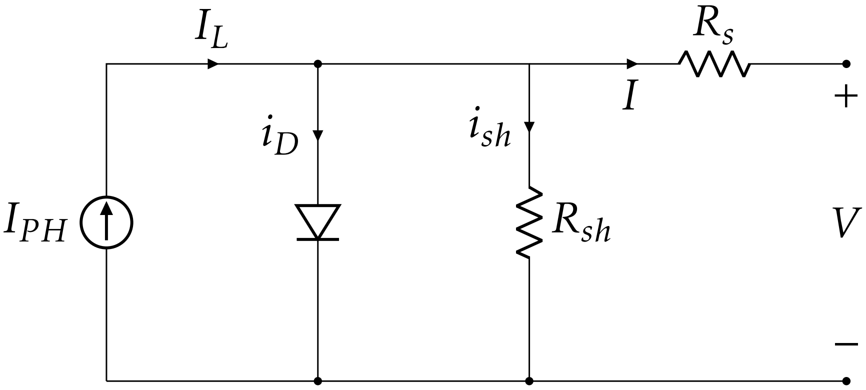

Figure 1.11–*The electrical scheme for the single diode model, assuming a single cell.*

The Single Diode circuit for modules

When several cells are connected with each other in serial, say n_S, Equation (1.8) reads:

$$\mathrm{I_m} = \mathrm{I}_{PH} - \mathrm{I}_0 \left[\exp\left(\frac{q.(\mathrm{V_m} + \mathrm{n}_S \times \mathrm{I_m} \times \mathrm{R}_s)}{\mathrm{m}.k.T_{\mathrm{cell}}.\mathrm{n}_S} \right) - 1 \right] - \frac{\mathrm{V_m} + \mathrm{I_m} \times \mathrm{R}_s \times \mathrm{n}_S}{\mathrm{n}_S \times \mathrm{R}_{sh}} \tag{1.9}$$

This way, real behaviour of cells are replicated at the module scale (the denomination *five parameters* model holds).

Bypass diodes between the bunch of serial connections also imply a parallel mode of operation. As shown in H. Tian et al., 2012, the single diode model is modified as follows when assuming n_P:

$$\begin{aligned}\mathrm{I_m} =& \mathrm{n}_P \times \mathrm{I}_{PH} - \mathrm{n}_P \times \mathrm{I}_0 \left[\exp\left(\frac{q.\left(\mathrm{V_m} + \frac{\mathrm{n}_S}{\mathrm{n}_P} \times \mathrm{I_m} \times \mathrm{R}_s\right)}{\mathrm{m}.k.T_{\mathrm{cell}}.\mathrm{n}_S} \right) - 1 \right] \\ & - \frac{\mathrm{V_m} + \mathrm{I_m} \times \mathrm{R}_s \times \frac{\mathrm{n}_S}{\mathrm{n}_P}}{\frac{\mathrm{n}_S}{\mathrm{n}_P} \times \mathrm{R}_{sh}}\end{aligned} \tag{1.10}$$

International industrial standards

The electrical parameters introduced in the various electrical models are decisive elements for qualifying the electrical performance of the modules, but the complexity of obtaining them is a problem for engineers who must either degrade his electrical model or make assumptions about the value of his parameters. The task is made all the more difficult by the fact that these parameters have temperature dependencies and tend to evolve over time due to the material degradation previously described. The main way to determine these parameters is to perform a flash test under Standard Test Conditions *STC*. The electrical performance of the module is measured under a controlled irradiation of $1000\,\mathrm{W\,m^{-2}}$ with a thermostat keeping it at 25 °C and under solar spectrum representative of an atmospheric air mass of 1.5 (say 1.5AM).

The data sheets given by module manufacturers use the Standard Test Condition to derive the so-called relative temperature coefficients for the short-circuit current α_{SC}, the open-circuit voltage β_{OC}, or even the maximum power γ_{mp}.

$$\begin{cases} \mathrm{I}_{SC} = \mathrm{I}_{SC-T_{STC}} \times [1 + \alpha_{SC} \times \Delta T] \\ \mathrm{V}_{OC} = \mathrm{V}_{OC-T_{STC}} \times [1 + \beta_{SC} \times \Delta T] \\ \mathrm{P}_{mp} = \mathrm{P}_{mp-T_{STC}} \times \left[1 + \gamma_{mp} \times \Delta T\right] \end{cases} \tag{1.11}$$

However, these conditions are not practical for operational purposes, as modules are rarely at 25 °C under conventional sunlight conditions. Therefore, there is a second standard more suited to these prerogatives under the name of the NOCT standard for Normal Operating Cell Temperature. The measurement of electrical (and thermal) performance is carried out for a module with 800 $\mathrm{W\,m^{-2}}$ sunlight and an ambient temperature of 20 °C, which is more realistic for the conditions encountered. The module is also mounted at a 45° angle on an open structure, allowing air to flow around it.

Other electrical modelling

It is known that the single-diode model lacks accuracy for low irradiance; therefore, varying irradiance may be more challenging to assess. To bypass this issue, some authors have considered the development of double-diode models that rely on the addition of another diode in parallel to the one already present in the single-diode model, as in Braisaz et al., 2011. When the enhancement of the electrical production is slightly enhanced in the case of silicium cells, other technologies of cells are better predicted through the double-diode model *(e.g., Cadmium telluride [CdTe])*. A major drawback for using the single-diode model for silicium cell is that the calculation complexity arises due to the computational effort to solve the electrical equation. Therefore they are not practical when one want to solve a large amount of time.

1.3.2/ Thermal Models

The modelling of the temperature of the PN junction is fundamentally linked to photonic and electronic effects, during which photons may or may not excite electrons and may or may not lead to the formation of a photocurrent. For example, the elements constituting these phenomena (thermalisation, Below Eg photons, Carnot Efficiency) are shown in clear details in Dupré et al., 2015b. At a macroscopic level, the photovoltaic cell absorbs a part of the incoming irradiance with respect to the absorptivity of the material. It results mainly in temperature increase and heat losses with the environment, plus a non negligible electricity production.

Heat Budget of Photovoltaics modules

Fundamentally, the Heat transfer in a solid system is from heat conduction; hence, assuming the temperature $T(x,y,z)$ at each point of the system and assuming the Fourier law with heat generation, the dynamic of the temperature can be written as follows:

$$\rho Cp \frac{\partial T(x,y,z)}{\partial t} = \lambda \times \left(\frac{\partial^2 T(x,y,z)}{\partial x^2} + \frac{\partial^2 T(x,y,z)}{\partial y^2} + \frac{\partial^2 T(x,y,z)}{\partial z^2} \right) + Q_{hS}(t) - E_{hs}(T(x,y,z),t) \tag{1.12}$$

In which the term on the left side includes the temperature dynamics in the solid, weighted by the density ρ and the thermal capacity Cp, λ is the thermal conductivity in the medium. The terms $Q_{hS}(t)$ and $E_{hs}(T(x,y,z),t)$ are, respectively, the heat source and the power production that is similar to a heat sink. In this situation, the module is considered to be made of an effective material gathering the properties of the real slabs of glass, EVA, silicium and so fourth.

The module is thin in the z direction and relatively homogeneous in the xy plane as shown in Figure 1.3. The Fourier law can be simplified as a 1-D equation as follows:

$$\rho Cp \frac{\partial T(x,y,z)}{\partial t} = \frac{\partial\left(\lambda\left(\frac{\partial T(x,y,z)}{\partial z}\right)\right)}{\partial z} + Q_{hS}(t) - E_{hs}(T(z),t) \tag{1.13}$$

This equation can be easily derived for the layers incorporated in the module, assuming a simple 1-D mesh as in Aly et al., 2018 in which a Finite Difference method allows the calculation of the photovoltaic cell with good accuracy ($RMSE \simeq 0.08\,°C$ under outdoor conditions). In practise, though, modelling the different layers is time-consuming. The authors in Aly et al., 2018 found a computational cost about ten times higher using their accurate method compared to the simplified modelling scheme. In addition to the number of layers simulated, the second costly line is the knowledge of $E_{hs}(T(x,y,z),t)$. When the single-diode model (or equivalent) is reputed to best simulate real cell behaviour, another affordable option is to describe the electrical production as a material-dependent variable. Therefore, a handy way to categorise the thermal model is to look at **how many layers are simulated**, **how electrical production is calculated**. A schematic view of these categories is given in Figure 1.12.

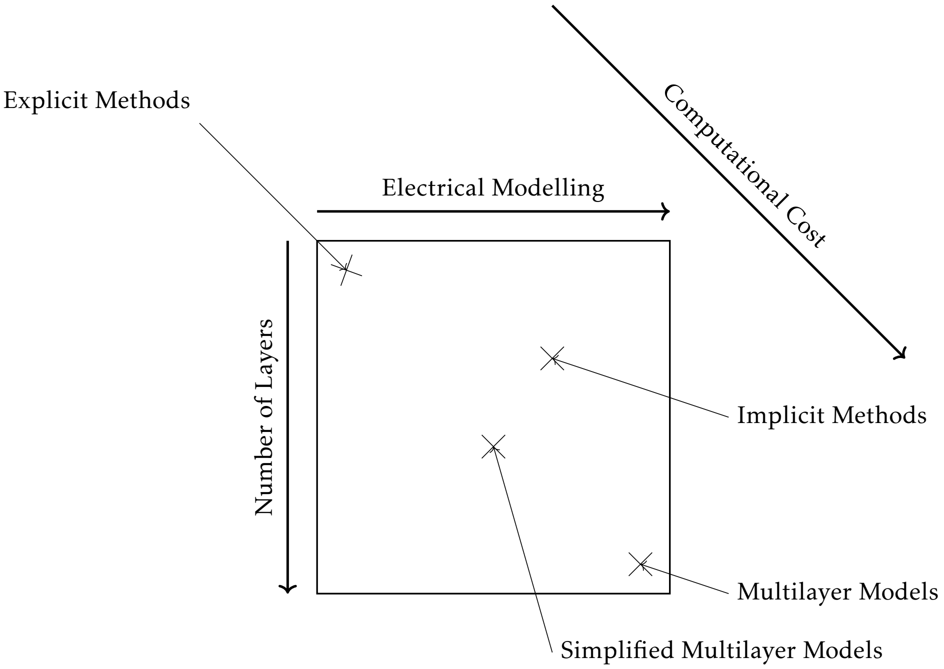

Figure 1.12–*Distribution of the existing modelling technics to determine cell temperature in outdoor conditions. The computational cost of the solution is proportional to the number of layers simulated in the module as well as the electrical modelling scheme.*

Explicit methods

Explicit model makes direct relationship between surface temperature and external conditions. Generally, this relationship is obtained by optimising a mathematical problem with or without constraints. The physical fields are represented as time-dependent vectors with independent components. Most of the time, the objective function $\vec{y}$ has a quadratic shape (RMSE, MBE, other). We can give a mathematical definition as follows:

$$\begin{cases} \text{Find } \vec{x}(t) = (x_1(t), x_2(t), ..., x_N(t)) \\ \text{Such that } \min\limits_{\vec{x} \in \mathbb{R}^N} \left|\vec{y}(\vec{x})\right| \end{cases} \tag{1.14}$$

In which $\vec{x}(t)$ is a time-dependent vector composed of N components $(x_1(t), x_2(t), ..., x_N(t))$ that are empirically selected, based on a physical guess or a priori arguments.

The simplest explicit model consists of relating the temperature of the photovoltaic module to the ambient temperature and the level of irradiation received. The best known model, genuinely demonstrated in Ross, 1976, integrates the Ross coefficient k between 0.02 and 0.0563 $\mathrm{K\,m^2\,W^{-1}}$ depending on the type of integration of the module as follows:

$$T_\mathrm{m} = T_\mathrm{amb} + k \times \phi_\mathrm{sw,poa} \tag{1.15}$$

Note that this equation was deduced from a dynamic experiment without wind action. Due to this lack of versatility, other models were developed to include the mean wind velocity. A full review of this type of method is available in Skoplaki and Palyvos, 2009. After the study by Ross et al., many attempts were made to describe the multiplier coefficient k in Equation (1.15). Among them, the link with the average wind velocity as proposed in Faiman, 2008 was largely shown as follows:

$$T_\mathrm{m} = T_\mathrm{amb} + \frac{\phi_\mathrm{sw,poa}}{U_1 + U_2 \times U_\mathrm{w}} \tag{1.16}$$

With U_1 and U_2 obtained using the linear regression between $\frac{\phi}{T_\mathrm{m} - T_\mathrm{amb}}$ versus wind speed. For example, in Faiman, 2008 the comparison of the model versus an experimental set-up has shown a robust linear trend ($r^2 = 0.63$) using $U_1 = 25\,\mathrm{W\,K^{-1}\,m^{-2}}$ and $U_2 = 6.84\,\mathrm{W\,s\,m^{-1}\,K^{-3}}$.

All these models share the same trends; ambient temperature and irradiation are the two main terms that affect module temperature (positive correlations), while the wind through its intensity acts as a regulator. In practise, the uncertainties on the input data (stochastic nature of wind and irradiation) and the fast dynamics of the system are not modelled, but are only interpreted through the chosen minimisation method. A quadratic method will thus tend to determine the best set of parameters, reducing the dispersion of results, partly due to these behaviours. The type of installation is also drowned in the set of coefficients obtained.

For floating photovoltaic applications, this type of method has been tested in Waithiru et al., 2018. The proposed results were as follows:

$$\begin{aligned} T_{m1} &= 2.0458 + 0.9458 T_\mathrm{amb} + 0.0215 \phi_\mathrm{sw,poa} - 1.2376 U_\mathrm{w} \\ T_{m2} &= 1.8081 + 0.9282 T_\mathrm{amb} + 0.021 \phi_\mathrm{sw,poa} - 1.221 U_\mathrm{w} + 0.0246 T_\mathrm{wat} \end{aligned} \tag{1.17}$$

With and without the water temperature in the explicit budget (note that temperatures are expressed in °C, Standard Units are used for the remaining variables). The input coefficient in front of T_wat is rather low compared to the other set of coefficients; therefore, the water temperature can be assessed as a low-magnitude element given the range of evolution throughout the day. Furthermore, the positive correlation appears to indicate a warming influence. Most importantly, the objective function is downgraded using T_{wat}, an explanation of this behaviour may be that information from the water inputs overfits the objective function[16].

Adaptations of this explicit model can also be made to improve the consideration of the thermal inertia linked to the variation in irradiation and the stochastic properties of the wind. For example, a strategy initially proposed in Veldhuis et al., 2015 and applied in Peters and Nobre, 2022 for the FPV proposes a correlation that includes both parameters characterising the effective radiative exchange temperatures, a phenomenology linked to the wind following an exponential law, and a method of taking into account the variation in temperature of the modulus by an exponential moving average. Thanks to this almost-physically based strategy, the action of water was found marginal in the floating case, in contrast to the role of wind regimes and installation setup.

One may note that the temperature obtained is not T_{cell}, but the module temperature considered as a single slice T_{m}. Even if it offers a good opportunity to make cross-validation work by comparing with RTD measurements glued on the rear module face, the cell temperature is different by a few centigrades. Determining the cell temperature relies on another model that allows one to express T_{m} in function of T_{cell}

Module to Cell

When assuming that T_{m} is representative of the temperature throughout the material, we hypothesise that $T_{surf} = T_{\text{m}}$, and especially $T_{\text{m}} = T_{\text{re}}$. A potential correction to the assumption is to consider a linear gradient within the module, since they are supposed to be homogeneous materials; it follows that the temperature depends on the location z as follows:

$$T_z = T_{\text{re}} + \frac{z}{z_{\mathcal{E}_{\text{m}}/2}} \times (T_{\text{cell}} - T_{\text{re}}) \tag{1.18}$$

with z the current height, $z_{\mathcal{E}_{\text{m}}/2}$ the half height of the module, and $(T_{\text{cell}} - T_{\text{re}})$ the difference in temperature between the cell and the rear side which must be measured. The advantage of this method is that it is a picture of a fully conductive mode of heat transfer in the module, thus it relies more on the materials/module technology than the mounting application. It is usually taken between 3 K (open rack/glass backsheet) and 0 K (insulated back/polymer backsheet) from empirical measurements. Assuming only conductive mode, the rear-side heat flux thus reads:

$$\phi_z = \frac{\lambda}{z_{\mathcal{E}_{\text{m}}/2}} \times (T_{\text{cell}} - T_{rear}) \tag{1.19}$$

Whence the density of heat flux ϕ_z is constant and λ is an average conductivity. However, the equation does not take into account the evolution of the environment.

An option developed in King et al., 2004 proposed to correct the reference temperature difference ΔT by the environmental condition and especially the level of plane of array irradiance $\phi_{\text{sw,poa}}$, as follows:

$$T_{\text{cell}} = T_{\text{re}} + \frac{\phi_{\text{sw,poa}}}{\phi^0_{\text{sw,poa}}} \times \Delta T \tag{1.20}$$

---

[16] Based on similar principles of minimisation of a mathematical objective function, neural network and data analysis methods are potentially suitable for dealing with these complex dynamic behaviours, but it goes beyond the scope of models in this work (data-driven models). The interested reader may refer to the work of May Tzuc et al., 2018 and Jeong et al., 2020.

Where $\phi^{0}_{\mathrm{sw,poa}}$ is a reference irradiation taken at $1000\,\mathrm{W\,m^{-2}}$. This strategy is practical as $\phi_{\mathrm{sw,poa}}$ is most of the time measured at the photovoltaic level, therefore the principle limitation of the explicit model is avoided (T_{m} instead of T_{cell}. Combining explicit and cell temperature model makes it possible to run electrical model later on with more precise temperature conditions.

Implicit methods

The implicit methods are based on the same criterion of modelling the temperature of a single homogeneous material as the explicit methods. This time, environmental inputs are associated with physical properties of the material and thermal phenomena that occur at the system level, hence **the electrical production has to be integrated in the implicit methods**. Starting from the initial Equation (1.13) and omitting the dynamic behaviour of the system and assuming homogeneity in the material, the heat budget is reduced to $Q_{hS}(t)$ and $E_{hs}(T(z),t)$. The thermal source element is determined as the irradiation in the plane of the module, weighted by the absorption of the silicium and the transmissitivity of the glass. The heat losses are from two contributors, the electricity production and the external radiations and convection, it reads

$$\tau\alpha\phi_{\mathrm{sw,poa}} = \eta_{\mathrm{cell}}(T_{\mathrm{m}}) \times \phi_{\mathrm{sw,poa}} + \mathrm{U}_{values} \times (T_{\mathrm{m}} - T_{\mathrm{amb}}) \tag{1.21}$$

In which τ and α are, respectively, the transmissivity of the glass and the absorptivity of the solar cell, η is the efficiency of the solar cell, and U_{values} is the external heat losses of the module (thermal radiation and convection). The concept of U_{values} is presented in more details in section 1.3.2.4.

The module temperature is then obtained under the following shape:

$$T_{\mathrm{m}} = T_{\mathrm{amb}} + \phi_{\mathrm{sw,poa}} \times \frac{\tau\alpha}{\mathrm{U}_{values}} \times \left(1 - \frac{\eta(T_{\mathrm{m}})}{\tau\alpha}\right) \tag{1.22}$$

The term *implicit* thus refers to the link between electricity production and temperature. It is a general practise to make use of this type of model, especially in inverse modelling when temperature and production are monitored and the objective is to determine the heat loss coefficient. Reference for floating photovoltaics would be the experimental works of H. Liu et al., 2018, Marco et al., 2021, Dörenkämper et al., 2021 in which an implicit method is assumed to simulate the different performance of technologies with respect to the cooling effect. It is important mentioning that these equations are similar to the model developed in Faiman, 2008 (including electricity production); **the U_{values} is constructed upon the difference in temperature between the surface of the module and the environment.**

Another method also integrated a U_{values} which is not based on the surface temperature but directly on the cell temperature. When this strategy is more precise, they cannot be compared to the model from Faiman, 2008; however, many authors combined these two models and make use of U_{values} without regard with the type of model solved[17].

On the U_{values} concept

The concept of U_{values}, originally used in the construction industry to characterise the insulation performance of a wall, is also frequently used to describe the global exchanges of modules with their surroundings:

$$\mathrm{U}_{values} \times (T_{\mathrm{m}} - T_{\mathrm{amb}}) = \alpha\phi_{\mathrm{sw,poa}}\,(1 - \eta) \tag{1.23}$$

---

[17] Ultimately it leads to bad temperature prediction and wrong electrical outputs...

However, in the major software used by the community PVsyst©, this equation is rearranged so that:

$$\mathrm{U}_{values} \times (T_{\mathrm{cell}} - T_{\mathrm{amb}}) = \alpha \phi_{\mathrm{sw,poa}} (1 - \eta) \tag{1.24}$$

in which U_{values} in the last equation is by construction greater than the one in Equation (1.23). Knowing that, The thermal loss coefficient is assumed to be a wind-dependent coefficient, therefore when using the PVsyst© model, the coefficients are denoted $\mathrm{U}_{values} = U_c + U_v \times U_{\mathrm{w}}$ meanwhile in the Faiman model, the coefficients are $\mathrm{U}_{values} = U_1 + U_2 \times U_{\mathrm{w}}$.

Assuming that there are no conductive transfers with outside structures, the U_{values} can be broken down into several sub-pieces, which refer to the fundamental heat modes under their lumped flavour as follows:

$$\mathrm{U}_{values} = \frac{h_{cv} (T_{\mathrm{m}} - T_{\mathrm{amb}}) + h_{rad} \left(T_{\mathrm{m}} - T_{sky}\right)}{T_{\mathrm{cell}} - T_{\mathrm{amb}}} \tag{1.25}$$

It is important to note that the effective temperature of exchange is still the ”module” temperature, as a lone slab of homogeneous material without temperature gradient. This property is quite challenging to deal with when referring to surface exchanges; therefore, the conductive analogy developed in King et al., 2004 as in Equation (1.18) can be used to this extent. Interestingly, the U_{values} strategy is well established in the community, but the functional form adopted is mainly similar to the fully convective linear ratio; an assumption is that $h_{cv} (T_{\mathrm{m}} - T_{\mathrm{amb}})$ moves quite faster in the real outdoor world than $h_{rad} \left(T_{\mathrm{m}} - T_{sky}\right)$ which evolves smoothly during the day with an increase in temperature. Therefore, a limitation of U_{values} is observable for the conditions of the evolving sky, the linear convective trend being overestimated to match this case.

A final mention on the parameter U_{values} is that some authors have tried to dissociate front and rear U_{values} and leads to good outdoor estimation as in Lindholm et al., 2021 for floating photovoltaics, as it reads:

$$\begin{aligned} \mathrm{U}_{values} = U_{fr} + U_{re} = & \frac{h_{cv}^{fr} \left(T_{mod}^{fr} - T_{\mathrm{amb}}\right) + h_{rad}^{fr} \left(T_{mod}^{fr} - T_{\mathrm{sky}}\right)}{T_{\mathrm{cell}} - T_{\mathrm{amb}}} \\ & + \frac{h_{cv}^{re} \left(T_{mod}^{re} - T_{\mathrm{amb}}\right) + h_{rad}^{re} \left(T_{mod}^{re} - T_{\mathrm{grd}}\right)}{T_{\mathrm{cell}} - T_{\mathrm{amb}}} \end{aligned} \tag{1.26}$$

This equation flavour allows for comparison of installation type in steady-state mode; hence, floating water contact installation was found to offer substantially greater U_{values} compared to aerial installation.

Dynamical Implicit methods

The implicit method is efficient when the module smoothly evolves in temperature (almost steady-state system) or when the studied time step is larger than the time constant of the material. When these requirements are not met, capacity behaviour must be included to record the thermal inertia of the system. Equation (1.21) is then rewritten as:

$$\mathcal{E}_{\mathrm{m}} \rho C p \frac{\partial T}{\partial t} = \tau \alpha \phi_{\mathrm{sw,poa}} - \eta_{\mathrm{cell}}(T_{\mathrm{m}}) \times \phi_{\mathrm{sw,poa}} - \mathrm{U}_{values} \times (T_{\mathrm{m}} - T_{\mathrm{amb}}) \tag{1.27}$$

This configuration is necessarily more expensive from a computational point of view because of the time derivative, but it is more reliable when the sky state is evolving. However, an existing drawback is present in the evaluation of module temperature under clear skies days, as little variation of incident irradiation decreases the accuracy of the modelling by a few tens of centigrade as in Jones and Underwood, 2002.

Multilayer models

Both explicit and implicit models make the trade-off of low computational time at the expense of approximation or abstraction of the heat transfer phenomenology. The assumptions about the operation of the system are often thermodynamic steady-state and temperature homogeneity, which requires an empirical connection law to determine the actual operating temperature of the cell. A *proper* use of these models is thus relatively thin, typical days with slow cloud state evolution (thermal inertia) and involves rather long time steps (10 minutes or more). Also, considering a thermal homogeneity of the two sides of the module is a risky option when one wishes to quantitatively know the influence of the cooling modes even more in a short time (1 minute or less). To eliminate these blocking elements, multilayer models propose to solve the initial transfer equation for all or part of the elements that make up the module. The dimensional approximation generally leads to considering this type of model in a 1-D format, and the authors have pushed the system in a three-dimensional format, in particular to study participating radiative behaviour (Weiss, 2015). We will limit ourselves here to the description of the one-dimensional multilayer model.

Thermal circuits

Multilayer models are presented mainly in terms of electrical/thermal analogy, so each layer of the system can be represented by a more or less elaborate set of resistive, capacitive, or source elements. Kirchof's law applies here not to current densities but to heat flux densities $\sum_{in}^{n=j}\dot{\Phi} = \sum_{out}^{n=j}\dot{\Phi}$. The thermal resistance of a layer is expressed as $R = \frac{T_{s1}-T_{s2}}{\dot{\Phi}}$, the form of the resistance depends on the mode of transfer considered in the layer; thus the layers in the module are represented more by the conductive resistance $R_{\mathrm{cd}} = \mathcal{E}/\lambda\mathcal{A}$.

The thermal capacity is expressed as ρCp, as for the implicit models, but this time in a discretised way for each layer. The boundary conditions of the system must also be defined phenomenologically unlike the explicit module. Keeping this electrical formalism, the boundary conditions can be described as resistances that apply only to the elements at the edge of the system and by convective and radiative resistances such as $R_{\mathrm{cv}} = 1/h_{\mathrm{cv}}\mathcal{A}$ and $R_{\mathrm{ir}} = 1/h_{\mathrm{ir}}\mathcal{A}$.

Generalized form

A consistent way of defining the multilayer model is proposed in Notton et al., 2005, it is adapted to all general thermal circuits assuming 3 or more layers. Assuming n nodes in the thermal scheme (T_{cell}, T_{eva}, etc.) and casting the node temperatures under a vector shape $\vec{T}$, the general form reads:

$$[C]\frac{\partial \vec{T}(t)}{\partial t} = [M]\vec{T}(t) + [S]E(t) \tag{1.28}$$

Whence $[C]$ is a diagonal matrix $(n \times n)$ that gathers the discretised terms ρCp, $[M]$ is a matrix $(n \times n)$ that contains the heat resistances, $[S]$ is a matrix $(n \times m)$ that involves the physical weight allocated to the vector of excitation $E(t)$ of shape m. For instance, the excitation vector may contain the plan of array irradiation at some points, ambient temperatures, etc.

In the initial work of Notton et al., 2005, the multilayer comprised 3 nodes (Glass, Cell, Tedlar) and showed good accuracy in the prediction of the temperature for the three layers. Similar results were achieved in Tina and Gagliano, 2016. Other works also add virtual points in front of both external faces (Tina et al., 2012), or add nodes at the EVA level (Gu et al., 2019).

1.3.3/ Existing Software and on the use of PVNOV®

Commercial software

Following the presentation of the fundamental equations that describe the temperature dynamics of photovoltaic modules, different modelling tools can be used to solve or couple the model with an electrical cell model, etc. The objective of this section is to show what the alternatives are and to provide a justification for the use of a particular model. In our study, it is desirable that the thermal model can be easily modified to take into account specific properties of the floating photovoltaic application. The first part of this section is dedicated to a quick overview of existing commercial solutions. Hereafter, the research reviews from Lalwani et al., 2010, Santiago et al., 2018 and Micheli, 2022, are supporting the analysis.

The commercial software most widely used is undoubtedly PVsyst® and is initially dedicated to modelling the electrical production of modules on the plant scale. It has the advantage of being the reference model for the financing aspect of PV developments. In recent inter-comparison analysis of photovoltaics model tools , the software was used in 70% cases to provide the estimation of the energy yield (Theristis, 2022). Interestingly, the results showed that a versatility of predictions occurs. It is concluded that the tool is not the only responsible for performance prediction, the modeller should also take care of the system that must be predicted using the most accurate sub-models coupled with precise data inputs. With regard to thermal predictions, an implicit thermal model is solved in order to feed the electrical model of the cells, this corresponds to Equation (1.24). One may note that the heat budget is written so that the cell temperature is solved. Therefore, the parameters included in the cooling process are specifically designed for the software. Other sub-models are also integrated in the tool to predict the yield of the power plants as accurately as possible: mismatch losses, soiling losses.

Beyond the land-based applications, PVsyst® does not have a model dedicated to floating photovoltaics, so users who wish to take into account the specificity of the environment must determine sets of parameters characteristic of their application (movement of structures, cooling of modules) and integrate them via user parameters or using an external step. We can autocite the work of Oliveira-Pinto and Stokkermans, 2020 which uses PVsyst® to study the bankability of FPV projects and linking the importance of the cooling effect in the economic modelling; or that of Dörenkämper et al., 2021 for characterising electrical production according to several climatic zones, including a new set of parameters to include the cooling effect in the calculation.

The main limitation of PVsyst®, from a thermal point of view, is the resolution of a simplified implicit equation system and the non-accounting of thermal inertia. These two parameters limit the use of the software for short periods of time. Furthermore, the boundary conditions of the system are described with a coarse formalism that does not differentiate between environmental heat sources. These intrinsic limitations of the software do not allow exploration of thermal phenomena in their complexity at the system boundary.

Other software packages incorporate a thermal formalism slightly different from PVsyst® and are designed to *internalise* electricity production as a heat sink in the thermal equation of the modules. For example, *PV*SOL* or *PVGIS* use thermal equations from *Faiman method*. It should be noted that the heat transfer coefficients are not equivalent between the PVsyst® model and the software based on the Faiman method, and these models tend to overestimate the module temperature[18]. Note that PV*SOL proposes a dynamic version of the thermal model by including a thermal-mass term. However, as with PVsyst®, the thermal model does not appear to be sufficiently versatile to explore heat transfers due to its rigidity in the heat transfers described.

PVNOV® software

The PVNOV® software is an in-house code originally presented in Matthieu Chiodetti, 2019 that solves the problem of predicting the energy yield of bifacial photovoltaics. To do so, an inverse ray tracing method is enforced to determine the irradiation at the modules surfaces (front and rear sides). Inverse ray tracing provides a robust tool for predicting structure albedo or mask shadows, as well as preserving computation time compared to simple ray tracing methods. Monofacial modules can also be implemented within the calculation tool. Irradiation prediction is launched as the principal module of the software, but the latter also integrate submodels that perform thermal and electrical calculations with regard to the power plant characteristics (strings, inverters, etc.).

The submodel dedicated to thermal modelling is based on the *BuildSysPro* library (Modelica language), see Plessis et al., 2014. This configuration can handle dynamics of multi-physical systems through a non-causal programming structure. The system causality being defined by the solver when the whole numerical structure is built, hence the flow of data in each sub modelling task (*e.g., convective transfer calculation*) is not a-priori assigned. When running a computation, the initial Modelica® language is translated into C language to speed up computational treatments. Using a nodal paradigm similar to the one enforced in software dedicated to buildings, the photovoltaic module is expressed as a resistive system composed of thermal resistances and capacitive elements. By doing so, the meaning of module temperature can be refined and material temperatures can be assessed. Surface temperatures are also parts of the thermal equation system and are used when calculating heat transfers with the environment. The latter feature is of great importance and is not currently available in commercial software to our knowledge [19]. However, exchange with the environment is reduced to lumped heat rates so that the field heterogeneity are averaged. To go ahead of this issue, PVNOV® proposes to solve the thermal and electrical equations for each cell. This strategy is computationally costly, but it allows one to better predict electrical production heterogeneity, especially at the array scale. Capacitor elements, as well as opportunities to modify the contribution of the environment to the heat budget of solar modules, are the main features that motivate the use of this modelling tool. Another key element is the possibility of separating the radiative kernel from the thermal and electrical ones, so that the cost of launching simulations can be reduced dramatically. Note that PVNOV® runs on windows OS but has recently been implemented on Linux machines. More details about the thermal kernel are given in Chapter 4.

---

[18] Theristis, 2022 shows that it is a common mistake when designing a PV plant

[19] Tools dedicated to scientific researches are more favourable to this structure, see **Tina2021**.

1.4/ Thermal Boundary Conditions in Numerical Models

The most of the attempts to deal with floating photovoltaics have been performed through modified boundary conditions, mainly: wind regime (in U_{values}) and water temperature. Following the description of physics-based models in the previous chapter, we have seen that boundary conditions are evolving from one model to the other. This section aims to show the different environmental elements that act on photovoltaic systems from a theoretical viewpoint. These elements are *de facto* linked to thermal transfer modes, so we will try to give an overview of these links. This chapter also provides an opportunity to introduce more precisely the role of convection in the thermal balance of the modules and its introduction into the thermal modelling tools.

As the volume of air becomes the system to be modelled, we introduce the physical equations of conservation classically used to describe the behaviour of air around photovoltaic modules, and we will remain confined to **standalone systems in this chapter**. Closely related to the modelling of the thermal boundary layer around the systems, a state-of-the-art of the two existing resolution methods, the empirical method and the theoretical method, is proposed. While the first one is related to experimental systems, the second one will be mainly shown in a numerical light thanks to Computational Fluid Dynamics (CFD) tools.

1.4.1/ Environmental Parameters and Thermal Modes of Transfers

In addition to the intrinsic parameters of the PV system, the installation parameters and the operation and maintenance parameters, the environmental parameters are elements that fundamentally affect the dynamics of the thermoelectric system (Hasan et al., 2022); their roles are related to physical transfers between the environment and the PV system. Implicit module equations have already highlighted the classical elements of incident irradiance in the module, ambient temperature, wind speed, and air humidity. These elements are obviously not of the same nature and do not act in the same way in the photovoltaic system, although their effect on the electricity yield can be seen. This behaviour mainly leads to the shape of existing models and the definition of a new set of coefficients with respect to specific applications (Coskun et al., 2017).

Irradiance (short wavelength) is classically the number one issue in cell models and is also a major component of the thermal model. Describing the irradiance that reaches the module necessarily requires solving *Radiative Thermal Equation* (RTE), which solves for the number of photons in a participating medium. Given the wavelengths involved and their electromagnetic properties, it is still common to model irradiation using empirical equations based on the path of the Sun, cloud conditions, and the quality of the atmosphere. Irradiation acts on the module as a heat source. The quality of the atmosphere is also described by the content of water vapour. Scattering phenomena are increased in humid situations. Thus, humidity as a boundary condition of the photovoltaic system is closely related to the radiative field. The clues on modelling short-wavelength irradiance are given in Appendix A.1.0.1.

Long-wave irradiance is not one of the major parameters included in thermal models; nevertheless, the latter is derived from the radiative thermal equation. Of course, solving the equation is often too costly and many atmospheric models are deployed to approximate its impact on the modules. One current assumption is to consider the atmosphere as a grey body that emits at ambient temperature, so that the vapour content in the atmosphere plays a principal role in the emissivity of the air layers.

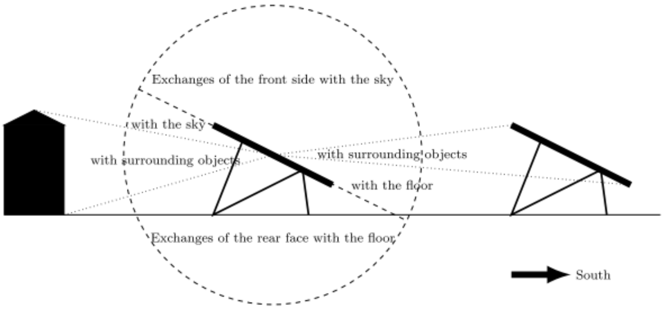

Figure 1.13–*Illustration of the radiative environment of photovoltaic modules, retrieved from (Weiss, 2015)*

When included in photovoltaic modelling as input data, long-wave radiation improves prediction accuracy (Driesse et al., 2022). The effect is much more emphasised at night as there are no overlapping sources in the heat budget of modules. It can be seen that long-wave irradiation has an indirect link with ambient temperature, the latter acting on the elements close to the PV installations. This is partly one of the reasons why thermal models describe nearby surfaces by the ambient temperature when surface temperatures are not available.

The last important parameter is the wind. Usually introduced in its mean velocity property, it is the dominant driver of advection-diffusion phenomena around the modules. The directionality properties are also of interest but are rarely integrated in the modelling. A more detailed description of the phenomenon is proposed in the next section.

Although one would like to know the influence of the physical fields on the photovoltaic system in an absolute way, all the physical fields introduced have their own temporalities on scales from the year (seasons) to the second. This disparity makes it difficult to compare heat transfer calculations between different scales; therefore, it is necessary to state the time step of the calculation in order to know to what extent the stochasticity of the fields is considered. For example, the study of the neural network of May Tzuc et al., 2018 leads to considering ambient temperature and relative humidity as the two main parameters of the module temperature models. The time step used being 30 minutes, the fields which have faster evolution's such as irradiation or wind are not finally the most representative of the temperature evolution of the system. For smaller time steps of the order of a minute as in Jones and Underwood, 2002, it appears that naturally stochastic quantities become key elements; it also becomes necessary to consider the thermal inertia of the system. The publication of Schuss et al., 2016 experimentally demonstrates the impact of the sampling rate of environmental data on the modelling of cell behaviour. Radiative and aeraulic fields are two elements whose knowledge in time steps less than 10 minutes improves the prediction of the electrical production of the cells. It should be noted that the air field is considered here as an element that moves the clouds and therefore acts on the radiative field. Under these conditions, acquisition frequencies on the order of 5 minutes are effective when the sky is considered clear. During cloudy periods, the integration time becomes problematic and data with a time step of 10 seconds give a good account of the evolution. In undersampling situations, the models are biased by the variability of the fields. This is more than ever stressed in moving photovoltaic applications such as vehicle integrated photovoltaics (Schuss & Fabritius, 2022), and this concern grows in floating photovoltaic applications to a lower extent due to wave/float interactions.

It should be noted that many other environmental effects act on the thermal of photovoltaic modules such as dirt and solid deposits on the modules. Although the former is related to an environment with particular chemical properties, bird droppings, or biofouling, solid deposits are more related to dust and fine volatile particles. The atmosphere plays a major role in their deposition on the module via its water content (humidity) and wind properties. However, these last two major environmental parameters will not be explicitly modelled in the framework of the thesis.

Therefore, this first section has highlighted the theory of model boundary conditions. These are generally models for atmospheric problems that are modified to take into account certain geometrical and technological specificities. In the following work, the short time scale is addressed, and the convective phenomenon is studied with more attention.

1.4.2/ Fundamental Equations for Convective Transfers

Thermal Boundary Layer

Convection is fundamentally related to the conduction/diffusion processes between a surface and a fluid in motion. The latter is an important candidate for the reachable convective intensity rate, since the bulk fluid motion contributes to the removal of the heat away from the surface. Surface geometry is a second key aspect since it acts on the local shear stress (i.e., local velocities) and ultimately on the distribution of ”thermal layers” above the surface. The thermal analogy of the velocity boundary layer leads us to define the convective density as follows:

$$\overline{\Phi}_{\mathrm{cv}} = \frac{-\lambda \frac{\partial T}{\partial y}}{T_{surf} - T_{\infty}} \times \left(T_{surf} - T_{\infty}\right) \tag{1.29}$$

in which $\left(T_{surf} - T_{\infty}\right)$ is the temperature difference between the solid surface and the temperature ”sufficiently away from the surface”, λ is the air conductivity, and $\frac{\partial T}{\partial y}$ is the temperature gradient at the surface. The rate of heat transfer in the boundary layer can be written as $\overline{h} = \frac{-\lambda \frac{\partial T}{\partial y}}{T_{surf} - T_{\infty}}$.

Two strategies coexist to obtain the information necessary to characterise the transfer by convection: the first one is based on empiricism, one seeks to solve a conservation of energy equation on a system either in outdoor or in controlled conditions; a second method is based on the thermal boundary layer theory in which one calculates the intensity of the conduction which transits from the solid medium to the liquid medium.

1.4.3/ Empirical Methods

The lumped strategy assumes the photovoltaic module to be a giant photovoltaic cell at constant temperature. In doing so, we can infer that the situation is similar to that in the case of a heated plate under atmosphere conditions. Therefore, the empirically based relation that limits aerial flow patterns and photovoltaic *as a flat plate* temperature can be written. Several authors have developed a test bench to this end for different configurations: open field structures (Test et al., 1981) or built-in modules (Sharples & Charlesworth, 1998), (Sartori, 2006). They interestingly remark a positive correlation between the temperature of the plate and the mean wind speed, in Test et al. this trend leads to:

$$\langle h_{fr}^{\mathrm{cv}} \rangle = 8.55 + 2.56 \times \overline{U_{\mathrm{w}}} \tag{1.30}$$

In which U_{w} is the wind captured one metre above the measurement set (in $\mathrm{m\,s^{-1}}$). However, the locations of the wind probe are more a matter of space availability around the system. It should reflect the wind field seen by the system; therefore, the rule of thumb is to acquire wind data at a significant location given the flow configuration.

However, a general conclusion drowned in almost every scientific report says that h_{fr}^{cv} should be redetermined for each geometry arrangement, as the methodology depends on the wind and the mounting system. Thus, many authors have derived their own convective heat ratios, in the case of a flat plate or directly over photovoltaic-based studies (Skoplaki & Palyvos, 2009).

When the Test et al. equation describes the wind effect on the module as *flat plate* at a constant temperature, which is mainly applicable on the front side of the module; rear-side phenomena are better described by free convective transfer. The boundary layer is controlled by the buoyancy-driven action of heated air in the direct vicinity of the module. One may consider a lumped coefficient in the same flavour as the Test et al. equation but including temperature difference instead of wind speed. The equation of Holman was made for this purpose and reads:

$$\langle h_{\mathrm{bs}}^{\mathrm{cv}}\rangle = 1.31\,(T_{\mathrm{m}} - T_{\mathrm{amb}})^{0.33} \tag{1.31}$$

Some variations can exist due to tilt considerations.

Although Equation (1.30) has the advantage of being easily integrated in thermal models, several drawbacks can be stated. First, using the correlation infers to position the wind probe at a location similar to the initial setup *(i.e., 1-meter above the module)*. This characteristic is supposed to be representative of the free field velocity; however, it depends on the nature of the near environment. Therefore, the correlation is rarely used with comparable wind inputs. The second drawback is raised when the wind speed is too low and tends to zero. In this situation, the correlation is out of its range of application; the constant number should be a good candidate of the free convective mode that should take place in this situation. Assuming that Equation (1.31) is better suited to encompass the no-wind situation, one may observe that the magnitude of the Holman correlation is twice lower than the constant value in Equation (1.30).

Non-dimensioned relations

One way of enlarging the range of use for empirical equations is to make them non-dimensioned. Therefore, comparing situations is made easier and fundamentally more general. Introducing the non-dimensioned numbers indicating the flow field conditions in terms of aerodynamical versus thermal prevalence, $Re = \frac{U_{\mathrm{w}}L}{\nu}$ and $Pr = \frac{\mu Cp}{\lambda}$, respectively, the Reynolds and Prandtl numbers, the heat rate of convective transfer can be determined using the non-dimensioned quantity for heat convective transfer:

$$\langle Nu\rangle_L = \frac{\langle h\rangle \times L}{\lambda} = f(Re_L, Pr) \tag{1.32}$$

In which Nu is the Nusselt number and L is a characteristic length over which the transfer takes place, similar to the characteristic length assumed in the Reynolds number. The advantage of this expression is the functional form of the relation. Reynolds number is, by construction, prescribed by the geometry and the free flow properties; meanwhile the Prandtl number relies on the thermal fluid properties. The form of the function of $f(Re_L, Pr)$ must be empirically assessed. This has been done by numerous authors for flat-plate geometries; for instance, in Gnielinski, 1975 the relation reads:

$$\langle Nu_{forced}\rangle_L = \sqrt{\left(0,664 \times Re_L^{0,5} \times Pr^{0,33}\right)^2 + \left(\frac{0.037 \times Re^{0.8} \times Pr}{1 + 2,443 \times Re^{-0,1} \times (Pr^{0,66} - 1)}\right)^2} \tag{1.33}$$

The correlations is valid when $10^4 < Re_L < 10^7$ and $Pr > 0.6$. When the wind velocity is low, the relation leads to $\lim_{U_w \to 0} Nu_{forced} = 0$, which by definition indicates that the convective coefficient is zero, based on the wind action. In addition to better capturing the natural behaviour of the wind, the notion of free stream is also a key information to derive good practise of measurement.

A major issue still remains about the free-flow turbulence and its influence on the Nusselt number intensity. Differences of as large as 20% of heat rates were observed for variations in free flow turbulence of up to 6% (Blair, 1983), (Osborne & Incropera, 1985). This information is even more critical as the behaviour is observed in wind tunnel experiments in which the turbulence level can be controlled to some extent and, above all, measured with extreme accuracy through Particle Image Velocimetry. These pieces of information are rarely available in real outdoor conditions, complicating the process of inferring accurate correlations for photovoltaic applications.

When the wind is too weak, the function f no longer depends on the Reynolds parameter, and it can be seen that the heat exchange is driven by buoyancy forces related to the temperature difference between the air on the surface and the overlying air. The Grashof number is used for this purpose:

$$Gr_L = \frac{g\beta\left(T_{surf} - T_\infty\right)L^3}{\nu^2} \tag{1.34}$$

For example, in the case of flat plates, Churchill in Churchill and Chu, 1975 proposed:

$$\langle Nu_{free}\rangle_L = \left(0.825 + 0.387 \times \sqrt[6]{K}\right)^2 \tag{1.35}$$

With:

$$K = Ra \times cos(\theta_m) \times \left(1 + \left(\frac{0.492}{Pr}\right)^{9/16}\right)^{16/9} \tag{1.36}$$

Whence $Ra_L = Gr_L.Pr$.

A variant of this correlation is also proposed in the case of Jones and Underwood, 2002 to take into account the natural convection that occurs mainly at the level of the rear face of the module. However, the convective boundary conditions in this case (transient monolayer model) are not intended to really cover the heat exchange that occurs specifically at one of the module surfaces. Thus, the two convective coefficients are combined in the same equation.

The use of dimensionless relationships provides a tool for combining the effects of the two convective phenomena on the same surface. This is particularly useful because the stochastic nature of the wind leads to indecision as to which phenomenon is driving the heat transfer. In the literature, we find the joint relation for flat plates such as $Nu^b = Nu^b_{forced} + Nu^b_{free}$, b chosen to 3. This strategy allows for covering the situation related to a weak flow while guaranteeing a realistic transfer rate when its intensity is sufficient to be the main actor of the heat transfer. This is the case, for example, in Mittag et al., 2019 and in the case of floating photovoltaics with one face of the module in direct contact with water (Lindholm et al., 2021).

Conclusions on empirical correlations

Empirical relations are powerful tools that can be used to describe convection in the case of photovoltaics. Some areas of improvement are still being studied to improve the determination of coefficients by adapted statistical studies (Akhsassi et al., 2018), taking into account the directional properties of the wind (Magare et al., 2018), and the geometrical dimensions of the solar array (Glick, Smith, et al., 2020).

1.4.4/ Theoretical Methods & Numerical Approximation

The theoretical approach is based on the description of the thermal boundary layer around the solid. In particular, it is through this approach that Blasius demonstrates the evolution of the Nusselt number as a function of the Reynolds and Prandtl numbers for the case of a flat plate subjected to a parallel flow, using the principle of similarity between the wall velocity difference and the height of the boundary layer (Blasius, 1908). With a slightly different method based on the integrated shape of the thermal boundary layer, Pohlhausen also shows the same result for this particular geometry (Pohlhausen & Angrew, 1921). However, these approaches are not particularly suitable for systems in which the turbulence regime evolves and local pressure forces challenge the shape of the dynamic boundary layer, although some authors have tried to use them to model photovoltaic systems (Dhaundiyal & Atsu, 2020). To take into account the fluctuations induced by the geometry of the problems, an evolution of the theoretical strategies consists of going back to the fundamental relations that translate the emergence of the dynamic and thermal boundary layers.

Numerical solutions of thermal boundary layers

Boundary layer can be approximated using numerical solvers that perform the calculation of Equation (2.1), Equation (2.2) and Equation (2.3). They are referred to as computational fluid dynamics (CFD) programmes, more details are provided about these programmes in Section 2.2.3. In the case of standalone photovoltaics, the principle works in the literature shed light on the flow dynamics around the module (so that a dynamic boundary layer is calculated), but also some authors have discussed thermal transfers. For instance, in Jubayer et al., 2016, several atmospheric flows are simulated and convective coefficients are calculated with notable differences when the turbulence regime becomes turbulent, the inhomogeneity of the heat rates along both module faces is also depicted: The leading edge benefits from a greater level of heat transfer along a certain distance depending on the wind flow. The heat rates evolve until they reach a constant value before the edge of the module. The direction of the wind θ_{w} also appears to modify the heat rates of convection; however, only two wind fields are studied: front and tail winds. An earlier publication focused on pressure fields had shown the difference that occurs due to perpendicular winds over the module (Jubayer & Hangan, 2014). More work has been conducted on the topic of cavity-induced effect in the case of integrated modules in a standalone building (Chowdhury et al., 2018). In the latter work, the reduction of wind-induced convective transfer is found to be greatly affected by the reduction of the cavity beneath the module. In this situation, convective transfer may be dominated by a free convective effect, so that the heat removal is reduced on the lower face. As a consequence, the temperature of the module may be higher and decrease the electricity conversion. Furthermore, the turbulence model becomes a critical element, as it modifies the estimation of the eddies (magnitude and location), as well as the wall-related conditions. The turbulence model $k-\epsilon$ model was used combined with a wall function to cover the viscous effects near the wall.

When almost all publications simulate a photovoltaic model as a thin plate, the role of the module frame in the intensity of $h_{\text{bs}}^{\text{cv}}$ is studied in Marinić-Kragić et al., 2018. It is found that the frame has a bad influence on the heat rates for weak wind regimes. However, the frame does not modify the heat rates observed on the rear side when a wind tail occurs. Furthermore, a contribution of Nazari and Eslami, 2021 indicates that drilling the frames can be strategic to guarantee aeraulic flow under the module; gains of 3.8 °C are obtained in the best cases compared to a frame without holes, especially at low wind speed.

The manner of taking into account the module from a thermal point of view is also from interest, either as a density of flux imposed structure or a fixed temperature system. When this is not a major concern in the early research stage, a thermoelectric model is probably a better option to consider. This coupling process was performed in Wu et al., 2017 with the observation of several boundary conditions and their impact on the flow structure and the heat rates of the module. As already pointed out in urban environment studies, coupling improves the knowledge of the fluid regime, so that a similar result was found. Interestingly, the surface coefficients for heat transfers were found almost similarly, which shows that considering basics scalar conditions is a reliable first-order approximation when studying steady-state systems.

1.5/ Summary

The state-of-the-art in thermoelectric models of photovoltaic is rather large and many models have been developed with a variable level of physical phenomena incorporated. The main contributors to the heat balance of the photovoltaic module have been presented. A first-level of state of the art showed that the contribution of the environmental parameters is not trivial and that they often overlapped each other. The quality of the input data also appeared to be a key element when one wants to model the system. Especially when the computational frequency sampling is *faster* than that of standard industrial modelling. In these conditions, radiative and aeraulic fields are the two elements that become preponderant in the calculation of the module temperatures for simulation time steps of the order of one minute. The main models used by the community do not allow one to fully specify the boundary conditions of PV module though. Only one detailed thermal model has been found in the literature adapted to FPV, but various attempt were also identified. A non-exhaustive summary is given in Table 1.1. The PVNOV® R&D model allows the boundary conditions to be defined with sufficient flexibility, and by doing so, the tool allows the calculation of the module and cell temperature, as well as the electrical energy produced at the DC side of the system. In the next chapters, the software will be used to address faster sampling frequency rates as well as describing the PV boundary conditions with an improved definition.

Method	Equations or Boundary Conditions (BC) adapted	Variables (BC)	Structure	Ref	Notes
Explicit	$0.943 \times T_{\mathrm{wat}} + 0.0195 \times \phi_{\mathrm{sw,poa}} - 1.528 \times U_{\mathrm{w}} + 0.3529$	$T_{\mathrm{wat}}, \phi_{\mathrm{sw,poa}}, U_{\mathrm{w}}$	NR	(Tim Umoette, 2016)	T_{cell} based / nearshore
	$2.0458 + 0.9458 T_{\mathrm{amb}} + 0.0215 \phi_{\mathrm{sw,poa}} - 1.2376 U_{\mathrm{w}}$	$T_{\mathrm{amb}}, \phi_{\mathrm{sw,poa}}, U_{\mathrm{w}}$	Medium-Footprint	(Waithiru et al., 2018)	T_{m} based
	$1.8081 + 0.9282 T_{\mathrm{amb}} + 0.021 \phi_{\mathrm{sw,poa}} - 1.221 U_{\mathrm{w}} + 0.0246 T_{\mathrm{wat}}$	$T_{\mathrm{wat}}, T_{\mathrm{amb}}, \phi_{\mathrm{sw,poa}}, U_{\mathrm{w}}$	Medium-Footprint		T_{m} based
	$T_{\mathrm{amb}} + a(1 + b \times T_{\mathrm{amb}})(1 - c \times U_{\mathrm{w}}) \times \phi_{\mathrm{sw,poa}}$	$T_{\mathrm{amb}}, T_{ap}, U_{\mathrm{w}}, \phi_{\mathrm{sw,poa}}$	NR	(Golroodbari & van Sark, 2020)	T_{m} based / nearshore
Implicit-U$_{values}$	$22.5 + 5.9 \times U_{\mathrm{w}}$	U_{w}	Large-Footprint	(Lindholm et al., 2021)	T_{cell} based ($T_{\mathrm{wat}} \simeq 20$ °C)
	$24.4 + 6.5 \times U_{\mathrm{w}}$		Free-Footprint		
	$25.2 + 3.7 \times U_{\mathrm{w}}$		Large-Footprint		
	$34.8 + 0.8 \times U_{\mathrm{w}}$		Large-Footprint	(Dörenkämper et al., 2021)	T_{m} based
	$18.9 + 8.9 \times U_{\mathrm{w}}$		Medium-Footprint		
	$35.3 + 8.9 \times U_{\mathrm{w}}$		Free-Footprint		
	Implicit - Multilayer Model				
	3-layer	$\phi_{\mathrm{sw,poa}}, T_{\mathrm{wat}}, T_{ap}, T_{sky}, U_{\mathrm{w}}$	Medium-Footprint	(Giuseppe Marco Tina, 2021)	\

Table 1.1–*Summary of existing models for thermal modelling in FPV literature. Note that all the unknowns are generally required in standard unit format (except temperature which is mainly in °C).*

As the thesis work focused precisely on convective problems, a second level of the state-of-the-art depicts the main developments on the subject of convective intensity prediction. Limiting ourselves to a standalone module, two characterisation methodologies have been put forward, empirical and theoretical/numerical methods. Although the first method is practical for software implementation, it requires representative facilities to be built. The second strategy is rather related to the resolution of the thermo-aerodynamic behaviour of the air mainly by using numerical tool; the method is expensive but offers a wider range of flexibility (influence of geometrical parameters on convection and wind field properties, etc.). In the following work, we will analyse in more detail the two strategies for the determination of convective phenomena, always keeping in mind the floating photovoltaic applications.

1.5/ References

Akhsassi, M., El Fathi, A., Erraissi, N., Aarich, N., Bennouna, A., Raoufi, M., & Outzourhit, A. (2018). Experimental investigation and modeling of the thermal behavior of a solar PV module. *Solar Energy Materials and Solar Cells*, *180*(June 2017), 271–279. https://doi.org/10.1016/j.solmat.2017.06.052

Aly, S. P., Ahzi, S., Barth, N., & Abdallah, A. (2018). Using energy balance method to study the thermal behavior of PV panels under time-varying field conditions. *Energy Conversion and Management*, *175*(July), 246–262. https://doi.org/10.1016/j.enconman.2018.09.007

Assouline, S., Narkis, K., & Or, D. (2011). Evaporation suppression from water reservoirs: Efficiency considerations of partial covers. *Water Resources Research*, *47*(7), 1–8. https://doi.org/10.1029/2010WR009889

Blair, M. F. (1983). Influence of free-stream turbulence on turbulent boundary layer heat transfer and mean profile development, part II—analysis of results. *Journal of Heat Transfer*, *105*(1), 41–47. https://doi.org/10.1115/1.3245557

Blas, M. A. D., Torres, J. L., & Prieto, E. (2002). Selecting a suitable model for characterizing photovoltaic devices. *25*, 371–380.

Blasius, H. (1908). *Grenzschichten in Flüssigkeiten mit kleiner Reibung* (tech. rep.). Zeitschrift für Mathematik und Physik.

Bontempo Scavo, F., Tina, G. M., Gagliano, A., & Nižetić, S. (2021). An assessment study of evaporation rate models on a water basin with floating photovoltaic plants. *International Journal of Energy Research*, *45*(1), 167–188. https://doi.org/10.1002/er.5170

Braisaz, B., Dupeyrat, P., Lindsay, A., & Radouane, K. (2011). AN ADVANCED MODEL OF PV POWER PLANTS BASED ON MODELICA®, 3644–3648.

Chatterjee, A., Keyhani, A., & Kapoor, D. (2011). Identification of photovoltaic source models. *IEEE Transactions on Energy Conversion*, *26*(3), 883–889. https://doi.org/10.1109/TEC.2011.2159268

Chowdhury, M. G., Goossens, D., Goverde, H., & Catthoor, F. (2018). Experimentally validated CFD simulations predicting wind effects on photovoltaic modules mounted on inclined surfaces. *Sustainable Energy Technologies and Assessments*, *30*(March 2017), 201–208. https://doi.org/10.1016/j.seta.2018.10.005

Churchill, S. W., & Chu, H. H. (1975). Correlating equations for laminar and turbulent free convection from a vertical plate. *International Journal of Heat and Mass Transfer*, *18*(11), 1323–1329. https://doi.org/10.1016/0017-9310(75)90243-4

Cooley, K. R. (1970). Energy Relationships in the Design of Floating Covers for Evaporation Reduction. *Water Resources Research*, *6*(3), 717–727. https://doi.org/10.1029/WR006i003p00717

Coskun, C., Toygar, U., Sarpdag, O., & Oktay, Z. (2017). Sensitivity analysis of implicit correlations for photovoltaic module temperature: A review. *Journal of Cleaner Production*, *164*, 1474–1485. https://doi.org/10.1016/j.jclepro.2017.07.080

Dhaundiyal, A., & Atsu, D. (2020). The effect of wind on the temperature distribution of photovoltaic modules. *Solar Energy*, *201*(October 2019), 259–267. https://doi.org/10.1016/j.solener.2020.03.012

Dörenkämper, M., Wahed, A., Kumar, A., de Jong, M., Kroon, J., & Reindl, T. (2021). The cooling effect of floating PV in two different climate zones: A comparison of field test data from the Netherlands and Singapore. *Solar Energy*, *214*(December 2020), 239–247. https://doi.org/10.1016/j.solener.2020.11.029

Driesse, A., Stein, J. S., & Theristis, M. (2022). Improving Common PV Module Temperature Models by Incorporating Radiative Losses to the Sky. (August).

Dupré, O., Vaillon, R., & Green, M. (2015b). Physics of the temperature coefficients of solar cells. *Solar Energy Materials and Solar Cells*, *140*, pp. 92–100. https://hal.archives-ouvertes.fr/hal-01281189

Faiman, D. (2008). Assessing the outdoor operating temperature of photovoltaic modules. *Progress in Photovoltaics: Research and Applications*, *16*(4), 307–315. https://doi.org/10.1002/pip.813

Giuseppe Marco Tina, L. M., Fausto Bontempo Scavo. (2021). Analysis of water environment on the production of floating photovoltaic plants. *Renewable Energy*, *175*(In Press), 281–295. https://doi.org/10.1016/j.renene.2021.04.082

Glick, A., Smith, S. E., Ali, N., Bossuyt, J., Recktenwald, G., Calaf, M., & Cal, R. B. (2020). Influence of flow direction and turbulence intensity on heat transfer of utility-scale photovoltaic solar farms. *Solar Energy*, *207*(November 2019), 173–182. https://doi.org/10.1016/j.solener.2020.05.061

Gnielinski, V. (1975). Neue Gleichungen für den Wärme- und den Stoffübergang in turbulent durchströmten Rohren und Kanälen. *Forschung im Ingenieurwesen*, *41*(1), 8–16. https://doi.org/10.1007/BF02559682

Golroodbari, S. Z., & van Sark, W. (2020). Simulation of performance differences between offshore and land-based photovoltaic systems. *Progress in Photovoltaics: Research and Applications*, (February), 1–14. https://doi.org/10.1002/pip.3276

Green, M., Emery, K., & Blakers, A. (1982). Silicon solar cells with reduced temperature sensitivity. *Electronics Letters*, *18*(2), 97. https://doi.org/10.1049/el:19820066

Gu, W., Ma, T., Shen, L., Li, M., Zhang, Y., & Zhang, W. (2019). Coupled electrical-thermal modelling of photovoltaic modules under dynamic conditions. *Energy*, *188*, 116043. https://doi.org/10.1016/j.energy.2019.116043

Hasan, K., Yousuf, S. B., Tushar, M. S. H. K., Das, B. K., Das, P., & Islam, M. S. (2022). Effects of different environmental and operational factors on the PV performance: A comprehensive review. *Energy Science and Engineering*, *10*(2), 656–675. https://doi.org/10.1002/ese3.1043

Jeong, H. S., Choi, J., Lee, H. H., & Jo, H. S. (2020). A study on the power generation prediction model considering environmental characteristics of floating photovoltaic system. *Applied Sciences (Switzerland)*, *10*(13). https://doi.org/10.3390/app10134526

Jones, A. D., & Underwood, C. P. (2002). A thermal model for photovoltaic systems. *Fuel and Energy Abstracts*, *43*(3), 199. https://doi.org/10.1016/s0140-6701(02)85831-3

Jubayer, C. M., & Hangan, H. (2014). Numerical simulation of wind effects on a stand-alone ground mounted photovoltaic (pv) system. *Journal of Wind Engineering and Industrial Aerodynamics*, *134*, 56–64. https://doi.org/https://doi.org/10.1016/j.jweia.2014.08.008

Jubayer, C. M., Siddiqui, K., & Hangan, H. (2016). CFD analysis of convective heat transfer from ground mounted solar panels. *Solar Energy*, *133*, 556–566. https://doi.org/10.1016/j.solener.2016.04.027

King, D. L., Boyson, W. E., & Kratochvil, J. A. (2004). Photovoltaic array performance model, SANDIA Report SAND2004-3535. *Sandia Report No. 2004-3535*, *8*(December), 1–19.

Klasen, N., Lux, F., Weber, J., Roessler, T., & Kraft, A. (2022). A Comprehensive Study of Module Layouts for Silicon Solar Cells under Partial Shading. *IEEE Journal of Photovoltaics*, *12*(2), 546–556. https://doi.org/10.1109/JPHOTOV.2022.3144635

Lalwani, M., Kothari, D., & Singh, M. (2010). Investigation of Solar Photovoltaic Simulation Softwares. *International Journal of Applied Engineering Research*, *1*(3), 585–601.

Lindholm, D., Kjeldstad, T., Selj, J., Marstein, E. S., & Fjær, H. G. (2021). Heat loss coefficients computed for floating PV modules. *Progress in Photovoltaics: Research and Applications*, (April), 1–12. https://doi.org/10.1002/pip.3451

Liu, H., Krishna, V., Lun Leung, J., Reindl, T., & Zhao, L. (2018). Field experience and performance analysis of floating PV technologies in the tropics. *Progress in Photovoltaics: Research and Applications*, *26*(12), 957–967. https://doi.org/10.1002/pip.3039

Lo, V., Orioli, A., Ciulla, G., & Gangi, A. D. (2010). An improved five-parameter model for photovoltaic modules Solar Energy Materials & Solar Cells An improved five-parameter model for photovoltaic modules. *Solar Energy Materials and Solar Cells*, *94*(8), 1358–1370. https://doi.org/10.1016/j.solmat.2010.04.003

Magare, D., Sastry, O., Gupta, R., Bora, B., Singh, Y., & Mohammed, H. (2018). Wind Effect Modeling and Analysis for Estimation of Photovoltaic Module Temperature. *Journal of Solar Energy Engineering, Transactions of the ASME*, *140*(1). https://doi.org/10.1115/1.4038590

Marco, G., Bontempo, F., Merlo, L., & Bizzarri, F. (2021). Comparative analysis of monofacial and bifacial photovoltaic modules for floating power plants. *Applied Energy*, *281*(October 2020), 116084. https://doi.org/10.1016/j.apenergy.2020.116084

Marinić-Kragić, I., Nižetić, S., Grubišić-Čabo, F., & Papadopoulos, A. M. (2018). Analysis of flow separation effect in the case of the free-standing photovoltaic panel exposed to various operating conditions. *Journal of Cleaner Production*, *174*, 53–64. https://doi.org/https://doi.org/10.1016/j.jclepro.2017.10.310

Matthieu Chiodetti. (2019). Predicting Yields of Bifacial Pv Power Plants – What Accuracy Is Possible?, 991–996.

May Tzuc, O., Bassam, A., Mendez-Monroy, P. E., & Dominguez, I. S. (2018). Estimation of the operating temperature of photovoltaic modules using artificial intelligence techniques and global sensitivity analysis: A comparative approach. *Journal of Renewable and Sustainable Energy*, *10*(3). https://doi.org/10.1063/1.5017520

Micheli, L. (2022). The Temperature of Floating Photovoltaics: Case Studies, Models and Recent Findings. *Solar Energy*, *242*(May), 234–245. https://doi.org/10.1016/j.solener.2022.06.039

Mittag, M., Vogt, L., Herzog, C., Pfreundt, A., Shahid, J., Neuhaus, D. H., & Wirth, H. (2019). Thermal Modelling of Photovoltaic Modules in Operation and Production. *PV Solar Energy*, (September), 9–13.

Nazari, S., & Eslami, M. (2021). Impact of frame perforations on passive cooling of photovoltaic modules: Cfd analysis of various patterns. *Energy Conversion and Management*, *239*, 114228. https://doi.org/https://doi.org/10.1016/j.enconman.2021.114228

Notton, G., Cristofari, C., Mattei, M., & Poggi, P. (2005). Modelling of a double-glass photovoltaic module using finite differences. *Applied Thermal Engineering*, *25*(17-18), 2854–2877. https://doi.org/10.1016/j.applthermaleng.2005.02.008

Oliveira-Pinto, S., & Stokkermans, J. (2020). Assessment of the potential of different floating solar technologies – Overview and analysis of different case studies. *Energy Conversion and Management*, *211*(November 2019), 112747. https://doi.org/10.1016/j.enconman.2020.112747

Osborne, D. G., & Incropera, F. P. (1985). Experimental study of mixed convection heat transfer for transitional and turbulent flow between horizontal, parallel plates. *International Journal of Heat and Mass Transfer*, *28*(7), 1337–1344. https://doi.org/10.1016/0017-9310(85)90164-4

Peters, I., & Nobre, A. (2022). Deciphering the thermal behavior of floating photovoltaic installations. *Solar Energy Advances*, *2*(November 2021), 100007. https://doi.org/10.1016/j.seja.2021.100007

Plessis, G., Kaemmerlen, A., & Lindsay, A. (2014). BuildSysPro: a Modelica library for modelling buildings and energy systems. *Proceedings of the 10th International Modelica Conference, March 10-12, 2014, Lund, Sweden*, *96*, 1161–1169. https://doi.org/10.3384/ecp140961161

Pohlhausen, E., & Angrew, Z. (1921). -. *Math. Mech.*, *1*, 115.

Ranjbaran, P., Yousefi, H., Gharehpetian, G. B., & Astaraei, F. R. (2019). A review on floating photovoltaic (FPV)power generation units. *Renewable and Sustainable Energy Reviews*, *110*(April 2018), 332–347. https://doi.org/10.1016/j.rser.2019.05.015

Reza Reisi, A., Hassan Moradi, M., & Jamasb, S. (2013). Classification and comparison of maximum power point tracking techniques for photovoltaic system: A review. *Renewable and Sustainable Energy Reviews*, *19*, 433–443. https://doi.org/10.1016/j.rser.2012.11.052

Ross, R. (1976). INTERFACE DESIGN CONSIDERATIONS FOR TERRESTRIAL SOLAR CELL MODULES, 801–806.

Ruschel, S. C., Gasparin, F. P., Costa, R. E., & Krenziger, A. (2016). Assessment of PV modules shunt resistance dependence on solar irradiance. *Solar Energy*, *133*, 35–43. https://doi.org/10.1016/j.solener.2016.03.047

Sah, C.-T., Noyce, R. N., & Shockley, W. (1956). Carrier Generation and Recombination in P-NV Junctions and P-N Junction Characteristics. *1*, 1228–1243. https://doi.org/10.1109/jrproc.1957.278528

Santiago, I., Trillo-Montero, D., Moreno-Garcia, I. M., Pallarés-López, V., & Luna-Rodríguez, J. J. (2018). Modeling of photovoltaic cell temperature losses: A review and a practice case in South Spain. *Renewable and Sustainable Energy Reviews*, *90*(March), 70–89. https://doi.org/10.1016/j.rser.2018.03.054

Sartori, E. (2006). Convection coefficient equations for forced air flow over flat surfaces. *Solar Energy*, *80*(9), 1063–1071. https://doi.org/10.1016/j.solener.2005.11.001

Schiro, F., Benato, A., Stoppato, A., & Destro, N. (2017). Improving photovoltaics efficiency by water cooling: Modelling and experimental approach. *Energy*, *137*, 798–810. https://doi.org/10.1016/j.energy.2017.04.164

Schuss, C., Eichberger, B., & Rahkonen, T. (2016). Impact of sampling interval on the accuracy of estimating the amount of solar energy. *Conference Record - IEEE Instrumentation and Measurement Technology Conference*, *2016-July*. https://doi.org/10.1109/I2MTC.2016.7520566

Schuss, C., & Fabritius, T. (2022). Impact of Environmental Conditions on the Degree of Efficiency and Operating Range of PV-Powered Electric Vehicles. *Applied Sciences (Switzerland)*, *12*(3). https://doi.org/10.3390/app12031232

Sharples, S., & Charlesworth, P. S. (1998). Full-scale measurements of wind-induced: Convective heat transfer from a roof mounted flat plate solar collector. *Solar Energy*, *62*(2), 69–77. https://doi.org/10.1016/S0038-092X(97)00119-9

Shockley, W. (1950). *Electrons and holes in semiconductors: With applications to transistor electronics*. van Nostrand.

Shongwe, S., & Hanif, M. (2015). Comparative Analysis of Different Single-Diode PV Modeling Methods, 1–9.

Skoplaki, E., & Palyvos, J. A. (2009). Operating temperature of photovoltaic modules: A survey of pertinent correlations. *Renewable Energy*, *34*(1), 23–29. https://doi.org/10.1016/j.renene.2008.04.009

Test, F. L., Lessmann, R. C., & Johary, A. (1981). Heat transfer during wind flow ower rectangular bodies in the natural environment. *Journal of Heat Transfer*, *103*(2), 262–267. https://doi.org/10.1115/1.3244451

Theristis, M. (2022). International Photovoltaic Modeling Intercomparison.

Theristis, M., Venizelou, V., Makrides, G., & Georghiou, G. E. (2018). Energy Yield in Photovoltaic Systems. *Mcevoy's handbook of photovoltaics* (pp. 671–713). Elsevier. https://doi.org/10.1016/B978-0-12-809921-6.00017-3

Tian, H., Mancilla-david, F., Ellis, K., Jenkins, P., & Muljadi, E. (2012). A Detailed Performance Model for Photovoltaic Systems Preprint. *Solar Energy Journal*, (July).

Tim Umoette, A. (2016). Design of Stand Alone Floating PV System for Ibeno Health Centre. *Science Journal of Energy Engineering*, *4*(6), 56. https://doi.org/10.11648/j.sjee.20160406.12

Tina, G. M., Marletta, G., & Sardella, S. (2012). Multi-layer thermal models of pv modules for monitoring applications. *2012 38th IEEE Photovoltaic Specialists Conference*, 002947–002952.

Tina, G. M., & Gagliano, A. (2016). An improved multi-layer thermal model for photovoltaic modules. *2016 International Multidisciplinary Conference on Computer and Energy Science, SpliTech 2016*. https://doi.org/10.1109/SpliTech.2016.7555927

Veldhuis, A. J., Nobre, A. M., Peters, I. M., Reindl, T., Ruther, R., & Reinders, A. H. M. E. (2015). An Empirical Model for Rack-Mounted PV Module Temperatures for Southeast Asian Locations Evaluated for Minute Time Scales. *IEEE Journal of Photovoltaics*, *5*(3), 774–782. https://doi.org/10.1109/JPHOTOV.2015.2405762

Waithiru, C. L., Jong Rok, L., Chang Sub, W., & Ahn, H. K. (2018). Prediction Model of Photovoltaic Module Temperature for Power Performance of Floating PVs. https://doi.org/10.3390/en11020447

Weiss, L. (2015). Modeling of a photovoltaic module under environmental conditions and optimisation of its performance.

Wu, Y.-Y., Wu, S.-Y., & Xiao, L. (2017). Numerical study on convection heat transfer from inclined pv panel under windy environment. *Solar Energy*, *149*, 1–12. https://doi.org/https://doi.org/10.1016/j.solener.2017.03.084

2 INTEGRATING THE FLOATING ARRAY IN THE ENVIRONMENT

> Everything is related to everything else, but near things are more related than distant things. (Tobler, 1970)
>
> *Waldo Tobler*

This chapter introduces the governing equations adapted to the study of the atmosphere near the surface of the Earth, where the photovoltaic modules settle. The principle methods of solving the Equations are presented under the flavour of Computational Fluid Dynamics so that the solver code_saturne and its capability in simulating the microclimate around the modules are presented. The waterbody induced effect on the atmosphere is mentioned and the state-of-the-art literature about determining the airflow in photovoltaic arrays is finally proposed.

Contents

2.1/ Introduction

Ambient environment is a key element controlling the thermal dynamics of the photovoltaic modules, and it is quite natural that the integration of the modules in a new environment offers particular feedbacks. At the edge of a bio-physical system triptych, it appears important to reduce the complexity of the complete system by investigating the systems independently or by simplified coupling. Figure 2.1 illustrates the main first-order feedbacks that can be extracted from the analysis of a coarse coupling between systems. The FPV technology without direct contact with water necessarily influences the choice of the main system to be described, the ambient air and the aeraulic flow acts mainly on the cooling of the modules by the thermal convection phenomenon. Nevertheless, this system remains complex in that it is an external flow that cannot be controlled: the interpretation of the stochasticity of the fields is a major problem in the description of this system. This acts both at the scale of the transport of quantities of interest for the description of boundary conditions (ambient temperature, humidity ...), and for the description of the mean flow at the level of a more complex photovoltaic system as when studying the photovoltaic plant as a whole. The coupling between the atmosphere and the lake is also challenging, especially when the lake is partially covered as it is the case when installing a PV plant. The evaporation potential is altered in a way that is difficult to quantify as the mechanisms at work are inter-correlated.

The numerical prism is mainly adopted in the work, thus the concepts of atmospheric flow and module/atmosphere/module and atmosphere/waterbody interaction are presented with the task of introducing useful and general elements of dynamic fluid mechanics. Microclimate modelling also requires a range of numerical tricks in order to keep the simulations of complex geometry computationally affordable. In this chapter, the literature on this subject will be discussed at length.

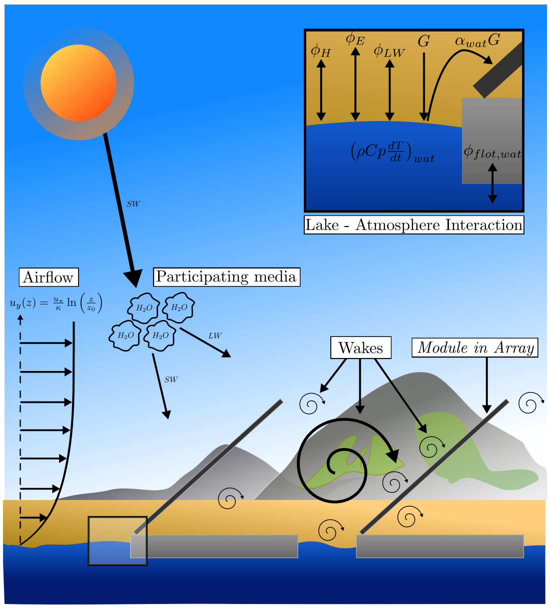

Figure 2.1–*Simplified schematic of the modified local conditions around FPV array. The waterbody interacts with the atmosphere so that the net budget of energy at the first layer of the waterbody drives the local conditions. The module configuration and distribution in array-shape also modify the wind regime observed by "in-array" modules.*

2.2/ Microclimate System and Modelling

The fluid surrounding the photovoltaic modules consists of a mixture of molecules, but is simplified by the designation of *air*. The properties of this environment can be addressed within the scope of the atmospheric boundary layer (ABL). Giving a clear definition of the ABL is complicated, although Gérard De Moor in De Moor, 2006 proposes some key aspects as follows:

- It consists of the fluid area in the direct vicinity of the surface. The notion of neighbourhood can be physically observed dynamically and thermally: the adherence of the fluid flow over the surface slowing down the fluid area through viscosity
- The fluid area is predominantly altered by the surface, mostly on the short time scales
- The flow regime is mainly turbulent, which has a significant effect on the efficiency of transport phenomena such as temperature and humidity
- The height of the boundary layer varies in space and time, a common assumption is to consider a height of one kilometre
- The flow and scalar parameters are continuous between the boundary layer and the surface - at the surface, the parameters are partially dictated by the properties of the atmospheric boundary layer, but also and especially by the *surface* (notion of energy balance, moisture).

Therefore, determining the airflow properties (velocity, turbulence, temperature, and humidity) is critical when one wants to understand what happens in the close environment of a photovoltaic installation. In the following, the term *microclimate* refers to *this close environment*. Characterising the airflow in the microclimate situation is even more important when considering installation that covers a larger range of spatial scale, the ABL flow evolving because of the surfaces encountered. One may consider, for instance, that the point measurements, which apparently describe well the behaviour of a standalone module, do not describe the physical field encountered at the full-array scale.

In the following sections, a mathematical description of atmosphere airflow is proposed as well as the tools and hypotheses that are admitted when addressing this subject.

2.2.1/ Fundamentals of Air Flow Behaviour in the Atmosphere

Conservative Laws: Navier-Stokes Equations

Assuming that airflow takes place in the earth reference frame in which $\vec{x} = (x, y, z)$ denotes the current point in the air volume Ω, the quantities of interest to describe the system are:

- The velocity and its spatial components, denoted $U = (u_x, u_y, u_z)$
- The potential temperature, denoted $\mathrm{T}_p = T.\left(\frac{\mathrm{P}}{\mathrm{P}_0}\right)^{\frac{-R}{Cp}}$
- The pressure, denoted P

It is also possible to get interest in describing particles or passive scalars in the volume; one of the most interesting aspects of the work is the mixing ratio of water vapour q (expressed in $\mathrm{kg\,kg^{-1}}$).

Considering the air as a continuous incompressible Newtonian fluid, conservative laws are in force so that the mass, the momentum, and the energy equations can be stated. They read:

$$\frac{\partial u_j}{\partial x_j} = 0 \tag{2.1}$$

For the conservative mass law in which ρ is the density of the air.

For momentum conservation ρu, three equations are implied, one per direction of the velocity vector. It reads:

$$\left(\frac{\partial}{\partial t} + u_j \frac{\partial}{\partial x_j}\right) u_i = -\frac{1}{\rho}\frac{\partial P}{\partial x_i} + \frac{\partial}{\partial x_j}\left[\mu\left(\frac{\partial u_i}{\partial x_j} + \frac{\partial u_j}{\partial x_i}\right)\right] - \frac{2}{3}\frac{\partial}{\partial x_i}\left(\mu\frac{\partial u_j}{\partial x_j}\right) + g_i + f_i \tag{2.2}$$

with the gravity vector g_i and external forces f_i[1]. With the exception of the pressure term in the right-hand part of Equation (2.2), the remaining part describes the advection process, so to speak, the convective term. The Newtonian nature of the fluid implies that the viscous stress tensor $\tau_{ij} = 2\mu S_{ij} - \frac{2}{3}\mu\frac{\partial u_k}{\partial x_k}\delta_{ij}$ is bound to the local strain rate $S_{ij} = \frac{1}{2}\left(\frac{\partial u_i}{\partial x_j} + \frac{\partial u_j}{\partial x_i}\right)$ through the molecular viscosity μ. The term δ_{ij} is the Kronecker delta, which reads $\delta_{ij} = 1$ when $i = j$ (cancel out otherwise).

Finally, using the potential temperature, the conservation of energy reads:

$$\left(\frac{\partial}{\partial t} + u_j \frac{\partial}{\partial x_j}\right) \mathrm{T}_p = \frac{\lambda}{\rho Cp}\frac{\partial^2 \mathrm{T}_p}{\partial x_j \partial x_j} + \Phi_{ext} \tag{2.3}$$

With Cp the heat capacity, the Fourier law $\Phi_i = \lambda\frac{\partial T}{\partial x_j}$, including the heat conductivity λ and an external heat source Φ_{ext}. Note that the equation can be written down for scalar conservative properties as well; diffusivity of scalar should be adapted (for instance, the Fick law for mass scalar).

Conservative laws are by nature chaotic due to the interaction of second-order derivatives with other fields. When the Reynolds number is high enough (bounded geometry configuration), the convective term in Equation (2.2) disturbs the flow with many eddies on a range of scales. That is to say, it is pretty much impossible to catch all the eddies in a high Reynolds Flow when one wants to simulate the airflow. Therefore, calculation of the fluid momentum, energy, and mass is rarely possible without assuming statistical field properties.

Reynolds Decomposition

Assuming that a field of interest is denoted Y (velocity, temperature, humidity, etc.), the Reynolds decomposition makes the separation between a mean value $\overline{Y}$ and a residual value Y'. The full field is written as follows:

$$Y = \overline{Y} + Y' \tag{2.4}$$

---

[1] *e.g., the Coriolis force* $-2\epsilon_{i,j,\beta}\Omega_j\overline{u_j}$ *can be integrated in* f_i*; however, it is set constant to zero here as the system is close to the Earth surface.*

The mean value must be understood as the ensemble average of the field obtained when the Navier-Stokes equation[2] is run several times and is as follows:

$$\overline{Y}(x,t) = \lim_{N\to\infty}\left(\frac{\sum_{i=1}^{i=N} Y^{(i)}}{N}\right) \tag{2.5}$$

Reproducing either numerical or experimental results is hard in practise. The ergodicity hypothesis can be applied when stationary flow is assumed; it eases the use of the Reynolds decomposition by assimilating the ensemble average to the temporal averaged. It reads:

$$\overline{Y}(x,t) = \lim_{T\to\infty}\left(\frac{1}{T}\int_0^T Y(x,t)\,\mathrm{d}t\right) \tag{2.6}$$

These statistical tools allow for simplifying the initial deterministic system of equations *(e.g., for modelling purpose)* and provide practical elements for assessing the bulk behaviour of airflow *(e.g., definition of atmosphere at constant flux)*.

Reynolds Averaged Navier-Stokes (RANS)

Using the Reynolds Decomposition and the Boussinesq hypothesis[3], the five conservative laws for the atmosphere flow under the Reynolds Averaged Navier-Stokes (RANS) shape read, for mass:

$$\frac{\partial \overline{u_i}}{\partial x_i} = 0 \tag{2.7}$$

For momentum:

$$\frac{\partial \overline{u_i}}{\partial t} + \frac{\partial\left(\overline{u_j u_i}\right)}{\partial x_j} = -\frac{\partial\left(\overline{u'_j.u'_i}\right)}{\partial x_j} - \frac{1}{\rho_0}\frac{\partial \overline{p}}{\partial x_i} + \nu\frac{\partial^2 \overline{u_i}}{\partial x_j \partial x_j} + g\beta\left(\overline{\mathrm{T}_p} - \mathrm{T}_p^{(0)}\right).\delta_{3i} \tag{2.8}$$

With β the thermal expansion coefficient. For energy:

$$\frac{\partial \overline{\mathrm{T}_p}}{\partial t} + \frac{\partial\left(\overline{u_j \mathrm{T}_p}\right)}{\partial x_j} = -\frac{\partial\left(\overline{u'_j \mathrm{T}'_p}\right)}{\partial x_j} + \frac{\lambda}{\rho_0 Cp}\frac{\partial^2 \overline{\mathrm{T}_p}}{\partial x_j \partial x_j} \tag{2.9}$$

In Equation (2.8), the term $\left(\overline{u'_j u'_i}\right)$ is called Reynolds stress and comes from Reynolds decomposition. It is a second-order component as it includes the velocity component twice. It is intimately bounded to the mean velocity $\overline{u_i}$ (first-order component) so there is no other way to express the Reynolds stress from another source of data when one wants to solve conservative equations[4]. The two major methods to solve this issue is to use turbulence models, which means solving more equations: first-order models imply solving two more equations (mainly turbulent kinetic energy k and dissipation rate ϵ or specific dissipation rate ω) and second-order models imply seven additional equations (one per Reynolds stress and a final one for ϵ).

---

[2] or the ground truth experiment

[3] low temperature variations in the fluid $T_0 + \delta T \simeq T$, therefore the buoyancy ρ does not vary with temperature and the reference buoyancy can be used ρ_0. However, the assumption is relaxed when buoyancy is multiplied by the gravity field g

[4] Non-linearity of the momentum equation is in operation, expressing the n-th component implies knowing the n-th+1 component and so fourth.

When one wants to use a first-order turbulence model, a current strategy is to define the turbulent viscosity ν_T and assume the Reynolds stress such that it reads:

$$\left(\overline{u_j'u_i'}\right) = -\nu_T\left(\frac{\partial u_i}{\partial x_j} + \frac{\partial u_j}{\partial u_i}\right) + \frac{1}{3}\overline{u_i'u_i'}\delta_{ij} \tag{2.10}$$

Then the kinetic energy and one of the dissipation rates can be modelled using an appropriate methodology , the ones used in the thesis are indicated in A.4.

In Equation (2.9), $\left(\overline{u_j'.\mathrm{T}_p'}\right)$ is the turbulent transport of energy that should also be solved. A strategy based on the definition of turbulent diffusivity reads as follows:

$$\left(\overline{u_j'\mathrm{T}_p'}\right) = -\frac{\nu_t}{Pr_t}\frac{\partial\overline{\mathrm{T}_p}}{\partial x_j} \tag{2.11}$$

Where the turbulent Prandtl number Pr_t, which depicts the influence of eddies on thermal diffusivity, must be assumed. Generally, it is set constant with an associated value of $Pr_t \simeq 1$.

The Universal Law of the Wall

Conservation equations describe the behaviour in the fluid domain. Very close to the walls of the system, the viscous effects tend to dominate the convective effects (as described in the previous chapter on the emergence of convection around a heated wall). Away from the wall, convective effects become dominant. This evolution is universal to all walls[5]: the wall law describes the evolution of the average velocity of the fluid with respect to the distance to the wall. To do this, several adaptations of the notation are practical:

- The friction velocity denoted $u_\star = \sqrt{\frac{\tau_w}{\rho}}$ where τ_w is the wall shear stress
- the dimensionless velocity denoted $u^+ = \frac{u(z)}{u_\star}$; note that $u(z)$ is parallel to the wall
- the dimensionless distance denoted $y^+ = \frac{yu_\star}{\nu}$.

Three regimes are assumed near the wall. First, the flow is laminar at distances $z^+ < 4$ and the dimensionless velocity profile follows $u^+ = y^+$. At distances larger than $z^+ > 50$, the dimensionless velocity profiles follow a logarithmic law in the theoretical form: $u^+ = \frac{1}{\kappa}\ln y^+ + C$. The constant C is set to 5.2 from empirical studies (smooth wall). In between $4 < z^+ < 50$, a buffer layer is assumed.

2.2.2/ Simplification of Atmosphere and Waterbody Systems

The Atmosphere at Constant Flux

From the Navier-Stokes equations, several hypotheses can be performed to simplify the first-order terms. These hypotheses, as well as the rearrangement of the momentum equation, are indicated in A.2.1. It leads to rewriting the momentum equation so that:

$$-\frac{\partial\overline{(u_x' \times u_z')}}{\partial z} + \nu \times \frac{\partial^2 \overline{u_y}}{\partial^2 z} = 0 \tag{2.12}$$

---

[5] In fact, they rely on hypothesis that are: the wall is a plane, the Reynolds number is large and no pressure gradient-related effect are appearing.

This simplified equation signifies that the fluxes of motion from turbulent momentum and viscosity are equal: the atmosphere is stated to be at Constant Flux. Mathematically, the latter equation can be rewritten so that the fundamental scale of friction velocity introduced in the prior section appears:

$$-\nu \times \frac{\partial \overline{u_y}}{\partial z} + \overline{u_z' \times u_x'} = -u_\star^2 \tag{2.13}$$

Classically, the velocity profile can be written in a logarithmic shape. This function derived from a functional analysis, see A.2.2, it reads:

$$\overline{u_y}(z) = \frac{u_\star}{\kappa} \ln\left(\frac{z - d_0}{z_0}\right) \tag{2.14}$$

whence $\kappa \simeq 0.42$ is the Von Karman constant, d_0 is the zero plane of displacement, and z_0 is the roughness length.

Atmosphere Stability

One may see that Equation (2.14) does not take into account the likely effect of temperature onto the velocity profile. A more general theory exists in the name of the *Monin-Obukhov similarity theory*, it expresses the mean velocity profile in the altitude as follows:

$$\frac{\partial u}{\partial z} = \frac{u_\star}{\kappa\,(z + z_0)} \phi_M(z/L) \tag{2.15}$$

in which $\phi_M(z/L)$ is a function that describes vertical motion in the atmosphere layer, called a stability function which includes the dimensionless number z/L in which L is the Obukhov Length, see Monin and Obukhov, 1954. The latter is a key player in the theory as it indicates whether the buoyant production or the shear production drives the turbulent kinetic energy in the atmosphere. Mathematically, it reads:

$$L = -\frac{u_\star^3}{\kappa \left(g/\overline{\mathrm{T}_p}\right) \overline{w'\mathrm{T}_p'}} \tag{2.16}$$

Three cases of atmospheric stability can be derived from Equation (2.15):

- the first has already been introduced in Equation (2.14) for the neutral atmosphere situation $\left(\frac{\partial \mathrm{T}_p}{\partial z} = 0\right)$. In this situation, no vertical motion is observed in the mean velocity. In other word: $\phi_M(z/L) = 1$.
- The second is the stable atmosphere $\left(\frac{\partial \mathrm{T}_p}{\partial z} > 0\right)$, so the buoyancy-driven flow has little effect on the vertical velocity gradient: $z/L > 0$
- The last is the unstable case $\left(\frac{\partial \mathrm{T}_p}{\partial z} < 0\right)$, a vertical gradient appears due to the thermal effect: $z/L < 0$.

A particular situation occurs when the shear stress is consistent, regardless of the stability function. The unitary dimension L being proportional to the third power of velocity friction, the stability function tends to zero as $\lim_{z/L\to 0}(\phi_M(z/L)) \simeq 1$. The same observation is also made when z is little in front of L.[6]

Hence, for consistent wind or for low atmosphere height, a neutrally stratified atmosphere is a good approximation of the atmosphere stability and the mean velocity profile in Equation (2.14) is verified.

Scalar Profiles

Similarly as the momentum equation, it is possible to determine a fundamental scale for the potential temperature, see Brutsart, 1982, it reads:

$$-\frac{\lambda}{\rho Cp} \times \frac{\partial \overline{\mathrm{T}_p}}{\partial z} + \overline{\phi_T} = Cste \rightarrow \mathrm{T}_p^\star \tag{2.17}$$

And for the water vapour:

$$-\frac{D_m}{\rho} \times \frac{\partial \overline{q}}{\partial z} + \overline{\phi_E} = q^\star \tag{2.18}$$

From these ideal atmospheric case, the scalar profile for temperature is:

$$\overline{\mathrm{T}_p^s} - \overline{\mathrm{T}_p}(z) = \frac{\phi_T}{\kappa u_\star \rho Cp} \ln\left(\frac{z-d_0}{z_T}\right) \tag{2.19a}$$

and for humidity:

$$\overline{q_s} - \overline{q}(z) = \frac{\phi_E}{\kappa u_\star \rho} \ln\left(\frac{z-d_0}{z_E}\right) \tag{2.19b}$$

Where $\overline{\mathrm{T}_p^s}$ and $\overline{q_s}$ are the potential temperature on the surface and the specific humidity on the surface, respectively. Both sensible heat flux ϕ_T and evaporative flux ϕ_E contribute to the atmospheric temperature and humidity gradient. A practical way to handle equations (2.19a) and (2.19b) is to define the thermal roughness length and the humidity roughness length as $\mathrm{T}_p^\star = \frac{\phi_T}{u_\star \rho Cp}$ and $q_\star = \frac{\phi_E}{u_\star \rho}$.

These three later dimensions are sufficient to parameterise the horizontally homogeneous atmosphere, and the vertical heterogeneous behaviour of the vectors and scalars.

Boundary Condition with the Waterbody

The properties of the atmosphere, as described in Equation (2.14), Equation (2.19a) and Equation (2.19b) in a simplified format, are mainly driven by the properties of the surface at the bottom of the atmospheric column. Unlike continental surfaces, water surfaces exhibit properties that change as a result of the volume of the underlying liquid. To simulate the first layer of water, a widely used method is to consider the water mass as a stack of layers; the upper layer is thus subject to thermal and mass exchange with the atmosphere, see Figure 2.1. which can be described in a bulk fashion as:

$$\mathcal{V}\rho Cp\frac{\mathrm{d}T}{\mathrm{d}t} = \mathcal{A}\alpha_{\mathrm{wat}}\Phi_{\mathrm{sw}} - \Phi_{\mathrm{lw}} - \Phi_e - \Phi_h \tag{2.20}$$

Where part of the short wavelengths $\mathcal{A}\alpha_{\mathrm{wat}}\phi$ and long wavelengths Φ_{lw} are absorbed by the water mass (associated to the volume $\mathcal{V}$). An assumption is that both radiative terms are absorbed in

---

[6] To give an idea, $L \simeq 10\,\mathrm{m}$ is a **very stable** atmospheric situation

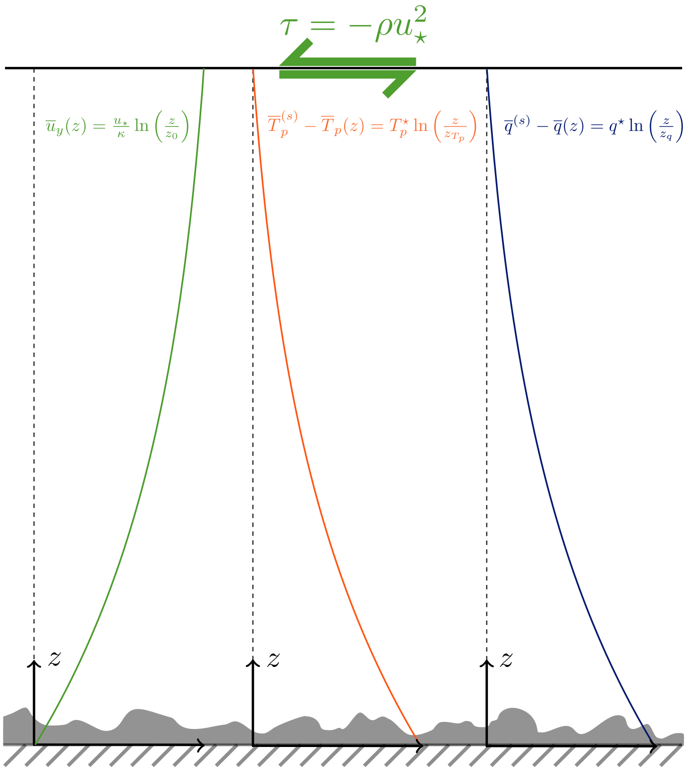

Figure 2.2–*Neutral Atmosphere at constant flux. The term τ refers to the atmosphere friction here.*

the first centimetres of the fluid. Depending on the water quality, this assumption can be altered by introducing an extinction coefficient on the first metre of fluid for the short-wavelength contribution. In addition to radiative properties, the upper layer also exchanges heat by convection and diffusion with the atmosphere in the form of sensible energy Φ_h and latent energy Φ_e.

Meanwhile, the surface temperature is mainly driven by the capacitive term on long-time scales[7], evaporative transfer exhibits faster time responses, especially during the day as it is closely bounded to water vapour diffusion and forced mass convection (Figure 2.3). Simulating the physics behind the phenomena stays complicated, especially for open-water situation, so that getting the knowledge of how much evaporation occurs on a given lake is principally achieved by empirical laws. The myriad of law shapes exist in the literature; see Wossenu and Assefa, 2012, here we put the light on the two major laws that are the Penman and Dalton laws, as they are the most currently employed.

Theoretical law: Penman's Law

The Penman law is originally based on a bulk heat equation at the ground level (mainly soil, but water also makes sense), and assumes that the irradiation gives energy to the H_2O molecules so that they can break their boundings and ultimately be transported to the air volume by the wind. The equation reads:

$$E_p = E_{p,R} + E_{p,A} = \left(\frac{s}{s+a\gamma}\frac{R_n}{\lambda}\right) + \left(\frac{a\gamma}{s+a\gamma} f_q(u)\Delta q\right) \tag{2.21}$$

---

[7] as shown by the left-hand side of Equation (2.20), the specific heat coefficient of water is $Cp \simeq 4187\,\mathrm{J\,K^{-1}\,kg^{-1}}$

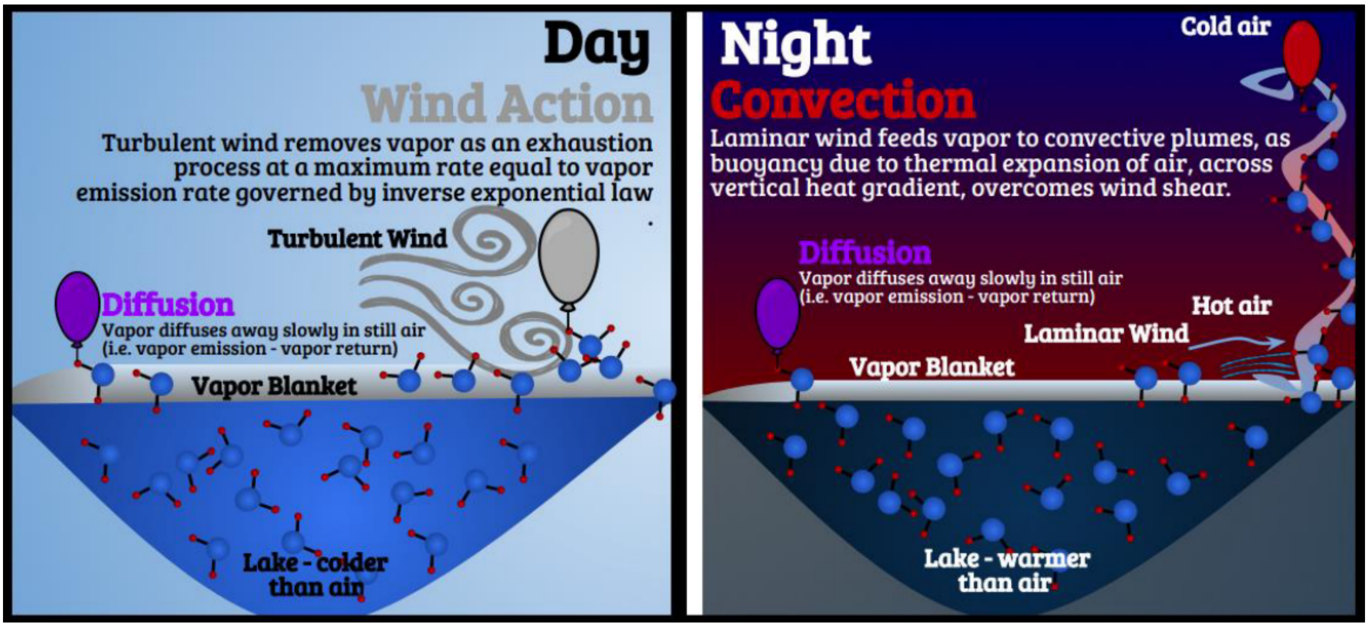

Turbulent wind removes vapor as an exhaustion process at a maximum rate equal to vapor emission rate governed by inverse exponential law

Vapor diffuses away slowly in still air (i.e. vapor emission - vapor return)

Laminar wind feeds vapor to convective plumes, as buoyancy due to thermal expansion of air, across vertical heat gradient, overcomes wind shear.

Vapor diffuses away slowly in still air (i.e. vapor emission - vapor return)

Figure 2.3–*Conceptualisation of evaporation processes and the related action that drives the process, retrieved from (Vimal & Singh, 2021). The balloons symbolise the action of diffusion (purple), forced mass convection (grey) and thermal convection (red).*

Here, $E_{p,R}$ and $E_{p,A}$ are the contributions of the heat budget side and the aerodynamic side of the process, respectively. R_n takes into account the net radiative transfer (short and long wavelength), meanwhile $f_q(u)$ is a function of the wind, empirically obtained. Parameters s and $a\gamma$ denote the slope of the saturation vapour curve at the temperature of the evaporating surface and the psychometric constant, respectively. The evaporation rate is given in $mm.day^{-1}$. Among the critical radiative and aerodynamic parameters, the surface temperature is also an important parameter hidden in the vapour pressure deficit.

Theoretical law: Dalton's Law

The Dalton law, first introduced in Dalton, 1802 is solely based on diffusion-advection processes as follows:

$$E_p = f_D(u) \times \Delta q \tag{2.22}$$

where $f_D(u)$ is also a mean velocity-based function. In a recent work (Vimal & Singh, 2021), the Dalton law was reviewed in contrast to the Horton law (Horton, 1915) with a slightly different shape as follows:

$$E_p = C\left(\overline{q}_S \times f_H(u) - \overline{q}\right) \tag{2.23}$$

with constant C. Such a law is found to be more efficient in short-timescale predictions, the supposition being that it should better catch the evaporation for large wind velocity, where the Dalton fails to catch the full behaviour. Both of these equations are called "Bulk-mean evaporation" methods or BME.

Experimental assessments for Open-water application

The theoretical laws are adapted to extrapolate the evaporative rate from a new waterbody when the temperature, irradiance and the wind function are hypothesised, or when one wants to monitor the evaporative rate of an existing reservoir when a calibration is available. Knowing the evaporative rate to precisely the degree is a requirement of experimental resources so that the theory can be adapted. Three main standards for measurements exist: the methods based on turbulence (From & Kinneret, 1993)[8], on the energy balance (J. F. Turner, 1966), or on satellite measurements (Wang & Dickinson, 2012). Several authors have experimentally validated the use of theoretical function with the help of calibrating materials as in Blanken et al., 2000 with Canadian lakes; the remaining questions remain in the equivalent form factor of exchange, which was shown to evolve according to the state of atmospheric stability around (Verburg & Antenucci, 2010) (that is, when the motor of motion is the buoyancy effect).

Interestingly, the sole aerodynamic term or the BME appears to be a better predicator of the latent flux than the full evaporative term E_p on short timescales (McGloin et al., 2014), (Vimal & Singh, 2021).

When waterbodies are covered

When the lake is covered by floating technology or by structures in direct contact with the water surface, the mechanisms of evaporation are altered. The evaporative intensity is generally lower than that on a conventional free surface. Many studies have been carried out on this type of system, for example, to determine the best coating of structures (Cooley, 1970), the best shape of obstacles (Assouline et al., 2010), or even the best system strategy (Helfer et al., 2009). In Assouline et al., 2010 and Assouline et al., 2011, the distribution of floating objects and the available space for water to evaporate show the same behaviour as in crop-related evapotranspiration through the stoma. The evaporation rate is proportional to the diameter of the ”pore” and not to the evaporating surface; This behaviour holds for the diameter up to the centimetre scale, while the dimensions of the stoma reach 100 µm.

Few studies of water evaporation with floating photovoltaics have also been performed, the floating solution being a key in the intensity of water retention. Confirming the trend observed for floating solutions versus suspended solutions, the evaporation rate is found to be superior in the latter technology in Bontempo Scavo et al., 2021. A Ciel & Terre floating solution is also found to reduce evaporation by an amount greater than 80 % in Yang et al., 2021.

Existing Numerical materials of Basin Evaporation

Simulating the evaporation of tanks is generally done in two ways, depending on the system that will be modelled later. The first method is to simulate the thermal behaviour of the first layer of water at the top of the tank; as discussed in the theoretical part. The simulation is concerned with hydrology, so the energy balance to be solved consists of the phenomena that occur in water, such as upwelling and horizontal diffusion. Modelling of these phenomena is beyond the scope of this thesis. However, we mention the existence of a one-dimensional lake model (vertical distribution of temperature, oxygen, and biological elements, horizontal homogeneity) such as GLM (Hipsey et al., 2019).

The second method consists of solving the diffusion-advection phenomenon of water vapour. The solvers of the Navier and Stokes equations are used for this purpose; the surface of the basin is considered to be at saturation vapour pressure (Glanz, 1973). This type of boundary condition

---

[8] it is theoretically easily achievable by using the Equation (2.18) and Equation (2.14), however the measurement setup requires a lot of costly materials and good command of data acquisition, see Aubinet et al., 2012.

(Dirichlet) is used in Condie and Webster, 1997 to determine the influence of the evolution of the roughness (soil to water) on the calculation of evaporation of a basin. In particular, it is shown that the horizontal gradients emanating from the smooth-rough evolution have a non-negligible impact on the total evaporation calculation. Around the shoreline, evaporation is reduced, without taking into account the possible recirculation zone that occurs due to the difference in height between the shoreline and the pond. A new law is proposed that takes into account this phenomenon; it is also reused in Hipsey and Sivapalan, 2003 as a support for the development of a function that takes into account the explicit windbreak at the shoreline. The wake zone is thus taken into account, and the Reynolds term is modelled by a K - E - l model (similar to the Mellor and Yamada model). Other authors do not explicitly specify the Dirichlet-type boundary condition; some seem to follow the same approach as for the passive scalar in temperature in order to determine a transfer rate as a function of a representative wind (**Vidal2010**); others directly solve the energy equation in the mixture (Tominaga et al., 2015) .

2.2.3/ Modelling the Microclimate through CFD

To simulate the airflow around floating module standing in array shape, one may write the conservative equations, associate the boundary conditions (waterbody, sides, atmosphere on the top) and try to solve it by hand, but a more common numerical approach stands in the use of Computational fluid dynamics solvers (CFD) able to solve the partial derivative systems. Obviously, computers have their own limiting attributes; probably the two major are: calculation capability and memory. Continuous equations are necessary to be discretised and some complex calculations must be modified[9] to reduce complexity. In this section, we shall endeavour to give a succinct presentation of the field of numerical fluid mechanics, as this subject can be approached from different angles. Therefore, we will limit ourselves to a general presentation of the mathematical mechanics at work, and we will invoke the main parameters that are dealt with.

Mathematical background

Several mathematical methods exist to perform the calculation relying on Eulerian or Lagrangian specifications, both in time and space (all dimensions). When the observer is looking at the flow without specifically following a given fluid parcel, a meshed space supports the calculation of the fluid state, the idea being to discretise equations that are by nature continuous. This corresponds to *Eulerian frame*. In this category, there are three methods to perform the discretization step: finite difference, finite volume, or finite element methods. Basically, finite differences rely on Taylor series to compute the derivative terms in the conservative laws; finite volumes rely on the flux-divergence theorem to perform a similar task; finite elements use integral flavour combined with weighted kernel functions (weak form), so that using improved numerical schemes is made easier compared to the finite volume. Although it is numerically more practical to use the finite-volume method, as the integral forms of the equations are always conservative, this is why the traction for CFD in microclimate study is still the use of the finite-volume method.

Lagragian frame on the other hand, allows one to follow fluid parcels throughout the space without mesh support. The idea being to divide the fluid into a set of discrete moving elements that are controlled by the same governing equations. The computation of derivatives is based on kernel functions that define the number of elements in the vicinity of the particle of interest, as well as their influence on the particle. There are several strategies such as *Smoothed Particle*

---

[9] always based on the physics behind!

Hydrodynamics (SPH) (**Violeau2012**), *Moving Particle Semi-Implicit method* (MPS) (S. Zhang et al., 2006), or even *Explicit Moving Particle Semi-Implicit method* (E-MPS) (Sainju & Regmi, 2014).

However, at the moment there is no clear support for this technique for microclimate modelling. However, there are some interests in modelling specific environments, such as coastal or marine environments (Luo et al., 2021) due to the ease of solving the free surface flow.

Generalities and Tools: on the use of code_saturne

The most widely used CFD tool for microclimate modelling is undoubtedly Envi-met software. In addition to solving conservation equations, the tool also integrates a radiative module, a pollutant transport model, and a range of soil models. For example, the action of the water body has already been studied for the purpose of thermal comfort in cities (Jacobs et al., 2020). However, the structure of the code prevents a more accurate and versatile use of the solution of the conservation equations, especially from the point of view of turbulence modelling. The main turbulence model is a $E-\epsilon$ model that does not allow a precise calculation of the kinetic energy in the walls, linked to the interaction with the atmosphere. A specific $k-\epsilon$ (RNG or Realisable) model has been implemented to solve this problem, but it does not seem sufficient to fully control the atmosphere versus ground interaction[10]. As said in Huttner, 2012: "users who are only interested in one specific element of urban microclimate can almost always find another software that delivers the desired results faster and possibly even more accurately". To determine specific thermoaerodynamic effects at the level of the floating photovoltaic power plant, several CFD tools appear to be relevant and can cover the microclimatic simulation. For example: Fluent/CFX and COMSOL (proprietary codes), Openfoam, code_saturne (open sources).

code_saturne is developed by the EDF R&D laboratory and provides an atmospheric module (Archambeau et al., 2004). The solver is based on the finite-volume approach, with a colocated arrangement for velocity and scalar fields. Equations (2.7),(2.8) and (2.9) are solved with the dry atmosphere flavour or even with the shape of the wet atmosphere. Moreover, code_saturne is known to be massively parallel and runs on distributed memory architectures (Neau et al., 2020). Therefore, it allows us to calculate microclimatic scales as large as the mesoscale. To complete the large resources available for microclimatic studies, a radiative solver that covers two- or three-dimensional simulations is also implemented.

The code_saturne solver is adapted to compute the Navier-Stokes equation but also provides several built-in models to perform radiative transfers or simulate ground behaviour. On the other hand, some authors have used code_saturne in a strong coupling manner to improve the calculation of code_saturne submodels. For example, in Daviau, 2016, code_saturne and *BuildSysPro* are coupled so that the heat of the building is better simulated and helps to capture the flow behaviour in the urban environment. Another coupling is performed in SOLENE-microclimat with the SOLENE code to solve the thermal radiation equation; see Miguet and Groleau, 2002.

Turbulence models

The Reynolds stress component is the elephant in the room when one wants to perform airflow modelling. Basically, three methods are used to solve Reynolds stresses (Equation (2.10)). The

---

[10] The interested reader may refer to the review of (Toparlar et al., 2017) to get an idea of the possibility of Envi-met and its range of applicability

first one consists of directly solving the Navier-Stokes equation without modelling the turbulence, the mesh size being such that the finest eddies (as well as the biggest) are caught. This strategy, Direct Numerical Solution (DNS), pain point is the calculation cost that does not allow for a large use of the method for flow with a high Reynolds number. A variation of the strategy consists in filtering the scale of the eddies to model. Large-Eddy Simulation (LES) assumes that the largest eddies must be calculated because they provide the largest part of the energy spectrum. On the other hand, the little eddies can be modelled through a subgrid model (Smagorinsky, ...). It leads to a cost-effective simulation, but mesh resolution is still a challenge in spreading LES at the industrial level. There is still a second strategy to model the Reynolds stress through algebraic relations, first-order transport equations, or second-order transport equations. The objective being similar in both cases, calculating the turbulent viscosity through assuming properties of the eddies behaviour (mixing length, kinetic turbulent energy, dissipating turbulent rate, characteristic frequency of eddies, etc.).

code_saturne embeds several methods to determine Reynolds stress, such as first-order[11] and second-order[12] models as well as large-eddy simulation and even DNS. The standard tuning of code_saturne is applied for all turbulence approaches. The parameters used hereafter are recalled in A.4.

Wall functions

When the Navier-Stokes equations are not solved directly, one issue still remains for the meshing cells that are located near the walls. From a technical point of view, the calculation of the Navier-Stokes equation is closely related to the distance of the cell centre to the wall so that the universal law of the wall described in Section 2.2.1.4 should hold with the *good level* of viscous effect. That is, a first cell located at $y^+ = 2$ must not integrate the same level of viscosity as a cell located at $y^+ = 50$. Therefore, wall functions are numerical bridges that ideally solve this issue by artificially describing the *proper* good level of viscosity[13].

A strength of code_saturne lies in the ability to adjust the wall functions and thus switch from one to the other with respect to the type of application involved. A.4 gives more details of the embedded laws in code_saturne. Scalars and vector fields are also attributed to specific wall functions.

Velocity wall functions

Considering a 2-D cell with a wall boundary condition on one side (fig. 2.4), and denoting d the distance from the wall to the centre of the cell I', $u_\star$ the friction velocity on the wall, the simplified bulk momentum equation in the first cell of the grid is as follows:

$$(\mu + \mu_T)\frac{\partial u}{\partial y} = \tau_w \tag{2.24}$$

---

[11] Eddy Viscosity Models

[12] Reynolds Stress Models

[13] it should be understand that in some cases that do not match the hypotheses given in Section 2.2.1.4, the wall function should add more or less viscous effect

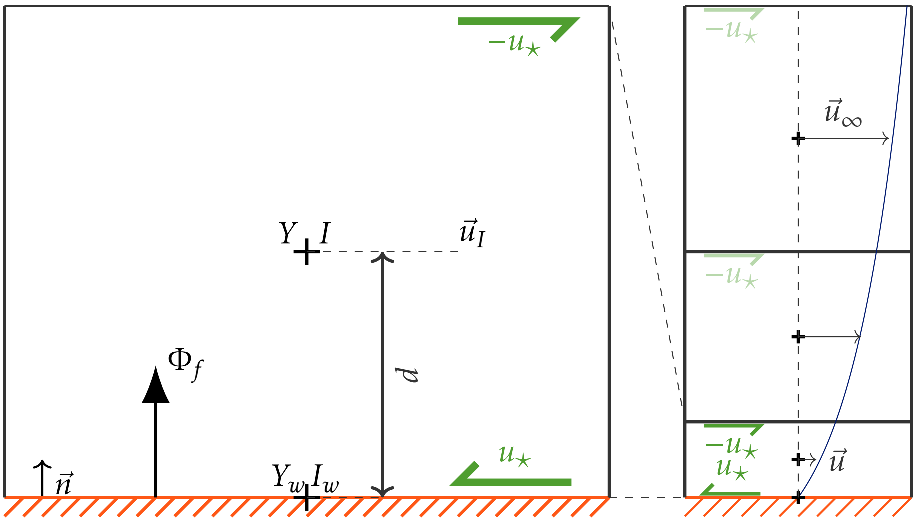

Figure 2.4–*Illustration of a wall-bounded cell and the associated numerical values used in code_saturne to compute the velocity and scalar. The first cell physical quantities are than used to determine the bulk motion in the flow above the wall (right-hand-side).*

Turning Equation (2.24) into non-dimensional using $u_+ = \frac{u_r}{u_\star}$[14] and $y_+ = \frac{y u_\star}{\nu}$[15], the dimensionless velocity profile is computed as:

$$\frac{y^+}{u^+} = \frac{y^+}{\frac{1}{\kappa} ln\left(\frac{y+z_0^{loc}}{z_0^{loc}}\right)} \tag{2.25}$$

Where z_0^{loc} is the local roughness of the wall in the case of a rough wall. code_saturne allows the user to choose between rough and smooth wall conditions, in this second case a linear velocity profile is assumed. More options are available when the user wants to declare a more realistic profile by tweaking an empirical two-layer law; for more details, see A.4 and the code_saturne user guide.

Scalar wall functions

The scalar function can also be applied in a fashion similar to the velocity wall functions. The general philosophy of code_saturne is to solve a one-cell heat budget using scalar diffusivities (laminar and turbulent), and it reads:

$$(\Phi_Y)_f = \int_\Omega \left(\kappa \frac{\partial Y}{\partial x_i}\vec{e_i} - \rho\overline{\vec{u}'Y}\right).S \tag{2.26}$$

where S is the shared surface of the cell with the wall boundary. The equation is made non-dimensioned such as:

$$\left(\frac{1}{\sigma} + \frac{1}{\sigma_T}\frac{\nu_T}{\nu}\right)\frac{\partial Y_+}{\partial y+} = 1 \tag{2.27}$$

with $Y_+ = \frac{Y-Y_w}{Y_\star}$. The scalar wall function $\frac{y_+}{Y_+}$ is used to determine the transfer rate coefficient as follows:

$$h_I^Y = \frac{C\mu}{d}\frac{y_+}{Y_+} = \frac{\kappa}{d} \times \frac{y^+}{Y^+} \tag{2.28}$$

---

[14] u_r is the velocity field projected within the wall plane

[15] It reads $\left(1 + \frac{\mu_T}{\mu}\right)\frac{\partial u_+}{\partial y_+} = 1$

in which C is the diffusion ratio of the scalar. Denoting the scalar roughness length $z_{0,Y}$, the turbulent number Prandtl/Schmidt σ_T and the non-dimensioned roughness length for the scalar Y as $y_{0,+} = \frac{\sigma_T}{\kappa\sigma}$, the computed scalar wall function is:

$$\frac{y^+}{Y^+} = \frac{y^+}{\frac{\sigma_T}{\kappa} ln\left(\frac{y_+}{y_{0,+}}\right) + \sigma y_{0,+}} \tag{2.29}$$

The dimensionless scalar profile $\frac{y^+}{Y^+}$ can also be modified by empirically determining two- and three-layer laws; see A.4 for more details.

2.3/ External Flows in Solar Arrays as Grid-Aligned Obstacles

2.3.1/ Lumped Theory of Roughness for Bluff-bodies

The parameters z_0 and d_0 in Equation (2.14) are of great interest, as they are intimately related to surface geometry (asperities, motif distribution [periodic, random], mean height); they allow one to characterise the influence of the surface on airflow. Tables of values of z_0 have been edited to cover various types of ground, from water surfaces to urban ones (Davenport, 1960) (initially constructed on the power law instead of logarithmic law constants), (Wieringa, 1992). These values are fundamentally not adapted to describe what happens in the vicinity of the surface; they only describe airflow above a certain level. The threshold above which the use of z_0 is valid to describe the wind velocity profile consists of a certain distance expressed on z_0 ($\simeq 20z_0$)(Wieringa, 1996) or on the height of the obstacle ($H+\Delta$ where H is the height of the obstacle, $\Delta \simeq [1.5, 4.5]$(Grimmond & Oke, 1999)). However, tables are rarely adapted to a specific environment composed of defined obstacles. Furthermore, it is not uncommon to observe the evolution of roughness over time, for example, in the case of croplands with interannual cycles, which ultimately results in a conductance disparity (Kim & Verma, 1990). Additionally, the obstacle motion modifies the z_0 value; this is especially the case with crops, canopies, or above water surfaces. This special case is covered by introduction within the z_0 determination of the wind speed (Q. Zhang et al., 2012) or when possible friction velocity (Charnock, 1955), (Amorocho & DeVried, 1981). Therefore, some authors have developed tools based on micrometeorological measurement or morphometric studies to determine z_0 values adapted to a given situation.

2.3.2/ Assessing the Roughness of an External Scene

Micro meteorological

Micro climatic strategies are based on anemometer measurement systems. The main wind components (mean and turbulent profiles) are used together with a set of adjoining assumptions to obtain the desired value. Here, the focus is on the roughness value and not the displacement height. A review of the main technique is given in Wieringa, 1996 The first consisted of directly applying the relation of Equation (2.14) using two anemometers at two different heights. It results in the following relation:

$$\frac{U_1}{U_2} = \frac{\ln(z_1/z_0)}{\ln(z_2/z_0)} \tag{2.30}$$

Standard anemometers can be used to make measurements. The second strategy based on turbulence uses the standard deviation of wind speed at a single location as follows:

$$\frac{\sigma_u}{U} = \frac{1}{\ln(z/z_0)} \tag{2.31}$$

The last strategy remains in the measurement of gustiness $G = \frac{U_{max}}{U}$ ($\langle G \rangle$ being the median of the time series) and assuming Gaussian wind variation with standard variation σ_u, it leads to:

$$z_0 = z_s \exp\left(-\frac{A f_T E_U}{\langle G \rangle - 1 + A - f_T A}\right) \tag{2.32}$$

whence f_T is a factor between 1 and 1.1 taking into account the time integration window, U_t, E_U, and A are, respectively, the wavelength of the gust (product of the duration t of the extreme gust and the average wind $\overline{U}$), the eccentricity of the gusts and an attenuation factor due to the operating parameters of the anemometer. Originally developed in Wieringa, 1973, other methods have been developed that refer to different gustiness assumptions as in Beljaars, 1987. The accuracy of the later method is generally dependent on z_0 itself; values of low magnitude z_0 can evolve dramatically (3 or 4 times), while high values of z_0 are more robust (the deviation 15% is evaluated in Verkaik, 2000).

Based on Equation (2.13) and the components of wind speed, it is also possible to directly describe the friction velocity $u_\star$, it reads:

$$u_\star = \left[\left(\overline{u'_y u'_x} \right)^2_{z_0} + \left(\overline{u'_z u'_z} \right)^2_{z_0} \right]^{0.25} \tag{2.33}$$

Morphometry of Obstacle Arrays

The morphometric strategy proposes linking aerodynamic parameters with geometric parameters that characterise obstacles: in particular, shape, number, and arrangement. It is thus relatively well suited to theoretical studies and allows for the prediction of aerodynamic characteristics based on elements that can be measured in the field. It is also adapted to cover rather large spaces when they are composed of periodic or relatively periodic elements. To validate this type of methodology, it is necessary to set up a micrometeorological strategy adapted to a certain point in the domain according to the angle of interest of the research (inter facial zone, atmospheric zone). in Grimmond and Oke, 1999, a review of the morphometric parameters is proposed and the main methods are listed, among which we find: methods based on the average height of obstacles $\overline{z_H}$, based on a combination of height and aerial fraction of the plan $\frac{\overline{A_P}}{A_T}$, based on a combination of the average height and the frontal area index $\frac{\overline{A_F}}{A_T}$ or based on the aspect ratio of the canyon $\frac{\overline{W}}{z_H}$. For example, a methodology based on the frontal index area proposed in Raupach, 1992 regarding the displacement of the zero plane and the length of the roughness is expressed as follows:

$$\frac{z_d}{\overline{z_H}} = 1 + \left\{ \frac{\exp\left[-(c_{d1} 2\lambda_F)^{0.5} - 1 \right]}{(c_{d1} 2\lambda_F)^{0.5}} \right\} \tag{2.34a}$$

$$\frac{z_0}{\overline{z_H}} = \left(1 - \frac{z_d}{\overline{z_H}} \right) \exp\left(-k \frac{U}{u_*} + \psi_h \right) \tag{2.34b}$$

$$\frac{u_*}{U} = \min\left[(c_s + c_R \lambda_F)^{0.5}, \left(\frac{u_\star}{U} \right)_{\max} \right] \tag{2.34c}$$

where ψ_h is the influence function of the roughness sublayer, c_S and c_R are the drag coefficients, and c_{d1} is a free parameter.

However there is no general rules driving the selection of one methodology in front of others, and, in addition, the versatility of the results is still weak for field studies. A major drawback being that measurements implies errors due to non-homogeneous flow states, and the complexity of the bluff body flow being not totally caught.

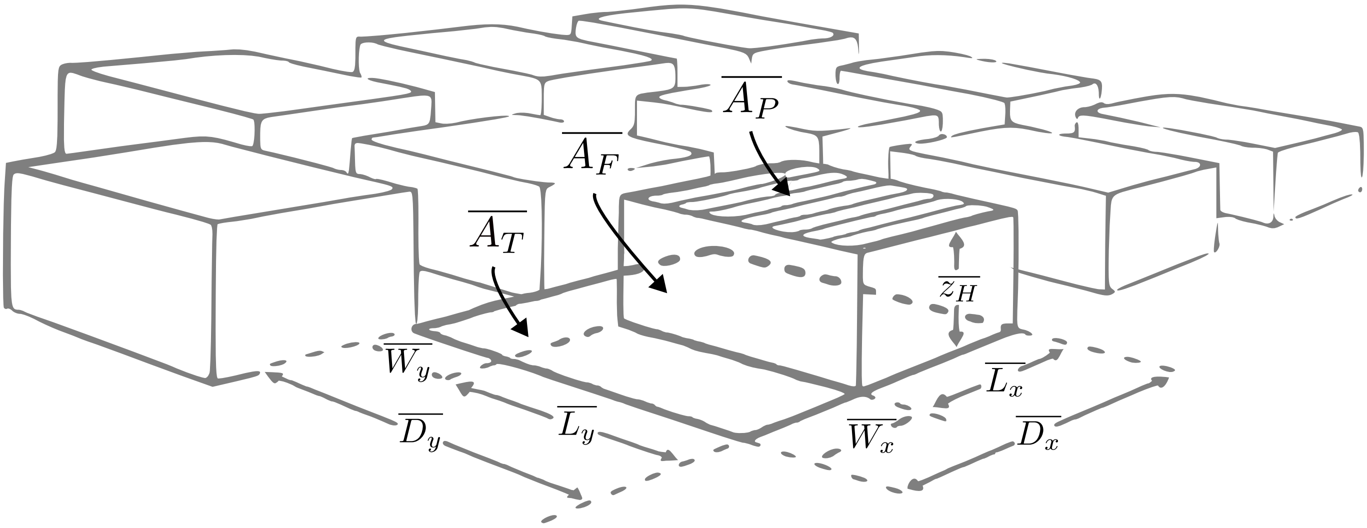

Figure 2.5–*Definitions of geometrical properties for a staggered array of buildings. Retrieved and adapted from (Grimmond & Oke, 1999)*

Theory of Local Airflow for Periodical Obstacles

Although the roughness length describes the influence of the ground roughness on the overall flow dynamics, no information is disclosed about the aerodynamic phenomena around the elements that obstruct the flow. These effects have been studied mainly in the case of urban flows in order to qualify the thermal exchanges in canyons whose geometrical shapes are essentially diverse. The reader interested in this subject can refer to the work of Merlier (Merlier, 2016). The complexity of these flows is not the subject of this thesis; however, we wish to describe here the main dynamic effects that are likely to be reproduced in the case of photovoltaic power plants, which are, in the same way as buildings, immobile structures.

In the case of two-dimensional blocking elements, several flow regimes can appear depending on geometrical criteria:

- A regime of isolated roughness in which the flow lines reconnect with the ground after the obstacle and those before reaching the next obstacle,
- A wake interference regime, a recirculation zone takes place between the elements, the lines do not reattach the ground and the flow is locally disturbed
- A skimming flow regime in which a vortex forms between the obstacles and is fed by the upper flow region.

Geometrical criteria are, most of the time, the height of the obstacle divided by the spacing distance. At the local scale (between obstacles and at their surfaces), several complex aeraulic phenomena appear, which are linked to the turbulence and kinetic energy of the flow. Among them, we can note the phenomenon of front, rear, and point stagnation as well as flow separation. In the first case, it concerns zones where the local fluid velocity is zero, while flow separation is mainly caused by geometries with sharp edges: the fluid boundary layer detaches the surface from the solid (this generally results in a wake zone).

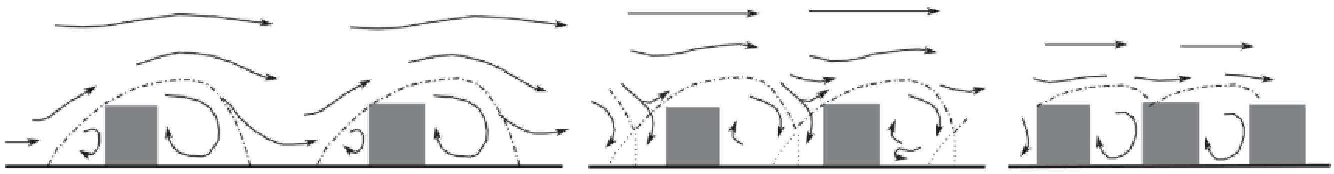

Figure 2.6–*The three standard flow regimes: the isolated roughness (left-hand side), the wake interference regime (middle) and the skimming regime (right-hand side). Retrieve from (Merlier, 2016).*

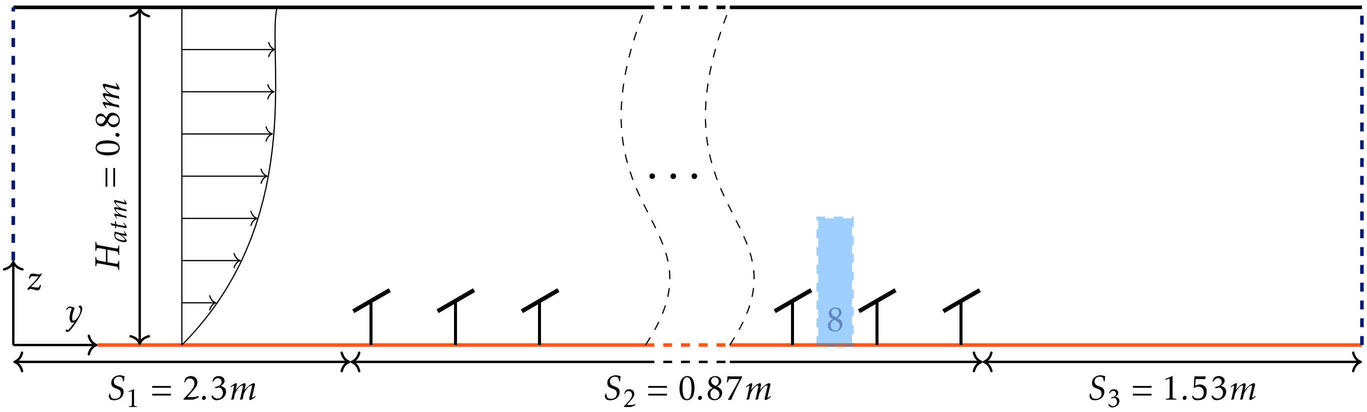

Figure 2.7–*2-D scheme of the wind tunnel experiment in Glick, Smith, et al., 2020. Modules are spaced by* 84 mm, *corresponding to a ground coverage ratio of* 58 %. *The inclination is set to* 30°. *Blue space shows the location of the PIV measurement (*8^{th} *to the* 9^{th} *row).*

2.3.3/ Principle Literature for Solar Arrays

The Portland Wind-Tunnel Experiment

The experiment consists of ten rows of thin plates as described in Figure 2.7, facing an atmosphere wind profile in a 800 mm per 1200 mm ($\mathcal{H}_{\text{atm}} \times L_{atm}$) wind tunnel. Plates are made of four layers, as the front and rear surfaces are aluminium-based materials. A Kapton heater allows one to control the heat flux imposed inside the module. The last layer is composed of aerogel insulation to mimic the effect of temperature elevation on the rear face of photovoltaic modules. The total dimensions of the system are 254 mm wide, 50.8 mm high and 5.3 mm in thickness; a row of the solar array is composed of four elements. The plates are held above ground at a distance of 38 mm. Various module arrangements are possible, mainly with different array tilts.

The experiment includes a particle laser velocimetry (PIV) system that allows one to determine, due to the displacement of inert particle swarming at the entrance of the wind tunnel, the instantaneous velocity at any point in the measurement space. The latter is constrained by the optical angle of the CCD camera (charge-coupled device); the measurement area obtained in the experiment is contained in a 2-D plane of approximately 20 cm square.

Two field views are carried out, the first being carried out upstream of the plant to monitor the inflow regime. The regime is controlled by the integration of roughened elements (metal and plastic chains) before the array and by a passive grid at the entrance of the test pipe. The turbulent intensity upstream reaches 11 %, while the velocity profile can be fitted with a logarithmic law such as $u_\star = 0.36\,\mathrm{m\,s^{-1}}$ and $z_0 = 5\,\mathrm{mm}$, which corresponds to a rough atmospheric boundary layer (considering the small size of the experiment).

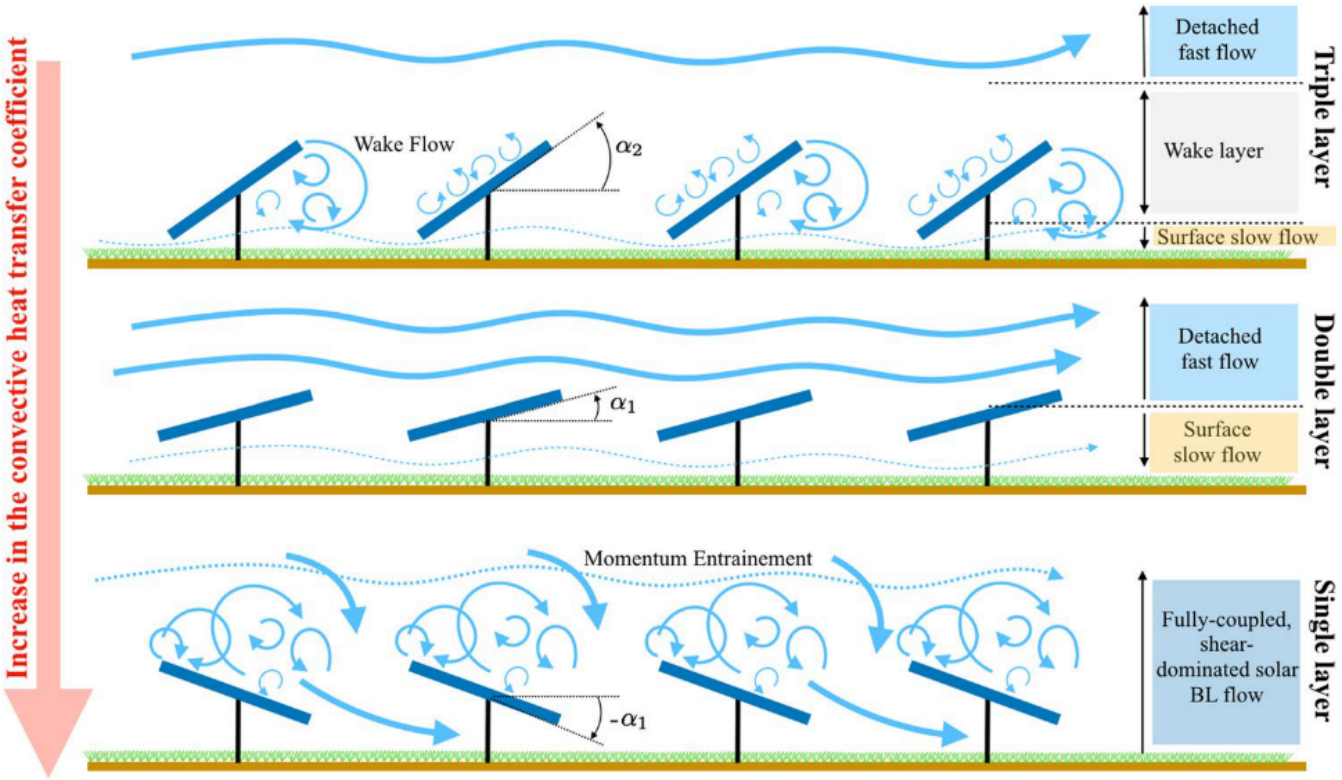

Figure 2.8–*Theoretical macrobehaviour of airflow in solar array retrieved from (Glick, Ali, Bossuyt, Calaf, et al., 2020).*

The second area of interest is located between the eighth and ninth rows of the array. The periodicity of the flow is supposed to be reached at this stage; the largest part of the recirculation zone is included in the measurement space. Since the PIV system cannot measure the velocity gradient adjacent to the wall, both on the floor and on the elements of the thin plate, part of the area of interest remains unmeasured.

A power density of $450\,\mathrm{W\,m^{-2}}$ is imposed in the centre of the thin plate through the heating system according to the nominal value of direct solar radiation ($\phi_{\mathrm{sw,poa}} = 1050\,\mathrm{W\,m^{-2}}$). The temperatures of the module element are measured at different levels through a copper-type T thermocouple constant. They are located in a cavity underneath the front surface of the thin plates (the cavity is filled with conductive silicone to ensure thermal contact) and at the heating system level.

Morphometric Theory in Solar Array

The setup is particularly suited to analyse the influence of the configuration and the intensity of turbulence on flow dynamics; it also gives a strong indication on the thermal performance of modules representative of the array (Glick, Ali, Bossuyt, Recktenwald, et al., 2020), (Smith et al., 2020). The flow shows three separate behaviours according to the module tilt and the wind direction. The first ”three-layer model” appears when the tilt remains relatively low (depending on the module height) and when the wind blows the front module faces. In this case, a submodule area, a wake zone, and an atmosphere area are experienced. The higher the tilt, the more the module tips act on the atmosphere area, so that the averaged wind profile in the lower part of the zone is linear with respect to the height direction. This influences both the front-module face and the rear-face in terms of overall turbulent mixing. When the tilt and the height between ground and module bottom are low, the three-layer model fades away and a ”two-layer model” is experienced. In this situation, the wake area is integrated into the surface flow area and reduces the bulk flow velocity. This can lead to more heat stored under the module as the fluid motion is reduced in this area. Finally, a single-layer model is obtained for the wind tail directions due to flow separation, which does not reattach between modules and suffers from wall constraints at the ground level.

A thermal resistance model is used to determine the surface heat exchange on the front and rear sides of the module element; for the front side, it is defined as follows:

$$Nu_{ad,up} = \frac{\frac{T_{Ht} - T_{up}}{R_{fnt}} \times L}{\lambda \times \left(T_{up} - T_{ref}\right)} \tag{2.35}$$

where $Nu_{ad,up}$ is the adiabatic Nusselt number for the front side of the module, T_{Ht}, T_{up} and T_{ref} are, respectively, the temperature of the heating system, the surface temperature and a reference temperature,R_{fnt} is the thermal resistance of the front material, L is a characteristic length based on the length of the element and λ is the air conductivity. Adiabatic Nusselt number superposes the local (element-wise) Nusselt number with a kernel function to take into account nonuniform temperature or heat flux within the staggered array (Anderson & Moffat, 1992). In the solar array experiment, this concept is built into the value T_{ref}, which is defined at the surface temperature of the eighth element when the element heater is turned off, but not the other elements. According to the layers indicated in these investigations, the magnitude of convective transfer evolves throughout the possibility of configuration. The first threshold is reached at tilts around 30°, the convective magnitude being maximum at the rear face level. Above, a pullback is observed. In contrast, the lower the tilt, the better the convective transfer on the rear side. For reverse wind, the gain on the rear face outperforms the loss observed on the front module side (-25%, 104%, respectively). An optimum between general exchange is found; however, it is not constant with respect to the Reynold number; the optimum interval is constrained between 0° and 10°. Both heat rates also observe a positive correlation with increasing turbulent intensity.

This analysis confirms the possibility of improving temperature management through system-level modifications; it also indicates that wind turbulence influences the system at the array level and should be assessed in an array-based evaluation of convective transfers. in Glick, Ali, Bossuyt, Recktenwald, et al., 2020, a correlation is defined for the nominal case observed in the wind tunnel:

$$\langle Nu \rangle_L = 0.0238 Re^{\frac{4}{5}} Pr^{\frac{1}{3}} \tag{2.36}$$

In a fashion similar to the flat-plate correlations for convective transfer depicted in the first chapter. However, the magnitude of the constant is found to be lower than that of the state-of-the-art correlations.

Full-Scale Experiment

Once at full scale, several issues are coupled with fundamentally turbulent issues related to the atmosphere: the availability of data on large systems and the relevance of point measurements are the two main issues. A first study on the performance of power plants related to the direction of the wind (Vasel & Iakovidis, 2017) has been carried out on the Hadley powerplant, [16], leads to

---

[16] the plant covers an area of 12 ha for more than 19,000 modules

the conclusion that electrical production is higher on a global scale when the wind comes from the south, behind the module; the maximum increase in electrical production is obtained at 24% of the nominal production for the elements to the north of the plant. As elements to the south of the plant are warmer than elements to the north in this situation, module temperature heterogeneity is assumed but not evaluated. From an experimental point of view, the wind measurement is carried out at about 7.5 m above the ground, and the ”south” or ”north” character is considered by splitting the wind rise into 2. These assumptions are consistent with the assumed development of the ABL (constant direction with height). A similar experiment carried out in Oxfordshire on a similar sized power plant also determined the same cooling phenomena (Waterworth & Armstrong, 2020). Interestingly, wind velocity was not found to correlate the power production; although the theoretical phenomenon includes temperature / power production.

Although previous publications allow us to give a trend of improved production due to cooler thermal operating conditions depending on the wind direction, the absence of thermal measurements prevents us from verifying the level of thermal heterogeneity at the scale of a park. As a result, some thermally related phenomena (cell degradation) have not yet been associated with the uncertainty of the temperature. To overcome this weakness in industrial projects and to have a reliable temperature estimate, thermal measurements must be dispersed on a global scale. An IEC61724:2021 standard states that six probes are needed to obtain a reliable average of the operating temperature of the modules. In Maeda et al., 2022, a prototype of 84 modules distributed in 3 strings was monitored over several seasons to determine the level of heterogeneity between the modules in the centre and the modules at the edge of the system. A mean absolute difference of 6.79 °C is measured and leads to an uncertainty of the order of 1.6% in electrical output. The temperature heterogeneity observed in the prototype is a function of the incident irradiance in the module; therefore, the most optimal operating conditions for electricity production are also those with the greatest uncertainty in terms of temperature. Of course, this situation is unrealistic for industrial situations, because of the absence of module lines in front and behind the measured system. The three atmospheric zones experienced by Glick are naturally absent from the full-scale experiment.

Numerical Simulation

Initially, the plant scale was studied to take into account the effects of aerodynamic loads on structures[17]. In fact, the objective functions of the studies are rather related to the aerodynamic coefficients Cd, Cl and Cm which describe the drag, lift and moment actions on the system[18]. In Shademan et al., 2014, a morphometric study is carried out on a subset of four strings for a single wind direction facing the module. Drag and lift coefficients are shown to be functions of the ratio $\mathcal{L}_\mathrm{m} \times \cos(\theta_\mathrm{m})$ to $\mathcal{S}_\mathrm{m} - \mathcal{L}_\mathrm{m} \times \cos(\theta_\mathrm{m})$ and that the lower this ratio, the more the forces applied to the structure are reduced. This effect is attributed to the emergence of a large pressure differential in front and behind the module, which directs the creation and intensity of a turbulence zone behind the obstacles. Of the four rows studied, the first two rows show relatively high edge effects compared to the following rows. Therefore, it is questionable whether an established regime is obtained at the end of the four rows studied. These results are obtained with a $k-\omega SST$ turbulence model with a mixed meshing strategy, structured for elements far from the modules, prismatic for elements close to them, and structured for cells adjacent to the panels. The main

---

[17] The industrial targets is to match the standards *IEC 61215* (that is, the 24kPa charge in a homogeneous wind field)

[18] Mathematically they read $C_x = F_x / \left(0.5 \rho U_\mathrm{w}^2 A\right)$ where F_x is the force acting on the module in a given direction

conclusion of this study is that, at the array scale, the geometrical parameters are key parameters in the flow patterns. The initial choice of the authors is a combination of $\mathcal{L}_{\mathrm{m}}$, θ_{m}, and $\mathcal{S}_{\mathrm{m}}$.

Using a fixed power plant geometry, Jubayer and Hangan, 2016 shows the formation of a new turbulent structure around the systems for oblique winds. These lead to change the perception of loads for elements *in the middle* of the power plant; the latter present higher levels of loads than for winds that come from perpendicular to the system. As the system consists of 5 rows of modules, the question of spatial homogeneity of the flow is still open, the computational cost to reach this number of rows reaching 1.5×10^6 cells for the coarsest mesh. We also note that the same turbulence assumptions are applied in Shademan et al., 2014. In addition to the first publication, it also seems that the direction of the wind θ_{w} may interact differently in the array system.

From a structural point of view, the effects of the wind on the modules have an impact on the vibrations of the whole system. Thus, as for the module simulation in a standalone situation, coupling with a structural mechanics calculation code allows one to highlight the preferential vibration frequencies in the power plant according to the directions and the recirculation zones. In Pascal, 2022, the coupling of the CFD and structural mechanics calculations shows that oblique winds are harmful to the photovoltaic cells, whereas tailwinds have an impact on the glass of the front modules. Taking into account all modules at the scale of the power plant, coupled with different atmospheric situations, thus allows for improved durability of the structures and their optimisation.

Recently, the topic of floating photovoltaics with a CFD approach was proposed in Lindholm et al., 2022 for the floating arrangements of Ciel et Terre®. This time, the topic of interest was the flow effect on convective transfers seen by the modules within the array. Compared to previous studies at the array scale, the structure is explicitly represented in the numerical simulation. Therefore, the flow is disturbed by the array of regular thin plates (18 strings are considered) and their respective mono-float systems. The wind direction is set to a constant such as $\theta_{\mathrm{w}} = 0°$ and the turbulence model is switched to the $k-\epsilon$ model. Radiative transfer was also integrated in the computation; therefore, they were able to derive a U_{values} linearly dependent on wind velocity as:

$$\mathrm{U}_{values} = 17.7 + \overline{U_{\mathrm{w}}} \times 5.5 \tag{2.37}$$

Even if the strategy in the work assumes a global U_{values} for the module, the wind-related coefficient is found to be higher than in any other installation. On the other hand, the constant value is rather low in front of experimentally calculated correlations. They also found a weak relation of the water temperature as a direct cooling factor on the module temperature, and it is stated that the direct effect can account for at most 1 °C in temperature decrease compared to a reference set-up. A final assessment gives credit to the impact of the structure on the reduction of heat removal efficiency; a loss of $3.2\,\mathrm{W\,K^{-1}\,m^{-2}}$ in the U_{values} is observed when comparing floating and non-floating installations. In this case, the use of a CFD approach allows us to investigate the preferential roots of the cooling of floating modules, low-range or macroscopic flow modifications, thermal radiations, etc.

2.4/ Summary

This chapter has highlighted the intrinsic complexity of describing the airflow around photovoltaic modules when they are configured as power plants. In order to simplify the system to be described, several assumptions have been presented which allow to correctly describe the asymptotic behaviour of the airflow under typical atmospheric conditions. The natural scales of the atmosphere have been introduced in this sense. In the following work, the atmosphere will be addressed in the light of the neutral atmosphere, which is a relevant representation when the driving force of the flow is related to frictional forces.

In addition to the chaotic nature and stochastic fluctuations that act on the dynamics of the atmospheric system, the modelling stage necessarily involves approximations that have a definite influence on the quality of the numerical simulation of the system. The closure of the conservation equations, especially for those of motion, as well as the simulation of the behaviour of the fluid close to the walls (modules, lakes), have been mentioned as the two major elements that make the numerical simulation an accurate and robust tool. While the first element is key in the notion of computational cost, the second element also acts on the relevance of the simulation of the interactions between the fluid and solid elements. In order to be able to completely control the two aspects, the qualities of the code_saturne software were introduced; we will endeavour in the continuation of the work to use its assets to unlock modelling which is usually too costly for the industrial companies.

Finally, the integration of photovoltaic power plants within the atmosphere has received relatively little attention in the literature, in contrast to standalone systems. Global scale studies especially on thermal prospective suffer from a lack of available data, they are mainly reserved to numerical mechanical evaluation (structure or module stresses). However, the latest work carried out at Portland University in wind tunnel is a good starting point for building reliable numerical representations. We will make use of these experimental results to support the proposed numerical implementation. From the point of view of numerical simulation, it is nevertheless noted that there is a lack of relation between the natural scales of the atmosphere and the arrangement of the modules in the shape of a utility-scale powerplant. Therefore, simulating the atmosphere airflow that blows the module in the array fall into the scope of the work.

2.4/ References

Amorocho, J., & DeVried, J. (1981). A new evaluation of the wind stress coefficient over water surfaces. *Journal of Geophysical Research*, *86*(C5), 4307. https://doi.org/10.1029/jc086ic05p04307

Anderson, A. M., & Moffat, R. J. (1992). The adiabatic heat transfer coefficient and the superposition kernel function: Part 1—data for arrays of flatpacks for different flow conditions. *Journal of Electronic Packaging, Transactions of the ASME*, *114*(1), 14–21. https://doi.org/10.1115/1.2905435

Archambeau, F., Méchitoua, N., & Sakiz, M. (2004). Code Saturne: A Finite Volume Code for Turbulent flows - Industrial Applications. *International Journal on Finite Volumes*, *1*(1).

Assouline, S., Narkis, K., & Or, D. (2010). Evaporation from partially covered water surfaces. *Water Resources Research*, *46*(10), 1–12. https://doi.org/10.1029/2010WR009121

Assouline, S., Narkis, K., & Or, D. (2011). Evaporation suppression from water reservoirs: Efficiency considerations of partial covers. *Water Resources Research*, *47*(7), 1–8. https://doi.org/10.1029/2010WR009889

Aubinet, M., Vesala, T., & Papale, D. (2012). *Eddy Covariance: A pratical Guide To Measurement and Data Analysis*. https://doi.org/10.1007/978-94-007-2351-1

Beljaars, A. C. M. (1987). The Influence of Sampling and Filtering on Measured Wind Gusts. *Journal of Atmospheric and Oceanic Technology*, *4*(4), 613–626. https://doi.org/10.1175/1520-0426(1987)004⟨0613:TIOSAF⟩2.0.CO;2

Blanken, P. D., Rouse, W. R., Culf, A. D., Spence, C., Boudreau, L. D., Jasper, J. N., Kochtubajda, B., Schertzer, W. M., Marsh, P., & Verseghy, D. (2000). Eddy covariance measurements of evaporation from Great Slave Lake, Northwest Territories, Canada. *Water Resources Research*, *36*(4), 1069–1077. https://doi.org/10.1029/1999WR900338

Bontempo Scavo, F., Tina, G. M., Gagliano, A., & Nižetić, S. (2021). An assessment study of evaporation rate models on a water basin with floating photovoltaic plants. *International Journal of Energy Research*, *45*(1), 167–188. https://doi.org/10.1002/er.5170

Brutsart, W. (1982). *Evaporation into the Atmosphere*. https://doi.org/10.1017/978-94-017-1497-6

Charnock, H. (1955). Wind stress on water. *Quarterly Journal of the Royal Meteorological Society*, *81*(350), 639–639. https://doi.org/10.1002/qj.49708135026

Condie, S. A., & Webster, I. T. (1997). The influence of wind stress, temperature, and humidity gradients on evaporation from reservoirs. *33*(12), 2813–2822.

Cooley, K. R. (1970). Energy Relationships in the Design of Floating Covers for Evaporation Reduction. *Water Resources Research*, *6*(3), 717–727. https://doi.org/10.1029/WR006i003p00717

Dalton, J. (1802). Experimental essays on the constitution of mixed gases ; on the force of steam or vapour from water and other liquids in different temperatures, both in a Torricellian vacuum and in air ; on evaporation ; and on the expansion of gases. *Manchester Literary and Philosophical Society*, 535–602.

Davenport, A. G. (1960). Rationale for determining design wind velocities. *ASCE Journal of the Structural Division*, *86*(5), 39–68.

Daviau, N. (2016). *Études fines des échanges énergétiques entre les bâtiments et l ' atmosphère urbaine* (Doctoral dissertation).

De Moor, G. (2006). *Couche limite atmosphérique et turbulence - Les bases de la micrométéorologie dynamique* (M. France, Ed.).

From, E., & Kinneret, L. (1993). Eddy Correlation System Measurements and Energy Budget Estimates. *Water Resources*, *29*(4), 901–910.

Glanz, D. J. G. T. O. (1973). Lincoln Lake ecologic study. *Water Resource Engineering*.

Glick, A., Ali, N., Bossuyt, J., Calaf, M., & Cal, R. B. (2020). Utility-scale solar PV performance enhancements through system-level modifications. *Scientific Reports*, *10*(1), 1–9. https://doi.org/10.1038/s41598-020-66347-5

Glick, A., Ali, N., Bossuyt, J., Recktenwald, G., Calaf, M., & Cal, R. B. (2020). Infinite photovoltaic solar arrays: Considering flux of momentum and heat transfer. *Renewable Energy*, *156*, 791–803. https://doi.org/10.1016/j.renene.2020.03.183

Glick, A., Smith, S. E., Ali, N., Bossuyt, J., Recktenwald, G., Calaf, M., & Cal, R. B. (2020). Influence of flow direction and turbulence intensity on heat transfer of utility-scale photovoltaic solar farms. *Solar Energy*, *207*(November 2019), 173–182. https://doi.org/10.1016/j.solener.2020.05.061

Grimmond, C. S. B., & Oke, T. R. (1999). Aerodynamic Properties of Urban Areas Derived from Analysis of Surface Form. *Journal of Applied Meteorology*, *38*(9), 1262–1292. https://doi.org/10.1175/1520-0450(1999)038⟨1262:APOUAD⟩2.0.CO;2

Helfer, F., Zhang, H., & Lemckert, C. (2009). Evaporation Reduction by Suspended and Floating Covers: Overview, Modelling and Efficienc. *Urban Water*, (16).

Hipsey, M. R., Bruce, L. C., Boon, C., Busch, B., Carey, C. C., Hamilton, D. P., Hanson, P. C., Read, J. S., De Sousa, E., Weber, M., & Winslow, L. A. (2019). A General Lake Model (GLM 3.0) for linking with high-frequency sensor data from the Global Lake Ecological Observatory Network (GLEON). *Geoscientific Model Development*, *12*(1), 473–523. https://doi.org/10.5194/gmd-12-473-2019

Hipsey, M. R., & Sivapalan, M. (2003). Parameterizing the effect of a wind shelter on evaporation from small water bodies. *Water Resources Research*, *39*(12), 1–9. https://doi.org/10.1029/2002WR001784

Horton, R. E. (1915). A New Evaporation Formula Developed. *78-4*, 196–200.

Huttner, S. (2012). Further development and application of the 3D microclimate simulation ENVI-met. *Mainz: Johannes Gutenberg-Universitat in Mainz*, 147. http://ubm.opus.hbz-nrw.de/volltexte/2012/3112/

J. F. Turner, J. (1966). Evaporation Study in a Humid Region, Lake Michie North Carolina. *Geological Survey Professinonal Paper*.

Jacobs, C., Klok, L., Bruse, M., Cortesão, J., Lenzholzer, S., & Kluck, J. (2020). Are urban water bodies really cooling? *Urban Climate*, *32*(January), 100607. https://doi.org/10.1016/j.uclim.2020.100607

Jubayer, C. M., & Hangan, H. (2016). A numerical approach to the investigation of wind loading on an array of ground mounted solar photovoltaic (PV) panels. *Journal of Wind Engineering and Industrial Aerodynamics*, *153*, 60–70. https://doi.org/10.1016/j.jweia.2016.03.009

Kim, J., & Verma, S. B. (1990). Components of surface energy balance in a temperate grassland ecosystem. *Boundary-Layer Meteorology*, *51*(4), 401–417. https://doi.org/10.1007/BF00119676

Lindholm, D., Selj, J., Kjeldstad, T., Fjær, H., & Nysted, V. (2022). CFD modelling to derive U-values for floating PV technologies with large water footprint. *Solar Energy*, *238*(April), 238–247. https://doi.org/10.1016/j.solener.2022.04.028

Luo, M., Khayyer, A., & Lin, P. (2021). Particle methods in ocean and coastal engineering. *Applied Ocean Research*, *114*, 102734. https://doi.org/10.1016/j.apor.2021.102734

Maeda, M., Nagaoka, A., Araki, K., & Nishioka, K. (2022). Practical and simplified measurements for representative photovoltaic array temperatures robust to climate variations. *Solar Energy*, *231*(October 2020), 243–251. https://doi.org/10.1016/j.solener.2021.11.035

McGloin, R., McGowan, H., McJannet, D., & Burn, S. (2014). Modelling sub-daily latent heat fluxes from a small reservoir. *Journal of Hydrology*, *519*(PB), 2301–2311. https://doi.org/10.1016/j.jhydrol.2014.10.032

Merlier, L. (2016). On the interactions between urban structures and air flows : A numerical study of the effects of urban morphology on the building wind environment and the related building energy loads To cite this version : HAL Id : tel-01368556.

Miguet, F., & Groleau, D. (2002). A daylight simulation tool for urban and architectural spaces-application to transmitted direct and diffuse light through glazing. *Building and Environment*, *37*(8-9), 833–843. https://doi.org/10.1016/S0360-1323(02)00049-5

Monin, A. S., & Obukhov, A. M. (1954). Basic laws of turbulent mixing in the surface layer of the atmosphere. *Tr. Akad. Nauk SSSR Geophiz. Inst*, *24*(151), 163–187.

Neau, H., Pigou, M., Fede, P., Ansart, R., Baudry, C., Mérigoux, N., Laviéville, J., Fournier, Y., Renon, N., & Simonin, O. (2020). Massively parallel numerical simulation using up to 36,000 CPU cores of an industrial-scale polydispersed reactive pressurized fluidized bed with a mesh of one billion cells. *Powder Technology*, *366*(March), 906–924. https://doi.org/10.1016/j.powtec.2020.03.010

Pascal, R. (2022). Effects of Wind Load on the Mechanics of a PV Power Plant. *WCPEC2022 Conf.*

Raupach, M. R. (1992). Drag and drag partition on rough surfaces. *Boundary-Layer Meteorology*, *60*(4), 375–395. https://doi.org/10.1007/BF00155203

Sainju, A., & Regmi, A. (2014). A Collision Model to Improve Stability of Explicit Moving Particle Simulation Method. (January 2016).

Shademan, M., Barron, R., Balachandar, R., & Hangan, H. (2014). Numerical simulation of wind loading on ground-mounted solar panels at different flow configurations. *Canadian Journal of Civil Engineering*, *41*(8), 728–738. https://doi.org/10.1139/cjce-2013-0537

Smith, S. E., Glick, A., Ali, N., Bossuyt, J., McNeal, J., Recktenwald, G., Calaf, M., & Cal, R. B. (2020). Configuration Effects on Flow Dynamics and Convective Behavior in Large-Scale Solar Arrays. *Conference Record of the IEEE Photovoltaic Specialists Conference*, *2020-June*, 2195–2196. https://doi.org/10.1109/PVSC45281.2020.9300740

Tobler, W. (1970). A COMPUTER MOVIE SIMULATING URBAN GROWTH IN THE DETROIT REGION. *Economic Geography*, *46*, 234–240. https://doi.org/10.1126/science.ns-13.332.462

Tominaga, Y., Sato, Y., & Sadohara, S. (2015). CFD simulations of the effect of evaporative cooling from water bodies in a micro-scale urban environment : Validation and application studies. *Sustainable Cities and Society*, *19*, 259–270. https://doi.org/10.1016/j.scs.2015.03.011

Toparlar, Y., Blocken, B., Maiheu, B., & van Heijst, G. J. (2017). A review on the CFD analysis of urban microclimate. *Renewable and Sustainable Energy Reviews*, *80*(June), 1613–1640. https://doi.org/10.1016/j.rser.2017.05.248

Vasel, A., & Iakovidis, F. (2017). The e ff ect of wind direction on the performance of solar PV plants. *Energy Conversion and Management*, *153*(October), 455–461. https://doi.org/10.1016/j.enconman.2017.09.077

Verburg, P., & Antenucci, J. P. (2010). Persistent unstable atmospheric boundary layer enhances sensible and latent heat loss in a tropical great lake: Lake Tanganyika. *Journal of Geophysical Research Atmospheres*, *115*(11), 1–13. https://doi.org/10.1029/2009JD012839

Verkaik, J. W. (2000). Evaluation of two gustiness models for exposure correction calculations. *Journal of Applied Meteorology*, *39*(9), 1613–1626. https://doi.org/10.1175/1520-0450(2000)039⟨1613:EOTGMF⟩2.0.CO;2

Vimal, S., & Singh, V. (2021). Re-discovering Robert E. Horton's Lake Evaporation Formulae: New Directions for Evaporation Physics. *Hydrology and Earth System Sciences Discussions*, (July), 1–37. https://doi.org/10.5194/hess-2021-234

Wang, K., & Dickinson, R. (2012). a Review of Global Terrestrial Evapotranspiration : Observation. *Reviews of Geophysics*, *50*(2011), 1–54. https://doi.org/10.1029/2011RG000373.1.INTRODUCTION

Waterworth, D., & Armstrong, A. (2020). Southerly winds increase the electricity generated by solar photovoltaic systems. *Solar Energy*, *202*(April), 123–135. https://doi.org/10.1016/j.solener.2020.03.085

Wieringa, J. (1996). Does representative wind information exist? *Journal of Wind Engineering and Industrial Aerodynamics*, *65*(1-3), 1–12. https://doi.org/10.1016/S0167-6105(97)00017-2

Wieringa, J. (1973). Gust factors over open water and built-up country. *Boundary-Layer Meteorology*, *3*, 424–441.

Wieringa, J. (1992). Updating the Davenport roughness classification. *Journal of Wind Engineering and Industrial Aerodynamics*, *41*(1-3), 357–368. https://doi.org/10.1016/0167-6105(92)90434-C

Wossenu, A., & Assefa, M. (2012). *Evaporation and Evapotranspiration - Measurements and Estimations*.

Yang, P., Chua, L. H., Irvine, K. N., & Imberger, J. (2021). Radiation and energy budget dynamics associated with a floating photovoltaic system. *Water Research*, *206*(September), 117745. https://doi.org/10.1016/j.watres.2021.117745

Zhang, Q., Zeng, J., & Yao, T. (2012). Interaction of aerodynamic roughness length and windflow conditions and its parameterization over vegetation surface. *Chinese Science Bulletin*, *57*(13), 1559–1567. https://doi.org/10.1007/s11434-012-5000-y

Zhang, S., Morita, K., Fukuda, K., & Shirakawa, N. (2006). An improved MPS method for numerical simulations of convective heat transfer problems. *International Journal for Numerical Methods in Fluids*, *51*(1), 31–47. https://doi.org/10.1002/fld.1106

Part II

Contributions

3 EXPERIMENTS

> Beauty is truth, truth beauty - that is all /
> Ye know on earth, and all ye need to know
>
> John Keats, *Ode on a Grecian Urn*

This chapter aims to describe the three measurement campaigns performed on floating set-up and at the laboratory. Measurement setups and data sets are introduced with a first level of data exploitation. An innovative measurement methodology is also introduced to improve the knowledge of the convective ratio.

Contents

3.1/ Introduction

Undoubtedly, monitoring floating installations offers a glimpse into the ground trough conditions experienced by the systems and their reactions to these multiple excitation. As the growing trend of FPV technology is recent, see Figure 14, the amount of monitoring data available in the scientific community is still low: They are also performed with a coarse level of refinement *(e.g., power production at array level, backsheet temperature of one module)* or in a low representativity configuration for the industry *(e.g., standalone floating module)*.

From the monitoring of a floating prototype from which general knowledge is deduced, with the emphasis given to the microclimate action on the cooling effect of FPV installation (Section 3.2), two other experiments were performed to specifically address heat rate measurements and reservoir-induced conditions using a plethora of scientific instrument setup.

Section 3.3, the solar platform newly installed on the laboratory roof in 2019 hosts the first photovoltaic experiment at *the scale of prototype array*. A set of sensors is installed to capture the near-environment from point measurements and to monitor the operational conditions of a representative module located in the middle of the prototype. The major experimental contribution of the thesis is presented as the first methodology capable of capture the convective heat rate at the front surface of the module with a better sampling frequency.

After completing this important proof-of-concept in a full-scale experiment, the innovative materials are deployed in a standalone setup launch at the FPV2 industrial site. Section 3.4 describes the floating raft that embeds the modules and presents the two sets of measurements for scientific monitoring of the atmosphere above the reservoir. This new level of refinement is dedicated to obtaining data with greater accuracy that allows us to optimise thermal models in the following sections.

3.2/ FPV1 Campaign: Evaluation of the Microclimate Effect

3.2.1/ Campaign Description

The FPV1 measurement campaign was an FPV project conceptualised, installed, and monitored by EDF R&D from September 2019 to mid-2022. The selected waterbody is located in Belgium and the water surface is approximately $4000\,\mathrm{m}^3$. The main objective of the campaign was to shed light on the global behaviour of an installation and to obtain first-level measurements from the production and temperature of the modules. In the context of the PhD thesis, the emphasis is given to the data exploitation of already existing data set in order to better understand the close environment of the floating set-up.

Hereafter, 6 months of monitoring are investigated in close detail between September 2019 and March 2020, and 36 days between August and September 2020. These periods are selected because they were poorly affected by data errors from electrical shutdowns. Although the investigation period is reduced, this initial database is assessed to provide sufficient quality and depth of data to perform validation of the thermal and electrical photovoltaic model.

As shown in Figure 3.1, the prototype is characterised by a free-standing structure composed of aluminium beams and HDPE floats. It is composed of side footpaths hosting SunnyBoy SMA inverters, the monitoring station settles on the back of the prototype; the structure is anchored to the embankment using ropes. The prototype hosts 3 rows of photovoltaic modules connected in series of 8 modules. Each are connected to an inverter and the DC power is recorded at this stage. The modules have a nominal capacity of 355 Wp, or 2800 kWp of output at the inverter input. They are initially orientated to the south with a constant tilt set to 30°. However, the effect of the wind on the structure and on the mooring lines changes the position of the system. A visual estimation of the wind-induced drift leads to the assumption of a deviation of the azimuth angle of about 5°.

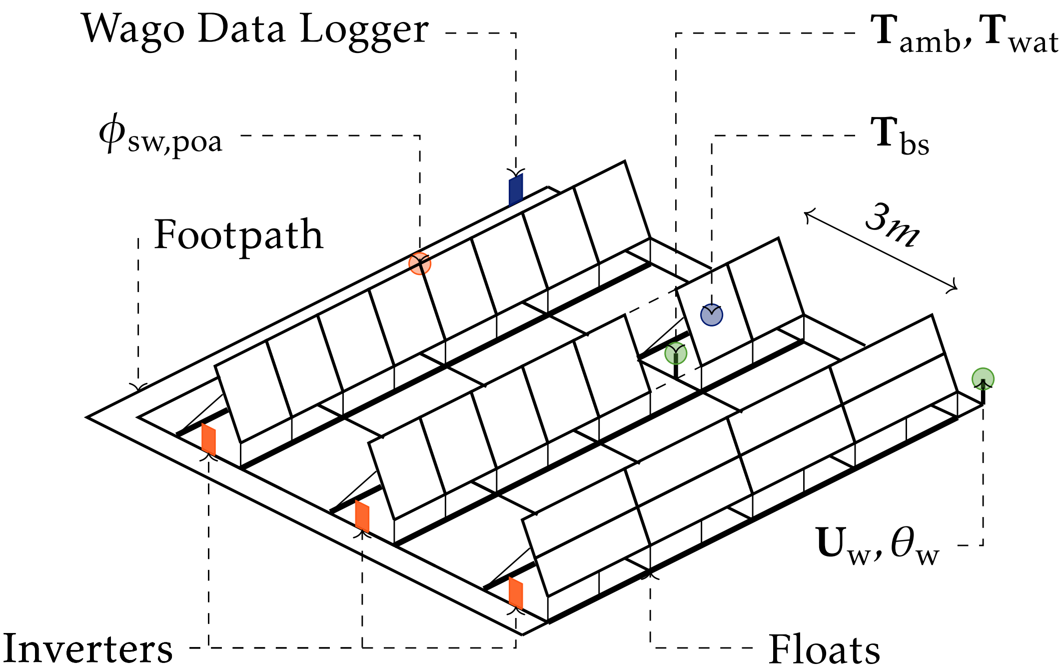

Figure 3.1–*Schematic of the FPV1 prototype and the instrumentation set-up.*

3.2.2/ Measurement Set-up

Location	Instrument	Parameters	Accuracy	Range	Sampling Timestep (s)
Module	RTD	$T^{6\to8}$	±0.3 °C	0 – 100°C	60
Sub-module	WXT534	U^{xy}_{wind},θ^{xy}_{w},T_{amb}, RH	3 %, 3 °, 3%, 3%		60
Water	RTD	$T^{9\to10}$	±0.3 °C	0 – 100°C	60
Back of Array	MS80-S	$\phi_{\mathrm{sw,poa}}$	10,00 %	300 - 2500 nm	60
Front of Array	WXT536	U^{xy}_{w},θ^{xy}_{w}	3 %, 3 °		60
Embankment	WXT534	U^{xy}_{w},θ^{xy}_{w}	3 %, 3 °		60

Table 3.1–*Details about the sensor used during the FPV1 campaign.*

The environmental measurement probes are located at several positions in the prototype and Table 3.1 summarises the elements and the technical characteristics of the equipment. A module of interest is located in the second row and is equipped with a PT100 sensor glued to the back of the module with double-sided aluminium adhesive. The weighted electrical production from the second string row is supposed to be representative of the real production of the module of interest. Under this module, a weather station and a PT100 sensor are installed in an immersion sleeve to monitor local thermoaerial conditions and water temperature, respectively. The weather station is located around 40 cm from the module and the water surface.

At the front of the installation, a 2D wind station is installed to measure a wind representative of the global mean field. Finally, an MS80-S sensor is installed in the tilt plane of the modules in the rear row of the prototype. A meteorological mast is also installed on the ground near the prototype to monitor the average wind, temperature, and local humidity. The acquisition loop lasts 1 min, and the data recovered by the acquisition logger correspond to the ones available in the data buffer of each sensor at the moment of querying. Therefore, $24 \times 60 = 1440$ records per probe are retrieved per day.

3.2.3/ Data Collected

To analyse the thermal mechanisms that drive the evolution of the module temperature, three temporal periods are dissociated according to the seasonality: autumn, the end of winter, and the end of summer. The first one runs from November 1 to November 30, 2019, the second one extends from March 1 to March 15, 2020 and the last one includes the period from August 8 to September 15, 2020.

Local Temperatures and Humidity Levels

First, we study the evolution of environmental conditions at the module level and, in particular, the measured components of humidity and temperature (ambient and underwater). Figure 3.2 and Figure 3.3 show the measured quantities averaged by days. Only day data are considered (data meet the criterion $\phi_{\mathrm{sw,poa}} > 30\,\mathrm{W\,m^{-2}}$). The evolution of humidity does not show clear evolution trends for each season, but it is observed that the average humidity level is more important for the fall period (approximately 76 % on average), while the summer period presents an average level of 12 points lower. We also notice that the variations during the day are much weaker during the first period, on the order of 11.2 % whereas in summer the variation reaches 15 %.

These amplitudes reflect the properties of daily evolution of this field. The level of humidity reaches a maximum in the early morning and a minimum late in the afternoon; this amplitude shows a more important accumulation of humidity in the *cold* period. The period of early spring is also critical for the moisture field, the daily changes are more marked than for the other seasons; this is mainly due to the evolution of the meteorology during this period from cold weather to a milder temperature. We also note that the difference in humidity level (and daily changes) between the water situation and the land measurement is relatively identical for the three periods (±0.3%) while the period at the end of winter shows more marked differences with a wetter condition over water of 0.8 % on average. We conclude that this last period is potentially key to observe particular phenomena over the basin (compared to a ground installation).

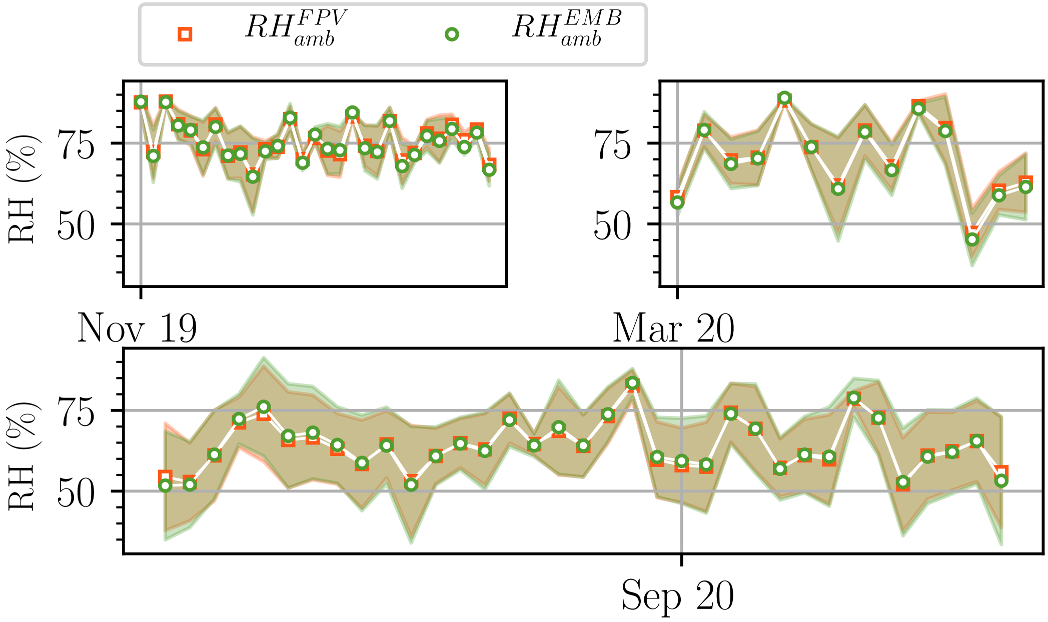

Figure 3.2–*Dynamics of the relative humidity, daily averaging has been applied for the three period samples.*

Figure 3.3 also shows the temperature trends for the three periods. This time various trends appear; the autumn and summer periods show decreasing evolutions, while the end of winter period shows a very slightly increasing evolution. In all three cases, the evolutions remain little marked, which is logical given the climate under which they are measured. On this temporal scale, it is interesting to observe that the water temperature is a delayed indicator of the ambient temperature, and those due to its thermal inertia, even if the investigated lake presents small dimensions (surface and depth). Logically, the average temperature levels above the water indicate temperatures of 8.5 °C, 8.8 °C and 20.9 °C that correspond to expected seasonal levels. The measurements of ambient temperature indicate seasonal levels of 8.1 °C, 8.5 °C and 20.3 °C, the lake-induced microclimate appears to have a slight warming effect. This is explained in particular by the water temperature, which on average is also higher for the three seasons (8.2 °C, 8.5 °C and 22.1 °C.

Solar Resources and Wind data

In support of the observation of the mean temperatures on site, the seasonal dynamics of the radiative field is presented in Figure 3.4. Radiative measurements clearly indicate different levels for the three seasons. The cold period shows an average irradiance of 194 W m^{-2} while the early

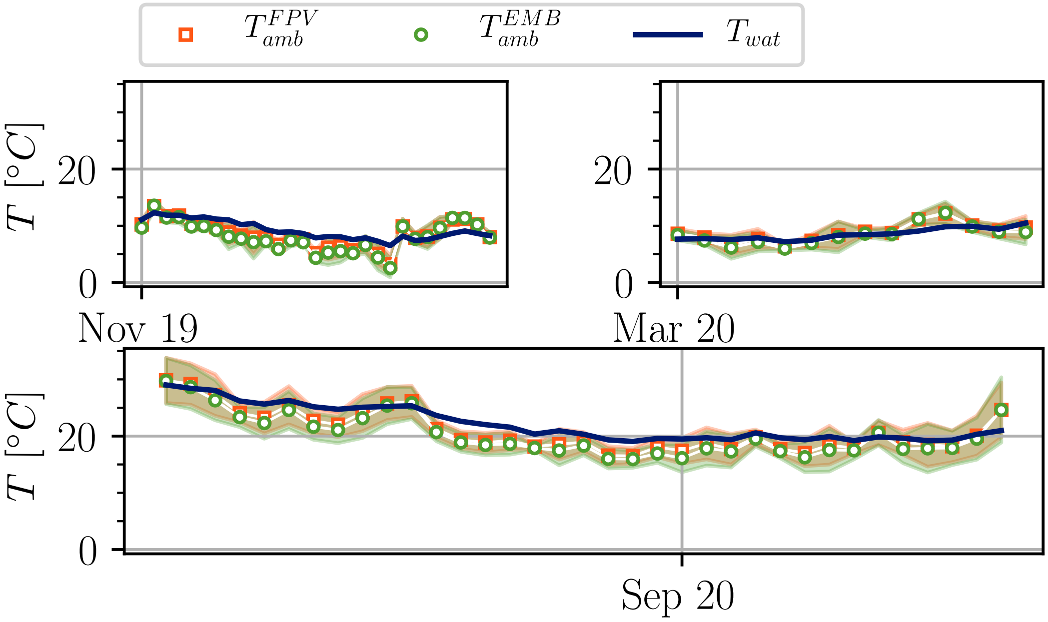

Figure 3.3–*Dynamics of temperatures (daily averages).*

spring and summer periods show respective levels of 260 W m^{-2} and 365 W m^{-2}. These observations make sense with respect to the temperate climate and also explain the observed ambient temperature trends. The cloudy tendency of the site is also integrated in these observations; this character is all the more prevalent in the summer period, where the daily variations are more volatile than during the cold season during which the cloud cover is persistent.

Figure 3.5a shows this character more precisely during the long summer period. In this figure, the radiative data are averaged per 10-min period and for all days of the period. The irradiance evolution range is also shown and shows that the radiative field is strongly affected by cloudy passages throughout the day. The evolution range of the irradiance reaches 720 W m^{-2} at the time when the mean irradiance reaches its maximum around 11 a.m. UTC. To be convinced of the presence of clouds, the PVLIB library is used to model the irradiation under clear-sky conditions, omitting possible masks. The evolution of the numerical irradiation shows that the difference is only related to the position of the Sun, which evolves during the period. The solar deficit observed between the measured field and the digitised one indicates that the evolution of the position of the sun is not the element that most alters the radiative field. It is concluded that cloud cover will be an important element to consider in numerical models in the future due to its daily variability.

Figure 3.5b shows the distribution of wind speeds by direction measured by the sensor on the raft. This distribution shows a preferred direction in the south and a largely minority reverse direction. The average speed is usually higher than 1 m s^{-1} during the period, while exceptionally high velocities higher than 4 m s^{-1} are observed at this height (40 cm above the water). These observations combine both the topological aspects of the site (prevailing historical south wind), microclimatic (canopy bordering the lake, aeraulic attachment zone in front of the southern part of the raft), and local (protection zone that comes from the raft). We can assume that the supply of forced convective phenomena will come mainly from the dominant direction and, consequently, that blocking phenomena may emerge in the middle of the power plant given the first row of modules upstream of the module of interest.

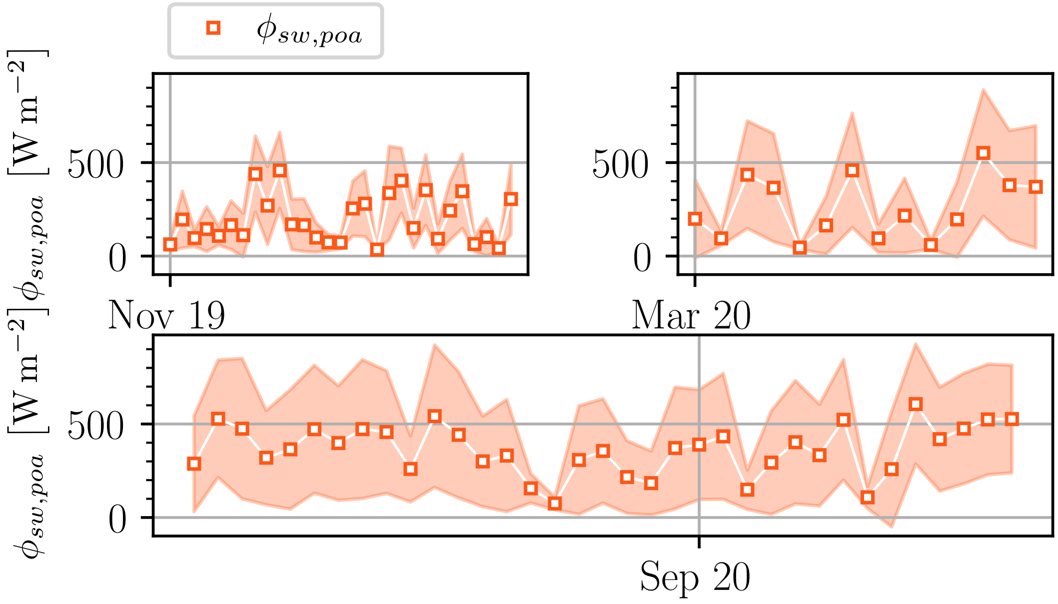

Figure 3.4–*Dynamics of irradiations (daily averaged).*

Data post-processing

Figure 3.6 shows the monitored data averaged over the day for the three seasons. Data are post-processed to be represented as a percentage of the maximum average value achieved over the three seasons; for the backside temperature, it is achieved in summer (T_{re} = 41.68 °C) while the maximum average output is achieved in early spring (P_m = 184.5 W). The maximum value in summer is slightly lower than the latter (P_m = 182.2 W), the difference could come from the module temperature differential between the two seasons. The temperature measured at the back of the module is much warmer on average during the summer period, reaching T_{re} = 27.8 °C with daily oscillations of T_{re} = 11.6 °C; while the late spring period shows an average of T_{re} = 13.0 °C and lower oscillations (T_{re} = 7.6 °C). The summer period shows classical operating regimes for photovoltaic installations, although the irradiance level fluctuates throughout the day due to the high concentration of clouds.

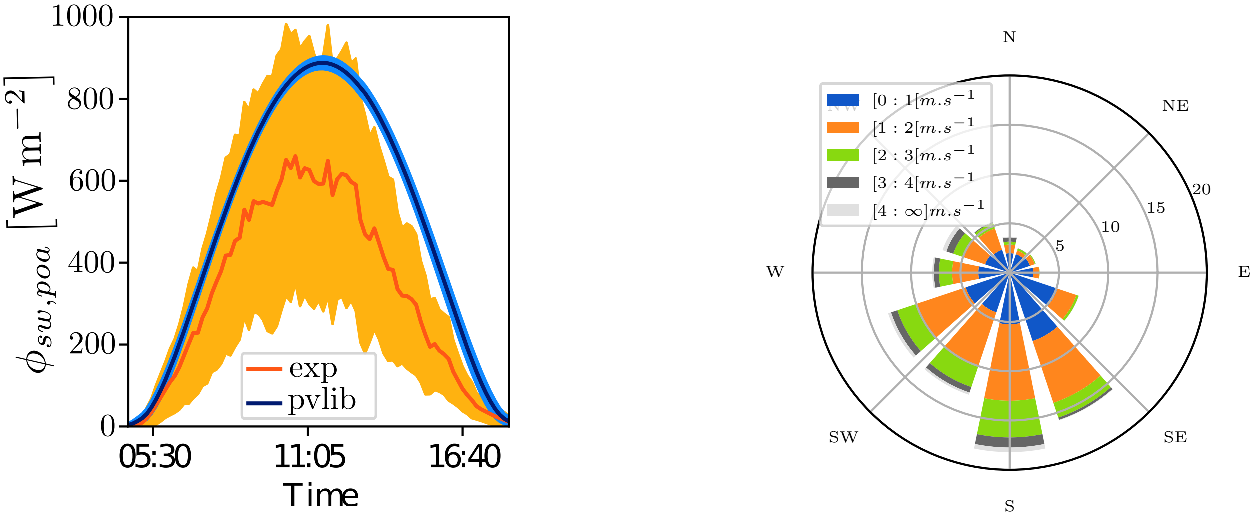

(a) *Averaged irradiation level measured $\phi_{sw,poa}$ (−) and its associated deviation (orange filled area). Numerical irradiation level is plotted for clear sky days (−), associated to a solar deviation (blue filled area)*

(b) *Distribution of wind experienced at the raft level with regard to the wind direction. 12 sectors are represented and five velocity bins are established per sector.*

Figure 3.5–*Local conditions experienced at the test site with comparison of optimal radiative levels from numerical clear-sky simulations.*

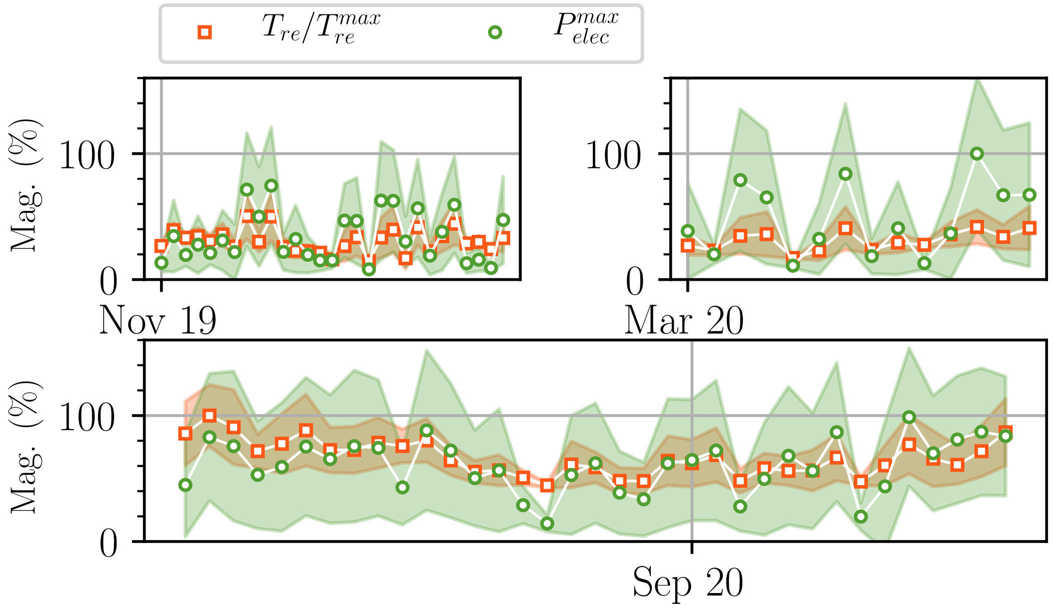

Figure 3.6–*Dynamic of the monitored fields for the module of interest*

3.3/ CETHIL Campaign: Measurements of Heat-Rates in Outdoor Conditions

3.3.1/ Campaign Description

The CETHIL measurement campaign is an experiment carried out jointly by the CETHIL laboratory and the TREE department of EDF R&D. It is taking place on the Solar Platform facility which is located on the roof of the CETHIL laboratory's building in Lyon. The platform is a versatile test facility that can monitor the urban microclimate using a range of instruments designed for atmospheric studies (LIDAR, Pyrheliometer), the measurement campaign inaugurates the testing facility. Measuring instruments can be plugged to the Solar Platform acquisition system as needed to study systems under real meteorological conditions, the measurement data is then retrieved on the laboratory server. The campaign consists of the monitoring of twelve photovoltaic modules, positioned in a bi-slope power plant layout. The ambition is to retrieve high quality data of electrical production and module temperature for a representative module in *array configuration*. Environmental parameters are also collected to describe the ambient conditions and offer some materials to perform numerical calculation of PV thermal behaviour. Finally, the campaign is mainly built to evaluate a new system of measurement based on heat-flux sensor. In the context of the PhD thesis, system conceptualisation, probe installation, system monitoring and data exploitation were performed; engineering of the photovoltaic structures, electrical branching and module flash-tests were performed by the laboratory engineers.

Laboratory's vicinity is characterised by high-buildings environment spaced by tree-lined walkways of varying lengths. Therefore, the platform is considered to be located in an urban fabric. The roof of the laboratory reaches a height of 13 m, and is protected by 110 cm acroteria. The platform is slightly elevated from the roof, with guard rails that secure the perimeter.

Figure 3.7 shows the orientation of the solar platform and the distribution of the modules; they are installed in a dual-sided east-west layout with a tilt of 12°. Two groups of 6 modules are established. The spacing between the groups is flexible, as are the rest of the structural dimensions, inclinations, and heights of the modules. In this study, a spacing of 1 m and a height of 1 m are considered. Within the same group, and in order to respect the proportions of the platform, three modules are orientated to the east, while the other three are orientated to the west. The spacing within the group itself is 10 cm, and the subgroups of three modules are spaced at 5 cm .

3.3.2/ Measurement Set-up

The experimental installation at CETHIL is based on the measurement of points of local thermal, aeraulic, and radiative fields. Table 3.2 summarises these sensors as well as a number of technical characteristics.

Thermal-Aeraulic monitoring

Thermal-aeraulic monitoring consists of collecting thermal-orientated data using K-type thermocouple and heat-flux sensors in different locations of the module of interest; aeraulic-orientated pieces of data are mainly from the 3-D anemometer in the array system. Six thermocouples are displayed along the module backsheet using a single-layer aluminium adhesive to hold the probe in contact with the surface. Three heat flux sensors are also bonded to the surface, one heat flux sensor is positioned on the backsheet in the centre of the module, while the remaining two heat

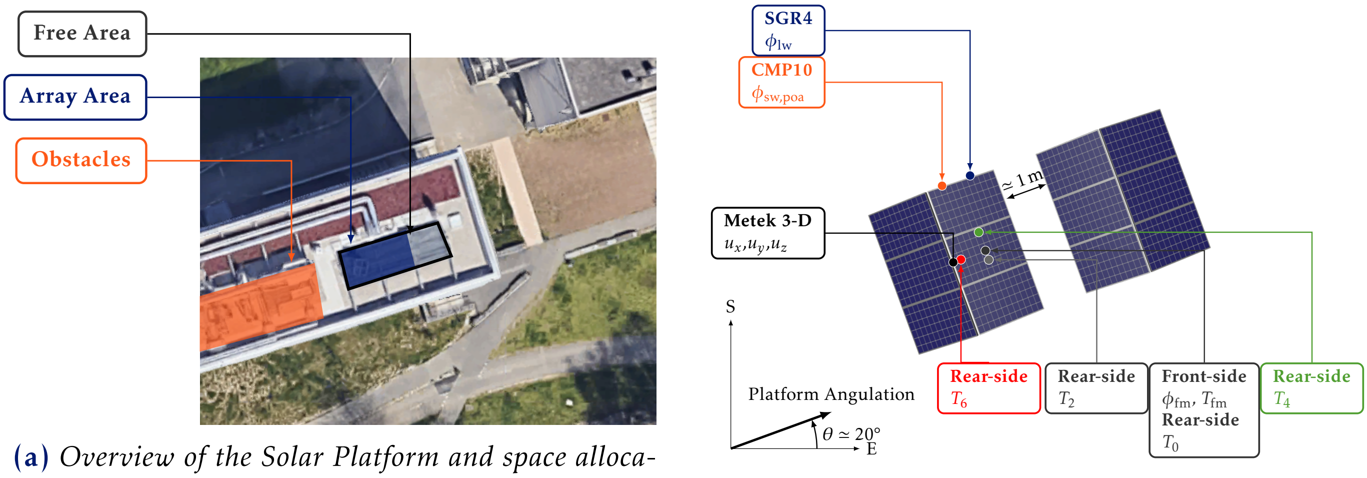

(a) *Overview of the Solar Platform and space allocations*

(b) *Sensor distribution across the array*

Figure 3.7–*Schematics of the local environment of the Solar Platform and the CETHIL campaign.*

Location	**Instrument**	**Parameters**	**Accuracy**	**Range**	**Sampling Timestep** (s)
Array level	SMP10	$\phi_{\mathrm{sw,poa}}$	$5\,\mathrm{W\,m^{-2}}$	285 – 2800nm	5
	SGR4	ϕ_{lw}		4500 – 42000nm	5
	TK	T_{amb}	±0.3 °C	0 – 100°C	5
PV module	heat flux sensor	ϕ_{fm}			5
	Metek 3D	u_x, u_y, u_z			5
	TK	$T^{1\rightarrow4}$	±0.3 °C	0 – 100°C	5
Resistive Charge					5

Table 3.2–*Summary of sensors installed and used for the CETHIL campaign.*

flux sensors are positioned directly on the front of the module. Thermal paste is applied to enhance thermal contact, so that the heat flux measured behind the probe is assumed to be the same as the flux that flows through the module by conduction. A silicone seal system seals the probes to prevent water infiltration into the system; during installation, a thermocouple is also integrated into the thermal paste under the heat-flux probes. The choice is made to focus on a single heat-flux sensor (front-side) and four backsheet temperature measurements. Wind situation near the module is recorded by the 3-D anemometer which is located 30 cm above the edge of the module of interest. As mentioned in Table 3.2, the acquisition time is limited to 5 seconds to diminish memory storage.

Radiative monitoring

Two radiative measurements are made: Short-wavelength and the long-wavelength measurements are both performed in the plane of the array. Nearby shading is weak and changes during the day. This is mainly a shading effect due to the bi-slope structure and the combination with a relatively low pitch. The pyranometry measurement is considered to be representative of the solar flux incident on the module of interest during the whole campaign, the surrounding buildings being relatively far away and the height of the Sun being sufficient to limit the effects of irradiation heterogeneities between the measurement and the module of interest.

Heat Flux Sensor Protocol and Post-Processing

The heat-flux sensors installed on the modules are instruments manufactured by the company CAPTEC. These sensors are based on the tangential gradient flux measurement technique. To do this, numerous micrometre-sized thermocouples are connected in series and installed between two copper plates that are sufficiently thick to guarantee the solidity of the measurement area. Temperature differences between the two surfaces cause a voltage difference at the thermocouple junction. The series connection thus ensures that the voltage difference is large enough to be characteristic of the temperature difference between the two sides of the system and the flux through the sensor can then be deduced. On the other hand, the copper size must be small enough not to induce a capacitive effect that would bias the measurement of the surface to be characterised. Therefore, the characteristic time of the system is very small compared to that of the adjacent thermal mass.

When positioned on a photovoltaic module, the heat flux sensor measures the conductive flux that is transmitted to the thin layer of air adjacent to the module, while absorbing part of the incident electromagnetic waves. These absorbed waves (short and long wavelengths) are not characteristic of the photovoltaic module, as the heat flux sensor has its own coating. In our measurement campaign, the copper plates are less than a millimetre thick, and the sensor positioning is made so that it does not modify electrical production level.

In order to deduce the convective transfer coefficient of the photovoltaic module by heat flux sensor measurement, the heat budget is solved as follows:

$$\phi_{\text{fm}} = \alpha_{\text{fm}}\phi_{\text{sw,poa}} - h_{cv}\left(T_{\text{fm}} - T_{\text{amb}}\right) - \epsilon_{\text{fm}}\left(\sigma T_{\text{fm}}^4 - \phi_{\text{lw}}\right) \tag{3.1}$$

whence ϕ_{fm} is measured at the heat flux sensor level, α_{fm} is the average absorptivity of the heat flux sensor and $\epsilon_{\text{fm}}$is its emissivity. These two latter radiative parameters are function of the coating, hence a special coating is applied on the sensible area. A black coating is applied as a spray, with a sufficient number of painting layer and sufficient drying time to ensure that each coating is dry and homogeneous (visual check). A commercial paint suitable for outdoor conditions is used. Two spectrometric protocols are then carried out in the laboratories to precisely characterise the emissivity and absorptivity properties of the paints. Their relative fragility prevented the direct introduction of the sensors into the visible and infrared spectroscopic control systems, so two samples with different roughness properties were made, the first in steel and the second in aluminium.

Spectral measurement in the visible range is carried out in the INL laboratory (Institut des Nanotechnologies de Lyon), the device allows reflexion of the samples in the vertical direction in the range $r_b^v \in [280;1100]\,\text{nm}$. The spectral measurement in the infrared spectrum is performed at the CETHIL laboratory, the measurement system also characterises the samples in the vertical direction over the range $r_b^i \in [4500;19000]\,nm$. The Kirchhoff law is applied to derive the emissivity of the samples.

The radiative measurements at the Solar Platform integrate the electromagnetic field between two boundaries that differs from the ones used in the spectral measurements. The short-wave band for the $CMP10$ sensor that goes from $\lambda_{CMP10_1} = 285\,\text{nm}$ to $\lambda_{CMP10_2} = 2800\,\text{nm}$, the long-wave band for the $SGR4$ sensor that goes from $\lambda_{CGR4_1} = 4500\,\text{nm}$ and $\lambda_{CGR4_2} = 42\,000\,\text{nm}$. Both absorbtivity and emissivity for the coating are derived using a weighting integral based on the spectral measurement. The hemispherical power of the heat flux sensor can be described as:

$$\epsilon_{\mathrm{fm}}(T_{\mathrm{fm}})E_b(T_{\mathrm{fm}}) = \int_0^{\infty} \epsilon_\lambda(T_{\mathrm{fm}}) \times E_{\lambda,b}(T_{\mathrm{fm}})\, d\lambda \tag{3.2}$$

From then on $\epsilon(T_{\mathrm{fm}})$ is the mean emissivity, $\epsilon_\lambda(T_{\mathrm{fm}})$ is the spectral emissivity, $E_{\lambda,b}(T_{\mathrm{fm}})$ is the blackbody spectral emission, and $E_b(T_{\mathrm{fm}})$ the total emissive power. A decomposition of the integral according to the cutting wavelengths for the $GCR4$ sensor gives:

$$\begin{aligned}\epsilon_{\mathrm{fm}}(T_{\mathrm{fm}})E_b(T_{\mathrm{fm}}) = &\int_0^{4500} \epsilon_\lambda(T_{\mathrm{fm}}) \times E_{\lambda,b}(T_{\mathrm{fm}})\, d\lambda \\ &+ \int_{4500}^{19000} \epsilon_\lambda(T_{\mathrm{fm}}) \times E_{\lambda,b}(T_{\mathrm{fm}})\, d\lambda \\ &+ \int_{19000}^{42000} \epsilon_\lambda(T_{\mathrm{fm}}) \times E_{\lambda,b}(T_{\mathrm{fm}})\, d\lambda \\ &+ \int_{42000}^{\infty} \epsilon_\lambda(T_{\mathrm{fm}}) \times E_{\lambda,b}(T_{\mathrm{fm}})\, d\lambda \end{aligned} \tag{3.3}$$

Assuming that the calculation of equation 3.1 is from interest when $T_{\mathrm{fm}} \in [300;350]K$, the fraction of emissive power of the first and the last terms of Equation 3.3 account at most for 2% and 5% in the total hemispherical power, respectively. Equation 3.3 is then reduced to:

$$\begin{aligned}\epsilon_{\mathrm{fm}}(T_{\mathrm{fm}})E_b(T_{\mathrm{fm}}) = &\int_{4500}^{19000} \epsilon_\lambda(T_{\mathrm{fm}}) \times E_{\lambda,b}(T_{\mathrm{fm}})\, d\lambda \\ &+ \int_{19000}^{42000} \epsilon_\lambda(T_{\mathrm{fm}}) \times E_{\lambda,b}(T_{\mathrm{fm}})\, d\lambda \end{aligned} \tag{3.4}$$

The blackbody radiation fraction is introduced as the ratio of the fraction of emissive power to the total hemispherical power emissive power integrated from $\lambda = 0nm$ to the wavelength of interest as follows:

$$F(\lambda_c, T) = \frac{\int_0^{\lambda_c} E_{\lambda,b}(T_{\mathrm{fm}})}{E_b(T_{\mathrm{fm}})} \tag{3.5}$$

Using this writing style and considering the spectral tables for the blackbody fraction, the fraction of emissive power associated with the spectral calibration at the laboratory is as follows:

$$F(\lambda_1, \lambda_2, T) = (F_{0\to\lambda_2 T_{\mathrm{fm}}} - F_{0\to\lambda_1 T_{\mathrm{fm}}}) = F(300 \times 19) - F(300 \times 4.5) \simeq 0.71 - 0.01 \simeq 0.70 \tag{3.6}$$

Hence the coating properties in the long-wave range is well known at least for 70%, the remaining portion between the cutting wave-length of the calibration set-up and the cutting wave-length of the CGR4 sensor accounts at most for 24% of the total hemispherical power. For this latter part, an arithmetic mean of the emissivity is hypothesized as follows:

$$\frac{\sum_{\lambda_{CGR4_1}}^{Cut_2} \epsilon_\lambda}{N_\epsilon} = \overline{\epsilon}_{Cut2\to CGR4_2} \tag{3.7}$$

Finally the emissivity that can be integrated in Equation 3.1 leads to:

$$\begin{aligned}\epsilon(T_{\mathrm{fm}}) = &\frac{\sum_{\lambda_{CGR4_1}}^{\lambda_{Cut_2}} \epsilon_\lambda(\lambda) E_{\lambda,b}(T_{\mathrm{fm}})}{N_\epsilon E_b(T_{\mathrm{fm}})} \\ &+ \overline{\epsilon}_{Cut2\to CGR4_2}(F_{0\to 42000} - F_{0\to 19000}) \end{aligned} \tag{3.8}$$

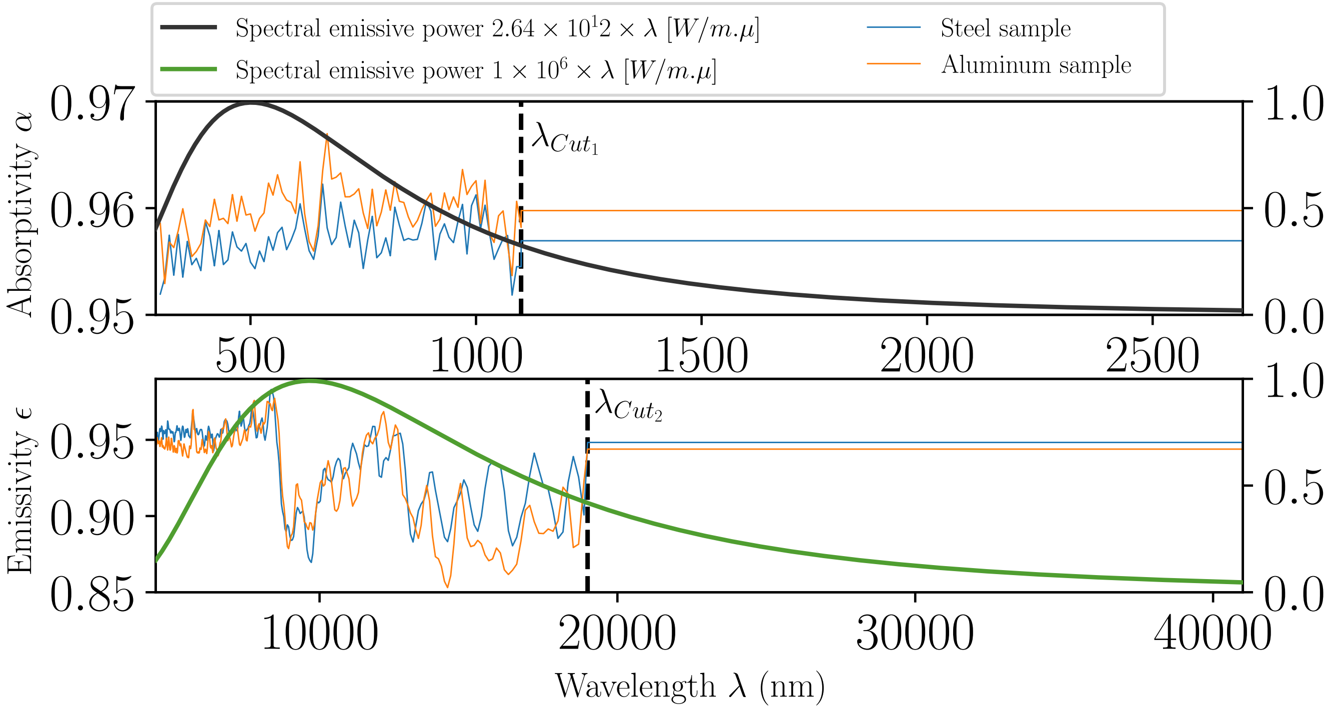

Figure 3.8–*Calibration of coatings in the visible spectrum (top subplot) and the infrared spectrum (bottom subplot) for the two sample materials. After the cutting wavelengths (occurring from experimental limitations), the emissivity and the absorptivity are extrapolated through a weighted-by-blackbody averaging procedure.*

The same procedure is performed to assess the absorptivity, the wavelength of interest is modified to match the characteristics of CMP10, the temperature of reference being $T_{Sun} = 5774\,\mathrm{K}$, it leads:

$$\begin{aligned} \alpha(T_{Sun}) = & \frac{\sum_{\lambda_{CMP10_1}}^{\lambda_{Cut_1}} \alpha_\lambda(\lambda) E_{\lambda,b}(T_{Sun})}{N_\alpha E_b(T_{Sun})} \\ & + \overline{\alpha}_{Cut1\rightarrow CMP10}\left(F_{0\rightarrow 2800} - F_{0\rightarrow 1100}\right) \end{aligned} \tag{3.9}$$

The integral reduction, similar to the procedure explained in Equation 3.4, leads to an uncertainty of $\simeq 2.5\%$ about the total hemispherical absorptivity in the UV part. The *infrared part* of the sun radiation being integrated in the input ϕ_{lw} and thus in the major part in the emissivity calculation.

The calibration ends with the estimation of the emissivity and the absorptivity of the coating for both materials, as indicated in Table 3.3. A first observation is that the material quality has little influence on both radiative properties, so it is concluded that the coating protocol is robust to different surface microstructure states. The average value of emissivity is used to qualify the long-wavelength coating feature, so that $\epsilon_{\mathrm{fm}} = 0.875$. In addition, in the work the absorptivity value of 0.9 is considered.

3.3.3/ Data Collected

The solar platform acquisition loop is calibrated to integrate sensor data every five seconds. Due to some minor issues with sensors, it was decided to concentrate on an acquisition period of 18

	Steel	Aluminum
$\alpha_{\mathbf{fm}}$	0,9	0,9
$\epsilon_{\mathbf{fm}}$	0,88	0,87

Table 3.3–*Summary of coating properties from the spectroscopy measurements.*

days from 18 May to 5 June 2022 to capture as much information as possible: 287810 datapoints are recovered. The period chosen also corresponds to the *warm* and sunny season, so the measurement methodology is evaluated in a favourable environmental context.

In the following, we propose to analyse the results of the measurements for a characteristic day to have a picture of the signal dynamics. We choose a day where the availability of the acquisition bay is rather good and where the environmental characteristics have a rather important dynamics (clouds, winds). The day of 22 May meets these criteria. With regard to the time series, a presentation in the form of a boxplot is also proposed for the time series of the data for 22 May, as well as for the full time series which includes the 18 days of studies. In the following, a filter is performed on the entire data set to keep only the instants where $\phi_{\mathrm{sw,poa}} > 30\,\mathrm{W\,m^{-2}}$.

Figure 3.9 shows the environmental characteristics of the short- and long-wave radiative fluxes, the electrical production, and the flux measurement directly at the heat flux sensor terminal. The short-wave radiative flux is the most important heat source and shows a classical evolution for a summer day, given the eastward tilt of the system. Thus, the solar bell is shifted towards the morning (left). The maximum flux reaches $1124\,\mathrm{W\,m^{-2}}$ over the entire period, the median value is $341\,\mathrm{W\,m^{-2}}$ while the median observed in 22nd May is $443\,\mathrm{W\,m^{-2}}$, which indicates that local conditions are even more degraded. The long-wave radiative flux is rather constant, the median of the measurements over the global period is $364\,\mathrm{W\,m^{-2}}$ which is relatively logical for partly cloudy skies. The usual amplitude is $55\,\mathrm{W\,m^{-2}}$, combined with dynamics similar to the short-wave radiative flux on short time scales (passage of clouds), and on nycthemeral scales. Thus, during the day, this heat source can be qualified as relatively constant compared to the other heat flows.

The electrical production shows a realistic dynamic compared to the normal operation of a photovoltaic module connected to an inverter and to the grid, and it is well correlated with the solar flux. On 22nd May, the median value is $96\,\mathrm{W\,m^{-2}}$, *(i.e., an operation strongly impacted by the cloudy evolutions)*. However, the median production during the entire period reached only $20\,\mathrm{W\,m^{-2}}$, the variable load ran into problems frequently. When the source of this irregular behaviour was not found, it is hypothesised that the MPPT trigger is not optimally parameterised so that irregular sky-states and brief increase or loss in irradiation provoked charge default.

Finally, the measurement of the heat flux with the heat flux sensor indicates a very important dynamic over much shorter time periods than the cloudy passages indicated above. The median value of the series indicates $24\,\mathrm{W\,m^{-2}}$ all in all, but the very unstable values reach important positive and negative levels: $\phi_{\mathrm{fm}}^{fr} \in \left[-148.79\,\mathrm{W\,m^{-2}}; 171.21\,\mathrm{W\,m^{-2}}\right]$.

Study of temperature measurements

Figure 3.10 shows the temperature dynamics of the thermocouples positioned under the module and the thermocouple positioned on the module, under the heat flux sensor. It can be seen that all of the thermocouples have the same values and almost identical behaviour. Some disparities

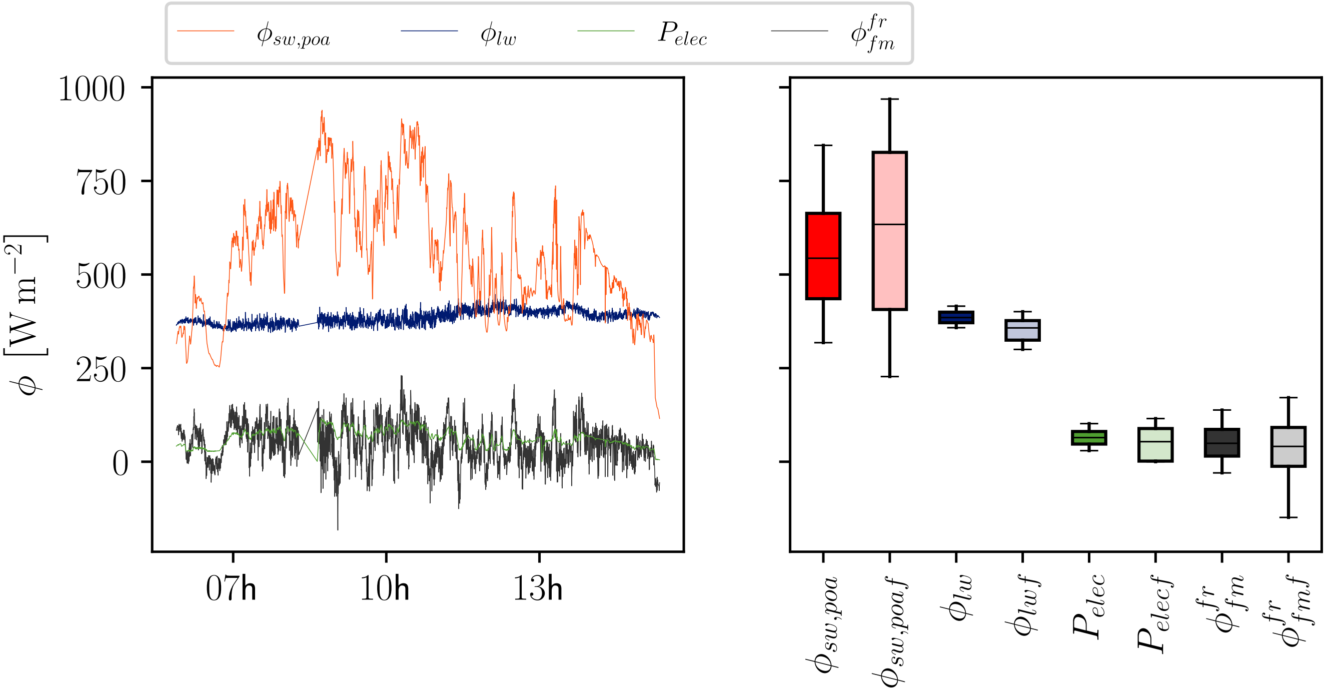

Figure 3.9–*Dynamics of the measured temperatures during the 22nd of May 2022. The right hand side shows the distribution of the flux with respect to the colour of the time series. The suffix $_f$ indicates the distribution for the full period of investigation, from the 18 of May to the 5 of June 2022.*

remain according to their positions, but the temperature difference never exceeds 3.2 °C. Thermocouples T0 and T6, which are located on a vertical line in the middle of the module, behave more similarly to thermocouples T2 and T4, which are off-centre. This phenomenon can be attributed to local heterogeneities (wind direction and intensity) and to local characteristics of cells (localised shading). Interestingly, we notice that the thermocouple under the heat flux sensor remains very close to the average of the four sensors under the module; on the day of 22 May their difference (median) is 0.93 °C, it reduces to only 0.66 °C over the whole 18-day period. There are still a few moments during which the temperature measured under the heat flux sensor is much higher than the temperature of the module, at most 8 °C. These observations are exceptional and we were unable to attribute them to a specific heat source.

Winds and heat rates

Figure 3.11 shows the dynamics of the wind components, as well as the dynamics of the recalculated convective transfer parameters from the 1-D heat balance on the photovoltaic module and the heat balance on the heat flux sensor. For all parameters, a resampling is performed for better readability of the temporal information, the *average* time step considered is 5 minutes. Deviations from the mean are represented by the highlighted areas. For these diagrams, additional filtering is performed to limit the instants where the convection coefficients are virtually infinite or negative (when the surface and ambient air temperature differences are close).

Wind components show the usual trend to which photovoltaic installations are subject, an average speed that alternates between periods around 0.5 m s^{-1} to instantaneous gusts reaching much higher speeds. On 22$^{\text{nd}}$ May, the fastest reading occurred at 2 p.m. and indicated an average speed of 4 m s^{-1}, which is half the maximum speed throughout the recording period. The read-

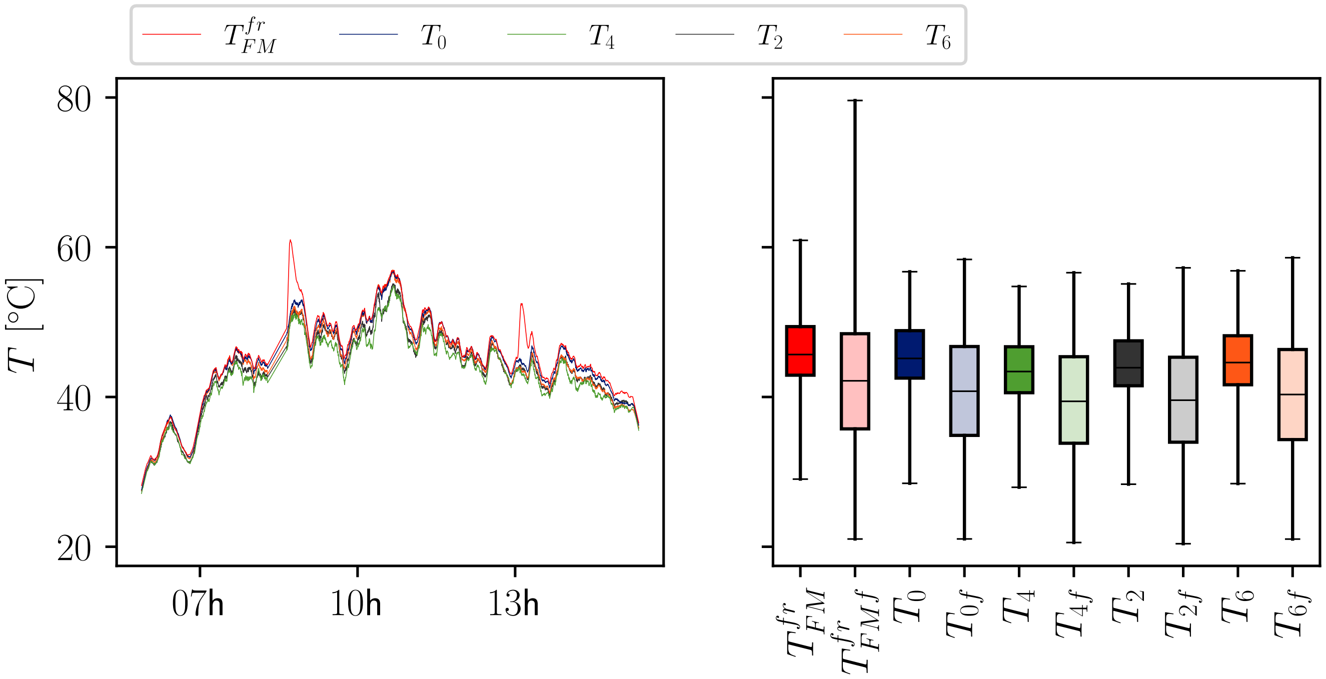

Figure 3.10–*Dynamics of the measured fluxes during the 22nd of May 2022. The right hand side shows the distribution of the temperatures with respect to the colour of the time series. The suffix $_f$ indicates the distribution for the full period of investigation, from the 18 of May to the 5 of June 2022.*

ing of the box plot also shows that the range of variation of the mean velocity is 1.5 m s^{-1}. It is sufficiently large for the observable transfer modes to evolve over the day. Another important indication provided by the component w is that the flow regime is indeed parallel ($\overline{w} \simeq 0\,\mathrm{m\,s^{-1}}$) and that the position of the system is not biased by the presence of modules less than 40 cm from the measurement zone, there is no noticeable recirculation zone. Therefore, the wind measurement is considered to be well representative of the flow regime observed by the photovoltaic module.

The recalculated convective parameters also show behaviours that are similar to the aeraulic flow. The observation of the time series shows, in particular, the sudden increase of the two recalculated coefficients from 14h when the average wind speed increases appreciably. A degradation of the intensity of the coefficients is also observed between 10 a.m. and 12 a.m. on the period when the wind speed is rather low. The transfer rates show a similar trend to the evolution of the average wind speed on both the particular day and over the entire study period, where the median values of the transfer rates follow the increase of the median value of the wind speed. An attempt can therefore be made to extend the correlation to the entire study period.

Surprisingly, we observe that the method of calculation by heat balance in the photovoltaic module presents greater amplitudes than the method of recalculation by heat sensors; this materialises as well on the specific day of 22$^{\mathrm{nd}}$ May, as on the whole period of study where the median of the convective coefficient by the heat sensor method is only 20.2 W K^{-1} m^{-2} against 23.9 W K^{-1} m^{-2} for the method 1-D module. This behaviour is attributed to the lower thermal inertia of the measurement probe compared to the inertia of the module. Thus, when there is a sudden change in cloud cover (or clearing), the probe temperature changes faster than the backsheet temperature of the module. The temperature difference between the system and the surrounding atmosphere is not biased, and the surface balance is better approximated by the new

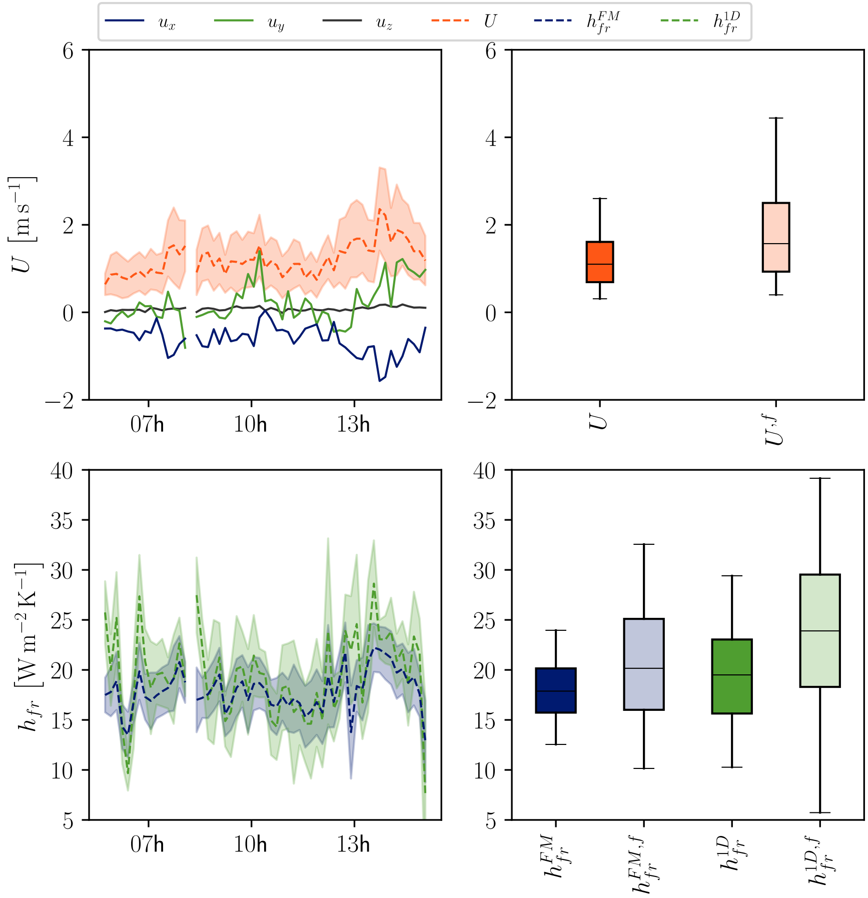

Figure 3.11–*Dynamics of winds components and heat rates the* 22^{nd} *of May 2022. The right hand side shows the distribution of the winds and the heat rates with respect to the colour of the time series. The suffix* $_f$ *indicates the distribution for the full period of investigation, from the 18 of May to the 5 of June 2022.*

measurement method.

Performance of the new measurement methodology

It is proposed to materialise the benefits of the new convective transfer rate measurement methodology by comparing its performance in reducing residuals when correlating the calculated field with the mean wind speed. Figure 3.12 shows this statistical character, as well as the predictions of the linearity coefficients u_c and u_v. Interestingly, it can be seen that the residuals of both methods are rather low, the r^2 hardly reaches a maximum value of 0.6 with the 1-D method by balance on the photovoltaic module at hourly time step. These results were expected given the estimates made in the literature, *e.g. in (Dörenkämper et al., 2021), the* r^2 *coefficients reach a maximum of 0.59*. Also similar to this publication, it is observed that the aggregation of data up to a sampling of 1 value per 10 min offers a better relevance than the aggregation of data at 1 minute, for the 1-D module method. The new method is also subject to this sampling rule, but the range of variation is much smaller. It is clear that the heat sensor methodology far outperforms the classical methodology for time steps up to 10 min. Beyond that, the heat sensor system does not increase the quality of the correlation obtained.

When looking at the linearity parameters, it can be seen that both methods offer relatively close parameter sets for both the constant and the mean wind speed dependent part. Both methods

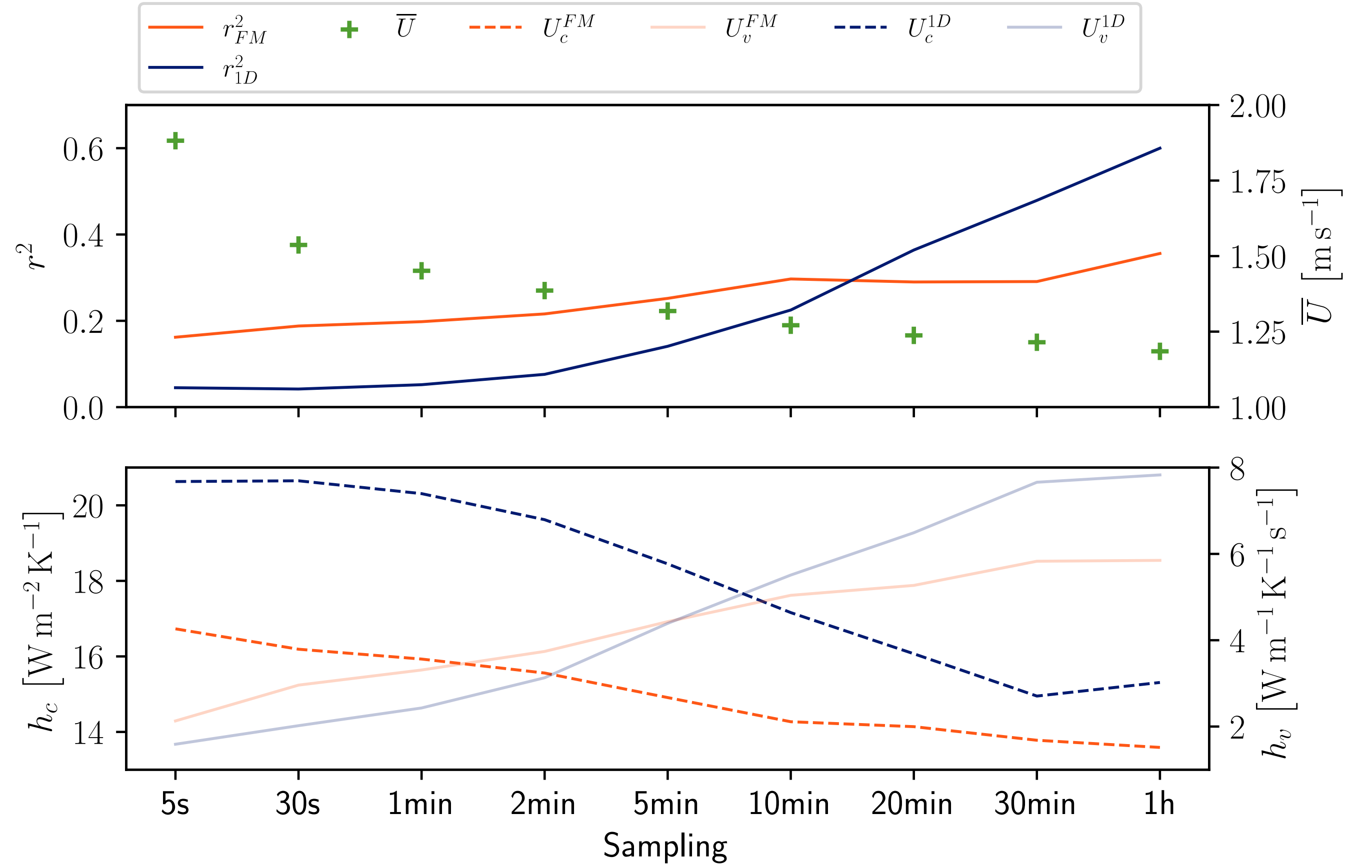

Figure 3.12–*Statistical performances of the new method of determining h_{fr}^{cv} in front of the data sampling (orange) Usual performances of the inverse 1-D thermal model is provided (blue). Linear trends are also indicated for both strategies.*

have much higher constant coefficients than the one proposed in Test et al., 1981. The wind-dependent coefficient is much higher for the 1-D photovoltaic methodology and much lower for the heat flux sensor methodology. This is a predictable behaviour for both methods if we consider that the lower module tilt in the experiment enhances forced convective transfers, as shown numerically in Jubayer et al., 2016. The average wind speed follows the downward trend noticed in the linearity coefficient, which depends on the wind speed. Both methods tend to reduce the variability of the calculation as a consequence of the reduction in variability of the aerodynamic input parameter. For small time steps, the wind-dependent coefficient is significantly larger and counteracts this variability at short time scales.

In conclusion, the new methodology provides an added value for measuring the convective coefficient in time steps below 10 min. This performance is explained by the sensor characteristics, which integrate local temperature differences much more quickly than with the conventional method. Therefore, it is relevant to test this methodology for photovoltaic applications on a minute scale to more accurately describe the convective coefficient on the front panel.

3.4/ FPV2 Campaign: Heat-Rate Monitoring of Standalone FPV

3.4.1/ Campaign Description

The measurement campaign *FPV2* is carried out in the French area of the Hautes Alpes. It is conducted by six stakeholders:

- The Department of Technology and Research for Electricity Efficiency (TREE) at EDF R&D
- The Center of Thermal Energy Sciences (CETHIL)
- The Department of Fluid Mechanics, Energy and Environment (MFEE) at EDF R&D
- The Centre d'Enseignement et de Recherches en Environnement Atmosphérique (CEREA)
- The National Laboratory of Hydraulics and Environment (LNHE) at EDF R&D
- The laboratory ATHOS Environment

The campaign focuses on the atmospheric and hydraulic study of the reservoir in which a floating photovoltaic project is being implemented since 2022[1]. The industrial stakeholders are as follows:

- EDF Renouvelables
- The EDF Center of Hydraulic Infrastructures (CIH)

The industrial project consists of the installation of 50,000 photovoltaic modules, it would be the first FPV project for EDF in France. The hosting reservoir is an hydropower station, it also allows to feed the crops in the reservoir's vicinity during the summer. The site is located at an altitude of 670 m, in a mountainous environment. The reservoir is 1250 m long and 380 m wide. Eastern part of the reservoir is occupied by the hydropower station and the turbining facility. The photovoltaic project aims to cover $20\times10^5\,\mathrm{m}^2$ of the water surface which is estimated to $30\times10^5\,\mathrm{m}^2$, with floating technology from Ciel et Terre®. The tilt of the modules is 12° with an azimuth angle towards the south.

In the PhD thesis context, an instrumented raft has been developed with the aim of collecting environmental data as well as monitoring FPV modules. As the installation takes place upfront to the industrial project commissioning, the monitored module are directly installed onto the raft. Conceptualisation, probes installation and data analysis of the measurement campaign have been performed within the PhD scope. Construction of the raft and electrical installation have been fully performed by the ATHOS Environnement laboratory. The raft structure consists of several floating HDPE blocks on which mounting plates are installed to allow the installation of a telescopic meteorological mast, acquisition closet, two batteries, and the monitored PV modules which are identical to those installed in the CETHIL campaign. Gravitational anchors are setting the raft in position, though hydropower pumping and turbining operation acts strongly on the water level; therefore the position of the system fluctuates from time to time. The measurement campaign is carried out for one month between May and June 2022.

---

[1] the array would be commissioned by 2023.

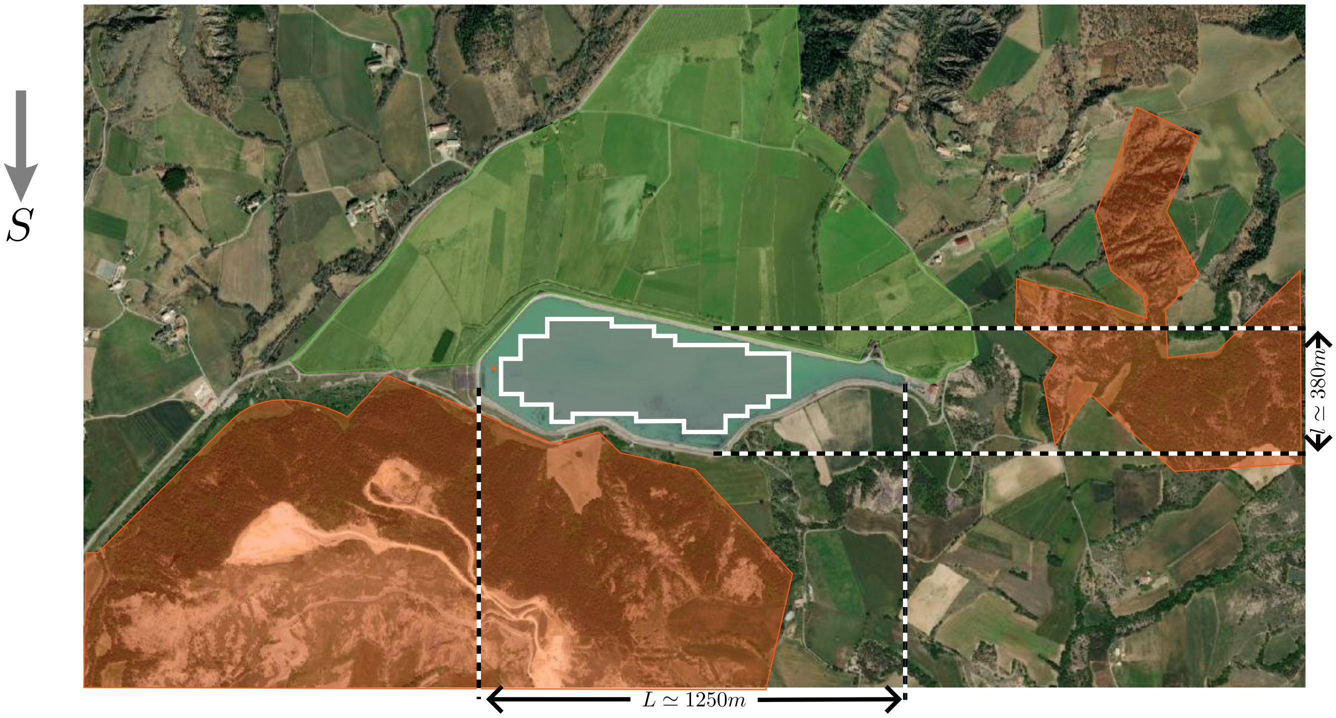

Figure 3.13–*Near environment of the FPV2 campaign. Mountains and crops areas are respectively depicted in orange and green. The gray surface shows the space to be covered by the array. The orange dot point in the western part of the lake shows the approximate location of the experimental measurement set-up.*

3.4.2/ Measurement Set-up

The measurement system includes a part dedicated to micro-meteorological monitoring, which is mainly installed on the measurement mast. The second part is dedicated to the temperature monitoring of the module, the sensors are mainly located on the back side of the photovoltaic modules. A summary of the probes installed for the campaign purpose is shown in Table 3.4.

Probes on the mast

The mast is installed with guy wires connected to the plate on the floats to reduce possible wind-related oscillations. Measurement instruments are strategically positioned to optimise mass distribution and minimise interference between sensors. Photography of the sensor hosted by the mast is available in Figure 3.14

The highest point on the mast is occupied by the 3-D ultrasound anemometer, with a measurement area approximately 3.1 m from the support plate. The sensor takes 10 measurements per second in all three directions of space. These characteristics make it possible to determine a point turbulence level at the level of the measurement zone, in addition to the instantaneous wind speed. In the following work, we will work with integrated turbulence data at the 10-minute time step. Its position is optimised to produce data that are as little altered as possible by the movement of the raft and for the other sensors.

On the southern part of the mast are installed the short and long wave radiation sensors. The MS-90+ radiative capture consists of two MS-90 and MS-80S sensors, connected by a computer (CBOX). MS-90 measures direct radiation, while MS-80S measures global radiation. The computer allows the combination of the two quantities to determine the diffuse field. The SGR4

Location	**Instrument**	**Parameters**	**Accuracy**	**Range**	**Sampling Timestep (s)**
Mast	MS-90+	$\phi_{DNI}, \phi_{GHI}, \phi_{DHI}$	10,00 %	300 - 2500 nm	60
	GMX600	$U_{\mathrm{w}}^{xy}, \theta_{\mathrm{w}}^{xy}, T_{\mathrm{amb}}, RH$	3 %, 3 °, 3%, 3%		60
	SGR4	ϕ_{lw}		4500 - 42000 nm	60
	Metek 3D	u_x, u_y, u_y			10^{-1}
	Fisheye				10
PV module	MS-80S	$\phi_{\mathrm{sw,poa}}$	10,00 %	300 - 2500 nm	60
	heat flux sensor	ϕ_{fm}			60
	RTD	$T^{1\to5}$	±0.3 °C	0 – 100°C	60
Floats	RTD	$T^{6\to8}$	±0.3 °C	0 – 100°C	60
Water	RTD	$T^{9\to10}$	±0.3 °C	0 – 100°C	60

Table 3.4–*Set of probes installed at the floating test site of FPV2.*

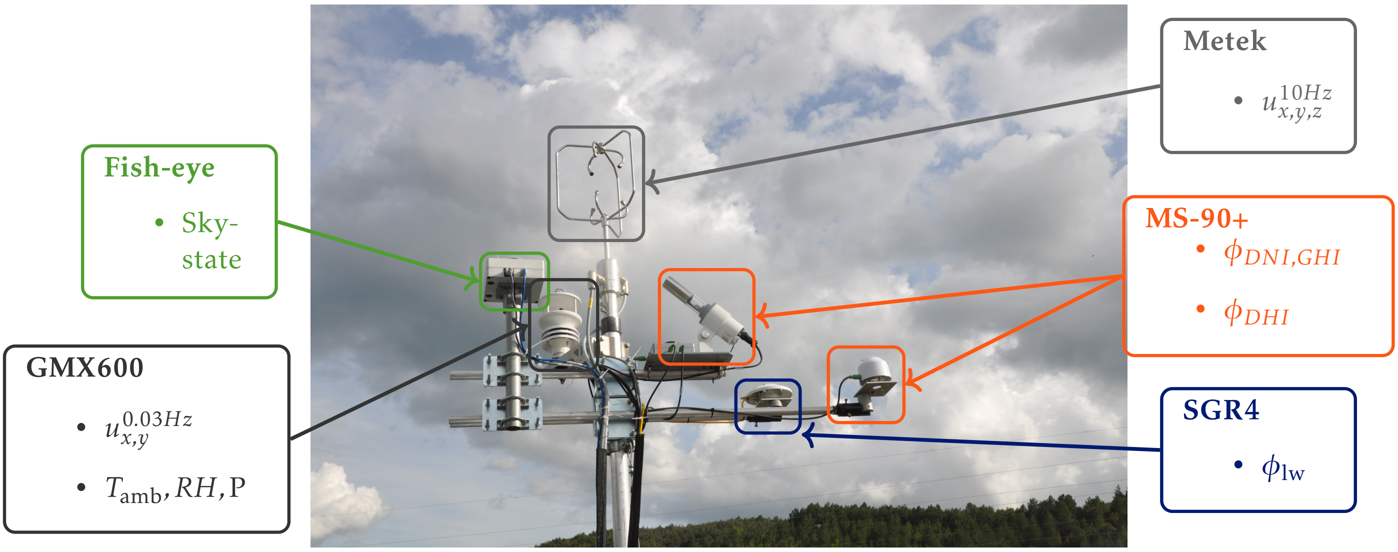

Figure 3.14–*Sensor installed on top of the mast.*

radiation sensor measures long-wave radiation in the half-sphere facing the sky.

To the north, the GMX600 meteorological station makes it possible to determine the ambient air temperature, the level of humidity, the air pressure, the presence of rain and also the wind characteristics in the two horizontal dimensions. However, the acquisition frequency is less important than for the three-dimensional system. Additionally, its position relative to the other sensors does not allow one to produce relevant measurements of wind characteristics when the wind comes from the south. In this situation, the three-dimensional sensor obstructs part of the incident field. A fisheye camera, also positioned to the north of the installation, scans the sky with a capture time of 10 seconds. Part of the sky is also obstructed by the 3D anemometer.

Data acquisition

Both the 3D anemometer and the fisheye camera are power and data intensive. Under these conditions, the monitoring system is split into two parts; the first one called *high frequency* is dedicated to the two previous sensors. All the other sensors on the raft are attached to the *low* *frequency* acquisition.

The high-frequency system consists of a PC and a modem for the daily transfer of wind data and sky images. Additional hard disk storage is built directly into the monitoring cabinet. A battery is also dedicated solely to high-frequency acquisition.

Module-level and raft-level sensors

The modules installed on the raft are used both to supply power to the various electronic elements that make up the whole system and to monitor the operating temperature. The module that is electrically connected to the low frequency branch of the acquisition system is riddled with RTD sensors bonded by a double layer of aluminium adhesive tape. The positioning of the sensors is chosen to capture the average behaviour of the module as closely as possible. A temperature sensor is also placed on the module dedicated to high-frequency acquisition to capture any malfunction between the two modules.

A second MS-80S sensor is also installed above the module through a plate screwed to the frame. The plate shares the same plane of incidence as the module, so the sensor makes a global measurement of the solar flux in the module plane. This measurement reduces the uncertainty on the yield and therefore on the operating temperature (no additional calculation of solar transposition).

Under the modules, RTD sensors are installed to evaluate the surface temperature of the floats at different positions. Two sensors are positioned on the front part of the floats to guarantee a minimum of incident irradiation during the day, and a last sensor is positioned on the back part to possibly give an indication on surface temperature heterogeneity.

3.4.3/ Data Collected

The dynamics of the environmental and operational measurements for the particular day of 1st June is represented below. This day is marked by alternating sky conditions and parasitic movement and is representative of site conditions on a global scale. In addition to the particular dynamics, statistical data for the entire measurement period are also represented.

Density of flux measured

Figure 3.16 shows the dynamics of the solar flux density measurements, the short wavelength in the module plane, the long wavelength and the heat flux sensor measurement; as well as the statistical elements of the particular series of June 1st, in addition to the global distribution. To avoid biasing the analysis by taking into account improper measurements (shading by the meteorological mast on the $\phi_{\mathrm{sw,poa}}$ probe), the statistics are calculated exclusively for the afternoon period (12 a.m. to 8:30 p.m.). Also, Figure 3.17 shows the state of the sky captured by the fisheye camera for three situations represented by vertical dotted lines (1 p.m., 3 p.m., 5 p.m.). Initially, we noticed that the solar curve is rather well represented with a maximum of 1221 $\mathrm{W\,m^{-2}}$ just before 12 a.m.. The shading caused by the presence of the mast is also noticeable during the period 8 a.m. to 12 p.m. and is reflected in the reduction of the solar flux density. A camera check during this same period confirms that the shading is not caused by an overcast sky. Therefore, it is wise to ignore this period. During the day, the sky becomes cloudier, Figure 3.17b shows a persistent cloud passing through the scene around 3 p.m.. Between the two moments captured

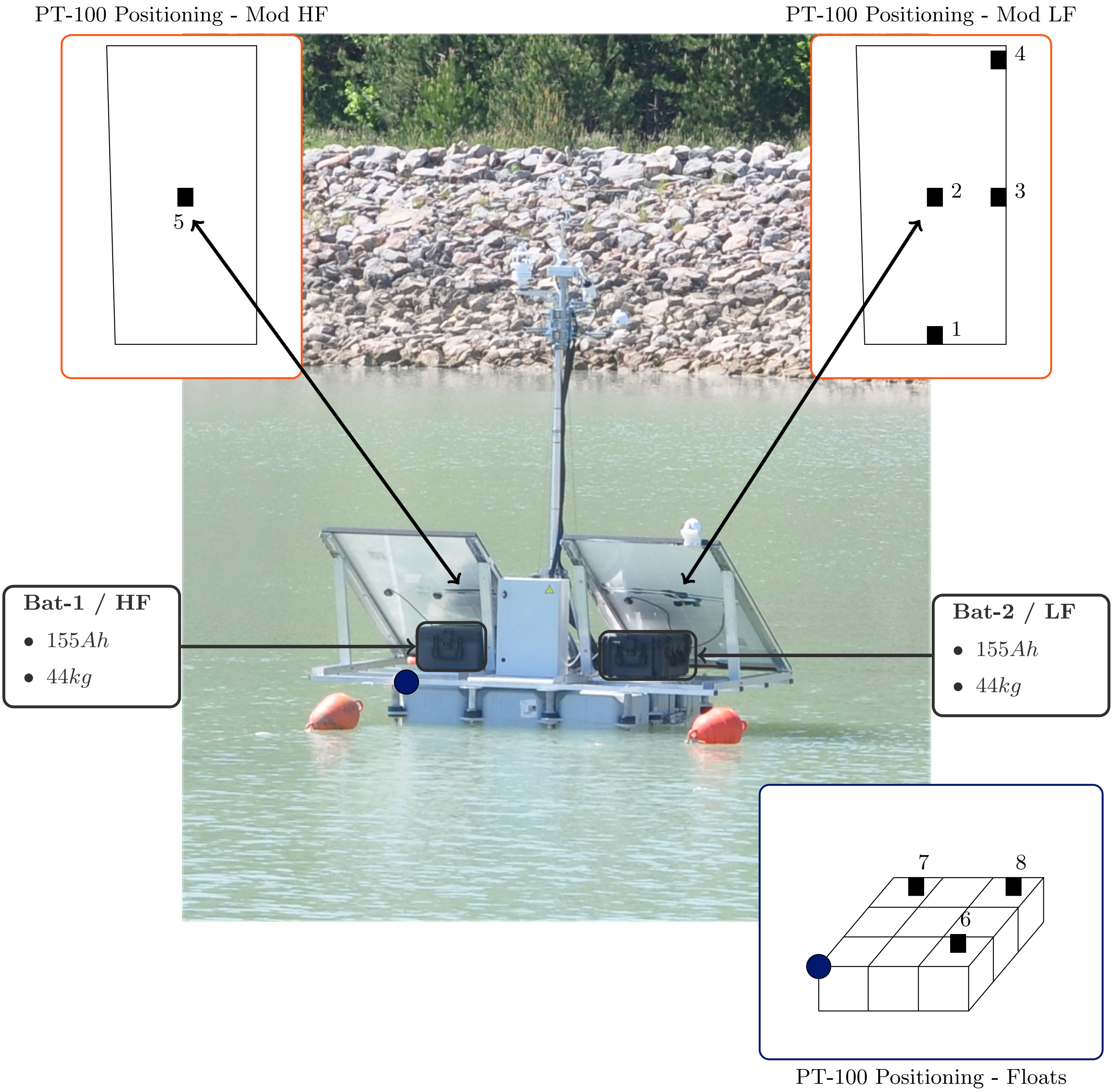

Figure 3.15–*Distribution of temperature probes and the MS-80S measuring the* $\phi_{sw,poa}$ *component.*

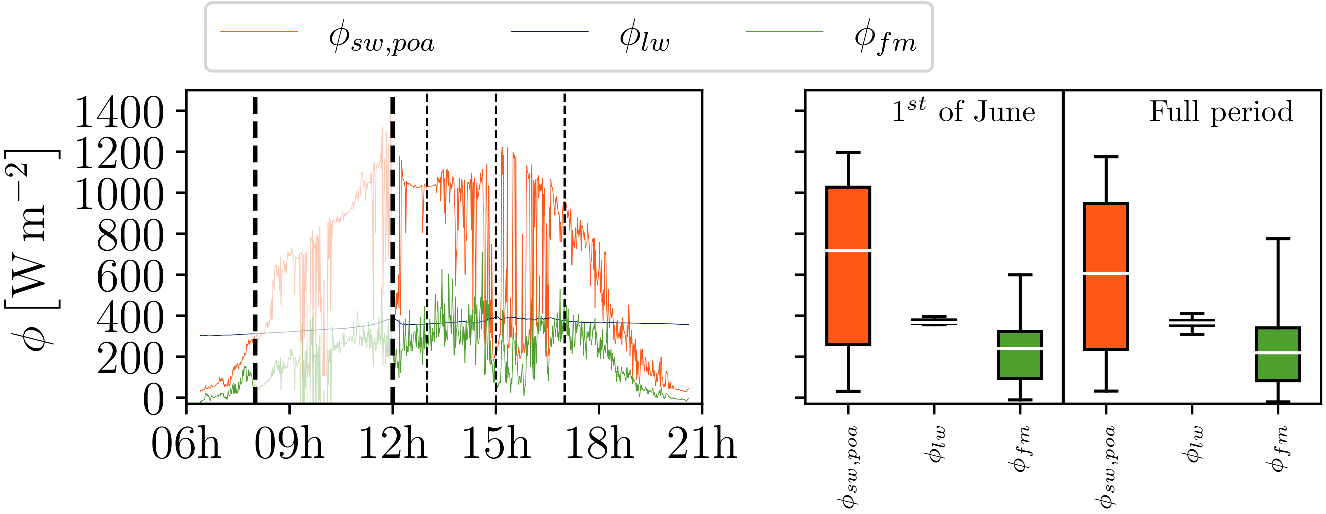

Figure 3.16–*Dynamics of flux density measurements over the 1^{st} of June: $\phi_{sw,poa}$ (−), ϕ_{lw} (−), ϕ_{fm}^{fr} (−). The distribution of datapoints are given for both the single day of study and the full dataset. Colours are similar to the time-series plot.*

by the camera, the raft has also moved; this is visible by noticing the displacement of the topographic landmark. This movement can also be seen in the quality of the radiative measurement - its dynamics show variations of the order of 50 W m^{-2} over short periods of time, 1 to 2 minutes. Instead, cloud areas are characterised by a brief but potentially persistent drop in radiative value, on the order of 500 W m^{-2}. Cloudy skies can also be visualised with variations of the order of 200 W m^{-2} and are more persistent - Figure 3.17c shows the latter case. In the following work, we will note that the representative daily irradiation of the site for the global period is 607 W m^{-2}.

At the same time, the heat flux sensor shows a behaviour similar to that observed at CETHIL, its dynamics is fast, and cloudy periods are also identifiable on this signal. The main range of variation is $\phi_{\mathrm{fm}}^{fr} \in [-2; 530]\,\mathrm{W\,m^{-2}}$ (whole period), with a median value of 218.6 W m^{-2}. It is interesting to note that the maximum value is about 200 W m^{-2} higher than the value measured in CETHIL. Although the data processing is slightly different (here only the afternoon measurements are considered), this shift is notable. Its explanation comes from the fact that there is no electric charge during the investigation period. Indeed, whereas the CETHIL module produced around 220 W during the measurement period, the FPV2 module is supposed to produce very little, given the level of charge of the batteries, which is assumed to be very high at this time of the day. Therefore, this power differential is released as heat and captured by the heat flux sensor.

Finally, the long-wave radiative flux shows relative constancy throughout the day, both during the day of interest and on a global scale. If we pay attention to the signal around 12 a.m. and 3 p.m., we notice small fluctuations of the order of 30 W m^{-2} which correspond to cloud passages (Figure 3.17b), for which the alliance between effective temperature and emissivity is more important than the same alliance for the clear sky. For the rest of the studies, we will retain a median global value of 364 W m^{-2}.

(a) *1 p.m. - Clear sky* **(b)** *3 p.m. - Cloud passage* **(c)** *5 p.m. - Evolving sky*

Figure 3.17–*Sky states captured during the 1st of June. The principle landmark (North Eastern Side of the "Montagne de Saint-Genis") is indicated by a white rectangle (True North direction).*

Temperature analyis

Figure 3.18 shows the temperature dynamics during the day for the different temperature sensors, an average is made for the sensors attached to the back of the module and the sensors attached to the floats in order to reduce the edge effects that are perceptible between the different positions of the systems. First, it can be seen that the average temperature measured on the module is consistent with the radiative evolution measured previously. The cloudy passages around 3 p.m. are transcribed by a notable drop of the order of 26 °C. The application of the spatial average shows that the signal between 8 a.m. and 12 a.m. undergoes a moderate alteration due to the shading on the module. However, this portion of the signal is not considered in the following case when this apparent robustness is not verified when working at the global scale.

The temperature dynamics of the floats show an evolving behaviour during the day. At first, at night and until early morning, the float is less warm than the water and remains warmer than the ambient air (and the module). At this time, the air acts as a cooling agent for the lake and a warming agent for the atmosphere. Around 9 a.m., the float becomes warmer than the lake and remains warmer than the air, the temperature difference is still greatly reduced. At this point, the float becomes a warming agent for the lake and its influence on the warming of the air is reduced, but it still exists. This behaviour can be seen in the median values for the global period; the float reaches a median temperature of 25.77 °C while the atmosphere reaches a temperature of 23.3 °C and 21.3 °C for water. In order to complete these observations, it is also necessary to mention the typical characteristics of the lake environment from which FPV1's experiment only partially benefited: the ranges of ambient temperature variations are important ($T_{\text{amb}} \in [16.4; 28.8]$ °C over the study day) and the water temperature presents a much stronger inertia ($T_{\text{wat}} \in [20.6; 23.9]$ °C over the study day). Situations leading to cooling effects during the day are therefore potentially more frequent and important, while the opposite effect during the night is also possible.

Wind regimes

Figure 3.19 shows the dynamics for the day of interest of the wind speed, the friction velocity, and the normalised turbulent intensity. For these measurements, data are averaged on a 10-minute basis, and therefore between 5999 and 6000 samples, denoted N, are integrated per datapoint. Wind velocity is calculated from the direction components as:

$$\overline{U_{\text{w}}} = \left[u_x^2 + u_y^2\right]^{0.5} \tag{3.10}$$

The friction velocity is computed from Equation (2.33).

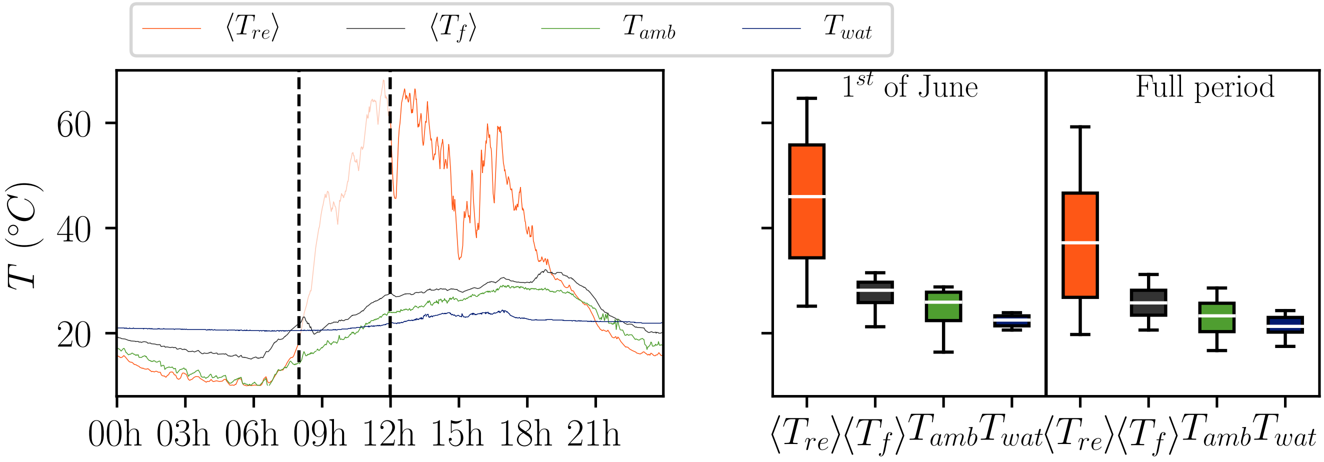

Figure 3.18–*Dynamics of temperature measurements the 1^{st} of June: $\langle T_{re} \rangle$ (━), T_{wat} (━), $\langle T_f \rangle$ (━) and T_{amb} (━). The distributions of datapoints are given for both the single day of study and the full dataset. Colours are similar to the time-series plot.*

The nycthemeral wind dynamics is well measured on the site, the average wind speed is rather low during the night with levels between $0.5\,\mathrm{m\,s^{-1}}$ and $0.9\,\mathrm{m\,s^{-1}}$, then during the day the levels are clearly stronger due to the usual atmospheric properties. The day of June 1^{st} proves to be a fairly conservative case with respect to the wind regime throughout the period; we observe that the median wind reaches $1.7\,\mathrm{m\,s^{-1}}$, while during the general period the median is $2.6\,\mathrm{m\,s^{-1}}$. This value, which will be retained for the rest of the work, only considers the daily winds; the winds observed during the night are excluded. From the prospective view of the atmosphere, the friction velocity reaches a median value of $0.25\,\mathrm{m\,s^{-1}}$ on the global scale, assuming that the turbulence involved by the mast and the raft is negligible in the calculation. The dynamics over the day of interest follows a similar behaviour as the averaged velocity, which is a normal behaviour, as the roughness value that is internalised in the computation is almost constant in the first approximation (roles of wind swell and crops permeability near the lake are dismissed). The range of evolution observed on the global scale extends to $u_\star \in [0.09, 0.52]\,\mathrm{m\,s^{-1}}$.

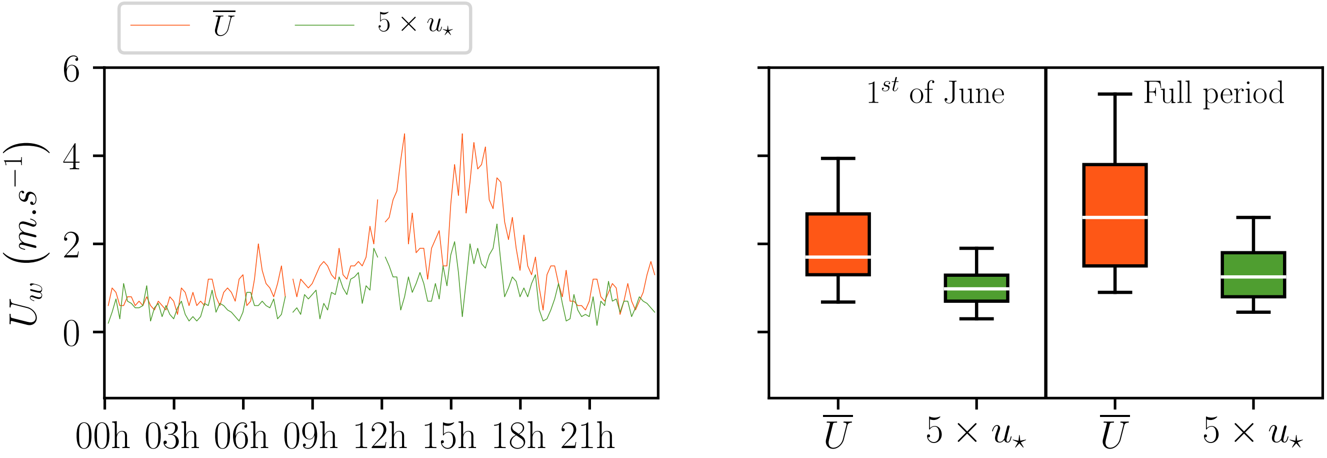

Figure 3.19–*Dynamics of high-frequency velocity measurements for the 1^{st} of June: U_w (━) and $u_\star$ (━). The distributions of datapoints are given for both the single day of study and the full dataset. Colours are similar to the time-series plot.*

To analyse the main wind direction, the data is collected in *coarse* sectors. The selected sector size is 90°, which allows maximum coverage of raft movements due to soft anchoring. An example of a change in wind direction due to the inclination of the raft is given in Figure 3.21. In this context, the part of wrong attribution of categories still exists, as highlighted by Figure 3.21c where the measured category is east, while the true category lies between the South and East bins.

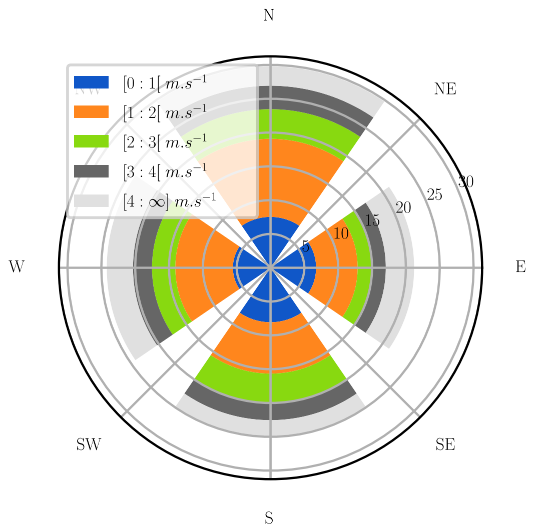

Figure 3.20–*Wind roses constructed with records from the daily period ($M = 3923$ measurements).*

Figure 3.20 shows that the main direction seems to be north with 30 % of the wind occurrences in the sector. This direction is rather logical from a microclimatic point of view; Figure 3.13 indicates that the southern area of the lake is open, the surrounding relief being rather favourable for the flow in this direction. The eastern direction has the fewest occurrences with 21 %. In addition to the microclimatic context, this is also the direction for which the raft has the least surface area exposed to the wind (drag reduction), so we cannot clearly attribute this low occurrence to the microclimatic context alone. By comparing the observations of the fish-eye camera with the direction measurements, it can be seen that the southern sector is a good candidate to host the prevailing wind directions.

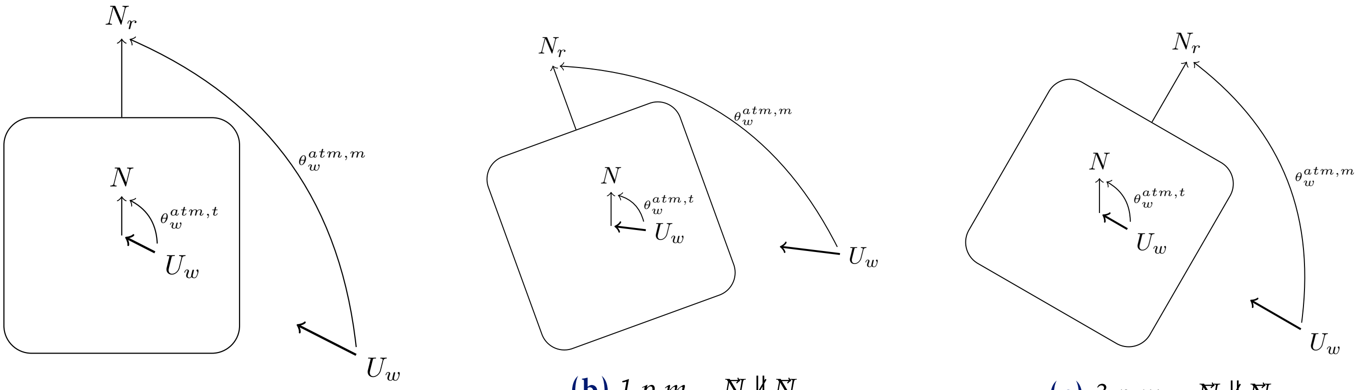

(a) $\vec{N} \parallel \vec{N}_r$

(b) *1 p.m. -* $\vec{N} \nparallel \vec{N}_r$

(c) *3 p.m. -* $\vec{N} \nparallel \vec{N}_r$

Figure 3.21–*Estimated yaw of the raft for different instants based on the fish-eye pictures on the 1st of June. Figure 3.21a indicates the calibration state in which* $\theta_w^{atm,exp} = \theta_w^{atm,t}$*, Figure 3.21b shows the estimated situation at 1 p.m. (assuming a yaw of* $-20°$*) , the recorded direction value is* $\theta_w^{atm,exp} = 117°$ *and* $\theta_w^{atm,exp} > \theta_w^{atm,t}$*, Figure 3.21c shows the estimated situation at 3 p.m. (assuming a yaw of* $20°$*), the recorded direction value is* $\theta_w^{atm,exp} = 90°$ *and* $\theta_w^{atm,exp} < \theta_w^{atm,t}$*.*

3.5/ Conclusion

Each of the measurement campaigns conducted during the thesis work has been specifically designed to a given objective, though they form a single unit that allows one to characterise photovoltaic floating applications.

First, the FPV1 campaign focused on the environmental background of FPV and the existing link with operating conditions. The campaign is segmented in three seasons, and the high-quality data (1-minute sampling) allow us to describe the scene with a satisfactory accuracy. However, the combination of climate conditions and the features of the test site appears to smooth the action of specific local environmental conditions. The records performed offshore and onshore will be used to simulate the thermal and electrical performances of the investigated setup in a next chapter.

Second, the CETHIL campaign sheds light on a new methodology to measure the convective heat rate on the front face of the module. A major advantage of the developed system is to make use of high-frequency sampling data so that it outperforms the state-of-the-art methodology. Under an acquisition time-step of 10-min, the new method offers a greater statistical efficiency, mainly by capturing the effect of brief thermal variations. Further investigations would lead to simulation of the module behaviour with the flux density recorded, and estimate the expected gain in prediction by doing so.

Finally, the FPV2 campaign addresses both the monitoring of thermal behaviour of floating module (though in standalone mode), and the microclimate effect of a representative lake for an FPV project. Either a low-frequency (1-minute sampling) and a high-frequency (10-Hz sampling) were installed, hence the campaign allows us to study the atmosphere dynamics and its link with the module conditions. Knowing that the FPV2 reservoir will host an FPV powerplant, the information collected through the campaign will be integrated into a microclimate model, using the atmospheric flow solver integrated in code_saturne, to predict the effect of positioning the FPV array. In this regard, Table 3.5 collects the enumerated measurements of interest in a bulk fashion.

Field	$\phi_{\mathrm{sw,poa}}$	T_{amb}	T_{wat}	$u_\star$	$\theta_{\mathrm{w}}^{\mathrm{atm}}$
Median	$607\,\mathrm{W\,m^{-2}}$	23.3 °C	21.3 °C	$0.25\,\mathrm{m\,s^{-1}}$	0°

Table 3.5–*Summary of the statistical data observed at the FPV2 Test-site.*

4 NUMERICAL MODELLING

> You can prove anything you want by coldly logical reason, if you pick the proper postulates.
>
> Isaac Asimov

This chapter describes the nodal and the CFD models used in the thesis work. The nodal model is dedicated to solve the thermal behaviour of FPV so that the boundary conditions are investigated in more details. The focus is put on standalone systems. The CFD models assimilate the PV module as single or several heated flat plates over which airflow dynamics is simulated. Those models are used to upscale the study to powerplant scale; elements of validation are discussed to support those developments.

Contents

4.1/ Introduction: Numerical Configuration Descriptions

When one wants to simulate the thermal dynamics of a photovoltaic system, thermal radiative transfers and convective transfers are embedded in the calculation either as a simple coefficient (U_{values}) or under a refined shape with separated influence. In the second case, correcting the thermal correlations to encompass the FPV application in PV prediction tool is favoured. In addition, the separated thermal modes allows one to determine corrective terms for each source of heat. Therefore, thermal models can be even more dedicated to the FPV thermal phenomena.

This chapter highlights the tweak introduced into the photovoltaic code developed at the laboratory so that the particular conditions over waterbodies are taken into considerations. From now one, it is assumed that radiative inputs are obtained through plane of array measurements (see 4). Therefore, the numerical radiative kernel is not addressed. The emphasis is placed on the thermal and electrical parts of the software. A presentation of the numerical parameters is provided and a validation step between thermal and electrical production from the numerical kernel and the data from the FPV1 campaign is carried out.

In a second stage, CFD models are developed with the ambition of assessing the convective transfers at the scale of the PV array. In this case, the volume of control is the air around the module. It is required that the numerical models are versatile so that different array geometry can be simulated. To do so, it assumed that the powerplant system is sufficiently regular in shapes so that a single motif of the array is a representative geometry of the full-scale system[1]. With this assumption in head, a full pre-processing step is implemented in SALOME® to construct the PV geometry based on simple inputs *(e.g., the module tilt θ_m, the module height $\mathcal{H}_m$, the module spacing $\mathcal{S}_m$)* and then meshing the geometry according to the air volumes of interest. With that being constructed, three numerical models are implemented in code_saturne with different objectives:

- The bi-periodic configuration seeks to calculate the average profiles of the physical fields (velocity, thermal and humidity) inside the photovoltaic power plants when the flow is spatially established (permanent state). The computational effort for this system is low, which means that several geometries could be investigated, it is suited to industrial use. The good practice of meshing is also investigated in more details for this numerical model.
- The 2-D plant configuration seeks to describe the spatial evolution of the physical field profiles. It is specially constructed to simulate the entrance region of the photovoltaic powerplant. The computational cost is higher, but it allows to show fields heterogeneity that are not captured through the bi-periodic simulations.
- The 3-D plant configuration seeks to stress the modelling atmosphere solver in order to compare the resulting fields with the wind tunnel experiment from Portland. The numerical cost is high and adapted to research purpose; it is a high-fidelity numerical reference.

In the three numerical models, the modules are heated flat plates assuming a constant density of heat flux. They are explicitly represented assuming a frame-less solution which means that the physical obstacles for the airflow are tilted rectangles (assuming a longitudinal 2-D slice of PV powerplant).

---

[1] to be convinced, the reader may see Figure 1.4, Figure 1.6 or Figure 1.5

4.2/ Photovoltaic Module 1-D

Calculation of thermo-electric dynamics is performed by the PVNOV® software (see Section 1.3.3.2). The ray tracing features is not used in this work as only monofacial cells are under investigation plus the source of radiative data is essentially composed of plane of array irradiance $\phi_{\mathrm{sw,poa}}$. Only the thermal and electrical model is involved as it allows: working with higher frequency sampling than other commercial software, defining the boundary conditions with precise thermal modes, coupling electrical and thermal dynamics (strong coupling).

The numerical structure is presented in Figure 4.1. Four file inputs are mandatory to launch the calculation: a meteo file that contains the environmental data, a module and inverters files with the characteristics of the systems and a parameter file including the tuning of the solver features. The first and the later files are the most important elements for thermal modelling, the module and inverter characteristics are more decisive for the electrical yield assessment; however failing in describing those two systems lead to modify the thermal budget and thus the temperature assessment. See A.3 for the syntax and numerical shape of mandatory files.

4.2.1/ Thermal Multi-layer Scheme

Module system

The thermal scheme is composed of five material layers which corresponds to the classical Glass/Backsheet module layout. The layers are therefore distributed (from top to bottom): Glass, ethylene-vinyl acetate (EVA), Silicium cell, EVA, Backsheet. All the thermal terms are written under the shape of a heat flux in $\mathrm{W\,m^{-2}}$, the area of exchange is defined by the product of the cell area and the number of cells in the module or the array. The stack of layers are cut into two pieces over which only conduction mode is considered. It is assumed that the conduction is 1-D (module width is little in front of the surface) and no contact resistance are integrated. The transient term is applied at the middle of the layers thanks to a thermal capacity. Figure 4.2b shows the distribution of thermal resistance R and capacity components $\rho\mathcal{V}Cp$. The conduction term reads $\phi_{cd} = \frac{\Delta T}{R^{cd}}$ and $R^{cd} = \frac{d/2}{\lambda}$ for each halved layer, the width d and thermal capacity λ are written out for each material in Table 4.1. The model is said *nodal* as described in Section 1.3.2.6.

Boundary conditions

Figure 4.2a shows a schematic of FPV situation with the emphasis on the thermal boundary conditions. With respect to the numbering in the figure, the heat transfers reads:

1. Short wavelength in the plane of array $\phi_{\mathrm{sw,poa}}$
2. Long wavelength exchange with the sky $\phi_{\mathrm{ir},fr}$
3. Front face convection $\phi_{\mathrm{cv},fr}$
4. Conduction $\phi_{cd,ext}$
5. Rear face exchange with the environment $\phi_{\mathrm{ir,re}}$
6. Rear face convection $\phi_{\mathrm{cv,re}}$

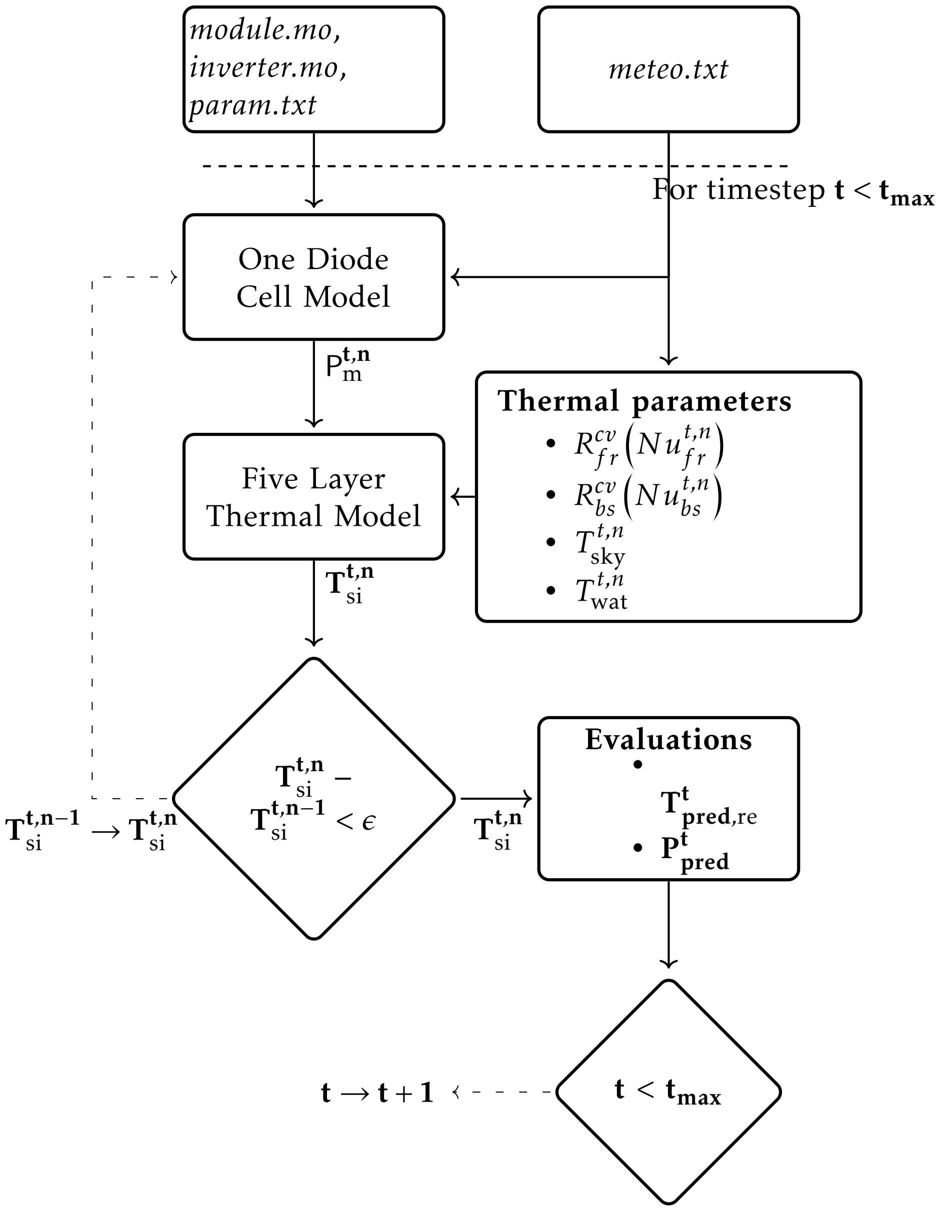

Figure 4.1–*Calculation structure for the 1-D photovoltaic module.*

The short-wavelength action is directly integrated at the cell level, the irradiation in the plane of array $\phi_{\mathrm{sw,poa}}$ is derived as ϕ_{cell} and reads: $\phi_{\mathrm{cell}} = \phi_{\mathrm{sw,poa}} \alpha \tau_{\mathrm{gl}} \tau_{\mathrm{eva}}$ Where τ_{gl} and τ_{eva} are the glass and the EVA total transmissitivities, respectively. A fix value of 0.95 is enforced for the product of the two total transmissitivities and the silicium total absorptivity α. Note that the energy yield (electrical) is removed at this stage.

The long wavelength exchange with the sky is applied to the top module layer. The heat radiative flux reads: $\phi_{\mathrm{ir},fr} = \frac{T_{\mathrm{sky}} - T_{fr}}{R_{fr}^{\mathrm{ir}}}$ with R_{fr}^{ir} and T_{sky} two functions which depend on the environment. Knowing that $R_{fr}^{\mathrm{ir}} = 1/h_{\mathrm{ir},fr}$, the heat radiative rate is obtained through a linearization process that reads: $h_{\mathrm{ir},fr} = FF\sigma\epsilon_{\mathrm{gl}}\left(T_{fr} + T_{\mathrm{sky}}\right)\left(T_{fr}^2 + T_{\mathrm{sky}}^2\right)$. Note that form factors FF are set to 1 when $\theta_{\mathrm{m}} \leq 30°$ to reduce time calculation[2]. The front heat flux $\phi_{\mathrm{ir},fr}$ is directly known at the FPV2

---

[2] From standard Farm Factor calculation for a plane with the sky hemisphere it reads $FF = \frac{1+\cos(30)}{2} \rightarrow FF \simeq 0.93$

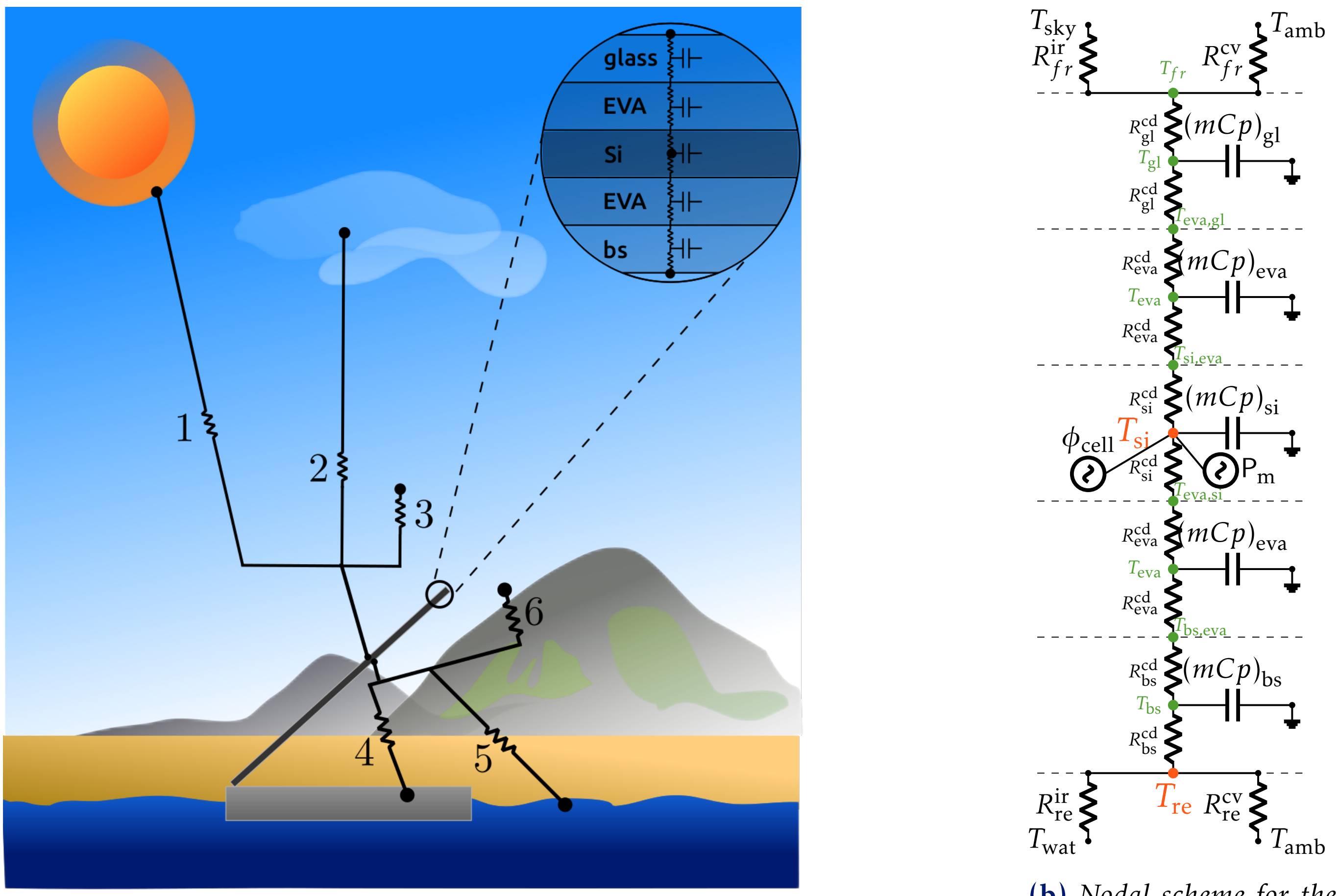

(a) *Illustration of the nodal scheme with explicit representation of the physical elements exchanging heat with the FPV module.*

(b) *Nodal scheme for the modules with the eleven unknowns (coloured).*

Figure 4.2–*Schematics of the thermal model developed for floating photovoltaics application.*

campaign using the pyrgeometer sensor, so the thermal scheme is modified in this case to directly admit the thermal flux in the calculation.

The convective heat transfer for the front face is calculated as $\phi_{cv,fr} = \frac{T_{amb} - T_{fr}}{R^{cv}_{fr}}$. The resistance term is expressed as the inverse of the heat rate $R^{cv}_{fr} = 1/h^{cv}_{fr} = \lambda/(Nu_{mix} \times \mathcal{L}_m)$. The correlation in (Gnielinski, 1975) is applied as a boundary condition of reference for the forced transfer. It takes into account the effect of forced convective transfers from laminar and turbulent regimes over an inclined flat plate, it reads:

$$\langle Nu_{forced} \rangle_L = \zeta \times \sqrt{\left(0,664 \times Re_L^{0,5} \times Pr^{0,33}\right)^2 + \left(\frac{0.037 \times Re^{0.8} \times Pr}{1 + 2,443 \times Re^{-0,1} \times (Pr^{0,66} - 1)}\right)^2} \tag{4.1}$$

The equation holds when $Re_{L,max} < 10^7$ and when the Prandtl number also verifies $Pr > 0.6$. The term ζ holds for tweaking the constant that comes from the functional analysis of the forced heat convective transfer. The standard case use the value $\zeta = 1$.

The conduction processes is set to 0 as it is assumed that the floating structure does not interact with the module thermally (insulators). This assumption is reinforced by the low area of contact between both systems. In addition that the other contributions are at least one order of magnitude higher than the conduction with the environment.

Material	**Subscript**	**Thickness** $\mathcal{E}$ (m)	**Density** ρ (kg m^{-3})	**Conductivity** λ (W m^{-1} K^{-1})	**Heat Capacity** Cp (J kg^{-1} K^{-1})	**Thermal Mass** $\rho \times \mathcal{E} \times Cp$ (J m^{-2} K^{-1})
Glass	gl	0,003	3000	1,8	500	4500
EVA	eva	0,000365	960	0,35	2090	732
Silicium	si	0,00017	2330	148	677	268

Table 4.1–*Thermal properties of PV materials, taken from (Armstrong & Hurley, 2010) and adapted from laboratory measurements.*

The long wavelength exchange with the environment is similarly determine as the front face exchange, it follows: $\phi_{\mathrm{ir,re}} = \frac{T_{\mathrm{wat}} - T_{\mathrm{re}}}{R^{\mathrm{ir}}_{\mathrm{re}}}$ with $R^{\mathrm{ir}}_{\mathrm{re}}$ and T_{wat}. Linearization process is also applied.

Finally the rear convective process is expressed under the same flavor as the front face convection transfer, $\phi_{\mathrm{cv,re}} = \frac{T_{\mathrm{amb}} - T_{\mathrm{re}}}{R^{\mathrm{cv}}_{\mathrm{re}}}$. This time, the correlation from (Churchill & Chu, 1975) is calculated:

$$\langle Nu_{free} \rangle_L = \chi \times \left(0.825 + 0.387 \times \sqrt[6]{K}\right)^2 \tag{4.2}$$

With:

$$K = Ra \times cos(\theta_{\mathrm{m}}) \times \left(1 + \left(\frac{0.492}{Pr}\right)^{9/16}\right)^{16/9} \tag{4.3}$$

The term χ is used to weight the free convective transfer, similarly as ζ for forced convective transfer. The standard case also use the value $\chi = 1$.

Main thermal components solved

The final system of thermal equation is composed by 11 equations, each one calculating the temperature at the interface between layers or at the middle location of the layers. The two main equation in our case are the middle silicium temperature and the backsheet temperature at the interface with the atmosphere, they read:

$$\begin{cases} \left(\mathcal{V}\rho Cp\frac{\partial T}{\partial t}\right)_{\mathrm{si}} = \phi^{top}_{cd,\mathrm{si}} + \phi^{bottom}_{cd,\mathrm{si}} + \phi_{\mathrm{cell}} - \mathrm{P_m} \\ \phi^{bottom}_{cd,\mathrm{bs}} = \phi_{\mathrm{ir,re}} + \phi_{\mathrm{cv,re}} \end{cases} \tag{4.4}$$

4.2.2/ Electrical Scheme

Single-Diode Model - Module level

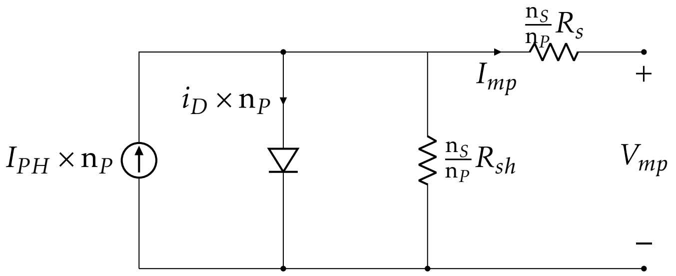

Figure 4.3–*Equivalent scheme of the electrical model enforced in the photovoltaics calculation*

The electrical model consists in a single diode scheme, based on the electrical parameters integrated in the module file. In the thesis, two different modules are used, their respective properties are summarised in the Table 4.2. The equations solved are the Equation (1.7) and Equation (1.10).

CAMPAIGN	n_S	n_P	I_{PH}	I_o	R_s (Ω)	R_{sh} (kΩ)	n
FPV1	72	1	$f^{(1)}(\phi_{\text{cell}}, T_{\text{cell}})$	$f^{(2)}(\phi_{\text{cell}}, T_{\text{cell}})$	$9,68 \times 10^{-5}$	1,28342	1.1
FPV2b	60	2	$f^{(3)}(\phi_{\text{cell}}, T_{\text{cell}})$	$f^{(4)}(\phi_{\text{cell}}, T_{\text{cell}})$	$4,46 \times 10^{-5}$	1,596	1.1

Table 4.2–*Electrical specifications for the module involved in the thesis work. Functions* $f^{(1)}$, $f^{(2)}$,$f^{(3)}$, $f^{(4)}$ *are based on flash tests of the modules for both campaigns.*

Inverter level

The right-hand side of the electrical model for the modules (Figure 4.3) is connected to the inverter so that the resistive load is adapted throughout the time. An algorithm framework is available in Modelica to perform this operation numerically; the AC power is an output of the full electrical model. The maximum power-point tracking is coded using a Particle Swarm Optimisation method which is available in the Modelica library. Our concern is only given to the DC side of the system as it is the best picture of the energy that is removed from the thermal budget at the module level. The MPPT being connected to the inverter, the latter has to be defined in order to generate a DC power.

A similar model as the one developed by SANDIA laboratory is enforced in Modelica, see (King et al., 2007). In a nutshell, the AC power is almost a linear function of the DC power, assuming a little curvature of the power transcription. An important point to mention is the maximum DC power, denoted P_{DCO}, at the inverter input. This information is integrated in the *inverter.mo* file from the inverter data-sheets. When the power at the module levels is greater than P_{DCO}, the power is clipped so that the maximum power outlet cannot be overshot. In consequence, the MPPT cannot reach the best theoretical load and the heat sink at the module level is downgraded (the module heats up).

For the FPV1 campaign, the P_{DCO} value filled in the *module.mo* file is $P_{\text{DCO}} = 2600\,\text{Wp}$ (SunnyBoy Inverter). For the FPV2 campaign, a fictitious power of characteristic of $P_{\text{DCO}} = 50\,\text{Wp}$ is filled in so that it should correspond to the maximum energy yield that can be absorbed by the module (the remaining part of the total electrical capacity is lost by heating). This threshold is chosen to match the afternoon condition of running when the battery is fully charged and the electrical production only feed the set of sensors.

4.2.3/ Solver Settings

Convergence and uncertainty

Thermal and electrical models are solved through iterative procedure through a finite difference scheme. Outputs of one module serves as inputs for the second until the error criterion is met ($\epsilon < 1e-4$)[3]. The latter must be satisfied for the main thermal unknowns in the nodal scheme. The nominal case is set to 1 °C, therefore the uncertainty for all the nodes are assumed to be 1×10^{-4} °C.

---

[3] The reader may refer to Figure 4.1.

Solver configuration and Numerical parameters

The finite difference scheme make use of the SUite of Nonlinear and DIfferential/ALgebraic equation solver CVODE (Hindmarsh et al., 2005). The solver is adapted to non linear and large scaled ODE systems, through variations of Newton-Krylov algorithms. Other solvers are available in the Dymola environment (DASSL, Runge-kutta 4, ...) but the CVODE solver has proven to be reliable in atypical situations when the ODE's become stiff.

4.2.4/ Solver Validation

Behaviour of the thermoelectric model is validated using a summer subset obtained during the FPV1 campaign. The physical boundary conditions described in the previous section are applied, and the modelled data are the backsheet temperature $T_{pred,\mathrm{re}}$ and the electrical production P_{pred}. They are compared with their experimental counterparts $T_{exp,\mathrm{re}}$ and P_{exp}, respectively. Figure 4.4 shows the results for both quantities. A first observation is that the thermoelectric produces an accurate picture of the two quantities under investigation. The linearity coefficients are higher than 0.89 and the r^2 coefficient indicates a very good accuracy for the electrical part, although the phenomenon of clipping is effective at high irradiation levels due to the inverter maximum power $P_{\mathrm{DCO}} < P_{DCmax} \rightarrow 2600\,\mathrm{Wp} < \underbrace{8}_{\text{Nb. of modules}} \times 355\,\mathrm{Wp}$. The temperature prediction is generally less efficient despite the complexity of the model, it tends to overestimate the actual temperature, particularly for low irradiation levels. This phenomenon is potentially due to a bad interpretation of the input conditions, to a deficiency in the thermal inertia taking into account (inconsistent time step) or to a hazardous behaviour of the electrical model at very low irradiation. This last option is preferred because of the intrinsic characteristics of the single diode model used.

This validation step shows that the implementation of the 1-D photovoltaic case study is rather consistent and that the main physical phenomena are correctly integrated in the model. The assumption made of a module with homogeneous physical properties in the transient regime is considered coherent and it is agreed that it is possible to use this model to represent the average characteristics of the photovoltaic module in a floating application, notably its backside temperature and its electrical output.

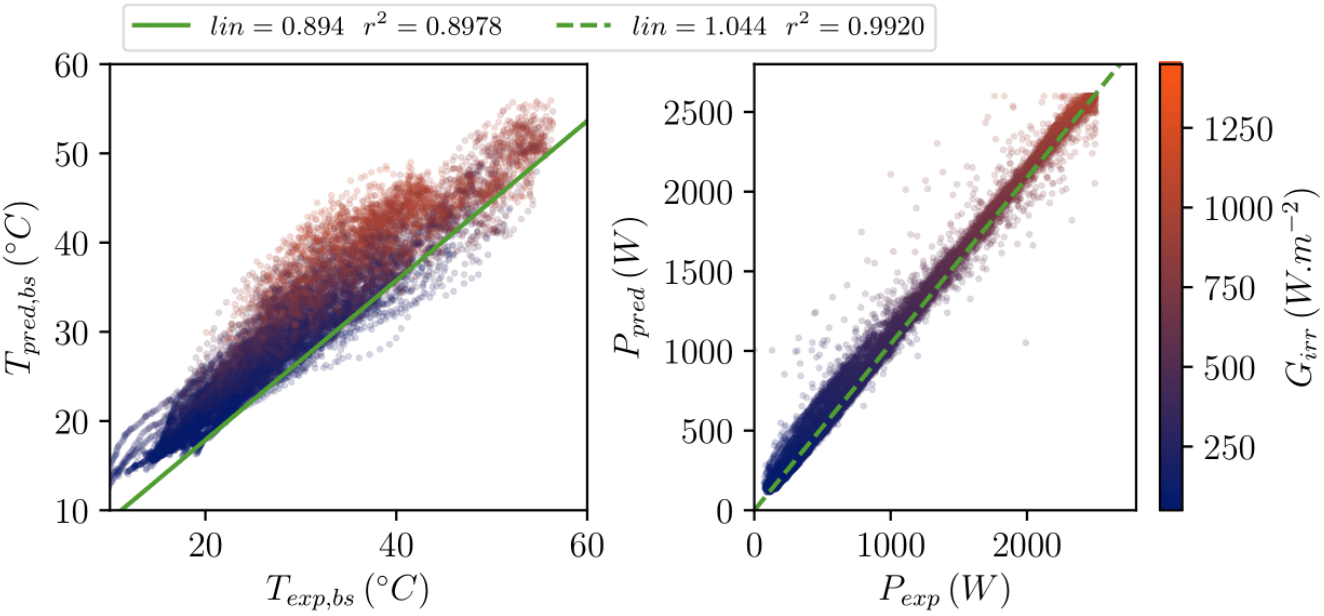

Figure 4.4–*Comparison of backsheet temperatures (right-hand side) and DC yield (left-hand side) coloured by measured irradiance field. Both comparisons are performed using the 1-D photovoltaic model applied over 17863 datapoints (1-min time step).*

4.3/ Single Heated Flat Plate 2-D

From now on, we are interested in the PV plant configuration as described in Figure 4.5. In contrast to Section 4.2, the medium to be modelled is the air adjacent to the module. Therefore, the fluid mechanics solver code_saturne is used. By analogy with the work related to the urban environment, three flow zones can be distinguished, the atmospheric flow zone developed upstream of the power plant, the heterogeneous flow zone with spatially evolving velocity profiles and finally a flow zone developed. All modules are represented by parietal heated plates and the arrangement of the modules is regular: the length of pitch $\mathcal{S}_\mathrm{m}$ is in effect throughout the power plant.

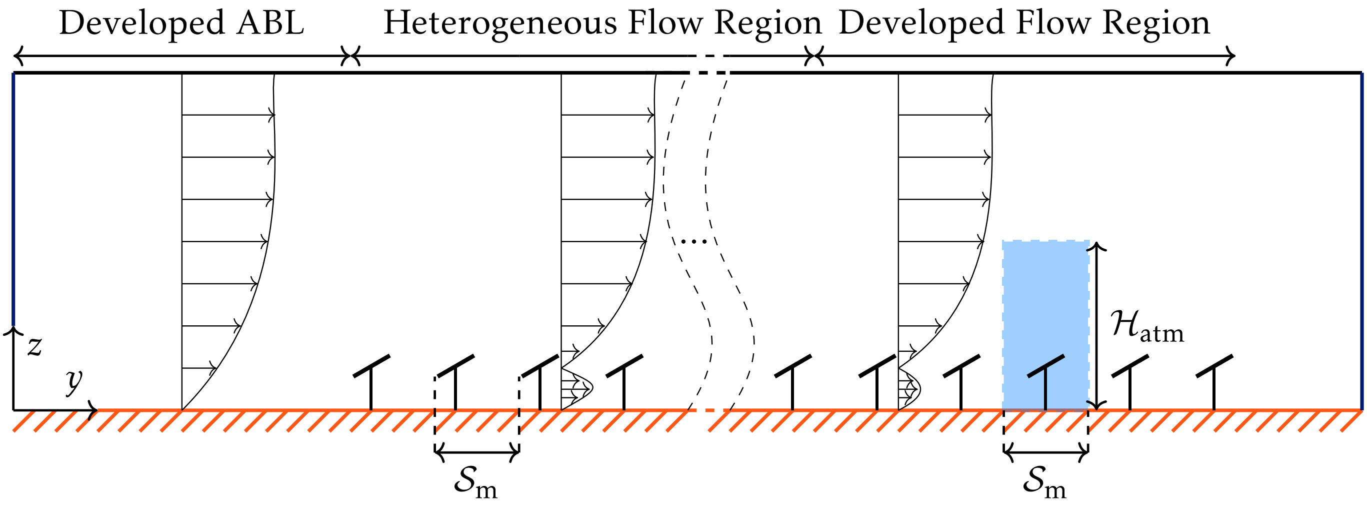

Figure 4.5–*Schematic illustration of the photovoltaic array in 2-D longitudinal view. The Heterogeneous Flow Region is the flow region affected by the change in geometry (flow field heterogeneous in space). The Developed Flow Region is the area where the spatial evolution of the flow is cancelled out. The area coloured in blue (■) shows the zone selected for the calculation of the* ***Single Heated Flat Plate*** *section.*

Firstly, we wish to characterise the Developed Flow Region which is assumed to be representative of the aeraulic conditions prevailing in an infinite power plant. However, it is assumed that costly computations are prohibited: The objective is to explore the airflow regime according to the set of geometrical parameters so that the airflow for FPV and land-based installations can be covered. Ultimately, the heat rates for the modules standing in the Developed Flow Region want to be estimated.

The next subsections are dedicated in introducing the pre-processing stages that are used in the study as well as the next sections (make use of regular spacing of modules in the array), then the specific conditions involved in the Single Heated Plate study are presented. Elements of validation are provided.

4.3.1/ Pre-processing Suite

In Figure 4.6, the steps that composed the numerical configuration are described. The preprocessing chain is similar for all the numerical configurations (2-D single heated plate, 2-D array of heated plates, 3-D Validation). The main preprocessing stages are performed in SALOME®[4]

---

[4] Version 9.7.0, identical for all modules.

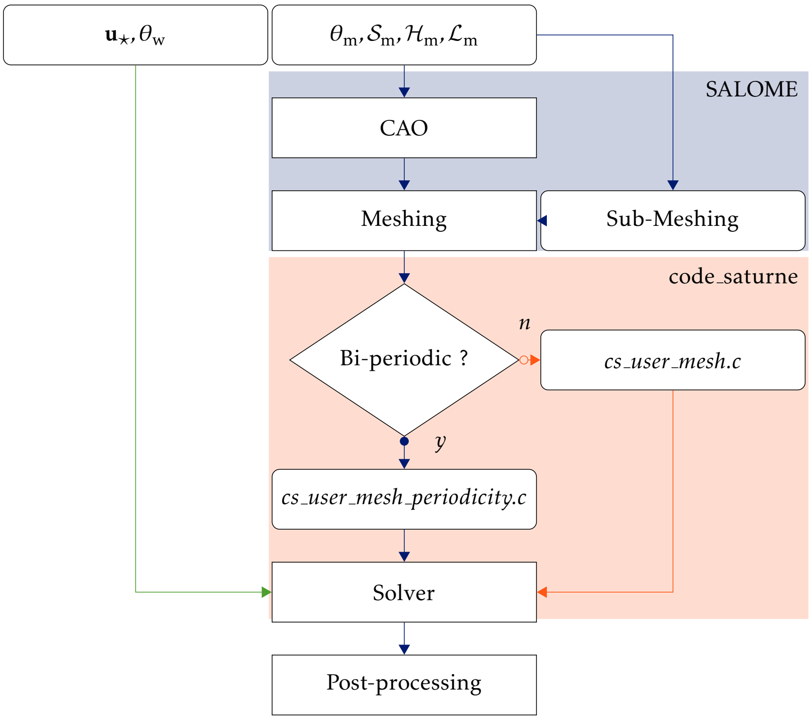

Figure 4.6–*Schematic of construction for the configuration systems. The initial pre-processing stages are shared by all systems. The code_saturne routine called when assuming specific pre-processing step are indicated.*

using the SHAPER® and SMESH® that are CAO and meshing software, respectively. These tools were used as they are easily scriptable in *Python* in order to perform multiple operations in a robust fashion.

The disparities in pre-processing steps for the numerical configuration are performed using the code_saturne solver. This sub-section shows the main preprocessing-chain and the particularity induced by the 2-D single heated plate in code_saturne.

The philosophy behind the suite being to construct an unitary motif (fully supporting the single heated flat plate case) and from that point performing supplementary simple operation such as copying, translating and sewing the discretized space of calculus.

Unitary Geometry configurations

The unitary geometry is parameterised as a two-dimensional channel, Figure 4.7a shows the variable that make-up the channel. The domain of calculus stands in the area $\Omega = [0, \mathcal{S}_m] \times [0, \mathcal{H}_m]$. The strings are represented by a rectangular hole of unit length $\mathcal{L}_m$ and width $\mathcal{E}_m$, oriented by an angle θ_m with respect to the axis $\vec{y}$. The centre of the hole is positioned at $(y_c, z_c) = \left(\frac{\mathcal{S}_m}{2}, \mathcal{H}_m - \frac{\mathcal{L}_m}{2}\sin(\theta_m)\right)$.

The dimensions of the single heated flat plate study rely on the type of the investigated application. Four cases are distinguished:

- The base case for ground mounted that takes into account full scale dimensions for a real photovoltaic powerplant.
- The FPV2 case that refers to the dimensions involved in the floating set-up of the industrial

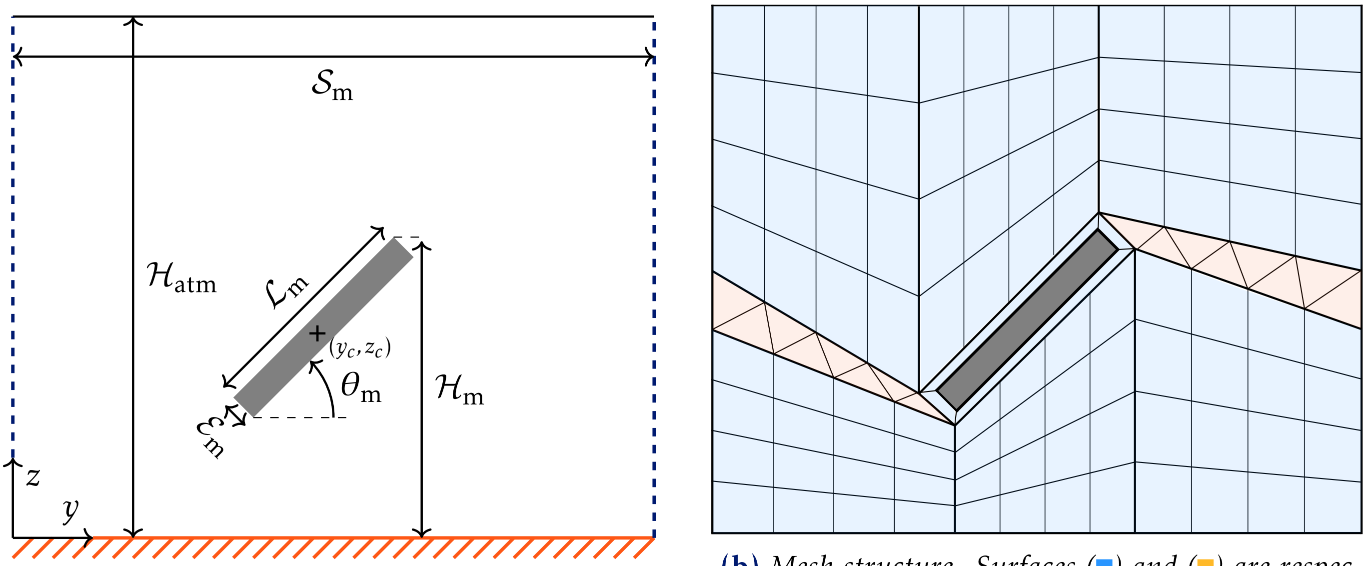

(a) *Parameterised geometry.*

(b) *Mesh structure. Surfaces (🟦) and (🟨) are respectively the location of hexahedrons and prismatic cells.*

Figure 4.7–*Sketches of the bi-periodic pre-processing stages.*

installation at FPV2.

- The morphometry case which is delimited by tilt, pitch and module height variations. It is later used to analyse the quantity of interest with regard to several feasible dimensions.
- The Validation case from the wind tunnel experiment in Glick, Smith, et al., 2020. The dimensions are a reduced scale from the base case for ground mounted case.

Table 4.3 summarises the dimensions that applied in each case. In this section, the focus is given to the base case for ground mounted. The construction steps, numerical settings and post processing quantities being similar for the floating case, choosing the full scale ground-mounted scheme allows to validate the numerical model with regard to the validation case. The floating case having no validation material to be compared with.

The geometry is made on the SHAPER tool. In order to improve the mesh creation in the next stage, the geometry is built-up to incorporate 12 sub-zones.

Dimensions	Experimental (Validation)	Ground Mounted (Full-scale)	Morphometry Case (Full-scale)	Floating (FPV2)
$\mathcal{L}_\mathrm{m}$ (mm)	50.8	1676.4	1676.4	1000
θ_m (°)	30	30	[10;35]	12
$\mathcal{H}_\mathrm{m}$ (mm)	63.4	2092.2	[362.1;2092.2]	362.1
$\mathcal{E}_\mathrm{m}$ (mm)	5.3	6	6	6
$\mathcal{S}_\mathrm{m}$ (mm)	87.4	2884.2	[1330;5400]	1330
$\mathcal{H}_\mathrm{atm}$ (mm)	800	7260	10000	7260

Table 4.3–*Summary of geometry dimensions for the simulated cases.*

Meshing - General Considerations

The finite volume - Eulerian - formalism of code_saturne requires a discretized mesh to support the calculation of the conservation equations (Equation (2.8)). The prior geometry step concludes on the determination of a 2-D feature with several sub-areas composed of four sides. The mesh construction step takes this properties into account to associates the geometry groups to a set of constraints that rely on the dimensions involved in the case under construction (see the dimensions in Table 4.3)

Naturally, it is preferred to optimise the discretized space through a structured mesh, as it would ease the solver operation. However, the geometry of the modules imposes deformations on the cells, especially when the tilt of the module is important. The critical points are located at the trailing edges of the module, so special attention is paid to these areas to reduce the deformation rate as much as possible, using a triangular generation algorithm. In order to guarantee a sufficient robustness for cell's properties within the full mesh, the sub-areas around the module are designed so that the size of the zone with triangle faces are large enough.

One of the important constraints in the construction of the mesh lies in the conformity criterion at the edges of the domain for which periodic conditions are applied. Each cell on the left of the domain must match its counterpart on the right. The shape of the module combined with the requirement of the maximum number of hexahedrons in the domain necessarily leads to the creation of prismatic sub-meshing zones to avoid both a significant warp at the trailing edges of the module, and a shift of the cells from the edges of the domain. Sub-meshes are supported by the sub-areas made during the geometry creation stage. The twelve areas are assigned a specific set of constraints to ensure that the average cell volume is swiftly evolving from the little cells at the module vicinity to the atmosphere. Cell shape is controlled at this moment, with the objective of reducing as much as possible cell warping by modulating the number of cells around sharp edges. Figure 4.7b shows the arrangement of the sub-mesh areas and the criterion of conformity in the Ground-Mounted case.

At this stage, the mesh is still supported by a 2-D geometry, hence it can be considered similar to a grid-mesh. To ensure that the volume of fluid method can be applied, the grid-mesh is arbitrary extruded so that the discretized space has a nominal length of 0.05 m in the $\vec{x}$ direction, covered by a single 3-D cell. The volume of control is defined in $\Omega = [0, \mathcal{S}_{\mathrm{m}}] \times [0, \mathcal{H}_{\mathrm{atm}}] \times [0, 0.05]\mathrm{m}^3$. The distance of 0.05 m is chosen with regard to the specific pre-processing stage in the configuration system of 3-D staggered arrays. The width has no influence over the calculation for the different configuration system whatsoever.

4.3.2/ Solver Settings

Conservation laws

In this study, the equation solved by code_saturne are the three conservation laws for the dry atmosphere: the mass conservation (Equation (2.7)), the momentum conservation (Equation (2.8)) and the energy conservation (Equation (2.9)). The humidity field is integrated as a fourth conservative equation assuming a passive scalar, it reads:

$$\frac{\partial \overline{\rho q}}{\partial t} + \frac{\partial \left(\overline{\rho u_j q}\right)}{\partial x_j} = -\frac{\partial \left(\overline{\rho u_j' q'}\right)}{\partial x_j} + \frac{\partial}{\partial x_j}\left(D_m \frac{\partial \overline{q}}{\partial x_j}\right) \tag{4.5}$$

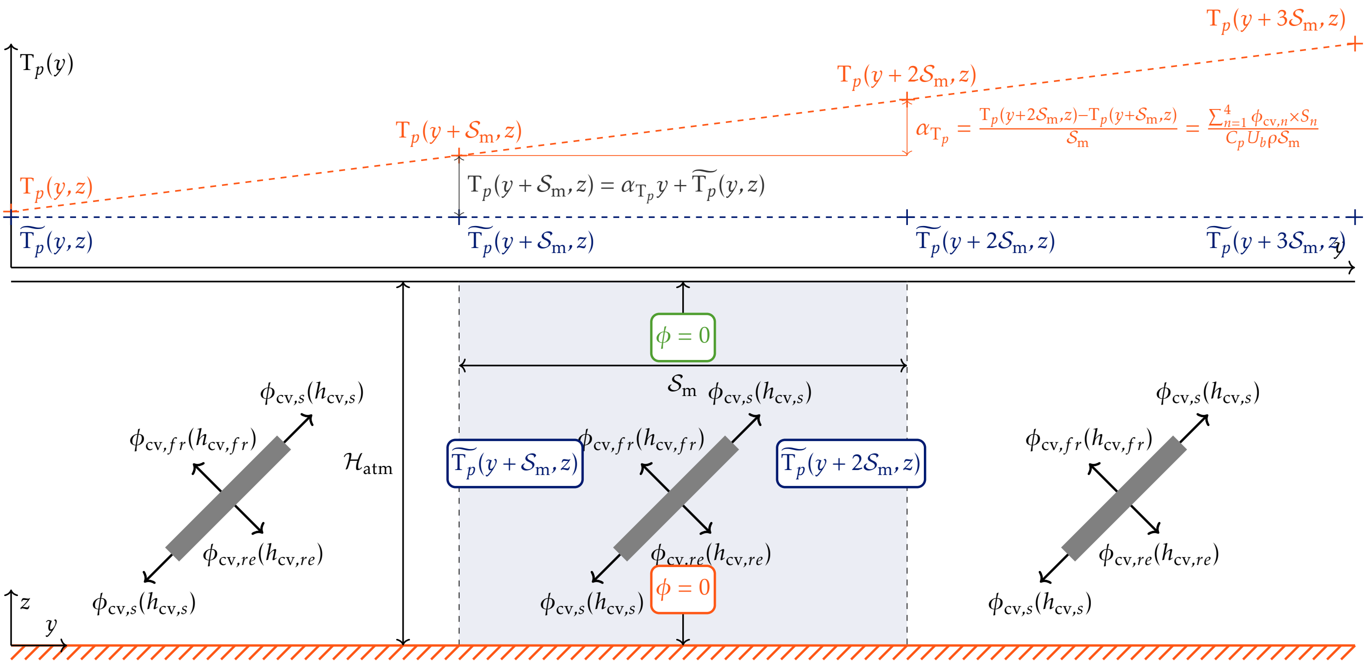

Figure 4.8–_Illustration of the temperatures in the streamwise direction. The periodic temperatures is constant throughout the powerplant. The potential temperature increases as the density of heat flux feed the macroscopic volume of air. It is hypothesised that the density of flux does not escape the control volume by the top and the bottom of the system._

note that the approximation of Boussinesq is applied in the momentum conservative equation.

The assumption of periodicity in this numerical configuration leads to solving the conservation equation system in a periodised form. We define the periodic quantities: $\widetilde{\vec{u}}$, $\widetilde{P}$, $\widetilde{T_p}$ and $\widetilde{q}$. All four conservation equations can be rewritten, however the conservation of energy requires modification to integrate periodised unknown $T_p(y,z) = y\alpha_{T_p} + \widetilde{T_p}(y,z)$. As shown in Figure 4.8, the advancement within the plant leads to constant and non-zero heat transfers between the periodic elements. Under these conditions, the temperature within a pattern increases as the pattern moves streamwise direction. Mathematically, the evolution in the streamwise direction of the difference in temperatures between two patterns can be written as :

$$\alpha_{T_p} = \frac{T_p(y + 2\mathcal{S}_m, z) - T_p(y + \mathcal{S}_m, z)}{\mathcal{S}_m} \tag{4.6}$$

Source term from bi-periodic considerations

The term α_{T_p} is computed using the conservation of energy law which reads:

$$\frac{\partial\left(\overline{\rho u_j T_p}\right)}{\partial x_j} + Cp\rho\overline{u_j}\frac{\partial \alpha_{T_p}}{\partial x_j} = \frac{\partial \Phi_j}{\partial x_j} \tag{4.7}$$

All calculus performed α_T reads:

$$\alpha_{T_p} = \frac{2 \times \Phi(\mathcal{L}_m + \mathcal{E}_m)}{Cp\rho U_b \mathcal{S}_m} \tag{4.8}$$

in which U_b the spatial mean velocity in the fluid domain. Mathematical proof is given in A.4.4.

Turbulence model

The Reynolds stress tensor is modelled using $k-\omega SST$ turbulence model. This choice is motivated by its ability of dealing with either a high-Reynolds or low Reynolds flows, especially below the module where the wake effect can affect the flow development leading to low velocity areas mainly in study cases with important $u_\star$. Another advantage stands in the typical $k-\epsilon$ turbulence behaviour away from the module compared to the low accuracy of $k-\omega$ turbulence models in the modelling of free turbulence. In addition, the computational costs is relatively affordable as it only a first order turbulence scheme. Hence, it fulfils the criteria of compromise between robustness and computational effort. In the case of high-Reynolds simulations, wall functions for velocity and scalars are activated, the formula available in code_saturne are enforced, see Appendix A.4.

Solver parameters

A first order time stepping scheme, implicit Euler, is used with constant time step. However, the time needed for the scalar fields to converge is determined as a function of the atmosphere height $\mathcal{H}_{\text{atm}}$ and the friction velocity $u_\star$, in addition to the mesh density. The final condition on the time-step is that the CFL condition stays under a value of 10. The SIMPLEC algorithm is enforced to couple the pressure and the velocity field (Doormaal & Raithby, 1984).

4.3.3/ Initial and Boundary conditions

Fluid States

The thermal and mechanical properties are set constant for the dynamic viscosity $\mu = 18.3\,\mu\text{Pa}\,\text{s}$, the specific heat $C_p = 1017\,\text{J}\,\text{kg}^{-1}\,\text{K}^{-1}$, the air conductivity $\lambda = 24.95\,\text{mW}\,\text{m}^{-1}\,\text{K}^{-1}$ and the water mass diffusion $2.82 \times 10^{-5}\,\text{m}\,\text{s}^{-1}$. The initial states are set as follows:

$$\begin{aligned} u(y,z) = v(y,z) = w(y,z) &= 0\,\text{m}\,\text{s}^{-1} \\ \text{T}_p(y,z) &= 15\,°\text{C} \\ q(y,z) &= 0\,\text{kg}\,\text{kg}^{-1} \end{aligned} \tag{4.9}$$

Boundary Conditions

Three types of boundary conditions are enforced: inlet, walls or periodic.

As shown in Figure 4.9, the boundary conditions of the periodic pattern read:

1 Periodic conditions are applied on the left-side and the right-side of the domain. It reads $\vec{u}(y=0,z) = \vec{u}(y=S,z)$, similarly, the temperature and humidity are equal at both sides of the domain.

2 Smooth wall condition is applied on the bottom of the domain, the no slip condition $\vec{u} = \vec{0}$ impact is modelled through a law of the wall on the velocity field. A no flux density condition is applied as well as a Dirichlet condition over the humidity field $q = 0$.

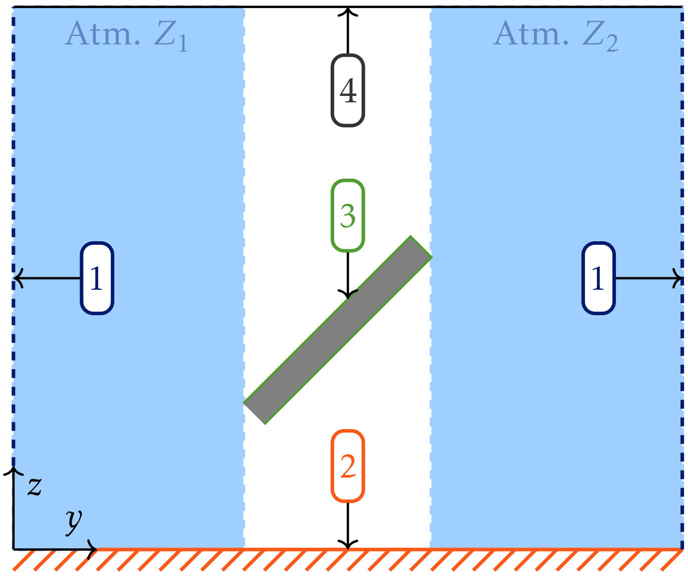

Figure 4.9–*Boundary conditions applied. Filled areas are used to calculate atmosphere-related outputs.*

3 Smooth wall conditions are applied for the four surfaces of the module motif. Similarly to the bottom of the domain, a law of the wall is applied to model the no slip condition on the velocity vector. This time, a constant flux is set at $\phi = 250\,\mathrm{W\,m^{-2}}$ or $\phi = 450\,\mathrm{W\,m^{-2}}$ depending on the study case.

4 Inlet condition is set at the top of the domain. The conditions over the velocity field are set according to the wind angle through the followings:

$$\begin{cases} \tau_x = -\rho u_\star^2 \times sin(\theta_\mathrm{w}) \\ \tau_y = -\rho u_\star^2 \times cos(\theta_\mathrm{w}) \\ w = 0 \end{cases} \tag{4.10}$$

The value of $u_\star = 0.36\,\mathrm{m\,s^{-1}}$ is set in the standard case. Adiabatic and Dirichlet conditions are set for the temperature field and the humidity ($q = 0$) respectively .

Post-processing information

Several quantities are extracted from the numerical simulations to characterise the influence of the flow on the module (convective intensities) and vice versa the influence of the module on the flow (velocity profile, scalar transport).

Flow influence over the module

The convective intensity is deduced from the knowledge of the flow on the wall of the module (imposed), both for the front and the back faces. It is calculated on each face of the two surfaces such that:

$$Nu_x = \frac{\Phi \times L}{\lambda \times (T_x - T_\infty)} \tag{4.11}$$

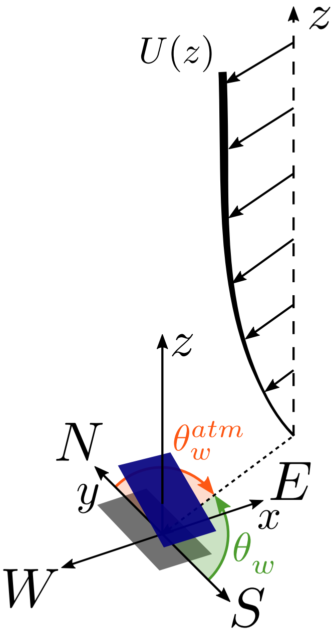

Figure 4.10–*Wind direction θ_w takes the module orientation toward the south as the nominal orientation. The atmosphere convention θ_w^{atm} is given with respect to the module orientation.*

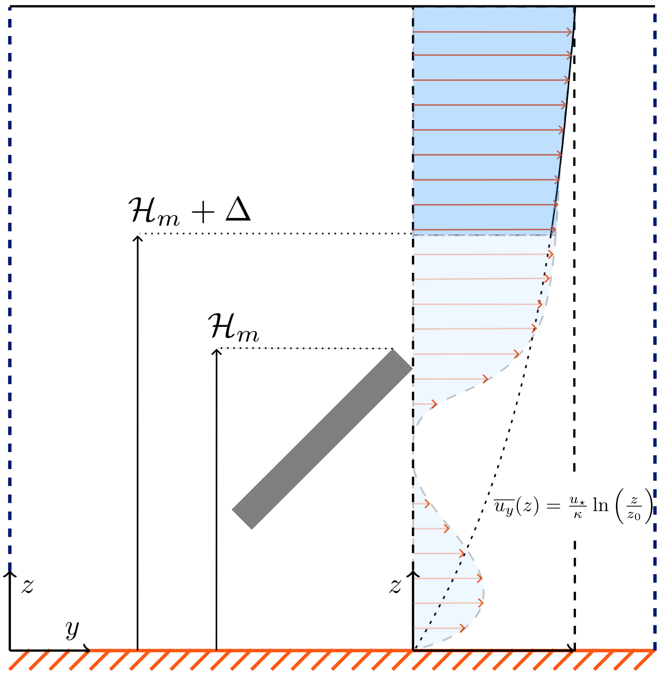

Figure 4.11–*Schematic of the post-processing operation for z_0 assuming the flow is in the y direction. The velocity profile is integrated from a distance $\mathcal{H} + \Delta$ to compute the value z_0, the wake area is not included in the calculation.*

Considering a classical characteristic length L and a reference temperature such that $T_{ref} = T_\infty$. An averaged value is calculated for both surfaces as follows:

$$Nu_L = \frac{1}{L} \int_{l=0}^{l=L} Nu_x \, \mathrm{d}l \tag{4.12}$$

Module influence over the flow

In the given configuration, the module is explicitly represented so that the flow *sees* a rigid obstacles: the flow streams hit the obstacle and, as described by conservative laws, pass through the top and the bottom of the periodic motif. The projected velocity according to the wind direction reading $U_\perp = u_x \cos(\theta_\mathrm{w}) + u_y \sin(\theta_\mathrm{w})$, the averaged velocity with respect to the altitude z becomes:

$$\overline{U}(z) = \frac{1}{S \times W} \int_{x=0}^{x=S} \int_{y=0}^{y=W} U \, \mathrm{d}x \, \mathrm{d}y \tag{4.13}$$

From the flow prospective and sufficiently away from the obstacle level, say h_{min}, the perturbation provoked by the obstacle is seen as a shift in the velocity profile. The heterogeneous repetition of motifs can be assimilated to an equivalent surface associated to specific roughness length. By doing so, the roughness length integrates the action on the flow dynamic from the modules. Its value is obtained by minimising the residual error between the velocity profile obtained by simulation, and the theoretical atmospheric log-law, it reads:

$$\ln(z_0) = \frac{\displaystyle\int_{z=h_{min}}^{\mathcal{H}_{\text{atm}}} \left(\ln(z) - \kappa \frac{\overline{U_\perp}(z)}{u_\star}\right) \mathrm{d}\Omega_z}{\displaystyle\int_{z=h_{min}}^{\mathcal{H}_{\text{atm}}} \mathrm{d}\Omega_z}. \tag{4.14}$$

Whence h_{min} can be expressed based on the geometrical properties of the microstructure. In other word, a surface which benefits from the calculated roughness is similar to the fully represented module from a flow dynamic prospective (considering large scale effects), this surface is said to implicitly represent the module action.

The spatially averaged temperature is also deduced by integrating all fields:

$$\overline{\mathrm{T}_p}(z) = \frac{1}{S \times W} \int_{x=0}^{x=S} \int_{y=0}^{y=W} \mathrm{T}_p \, \mathrm{d}x \mathrm{d}y \tag{4.15}$$

Post-processing of the average evaporative ratio is based on the code_saturne methodology for the wall function adapted to passive scalar, it reads:

$$\langle h_S^E \rangle = \frac{1}{S} \int_{l=0}^{l=S} h_s^E \, \mathrm{d}S \tag{4.16}$$

whence h_s^E is the local evaporative ratio calculated by code_saturne based on the cell property, the local shear velocity and the law of the wall as follows:

$$h_s^E = \frac{\mu}{\rho \overline{I'F}} \frac{y^+}{q^+} \tag{4.17}$$

Recall that $y^+ = \frac{y u_\star}{\nu}$ is the non-dimensional distance from the cell centre to the wall and $q^+ = \frac{q - q_{wall}}{q^*}$ is the dimensionless profile of humidity.

4.3.4/ Validation

Mesh sensitivity

A mesh sensitivity analysis is performed to determine the optimal number of cells. The term "optimum" refers to the quality of the output quantities in relation with the calculation cost. For a given geometry, the size number modifies the mean cell volume. Considering that analysing all the configurations inspected in the work requires running too many simulations with regard to our computing availability, only the two standard configurations are investigated. Both situations allow one to study quite different geometries with typical parameters; hence, we hypothesise that the configuration in between would experience similar meshing effects. To some extent, the analysis for the ground-mounted case can be used for the validation case of wind turbines. The boundary conditions for the standard atmosphere are enforced ($u_\star = 0.36\,\mathrm{m\,s^{-1}}$, $\theta_{\mathrm{w}} = 0°$).

Five meshes are constructed for both configurations. The discretised spaces with lower quality support the making of the high-quality meshes. A maximal form factor of 6 is set in the whole domain, this limit being reached in the atmosphere area; the module area benefits from a higher quality meshing for both configurations and for all the meshes in the sensitivity analysis. Comparatively, ground-mounted like meshes are evaluated over a larger range of cell number than the FPV2 configuration as it is latter used with a stronger emphasis.

Evaluation of the quantities of interest is performed in relation to the higher quality mesh. The error values are calculated for the quantities z_0, h_{fr}^{cv} and $h_{\mathrm{bs}}^{\mathrm{cv}}$ referring to the mesh i, and it reads:

$$\epsilon_{rel} = \frac{\left|z_0^{HQ} - z_0^{i}\right|}{z_0^{HQ}} \tag{4.18}$$

$$\epsilon_{rel} = \frac{\left|h_{fr}^{\mathrm{cv}\,HQ} - h_{fr}^{\mathrm{cv}\,i}\right|}{h_{fr}^{\mathrm{cv}\,HQ}} \tag{4.19}$$

$$\epsilon_{rel} = \frac{\left|h_{\mathrm{bs}}^{\mathrm{cv}HQ} - h_{\mathrm{bs}}^{\mathrm{cv}i}\right|}{h_{\mathrm{bs}}^{\mathrm{cv}HQ}} \tag{4.20}$$

As ϵ_{rel} related to convective transfers can directly suffer from the behaviour of the $k-wSST$ turbulence model, $y_{+,MAX}^{fr,\mathrm{re}}$ and $\overline{y}_{+}^{fr,\mathrm{re}}$ are also calculated. The trade-off criterion with respect to computational cost refers to a rough estimation for the efficient use of code_saturne. Optimisation in computational time is possible by parallelisation within the limit of 10,000 cells. Therefore, the computational cost will be considered to increase significantly when the X-mesh contains 10,000 more cells than the Y-mesh. This strategy does not take into account the computation time required to achieve convergence, which is significantly affected by: the configuration, the air boundary conditions, and the height of the domain.

The results of space discretization are displayed in Figure 4.12 for both configurations.

The mesh sensitivity analysis for the quantity z_0 is performed using $h_{min} = 2 \times \mathcal{H}_{\mathrm{m}}$ in Equation 4.14, it appears that increasing the mesh quality has a very strong influence on the value of the integrated quantity. The ground-mounted configuration is slightly less influenced; the coarsest mesh has an error of 38%, while it amounts to 59% for the FPV2 configuration. This level of uncertainty in the value of z_0 is observed in the literature, so orders of magnitude are globally respected regardless of the size of the mesh.

For the quantity h_{fr}^{cv}, the two configurations show similar trends. The finer the mesh size, which results in a decrease in y_+ at the wall level, the more efficient the quality of the quantity calculation. Neither of the two situations shows a global Low Reynolds behaviour, which is relatively logical considering that the air flows faster over this surface given the standard atmospheric boundary conditions used. The orders of magnitude are within the ranges given in the literature to quantify the precision of h_{cv}, namely $\epsilon \simeq 20\%$. The coarsest mesh for the ground-mounted configuration exceeds this threshold by 5%. However, the marginal differences between the fine meshes are small before the best accuracy is obtained. The increase in computational cost is exponential, so the trade-off is a lower computational cost with a slightly larger error. For the FPV2 configuration, the increase in computational cost compared to the gain in efficiency (12%) is acceptable up to the median mesh size.

The quantity $h_{\mathrm{bs}}^{\mathrm{cv}}$ the two configurations also show similar trends, and spatial refinement improves the consideration of near-wall phenomena. This observation must be balanced for the ground-mounted configuration, where the coarsest mesh obtains results comparable to those of the fine

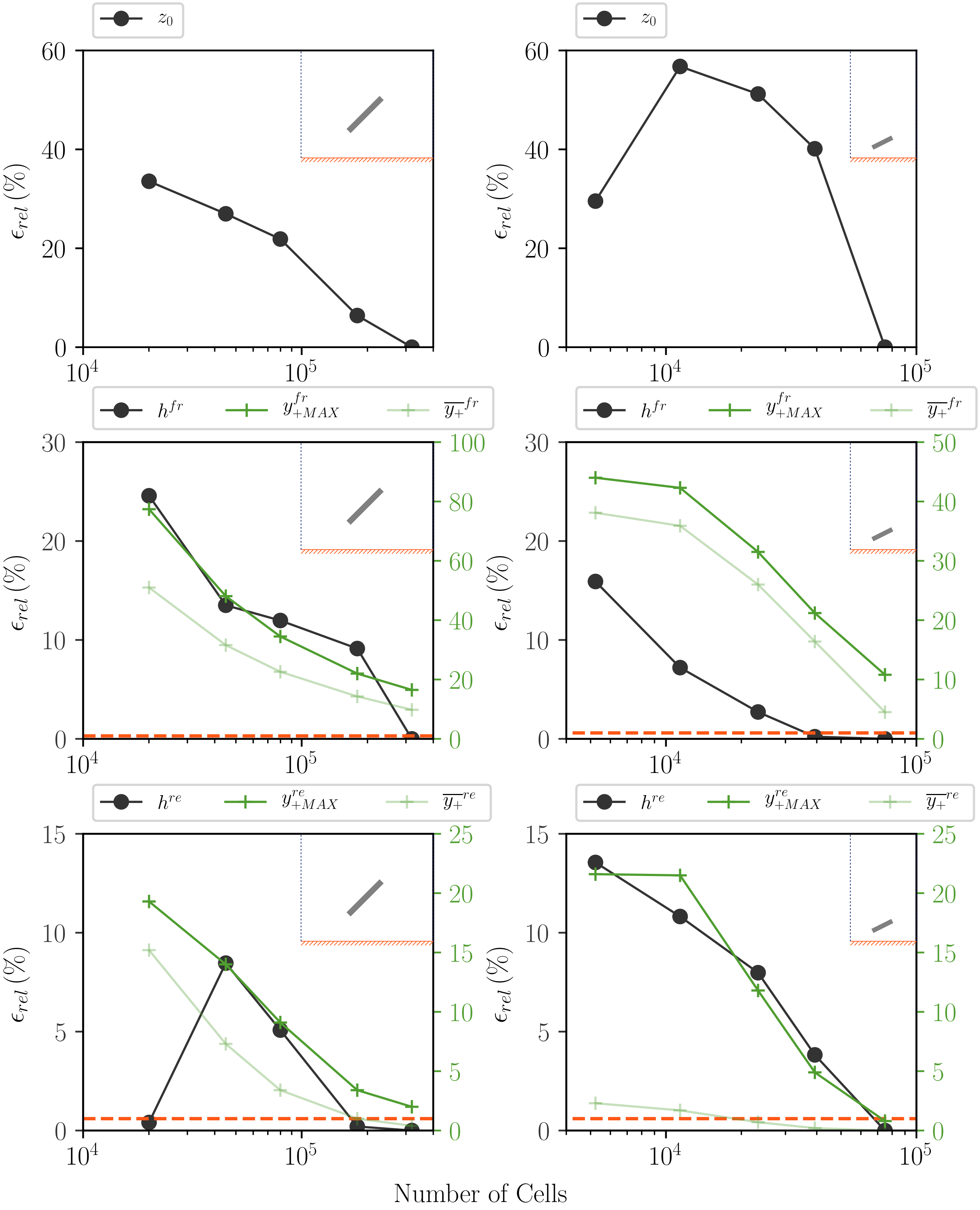

Figure 4.12–*Sensitivity analysis of the meshing contribution on the uncertainty of quantities of interest (all the runs are performed with* $CFL_{max} < 10$*). The right-hand side of the plot is dedicated to the Ground Mounted-like geometry, the left-hand side shows the FPV2 case study. The axes for the four subplots devoted to convective parameters are organized as follows: relative errors compared to* h^{HQ} *are indicated on the left axis,* y_+ *values are indicated on the right axis. The dashed orange lines read on the right axis and show the threshold of high to low Reynolds format of the* $k-\omega\,SST$ *turbulence model.*

mesh, which can be explained by the fact that the macroscopic conditions are similar (eddies) for these two refinements. We also notice that the fine meshes are bound to evolve as low Reynolds meshes. This does not seem to affect the efficiency of the calculation of the convective intensity in a strong footprint or in an open system situation. We conclude that the turbulence model is well suited to the general situation of the study. The increase in computational cost compared to the gain in efficiency of the prediction of this quantity for the FPV2 configuration is relatively interesting; the median mesh allows one to gain 6% in accuracy compared to the lowest quality mesh.

Finally, the spatial criterion leads to the use of a coarse mesh for the ground-mounted configuration, while the median mesh is chosen for the FPV2 configuration.

A further analysis was carried out on the shortlisted meshes of interest to estimate the action of the time-stepping discretization over the calculated quantities. It was shown that CFL_{max} should be kept below a threshold of $CFL_{max} < 20$ to optimise the calculation of $h_{\text{bs}}^{\text{cv}}$ and h_{fr}^{cv}, and $CFL_{max} < 10$ to reduce the uncertainty in the calculation of z_0 due to time discretization at less than 10%.

Comparisons

Figure 4.13 shows the mean velocity profile and the profile of the shear component of the Reynolds tensor, obtained from the bi-periodic numerical simulation; experimental data are retrieved and plotted from from Glick, Smith, et al., 2020. The boundary conditions applied to the model are identical to the conditions measured in the wind tunnel experiment. For comparison purposes, the data are normalised so that the reference height is at the trailing edge of the module, the velocity is normalised from the maximum observed velocity. For the numerical simulation, the full scale is considered, resulting in a module thickness smaller than that chosen for the wind tunnel experiment. The measurements available in the experiment are shown in the figures.

First, it can be seen that the numerical model corroborates the trizonal structure established in the literature. The submodule zone shows low velocities and a decrease in shear stress until the wake zone. The latter shows the presence of a recirculation zone ($u_y/U_0 \simeq 0$), while an increase in shear stress occurs due to the interaction between the atmosphere and the tilted module. The last atmospheric zone shows a classical logarithmic profile.

However, the numerical simulation fails to obtain the correct velocity and turbulence levels. This is probably due to the use of the $k-\omega SST$ turbulence model, whose modelling induces uncertainty about the creation of turbulence at the flow interaction level with the plane module. Another source of numerical error lies in the use of a smaller thickness for the module compared to the experiment. This may explain the difference in obtaining the height that verifies the absolute velocity minimum. These differences in relative height are also found in the shear profile, whose local extrema are below the experimental extrema. A surprising feature is the inversion of the velocity profile below the module, which is characterised by the dotted line. This situation is not found in the wind tunnel experimentation; however, this phenomenon does not seem to be naturally attributable to the turbulence modelling or to the difference in geometry. Two hypotheses can be envisaged: the equations solved in code_saturne are not complete, or the physical assumptions are inadequate. This hypothesis can be studied by simulation of a representative case of the wind tunnel for which the turbulent phenomenon is modelled with a more efficient method or solved directly. The second assumption is that the experimental system is not representative of a periodic case (i.e. the flow has not reached an established steady-state representative of an infinite plant). This assumption is difficult to verify unless a wind tunnel experiment is developed and elements are added.

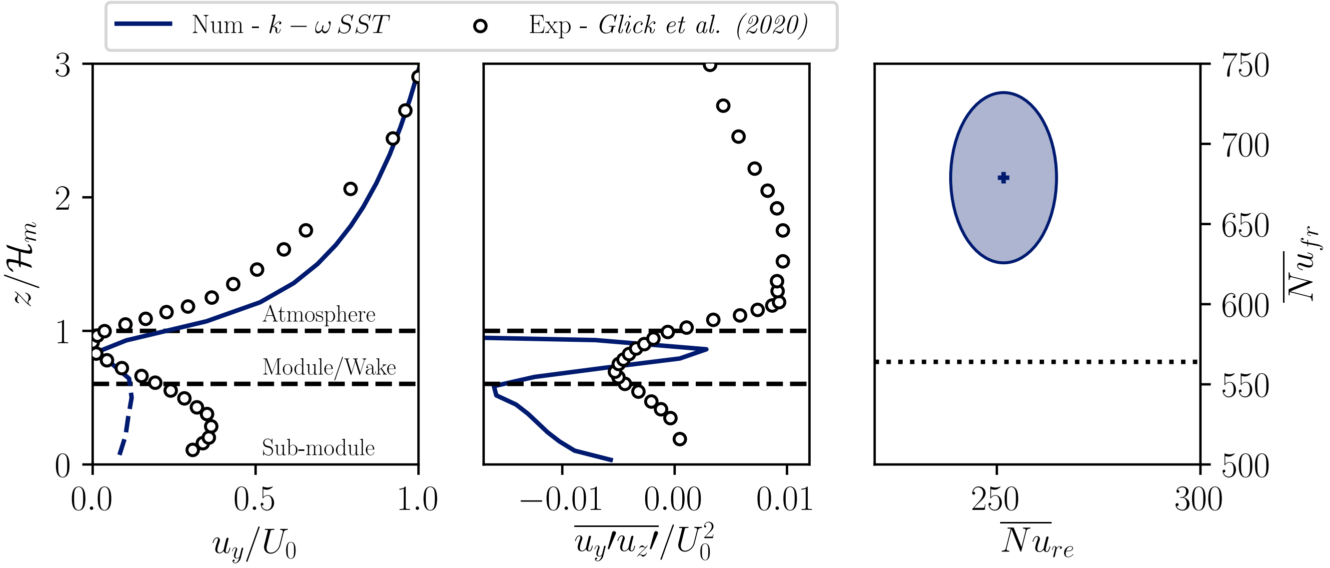

Figure 4.13–*Streamwise velocity and turbulence profiles. Similar windows of integration are used.*

Figure 4.13 shows the results for the calculation of the convective coefficients in front and rear, averaged along the surfaces, for the two-period simulation. The result for the front-face coefficient, obtained in the wind tunnel experiment, is rescaled with respect to the characteristic length of the numerical simulation and is indicated by a horizontal dashed line. It can be seen that the convective coefficient of the front face is predicted with the right order of magnitude in the numerical experiment, a difference of the order of 20 % is reached, which falls within the uncertainties commonly described for the quantification of convective coefficients.

Taking into account the previous results on the mechanical properties of the flow, this difference can be explained by the lower height at which the extrema are obtained; they are found more strongly in the central part of the wake zone. This character is found in a lower position of the detachment points of the flow during its interaction with the module. There is also a difference in intensity between the convective coefficients of the front and rear faces for the numerical simulation, which is typical of the difference obtained for the wind tunnel experiment. We conclude that the thermal turbulence model is appropriate for further studies.

Summary

The parameterisation of the biperiodic simulation is rather consistent with the real physical situation. The typical aerodynamic entrainment of the atmosphere, coupled with a relatively reliable turbulence model, provides good orders of magnitude for the quantities of interest investigated. However, some flow regimes are not conserved, such as the flow under the module and friction. In these circumstances, a high-fidelity model must be established to determine the real influence of the chosen turbulence model, geometry, and experimental reference on the quality of the results. However, it turns out that the orders of magnitude of the thermal regimes are preserved in the numerical simulation, at least for the front side of the module. Therefore, this heated plate formalism can be used with an atmospheric profile representative of a PV power plant flow to characterise the evolution of the coefficient as a function of the plant geometry.

4.4/ Array of Heated Flat Plates 2-D

The previous section showed that a low-cost bi-periodic representation was feasible in order to reduce the complexity of a scaled calculation. However, the velocity and turbulence fields showed discrepancies with the wind tunnel experiment. In this section, we propose to make this first representation more complex by explicitly representing all the modules of a photovoltaic power plant built in similarity with the wind tunnel experiment. The construction steps of the numerical case are recalled, and the new features are also introduced. The data set is also modified to coincide with a wind tunnel problem.

In doing so, this section has two main purposes. Firstly, we want to be able to model the inlet of the power plant with respect to the wind direction. Second, we want to reduce the set of assumptions that surround the results of the periodic version of the problem: scaling effects, accuracy of the turbulence model, and failure of the aeraulic solver assumptions. To do this, a validation step is carried out in order to evaluate the relevance of the numerical case implemented.

4.4.1/ Geometry configuration and Pre-processing Steps

The construction of the geometry is mainly based on the initial geometry of the standard situation on the ground, using full-scale dimensions as indicated in Table 4.3. All supplementary operations, as depicted in Figure 4.6, are performed on code_saturne.

To do so, a *cs_user_mesh.c* preprocessing file is added in the code_saturne pre-calculus step. It contains specific meshing operations such as: copy and translation of the cells, group tags outweighed (for purposes of boundary conditions), and extrusion of cells in the streamwise direction. The main idea is to copy the initial cell locations and translate them at $n \times \mathcal{S}_\mathrm{m}$ distance in the streamwise direction so that the faces of the cells are always in full contact with another cell (conformity requirement), identify the cells that were genuinely devoted to periodic boundaries and renaming them so that they can be sewed between unitarian motifs. The extrusion steps are performed to ensure a good distance from the first and last module rows to the boundary conditions in the streamwise direction. The calculation ended up in code_saturne mesh native format (*mesh_output.csm*) which contains a longitudinal section of a solar array with only one cell normal to the plan ($\vec{x}$). The space occupied by the modules, as well as the front and rear solar array, is chosen to optimise the calculus over several cores and maximise the number of explicitly represented modules. They are shown in Figure 4.14.

4.4.2/ Solver Settings

As for the bi-periodic case, the $k-\omega SST$ turbulence model is assumed with a high and low Reynolds formalism; therefore, a law of the wall is integrated. A constant timestep of $\Delta t = 2 \times 10^{-3}$ s is enforced to ensure $CFL_{max} < 10$. The permanent regime is observed through the calculation of the residuals for velocity, temperature, and humidity.

4.4.3/ Initial and Boundary Conditions

Boundary Conditions

The set of boundary conditions for the numerical solar array is fundamentally different from the biperiodic case, as the atmosphere velocity profile is imposed at the inlet; there is no "atmosphere"

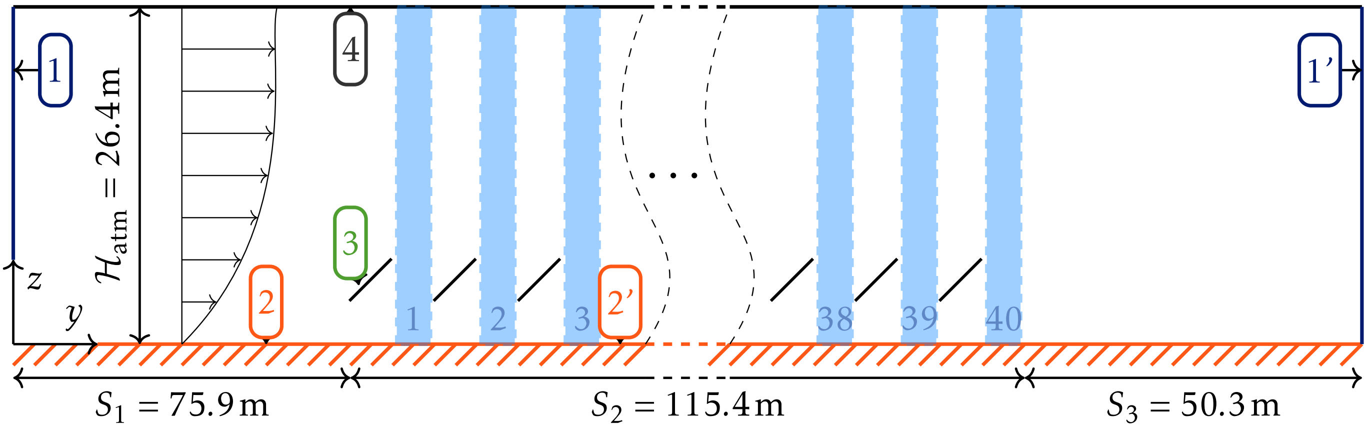

Figure 4.14–*Schematic of the numerical array investigated in the 2-D solar array configuration.*

equilibrium made between the top of the atmosphere down to the array. From the notation in Figure 4.14, the conditions read:

$\boxed{1}$ Inlet condition is assumed on the left of the domain, a logarithmic velocity profile is given as $u(z) = \frac{u_\star}{\kappa} \ln\left(\frac{z}{z_0}\right)$ with $u_\star = 0.36\,\mathrm{m\,s^{-1}}$ and $z_0 = 0.165\,\mathrm{m}$. The temperature is assumed constant and no humidity profile is enforced.

$\boxed{1'}$ Outer condition is assumed on the right hand-side of the volume. The condition is coded as $\frac{\partial^2 P}{\partial n \partial \tau} = 0$ in which n is the outward normal vector and τ is any vector in the boundary face.

$\boxed{2}$ A rough wall is assumed with a roughness value of $z_0 = 0.165\,\mathrm{m}$. Dirichlet conditions are fixed for the temperature and for the humidity $q = 1$. This wall setting extends from the inlet section to the first cell under the first module. A similar condition is applied from the cell under the last module to the outlet.

$\boxed{2'}$ A rough wall is assumed with a roughness value of $z_0 = 0.01\,\mathrm{m}$. The Dirichlet conditions are fixed for the temperature and for the humidity $q = 1$. This wall setting goes from the first cell under the first module to the last cell under the last module

$\boxed{3}$ A smooth wall is enforced with a Neuman condition on the temperature field such as $\phi = 250\,\mathrm{W\,m^{-2}}$, a Dirichlet condition is fixed for the humidity scalar.

$\boxed{4}$ A smooth wall condition is applied with adiabatic conditions on the temperature scalar and a dirichlet condition is set for the humidity scalar as $q = 0$

4.4.4/ Validation: Velocity Profiles

Figure 4.15 shows the results of the integrated velocity profiles for the wind tunnel experiment, as well as for the numerical simulation of the full-scale case. The same integration spaces are

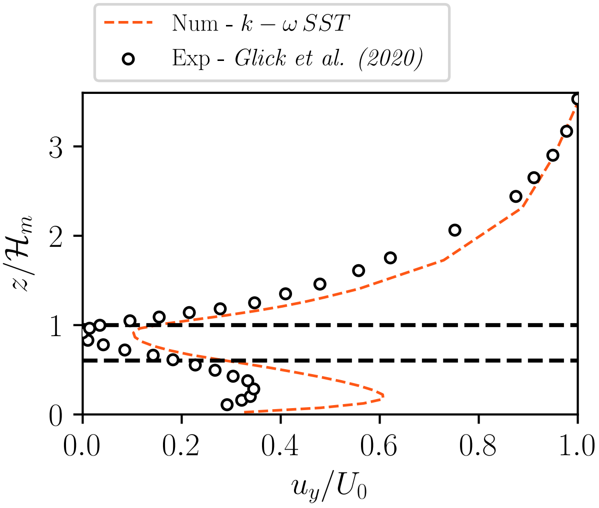

Figure 4.15–*Comparison of the streamwise velocities obtained in the wind tunnel experiment and the one obtained through the 2-D array simulation. Both fields are recovered between the 8th and the 9th row. Horizontal lines indicate the module tops and bottoms.*

considered, i.e. the inter-pitch space between the 8th and 9th module rows. As for the periodic case, all three flow zones appear in the numerical simulation, but this time the zone under the module is adequately represented from the phenomenological point of view. Qualitatively, the velocity levels are overestimated both below the modulus (factor of order 2), and in the wake zone. The local minimum is obtained at the right height, just below the $\mathcal{H}_\mathrm{m}$ height. It is recalled that for this simulation, the thickness of the module is similar to the one enforced in the wind tunnel experiment (1:33 scale). Thus, the hypothesis of a numerical dimensional difference at the origin of the field differences observed in the previous bi-periodic case is not verified. The overestimation of the atmospheric layer above the modules is smaller than the differences in other parts of the velocity profile, the order of magnitude is of the order of 25 %. Knowing that the turbulence model $k-\omega\,SST$ is a turbulent model of the order one, we deduce that the proposed simulation is rather consistent with the real wind tunnel case. A better turbulence model must be studied to fully verify the relevance of the aerodynamic solver. The bi-periodic case is still valid from this central 2-D simulation, given the evolution of the velocity profiles as we move streamwise, through the powerplant. The conditions to establish the aerodynamic profile are still questionable.

4.5/ High-fidelity Modelling: Large-Eddy Simulation

Validation of the numerical solver is a mandatory step in assessing the accuracy of the physical field calculated in the field volume. This is more than true because the results given by the bi-periodic scheme can be attributed to two roots: numerical modelling deviation or failure in obtaining periodic conditions in the wind tunnel implementation. The 2-D wind tunnel numerical simulation has also shown that the second option can be the ultimate root of such deviation; however, the turbulence model is also a good candidate in the deviation process.

In this section, the wind tunnel experiment of Glick, Smith, et al., 2020 is implemented in code_saturne using the Large Eddy Simulation turbulence scheme. This time the wind-tunnel scale is adopted; therefore, the purpose of the numerical experiment is to reproduce the velocity and main turbulence profiles, as well as to reproduce the heat transfer rate obtained. By doing so, we intend to declare that the code_saturne atmosphere solver is well adapted to make the calculation and that the roots of divergence seen in the calculated outputs within the prior simulations are due to turbulence modelling and failure to obtain established wind regimes.

4.5.1/ Geometry Configurations

The geometry of the wind tunnel experiment is reproduced with little adaptation. It is numerically based on the combination of conformed meshes side by side as shown in Figure 4.16. The unitary motif, similar to the one introduced in Subsection 4.3.1.1 is used with the following dimensions : $\mathcal{L}_\mathrm{m} = 50.8\,\mathrm{mm}$, $\mathcal{E}_\mathrm{m} = 5.3\,\mathrm{mm}$, $\mathcal{H}_\mathrm{m} = 68\,\mathrm{mm}$, $\mathcal{S}_\mathrm{m} = 84\,\mathrm{mm}$, $\theta_\mathrm{m} = 30°$, and $\mathcal{H}_\mathrm{atm} = 800\,\mathrm{mm}$. The maintaining structure is omitted in the numerical geometry in order to reduce the complexity of the meshing procedure, this hypothesis is supported by the low number of maintaining frames. A second unitary motif representing the edges of the module rows is created with a conformed mesh. The operation of copying, translating, and sewing is performed in the latter order to create the volume of control, and is therefore defined in $\Omega = [0,4700]\times[0,800]\times[0,1200]$, with the exception of the ten rows of modules.

4.5.2/ Supplementary Step for Pre-processing

The original pre-processing chain is reused to build the unit geometry as dimensioned in the wind tunnel experiment. Instead of using a periodic representation, an additional meshing step is implemented using a *cs_user_mesh.c* file. A second unit mesh is created with respect to the cell positions of the unit mesh, including the photovoltaic obstacle, hereafter: intermodule mesh. In the latter case, the space initially allocated to the module is filled with hexahedral cells. This particular mesh is used to construct the edges of the wind tunnel, which does not include a module, to take into account possible edge effects at the level of the study plane.

Two functions are then implemented in the *cs_user_mesh.c* file, the first consists of the reproduction of the construction steps of the 2-D power plant, applied for the two unit meshes (module and intermodule); thus the ten rows of modules are created by reproduction of the initial pattern. In the same way, 10 intermodule spaces are created and assembled. This step also includes an extrusion along the axis of the modules, so that three blocks of cells are created which include in ascending x-order: an intermodule space, a module area, and an intermodule space. This arrangement spans the length of the wind tunnel, with each cell spaced by 5 mm along this axis. The second function consists of adjusting the dimensions of the mesh by extrusion along the $\vec{y}$

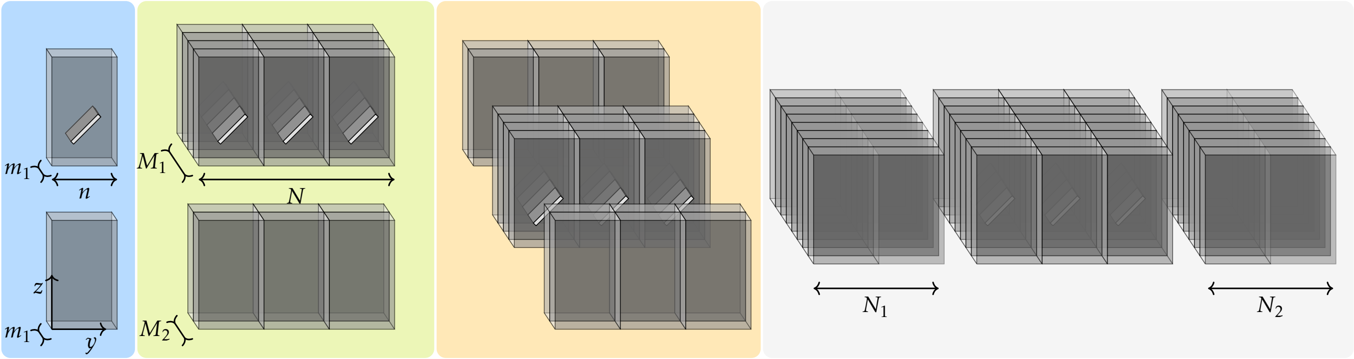

Figure 4.16–*Pre-processing chain: unitary geometry construction and meshing operations. The final stage of the chain ends up with the creation of a calculation mesh with respect to the dimensions described in the experiment*

axis and along $\vec{z}$ to meet the desired dimensions. The surface areas of the mesh (before the modules, under the modules, and behind the modules) are also parameterised in this second step. Finally, a multiplication operation is carried out to reduce the volumes of the cells and consequently increase their numbers, preserving the shape of the volumetric cells. The combination of functions and the joining procedures are shown in Figure 4.16.

The total number of cells is 24 671 104 cells.

4.5.3/ Governing Equations, Initial and Boundary Conditions

Governing Equations

The computational model used in the model validation section is based on the resolution of the Navier-Stokes equation using Large-Eddy Simulation, and a spatial and scale filter is applied. In this section, the field u is decomposed into a solved part denoted $\overline{u}$, and an unresolved part denoted u'; the filtering operation does not satisfy the Reynolds decomposition.

The system of solved equations can be written as follows :

$$\begin{cases} \dfrac{\partial \overline{u}_i}{\partial x_i} = 0, \text{for } x \in \Omega \text{ and for } t \geq 0 \\ \dfrac{\partial \overline{u}_i}{\partial t} + \overline{u}_j \dfrac{\partial \overline{u}_i}{\partial x_j} = -\dfrac{1}{\rho} \dfrac{\partial \overline{p}}{\partial x_i} + \nu \dfrac{\partial^2 \overline{u_j}}{\partial x_i \partial x_i} - \dfrac{\partial \tau'_{ij}}{\partial x_j}, & \text{for } x \in \Omega \text{ and for } t \geq 0 \\ \rho Cp \dfrac{\partial \overline{\mathrm{T}_p}}{\partial t} + \dfrac{\partial \left(\overline{u_j} \overline{\mathrm{T}_p} \right)}{\partial x_j} = \lambda \dfrac{\partial^2 \overline{\mathrm{T}_p}}{\partial x_i \partial x_i} + J_\phi, & \text{for } x \in \Omega \text{ and for } t \geq 0 \end{cases} \tag{4.21}$$

With Σ_i^j the surfaces of the module obstacles and Σ_k the surfaces of the wind tunnel experiment. Note that Σ_i is the surface that corresponds to the entrance of the wind tunnel. The hypothesis of Boussinesq is applied (density differences are ignored when not multiplied by gravity). The domain of application Ω is described in Figure 4.17. The Smagorinsky model is used to model the unresolved scale and, more precisely, the term τ'_{ij}. It reads: $\tau'_{ij} = \overline{u_i u_j} - \overline{u}_i \overline{u}_j = 2 \times \nu_t \left(\dfrac{\partial \overline{u}_i}{\partial x_j} + \dfrac{\partial \overline{u}_j}{\partial x_i} \right)$

in which ν_t is the subgrid-scale viscosity as follows:

$$\nu_t = (C_s\Delta)^2\sqrt{\frac{1}{2}\left(\frac{\partial \overline{u}_i}{\partial x_j} + \frac{\partial \overline{u}_j}{\partial x_i}\right)} \tag{4.22}$$

Whence C_s is set to 0.065 and Δ is the filter width.

Similarly, the filtered scalar transport for T_p includes an eddy diffusivity model so that $J_{phi} = \frac{\nu_t}{Pr_t}\frac{\partial \mathrm{T}_p}{\partial x_i}$. The turbulent Prandtl number is taken so that $Pr_t = 1$.

Initial and Boundary Conditions

The boundary conditions applied to the outer surfaces denoted Σ_i, $\Sigma_{-1\rightarrow 4}$ for the input and the 5 sides of the cubic area, respectively, as well as the conditions applied to the inner surfaces denoted $\Sigma_{5\rightarrow 9}^{[1]\rightarrow[10]}$ are summarised in the following system:

$$\begin{cases} u = 0, & \text{for } x \in \Sigma_{-1\rightarrow 3} \vee \Sigma_{5\rightarrow 9}^{[1]\rightarrow[10]} \text{ and for } t \geq 0 \\ \vec{\phi}\cdot\vec{n} = \phi_{mod}, & \text{for } x \in \Sigma_{5\rightarrow 9}^{[1]\rightarrow[10]} \text{ and for } t \geq 0 \\ u_{i=1,2} = 0, & \text{for } x \in \Sigma_i \text{ and for } t \geq 0 \\ u_{i=3} = \frac{u_\star}{\kappa}\ln\left(\frac{z}{z_0}\right), & \text{for } x \in \Sigma_i \text{ and for } t \geq 0 \\ \mathrm{T}_p = \mathrm{T}_p^{(c1)}, & \text{for } x \in \Sigma_{i,-1\rightarrow 4} \text{ and for } t \geq 0 \\ p = p_0, & \text{for } x \in \Sigma_4 \text{ and for } t \geq 0 \end{cases} \tag{4.23}$$

The ceiling Σ_{-1}, right side Σ_1, left side Σ_2, below module area Σ_3 are considered smooth walls. The modules are also considered smooth walls, and a Neumann condition is applied for the front, rear, and side surfaces. The upward area Σ_0 is considered a rough wall with an associated $z_0 = 5\,\mathrm{mm}$ to mimic the chains that lie on the surface in the experiment.

4.5.4/ Solver Settings

A constant time step of $5.95 \times 10^{-4}\,\mathrm{s}$ is considered, which led to a maximum CFL number of 2.46 the top of the atmosphere layer. At the module level, the CFL is lower than 1 throughout the array. The total duration of the experiment is 28.1 s and time averaged values are integrated from 10 s to the end. The SIMPLEC algorithm is also used to perform pressure-velocity coupling. A second-order time scheme is also used; see (Amino et al., n.d.).

4.5.5/ Atmospheric Solver Validation

The objective of the High-Fidelity Simulation is to reproduce the quantities of interest that are found in the wind tunnel experiment. To do so, the mean wind speed profiles and the Reynolds Shear Stress profiles are compared at two locations: before the array and at a given location within the array. The same windows of integration between the simulated and the experimental study case are applied, in the middle of the wind tunnel width. Note that the integration window in

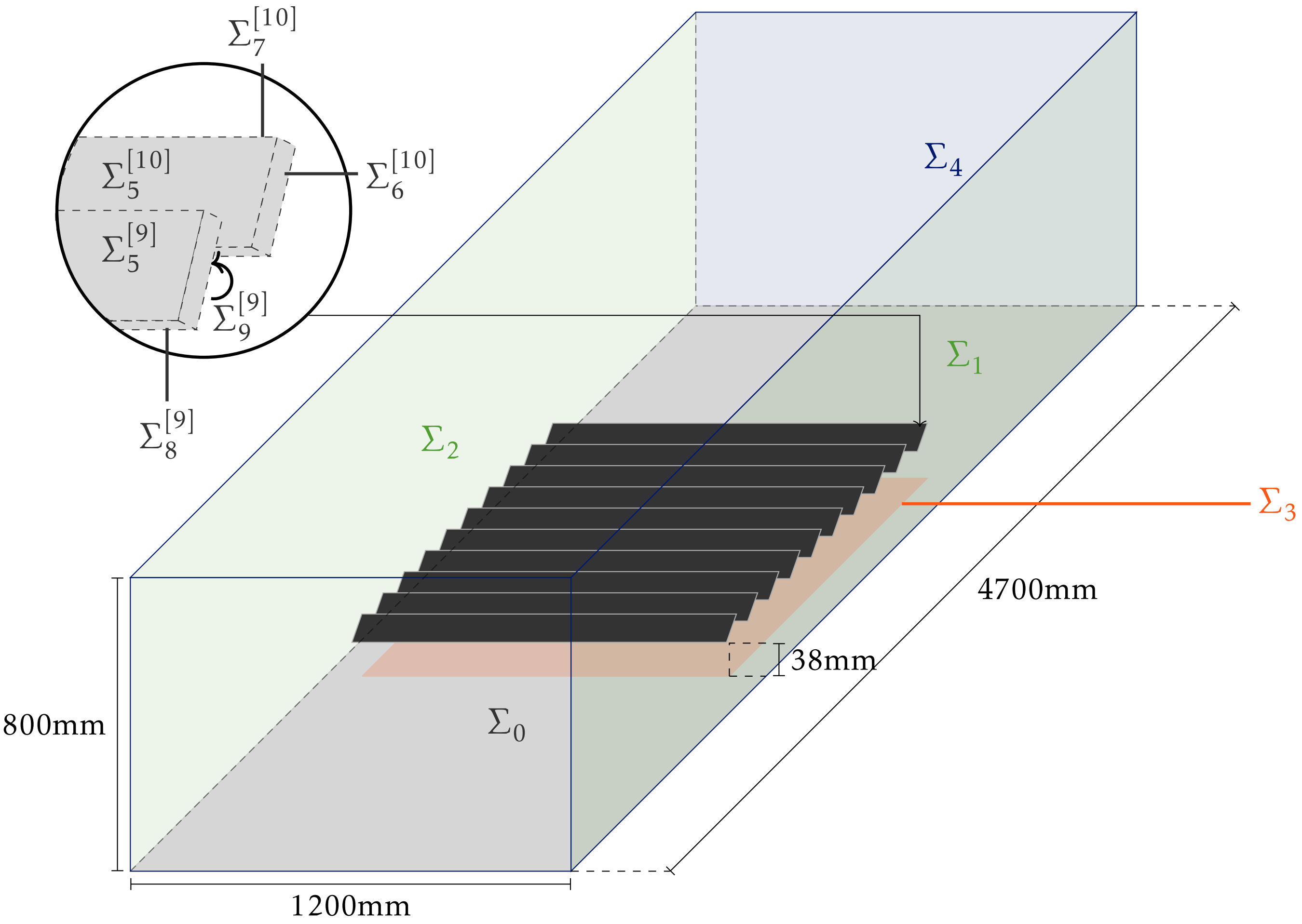

Figure 4.17–*Schematic of the numerical wind tunnel in 3-D, the volume of control* Ω *is bounded by the surfaces* Σ.

the simulated case is bigger in the width direction so that the number of cells integrated when aggregating the field is larger.

The profiles are given using a non-dimensioned height based on the maximum height of the obstacle $\mathcal{H}_\mathrm{m}$. A nominal velocity U_0 is defined at the height $z/\mathcal{H}_\mathrm{m} = 3.2$, thus the results are given as non-dimensional values. The nominal velocity of the simulation was slightly lower than that of the real experiment; therefore, the Reynolds number for the flow was estimated at $Re_L \simeq 8000$.

Momentum before the array

Figure 4.18 shows the non-dimensional profiles before the array of modules for both numerical and experimental situations. The numerical mean velocity follows a logarithmic law, whereas the experimentally obtained velocity profile has a power-law shape. The simulated field before the array is underestimated for altitudes lower than $z/\mathcal{H}_\mathrm{m} \simeq 1$. For large values of $z/\mathcal{H}_\mathrm{m}$, the numerical profile slightly overestimates the experimental velocity. This result shows that using the ideal velocity profile coupled with the wall function in the entrance region of the wind tunnel is efficient in reproducing the quantities from the experiment. Furthermore, the flow at the location of integration is assumed to be fairly spatially developed; no effect from the wind tunnel sides are experienced.

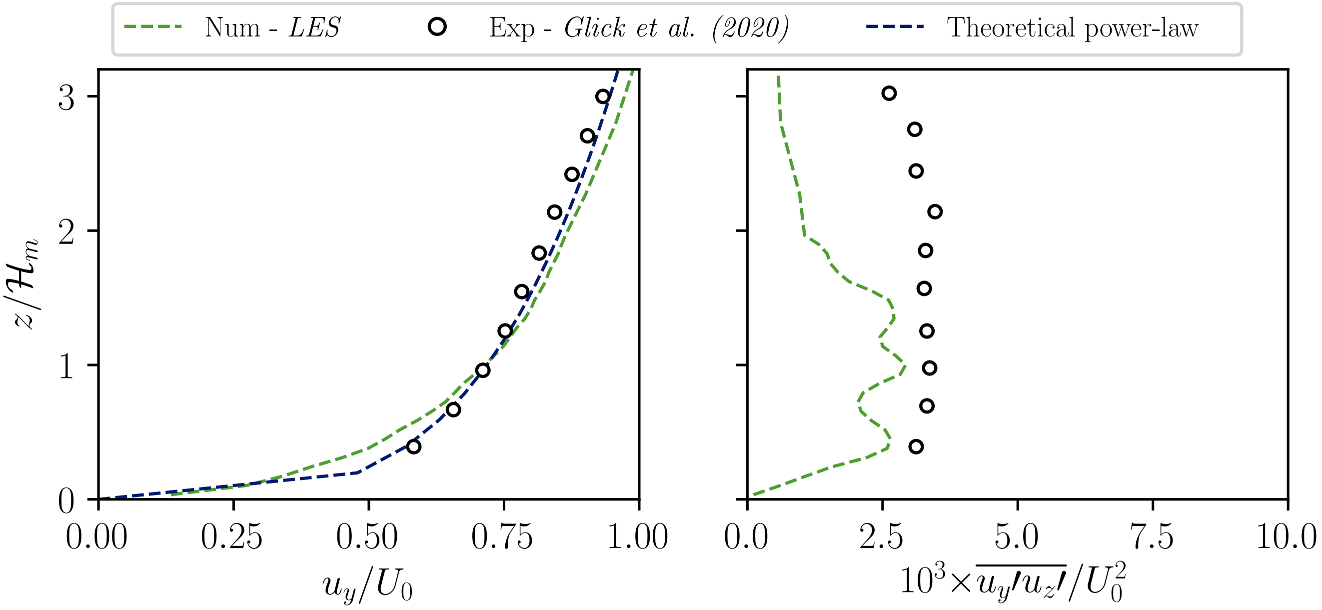

Figure 4.18–*Comparison between numerical and experimental velocities and Reynold stresses from the integration of fields before in the entrance region, before the array of modules.*

In general though, the turbulence level lacks of strength at the module height level; it is also found very low when $z/\mathcal{H}_\mathrm{m} \simeq 2$. This behaviour is classical when no vorticity is included in the LES setup and the entrance region is not sufficiently long to reproduce the mixing. An option to consider in the future would be to include a synthetic or equivalent strategy to catch a better level of turbulence at the beginning of the array. Due to the explicit representation of the modules in the system, it is assumed that the main turbulence source is produced by the flow dynamic interacting with the geometry; The lower turbulence level at the entrance location would modify the heat-rate for the first modules and rapidly be forgotten by the flow.

Momentum within the array

Figure 4.19 shows the non-dimensioned profiles within the array of modules for both numerical and experimental situations. The mean velocity profile shows good consistency with the experimental profile. The three flow zones are faithfully reproduced both in intensity and phenomenology: the module subzone shows a local maximum around $z/\mathcal{H}_\mathrm{m} = 0.3$, the wake zone shows a local (and global) minimum at $z/\mathcal{H}_\mathrm{m} \simeq 0.95$, and the transition/atmospheric zone follows a logarithmic law. Such a match between numerical and experimental profiles demonstrates the ability of the high-fidelity simulation to reproduce the flow dynamics and the interaction between the complex flow in the array with the regularly spaced geometry. The governing equations and the hypotheses made are fairly competitive so that it is considered that the atmospheric solver is consistent. Figure 4.20 pushes the assumption by showing that the distribution of velocity in the streamwise direction is also reproduced with a good level of similarity, especially in the wake area. The prediction of flow direction reversal at the trailing edge of the 8th module is caught. The flow regime in the direct vicinity of the 9th module also obtains the same non-dimensioned velocity between $U_\mathrm{w}/U_0 \in [0, 0.2]\,\mathrm{m\,s^{-1}}$, the upper part of 9th module gets the greatest flow regime with levels of around $U_\mathrm{w}/U_0 = 0.3$. Apart from the ceiling boundary conditions that were unlikely to act on the flow regime at this altitude level due to the distance of the modules, the boundary conditions applied at the module and ground level are also competitive in producing the good

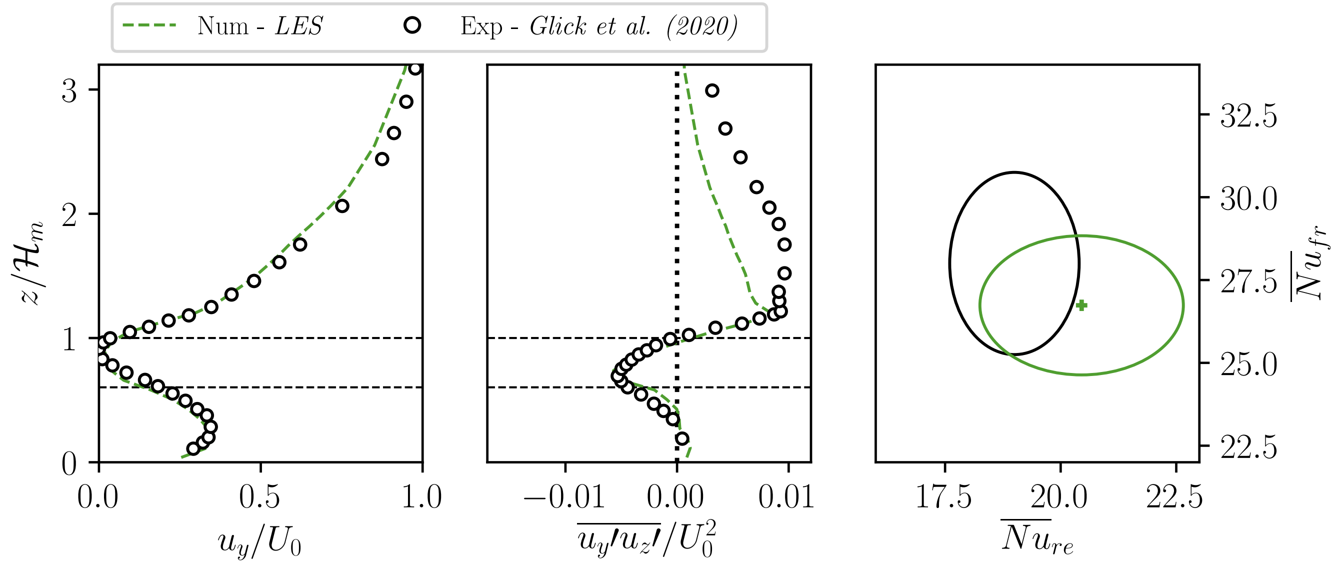

Figure 4.19–*Comparisons between numerical and experimental velocities (left-hand side) and Reynolds stresses (right-hand side), integrated between the 8th and the 9th row of the module array.*

level of interaction.

This level of turbulence is shown in right-hand side of Figure 4.19 and in Figure 4.21. The level of mixing is accurately model below the module, in the wake area and slightly above the system. After hitting a maximum value around $z/\mathcal{H}_\mathrm{m} \simeq 1.2.$, the simulation of the atmosphere lacks of accuracy and the turbulence level is found to be lower than in the experimental study case. Here, the boundary condition from the wind tunnel input is the main contributor of the turbulence flaw. The local creation of turbulence from the module and atmosphere interaction is the main source of the mixing level, as demonstrated by the yellow area in Figure 4.21 and its poor size in the simulation. The kinetic energy of the atmosphere feeds the turbulence field and improves the size of the maximum turbulence intensity location.

Thermal exchange within the array

Figure 4.19 shows the intensity of convective transfers evaluated on the front and rear sides of the element located in the 8th row. A similar simulation has been performed to evaluate the kernel function to incorporate in T_{ref} using an inert module within the stack of elements. The numerical Nusselt number is obtained as follows:

$$Nu_{ad,up} = \frac{-q_{up} \times L}{\lambda \times \left(T_{up} - T_{ref}\right)} \tag{4.24}$$

With $-q_{up}$ the value of the Neumann boundary condition. An average temperature T_{up} has been used in the simulation to encompass the heterogeneity along the face of the elements. Both the front- and rear-side intensities are of the same order of magnitude, assuming uncertainties of both the experiment and the numerical simulation. The uncertainties of the simulation were estimated on the basis of the temperature difference along the element planes. The good performance of the velocity and Reynolds stress estimation depicted in Figure 4.19 leads to good accuracy in

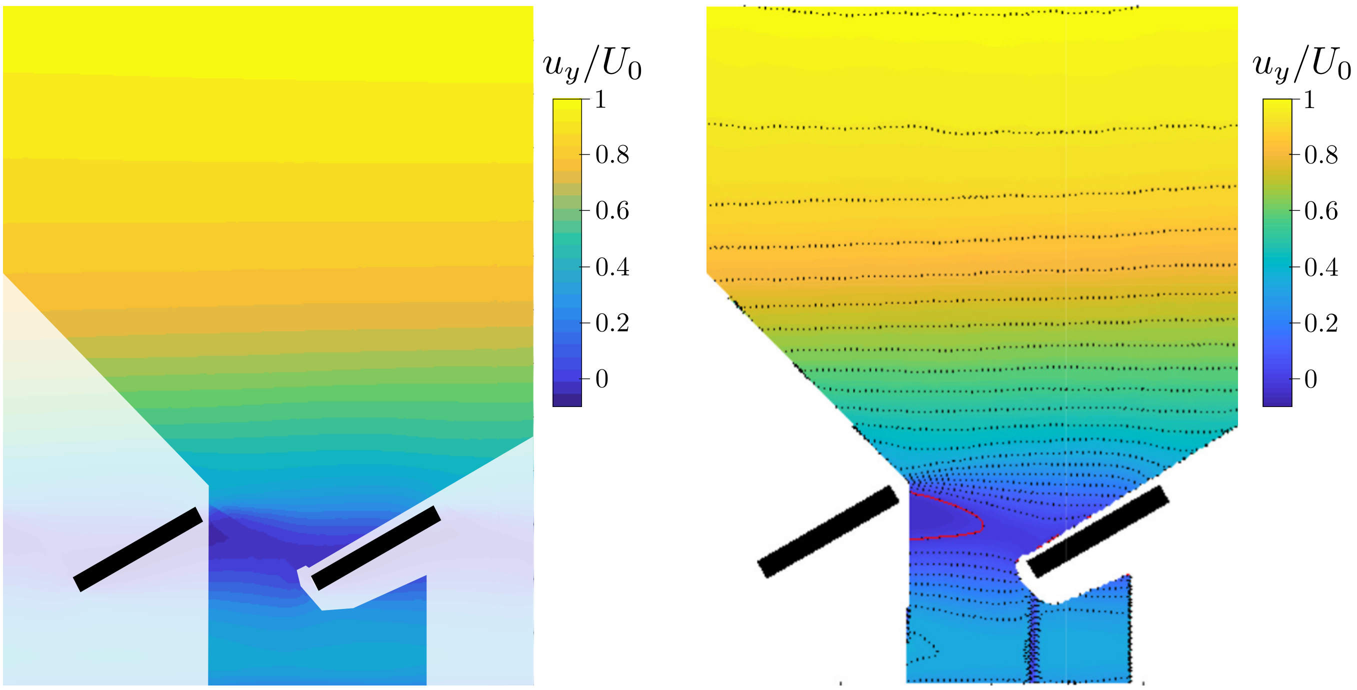

Figure 4.20–*Comparison of averaged velocity fields in the streamwise direction between the high fidelity modelling (left-hand side) and the experimental set-up retrieved and adapted from (Glick, Smith, et al., 2020) (Fig. 10.a).*

estimating the rear-side exchange; however, the front-side exchange has a downgraded quality probably due to the level of turbulence that differs slightly in the transition layer.

Conclusion and Perspective

The comparison of results between the ground truth experiment and the high fidelity numerical scheme shows that the code_saturne solver is well adapted to catch the complex flow behaviour within the stacked array of module elements.

Furthermore, even if the high-fidelity scheme can be enhanced by integrating accurate inflow vorticity, the fields of interest appear to be poorly modified by an inaccurate vorticity level in the upper part of the atmosphere. The most important mixing is captured through the interaction of the stacked array with the atmosphere.

It is worth mentioning that the boundary conditions that are enforced in the simulation are good candidates to reproduce the real conditions; so to speak, the wall functions are efficient in artificially improving mixing level for the cell near the surface. This strategy saves cost in refining the mesh especially in the *LES* context, which is greedy in computing resources. In addition, the geometry constructed by tweaking the pre-processing steps for the unitary motif to recreate the 3-D volume of control also appears to be relevant in terms of *explicit* boundary conditions.

In perspective of the high fidelity modelling, a next step would be to reproduce the good level of turbulence as input conditions. When a synthetic model can be activated in code_saturne, tuning the input remains time consuming, the second approach in two-steps (reproducing turbulent intensity by looping the entrance region) can ease the time needed, but surely requires computational resources. In any case, relaxing the turbulence level at the input level would help to know to what extent the *Developed ABL* field should be known to determine the heat rate for the module

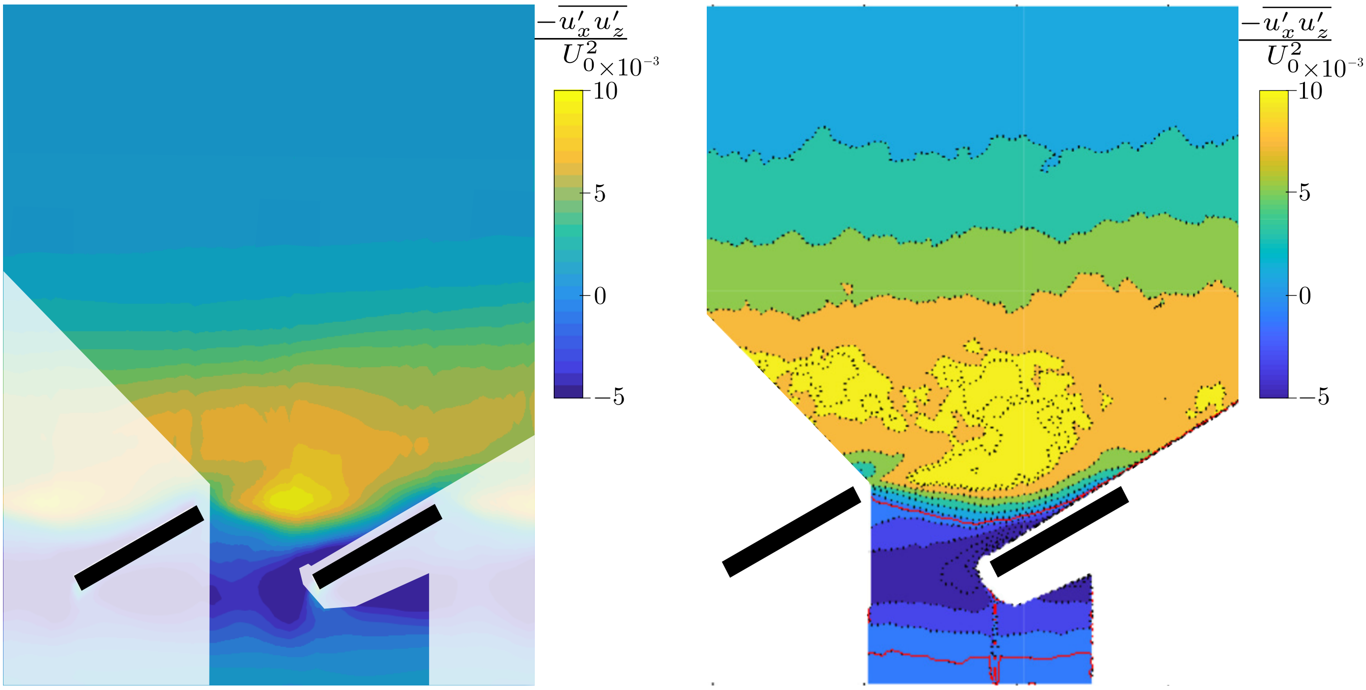

Figure 4.21–*Comparison of Reynolds Stress fields in the streamwise direction between the high fidelity modelling (left-hand side) and the experimental set-up retrieved and adapted from (Glick, Smith, et al., 2020) (Fig. 10.a)*

at the infinite location in the array.

4.6/ Conclusion

In this chapter, the computational frameworks dedicated to the study of photovoltaic yield and the estimation of thermal convection in power plants have been introduced and validated by comparison with in-situ or high-fidelity experiments.

Firstly, it has been shown that the initial thermoelectric modelling tool has all the qualities required to be able to explore thermal boundary conditions more accurately. A first level of exploration has been introduced with the integration of additional parameters in the initial sub-models, in the bricks dedicated to forced and natural convection, as well as in the long-wave radiative bricks. These modifications make the numerical tool more complex. The experimental validation via comparison with in-situ temperature and production measurements showed that the model was reliable, the next chapter aims at working on the proposed numerical sub-bricks to conjecture on the thermal boundary conditions to be applied in the FPV.

In a second step, a model suite based on the fluid mechanics solver code_saturne has been developed. It allows reproducing the wind profiles inside a PV plant, assuming that the latter are hot plates, regularly spaced. The main bi-periodic model was built to solve the computational cost problem associated with the multiplication of numerical cells to be computed to reach full scale. Forcing the flow by applying a frictional constraint coupled with the use of adequate boundary conditions yields dynamic profiles that are consistent with the high-fidelity experiment, the aeraulic flow zones in the literature power plant are reproduced for the atmospheric part while the sub-modules zone as well as the recirculation zone show discrepancies with the experiment.

Two additional models were built to stress the periodicity assumptions. Using the scalability properties of the bi-periodic case, a semi-infinite plant case was constructed. All three dynamic zones were obtained, but flow velocity variations could also be identified, mainly below the module and in the wake area. As these zones describe the flow regime near the modules, uncertainties in simulating those areas are detrimental when one wants to estimate the heat rates of modules. Assuming the high-fidelity experiment to be valid, the semi-infinite study provides an insight on the role of turbulence modelling in the simulation uncertainty. However, contrary to the biperiodic scheme, such a model can indicate the extent of heterogeneous flow in the array so that this property will be investigated in more detail in Chapter 6. The question will be: in which extent the developed flow regime is a proper assumption in real study case and how it is really evolving (length)?

To conclude, a high-fidelity simulation was carried out to secure the role of turbulence in the simulation. Using a LES turbulence scheme, the dynamic profiles and heat exchange results of the reference flat plate with the atmosphere were correctly captured by the solver. The adequacy of the latter model with the literature experiment suggests that the *fully developed flow* criterion is not met in the experiment. From this assumption, it appears that there is a good chance that the bi-periodic case is representative of the real behaviour of modules when the array is long enough so that the flow is fully developed. For this reason, the bi-periodic array simulator will be based on the $k-\omega SST$ model to represent the floating photovoltaic array in Chapter 7.

5 Thermal Boundary Conditions for Standalone FPV

> Are the geoengineers modern-day Phaetons, who dare to regulate the Sun, and must be struck down by Zeus before they destroy the earth? Or has the perfection of our rational capabilities forever silenced Nemesis?
>
> Clive Hamilton in Hamilton, 2010

This chapter presents an analysis of the results of the estimation of the cooling effect for standalone floating PV. It covers the effect of ambient temperature and the evolution of convective and radiative heat transfer modes.

Contents

A part of the results presented in this section is presented in:

Amiot, B., Le Berre, R., & Giroux-Julien, S. (2022). Evaluation of thermal boundary conditions in floating photovoltaic systems. Progress in Photovoltaics: Research and Applications, (April), 1–18. https://doi.org/10.1002/pip.3631

5.1/ Introduction

The use of a detailed physical model to describe the different thermal transfer modes allows to capture the dynamics of the PV module with a higher degree of accuracy than the dominant methodology in the PV community. A quick review of this formalism applied to our experiments is available in the appendix A.5 to support this assessment that we seek to overcome with the deployment of more sophisticated models. This section is built on the exploration of thermal boundary conditions and microclimatic effects to identify modifications to the FPV thermal models.

A first element of the study is the heat input from the lake through thermal transfer of sensible energy to the atmosphere. Known to be a system that acts as a heat sink for the atmosphere in order to justify a passive cooling effect, the instrumentation implemented on the FPV1 site allows the reconstruction of these passive effects at several scales of interest including the seasonal scale, which is not supported by the specialised literature.

The breakdown of the thermal model offers a second scale of development which acts on the heat and cooling sources embedded in the thermal model of the FPV. Although global cooling coefficients have shown improved cooling for FPV, very few authors have attempted to disentangle the thermal effects to derive corrections to the classical models. To overcome the natural limitations of using thermal models and loss functions when splitting thermal modes, a simple classification method is formulated to ensure that the corrections to convective and radiative correlations are representative.

Also, the tweak of the thermal model with measurements derived from convection and long-wave radiative exchanges carried out on the FPV2 site also responds to the construction of corrections to the empirical convective correlations that drive the thermal balance of the modules. The relevance of the corrections produced is emphasised here in that they take into account specific geometric and environmental conditions while being made from accurate and robust sensors not usual for the application.

5.2/ Assessment on Microclimate *Cooling Effect*

5.2.1/ Case Study and Hypotheses

To determine to what extent the local temperature is cooled by the presence of the lake, the following hypothesis is proposed: *the thermal stability between the waterbody and the ambient influences the temperature difference between the ambient above the waterbody and the surrounding area.* This hypothesis makes it possible to approach both the cooling phenomenon and the warming phenomenon. Moreover, evaporative transfer is directly induced within the hypothesis due to its action on the unsaturated air volume in the water vapour.

To evaluate the assumption, subsets of the data set obtained during the FPV1 campaign are elaborated. They correspond to different seasons for which the waterbody has either an atypical behaviour with respect to the ground surface or a similar behaviour. The *autumn* period starts on 1 November and ends on 1 December, the *spring/winter* period runs from 1 March to 15 March and the *summer* period runs from 1 September to 30 September.

All subsets are chosen for the large number of valid measurements. A microclimatic effect is deduced from the difference in temperatures between the offshore and onshore measurements ($\Delta T_{FPV-EMB} = T_{\text{amb}}^{FPV} - T_{\text{amb}}^{EMB}$) and the thermal lake stability measurements ($\Delta T_{FPV-wat} = T_{\text{amb}}^{FPV} - T_{\text{wat}}$). Meteofiles are built based on these seasonal subsets using the ambient temperature for offshore location (FPV simulation) or embankment location (ground-mounted simulation). They follow the required syntax described in Listing A.1. Physically speaking, the thermal constructions are summarised under the circuit analogy in Figure 5.1. All parameters are taken constant within each season assessment, except for ambient temperatures.

5.2.2/ Microclimate *Cooling Effect*: Seasonal Observation

The two temperature differences $\Delta T_{FPV-EMB}$ and $\Delta T_{FPV-wat}$ are observed as samples that are part of continuous processes. First, we would like to evaluate the contingency of the two temperature differences so that the microclimate effect is deduced from the waterbody stability criteria. The contingency for the samples of observation is studied by the chi-square law with 4 degrees of freedom; the null hypothesis is that the microclimatic temperature differences are independent of the stability of the waterbody. The number of degree-of-freedom is arbitrarily chosen; the objective is to differentiate clear deviations between parameters; however, this criterion is constrained by the relatively low number of observations. The null hypothesis condition holds when $Y^2 < \chi^2 = 9,49$, if the threshold is exceeded, correlations can be observed between the two parameters.

The result of the contingency test is presented in Table 5.1. The statistical test analysis shows that the stability of the waterbody is correlated with the microclimatic temperature difference (fall $Y^2 = 5419.0$, spring $Y^2 = 1174.1$ and summer $Y^2 = 4175.7$), the Tschuprow coefficient also shows that the link between the two parameters is rather strong. This is even truer for the fall season, for which the coefficient is around 1, the link is less strong for spring (0.57) and slightly higher for summer (0.67). The pond is, in fact, a source of heat that *lags* behind the ambient temperature in autumn, whereas in the other two seasons the interseasonal effect is reduced, evaporation also participates in the reduction in temperature and is more strongly reflected in the dry seasons.

An important observation is that the waterbody temperature tends to favour warming of the local climate, whereas the cooling effect is much less favoured. The observation is similar for the

	$T^{FPV}_{amb} - T^{EMB}_{amb} > 1$	No Effect	$T^{FPV}_{amb} - T^{EMB}_{amb} < -1$
Fall			
$T_{wat} - T^{FPV}_{amb} > 0$	**5863** *(657,4)*	878 (919,4)	63 (145,4)
$T_{wat} - T^{FPV}_{amb} = 0$	393 (98,2)	627 (197,8)	24 (6,0)
$T_{wat} - T^{FPV}_{amb} < 0$	147 (1277,1)	2072 (1661,0)	303 (456,8)
Spring			
$T_{wat} - T^{FPV}_{amb} > 0$	**1570** *(167,1)*	711 (131,6)	25 (39,4)
$T_{wat} - T^{FPV}_{amb} = 0$	1004 (1008,5)	460 (79,5)	7 (39,1)
$T_{wat} - T^{FPV}_{amb} < 0$	1006 (297,5)	2267 (227,8)	**226** *(83,7)*
Summer			
$T_{wat} - T^{FPV}_{amb} > 0$	**9435** *(430,5)*	1238 (631,6)	10 (547,0)
$T_{wat} - T^{FPV}_{amb} = 0$	837 (8,1)	448 (70,6)	9 (51,8)
$T_{wat} - T^{FPV}_{amb} < 0$	3138 (612,0)	2699 (773,1)	**978** *(1051)*

Table 5.1–*Number of observations of temperature differences above the pond and on the embankment versus the temperature difference between the water and air above the pond for three seasons. The χ^2 part of the observation is written in parentheses.*

three seasons. In spring, it can be observed that the effects of microclimatic cooling are favoured compared to the hypothesis of independence (226 > 83.7), this behaviour can be attributed to the storage property of the basin. As the basin is at low temperature after the winter season, radiative heating during the daytime period induces faster heating of the air on land than over the water.

In summer, the cooling effect is not favoured by the behaviour of the water (978 < 1051), the independence is relatively small. It is assumed that the vegetation around the measurement area on land must interfere more widely for this season so that the shift in ambient conditions is weaken. In the observed situation, it seems that the waterbody induces a seasonal pattern that has the greatest influence during the *cold* season; the pond is more frequently a heat source than a heat sink. There are obviously more instants that are concerned with substantial cooling effect due to ambient shift in the summer period; however, the statistical study shows that the criterion of independence is not met. The cooling effect due to the microclimate is not constant throughout the year.

5.2.3/ Microclimate *Cooling Effect*: Daily Observation

The daily pattern of temperature varies from time to time in magnitude, mainly due to solar forcing. Therefore, performing a contingency study is less relevant. Therefore, we use the photovoltaic model to assess daily variability. Three typical days are classified for each subset. They are selected as representative candidates for a reliable microclimatic cooling effect as the condition $T^{FPV}_{amb} < T^{EMB}_{amb}$ is matched at some points during the sunny period.

The statistical indicators shown in Chapter 3 are applied to assess the precision of the prediction temperature with the temperature of the back sheet. The indicators are calculated between two timestamps during which microclimatic cooling occurs. These periods are seasonal dependent, but a similar pattern is assumed: a first period goes from midnight to the morning and encom-

	BC T_{amb}^{FPV}	BC T_{amb}^{EMB}
Fall		
$RMSE\left(T_{bs}^{exp} - T_{bs}^{num}\right)$	1.51 °C	1.93 °C
$MBE\left(T_{bs}^{exp} - T_{bs}^{num}\right)$	2.01 °C	2.36 °C
$T_{amb}^{FPV} - T_{amb}^{EMB}$	0.5 °C	
Spring		
$RMSE\left(T_{bs}^{exp} - T_{bs}^{num}\right)$	1.95 °C	1.94 °C
$MBE\left(T_{bs}^{exp} - T_{bs}^{num}\right)$	2.54 °C	2.52 °C
$T_{amb}^{FPV} - T_{amb}^{EMB}$	0 °C	
Summer		
$RMSE\left(T_{bs}^{exp} - T_{bs}^{num}\right)$	1.38 °C	0.73 °C
$MBE\left(T_{bs}^{exp} - T_{bs}^{num}\right)$	1.97 °C	1.59 °C
$T_{amb}^{FPV} - T_{amb}^{EMB}$	−1 °C	

Table 5.2–*Summary of the simulation performances given the temperature selected as the "ambient temperature" with respect to the seasonal subset. Statistical indicators are calculated on the basis of the likely occurrence of thermal inversion at the waterbody level.*

passes the nightly temperature drift of the water mass, a second period spreads from the end of the first period to the late afternoon, and a last period is finally calculated with the remaining part of the day. The second period is investigated more deeply because it concerns the daily pattern, which is related to the production of photovoltaic electricity.

The results of the statistical indicator within the time period of interest for the three seasons are given in Table 5.2, a graphical output is shown for the summer period only in Figure 5.2. The first observation is that the temperature change in the microclimate occurs during the second temporal range. The first and third windows always show a greater average temperature difference. This point credits the seasonal microclimate effect, since the fall period shows the lowest temperature difference with $\Delta T \simeq 0.5\,°C$ while the summer period obtains the highest daily difference, $\Delta T \simeq 1.4\,°C$ (–). RMSE and MBE show that FPV-based temperature conditions are not always the best estimator, especially in summer, where the embankment condition offers a better fit for both indicators ($|RMSE^{EMB}| < |RMSE^{FPV}|$ and $|MBE^{EMB}| < |MBE^{FPV}|$). Although the temperature difference between water and air is the largest (−1.0 °C), the behaviour of the photovoltaic module shows a warming effect of more than 1 °C in the late afternoon (–). The cooler season is not affected by this phenomenon, and the buffering effect induced by the thermal capacity of the lake, which tends to dampen the temperature evolution over the lake, is greatest in the fall period and observable in the backsheet temperature prediction. At this time, the air temperature obtained at the pond level is the best estimator and appears as a warming effect. The observations for the end of the winter-spring period do not show special trends that can be associated with neither cooling nor warming effects; the statistical indicators are identical.

Therefore, the only cooling effect observed is obtained in summer, but according to the 1-D simulation, the backsheet temperature is not better predicted at this moment. Instead, a warmer

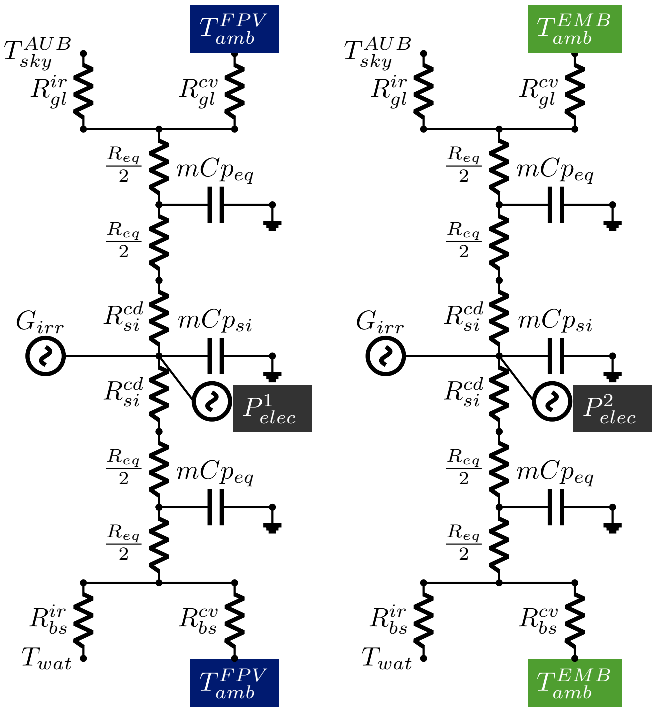

Figure 5.1–*Resistive analogy of the models enforced to evaluate microclimate cooling gains.*

temperature seems to be a better estimator of the effective convective temperature of exchange. A speculative hypothesis is that the measurement stations are more or less affected by the surrounding environment, so that the air temperature captured by the meteostation above water suffers from other thermal modes such as direct radiation or convective transfers. Another explanation could be that there is local temperature buffering so that the air temperature below the module differs substantially from the temperature in front of the system; the magnitude of the difference would have been greater if floating structures had been installed to avoid heat removal around the rear module side. More measurements are needed to determine the reason for this observation.

5.2.4/ Modification of the Energy Yield

The simulations performed during the previous study were reused; the focus was on the electrical performance calculated by the single-diode model. Assuming that T_{amb}^{FPV} is the best image of the effective convective temperature, it is possible to calculate *yield gain* during the cooler period. The temporal plot in Figure 5.3 shows a slight production gain (🟦), up to 5.3 W for the entire module row. It corresponds to a maximum gain $\Delta P \simeq 0.2\%$, the mean value estimated at $\Delta P \simeq 0.15\%$. As in Figure 5.2, the most important temperature decrease is obtained in the late afternoon and corresponds to the maximum cooling effect experienced by the electrical yield. The reversal trend is observable before 11 a.m., the production yield decreasing due to the temperature change (🟧). The same calculations are performed for the two other climates, and the results are shown in Table 5.3.

This first strategy to refine the definition and estimation of the cooling effect shows that the full-year time scale is not appropriate to estimate gains in electrical production due to local passive cooling. A seasonal view of the problem shows that the cross-comparison between an onshore reference system and a photovoltaic system depends on the waterbody behaviour. On a typical day

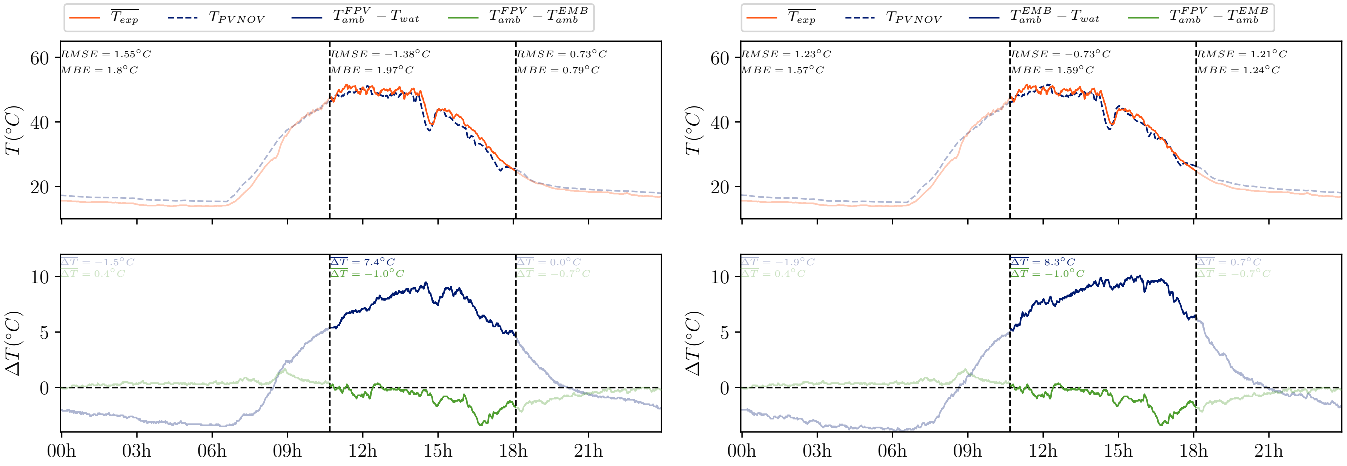

(a) $T_{amb} = T_{amb}^{FPV}$ *(offshore location)*

(b) $T_{amb} = T_{amb}^{EMB}$ *(onshore location)*

Figure 5.2–*Backsheet temperatures from 1-D simulations compared to experimental measurements for the summer subset. The two parameters chosen as candidates for microclimate cooling are also presented* $(\Delta_{FPV-EMB}, \Delta_{FPV-wat})$

	Fall	Spring	Summer
$\Delta\overline{T}$ (°C)	0,5	0	-1
ΔP_m	-0,11%	0,02%	0,15%

Table 5.3–*Seasonal cooling effect observed as a result of microclimate shift*

scale, the gain is even less obvious, and strong local warming tendencies can be observed, especially in the morning, when the nycthemeral cycle inertia is important. The trends in this cooling are rather perceptible over long frequencies on the scale of the day, whereas the phenomenon of amplification linked to the season runs over several dozen days. The maximum average electrical gain related to seasonality is estimated at 0.15%, but this gain is observable at strategic moments for photovoltaic production, with the warming phenomenon occurring more in the morning at times of low solar activity.

However, this first study is not fully characteristic of a floating photovoltaic power plant, the study lake is relatively small and shallow. This is characterised by a rapid surface temperature evolution on a seasonal scale, while radiative forcing remains the dominant element in this evolution on a daily scale. Furthermore, the evaporative phenomenon is not directly observed; it is the air temperature above the lake that contains this information. Although it is assumed that evaporation is relatively little reduced by the presence of the modules (low footprint), the location of the lake and the surrounding vegetation are not factors that point in the direction of high lake evaporation, but rather towards a reduction of this effect (ambient humidity, lower wind speed).

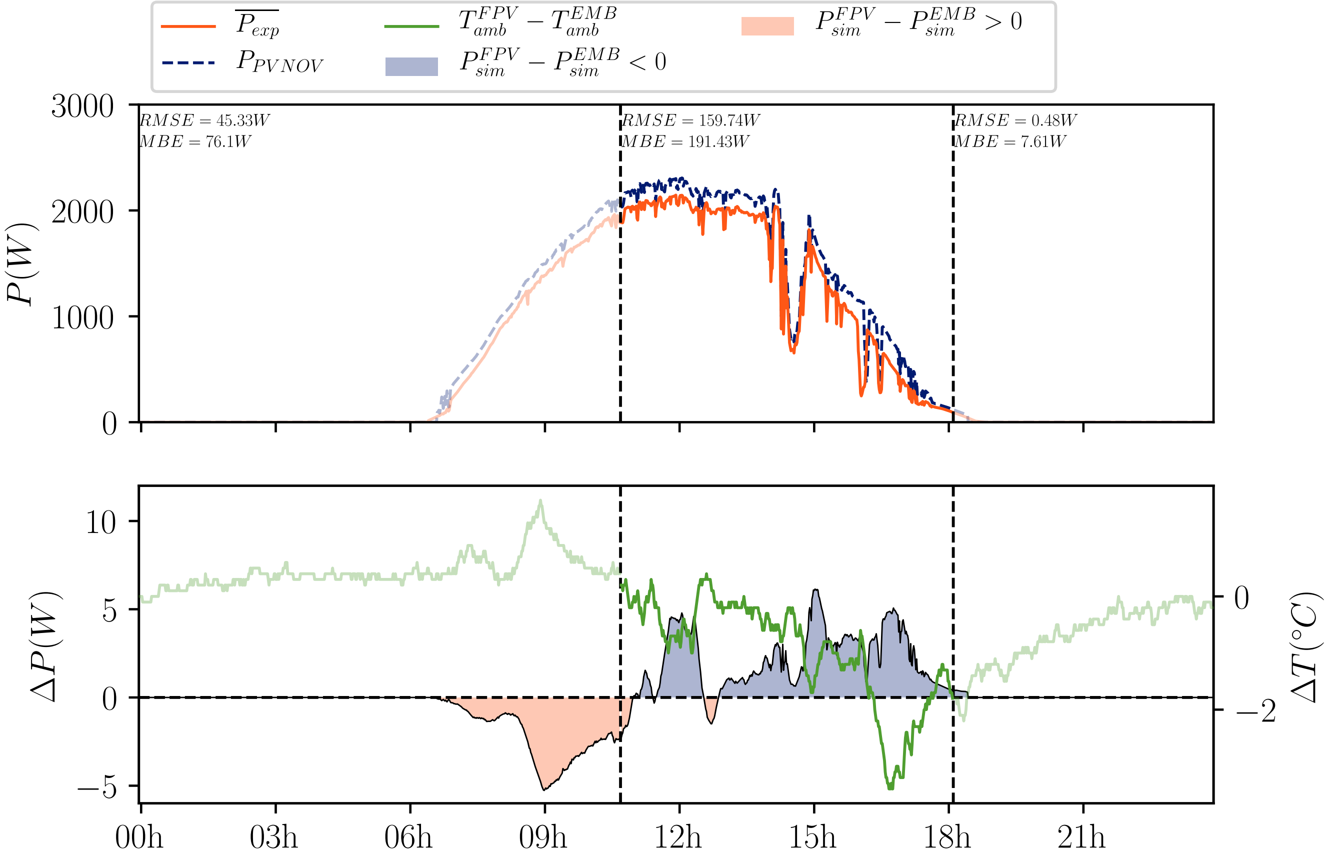

Figure 5.3–*Estimation of cooling effect due to microclimate ambience in summer based on two runs of photovoltaic model with various ambient temperature inputs. Energy yield is given at the string level so that the difference in energy yield from two simulations* (ΔP) *is based on the total string yield. Differences between waterbody and ground ambient temperatures are more important during the afternoon so that the greater cooling effect shows up in the meantime.*

5.3/ Correction of Convective Correlations based on Nodal Model

The literature regularly proposes to model the cooling effect in a simplified form with the parameter U_{values} coupled with empirical research. We have shown in Chapter 1 that the use of this tool is sufficient to describe the cooling of photovoltaic systems as long as the time scale is large enough. However, the strategy is limited by the structure of the inverse thermal model used. More sophisticated models are needed to reduce temporal scales and solve larger spatial scales, in particular, through the induction of suitable convective modes.

This section proposes to highlight different empirical strategies to describe the convective intensity seen by floating photovoltaic modules. The first part is devoted to a description of the thermal models and the proposed evolutions. Therefore, physical systems are described that support the application of empirical methods. While the classical method is applied to determine the cooling trends in a second part, the two new strategies are described in the following subsections. Contributions to the thermal prediction quality of these two strategies are compared with the reference classification proposed in (H. Liu et al., 2018) for installations FPV1 and FPV2.

5.3.1/ Calculation of Heat Rates, Data Filtering and Hypotheses

Optimised 1-D modelling

The optimised thermal modelling is constructed following the simulation and statistical sorting depicted in Figure 5.4. First, the multilayer thermal model presented in Section 4.2.1 is run iteratively for several couples of weighting parameters (χ, ζ), the backsheet temperature outputs are stored after each run. These runs are performed using the parameter sweep option in Dymola® so that multi-threading improves the simulation time.

Then, the best runs are evaluated based on the minimisation of statistical indicators. They are obtained by comparing the output of simulations with the experimental measurement considering only daytime values.

Then, a filtering step consists in separating the errors of the prediction into three categories that refer to the convective modes observed at each instant, and the Richardson dimensionless number is applied for that purpose. According to the Richardson value, the error is associated with one of the tree bins as follows:

$$\begin{aligned} Ri \leqslant 0.1 &\rightarrow Forced \\ 0.1 < Ri < 1 &\rightarrow Mixed \\ Ri \geqslant 1 &\rightarrow Free \end{aligned} \tag{5.1}$$

In order to declare a couple of weighting parameters as the best option and therefore the most reliable to correct the existing correlation, statistical estimators are computed for each bin of errors. The final stage consist in finding the best trade-off in the space of result that avoids the phenomenon of compensating the error between bins. It is hoped to obtain the lowest Mediane indicator for each bin, as well as no asymmetry in the error distribution.

Quasi-direct heat flux sensor correlations

As a result of the methodology set up to recover the convective coefficient from the heat flux sensor measurement at CETHIL, the same operation is carried out at the FPV2 test site. As the

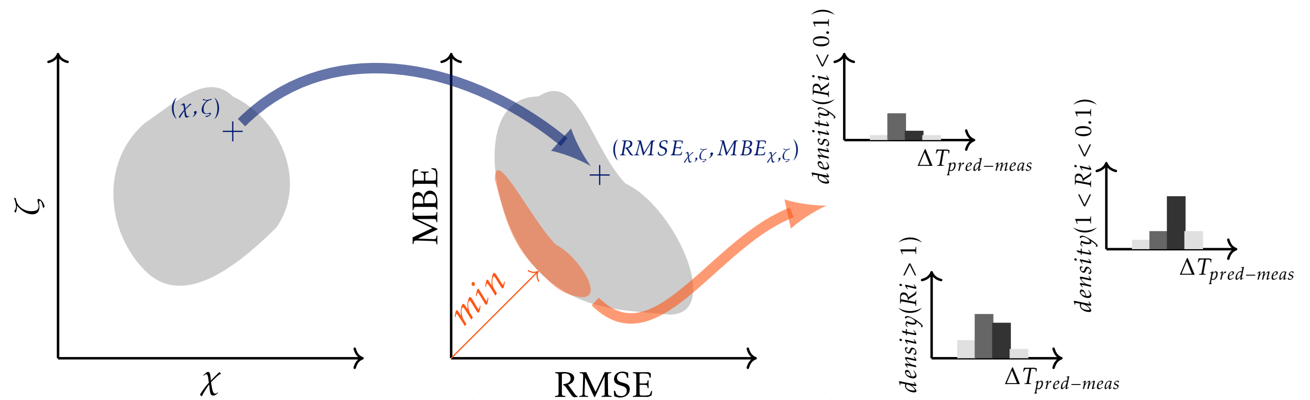

a) Feasible design space b) Feasible objective space c) Dimensionless numbers categorization

Figure 5.4–*Schematic view of the parameter selection for convective actions. The parameter sets obtaining the best scores in temperature predictions are sorted out according to the Richardson number calculated theoretically and based on the experimental available measurements.*

acquisition time of the experiment is shorter than 10 minutes, we hope that the behaviour regarding the reliability of the measurement will be effectively verified. Furthermore, the FPV2 measurement system does not allow us to know the electrical power delivered by the module. This assumption is not necessary to determine the convective ratio, but it allows us to close the thermoelectric system of the module. Therefore, we can apply the multilayer model by integrating the convective boundary conditions described by the heat flux sensor. **In this strategy, the knowledge of the wind characteristics are not necessary, it is totally replaced by the calculated convective coefficient.**

We reuse the same radiative information as that developed in Chapter 3 for the measurement system, the system having been designed identically to that placed in the CETHIL campaign. As the thermocouple used to recover the temperature of the heat flux sensor is not operational, the temperature of the module is used to tweak the temperature of the heat flux sensor. As demonstrated in the CETHIL experiment, the real temperature difference between the module and the heat flux sensor remains lower than 0.9 °C during the sunny period. To guarantee the stability of the numerical calculation, in the periods where the calculated coefficient is usually forced to $0\,\mathrm{W\,K^{-1}\,m^{-2}}$ *i.e., when the coefficient tends to infinity because the temperature difference with the outside is low*, the function of Test et al. is applied. Therefore, the calculated h^{cv}_{fr} function is continuous. An additional retrospective check is performed to verify that the time period of interest in FPV2 is not influenced by this decision.

The new function for h^{cv}_{fr} is entered into the *meteo.txt* file as a column that replaces the U_{w} column.

5.3.2/ Distribution of Convectives Modes

FPV1 distribution

Figure 5.5 shows the statistical indicators obtained by comparing $T_{pred,\mathrm{re}}$ and $T_{exp,\mathrm{re}}$ at the FPV1 test site. A heatmap cell corresponds to a single simulation from which the (ζ,χ) coefficients are applied to the boundary conditions. The border of the figure shows the performance of the nominal case $(\zeta,\chi) = (100,100)$ (top border) and the optimised case $(\zeta,\chi) = (120,150)$ (right border).

Looking at the Mean Bias Error of simulations, the frontier of the optimised cases ranges from

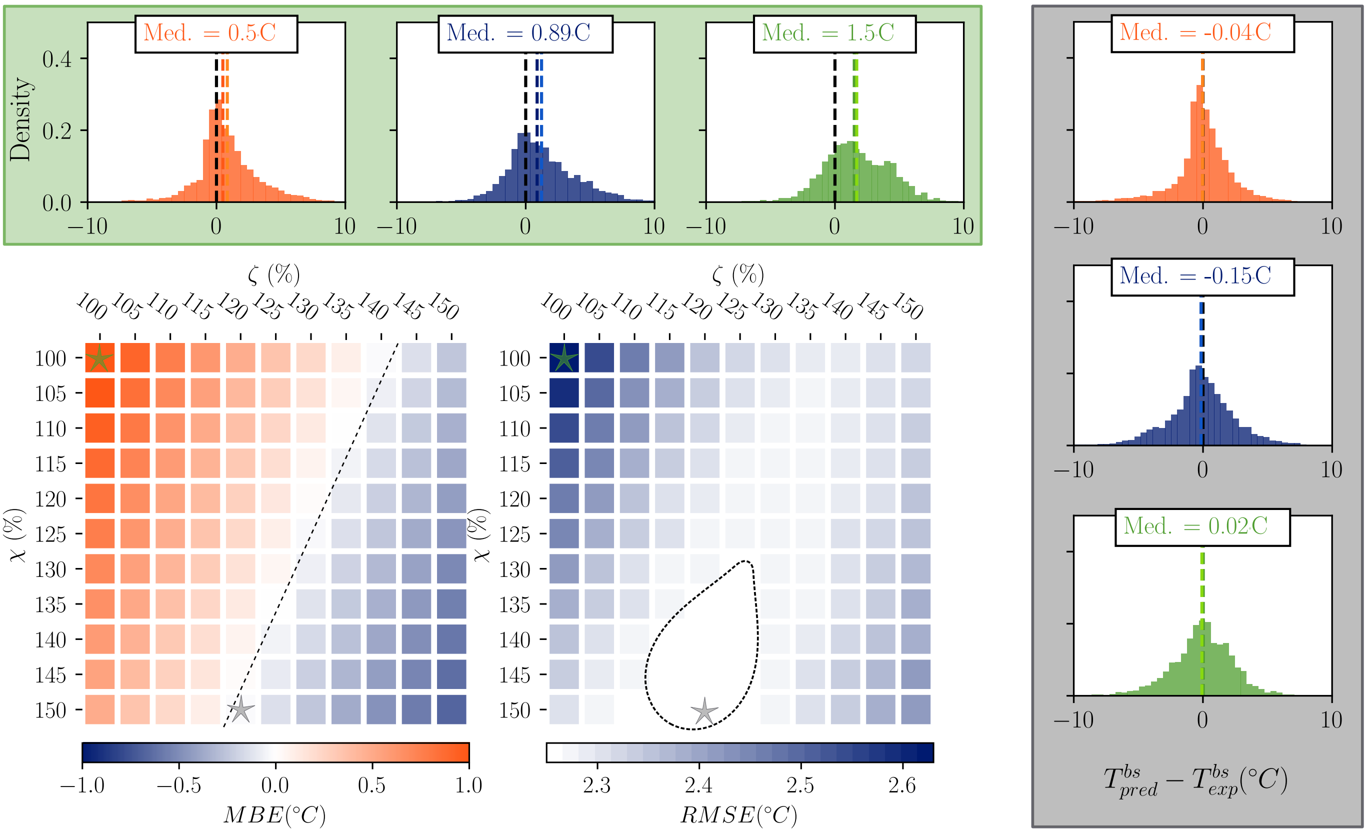

Figure 5.5–_Application of the statistical framework to derive meaningful weighting parameters for both convective heat modes in the FPV1 case study._

the parameters $(\zeta, \chi) = (140, 100)$ to $(\zeta, \chi) = (120, 150)$. The line spreading from one end to the domain to another can be explained by the low sensitivity to the natural convective region of the framework. Therefore, these coefficients have a lower influence on overall performance. From the Root Mean Square Errors, it appears that the deviation simulation is minimised in a region bounded by cells $(\zeta, \chi) = (110, 150); (125, 130); (125, 150)$. The region around $(\zeta, \chi) = (125, 150)$ corresponds to the previous assessment with the MBE indicator, so the area is selected for further research based on clustering selections.

The error distributions for the nominal case $(\zeta, \chi) = (100, 100)$ are shown for the three modes of convection (forced in Figure 5.5.a, mixed in Figure 5.5.b and free in Figure 5.5.c). The distribution for the forced convective category falls between a Cauchy and a Gaussian distribution as the peak density is narrowed and the tails decay rapidly. The error bias is less pronounced than in the other category (0.84 °C vs. 1.23 °C and 1.69 °C), but it remains positive. Therefore, the initial prediction includes heat mechanisms that are lower than those in the real-world experiment. The two other distributions are closer to Gaussian distributions as the peak density is reduced. It can be appreciated that the prediction of the free convective case is poorly achieved compared to the other thermal modes, so situations with lower wind would include a larger bias in the prediction.

The case $(\zeta, \chi) = (120, 150)$ provides the best bias reduction for the three error distributions (forced in Figure 5.5.d, mixed in Figure 5.5.e and free in Figure 5.5.f). The most significant evolution is obtained for the free convective case with an average bias correction of 1.61 °C. A prediction gain of 1.08 °C is also obtained for the mixed convective category. The optimised model improves the error distributions with a stronger density peak around $\Delta T = 0$ °C compared to the initial distributions. An important point to mention is that the statistical compensations between thermal modes are eliminated so that the correlation weights are representative of each thermal in a separate fashion. The greater trend observed for forced convective action is attributed to the free footprint geometry that allows the wind to develop without obstacles around the modules. In addition, the turbulent intensity is admitted to be greater offshore, and it would also participate in the result obtained. However, the magnitude of enhancement is within the calculation uncertainty limits defined for convective rates; the proposed strategy has only reduced the calculation uncertainty by not considering unproper thermal modes. Therefore, the causal reasons of the enhancement are still speculative. In the case of free convective heat rates, it appears that the range of enhancement is large in front of the nominal case. A speculative hypothesis is the ability of the air temperature to dissipate in the vicinity of the installation. In case of thermal buffering action, it is likely that the nominal correlation would be reduced with respect to the level of insulation around the backside of the modules.

FPV2 distribution

The similar experiment is performed on the FPV2 dataset, Figure 7.10 shows the statistical results as well as the heat modes distributions for the nominal and the optimised case on the top and right borders, respectively.

The region of lower statistical results is located along a line from $(\zeta,\chi) = (95,105)$ to $(\zeta,\chi) = (113,50)$ for the MBE indicator. The RMSE also performs well around the similar line of parameter; however, the display of best values is larger, especially in the lower-value region. Compared to Figure 5.5, it appears that the spread for both indicators is significantly lower in the FPV2 case for the MBE indicator; the upside down effect is captured for the RMSE indicator so that we can speculate that the magnitude of the wind velocity has an influence on the quality of the developed strategy. As introduced in Chapter 3, the magnitude at the FPV2 site is more important than for the FPV1 site. Statistically, the inverse thermal model would suffer from larger temperature reduction due to a stronger trend in the forced correlation; this phenomenon is caught through the MBE error, for instance.

The best match for both coefficients is obtained for the pair $(\zeta,\chi) = (104,75)$; it is worth mentioning that the parameter couples reduce the compensation phenomenon at most between forced and free action. When comparing the bins between the nominal case and the optimised one, it is noticed that the forced class benefits of lower statistical estimator(-0.08 °C vs. -0.39 °C). On the other hand, the free convective class is dramatically optimised (-1.21 °C vs. 0.27 °C), it is concluded that the coefficient set over the free convective transfer has a real significance (in this case, reduction of the free convective transfer), when the enhanced trend on the forced convective transfer is more or less cancel out. In the studied case, the raft structure is complex around the module of interest and especially near the rear side. The electrical battery produces an obstacle for fluid flow so that it is speculated that the free transfer occurs with a degraded regime.

5.3.3/ Faster Frequency Sampling

Figure 5.7 shows the temperature dynamics predicted from the numerical experiment with the new function h^{cv}_{fr} for the day of 28 May (−). For comparison, the experimental results (−) and the temperature deduced from the simulation using the optimisation of convective parameters (−) are also shown. This day is characterised by a radiative flux that undergoes some cloudy passages. With the absence of anchoring that induces movement of the azimuth angle of the

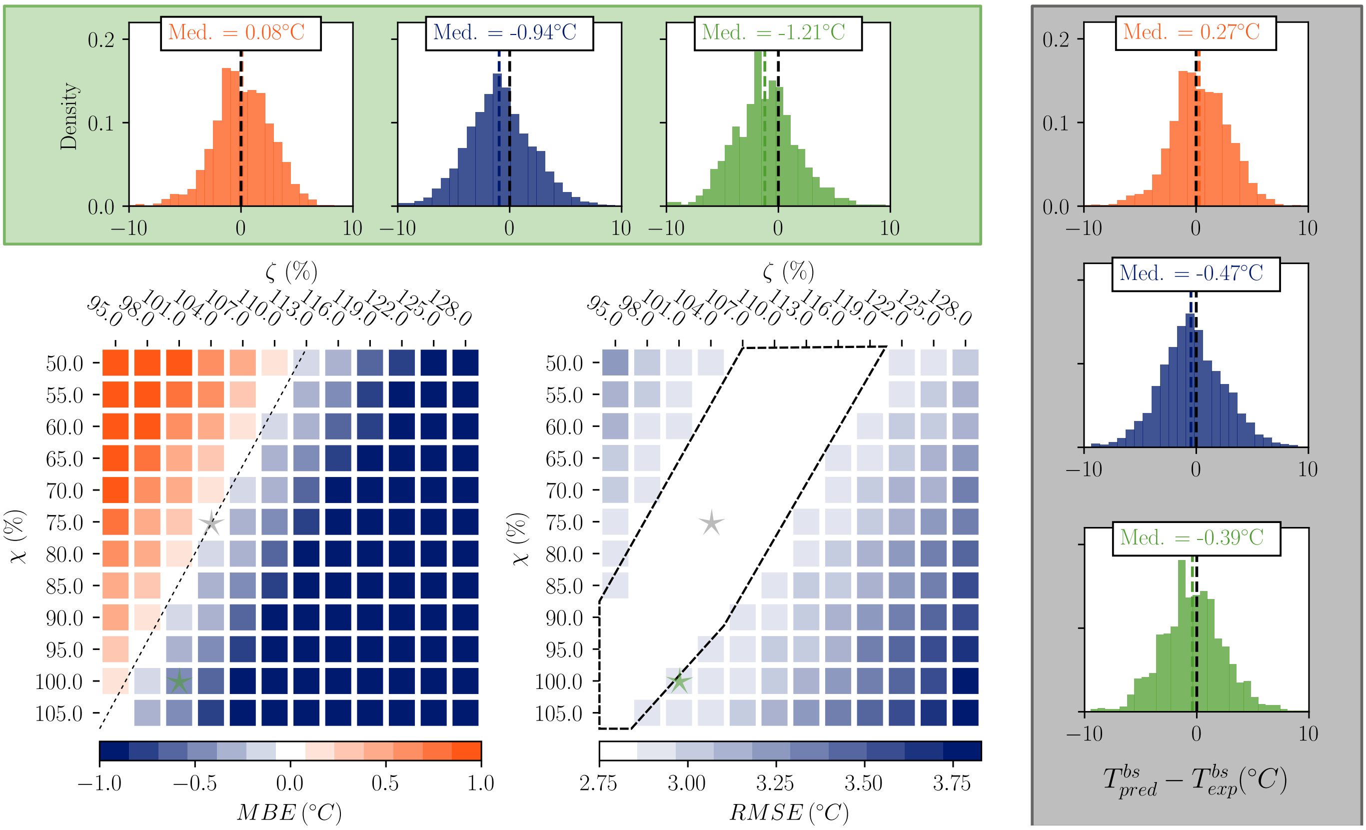

Figure 5.6–*Application of the statistical framework to derive meaningful weighting parameters for both convective heat modes in the FPV2 case study.*

module, the experimental temperature undergoes important variations during the day (14 °C between 12p.m. and 1a.m. for example). We observe that the predicted temperature of the new h^{cv}_{fr} is very consistent with the experimental temperature during the afternoon. On the other hand, at the same time, the methodology based on the optimised convective coefficient is parasitised by the wind field. As we have seen, the latter method is limited when the wind variations are abrupt. Therefore, the heat flux sensor method is more robust in dealing with short-term dynamics.

However, the coincidence between the predicted temperature and the experimental temperature is slightly biased by the use of the backside temperature in the calculation scheme. However, observation of the forbidden period between 8 am and 12 pm indicates that although the actual temperature is used in the calculation of h^{fm}_{cv}, the evolution of the temperature prediction tends more to follow the temperature obtained with h^{clas}_{cv}, which does not use any information on the actual temperature of the module. Thus, this bias can be considered rather small.

However, since the methodology does not use information on the air field, the method emphasises the real convective phenomenology. This argument is all the more valid when we are interested in the evolution of the temperature difference between the numerical and experimental schemes. From 12 a.m. onwards, the variations in the difference are much less exacerbated than the variations obtained with the initial numerical scheme. When the deviation of the new method is important, for example around 1 p.m. with a deviation $\Delta T^{fm} \simeq 2.5$ °C (🟩), an abrupt variation of the initial method is observed $\Delta T^{clas} \simeq 4.0$ °C (–). This is the translation of a better consideration of the aeraulic phenomenon with the new methodology.

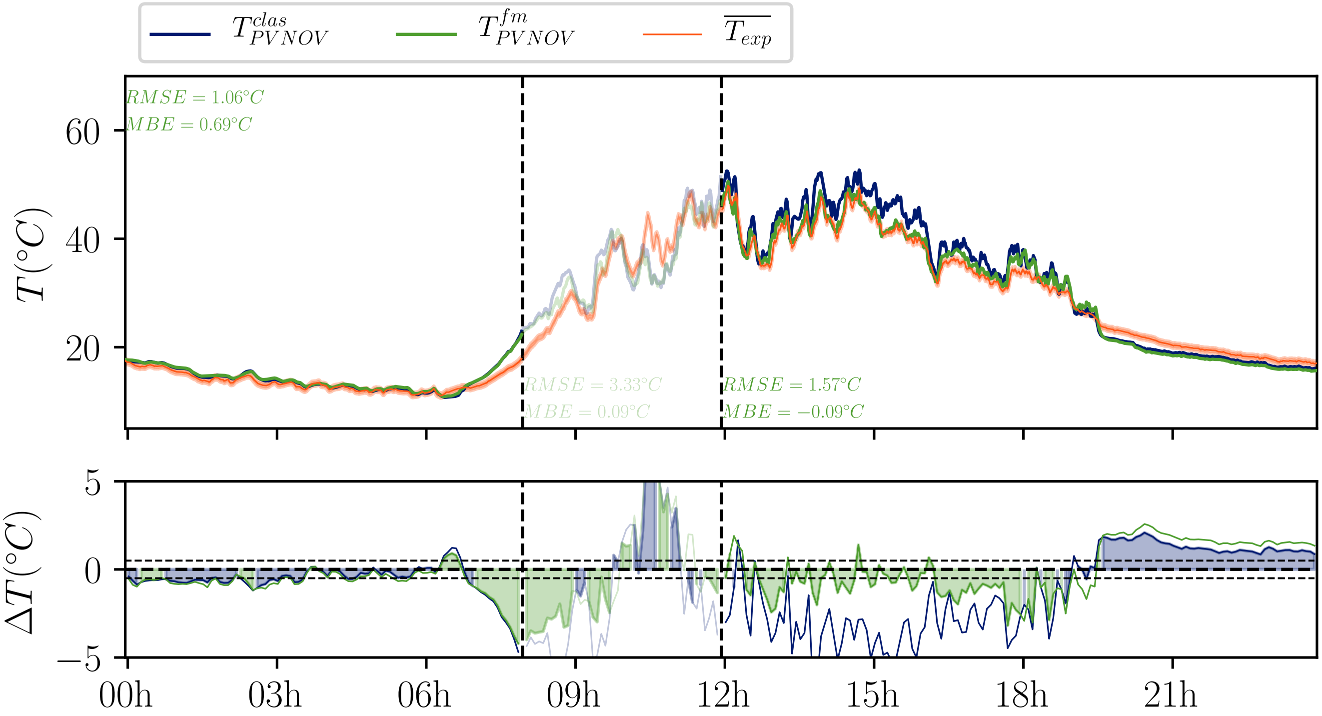

Figure 5.7–*Cross-comparisons of backsheet temperatures obtained though the flux-metre method or the optimised method versus the experimental temperature measured at FPV2.*

Analysis of the entire study period improves temperature prediction using the heat flux sensor of $RMSE = 2.44\,°\mathrm{C}$ and of $MBE = 0.05\,°\mathrm{C}$, while the previous method performed less well $RMSE = 2.7\,°\mathrm{C}$ and $MBE = -0.33\,°\mathrm{C}$. Therefore, it is concluded that h_{cv}^{fm} is more relevant to represent the convection at the front of the floating PV module for the prediction time step used (1 minute).

From the results of cross-validation, a theoretical linear law is constructed that minimises the residuals of the statistical series $h_{fr}^{\mathrm{cv}}\left(\overline{U_{\mathrm{w}}}\right)$. This new law is created from the time series with a time step of one minute. To ensure that the law is relevant without integrating a theoretical correlation to support inconsistent values, the statistical series used only considers h_{fr}^{cv} calculated between 12 a.m. and 6 p.m.. Agglomeration of the data at the 10-minute time step, coupled with averaging, allows a significant increase in linearity ($r^2 = 0.19 \rightarrow r^2 \simeq 0.4$). We prefer to use the minute time step because it is the one that is assumed to be imprecise without the use of a particular strategy as adopted in his work.

The linear law and the distribution of the statistical series are presented in Figure 5.8. The spread of h_{fr}^{cv} is important; the maximum value of the series reaches $88.1\,\mathrm{W\,K^{-1}\,m^{-2}}$ *i.e., around 10 times the nominal value of the empirical relation of Test et al.* However, more than 90% of the series is situated between $7.6\,\mathrm{W\,K^{-1}\,m^{-2}}$ and $36.5\,\mathrm{W\,K^{-1}\,m^{-2}}$, with a median value of $16.7\,\mathrm{W\,K^{-1}\,m^{-2}}$, i.e. 60% higher than the nominal value of Test et al.

The observation of the distribution of point densities indicates important support zones around $0.9\,\mathrm{m\,s^{-1}}$ and $1.5\,\mathrm{m\,s^{-1}}$ with similar convective ratios between $9\,\mathrm{W\,K^{-1}\,m^{-2}}$ and $14\,\mathrm{W\,K^{-1}\,m^{-2}}$ (■). For more intense winds, support values are also identifiable at $2.1\,\mathrm{m\,s^{-1}}$, $2.6\,\mathrm{m\,s^{-1}}$ and $3.3\,\mathrm{m\,s^{-1}}$ with increasing ratios $10.5\,\mathrm{W\,K^{-1}\,m^{-2}}$, $16\,\mathrm{W\,K^{-1}\,m^{-2}}$ and $19\,\mathrm{W\,K^{-1}\,m^{-2}}$ (■). Linear regression gives a law whose coefficient of linearity is $2.51\,\mathrm{W\,K^{-1}\,m^{-2}}$ (–), it is almost identical to that of the law

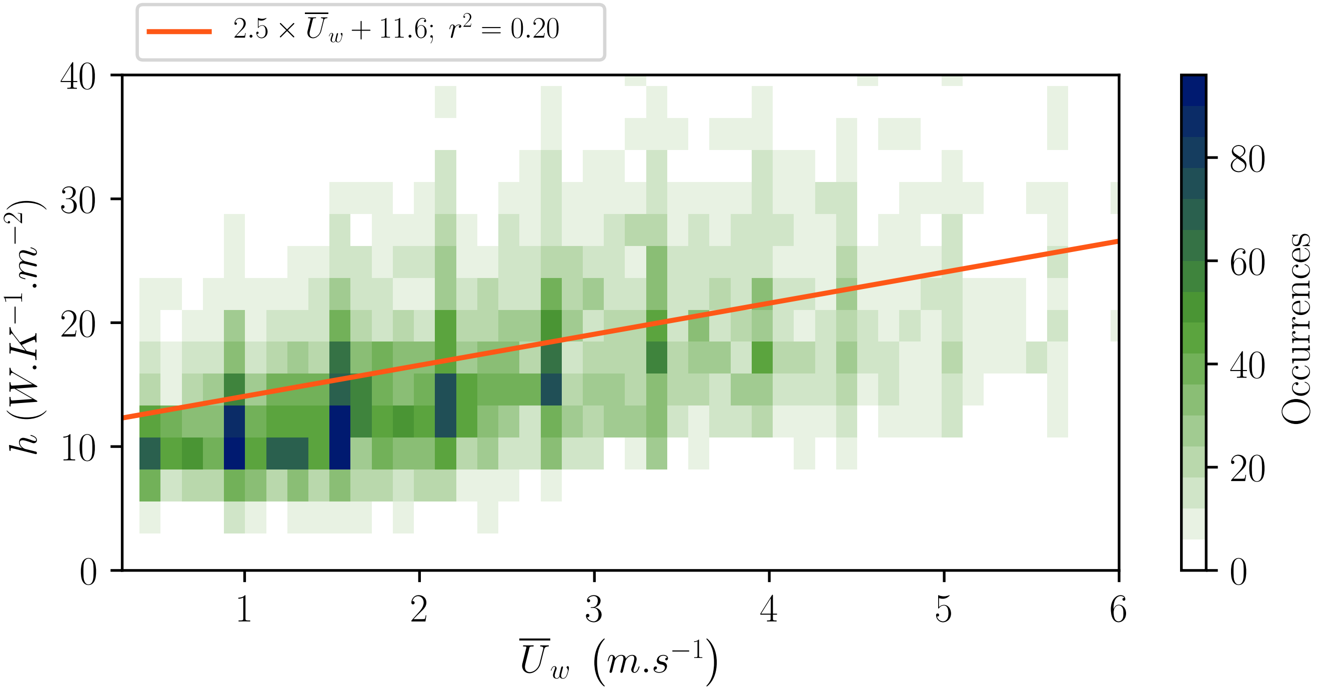

Figure 5.8–*Statistical distribution of empirical h^{cv}_{fr} correlated with the mean wind speed.*

of Test et al. 2.55 $\mathrm{W\,K^{-1}\,m^{-2}}$. However, the offset is more than 3 points higher, the law gives :

$$h^{\mathrm{cv}}_{fr} = 2.5 \times U_{\mathrm{w}} + 11.55 \tag{5.2}$$

It can be seen that the support points are all below the linear law; this is explained by the spread of the statistical series in the upper part of the diagram. Therefore, we expect to have a more insistent behaviour in the temperature reduction via this empirical law.

In conclusion, it can be seen that the new methodology allows us to recover a linear law that associates the convective coefficient with the mean wind speed, while offering a higher reliability of the law for the acquisition frequency (1 min). The nominal value of the law is higher than the previous law of Test et al. which suggests that the cooling of the system in a standalone version is better on water than on a structure on land. The order of magnitude is around 26.6% such as:

$$\frac{\left|h^{Test}_{cv}\left(U_{\mathrm{w}} = 1\,\mathrm{m\,s^{-1}}\right) - h^{FM}_{cv}\left(U_{\mathrm{w}} = 1\,\mathrm{m\,s^{-1}}\right)\right|}{h^{Test}_{cv}\left(U_{\mathrm{w}} = 1\,\mathrm{m\,s^{-1}}\right)} = \frac{|11.11 - 14.07| \times 100}{11.11} \simeq 26.6\% \tag{5.3}$$

Figure 5.9 summarises the results of the developed correlations from the 1-D thermal optimisation process and the heat flux measurement relation with respect to the measured wind velocity. The function of the U_{values} methodology is also indicated, and the thermal radiative part is removed for the purpose of this summary.

A first observation is that all equations (even the theoretical ones) are in the same range of evolution with a maximum difference of 8 $\mathrm{W\,K^{-1}\,m^{-2}}$ for strong winds. It is assumed that the phenomenology of convection usually performed for land-based photovoltaics is relevant in the case of floating photovoltaics. The Gnielinski formulas (basis and optimised) behave differently than linear relations at low wind regimes, as they describe the laminar flow regime which is less favourable in heat rates compared to the turbulent portion. Considering that the mean wind reaches 2.6 m s^{-1} at the experimental site (up to 4 m s^{-1}), the differences between the equations are rather low in this segment. The principal differences arise from the functional form that are admitted in the process of making the equations. It is noted that the performance of the U$_{values}$ methodology is close to the trend found by the heat flux sensor, the difference is up to 4.3% at the median wind velocity measured on site. In the lower velocity segment, the heat rate is found to be higher by the heat flux sensor, the error in the 1st quartile is around 10%. In this case, the deployment of the heat sensor methodology is comparable with the use of the bulk methodology in terms of performance; it is hypothesised that the observation comes from the frequency sampling of 1 min, which made the U$_{values}$ methodology reliable. Another point is that the wind is strong and constant, which allows turbulent regime to appear most of the time, and this way the permanent regime of module functioning is reached more rapidly. It does not totally explain the difference in trend obtained by the optimised 1-D system compared to the other empirical curves. It is assumed that the one of the issues faced by the method is to deal with the low wind regimes, as the linear trend is comparable to the U$_{values}$ system for strong winds. In this case, it is thought that the Gnielinski functional form constrains the level of heat rate with consideration of both regimes evolution.

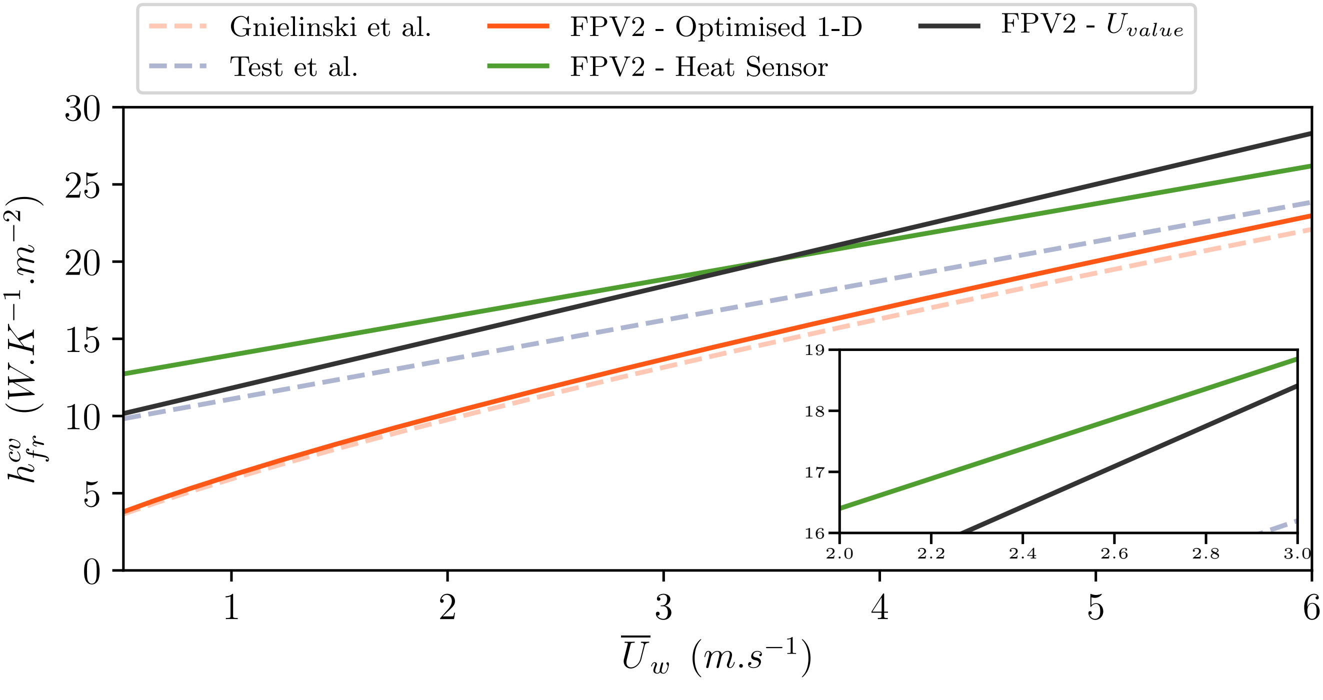

Figure 5.9–*Comparisons of h_{fr}^{cv} obtained with the two methodologies developed and the bulk methodology from Appendix A.5. The functions from the literature are indicated. The internal plot emphasises the difference of h_{fr}^{cv} for the mediane wind velocity encountered at FPV site.*

5.4/ Radiative Cooling and Warming

As discussed in Chapter 1, the choice of the thermal radiative boundary condition is also critical to understanding the thermal mechanisms that act on floating photovoltaic modules. In the literature, it is assumed that the water temperature is a good indicator of the effective temperature at which the aqueous medium irradiates nearby elements and thus the modules. It is necessary to choose the best boundary condition, the one that best describes the effective irradiation of the soil, to optimise the prediction of the thermal dynamics of the FPV modules.

This section aims to question the relevance of using the water temperature as the best estimate of the effective exchange temperature, especially by contrasting the radiative boundary condition of the sky, which is also a predominant cooling source for the systems. An assumption made in this section is that the evaporating water mass changes the set of correlations suitable for describing the radiative transfer with the sky.

5.4.1/ Emissivity-based Models for FPV Boundary Conditions

This study is based on the use of FPV2 data sets to describe an empirical radiative boundary condition and FPV1 data sets to determine an empirical correlation by statistical optimisation, similar to the convective phenomenon. In both cases, the model that describes the atmosphere as a grey body that radiates with an emissivity ε_{atm} is used. As a remainder, these models are constructed upon the sky temperature formula and the sky downward irradiation as follows:

$$\phi = \sigma T_{\text{sky}}^4 = \sigma \varepsilon_{atm} T_{\text{amb}}^4 \tag{5.4}$$

whence $\sigma = 5.67 \times 10^{-8}\,\mathrm{W\,m^{-2}\,K^{-4}}$ is Stefan's constant. As seen in Chapter 1, there exist several methods of linking emissivity to field measurements; here, we select the method involving only two fields, ambient temperature and relative humidity, since they are two fields usually available in weather stations.

Name	T_{sky} **Function**	**Climate**	**References**	**ID**
	ε-based models			
Bliss	$T_{\text{amb}} \times \left(0.8 + 0.00396 T_{dp}\right)^{0.25}$	Arid	(Bliss, 1961)	1
Berger	$T_{\text{amb}} \times \left(0.77 + 0.0038 T_{dp}\right)^{0.25}$	Temperate	(Pandey et al., 1995)	2
Chen	$T_{\text{amb}} \times \left(0.736 + 0.00577 T_{dp}\right)^{0.25}$	Continental	(Chen et al., 1995)	3
Berdhal	$T_{\text{amb}} \times \left(0.727 + 0.006 T_{dp}\right)^{0.25}$	Tropical	(Martin & Berdahl, 1984)	4

Table 5.4–*Sky temperature functions supporting radiative analysis.*

The functional form based on a linear relation between the emissivity and the temperature of the dew point can be expressed as follows:

$$\frac{T_{\text{sky}}^4}{T_{\text{amb}}^4} = A + B \times T_{dp} \tag{5.5}$$

The effort is given to determining A and B with the best accuracy as possible.

5.4.2/ Correction of Atmosphere Emissivity from FPV1 Campaign

Optimising procedure in forced in the convective assessment can be re-performed for the radiative boundary conditions. This time, weights are given to the coefficients A and B and the convective transfer parameters are set constant to the values obtained during the convective case of FPV1 (that is, $(\zeta,\chi) = (120,150)$). For this part, the water temperature is used as the radiative As for making accurate correction of correlation for the convective transfer, it may be incorrect to weight emissivity magnitude without concerns on the real source of radiative heat. This is more than true in the FPV1 case in which no accurate measurements are performed for the long-wavelength radiation. The strategy is developed to separate the preferential radiative source using the dimensionless number K_t, the clearness index, defined in (**Colliver1991**). It reads:

$$K_t = \frac{\phi_{\mathrm{sw,poa}}}{I_{sc}\epsilon cos(\Theta_z)} \tag{5.6}$$

where $I_{sc} = 1367\,\mathrm{W\,m^{-2}}$ is the solar constant at the top of the atmosphere, ϵ is a correction factor for the eccentricity of Earth and Θ_z is the solar zenith angle. Unlike the Ri number, the clearness index is not derived from a dimensional analysis. A K_t value tending toward zero indicates a large portion of clouds, while a K_t close to one indicates a clear sky situation. The C category of the sky state reads:

$$C = \begin{cases} Night, & \text{if } \phi_{\mathrm{sw,poa}} < 50\,\mathrm{W\,m^{-2}}, \\ Cloudy, & \text{if } \phi_{\mathrm{sw,poa}} > 50\,\mathrm{W\,m^{-2}} \text{ and } K_t < 0.5, \\ Clear-sky, & \text{if } \phi_{\mathrm{sw,poa}} > 50\,\mathrm{W\,m^{-2}} \text{ and } K_t \geqslant 0.5, \end{cases} \tag{5.7}$$

Same selection steps as for convective parameters are performed. The couple of variables is denoted (A,B).

Figure 5.10 shows the global statistical results for 80 simulations with evolving A and B parameters. The initial space of variables is established by looking at the magnitude of both parameters in the relations given in the literature (Table 5.4). It is observed that the emissivity parameter is greater than all the proposed functions in the literature; the closer function is the one from Bliss et al. which is reputed to include too important weight due to the arid climate experienced for the empirical law. Importantly, the laws that are built for temperate climate are the most far from the optimal frontier obtained along the line $(A,B) = (0.81,4\,5e-3)$ to $(A,B) = (0.77,7e-3)$. It is necessary to enhance the sky temperature in this case; it can be appraised as a need to account for a radiative warming effect due to the vapour content in the vicinity of the module.

Following a similar analysis for convective work, the optimised case is based on the most accurate trade-off obtained when separating the simulation results in the three categories. Figure 5.11 shows the distribution of results for the nominal case and the best match obtained with the couple $(A,B) = (0.8,5e-3)$. When the initial set incorporates a statistical compensation between the clear sky situation Figure 5.11.a and the cloudy category Figure 5.11.b ($Med.T = -0.8\,°\mathrm{C}$ vs. $Med.T = 1.13\,°\mathrm{C}$), this behaviour is reduced in the optimised case Figure 5.11.d and Figure 5.11.e ($Med.T = 0.45\,°\mathrm{C}$ vs. $Med.T = 0.17\,°\mathrm{C}$). The distribution of errors is improved in the optimised case, especially for the cloudy and the night cases in which the bias is largely reduced by almost 1 °C. The strategy does not perform with similar accuracy for the clear-sky bin, the initial distribution is at first sight quite challenging to address (large display, no clear mediane nor mean values). In the proposed strategy, there are no weight differences induced by the category chosen,

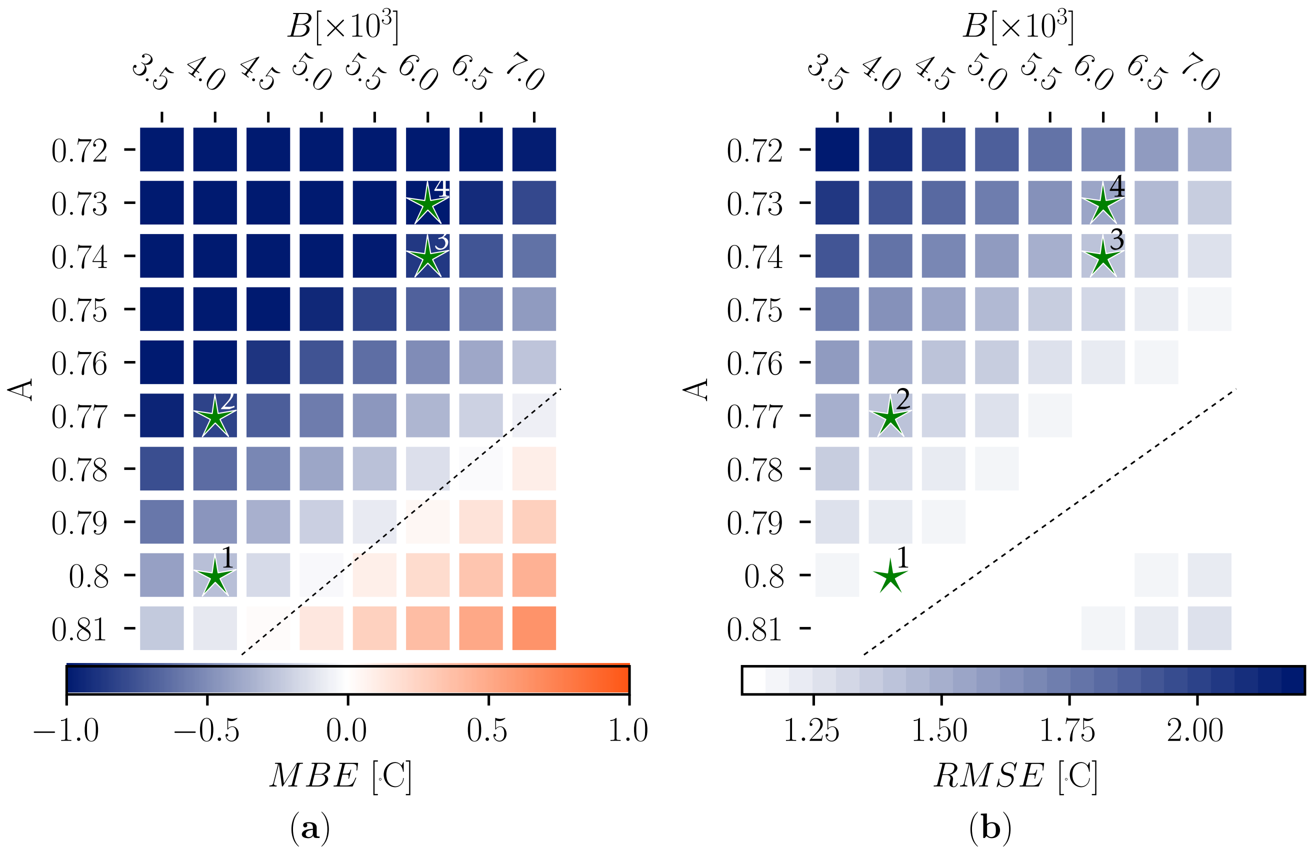

Figure 5.10–*Parametric exploration of the space of objectives for the ε-based model.*

so that only the bias of the whole dataset is reduced to optimise the function. It is speculated that this strategy should be forced to act on the large display of the clear-sky bin. For the Aubinet formula, it is a good choice to consider the value K_t to do this. However, the sky state model would induce a new parameter; the choice in our work is not to overload the radiative model so that the complexity is kept low. This is highly preferable to be able to compare results between cases.

5.4.3/ Correction of Atmosphere Emissivity from FPV2 Campaign

In the FPV2 case, the inverse thermal model is not necessary, as the measurement station incorporates the measurement of the ambient temperature and the temperature of the sky. Therefore, the ratio of sky temperature to 4^{th} power and ambient temperature to 4^{th} is easily achievable.

The result of the post-processing of these measurements is available in Figure 5.12. This highlights a distribution of the apparent emissivity of the atmosphere as a function of the temperature of the point recalculated from knowledge of the ambient temperature and the relative humidity. Initially, a very high concentration of points around the apparent emissivities 0.78 and 0.82 is observed, while the distribution presents a total spread between 0.72 and 0.85. The linear positive relationship that appears between the average emissivity and the temperature of the dew point has the following characteristics: $A = 0.741$ and $B = 0.0062$. This places the correlation in the same order of magnitude as the Berdhal and Chen relationships initially constructed in tropical and continental climates, respectively. The statistical r^2 indicator achieves a value of 0.5 so that the linear trend is low and a more complex relation can be imagined to enhance the structure of the formula (e.g., integrating the K_t value in the equation). It is important to mention that there

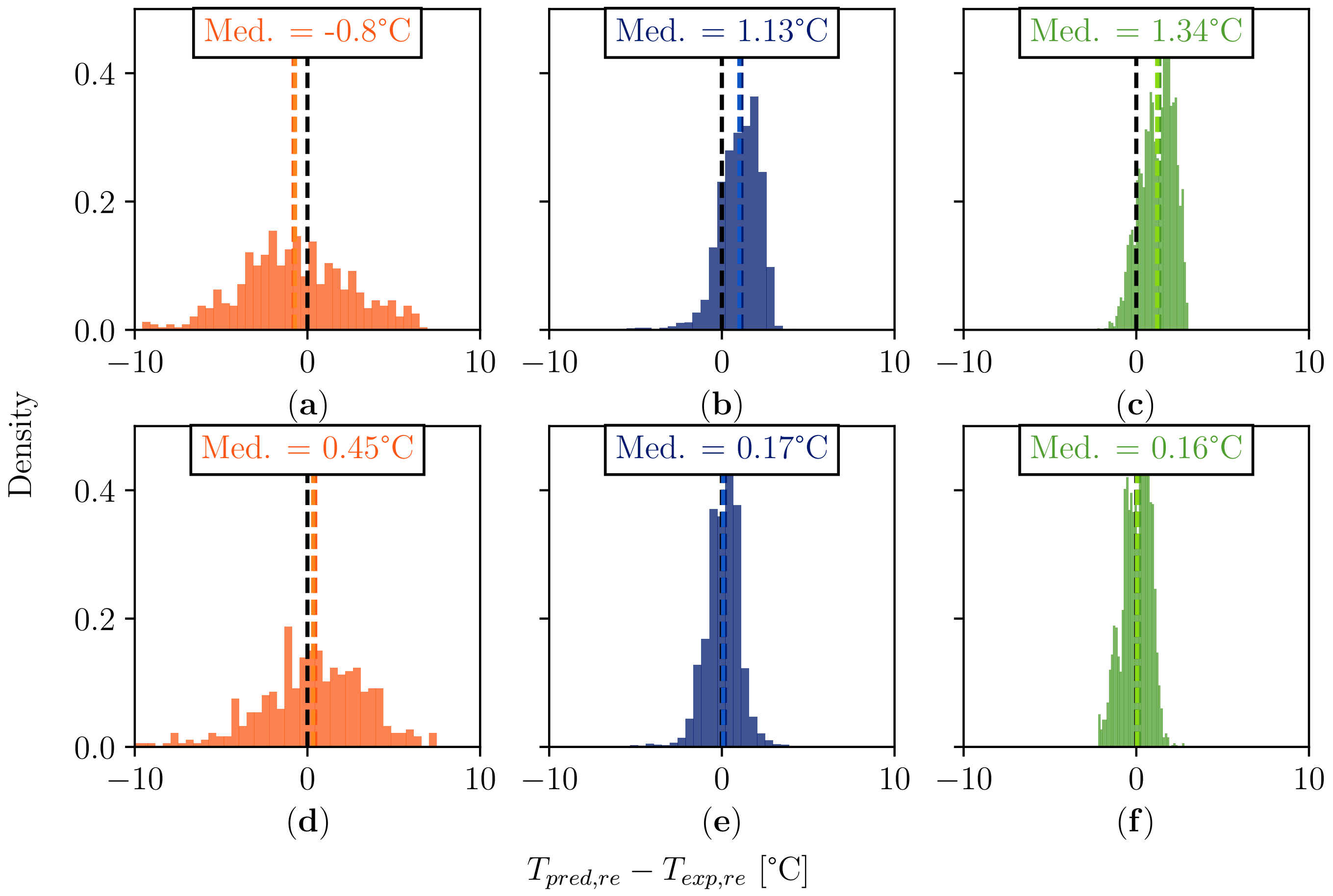

Figure 5.11–*Error distributions for the model with* $T_{sky} = T_{sky}^{Aubinet_1}$ *(a,b,c) and* $T_{sky} = T_{sky}^{opti}$ *(d,e,f)*

is a non-negligible part of the dataset in the upper part of the plot (above the trend line), and especially at low magnitude temperature. These features (larger emissivity and low dewpoint temperature) reflect the morning situation when the vapour content in the atmosphere is important and almost saturated as a result of the temperature. In this situation, the participating media has a larger influence. Such an observation is not possible to perform in the FPV1 case due to the inverse thermal model used and the lack of long wavelength measurements.

The climate appears to be a relatively minor element in the description of the effective emissivity of the atmosphere; the site of FPV2 experiences a climate that evolves during the investigation period (rather than a dry Mediterranean-type climate). On the other hand, we notice that the parameter directly related to humidity has a higher magnitude than for all other relations. It is assumed that this behaviour is related to the magnitude of the potentially weaker daily evolution on the lake considering the evaporation that occurs there.

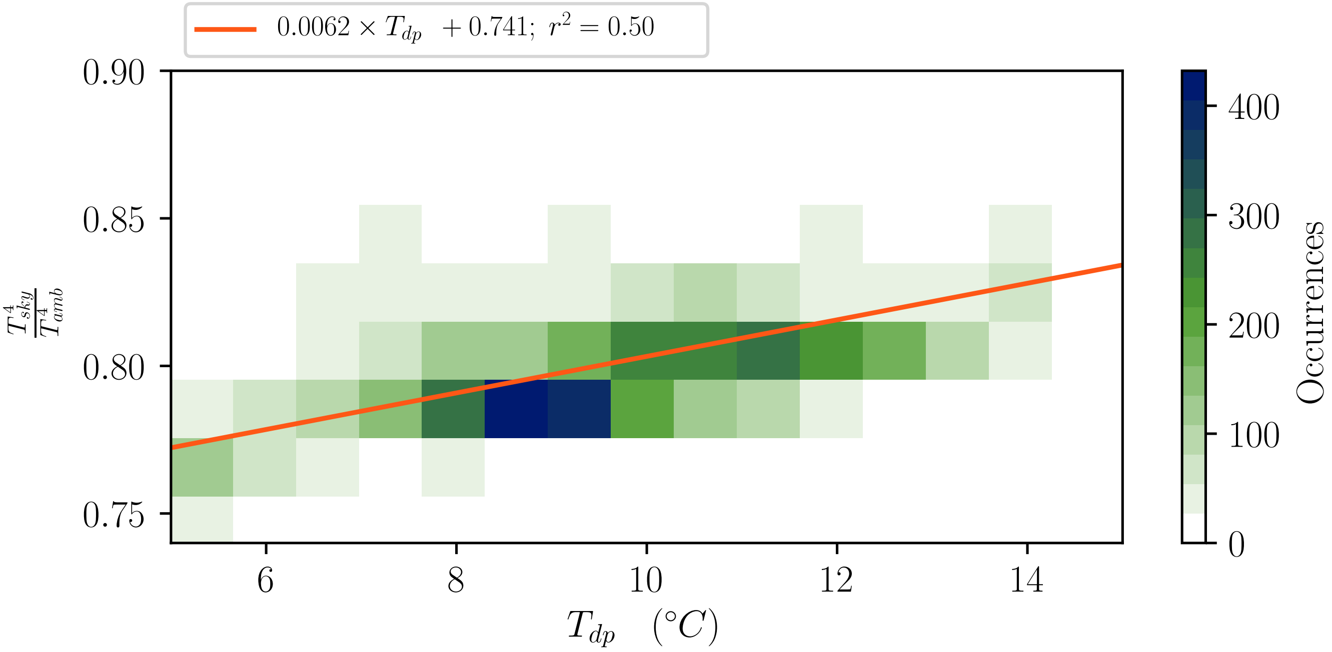

Figure 5.12–*Statistical optimisation of the sky function based on* ε_{sky} *format for the FPV2 experiment.*

5.5/ Conclusion

The first goal of this chapter was to describe the main elements that affect the heat evolution of floating photovoltaic modules under the spectrum of standalone FPV systems. Then, a second objective was to apply a detailed thermal model so that the boundary conditions of the model could be investigated in more detail.

Based on data collected from the experimental prototype in a small pond and in a temperate climate, a low magnitude of the cooling effect was found when selecting a representative day of operation for different seasons. A higher energy yield of around 0.15% was obtained for the summer period when the multilayer thermal model took into account the microclimate effect. The upside-down effect was also demonstrated in cold season, the energy yield was found to be reduced by up to -0.11%. In the work, the microclimate shift occurs from thermal instability between *continental ground* and *water surface*, it is likely to obtain another level of cooling in different climates and seasons. However, it was pointed out that daily thermal instabilities are not equal between the investigated seasons. The thermal capacity of water coupled with the waterbody dimension appears to play a major role in the daily pattern of microclimate cooling for floating PV.

To better encompass the effect of external conditions on floating setup without using a global U_{values} strategy due to its native lack of versatility, two new methodologies were proposed to determine empirical correlations. The first focusses on the optimisation of the multilayer thermal system using adapted key performance indexes, dimensionless based. The strategy revealed that forced convective transfers increase from 4% to 20% at most for FPV compared to land-based, the impact of free convective transfer was found to be greater in free rack configuration and lower in large footprint situations. The developed strategy can enhance the prediction of thermal effect thanks to these boundary condition separation strategies. The second methodology was based on a new sensor that can derive convective values with a faster sampling rate. This method was applied to a floating experiment, and a new correlation with a greater magnitude compared to the literature was found. The second strategy opens the door to improved thermal monitoring by directly integrating the stochasticity of the wind within the heat rate correlation.

A last investigation was the boundary condition for thermal radiative transfers. The effect of thermal radiation seems to behave differently in a participating microclimate such as the one in force in floating photovoltaic application. When the dimensionless categorisation has shown that night and cloudy sky benefit of strong effect from improved humidity level (hardly caught by nominal correlations), the clear-sky situation was not found to be dictated by the humidity level but by the clearness index; the latter being dismissed in our model to keep it simple. When the analysis of the thermal radiations in the FPV2 study case was conducted, it was found that the initial climate assumption was also not efficient in predicting the magnitude level of the sky correlation. The weight of the humidity was found to be lower than during the first thermal radiation case, so more work would be needed to explore the impact of the microclimate on the thermal radiation evolution throughout the day and due to the photovoltaic array configuration. For example, a refined simulation of radiative transfers with respect to simulated humidity level near the installation can be a first shot in this direction.

6 AIRFLOW AND CONVECTIVE PERFORMANCES IN SOLAR ARRAYS

> Even a broken clock is right twice a day
>
> Alan Turing in *The Imitation Game*

This chapter presents an analysis of the results of the thermoaerodynamic methodology specific to the PV plant scale. It considers the regimes of the airflow in typical PV plant cases and makes comparison between land-based and FPV airflows, the consolidation elements of the scaling-up methodology, and the influence of geometry on the thermal correlations.

Contents

6.1/ Introduction

By easing the calculation of airflow at the array level, it becomes now possible to investigate the cooling effect of convective transfer at an industrial level and evaluate the difference in intensity between land-based and floating applications. Meanwhile, it is unlikely to separate the exchange potential from the heat rate under normal operating conditions because only a numerical model can perform this job at low cost and without specific geometrical requirements. Therefore, the FPV2 design of the industrial system and the full-scale land-based system experienced in (Glick, Smith, et al., 2020) are reproduced and investigated under typical environmental conditions to make a comparison of the two distinct applications.

Although the bi-periodic method offers a practical opportunity to scale-up the research investigation, the main counter-effect is the loss of the flow information before the flow establishment area: Convective transfer is heterogeneous in nature. To get a glimpse of the heterogeneous behaviour, we simulated the numerical land-based array with the desire of capturing key thermal structures for heat transfers. Increasing the complexity means increasing the cost, the simulation is devoted to giving a range of uncertainty of the heat rates with respect to the bi-periodic simulation.

Before going through the main results of the chapter, a little diversion is made to increase the reliability of the computation by investigating the role of secondary unknowns that can act on the output. This allows to secure the bi-periodic computations before launching the exploration of first-order parameter for the airflow structure.

The final part of the chapter relies on a morphometric study based on a land-based solution so that the main geometric parameters are investigated in more detail. Precisely, the morphometry is performed for the entire combination of atmosphere wind directions. This allows one to evaluate the preferential contributor over the dynamics and the heat-rate output with regard to the periodic obstacle shape. A very last stage also shows the heat rates of front module faces with respect to the FPV2 geometry, with the ambition of constructing floating-designed correlations for all the outputs (dynamics, heat rates, evaporation).

6.2/ Array Level Airflow: Comparison between Land-based and FPV

6.2.1/ Geometry of Considered Study Cases

This section aims to compare the two types of installation, land-based and FPV, according to incident velocity profile assumptions; the thermal conditions are also equivalent. The representative geometry of the land-based case is chosen as the full-scale case of the wind tunnel experiment, these quantities are available in Table 4.3. This geometry is convenient because it also allows us to support the comparison of the numerical results with the experiment considering the transition to full-scale. It is also chosen to represent the FPV case by the geometry of the FPV2 industrial site, available in Table 4.3. The wind conditions are applied at the top of the domain, they are described by:

$$\begin{cases} u_\star \in [0.36, 0.67, 0.98] \\ \theta_\mathrm{w} \in [0, 180] \end{cases} \tag{6.1}$$

The standard boundary conditions $u_\star = 0.36\,\mathrm{m\,s^{-1}}$ and $\theta_\mathrm{w} = 0°$ are similar to the validation case in Glick, Smith, et al., 2020.

6.2.2/ Analysis of Momentum Conservation

Figure 6.1 shows the simulated wind fields in the case of representative periodic systems of the fictive land-based power plant and the case study FPV2. For identical atmospheric friction conditions, the velocity at the top of the field is higher in the FPV2 configuration, on the order of 33%. The combination of low tilt θ_m and height $\mathcal{H}_\mathrm{m}$ reduces the wind load on the floating configuration so that atmospheric flow can accelerate with greater magnitude.

The recirculation region shows a vortex in both cases. From an altitude point of view, it is bounded between dimensionless heights $z/\mathcal{H}_\mathrm{m} \simeq 0.7$ and $z/\mathcal{H}_\mathrm{m} \simeq 1$. The size of the vortex seems to evolve as a function of the angulation of the tilt, the ground-mounted case showing a larger eddy with associated faster fluid motion due to the constraint $\theta_\mathrm{m}^{GM} > \theta_\mathrm{m}^{FPV}$. Convective transfer benefits from greater velocity magnitude; in that case, the emphasised velocity takes place at the front face of the module below the medium height[1]. This is due to the formation of a stagnation point around this module height. The low pressure area is then larger around the lower part of the land-based geometry so that it can indicate a more important convective transfer in this situation.

On the upper part of the module, both the atmospheric flow and the recirculation area feed the area. The floating configuration benefits from a greater kinetic energy in this zone; therefore, the tip of the module may experience a larger wind-driven effect on thermal transfer. In comparison, the upper part of the module in the ground situation shows a reduced stream-wise velocity. We can hypothesise that angulation θ_m is the most influential parameter for the location of the stagnation point and the distribution of the active area along with the convective transfer will be emphasised. Low angulation moves the vortex down and reduces the velocity in the lower part of the module but enhances the upper part. The larger tilt offers a larger obstacle for the stream-wise flow, and the vortex is quite more important. When it tends to reduce the place offered for convergence between wake area and free-flow region, the velocity in the lower part of the module takes advantage from the higher altitude of the stagnation point.

---

[1] Mathematically: $\mathcal{H}_\mathrm{m} - \mathcal{L}_\mathrm{m} \times \sin(\theta_\mathrm{m})$

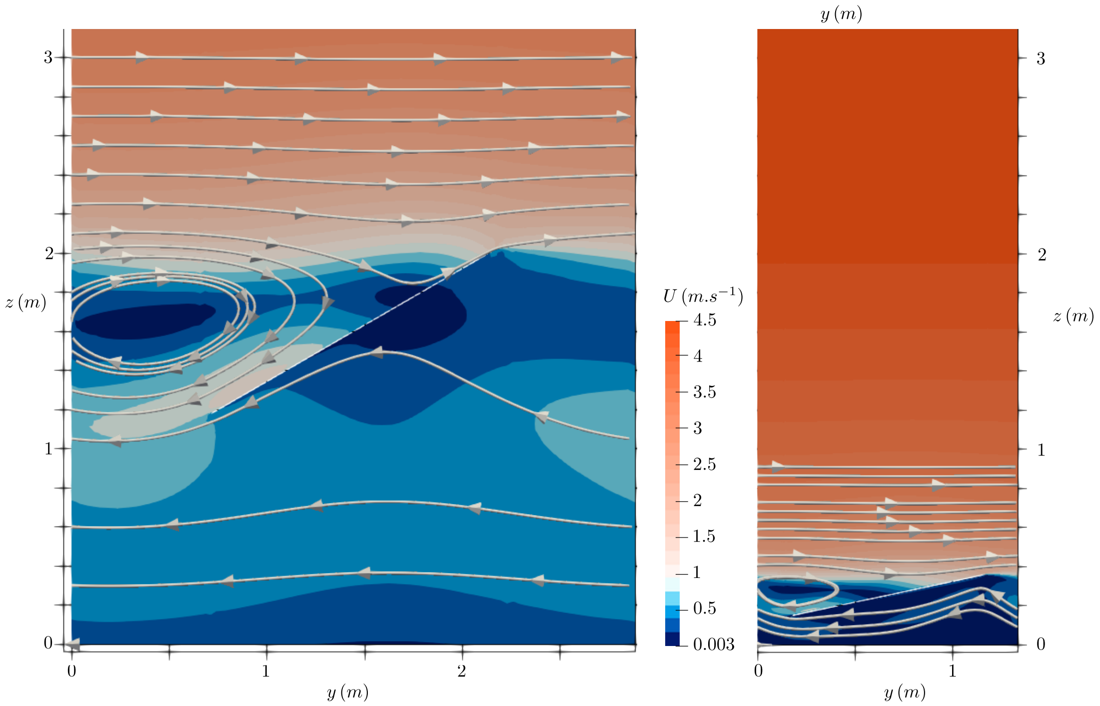

Figure 6.1–*Snapshot of Velocity fields at convergence for ground mounted configuration (left), and floating configuration (right). Streamlines indicate the flow direction within the three flow regions (free-flow, recirculation, sub-module).*

When the three segmented areas for flow regimes appear in land-based experiments[2], one may raise the question that in the FPV2 geometry, the submodule flow is not significant; therefore, the assumption of three areas could be reduced to two areas. The lower magnitude of the vortex features in the FPV2 case also gives some elements in this sense, as the intensity of the reversed direction flow has also an influence on the vortex dimension. From this observation, it is stated that the combination of geometrical properties is responsible for the shape of the flow region. As a consequence, it is likely to have a large influence on convective efficiency.

A key element raised by the numerical experiment is the flow direction in the sub-module zone. The numerical simulations show clearly that the flow direction is reversed from the initial direction so that it differs from the experiment in wind tunnel made by Glick et al. One explanation of this special behaviour is that inflow and outflow conditions are not reproduced in the bi-periodic simulation, conversely to the wind tunnel experiment in which a pressure gradient drives the airflow. With this lack of information, which is realistic for a module located at an infinite location in the solar array, the flow direction is solely constrained by the geometrical shape of the module obstacle.

6.2.3/ Heat Rates Evolution on the Plates

The supply of kinetic energy is variable on both sides of the module due to the formation of a recirculation zone and the location of the detachment point on the front surface as shown in Figure 6.1. In the particular case of FPV2, it is interesting to know whether the average value of the convective transfer rate is representative of local losses. Figure 6.2 shows a normalised represen-

---

[2] the free flow above the module, the wake zone, and the constrained flow behind the module or in the submodule area.

tation of the convective transfer rate as a function of air supply, for both sides of the module. The observation of the evolution of the convective transfer rate on the front face shows that the recirculation zone at the bottom of the module strongly degrades the transfer locally. The segment $x_m < 0.3\,\mathrm{m}$ shows a transfer rate of on average 25% lower than the maximum rate obtained at the top of the module; the distribution is not homogeneous and evolves almost linearly between the minimum rate and the end of the segment. The area between $0.3\,\mathrm{m} < x_m < 0.9\,\mathrm{m}$ has an average convective rate of 92%, which is rather constant, indicating that choosing an average value for the transfer rate is rather realistic. This observation also supports the positioning of the thermal sensors in these parts of the module to ensure a representative measurement, especially for the heat flux sensor system. The location $x_m > 0.9\,\mathrm{m}$ shows higher exchange rates than the rest of the module, as expected from the flow lines, which can be explained by an atmospheric air supply. The latter contains more kinetic energy, especially in the case of floating photovoltaics, where the module tilt is low. Therefore, this representation shows that the recirculation zone has a rather negative effect on the convective transfer rate on the front side for the FPV geometry. It is assumed that a larger recirculation area (size and energy) could change this statement, especially in the case of ground-mounted PV. In the FPV case, the supply from the atmospheric zone dominates the convective transfer on the front side. We also notice that the variation in kinetic energy in the domain has no influence on the front-side transfer rate, and the distribution of transfer rates remains invariant. This point is decisive for future work; we will be able to use convective atmospheric laws weighted by the friction velocity while keeping the invariance property of the heat transfers in the front face.

The rear face shows some differences with the front face. The maximum heat-rate is obtained at the module tip, but the evolution from the lowest exchange rate to the highest is very localised. The local transfer rate is rather constant for $x_m < 0.8\,\mathrm{m}$ of the length of the supply at $u_\star = 0.98\,\mathrm{m\,s^{-1}}$. For lower speeds, the area extends up to $x_m < 0.96\,\mathrm{m}$. Moreover, the intensity differential is stronger in the case of a high wind speed, and the recirculation zone acts with a stronger influence in this case. However, it can be seen that the middle zone of the module has a constant distribution, so the installation of sensors in this zone is consistent with obtaining an average image of the convective transfer, especially for the temperature probes. Finally, it also makes sense to assume an average convective behaviour on the rear face as long as the total aeraulic supply does not exceed the threshold value of $u_\star = 0.7\,\mathrm{m\,s^{-1}}$. Above this threshold, the distribution of temperature alters the mean value so that the local increase in heat-rate is localised and not representative of the system.

This analysis is also carried out for different wind directions and is presented in Figure 6.3, with the friction velocity set constant to $0.36\,\mathrm{m\,s^{-1}}$ and therefore below the critical threshold for the analysis of the rear face of the module. The first observation for the front side of the system shows that the distribution of the transfer rates follows the same characteristics as a function of the wind direction. The maximum transfer rate is reached for the upper edge of the module, even if this is not considered the *trailing edge* when the wind direction is $\theta_\mathrm{w} = 180°$. This observation confirms the fact that the atmospheric zone provides a very important part of the kinetic energy for heat transfer and that the recirculation zone has a rather reducing effect on the transfer. For all wind directions, it seems that the constant rate zone extends largely between $0.3\,\mathrm{m} < x_m < 0.9\,\mathrm{m}$; the assumption of constant transfer rate appears to be consistent for all situations on the front side.

The rear of the module is much more challenging, and the direction of the wind appears to be an element that modifies the aerodynamic processes and heat transfer. A zone of constant transfer rate is established globally between $0.1\,\mathrm{m} < x_m < 0.8\,\mathrm{m}$ with variations depending on the air field.

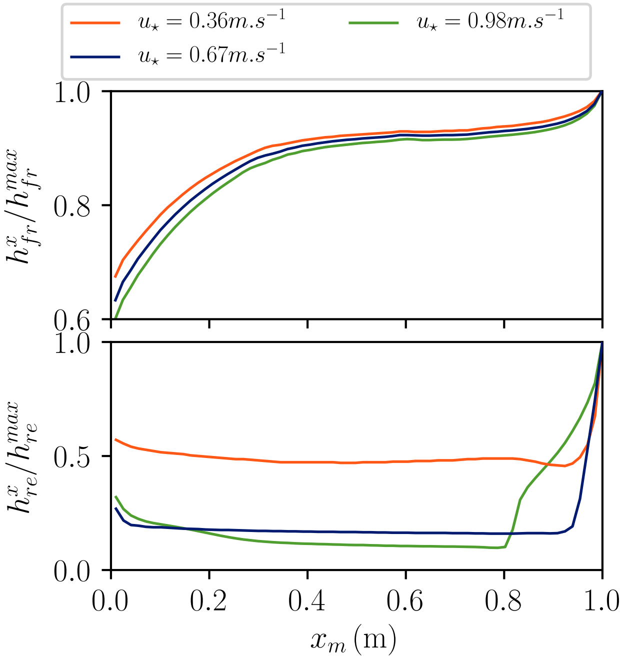

Figure 6.2–*Normalised heat rate distributions with respect to friction velocity for the front and rear surfaces, top and bottom plots, respectively ($\theta_w = 0°$).*

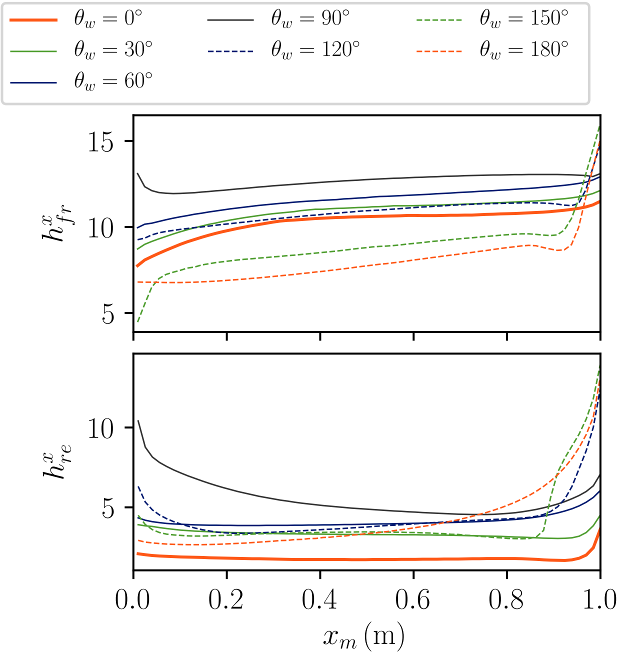

Figure 6.3–*Heat rate distributions with respect to the wind direction for the front and rear surfaces, top and bottom plots, respectively ($u_\star = 0.36\,\mathrm{m\,s^{-1}}$).*

This point is important in relation to the measurement of the thermal fields in the middle of the module and confirms that this is a position that captures the thermal operation of the module. The difference in obtaining the global and local maxima shows the evolution of the recirculation zone in position and magnitude; while crosswinds mainly show an absence of recirculation area due mainly to the bi-periodic numerical scheme used (establishment of the air field in the direction normal to the plane). The tailwinds show that the recirculation zone is weakened and is moving downward. The distributions of heat-rates obtained allow us to consider that the mean transfer rate is a good representation of the system operation. However, it may be from interest to consider the median value in some extents like for back winds.

6.2.4/ Averaged Heat Rates Evaluations

Figure 6.4 and Figure 6.5 show the results obtained for the two configurations front and rear faces. Elements from the literature are also integrated into the plot for comparison purposes. The reference velocities are obtained at similar heights 3.5 m, assuming an idealised velocity profile. On top of this strategy, extrapolation of mean heat-rate behaviour is assumed for the range of velocities below the minimal velocities of reference. The computational time scales conversely to the friction velocity; hence these ranges are very costly to reach. Note that the height of the reference velocity coincides with the experimental conditions of the method developed in (Test et al., 1981) for the ground-mounted case.

The first assessment consists of notifying the good agreement of the ground-mounted heat convective rate in front of the one derived from the wind tunnel experiment by Glick et al. The uncertainty is around 7% for the first non-extrapolated measurement point. The use of a finer mesh would surely reduce this gap. The deviation is greater for stronger winds, reaching 21% for a reference wind of $\overline{U_\mathrm{w}}^{(10)} = 9.9\,\mathrm{m\,s^{-1}}$. The deviations remain within the acceptable uncertainty

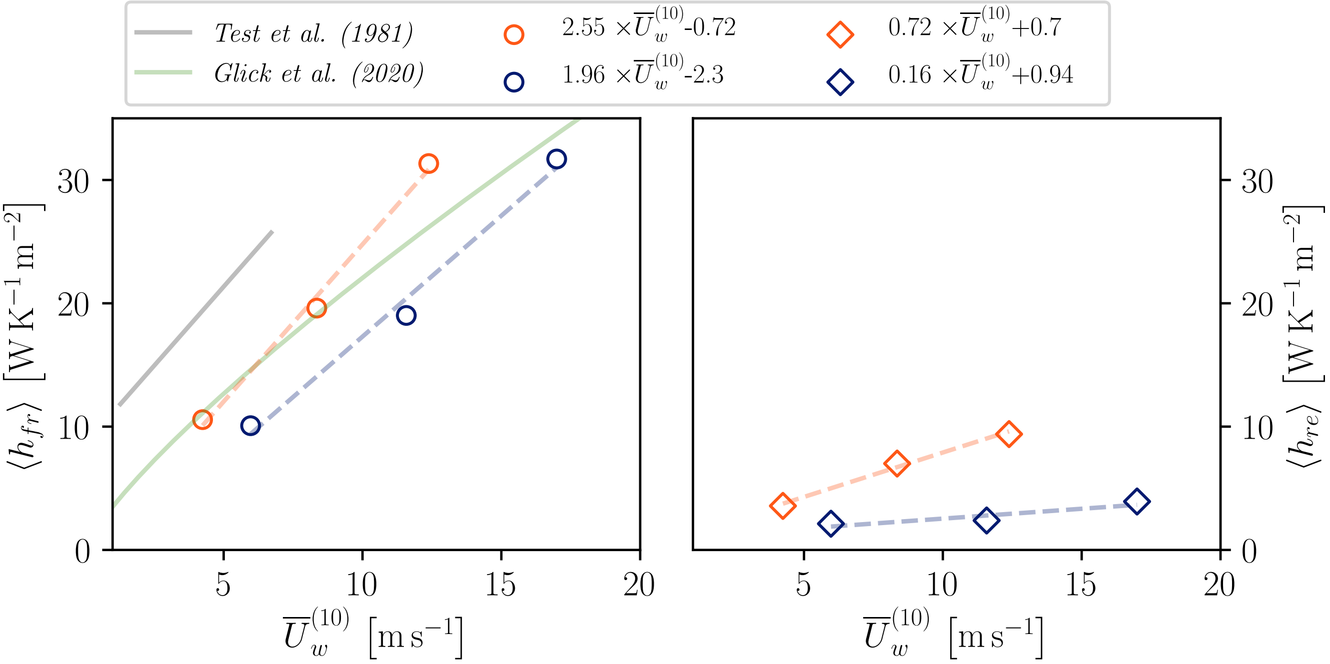

Figure 6.4–*Numerical comparisons of heat transfer rates obtained over the front module surface (left-hand side) and the rear module surface (right-hand side) for the ground mounted like situation (orange coloured) and the FPV2 case (blue coloured), $\theta_w = 0°$. Linear relations determined in the literature for the standalone situation (Test et al., 1981), and the wind tunnel experiment (Glick, Smith, et al., 2020), are also indicated.*

limits for determining the convective ratio. The periodic model, which stands for an infinite solar array module, is considered valid for the thermal part.

The periodic model also confirms the difference in thermal performance between a power plant system and a standalone system characterised by the correlation of Test et al. The linear regression shows a rather constant difference of the order of $6\,\mathrm{W\,K^{-1}\,m^{-2}}$, the difference is far from negligible for the usual temperature differences in operation (20 to 30 °C). The theoretical convective approach assumed through the CFD calculation emphasises the notable difference in photovoltaic applications with respect to the macroscopic wind structure and its effect on thermal efficiency.

The convective transfer rate is higher in the ground-mounted solution than in the FPV2 solution, regardless of the direction of the wind and the surface of investigation. When adding the front and back face rates, an increase of 42% is observed for the first solution in a headwind and 32% for a tailwind. The FPV2 geometry suffers from a lower exchange on the rear face. One hypothesis is that the ground interacts with the bulk flow and restricts the development of the submodule airflow regime. In Figure 6.4, the low-magnitude velocity zone around the rear face is clearly seen as the main contributor to lower solution performance. The free-flow velocity is no more representative of the heat exchange under this condition. A significant heat-rate downgrade for the floating geometry is also observed over the front face for headwind flow. The result is a little counterintuitive, as one would expect to obtain a stronger supply of the local flow from the atmosphere in a low-tilt plant as in the FPV2 case. A second reason for the explanation can be found in the lower pitch of the power plant; the supply area of the recirculation region is less exposed to the free-flow; therefore, the region contains less kinetic energy, which results in lower performance.

The difference in transfer at the front when the wind blows the module from the back is much less significant; both configurations have similar performances with a slight advantage for the ground-based solution. It is assumed this time that the tilt of the module plays a negative role in the development of the flow, it brings a significant level of turbulence due to an aeraulic blocking effect, especially when the tilt is large, as in the ground-mounted case. A lower tilt allows the flow to settle around the front surface more quickly, producing a better engine for convective transfer. On the rear face, both configurations achieve significant increases in transfer rate, the ground influence especially for the FPV2 system is weakened.

In general, the influence of the wind appears to produce a substantial gain in the general transfer rate of 20% for the back winds in the case of the FPV solutions. This gain is only 2% for the ground-mounted solution. A detailed analysis shows that the recirculation zone, when fed by rear-side winds, allows a large increase in heat rates. From the FPV case, the intensity expansion is observed to double for low-magnitude winds. A large footprint floating solution would have threshold conditions under forced convective transfers predominant. This triggers an important level of heat sink effects from macroscopic flow momentum. For open structures, the same behaviour is not necessarily triggered, as the flow still benefits from a sufficient feeding source of momentum due to the larger space available for the flow.

The conclusion of these comparisons is that the FPV solution provides significantly poorer convective performance than the ground-based solution when looking at the array level. Having a lower tilt leads to a better performance for tailwinds, but it does not allow one to challenge a ground-based module with a high tilt and a relatively large pitch. Periodic modelling proves to be a satisfactory approach, although the driving force of the flow is not a pressure difference but an imposed friction velocity. The comparison with Glick's experiment shows that the main design elements of the flow (wind characteristics and geometrical characteristics) are rather representative. Thus, it is rather relevant in the first approach not to consider the interaction between radiation and flow, although this is a key phenomenon in microclimatic studies.

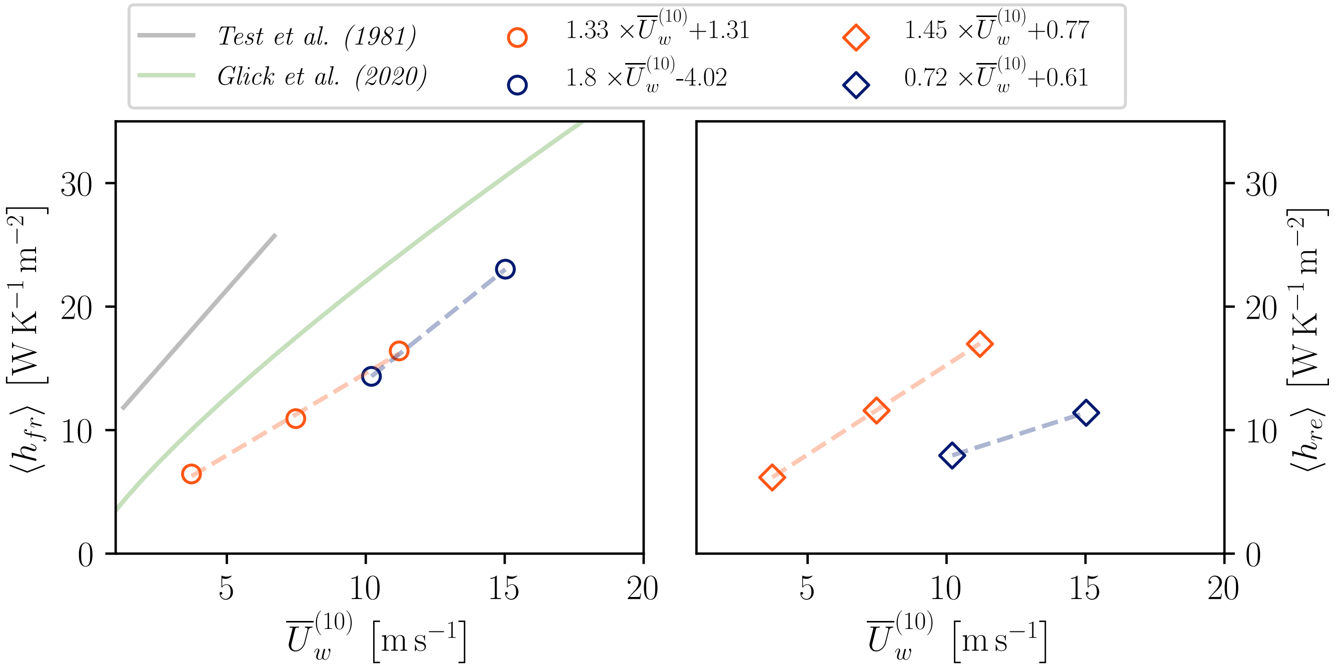

Figure 6.5–*Numerical comparisons of heat transfer rates obtained over the front module surface (left-hand side) and the rear module surface (right-hand side for the ground mounted situation (orange coloured) and the FPV2 case (blue coloured), $\theta_w = 180°$. Standard correlation from Glick and Test publications are given as indication.*

6.3/ Heterogeneity of Dynamics and Thermal Quantities in Solar Array

It should be noted that the developed numerical models refer to a representative module under steady state, because of the dynamic and thermal interactions upstream of it. This strategy does not allow to go back to the upstream state: the dynamic and thermal heterogeneity before the representative module is forgotten. If we want to have an idea of this evolution, we can use an explicit modelling of a numerical power plant, as proposed in Section 4.4, but in doing so, the computational cost will definitely be greater than for the bi-periodic case. We therefore limit ourselves to a representative case in order to support our periodic model in the following. A priori, we expect to have greater heterogeneity for the land-based case than for the FPV case because of the dimensions that are more conducive to the development of a flow below the plant. Therefore, we wish to estimate conservative uncertainty bounds on the main quantities of interest in our FPV study.

6.3.1/ Airflow Dynamics in Explicit Array

From the 2-D plant simulation in Section 4.4, we observe the roughness quantities and thermal scaled numbers as a function of the position studied in the plant. Figure 6.6 shows the dimensionless wind profiles in the 2-D plant for seven positions. These positions are described by a number that corresponds to the volume of air that lies after the module numbered n and before the $n+1$ module, see Figure 4.14. The figure also shows the idealised wind profiles from the roughness calculation at each position. Naturally, the calculated roughness length is not constant in the power plant as a function of the alteration of the wind profile; the value decreases as the power plant progresses until it reaches a constant value from the 21^{st} module. The first profile shows that the obstacle has a strong influence on the flow, so the logarithmic law and the calculated roughness length are not representative of the influence of the obstacle on the flow. Around the obstacle, the flow is accelerated, whereas the distant atmosphere is not influenced by the obstacle. As we move forward in the power plant, the velocity around the module decreases until it reaches a stable evolution from the 21^{st} module for the atmospheric part (above the module). At this point, the atmosphere far from the modules perceives the obstacles from the point of view of dynamics. It is interesting to note that the distant velocity profile has a predominant weight in the roughness calculation, whereas the atmosphere close to the module is less important due to the volume integration method. In the case of the study, an atmospheric integration is carried out from $h_{min} = 2 \times \mathcal{H}_{\text{m}}$. Since the most important impact on the atmospheric profile during the evolution of the power plant is observed in the wind field just above the module, it is worth asking what the role of height h_{min} is in the calculation of z_0.

In all cases, the submodule area is not represented by the roughness length; it is only from the 26^{th} row onwards that the submodule flow sees a reversal in direction, as modelled in Figure 6.1. The turbulence model used is not indifferent in obtaining these quantities, and it is assumed that the propagation of turbulent effects has an important effect on obtaining a steady state. The ideal periodic model is therefore a special case which is valid from a certain number of modules, in this case we will take the value of 26 modules.

To better visualise the dynamic heterogeneity within the plant, Figure 6.7 shows the evolution of the calculated roughness length at all atmospheric positions and with different levels of integration to perceive its impact on the calculated values. This representation is effective in seeing the different flow modes before reaching a permanent steady state. The perturbation of the atmosphere is well progressive from one space to another and four dynamic modes are visualised.

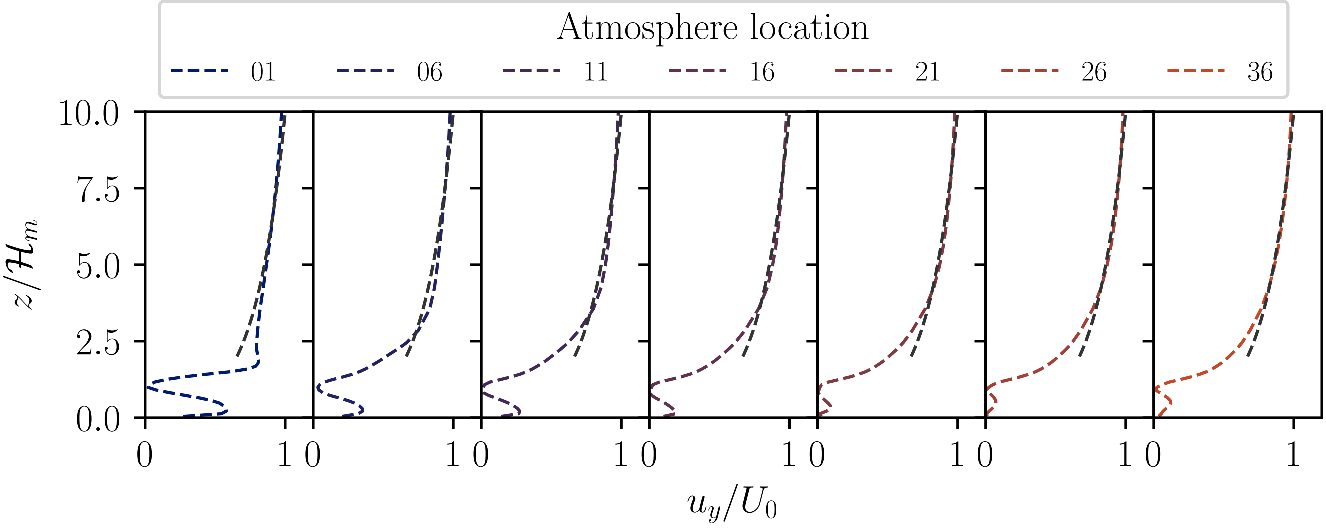

Figure 6.6–*Evolution of the velocity profile within the numerical 2-D array for 7 locations. Roughness length outputs are calculated and ploted for each profile.*

The first five modules show a strong impact on the flow, the averaged curve decreases sharply, 27% relative evolution, before adopting a gentler decreasing slope for the next 20 modules (14% relative). From the 26th row onwards, the flow is established and small variations are observed on the order of a few tenths of a percent. At the end of the array, an inflection of the curve is visualised due to the absence of an obstacle behind the system, the flow slows slightly, one observes a relative increase of 5% for the calculated roughness value.

The ideal value is not reached after 5 to 7 obstacles, as may be the case in experiments where the explicit roughness is stuck to the ground, the number of obstacles being more important. Capturing heterogeneity thus requires *more* calculation resources; in this case, modelling 26 modules in our case requires an effort of at least $20e3 \times 26 = 520e3$ cells without counting the upstream zone necessary for the establishment of the aeraulic entry conditions. An inherent limitation of our result is the turbulence model used which acts in a non-zero way on the establishment of the flow; one can expect to have variations on the position of obtaining the aeraulic establishment. Given the performance of the high-fidelity simulation in Section 4.4, it can be expected that the establishment will occur before the 26th row, as the latter predicts the correct velocity levels for the experimental study, while the $k-\omega SST$ model overestimates the flow dynamics in the three zones of interest.

The observation of the minimum integration height is also interesting; we notice that the lower the minimum height, the more there is a tendency to overestimate the roughness value. To follow up on the observations made in Figure 6.6, this result can be explained by the higher weight given to *bottom* of the velocity curve, which is strongly influenced by the obstacles. By choosing a significant height, the impact of this numerical degradation is reduced, and we converge towards a quasi-similar roughness from 3 to 4 minimum heights. This corresponds effectively to the observations in the literature, which advise 4 times the height of the obstacle when the latter is stuck to the ground. The averaged curve indicates that the uncertainty in selecting a minimum height that is too low leads to differences of the order of 6% in relative terms. This property is important because a high minimum height requires a sufficiently high space to integrate the flow . This necessarily has a cost for the numerical simulation, especially in the periodic case

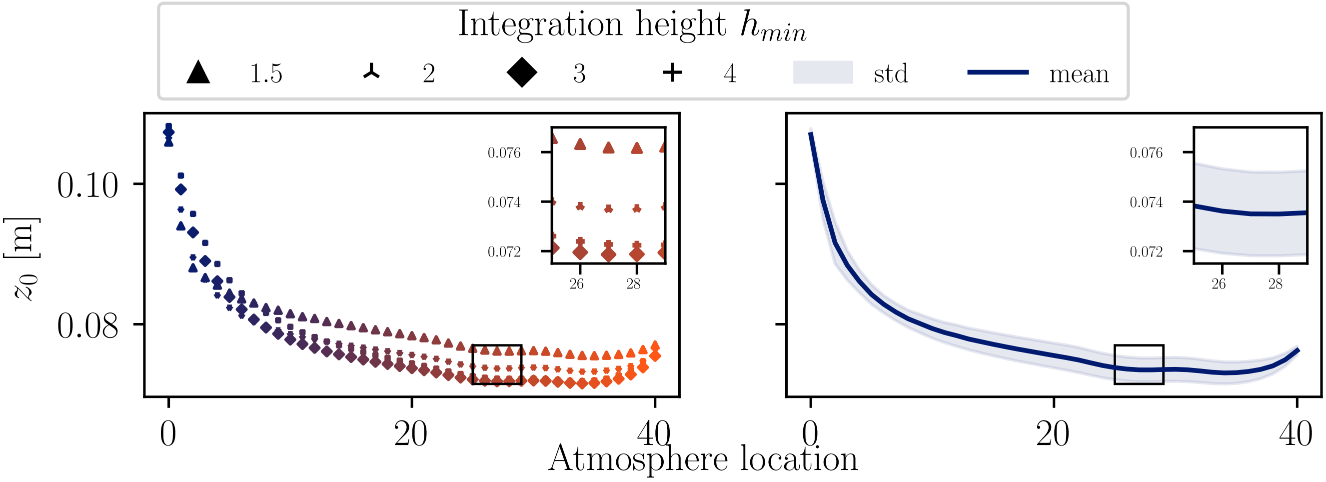

Figure 6.7–*Evolution of the roughness length calculated for all positions in the array, using four integration heights (left-hand side). Average and deviation values are plotted on the right-hand side.*

where one wishes to limit the cost of the simulation as much as possible. Another important criterion is that the selection of a minimum height does not influence the progression of the calculated heterogeneity in the plant; the levels of influence on the dynamics follow the same evolution for one or the other height chosen by the user. The heterogeneity calculation in our study does not take into account the phenomena under the modules, in particular the inversion in the direction of the flow. This property could have an influence on the phenomena near thermal and evaporative walls in the future.

6.3.2/ Thermal Heterogeneity from Explicitly Represented Array

In the continuity of the dynamics study, the evolution of the heat transfers for the 40 modules can be inspected, Figure 6.8 shows in particular the evolution of the heat transfers at the front and rear of the plant, as well as the performance of the periodic model adapted to the same geometry. As in the previous figures, the heat transfers show heterogeneity along the whole plant. The intervals related to similar behaviours are slightly different from the dynamics; we notice in particular that only the first two modules of the power plant have thermal performances largely superior to the rest of the system, mainly for the exchange with the front face. From the third module onwards, the dimensionless numbers for the front face are in a range between $Nu \in [400;750]$ with fluctuations caused by the evolution of the local dynamics in the system. At the end of the 26th modules, the spread of the convection is reduced in the interval $Nu \in [575;675]$, which corresponds to the third dynamic zone studied previously. For the latter, where the flow is assumed to be established, we find that the periodic model is rather efficient in describing the transfer levels (front and back face). For the back face, it seems that two groups emerge from the system: the first group upstream of the power plant obtains cooling rates between $Nu \in [630;280]$ with a decrease during the advancement of the power plant; the second group in the second half of the system presents a rather strong convergence around $Nu_{re} \simeq 180$. We thus obtain the two influences of the dynamics between a progressively decreasing wind regime, up to a reversal of the direction and an establishment of the dynamics which results in a convergence of the heat exchange. In all cases, the scaled numbers in the literature do not correspond to what is obtained in the plant, and the first modules are in the same order of magnitude concerning the front-side exchange, but this property is quickly erased and the order of magnitude is no longer valid from

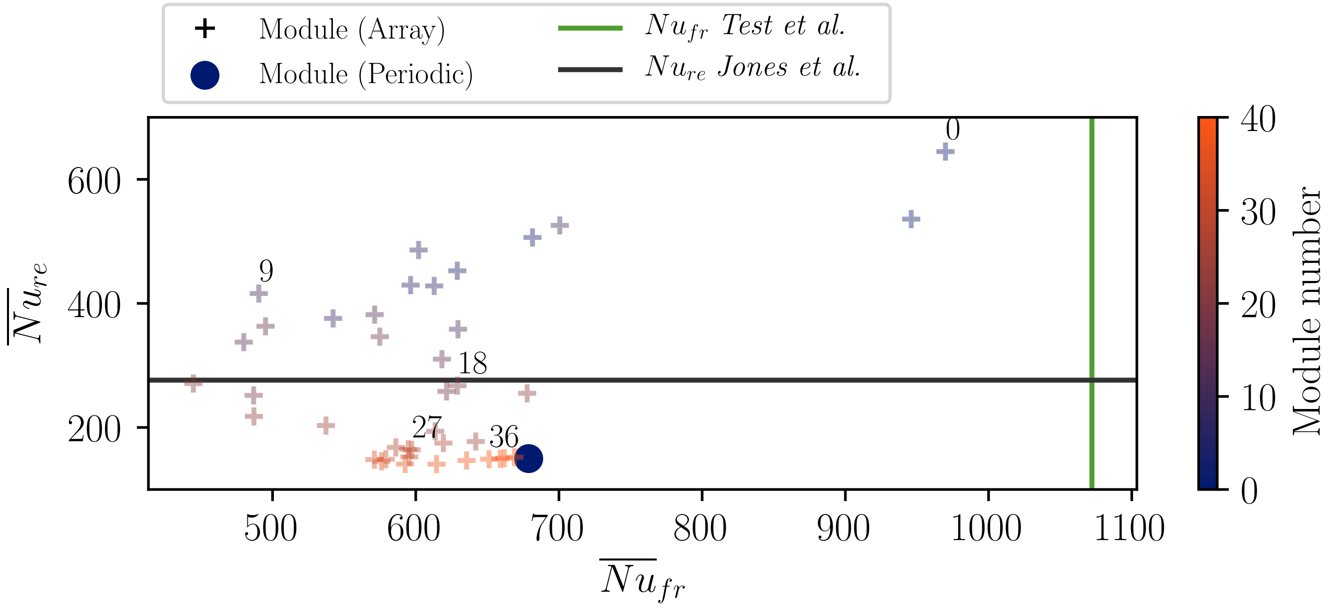

Figure 6.8–*Dimensionless heat transfers for the 40 modules in the simulation. Correlations obtained from the literature for both front and rear faces are indicated by vertical and horizontal lines. The values obtained using the periodic case are also shown in the Figure.*

the third module onwards. The overestimation of the backside transfer allows the error on the frontside correlation to be reduced at the module scale. This is valid for the first modules; while at the bottom of the plant the transfer is slightly lower than what is obtained in the literature, it is assumed that this is a corollary effect to the increase in local ambient temperature due to the heating of the modules.

There is undoubtedly dynamic and thermal heterogeneity in the plant; the modules facing the flow have higher cooling levels, while those in the recirculation zones have lower cooling levels. The ideal periodic system achieves the correct magnitudes for both the front and back face exchanges, thus capturing the nominal thermal operation of the system at the plant scale. Capturing thermal heterogeneity is expensive; here, the study is limited to an incident wind field, a typical configuration in the literature, and an optimal thermal operation for the modules. In reality, it would be necessary to repeat this study for different incident wind fields (including angulation), different geometrical configurations, and evolving thermal functioning depending on the cooling perceived by the module. Moreover, we can expect to have different convective mode emergences in the power plant, especially at the back side, due to the effect of the module temperature on free convection. Due to the land-based configuration chosen, it is assumed that the results obtained (dynamic and thermal) are conservative when considering the FPV due to a more compact geometry and a reduced flow regime under the module. Therefore, the assumption of long-range heterogeneity in FPV plants is probably reduced. This does not solve the problem of the computational cost of estimating this heterogeneity; we are interested in determining this heterogeneity at lower cost in Chapter 7.

6.4/ Unravelling the Numerical Parameter Set for Efficient Up-scaling Methods

6.4.1/ Case Features

The methodology to define a characteristic roughness with respect to the explicit system depends on the volume of air integrated. Two parameters are taken into account, the height selected by the user Δ, from which it is judged that the average wind speed is no longer influenced by the turbulence zone overlying the system, as well as the maximum height of the atmospheric domain. The first parameter is relatively transparent for the use of the methodology; we propose to examine its influence on the calculation of z_0 by adding an additional routine in *cs_user_extra_operations.c*. The second parameter is certainly more critical, it requires the reconstruction of a mesh, and therefore there is a potential risk with regard to the numerical stability of the methodology.

Therefore, it is proposed to create a study based on the standard *ground-mounted* case, in which the direction and speed of the wind are unfavourable for the convergence of the atmospheric boundary layer around the obstacle. The standard wind speed obtained with an imposed friction boundary condition of $u_\star = 0.36\,\mathrm{m\,s^{-1}}$ is a good compromise between *low* speed (potential buoyancy-driven flow) and realism (average speed around $2.5\,\mathrm{m\,s^{-1}}$ at one metre above the system). The most unfavourable wind direction for the atmospheric boundary layer is the direction in which the rear face of the module is facing the wind (i.e. $\theta_\mathrm{w} = 180°$), in this situation the displacement of the streamlines above the module is greater than in any other situation.

Four atmospheric heights are selected such that $\mathcal{H}_\mathrm{atm} \in [7.26, 10, 12, 15]$. They require the initial system to be remeshed. We choose not to reintroduce additional cells with respect to the initial 7.26 m height system to avoid a burden on the numerical calculation. The construction of the meshes according to a geometric law in the z direction tends to reduce the bias of this decision, the grid around the obstacle keeps a consistent form factor with respect to the adjacent cells, while the *atmospheric* mesh is less sensitive to air motion in the $\vec{z}$ direction.

Eight integration steps are also selected, the first step starts from $h_{min} = \mathcal{H}_\mathrm{m}$ while the last step is defined by $h_{min} = \mathcal{H}_\mathrm{m} \times 4.5$. The first step does not satisfy the conditions set in the literature ($h_{min} = 1.5 \times \mathcal{H}_\mathrm{m}$ minimum), but is placed *a priori* at a distance $z > 50 \times z_0$, so we expect to be able to obtain a logarithmic distribution from this threshold.

6.4.2/ Analysis of Minimal Height Integration

Figure 6.9 shows the results of the case study in an explicit representation for the 4 selected heights; the roughness lengths calculated on each explicit profile are integrated in a logarithmic analytical representation. For this exercise, the minimum integration height is chosen at $h_{min} = 2 \times \mathcal{H}_\mathrm{m}$. For the sole purpose of understanding, the extension of the analytical law under the minimum integration height is also represented.

The methodology described in the work seems to converge toward the definition of a roughness length of the order of $z_0 \simeq 0.05\,\mathrm{m}$ for the cases where the height of the atmosphere is equal to or greater than 10 m. The case in $\mathcal{H}_\mathrm{atm} = 7.26\,\mathrm{m}$ shows a calculated roughness on the order of 0.1 m *(i.e., double that of the other tests)*. Once dimensioned, the difference in speed between the profiles remains around $\Delta\overline{U_\mathrm{w}}(7m) \simeq 0.7\,\mathrm{m\,s^{-1}}$.

By numerical construction, velocity profiles with high atmospheric heights take longer to converge, as the balance of Reynolds stress forces takes place over a longer length. The time required

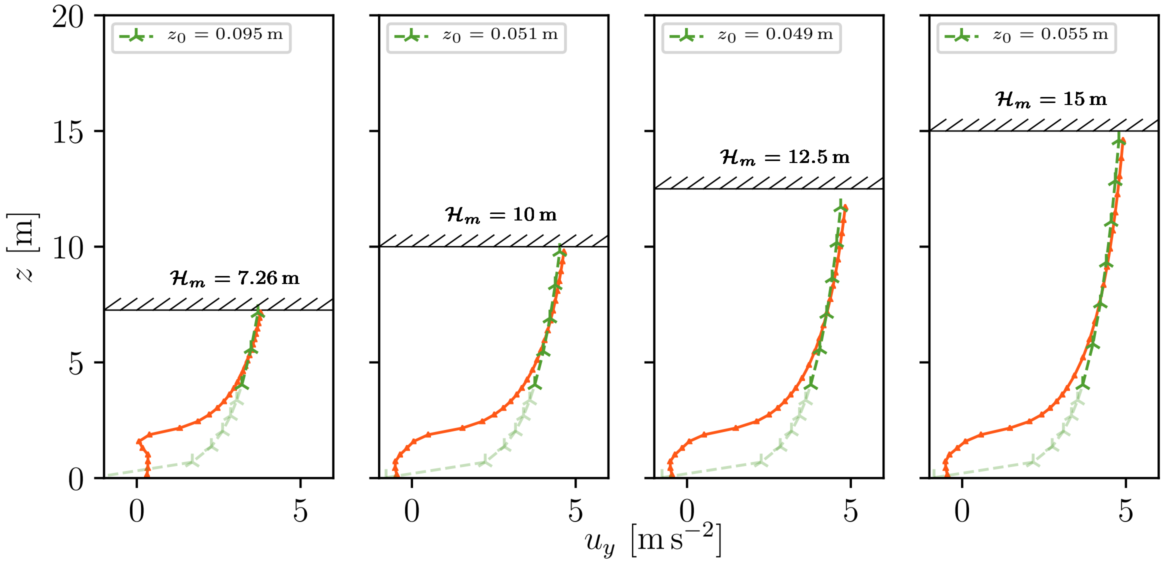

Figure 6.9–*Velocity profiles for the simulation of four atmosphere heights in the ground-mounted configuration, $\theta_w = 180°$. z_0 value is determined by integrating from the height $z/\mathcal{H}_m = 4$ (⅄). Hypothetical velocity field below the threshold is given as an indication (⅄).*

to reach equilibrium of the stresses is 60% greater for the $\mathcal{H}_{\text{atm}} = 15$ m case, compared to the $\mathcal{H}_{\text{atm}} = 7.26$ m case. Thus, a proper application of the methodology requires taking this parameter into account to optimise computational resources.

Another important observation concerns the submodule profile; it can be seen that the low wind area suffers a major effect when the domain size is less than 10 m. The inversion of the velocity profile does not operate; the wind direction is identical between the two sup and submodule flow areas. The inversion of the velocity profile is found in the cases where the atmosphere is higher; this necessarily has an influence on the creation of turbulence at the obstacle and consequently provides an explanation for the divergence of values for the calculated roughness between the different domains. Given the consistency of the study results z_0 for the different large domains, it is assumed that the behaviour obtained with a 7.26 m domain is not representative of the situation. Therefore, the methodology must be applied with a sufficiently large domain to avoid this situation.

A second rule of use appears when we observe the evolution of the roughness integration calculation for different heights of h_{min}. In general, the more profiles integrated from a high height, the lower the roughness determined. They seem to converge towards a nominal value around 0.045 m for the cases with high atmospheric heights. The nominal value of the case with an atmospheric height of 7.26 m also converges to a roughness height of about 0.09 m. Between two consecutive integration heights, the difference in the calculated value of z_0 is reduced so that the gap is only a few tenths of a millimetre from $h_{min} = 4 \times \mathcal{H}_{\text{m}}$, and this for all atmospheric domains. This observation corroborates the use of a methodology with an atmospheric height sufficient to integrate the velocity profile, at least from $z_{min} = 2 \times \mathcal{H}_{\text{m}}$. If possible, the integration condition $z_{min} = 4 \times \mathcal{H}_{\text{m}}$ should be preferred to obtain consistent results with respect to the applied logarithmic regression method. It should be noted that even if the integration volume is small compared to the total control volume, no subsidiary effect is observed for the calculation of z_0.

The rules for the rest of the work will be respected. For the ground-mounted test case, the height of 10 m seems to be a good compromise to obtain a consistent roughness while reducing the calculation time.

6.4.3/ Verification of Friction Velocity Independance

From Equation 4.14, the roughness length is a function of $u_\star$. Considering that the solar park does not move due to wind-module interactions, the calculation of z_0 using the recall methodology must not diverge from one $u_\star$ condition to the other. The Figure 6.10 shows the behaviour of the wind profile according to three $u_\star$ conditions for the floating case. It is observable that the dimensionless profiles are identical above the dimensionless height $z/\mathcal{H}_\mathrm{m} = 1$. Discrepancies between curves are due to flow states and numerical deviations from spatial meshing.

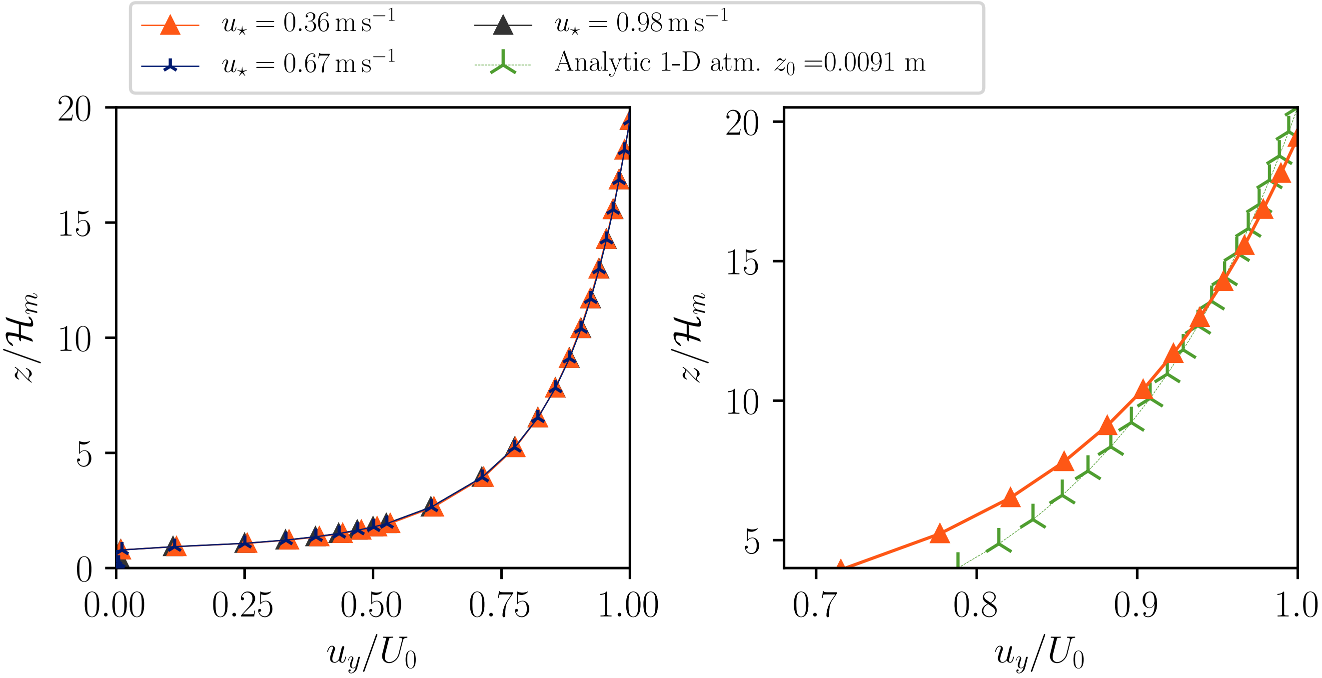

Figure 6.10–*Evolution of dimensionless wind profiles according to three velocity conditions at the top of the atmosphere (left-hand side). Comparison of wind profile obtained with* $u_\star = 0.36\,\mathrm{m}$ *and the analytic law determined by the* z_0 *value from the upscalling methodology.*

6.5/ On the Geometry of Solar Arrays for Dynamics and Thermal Quantities

6.5.1/ Role of the Module Height $\mathcal{H}_\mathbf{m}$

Following the first studies on the FPV2 cases and the ground-mounted test case, we wish to determine the minor morphometric elements *i.e., those which will exert a negligible influence on certain quantities of interest*. In this way, we wish to reduce the number of configurations of interest for the final morphometric study. We propose to study a configuration consisting of a constant tilt of 10° and whose pitch and height of the modules evolve between bounds representative of FPV and GM applications. We choose to refer to an occupancy rate between 80 % and 40 % and therefore a pitch of 2.1 m to 4.2 m by choosing a module length of 1.68 m. Assuming that the ground interferes with the flow in the case of FPV2, it is proposed to position oneself at a greater height so as to find an established under-module flow area, the energy supply of which directly intervenes in the airflow balance. Several airflow situations are also studied in order to characterise the quantities of interest in relation to realistic external situations. Three friction velocities and two wind directions are included as boundary conditions, as in the previous study. As friction velocity has no influence on the quantity of interest z_0, the focus is on global convective transfer.

Figure 6.11 and Figure 6.12 show the results obtained for the convective transfer rates in the front (left side) and back (right side), assuming a wind direction θ_w of 0° and 180°. Due to the computation time needed to obtain an established wind profile in the studied configurations, the numerical calculation points are extrapolated for wind fields with a speed lower than $4\,\mathrm{m\,s^{-1}}$ at 1 m above the modules. The trend linking the convective transfer rate to the reference velocity is always positive, with on average lower degrees of evolution than for the theoretical case. This finding must be weighted against the case where the occupancy rates are low or the relationship has a larger growth factor than the reference. This is the result of the evolution of the flow in the plant from a skimming type to a wake type. The more the flow transits towards a wake type, the more efficient the transfer is and tends to be closer to a standalone case. A second important observation is the weak relationship between the height of the modules and the transfer rate, both for the two sides of the modules regardless of the wind direction. Our result shows that the disturbance of the wind field in the power plant is *insensitive* to the height of the obstacle, assuming a disjointed obstacle. This result will have to be visualised using the scaling methodology. The backside also benefits from the absence of any geometric "constraint" from the ground (or other structures) that could interfere with the flow by slowing it down.

In general, the direction of the wind influences the transfer from both sides; when a surface is swept first, it exchanges more energy than when it is hidden from the main flow direction. Interestingly, the backside convection will always be weaker than the frontside convection, even if the latter is in the opposite direction of the flow. This behaviour can be observed for skimming-type flows and its influence tends to reduce when the configuration allows a wake-type flow. Assuming that the sum of the coefficients of the two faces is physically realistic (homogeneity of the surface temperature at the front and at the back), we observe that the global convective transfer is strongly dependent on the wind speed and its direction. The reference winds with a speed between $1\,\mathrm{m\,s^{-1}}$ and $4\,\mathrm{m\,s^{-1}}$ have a better efficiency in cooling the power plant modules when their directions are at $\theta_\mathrm{w} = 180°$. This observation is even more true when the occupancy rate is low, since the low-wind zones are reduced in size and relocated with respect to the *module* zone. Above $4\,\mathrm{m\,s^{-1}}$ the gains are marginal and the winds whose direction is $\theta_\mathrm{w} = 0°$ contribute to better cooling.

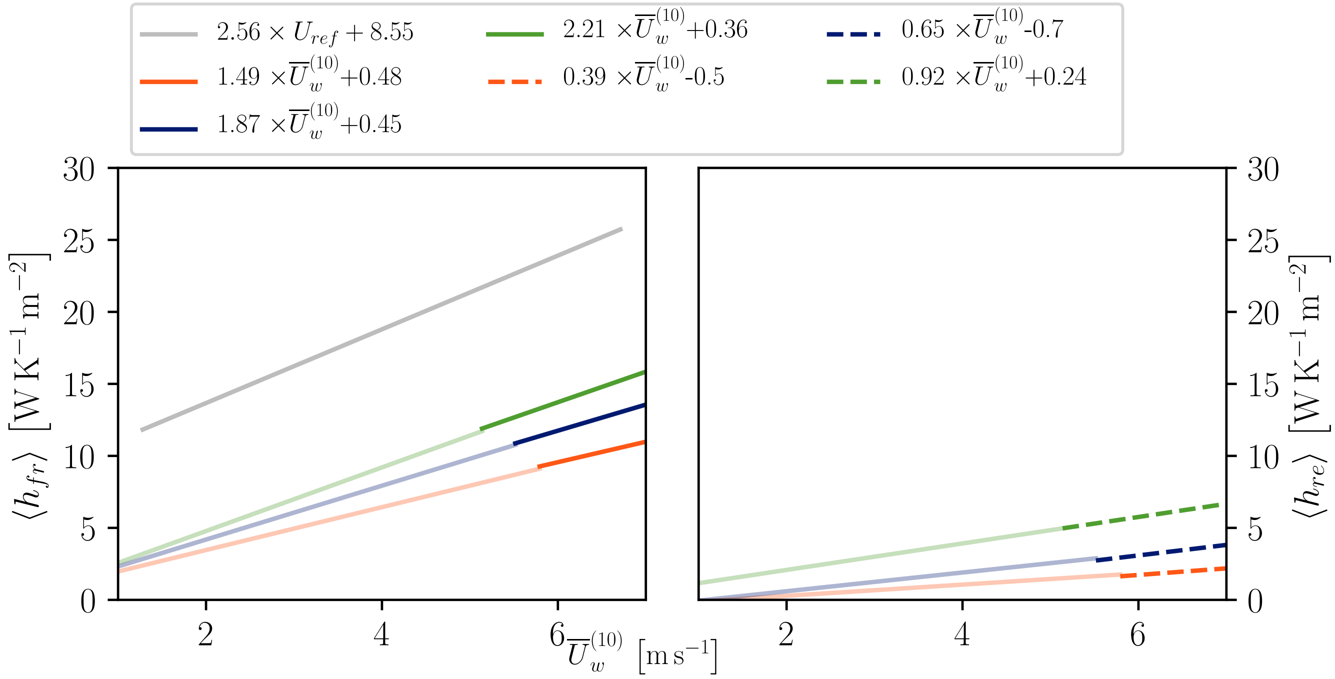

Figure 6.11–*Simulation of heat rates for the front face (right-hand side) and the rear face (left-hand side), when wind blows with an attack angle of* $\theta_w = 0°$. *The module height is fixed to* $\mathcal{H}_m = 1.15$ m, *and a fixed tilt is assumed as* $\theta_m = 10°$. *Different pitch values are elaborated:* 2.1 m (−), 2.884 m (−) *and* 4.2 m (−).

As a conclusion of this morphometric case, several configurations have allowed us to highlight the weak influence of the module height on global convective transfer. Thus, we can reduce the design of the morphometric experiment for configurations with constant height, higher than the height of the FPV2 case study for which the soil condition influences the aeraulic development mainly in the rear face. With winds representative of the classical configurations, the pitch remains a preponderant element in the establishment of a stationary flow regime. It also appears that this numerical study is in line with research conducted with ground-based power plant configurations for which the prevailing winds *behind the module* offer lower module temperatures. Specific conditions seem to be conducive to the development of such phenomena, mainly low wind speed conditions and high pitches.

6.5.2/ Design of Experiment : Description and Construction

From the previous results, the design of the experiment is established to cover plant configurations in pitch and tilt as follows: $\mathcal{S}_\mathrm{m} \in [2.1, 2.884, 4.2]$m and $\theta_\mathrm{m} \in [10, 20, 30]$ °, keeping the median height in the module constant. The height $\mathcal{H}_\mathrm{m}$ evolves between two configurations due to the tilt θ_m, the maximum difference is 27.4 cm, which is below the 60 cm evolution of the previous test case, so the observable effects on the quantities of interest are not attributed to the height difference but to the evolution of the other geometrical parameters. The simulation is bi-periodic, the frictional stress imposed at the top of the computational domain is made proportional to the wind angle θ_w, thus the configurations are evaluated for 7 incident winds, the frictional velocity is constant and equal to 0.36 m s^{-1}. Finally, the design of the experiment is made up of $3 \times 3 = 9$ configurations for which 7 cases are evaluated, 63 numerical simulations are necessary and each simulation takes approximately 5 hours.

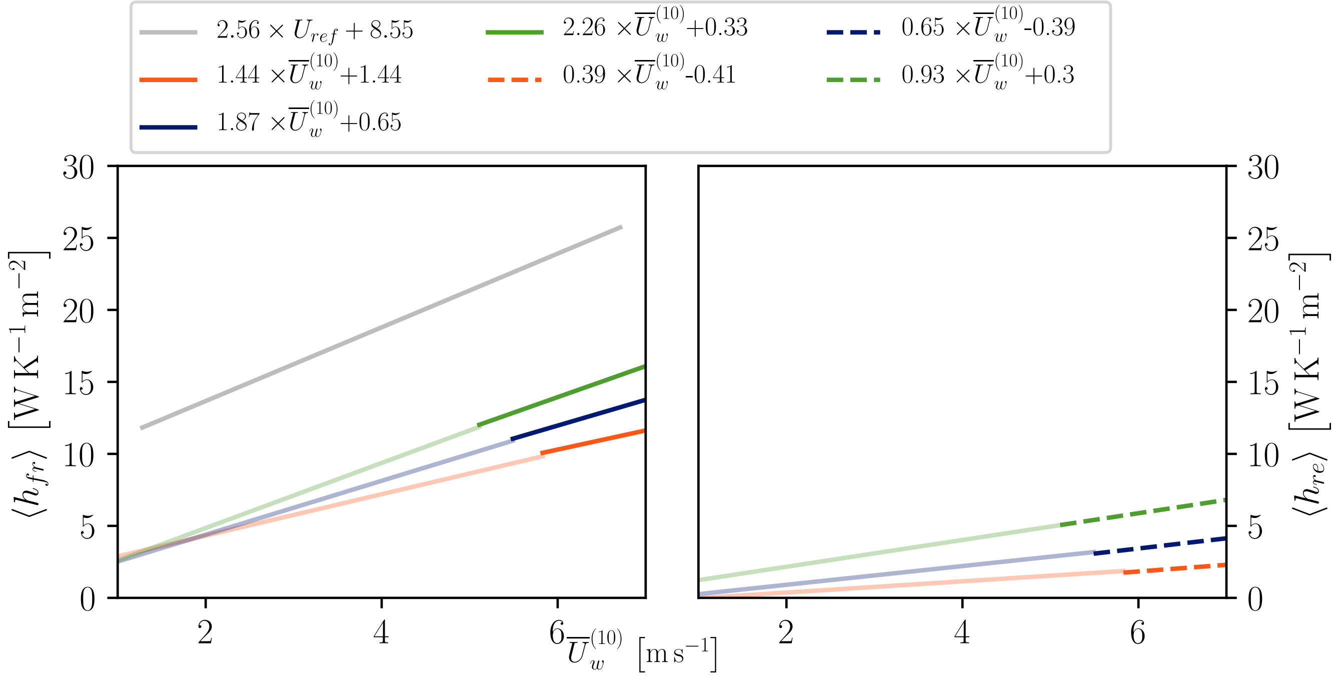

Figure 6.12–*Simulation of heat rates for the front face (right-hand side) and the rear face (left-hand side), when wind blows with an attack angle of $\theta_w = 0°$. The module height is fixed to $\mathcal{H}_m = 1.75\,\mathrm{m}$, and a fixed tilt is assumed as $\theta_m = 10°$. Different pitch values are elaborated:* 2.1 m (−), 2.884 m (−) *and* 4.2 m (−).

6.5.3/ Geometry Configuration and Flow Dynamics

First, the result of the dynamic interaction between the atmosphere and the configurations is considered. Figure 6.13 shows the results of the roughness calculation for all configurations, from the highest solar occupation rate to the lowest. A clear evolution of the interaction is observed as a function of the angle of attack of the wind θ_w, it is weak when the winds are transverse to the power plant, the order of magnitude is the tenth of a millimetre, and increases until interactions on the dynamics of the order of a centimetre are obtained. Between the two directions perpendicular to the module, the calculated roughness is greater for the winds hitting the system from the back. **These rules are independent of the geometric configuration**.

In the case of parallel winds ($\theta_\mathrm{w} = 90°$), the geometry of the power plant influences the value of the interaction at the margin, there is also an independence of the dynamic interaction between the atmosphere and the system, and it is assumed that the addition of a supporting structure will lead to a higher interaction.

For perpendicular or near-perpendicular winds ($\theta_\mathrm{w} \simeq 0°$), the interaction of the system with the atmosphere is not independent of the geometry. It can be observed that the largest module tilt is almost always the one that leads to the largest roughness value, whereas the smallest tilt almost always leads to the smallest value. The difference between the two tilts is almost an order of magnitude. The range of roughness evolution is wider for high-slope configurations.

The space between the modules is also an influencing parameter for these incident winds. It can be seen that the lowest occupancy rate has a greater influence on the dynamics than the packed solutions. As for the angulation, this difference is expressed by half an order of magnitude and mainly for the winds coming from the front of the module.

These numerical experiments show that the interaction on the dynamics of a PV plant cannot be considered constant and that a relationship between the interaction and wind direction is necessary to anticipate the correct orders of magnitude of the wind speed in plants. Knowing the geometrical configuration brings additional information on the value of the interaction; however, in our experiment, only one order of magnitude is crossed between the configuration $(GCR, \theta_{\mathrm{m}}) = (40\%, 30°)$ and $(GCR, \theta_{\mathrm{m}}) = (80\%, 10°)$, contrary to the two orders of magnitude crossed by simple knowledge of the direction of the wind. It supports the idea of creating functions so that $z_0 = f(\theta_{\mathrm{w}})$.

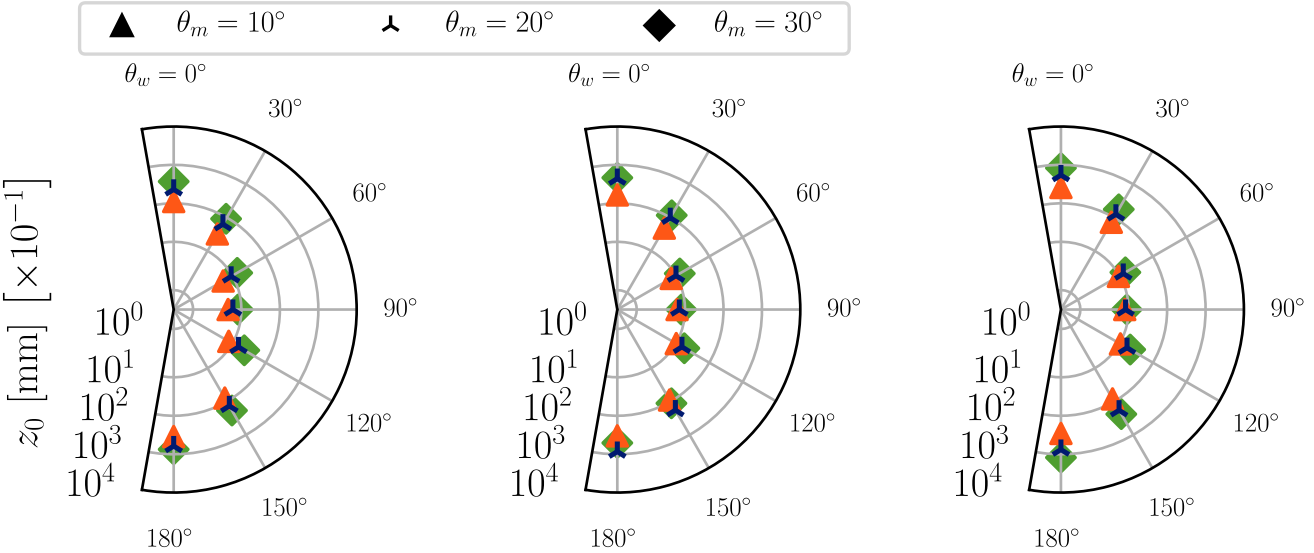

Figure 6.13–*Roughness length calculated for the 63 simulations of the morphometric evaluation, configurations are distributed from the right subplots to the left: GCR = 80%, GCR = 60%, GCR = 40%. Each marker corresponds to a single calculation, the associated configuration tilt is given by the marker shape. The polar axis gives the wind direction of the simulation assuming the convention given in chapter 6 ($\theta_w = 0°$ means wind blowing the module surface facing the sky).*

6.5.4/ Geometry Configuration and Heat-rates

Using the batch morphometric simulations, we want to determine the influence of geometric parameters on the convective intensity. For this study, the wind speed is necessarily different from one situation to another; the base vectors of each simulation are $u_\star$ and z_0. Figure 6.14 presents the results of the convective intensity in the front; we are interested in the result $\langle h_{fr} \rangle$, with $u_\star = 0.36\,\mathrm{m\,s^{-1}}$. We first observe that the coefficient has an inverse evolution to the experiment for z_0, the maximum values of $\langle h_{fr} \rangle$ are observed for the side winds, whereas the winds perpendicular to the module give lower coefficients. The configuration that offers the worst cooling is obtained with $\theta_{\mathrm{m}} = 30°$ and $\mathcal{S}_{\mathrm{m}} = 2.1\,\mathrm{m}$, with a wind direction perpendicular to the modulus $\theta_{\mathrm{w}} = 180°$, the order of magnitude is $5\,\mathrm{W\,K^{-1}\,m^{-2}}$. This result is quite logical, in this configuration the module assembly has a very large influence on the aerodynamic field and the energy supply in front of the module is to the advantage of the rear side of the module. The best cooling is obtained for $\theta_{\mathrm{m}} = 10°$ and $\mathcal{S}_{\mathrm{m}} = 4.2\,\mathrm{m}$ a wind direction at two thirds of the front face such that $\theta_{\mathrm{w}} = 60°$. This time, the coefficient is three times greater than previously with $15\,\mathrm{W\,K^{-1}\,m^{-2}}$. The range of evolution of the coefficient is more restricted compared to the evolution observed in z_0 for which we observed different orders of magnitude.

Geometrically, it can be seen that the tilt of the module does not have a real influence on convective transfer below $\theta_\mathrm{m} = 20°$, there is, however, a more important margin for θ_m between 20° and 30°, which reaches $\Delta\langle h_{fr}\rangle \simeq 3.5\,\mathrm{W\,K^{-1}\,m^{-2}}$ at the maximum for perpendicular winds such as $\theta_\mathrm{w} = 180°$. This last result reflects the variation in the kinetic energy supply to the front of the module as visualised in the standard case in 6.2. The less pronounced tilt tends to improve the supply in the zone and to reduce the formation of a recirculation zone. The influence is even null for winds on the side $\theta_\mathrm{w} = 90°$, in this last situation the flow is almost not influenced by the module and no recirculation zone seems to form around the system, regardless of the geometry.

The same observations are made with respect to the influence of the pitch on the convective intensity obtained. The trend observed is an increase in the convective coefficient when the pitch increases, the orders of magnitude vary from one tilt and one wind to another, and we can observe an average increase of $\Delta\langle h_{fr}\rangle \simeq 3\,\mathrm{W\,K^{-1}\,m^{-2}}$ between the pitches 2.1 m and 4.2 m. This observation can be attributed to the displacement of the recirculation zone in front of the modules as the tilt increases. Eventually, an *infinite* pitch should resolve to a typical convective coefficient of a module in standalone mode.

Macroscopic aeraulic flow in the power plant is not neutral in determining the observable cooling intensity in plants. The convective intensities are consistent with the empirical relationships obtained in a standalone module format, and some geometrical configurations obtain significant intensity reductions. Pitch and tilt are the two main geometric elements, and their combination is expected to affect the positioning and size of the vortex around the module and thus the air friction on the front of the module. However, the side winds at the power plants are little (if any) influenced by the geometry. This phenomenon is physically explainable by the very low alteration of the wind profile in this situation (as measured by the z_0 morphometry), the vortexes that are created around the systems have modest kinetic energy feeds due to the low aeraulic interaction.

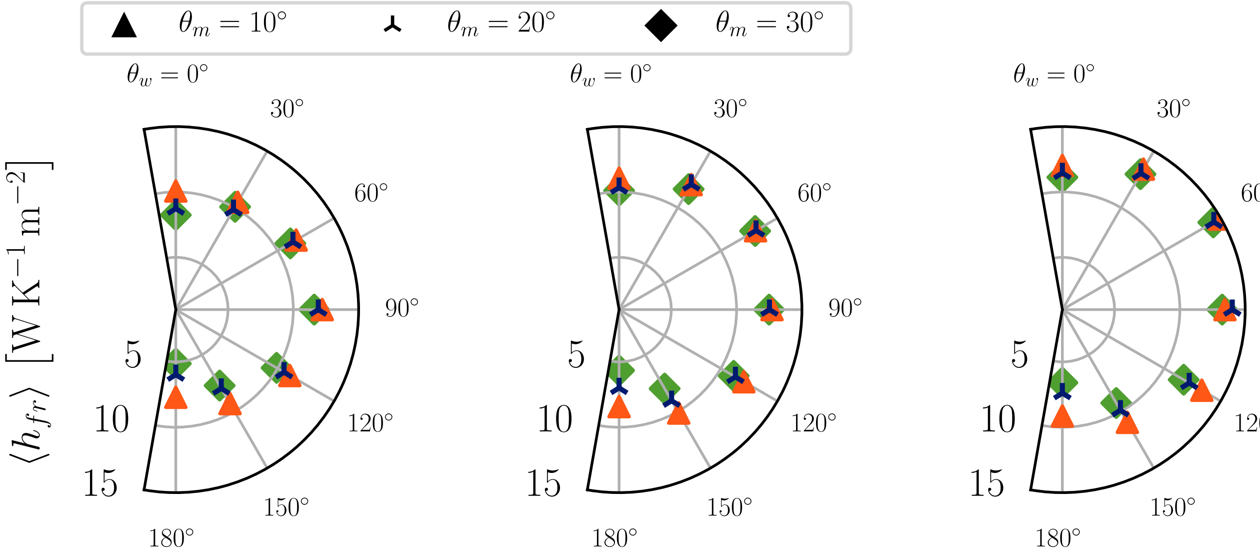

Figure 6.14–*Convective heat rates of the front face calculated from the 63 simulations of the morphometric evaluation. See Figure 6.13 for the details about subplot arrangements.*

In a second step, the convective coefficient obtained in the same simulation is studied for the rear side of the module. Figure 6.15 shows the results. Similarly to the previous study, we observe a relation of the convective coefficient inverse to the evolution of z_0. A strong point of divergence from the previous study lies in the evolution of the coefficients as a function of the pitch, the convective intensity can evolve from simple to double between two configurations with the same θ_m. The most important intensities are also obtained in mirror image compared to the previous study; the winds at the back of the module produce better cooling than the winds facing the module.

The worst configuration in terms of cooling performance is obtained with headwinds and a low pitch and tilt combination; it reaches at least $\langle h_{re} \rangle = 1\,\mathrm{W\,K^{-1}\,m^{-2}}$. In this situation, the bi-periodic model does not seem to be adapted to the representation of the convective phenomenon, it is assumed that the flow coming from the thermal effects is more efficient than the aeraulic effects forced by the wind, and thus that the recirculation zone around the backsheet is rather directed by a thermal effect. With RANS modelling, it is expected that this type of situation will be influenced by the turbulence model used.

The best cooling configuration is obtained with winds coming from two thirds of the rear face of the module when the pitch is important, the order of magnitude of the convective intensity reaches $12.5\,\mathrm{W\,K^{-1}\,m^{-2}}$. We also notice that the tilt is not the most influential parameter when the pitch is sufficiently large. This observation may be the result of the lack of influence of the recirculation zone on the rear face because the distance of the vortex from the surface is too great or the dimensions are not large enough.

A comparison of the intensity of the front and rear face coefficients shows that the front-face coefficient is almost always the dominant parameter, but there is no order of magnitude difference (if we omit the cases where our model seems less relevant because it is driven by thermal phenomena). e.g.: the configurations $\theta_\mathrm{w} = 0°$ and $\theta_\mathrm{w} = 180°$ with $\theta_\mathrm{m} = 10°$ and $\mathcal{S}_\mathrm{m} = 2.1\,\mathrm{m}$). Thus, regardless of the configuration, it is necessary to model the two convective transfers in the heat balance of the module.

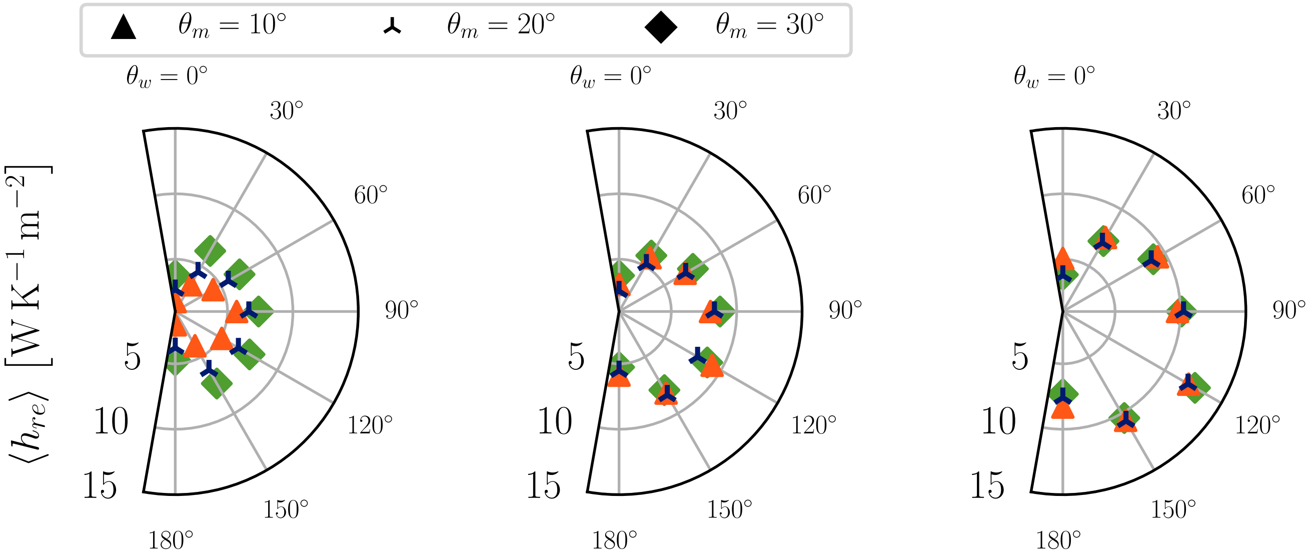

Figure 6.15–*Convective heat rates of the rear face calculated from the 63 simulations of the morphometric evaluation. See Figure 6.13 for the details about subplot arrangements.*

Although the friction condition imposed at the top of the atmosphere is realistic, the airflow through the system is necessarily dependent on the roughness created by the periodic scheme.

The point of view of the atmosphericist is relevant and practical at the scale of the array (as for z_0); however, it is not very practical at the scale of the photovoltaic practitioner, whose measurements usually stop in a wind and a typical direction. Therefore, to compare the convective performance by adopting a photovoltaic frame of reference, it is more convenient to describe the air field by an air flow rate or an average velocity *i.e., reference velocity*, as described by Test et al. From the first batch of simulations, the reference velocities are reconstructed from the analytical logarithmic law for a height of 3.5 m. Naturally, winds parallel to the module present higher flow velocities due to the lower roughness of the pattern; the convective coefficients are mechanically more important for these configurations.

In order to compare the convective performances for similar flows, a second series of 63 simulations is carried out for the same geometrical configurations. The shear stress at the top of the domain is taken to be greater $u_\star = 0.77\,\mathrm{m\,s^{-1}}$. The periodic scheme thus converges more rapidly.

With the 126 simulations, linear relationships between the convective parameter and the reference wind are constructed for each geometric combination; as in the previous sections, linear extrapolations are essential for all configurations to have wind speeds low enough to be representative of the usual local conditions of outdoor operations, but also large enough so that the main motion vector does not become the temperature differences. The results of the regressions are presented in Figure 6.16.

A first observation of this morphometric study is that the absolute values of the convective transfer rates at the front are rather similar for all the configurations studied. The constant value generally comprises between 0.5 and 2.5 , while the wind speed-dependent value also comprises between these limits. A similar pattern is observed for all configurations; the wind directions that are the most perpendicular to the module always have the highest transfer rates; this is even more true when the situation is characteristic of a ”free footprint” solution with a large pitch and a high tilt rate. In other directions, the morphometric elements have less influence, and there is a certain invariance of the transfer rates to the morphometry for these directions. This result can be explained by the face of the module that interests us, in fact, we have already mentioned the low transfer rate for the back winds to the module because of the predominance of the recirculation zone in this situation.

The comparison of the plot curves from left to right shows that pitch is the element that modifies the average transfer rate the most, while the evolution from top to bottom shows that the influence of tilt is weak; except when pitch is already important. It is in the latter situation that the highest average convective transfer rates are obtained. Note that the difference in convective intensity is more than four times greater in the most favourable morphometric case ($\theta_\mathrm{w} = 0°, \mathcal{S}_\mathrm{m} = 4.2\,\mathrm{m}, \theta_\mathrm{m} = 30°$ and $U_\mathrm{w} \simeq 6\,\mathrm{m\,s^{-1}}$) than in the most unfavourable case ($\theta_\mathrm{w} = 0°, \mathcal{S}_\mathrm{m} = 2.1\,\mathrm{m}, \theta_\mathrm{m} = 10°$ and $U_\mathrm{w} \simeq 1\,\mathrm{m\,s^{-1}}$), this observation shows that the common practise of considering a constant global transfer rate can lead to strong uncertainties. Taking into account the dependence of the global rate on the wind speed does not erase all the uncertainties, in fact, if we compare the previous favourable morphometric case with the unfavourable case with identical wind speed $6\,\mathrm{m\,s^{-1}}$, the difference in intensity is almost doubled. This indicates that the choice of the thermal coefficient is key and depends in a non-negligible way on the macroscopic geometry. This modification is attributed to the evolution of the flow from a rather wake flow regime demonstrated by Glick, Smith, et al., 2020 to a regime that tends towards skimming flow for spaced morphometries called ”free footprint”. In the latter situation, the flow around the front face is improved, our study shows that this is mainly the case for perpendicular wind directions and to a lesser extent

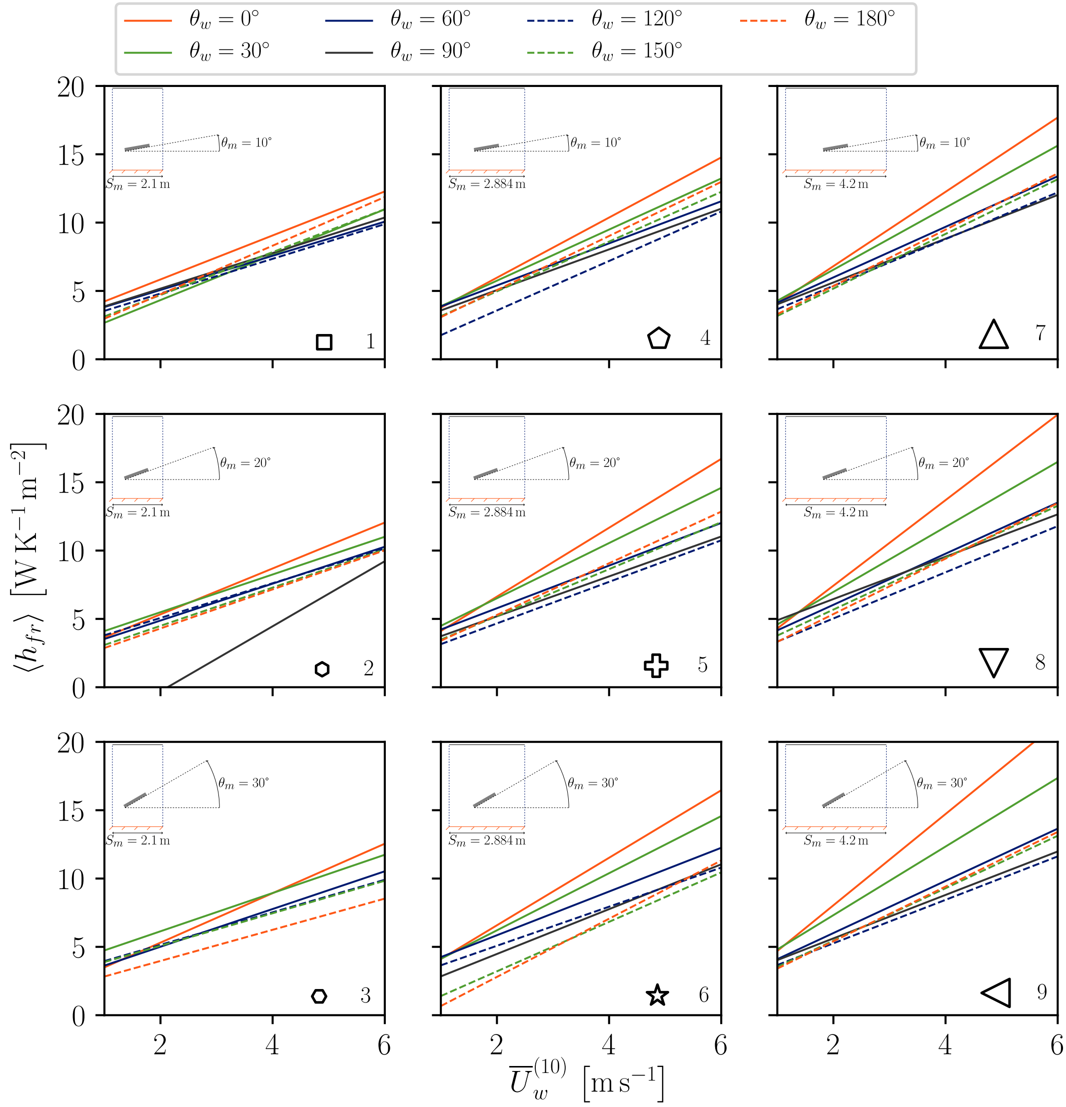

Figure 6.16–*Linear regression of front-side heat-rates for the nine land-based layouts. Each configuration is simulated for seven wind directions θ_w. One motif located on the right-downside corner is given as indication for each central layout.*

in the rest of the wind directions. However, it is also noted that the reference frame adopted in this situation is not fully adapted to the scale of the PV plant, the atmospheric forcing being dramatically different between the cases of perpendicular winds in the ”free footprint” situation and in the ”large footprint” situation. In the latter situation, reaching high wind speeds requires more effort from the atmosphere, whereas the effort is lower in the former case. Therefore, the morphometric comparison is useful for the practitioner whose knowledge of friction velocity is unknown.

For the FPV2 layout, Figure 6.17 shows the cooling performance for each angle of wind for the front and back of the system. A direction-averaged correlation is proposed so that the mean thermal interaction is deduced. Heat-rates on the front side of the system are greater than the one over the rear-side on average. Transverse winds drive the averaged coefficients to greater values whereas perpendicular winds have greater influence on one side or the other depending on the normal module direction. Both land-based and FPV thermal behaviours are similar in this extent.

It is noted that the FPV layout benefits of lower correlation magnitudes compared to the land-based configuration. When this assessment was mentioned for a single wind direction $\theta_\mathrm{w} = 0°$ at the beginning of this section, the thermal behaviour is extended to all the wind direction situation in this study. The term of *wind cooling effect* for floating photovoltaics is challenged here, the type of layout highly modify the wind influence over the modules. When in Chapter 6 the correlation for a standalone module was found greater offshore than the literature-based correlation, the airflow regime was assessed to achieve better heat removal due to stronger mean flow velocity and possibly higher level of turbulence mixing. The numerical study though shows that the layout breaks the wind profile either the mean velocity and the turbulence profiles. The convective cooling is degraded and does not depend much on the flow regime at the entrance region of the array, but more on the layout of the array. Therefore, the low tilted, pitch and heights of the floating configuration are detrimental to enhance wind interaction with the module as obstacles. *Wind cooling effect* is assessed to be not appropriated to describe the lower temperature observed in FPV in array-configuration.

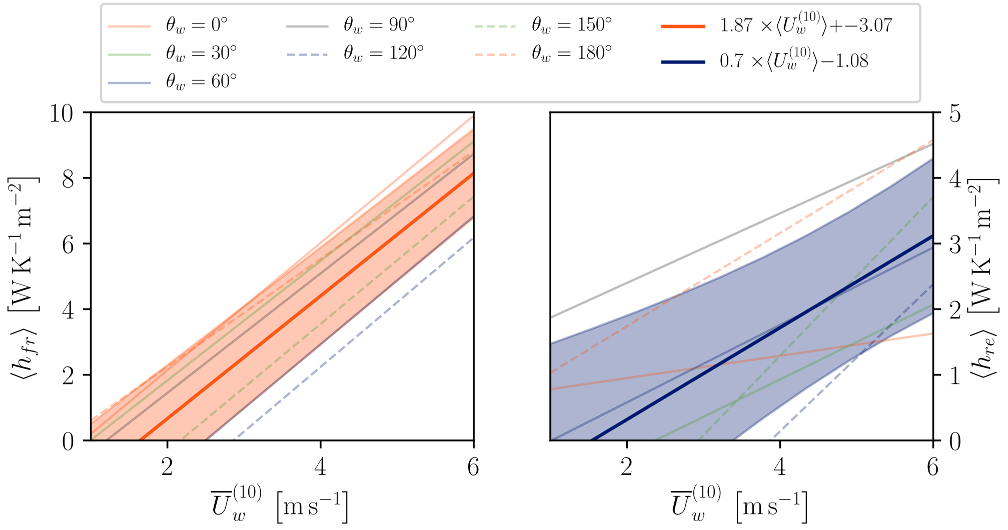

Figure 6.17–*Heat-rate performances for both sides of the FPV module in array configuration assuming seven wind directions. Front side heat rates are indicated on the left hand-side whereas rear-side heat rates are indicated on the right-hand side.*

Given a constant wind velocity value at 10 m, for instance $\overline{U_\mathrm{w}}^{(10)} = 5\,\mathrm{m\,s^{-1}}$, it is possible to compare the heat-rate performances for all land-based configurations including the FPV layout, assuming direction-averaged coefficients. Figure 6.18 shows the heat rates for both module sides in these situations. The dispersion of heat-rates is more important on the rear-side than over the front. For this specific wind regime the relative evolution of rear-side reaches 78% when the front-side shows a maximum relative error of 33%. It is observed that the greater the pitch, the greater the rear-side heat rates are obtained and conversely low pitchs are detrimental to obtain good level of rear-side heat rates. Interestingly, the tilt shows a lower influence on the array performance as both $\theta_\mathrm{m} = 10°$ and $\theta_\mathrm{m} = 30°$ can obtain similar heat rate magnitudes, especially on the front side (case 4 and case 9). As for urban flows, it is likely that more elaborated dimensional values (area or length ratio) could be created to quantitatively represent *insulated footprints* or *free footprints*. The FPV layout for instance is assessed to be a *large footprint* at least, which is confirmed by the low heat-rate magnitudes for the front-side and more importantly for the rear-side. From these observations, the *Cooling effect* in array configuration are ,for a large matter, a question of rear-side exchange so that *free-footprint* FPV layout may experience noticeable lower temperature over waterbodies if the airflow can remove heat efficiently behind the photovoltaic system. The FPV layout with a lower module height than the other land-based configurations may be a subject of downgraded heat rate below the module. A thermal buffer layer can settle behind the system and reduce dramatically the convective transfer levels. This situation is though one limitation of the proposed simulation as it induces that free-convective transfer may lead the rear-side exchange; the array simulator should be modified in consequence so that the heat flux becomes a natural scale of the simulation.

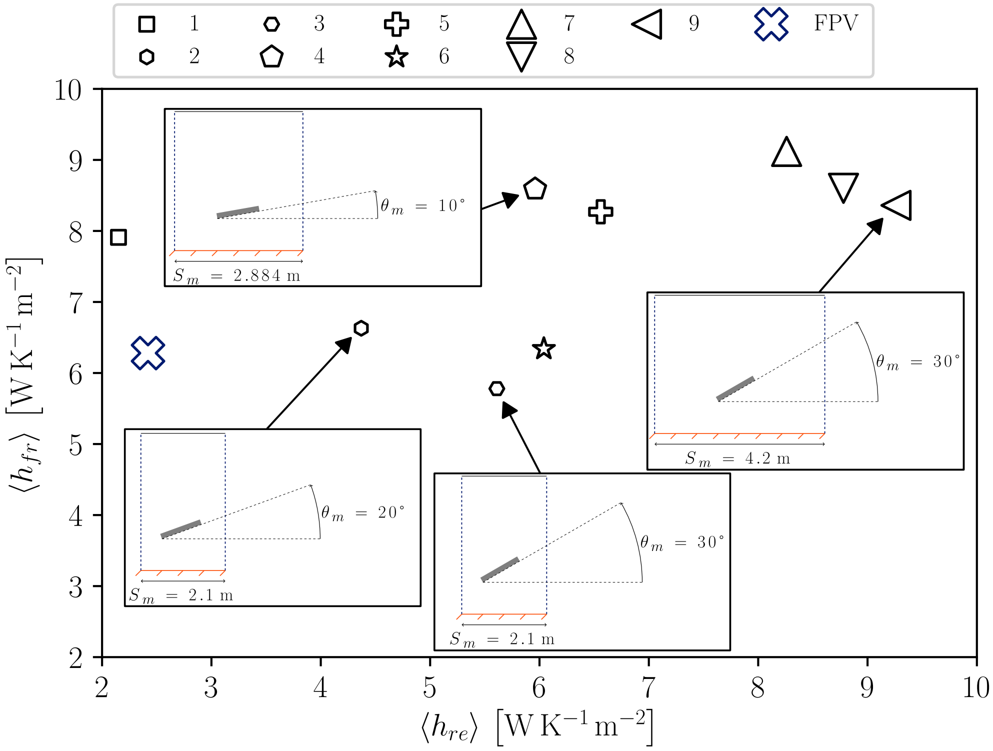

Figure 6.18–*Example of geometry performances according to the front and rear heat-rates obtained using the morphometric analysis. The performances of the Floating PV layout are also indicated.*

6.6/ Conclusion

The new method adapted for array-scale simulation has been applied to evaluate the effect of convective cooling in FPV and land-based systems. Both situations exhibit a lower level of convective cooling than the levels obtained through literature-based correlations for standalone systems. These results were significantly lower for the FPV case, and it is hypothesised that the rear face is a key factor in the thermal performance of these specific configurations. When the simulation runs over the assumption of fully developed flow in the array, supplementary material has been built to study the array-scale flow behaviour using explicit representation of forty modules. Heterogeneous flow was pointed out with strong variations with regard to the thermal heat rates produced. The fully developed flow is found to be obtained at long distances in the array so that design of the array seems to be a key driver in the magnitude of the convective cooling. These numerical experiments were conducted on land-based geometry, so that it should be a conservative hypothesis for the fully developed length compared to the FPV geometry; the cost of performing those simulations is less affordable than the new method developed.

Using the full-array representation and flow validation in Chapter 4, it is assumed that the length of heterogeneous flow is a function of the turbulence representation. For example, 26 modules were necessary to fully develop the flow state with the $k-\omega SST$ turbulence model. $k-\omega SST$ overestimates flow velocities in the array, it is likely to obtain a fully developed flow before the 26th module (especially with the FPV geometry). Second-order turbulence models should be investigated in more detail to increase the simulation accuracy. Nevertheless, the generally accepted threshold to obtain fully developed flow of the order of 5 to 7 obstacles (heat exchangers) seems to be unrealistic in the case of PV systems in an external atmosphere with three flow zones. Below the modules, the sub-module zone is difficult to capture. The developed method is clearly adapted to the simulation of the front heat-rates as it suffers less from the sub-module flow.

When the objective is to keep the computation as low as possible with the new methodology, limitations were observed in the precision of the simulation due to secondary parameters such as integration and domain heights, respectively, denoted z_{min} and h_{min}. They should be selected with caution. Indeed, the integration height is not trivial to determine in relation to the geometry of the powerplant $\mathcal{H}_\mathrm{m}$, θ_m, $\mathcal{S}_\mathrm{m}$: A large value of z_{min} requires more calculation cells. Assuming $\mathcal{H}_\mathrm{m}$ as a characteristic length, the minimum atmospheric height for the periodic system was found to be $h_{min} \simeq 4 \times \mathcal{H}_\mathrm{m}$ in order to secure the flow dynamic. Flow inversion in the submodule zone is not reproduced if the threshold is not respected. Another key aspect was verified using the new methodology by securing the invariance property of the calculation with respect to the friction velocity at the top of the domain. The next step will be to scale the effect of the power plant on the flow dynamic with respect to the atmospheric reference frame.

Finally, a morphometric study has been carried out to understand which geometric aspects of the power plant are the most important to determine the level of convective cooling. By reducing the field of possibilities to the influence of the module angulation and the intermodule distance, the combination of the two geometric parameters was found to modify the flow type from a wake flow/skimming regime with a reduced thermal effect on the power plant to a free/wake regime with improved cooling. Front-side heat rates were not found to evolve in a range of magnitude due to geometry configuration, but fine tuning of geometrical dimensions can be achieved to improve thermal management of the full-scale system. All wind directions were investigated for this quantity of interest, and geometry appeared to have a lower impact on the cooling magnitude when crosswinds occurred. This property should be investigated in more detail in the future, especially by complexifying the geometry with structural elements (frames, aluminium posts) in order to effectively capture the additional disturbances in the transverse plane.

The methodology applied in the FPV standard layout finally showed that direction-averaged heat-rates are lower than the heat-rates of land-based layouts. From this assessment, it was hypothesised that the term *wind cooling effect* should be used with cautious to explain the temperature differences observed in real-world FPV experiments. In array configuration, the combination of geometrically low tilt and pitch coupled with a lower height badly affect the front-side heat rate and mainly the rear-side heat rate. The results should be consolidated to ensure that the forced convective mode prevails even on this face. The numerical methodology proves to be a first element that allows us to address the scale of the power plant with a controlled cost and adapt to the industry. Moreover, the impact of wind direction being caught with the method and shows some non negligible variation in the magnitude of heat rates, it is possible to build specifically designed correlations that takes into account the air flow regime and direction. This will be addressed in the next Chapter 7.

7 FROM MODULE TO ARRAY: IMPLEMENTATION IN MICROCLIMATE CFD

> Le vent se lève, il faut tenter de vivre !
>
> Paul Valéry, *Le Cimetière Marin*

This chapter presents the results of the interaction between the geometrical configuration of FPV2 and a representative atmospheric flow measured *in-situ*. New geometrically-based wall functions are developed to simulate the influence of the floating array on the atmosphere flow. The evolution of front module faces at the array scale is estimated as well as the level of evaporative transfers.

Contents

7.1/ Introduction

The technique developed to simulate air flow in the photovoltaic array when the flow is established is a first piece to capture the level of heat transfers from aeraulic sources. As in many external applications, the length of the flow establishment is uncertain due to the stochastic nature of the wind; therefore, the thermal transfers from the module at an infinite location in the array lacks of reliability to describe the array scale: The heterogeneity of the airflow regimes must be investigated on a proper full-scale. This means simulating the airflow in all the macroscopic regimes such as the entrance regions, the established flow area, and the end of the array of obstacles. However, addressing all those zones requires a lot of computational resources when one wants to represent the modules explicitly: The number of mesh cells scales with the number of modules and the level of precision required. The objective is to create an estimator to capture the distribution of the thermal heat rates induced by the airflow regimes and their evolutions at the full array scale.

This chapter seeks to overcome the prohibitive computational cost of simulating the flow as if the modules were represented explicitly, in a configuration of a full-scale powerplant. The chapter is supported by the case study of the floating power plant FPV2, from which a number of measurements presented in Chapter 3 have been collected to qualify the environment above the basin. The topography of the reservoir is digitised at the microscale, and the dry atmosphere model is used to determine the flow regimes, as well as the diffusion of passive scalars of humidity and temperature in the air volume. Reduce computational cost is achieved by using a $k-\epsilon LP$ turbulence model coupled with a suitable set of boundary conditions and wall functions with respect to the initial FPV2 geometry simulation. The subscript ex is used to describe the results of those simulations in which the modules are **explicitly** represented. Wall functions and post-processing computations are performed to incorporate the information from the explicit simulation, to the 3-D microclimate simulation; therefore, the subscript im indicates that the boundary conditions and the wall functions are adapted to the 3-D situation. In other word, modules are **implicitly** represented so that their action on the atmosphere flow is conserved. To this end, three techniques are constructed:

- A roughness law designed for the geometry of FPV2, obtained by the homogenising method presented in Chapter 4, which takes into account the direction of the velocity.
- A wall function for the humidity field, which allows to reproduce the evaporative transfer reduction under the modules of the floating powerplant. It also takes into account the wind direction at the module level
- The thermal production of the powerplant imposes a volume heat source term on the air. Correlations are built up to reproduce the convective heterogeneity of the panel temperature in a post-processing step.

The methodology developed for the three fields of interest is applied to the FPV2 study case; however, they are also applicable to other study cases by recreating correlations for another configuration following Chapter 4. **The process described in this chapter is reproducible for other situation.**

7.2/ Computational Settings of FPV2 Microclimate

The 3-D microclimatic scale requires the implementation of a set of good simulation practises in order to obtain computed fields that are representative of real physics. In this first part, we introduce the main features of the FPV2 test case.

7.2.1/ Geometry and Meshing

As mentioned in Figure 3.13, the FPV2 floating array is located in a hilly region of crop fields and wooded hills. The steepest mountains are located at distances of approximately 10 km, the test case is constructed considering a radius of 2.5 km around the centre of the lake. Figure 7.1a shows the relief around the lake. The high points near the site are located in the southern part of the lake. The contour lines indicate that the area to the north of the lake, which consists mainly of agricultural land directly adjacent to the lake, is fairly flat. The lake is surrounded by embankments, the sides of which are not discernible in the figure, as is the water level in the reservoir. The latter fluctuates from day to day as a result of the daily electrical turbine production, so we will take a fixed height in the following studies.

The levelling data is obtained from open-source maps with a 25-meter resolution by the National Institute of Geography (IGN). The obtained geometry is then meshed using a specific script, and a 2-D mesh is created. The script ensures the conformity of the created cells, and the netgen mesher is also called when triangular meshes must be built in order to reduce cell warping. A circular space is established around the centre of the lake; This space guarantees the initial topography with a resolution of 25 m per cell side. A flat band is added around the space for computational optimisation purposes due to boundary condition issues that exist in this type of simulation; 60 m side cells are considered here. The floating elements of the lake are integrated as specific surfaces whose mesh size is refined to 5 m per side, to increase the resolution of the field calculation. Surfaces adjacent to the islands and the lake are also shown to improve the resolution at the edges of the basin, taking 15-metre-square cells with geometric refinement as we move towards the floating island areas. Figure 7.1b shows the result of the mesh script with refined areas. In the z direction, the mesh is made up of 33 cells, the altitudes of the faces follow a geometric sequence with a common ratio of 1.2. The height of the first cell (from bottom to top face) is 1 m. The total mesh is composed of 1 357 983 cells with only 2.02% prismatic cells, the remaining are hexahedra.

7.2.2/ Boundary Conditions and Initial State

Sides and top conditions

The geometry of the cylinder allows us to apply the velocity inlet or pressure outlet depending on the direction of flow *(i.e., automatic inlets/outlets)*. For inlet cells, logarithmic velocity profiles are applied. It is parameterised by a velocity friction $u_\star = 0.25\,\mathrm{m\,s^{-1}}$ and a large-scale mean roughness $z_0 = 0.1\,\mathrm{m}$. The velocity value reached at the top of the profile is set as a Dirichlet condition at the top of the domain. Constant temperatures and humidity levels are assumed on the side and top of the domain.

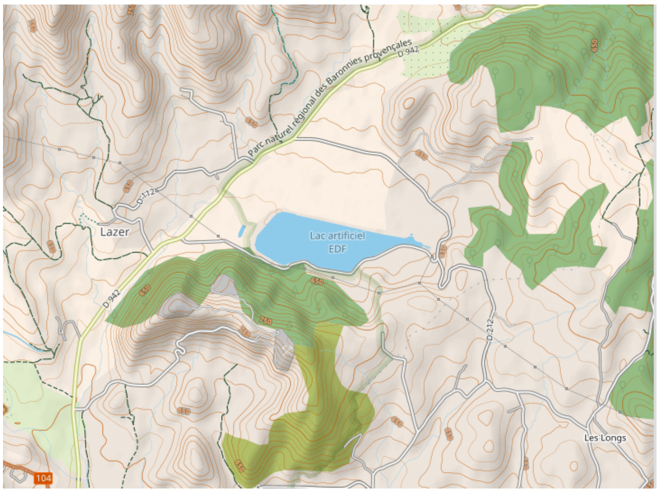

(a) *Map of FPV2 Area retrieved from Open Street Map*

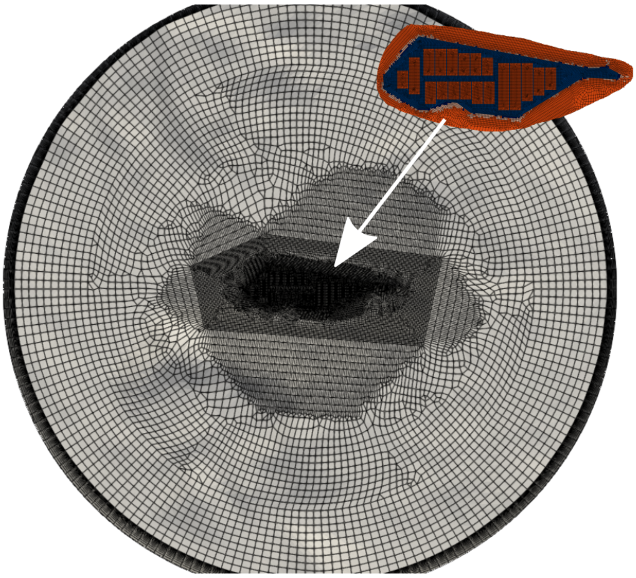

(b) *Mesh structure of the FPV2 microclimate case*

Ground conditions

Ground conditions are established based on reading of the ground occupations available in the THEIA database. Reading is carried out at the beginning of the code_saturne preprocessing stage, and land parcels are assigned to a virtual numerical field. A pre-processing operation is carried out in order to match the virtual field to a particular roughness. For this step, two types of soil are dissociated: forests whose roughness is set at $z_0 = 0.75\,\mathrm{m}$ and fields ($z_0 = 0.05\,\mathrm{m}$). For these two zones, the scalar quantities are fixed at $\mathrm{T}_p = \mathrm{T}_{p,amb}$ and $q_w = 0\left(\mathrm{kg\,kg^{-1}}\right)$; a rough wall law is also applied. A Charnock-type roughness condition is applied on the lake surface, such as $z_0 = 0.012 \times \frac{u_\star^2}{9.81}$, see Charnock, 1955. The Glanz and Orlab scalar law combined with a rough wall law is applied for the specific humidity, it reads: $q_{w,s} = 1.35 \times 10^5 \times exp\left(\frac{-4157}{T_{\mathrm{wat}}-33.91}\right)$ with $q_{w,s}$ in $\mathrm{kg\,kg^{-1}}$ and T_{wat} in K, see Condie and Webster, 1997. A temperature Dirichlet is also applied. In the photovoltaic island area, the initial conditions of the lake are swallowed. A wind angle-dependent roughness law is created, while the rough wall function is modified to account for the evaporation under the modules. These two features are discussed in the next section. It is noted that, in order to respect the bi-periodic studies of the previous section, a zero thermal flux condition is applied to the ground. The heat released by the modules is introduced into the system as a volume source adjacent to the faces associated with the plant.

	Colour	z_0 (m)	T_p Condition	q_w Condition $\left(\mathrm{kg\,kg^{-1}}\right)$
Reservoir	blue	$0.012 \times \frac{u_\star^2}{9.81}$	$\mathrm{T}_p = 294.45\,\mathrm{K}$	$q_w = q_{w,s}$
Forest	grey	0.75	$\mathrm{T}_p = 296.45\,\mathrm{K}$	$q_w = 0$
Crops	green	0.05	$\mathrm{T}_p = 296.45\,\mathrm{K}$	$q_w = 0$
Solar array	orange	$z_0(\theta_{\mathrm{w}}^{\mathrm{atm}})$	$\Phi = 0\,\mathrm{W\,m^{-2}}$	$q_w = q_{w,s}$

Table 7.1–*Characteristics of the surface mesh for the different areas represented in Figure 7.2*

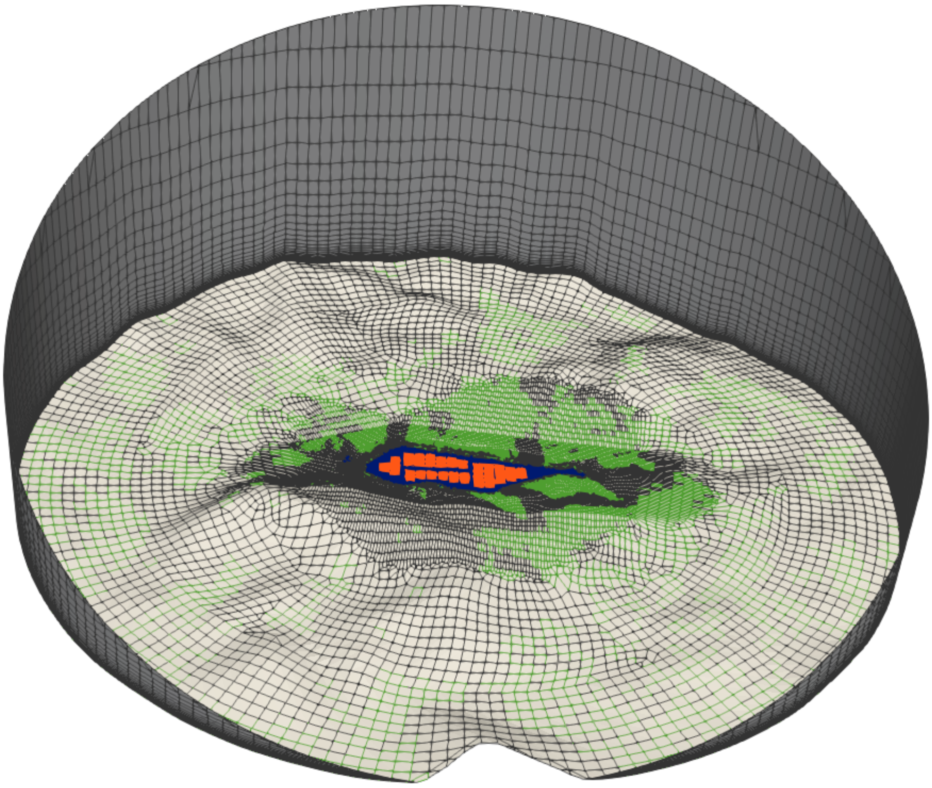

Figure 7.2–*Schematic of the boundaries of the control volume. The bottom boundary conditions are coloured accordingly to the land-use enumerated in Table 7.1.*

Volume conditions

Cells are initialised on the basis of the theoretical velocity profile and scalar profiles at the boundaries of the domain.

7.2.3/ Computational Parameters

Source terms

The heat source from the modules to the atmosphere is integrated into the cells whose bottom edge is tagged as the surface of the solar power plant. The source term ϕ in the equation (2.3) is adapted for each of these cells, it reads ϕ_{im}. The heat flux delivered by cells is calculated from the size of the bottom surface of the cell and the unit heat flux of an explicit pattern, denoted ϕ_{ex}. It is recalled that the flux density delivered in the explicit pattern must be weighted by the area over which a plant pitch is established. Considering a flux density Φ of $250\,\mathrm{W\,m^{-2}}$ per face of the module ($\mathcal{L}_\mathrm{m} = 1\,\mathrm{m}$) and a pitch of $\mathcal{S}_\mathrm{m} = 1.33\,\mathrm{m}$, the flux density becomes $\phi_{ex} \simeq \Phi \times 2 \times \mathcal{L}_\mathrm{m}/\mathcal{S}_\mathrm{m} \rightarrow \phi_{ex} \simeq 376\,\mathrm{W\,m^{-2}}$. The source term becomes $\phi_{im} = S_c \times \phi_{ex}$ in which S_c is the edge surface of the cell in the simulation where the power plant is implicitly represented. Note that the density of fluxes other than that from the module surfaces is considered to be negligible in ϕ_{ex}. These operations are performed in a user file *cs_user_source_term.c*.

Note that the choice of including a source term instead of including a Neumann condition for the solar array cells is made with regard to the ease of later integrating realistic boundary conditions, based on ground or lake models. In the case study, doing one or the other does not interfere with the solutions or the calculation procedure.

Numerical schemes

The RANS equations are solved in the dry atmosphere flavour; the closure turbulence model $k-\epsilon LP$ (Guimet & Laurence, 2002) is applied to determine the Reynolds stress. The pressure-velocity coupling is handled with the SIMPLEC algorithm. Second-order convective schemes are enforced for velocity and scalars. A first-order time scheme is used (Euler implicit; see (Amino et al., n.d.)).

7.3/ A New Method to Upscale PV Array Impact on the Micro-meteorology

In this section, the work carried out in the previous chapter is rearranged in order to construct wall functions capable of reproducing the effects of the FPV2 floating plant on the macroscopic airflow. Three relations are constructed, they correspond to the effects on the dynamics, on the evaporation, and on the heat exchange at the front face of the modules. In this section, the point of view adopted is that of the atmosphere so that we seek to determine relationships that are invariant to the atmosphere natural scales. The assumptions of the neutral atmosphere and operating conditions associated to high Reynolds values are elaborated.

7.3.1/ Wall Function for Momentum Using a Wind Direction Roughness

In the previous chapter, we discussed the influence of plant geometry on the roughness parameter. We also studied the robustness of the method for determining roughness as a function of external parameters such as atmosphere height $\mathcal{H}_{\text{atm}}$ or friction velocity $u_\star$, which was the boundary condition at the top of the domain. In Figure 6.10, we showed that the roughness length was invariant with this atmospheric parameter. Following this logic, we propose to calculate the roughness parameter for the FPV2 geometry as a function of all possible wind angles. From an atmospheric point of view, we must transpose the angles into the atmospheric reference frame, which is enforced in code_saturne.

The results of the simulations carried out to analyse the convective evolutions of the FPV2 geometry are adapted to the atmospheric frame. Figure 7.3 shows the evolution of roughness lengths as a function of the wind angle. It is recalled that the photovoltaic system faces south; therefore, the atmospheric wind $\theta_{\text{w}}^{\text{atm}} = 0°$ corresponds to a wind coming from *behind* the module.

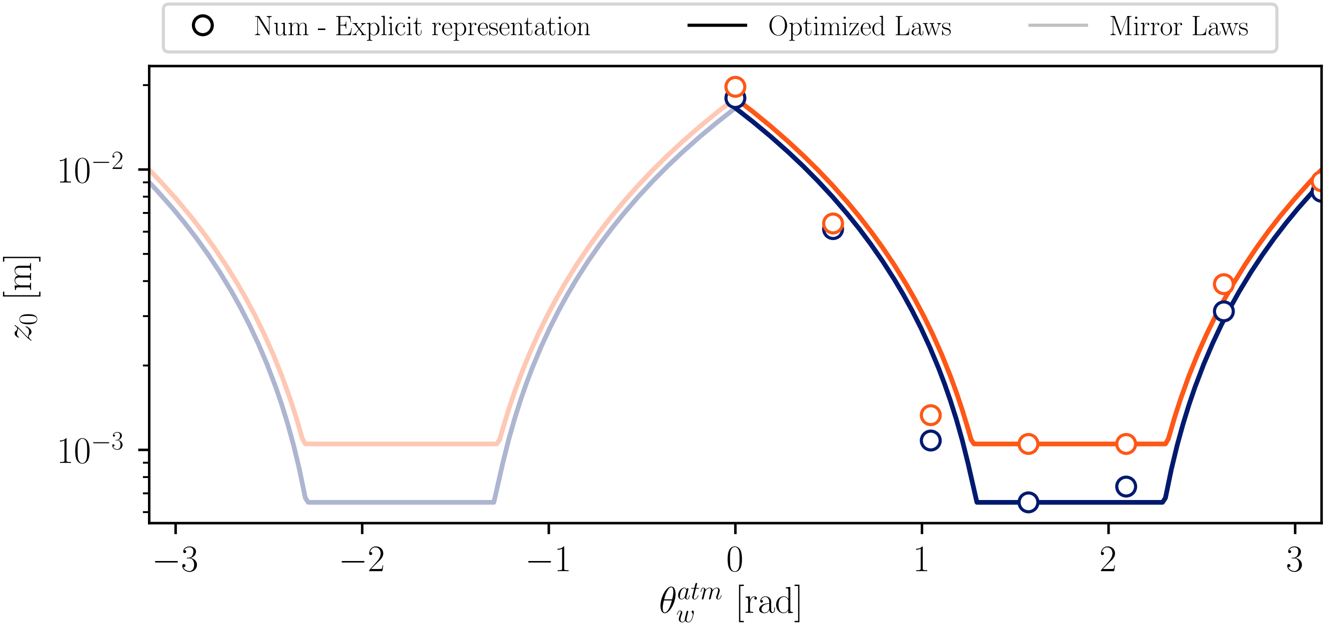

Figure 7.3–*Evolution of the ratio of roughness length per the friction velocity with regard to the wind angle (written with the atmospheric convention); obtained from the simulation of the explicit case. The solid lines* –, –, *show the second-order fitting functions for respectively* $u_\star = 0.36\,\text{m}\,\text{s}^{-1}$, $u_\star = 0.67\,\text{m}\,\text{s}^{-1}$. *Transparent lines are the reciprocal functions.*

The results of the simulations show that the invariance of the relative roughness is rather good for the perpendicular winds ($\theta_{\mathrm{w}}^{\mathrm{atm}} \in [0°, 30°]$). Small errors are still noticeable and can be related to a small difference in convergence between the two simulations. The errors are larger for crosswinds, but the orders of magnitude remain consistent between the simulations. The maximum influence of the structure on the aeraulic profile occurs when the winds are perpendicular to the module in a direction $\theta_{\mathrm{w}}^{\mathrm{atm}} = 0°$. This result agrees with the simulations carried out in Section 6.5.4. The influence then decreases as the wind direction changes, with the minimum reached for directions transverse to the module. Then again a local maximum is reached for crosswinds blowing at the front of the modules. It is noted that the orders of magnitude of the maxima are consistent with each other; they are only approximately one order of magnitude apart from the global minimum. In this particular configuration, the same behaviour assessed with the ground morphometry study is observed: the influence of the power plant on the atmosphere varies according to the directional characteristics of the atmosphere and those in a significant way. These observations corroborate the results demonstrated in Figure 6.13.

A second-order polynomial law is proposed to describe the continuous evolution of roughness as a function of the direction of the wind. The most conservative law with respect to the influence of the system on the flow dynamics fitted using $u_\star = 0.67\,\mathrm{m\,s^{-1}}$ reads :

$$\begin{cases} z_0 = 5.76{\theta_{\mathrm{w}}^{\mathrm{atm}}}^2 - 20.64\theta_{\mathrm{w}}^{\mathrm{atm}} + 17.97, & \text{for } \theta_{\mathrm{w}}^{\mathrm{atm}} \in [0; r_1] \cup [r_2; \pi] \\ z_0 = 1.05, & \text{for } \theta_{\mathrm{w}}^{\mathrm{atm}} \in [r_1; r_2] \\ z_0 = 5.76{\theta_{\mathrm{w}}^{\mathrm{atm}}}^2 + 20.64\theta_{\mathrm{w}}^{\mathrm{atm}} + 17.97, & \text{for } \theta_{\mathrm{w}}^{\mathrm{atm}} \in [-r_1; 0[\cup [-\pi; -r_2] \\ z_0 = 1.05, & \text{for } \theta_{\mathrm{w}}^{\mathrm{atm}} \in [-r_2; -r_1] \end{cases} \tag{7.1}$$

With z_0 in mm and $\theta_{\mathrm{w}}^{\mathrm{atm}}$ in rad. Two threshold values are established to remain in $\mathbf{R}_+^*$. They are fixed by the minimal numerical value of z_0. $r_1 \simeq 1.49$, $r_2 \simeq 2.10$ being the two roots of the second-order equation.

Before introducing the law directly into the microclimatic mesh, a final step consists of testing its effectiveness in a simplified case of a 1-D atmosphere.

From now on, let *exp* and *imp* be the subscripts that correspond to simulations carried out with an explicit representation of the modules (or ”full representation”), and simulations carried out with an implicit representation of the modules (1-D atmosphere or 3-D microclimate).

The 1-D atmosphere case is constructed from the same initial and boundary conditions as the explicit case. The roughness law is applied to the cell at the bottom of the domain[1]. The 1-D atmosphere model is simulated for the 7 wind directions incident to the explicit model. Figure 7.4 shows the wind profiles obtained by the implicit model using the numerical law, compared to the explicit model. Ideally, the implicit 1-D atmosphere model should result in a logarithmic profile that can also be represented analytically using Equation (2.14) by modulating the value of z_0.

We first check that the method of determination of z_0 by the explicit model is consistent because of its suitability to the atmospheric analytical model. The working hypotheses are well verified. The implicit model also shows a very good agreement of the velocity profiles with the analytical model for all wind directions. The best estimates are valid for the perpendicular winds, whereas the slight differences found when creating the numerical law remain valid for the crosswinds. The

---

[1] Numerically, this corresponds to overloading the roughness value of the wall law in *cs_user_boundary_conditions.c* by calling the function f_roughness[f_id] where f_id represents the ground face

maximum difference between the profiles reaches 11% in the worst case ($\theta_{\mathrm{w}}^{\mathrm{atm}} = 90°$). Therefore, the implementation of the numerical law is considered sufficiently robust, and its use will be favoured in the most favourable circumstances possible (perpendicular winds established).

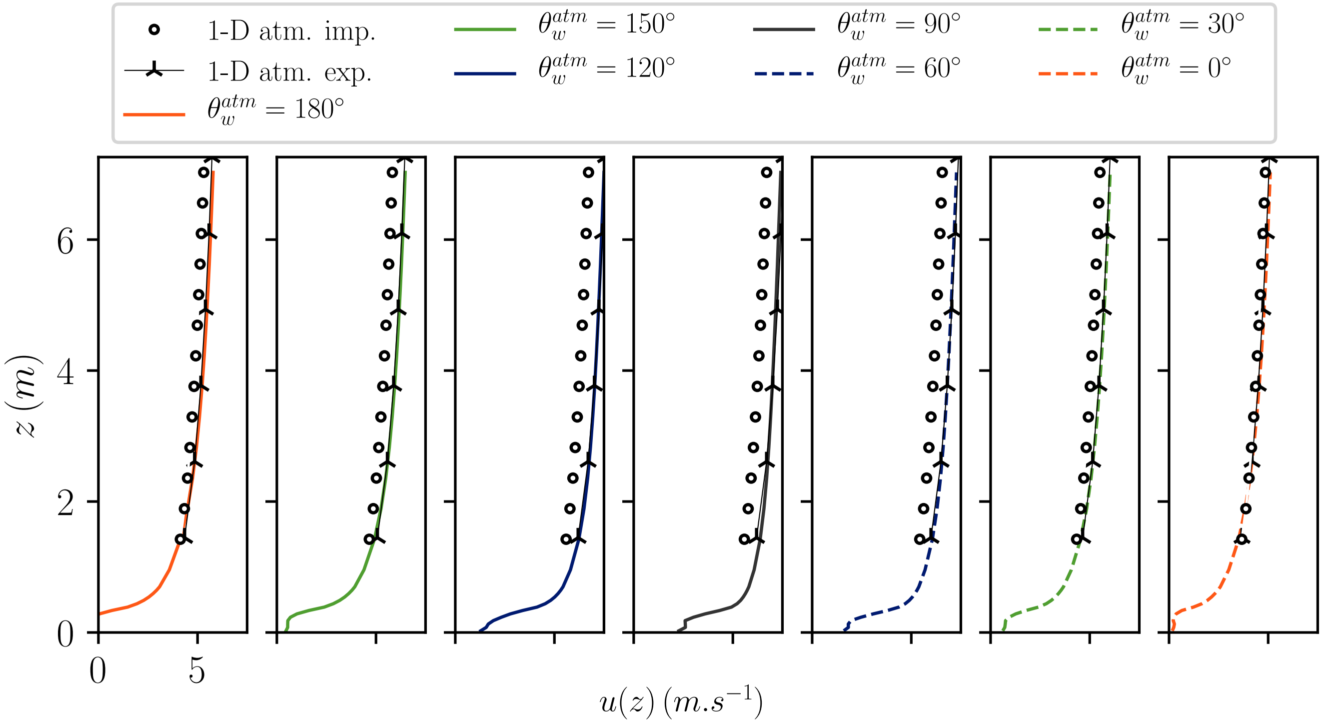

Figure 7.4–*Velocity profiles for explicit simulations of FPV modules and implicit simulations using the numerical law developed in Equation* (7.1)*. Each subplot corresponds to a specific wind direction from* $\theta_w^{atm} = 180°$ *(left-hand side) to* $\theta_w^{atm} = 0°$ *(right-hand side).*

It is concluded that the methodology developed for the calculation of roughness is consistent for winds perpendicular to the modulus. This result supports the validation of the methodology with respect to the value of $u_\star$, while extending the application spectrum to additional directions. The effect of crosswinds on the plant is less well captured. The latter phenomenon can be related to the small footprint of the structure with respect to the wind profile and the bi-periodic methodology. The High-Reynolds assumption is no longer necessarily suitable under these conditions ($Re_\star \simeq 10 \times U_\infty$). It is assumed that the integration of additional elements in the longitudinal plane could improve the prediction by naturally increasing the roughness value. In our floating case, floating or load-bearing structures could be considered. The deviation between implicit models and the analytical law also supports the weakness of the numerical wall law for very low z_0 values (i.e., without any overloading of the roughness value).

— 7.3.2/ Wall Function for Humidity Adapted to Half-opened Structures —

Recalling that for a prescribed geometry, the rates can be expressed with the dimensionless parameters:

$$Sh = f\left(Re_L, Sc\right) \tag{7.2}$$

The Reynolds friction number can be written as $Re_\star = u_\star z_0/\nu$ and the Sherwood number can be expressed as: $S_h = h_E L/D_m$ where L is the characteristic length of evaporative transfer. Rearranging the terms in the prior equation, we can write:

$$S_h(Re_L) \implies \frac{h_E L}{D_m} \propto \frac{u_\star z_0}{\nu} \tag{7.3}$$

Seeing that $h_E/u_\star \propto \frac{D_m z_0}{\nu L}$, the ratio $h_E/u_\star$ is by nature invariant.

The transfer rates for both cases can be written as follows:

$$\begin{cases} \left(h^Y\right)_{ex} = & \frac{\kappa}{\mathcal{H}_{\text{atm}}} \times \left(\frac{y^+}{Y^+}\right)_{ex} \\ \left(h_I^Y\right)_{im} = & \frac{\kappa}{d} \times \left(\frac{y^+}{Y^+}\right)_{im} \end{cases} \tag{7.4}$$

Where $\left(h_I^Y\right)_{ex}$ is calculated over the entire length of the atmosphere $\mathcal{H}_{\text{atm}}$, on the other hand, $\left(h_I^Y\right)_{im}$ is calculated solely for the first cell height d on the implicit surface. When scaling the wall function, the objective is to keep the scalar profile consistent. Mathematically, it reads:

$$\left(h_I^Y\right)_{im} = \left(h_I^Y\right)_{ex} \times \frac{\mathcal{H}_{\text{atm}}}{d} \times \frac{(y^+)_{ex}}{(y^+)_{im}} \tag{7.5}$$

Rearranging the terms in the previous system of equations, one may see that the quantity $\left(h_I^Y\right)_{ex}/(Re^*)_{ex}$ is constant for different $Re*$ as follows:

$$\left(\frac{h_I^Y}{Re^*}\right)_{ex} = \frac{\kappa}{\mathcal{H}_{\text{atm}}} \times \left(\frac{1}{Y^+}\right) \tag{7.6}$$

As a consequence of Equation (A.53) and Equation (7.3).

In Equation (7.5), the term $\left(h_I^Y\right)_{ex}$ is computed using a resistive analogy. Figure 7.6 shows the philosophy of the operation, the evaporative term being expressed at a fictitious surface height between the tip of the module and the bottom. The evaporation is as follows:

$$\begin{cases} \phi_E = \dfrac{\left(q_{=1} - q_{z_m}\right)}{R_{\text{m}}} \\ \phi_E = \dfrac{\left(q_{z_m} - q_{=0}\right)}{R_{\text{atm}}} \end{cases} \tag{7.7}$$

From the system (7.7), it reads:

$$q_{z_m} = \frac{R_{\text{atm}} q_{=1} + R_{\text{m}} q_{=0}}{R_{\text{m}} + R_{\text{atm}}} \tag{7.8}$$

Hence, the evaporative flux can be rewritten as:

$$\phi_E = \left(\frac{R_{\text{atm}} R_{\text{m}}}{R_{\text{atm}} + R_{\text{m}}}\right) \times \left(q_{=1} - q_{=0}\right) \tag{7.9}$$

From which a dimensionless humidity law can be derived as:

$$\frac{y^+}{q^+} = \frac{\mathcal{H}_{\text{m}} u_k}{\nu} \frac{q_\star}{q\left(z = \mathcal{H}_{\text{m}}\right) - q_{sol}} \tag{7.10}$$

with $y^+ = \frac{\mathcal{H}_\mathrm{m} u_k}{\nu}$.

Several tests are carried out to determine the optimal height to calculate evaporative resistance. As the system is regular, but has areas of varying degrees of air recirculation depending on the direction of flow, it is decided not to complicate the problem by selecting the median height at the module. This height provides effective results in all directions of the wind. Figure 7.5 shows the results of the evolution of the evaporative transfer parameter assuming the median height as reference. Similar orders of magnitude are observed for the points obtained by the simulation, mainly for the winds perpendicular to the module. A divergence of results is noticeable for winds blowing on the back side, transverse to the module. The model with the lower friction velocity gives a higher prediction of the evaporative coefficient, while the higher velocity gives smaller magnitude coefficients. Two hypotheses are possible here, the model has not yet reached a steady state, or the methodology has a weakness in capturing near-wall phenomena when the wind profile observes a recirculation zone in the vicinity of the studied surface. The second hypothesis appears to be the most likely one, as it implies a certain dependence on the turbulence model and the selected model not being specifically robust to capture this type of recirculating flow.

These significant differences inevitably lead to a difference in the $h_E/u_\star$ connection laws. The law determined from the points with $u_\star = 0.36\,\mathrm{m\,s^{-1}}$ obtains a stronger magnitude in general than the law with $u_\star = 0.67\,\mathrm{m\,s^{-1}}$, we will select the first one for the sake of consistency, while keeping in mind that it is a rather pessimistic assumption when trying to quantify gains in water conservation in the reservoir. It is defined as :

$$\begin{cases} h_E/u_\star = -6.39{\theta_\mathrm{w}^\mathrm{atm}}^2 + 16.77\theta_\mathrm{w}^\mathrm{atm} + 15.18, & \text{for } \theta_\mathrm{w}^\mathrm{atm} \in [0;\pi] \\ h_E/u_\star = -6.39{\theta_\mathrm{w}^\mathrm{atm}}^2 - 16.77\theta_\mathrm{w}^\mathrm{atm} + 15.18, & \text{for } \theta_\mathrm{w}^\mathrm{atm} \in [-\pi;0[\end{cases} \tag{7.11}$$

The law shows adequate behaviour with respect to the observed evolution of the numerical evaporation rates, with a local maximum obtained when the aerodynamic drag is very low, which is the case for crosswinds. The law tends to be ahead of the experimental point and to obtain a global maximum for wind directions slightly behind the module. The direction of the wind behind the module is more impactful for the evaporation, and it is assumed that the increase in turbulence in the area under the modules is one of the causes of this phenomenon. On the contrary, a floating plant with winds facing the front face of the module appears as a rather compact aerodynamic structure that prevents evaporative development.

Following the same strategy as for the calculation of the roughness coefficient as a function of wind direction, the methodology is first applied to the implicit atmospheric case, ensuring that the evaporative transfer rate and the roughness parameter are varied in accordance. In this way, it is expected that the water vapour transport is identical to that obtained in the implicit case. As the boundary conditions between the two cases are identical, it is also expected that similar mass fraction profiles will be obtained.

This experiment was unsuccessful with direct use of the evaporative law. Although orders of magnitude were respected, the numerical transfer rates were lower and resulted in the development of a moisture profile that was too low in magnitude. Therefore, a relaxation law was introduced to modulate the evaporation rate. A multiplicative constant was added to Equation (7.11). The value of 2.6 was chosen.

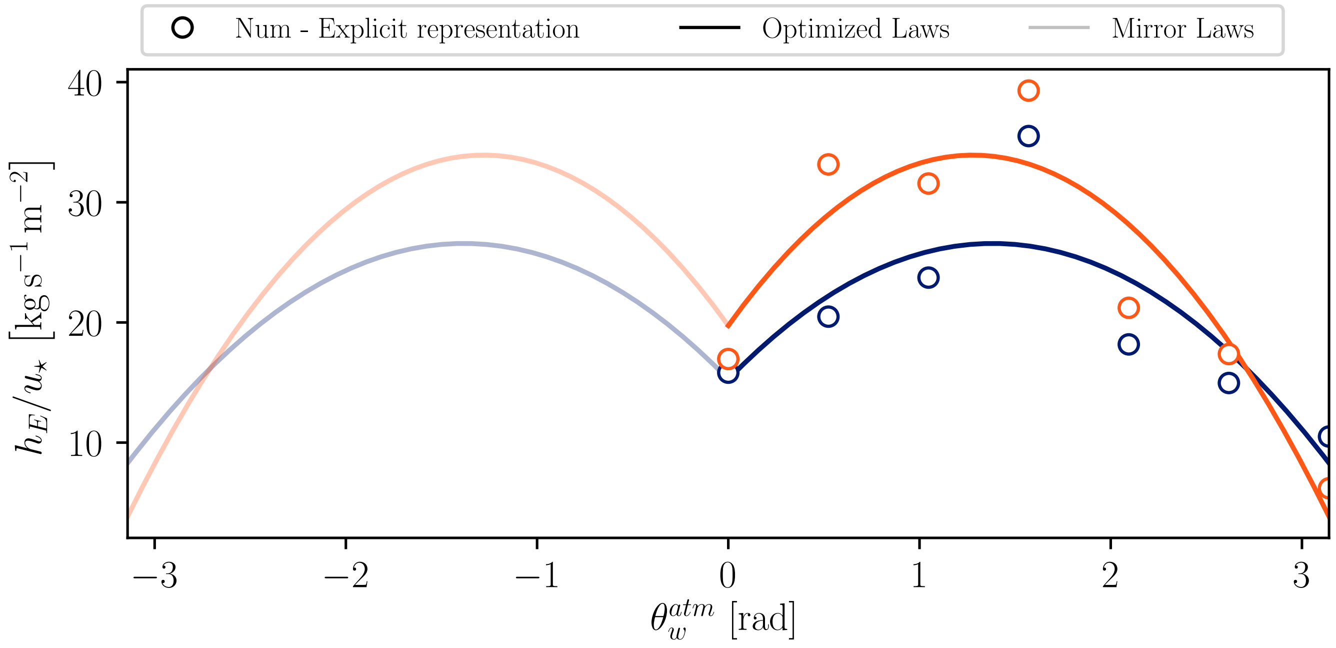

Figure 7.5–*Numerical laws adapted for the evaporative rates of transfer h_E*

Figure 7.7 shows the mass fraction profiles compared for the two representations of the plant, and those as a function of the direction of the atmospheric wind. The profiles obtained with the implicit method show a good consistency on the part that develops according to a logarithmic law and for all wind directions. Near the surface, the implicit method shows orders of magnitude similar to the explicit method, and the coherence is only effective after a height of 1 m, which corresponds globally to the distance foreseen for the integration of the fields in the roughness calculation. It can be concluded from this simplified experiment that the numerical evaporation rate is consistent for a large-scale application. Note that the use of a relaxation law is necessary to modulate the integration height of the mass fraction, which can be compared with the reproduction of a turbulent phenomenon that acts on the transport of the vapour near the modules. The absence of a law inevitably leads to inconsistency in the results, but it should be noted that the order of magnitude remains consistent with the explicit law.

7.3.3/ Reconstruction of the Panel Surface Temperature

Recalling that for a prescribed geometry, the heat rates can be expressed with dimensionless parameters:

$$Nu = f\left(Re_L, Pr\right) \tag{7.12}$$

Therefore, the Reynolds number can be written as: $Re_\star = u_\star z_0/\nu$ and the Nusselt number can also be expressed as: $Nu = h_{fr}^{\mathrm{cv}} L/\lambda$. Rearranging the terms in the prior equation, we can write:

$$Nu = f\left(Re\right) \implies \frac{h_{fr}^{\mathrm{cv}} L}{\lambda} \propto \frac{u_\star z_0}{\nu} \tag{7.13}$$

Seeing that $h_{fr}^{\mathrm{cv}}/u_\star \propto \frac{\lambda z_0}{\nu L}$, the ratio $h_{fr}^{\mathrm{cv}}/u_\star$ is by nature invariant.

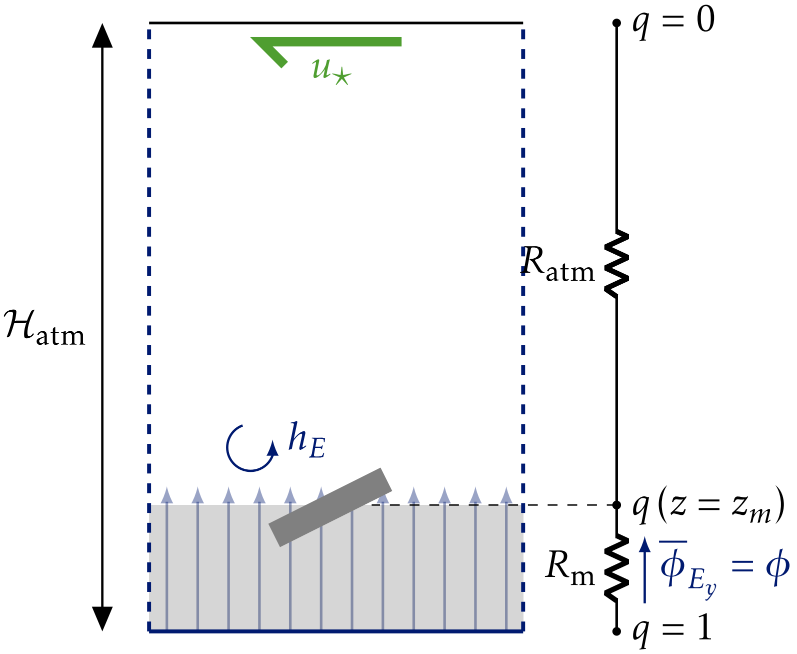

Figure 7.6–*Schematic of the resistive analogy for the calculation of* $h_{\mathrm{E}}(\mathcal{H}_{atm}, u_\star)$

In the previous chapter, the point of view of the power plant was adopted. Thus, the calculation of the convective transfer rates was obtained directly by numerical calculation using the value on the surface of the module and a reference temperature. The convective transfer rate determined was therefore of the form $\phi_H^{(1)} = h_{fr}^{\mathrm{cv}}(u_\star, \theta_{\mathrm{w}})\left(T_{fr,1} - T_{REF,1}\right)$. We will write $h_{fr}^{\mathrm{cv}} = h_{fr}^{cv}$ to quote this construction of the transfer rate. The set of boundary conditions adopted in the 3-D case does not allow the use of the surface temperature because it does not correspond to the temperature of the modules but to a representative ground temperature for the dynamic and thermal development of the atmosphere. It is necessary to construct the transfer rate law from the representative temperature with respect to the atmosphere when introducing a volume heat source that represents the heat loss of the photovoltaic modules. In these circumstances, this representative temperature is determined by comparing the potential temperature profiles obtained with the explicit representation of the modules against the profile obtained with the implicit representation, reusing the one-dimensional atmospheric case developed in the previous two subsections.

Figure 7.8 shows these two cases for all wind profiles entering the module. Note that the objective of this manipulation is to find concordant temperatures between the two representations, as the atmospheric profiles are not necessarily identical. In all cases, the profiles obtained by implicit laws intersect those obtained by the explicit law at variable heights z. They are all contained in a space $\mathcal{H}_{\mathrm{m}} < z < 2\mathcal{H}_{\mathrm{m}}$. The shape of the atmospheric profiles obtained by the implicit methodology is rather in agreement with those obtained by the explicit methodology, the profiles do not cross each other when going up in altitude. The most practical representative temperature is approximately $z \simeq 1.5\mathcal{H}_{\mathrm{m}}$ and thus of the order of 0.5 m. We will note this temperature $T_{REF,2}$.

Knowing $T_{fr,1}$ from the explicit model, the heat flux density delivered to the atmosphere at the height of the first cell of the 3-D microclimatic case is transferred to a more convenient form for the atmospheric problem as:

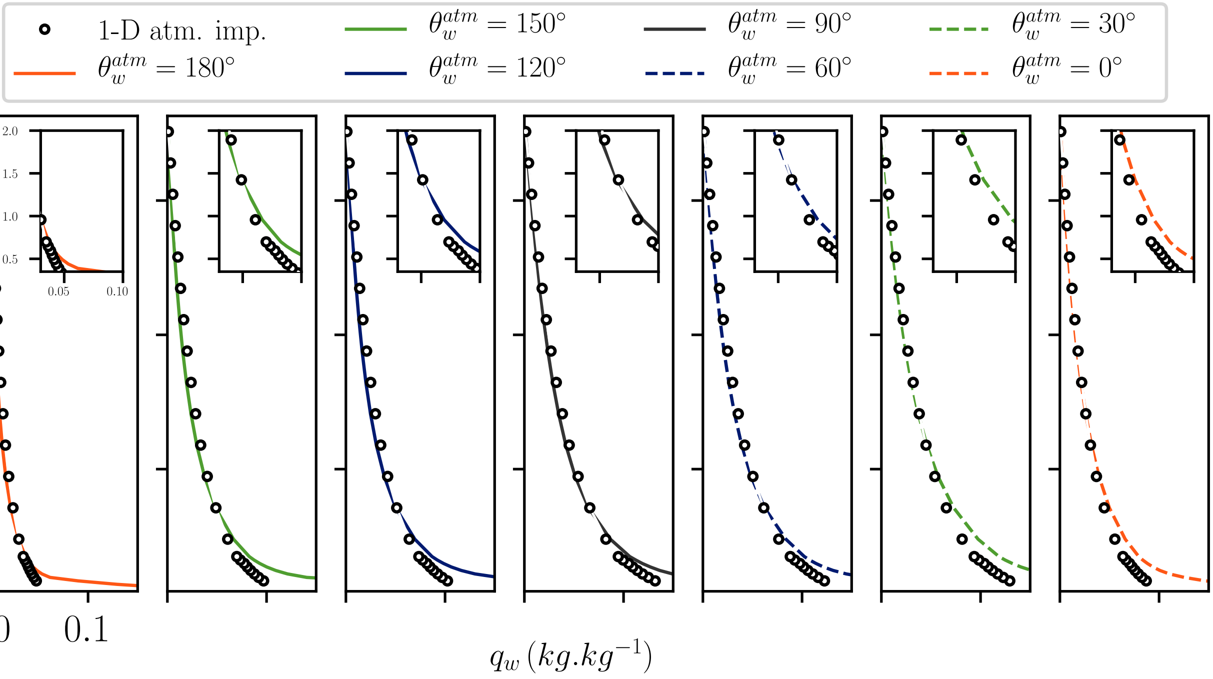

Figure 7.7–*Humidity profiles for all wind directions from* $\theta_w^{atm} = 180°$ *(left-hand side) to* $\theta_w^{atm} = 0°$ *(right-hand side). They are obtained with the explicit bi-periodic model (solid lines) and with a 1-D atmosphere model whose ground roughness condition is overloaded by the wall law defined by Equation (7.6).*

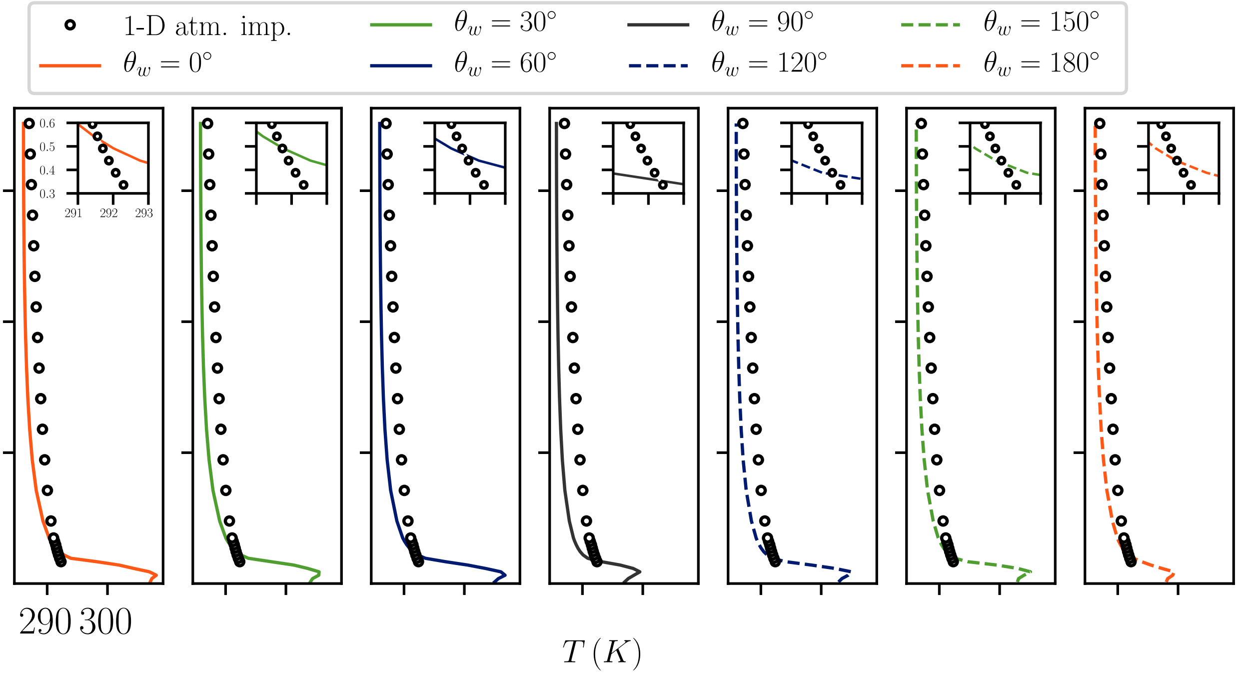

Figure 7.8–*Comparison of temperature profiles between 1-D atmosphere simulation including a volume heat source at the first cell above the ground and the simulation with ex modules. Seven wind directions are investigated from* $\theta_w^{atm} = 180°$ *(left-hand side) to* $\theta_w^{atm} = 0°$ *(right-hand side).*

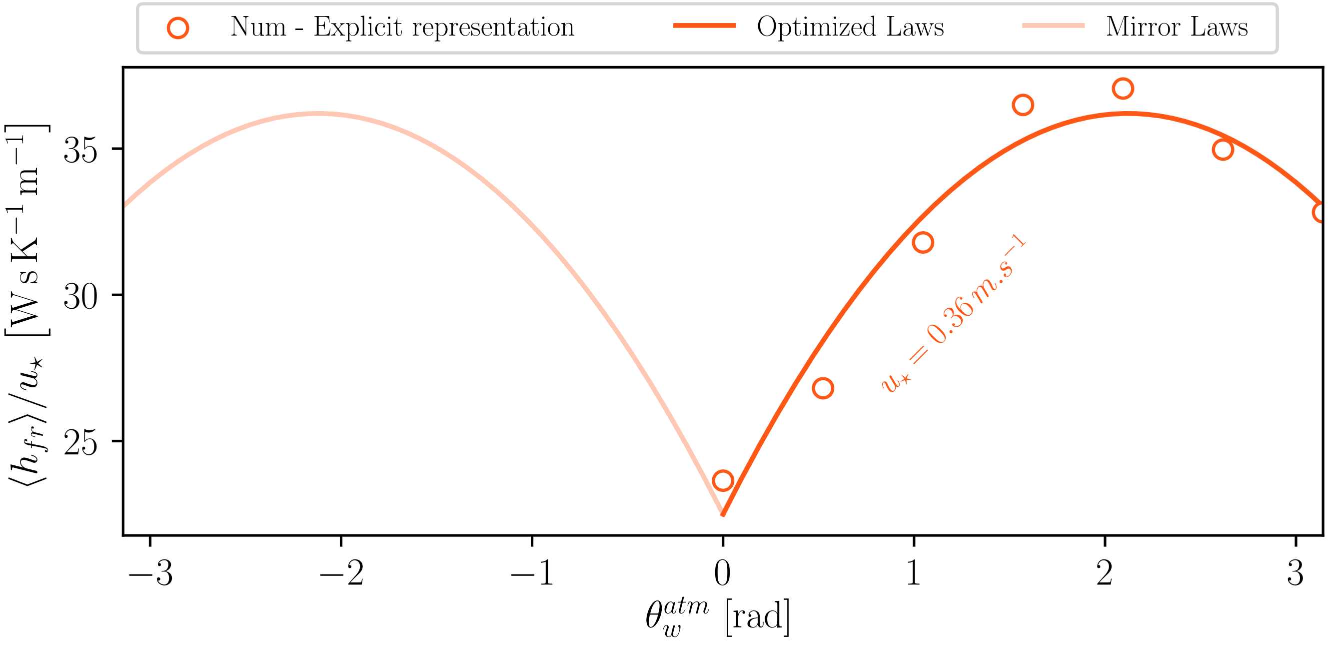

Figure 7.9–*Evolution of the ratio of front convective rate per the friction velocity with regard to the wind angle (written with the atmospheric convention). The solid lines (−) shows the second-order fitting functions for respectively* $u_\star = 0.36\,\mathrm{m\,s^{-1}}$. *Transparent line is the reciprocal function.*

$$\phi_H^{(1)} = h_{fr}(u_\star,\theta_\mathrm{w})\left(T_{fr,1} - T_{REF,2}\right) \tag{7.14}$$

Considering that the average height of the first cell above the surface on the 3-D microclimate scale is approximately 0.45 m which corresponds to approximately 10% of the height necessary to obtain the representative temperature $T_{REF,2}$ in the explicit model. The application of this law in the explicit case allows us to obtain the value h_{fr}^{cv}. Figure 7.9 presents its application, considering the invariance of $u_\star$, for all wind directions of the treated problem, as well as the second-order law that verifies the experimental numerical points. As expected, the convective transfer coefficient for the front face shows a local minimum when the atmospheric wind sweeps the module perpendicularly through the back face. The maximum is obtained for crosswinds and rather from the front of the module. This law is logical and follows the developments of the last chapter, this time with the atmospheric view of the system. The equations of the optimised law give :

$$\begin{cases} \dfrac{h_{fr}^{\mathrm{cv}}}{u_\star} = -3.05\theta_\mathrm{w}^{\mathrm{atm}^2} + 12.9\theta_\mathrm{w}^{\mathrm{atm}} + 22.5, & \text{for } \theta_\mathrm{w}^{\mathrm{atm}} \in [0;\pi] \\ \dfrac{h_{fr}^{\mathrm{cv}}}{u_\star} = -3.05\theta_\mathrm{w}^{\mathrm{atm}^2} - 12.9\theta_\mathrm{w}^{\mathrm{atm}} + 22.5, & \text{for } \theta_\mathrm{w}^{\mathrm{atm}} \in [-\pi;0[\end{cases} \tag{7.15}$$

To remain consistent with the use made of it afterwards, it will be recalled that the law makes it possible to return to the surface temperature of the module by the function :

$$\phi_H^{(2)} = h_{fr}(u_\star,\theta_\mathrm{w})\left(T_{fr,1} - T_{REF,2}\right) \tag{7.16}$$

In which $\phi_H^{(2)}$ is the heat source identical to the heat power delivered by the explicit modules, weighted by the size of the unit plant pattern. As a reminder, the heat flux density seen by the atmosphere includes both the module and the pitch attached to it. The latter is assumed to be an adiabatic surface for the purposes of the experiment.

7.4/ Assessment on the Physical Field Heterogeneity

In this section, we propose to study the heterogeneity phenomena that occur in the full-scale FPV2 power plant; the up-scaling methodology is implemented to capture array heterogeneity. In contrast to Section 6.3, heterogeneity is assessed over a larger distance and at a lower computational cost. The focus is put on the thermal heterogeneity (front-face temperatures); evaporative transfer magnitude is also discussed. It is decided to simulate only a single atmospheric condition with respect to the measurement campaign ($u_\star = 0.25\,\mathrm{m\,s^{-1}}$, $L_{MO} = 1$ and $\theta_\mathrm{w}^\mathrm{atm} = 0°$); however, other conditions can be implemented, as the up-scaling methodology has been made invariant to $u_\star$ and the variation of the quantities of interest with respect to $\theta_\mathrm{w}^\mathrm{atm}$ is already implemented.

7.4.1/ Spatial Evolution of Module Temperatures

From the representative boundary conditions of the FPV2 measurement campaign and by up-scaling the thermal conditions of the ground truth modules ($\Phi = 250\,\mathrm{W\,m^{-2}}$); the ambient temperature and wind velocity fields are obtained. The application of post-processing operations described in Section 7.3.3 gives the temperature level for the front face of the modules.

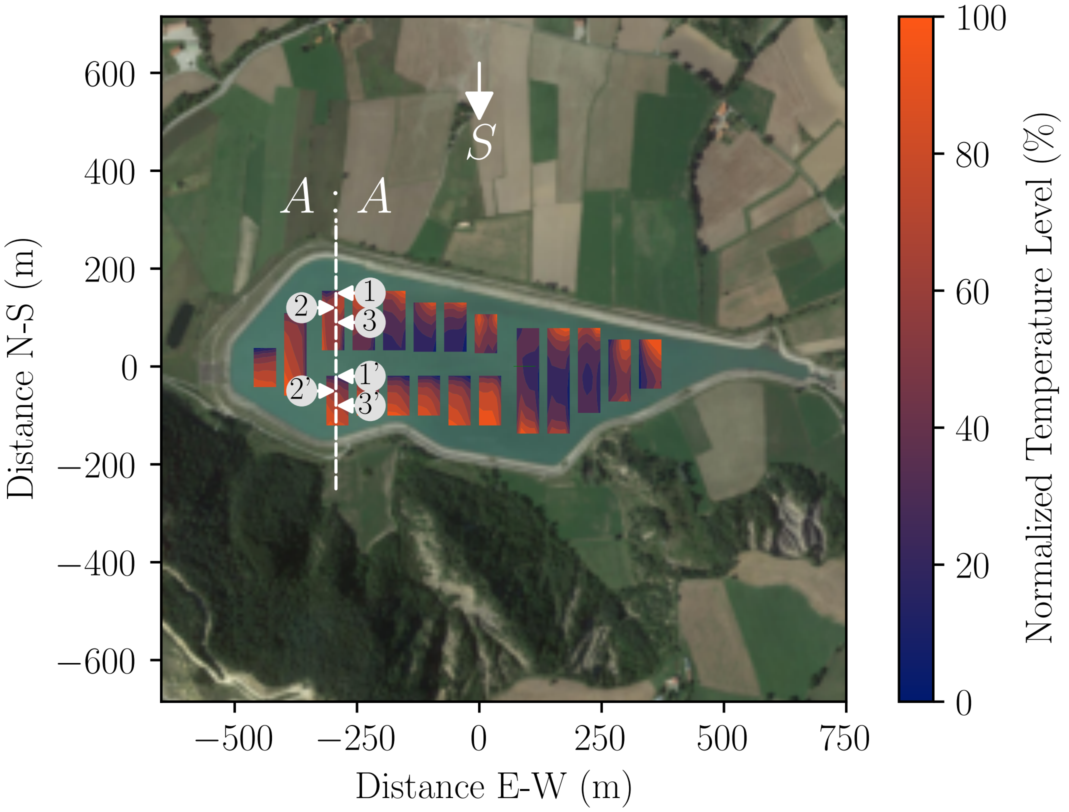

Figure 7.10–*Snapshot at* $ts = 4140\,\mathrm{s}$ *of the normalised temperatures of front module surfaces for the complete array at the FPV2 industrial site. The wind blows the array such as* $\theta_w^{atm} = 0°$. *A longitudinal cut is performed in the middle of the array to further investigation (A:A).*

Figure 7.10 shows in particular a snapshot of the normalised temperature when the steady state is reached. Normalised temperature is defined as: $T_{norm} = T_c - T_c^{min} / \left(T_c^{max} - T_c^{min}\right)$. It can be seen that the temperature distribution in the plant is not homogeneous, even within the floating sub-islands. Moreover, it seems that the evolution does not necessarily follow the direction of the flow as observed in the previous chapter. The islands to the north of the power station obtain warmer temperatures to the north than to the south, while the evolution of the islands to the north is reversed. Other blocks located more to the east show rather complex evolution with cold spots in the middle of the sub-blocks. The first conclusion is that macroscopic aeraulic movement influences the power plant even at distances more important than those obtained in the previous chapter ($\simeq 75\,\mathrm{m}$), it turns out that the heterogeneous regime is valid in all floating power plants. Here, the local effects of the modules on the flow are taken into account, in particular, the variations of wind angulation above the surface, which can be caused by the relief adjacent to the system. This was not the case in the previous chapter, which may explain the length of the heterogeneity found here.

When correlating the geographical positions of the hot and cold zones with the normalised temperature distribution in Figure 7.11, it can be observed that two particular regimes are frequently observed: a hot regime with a normalised temperature around 0.4 and a cold regime that remains around 0.25. Although the warm regime is clearly identified to the south of the southern islands and to the north of the northern islands, the cold regimes occur in the centre of the eastern islands and to the north of the southern islands. This observation corroborates the hypothesis that the established regime is not reached in the power plant, or else, in a very summary way at the end of the southern islands, we should have obtained a very pronounced Cauchy curve if this had been the case. Interestingly, the role of thermal management in the temperature distribution curve can be seen: the peak of cold modules is all the greater as many modules are located in the middle of the reservoir and benefit from the acceleration of the wind speed due to the low roughness of the water. The maximum temperatures obtained in Figure 7.11 are strangely obtained in the very north of the system, indicating either a numerical weakness in our approach or a topographic feature that acts significantly at these locations. Notable relief features include the change in roughness between the surrounding fields and the reservoir and the height of the reservoir relative to the adjacent pier. The first case is an implicit relief, which can be pre-processed during the calculation, while the second case is an explicit relief, which is difficult to preprocess. Following the specialised literature on hydrology as introduced in Chapter 1, it is likely that the condition on the location of the sub-islands does not verify the rule-of-thumb law $10 \times h_{embankment}$ from which the flow becomes constant.

7.4.2/ Stream-wise Evolution of Physical Fields

As shown in Figure 7.10, the A:A section line is used to visualise the evolution of the wind speed field and the scalar profiles at different points. Firstly, we focus on the longitudinal section shown in Figure 7.12 where the average wind speeds are represented. The difference in height between the embankment line and the water surface is clearly visible, which is 9 metres at this point, and therefore disturbances of the wind field are expected up to 90 metres after the embankment. First, it can be seen that a large recirculation zone is obtained at the northern edge of the lake, which is characterised by low average speeds at this location. At the beginning of the island, represented by the approximate line $x = 160\,\mathrm{m}$, the wind speed is disturbed; the isocontour lines are shifted upward. The beginning of the power plant is therefore subject to a weaker aeraulic regime at this location: this explains the temperature behaviour observed in the previous section for the northern islands. In fact, the embankment has a relatively constant height on all sides of the tank. We also note that the field lines decrease along the flow until they reach the end of the

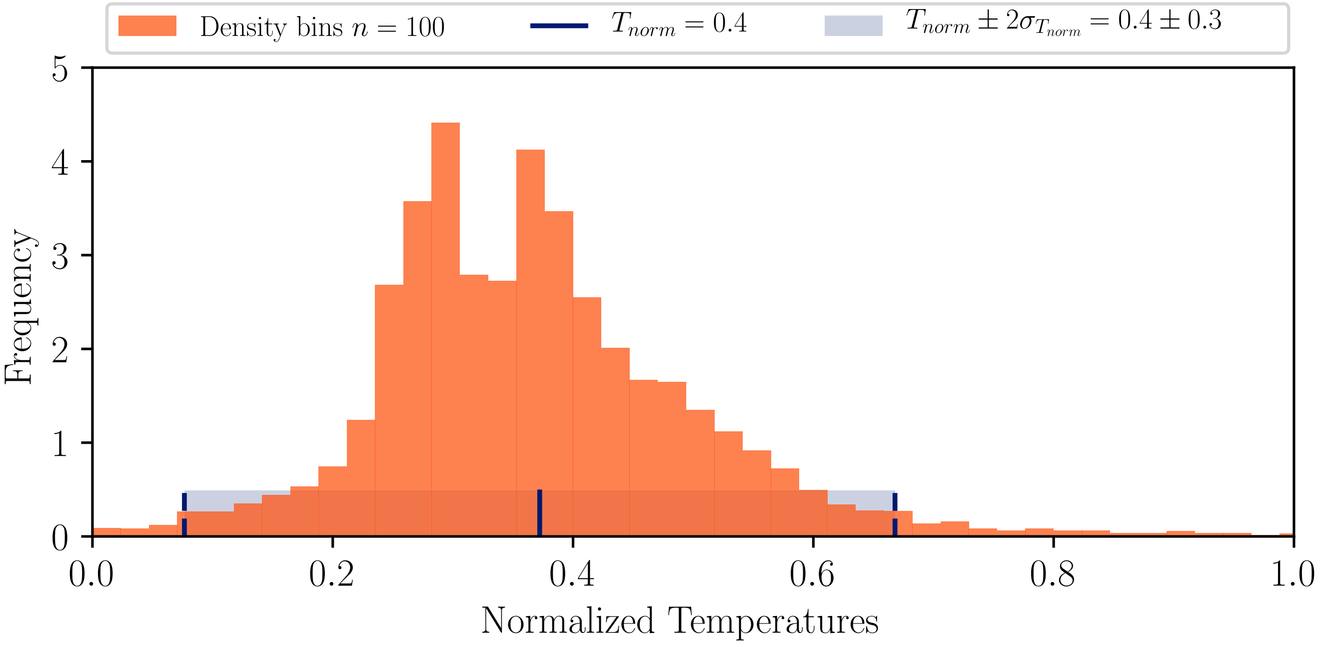

Figure 7.11–*Temperature predictions at the array scale for the nominal case study. The sum of the stick area is equal to one.*

first floating island; thus, we conclude that the temperature observations are indeed linked to the emergence of a recirculation zone that persists along the system.

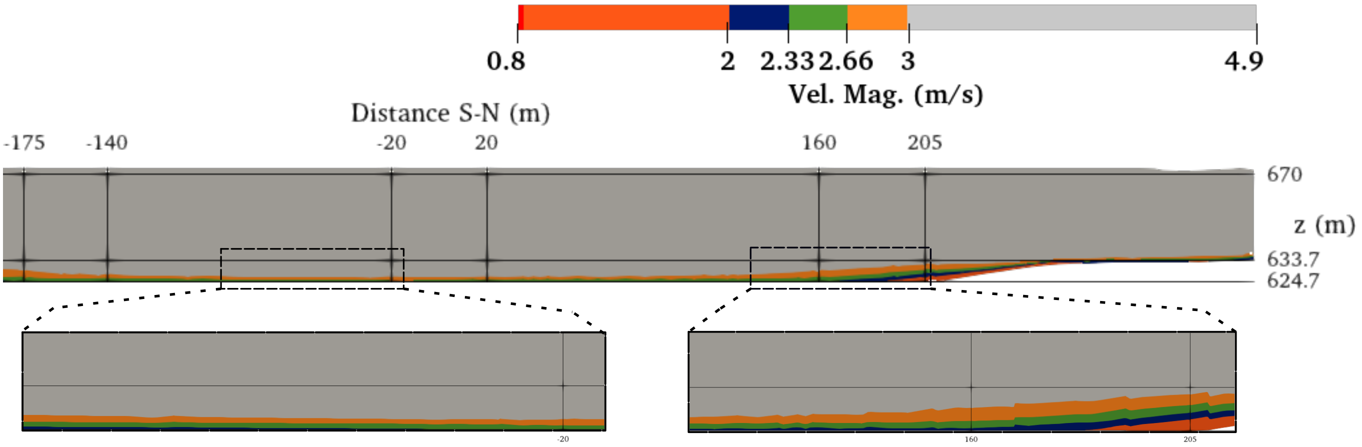

Figure 7.12–*Longitudinal cut of the atmosphere above the reservoir and the embankment. The location indicated on the snapshot corresponds to the approximate locations of the islands. The vertical line $x = 205$ m corresponds to the beginning of the reservoir as it is simulated in code_saturne. The colorbar shows the flow magnitude and its spatial evolution when the simulation is converged.*

In the second part of the lake where the second island is located, represented from the $x = -20$ m line, the airflow shows a weak upward evolution in the direction of the flow. This difference appears to be relatively small, as the roughness of the plant is not very high compared to environments with dense and high obstacles. Nevertheless, this evolution is well representative of the initially expected behaviour: the power plant acts as a brake on the flow dynamics, moreover compared to the initial lake surface which has a naturally reduced roughness. At the southern edge of the power plant, the flow does not seem to be fully established, and the field lines are still evolving at the end of the photovoltaic segment. The assumption of flow establishment after 5 modules is not validated in the case study. The length of flow establishment obtained in the explicitly represented land-based array (Section 6.3, 26 modules) is not valid for the study case. More than 40 modules are traversed along the southern sub-island without obtaining a converged front module temperature.

It is assumed that settlement conditions are functions of the geometric parameters of the power plant and that a lesser influence on the flow dynamics of the FPV geometry does not improve the achievement of a fast flow establishment. Under these conditions, the ”ideal” vision of the system is difficult to achieve for FPV plants whose island geometry depends on parameters that go beyond simple thermal management (bathymetry, available surface).

Figure 7.13 shows the atmospheric profiles (velocity magnitude, potential temperature and vapour density) at the six positions identified along the A:A line. The positions are elaborated with regard to the streamwise flow; points 1 and 1’ are representative of the entrance region of the flow above the north and south islands, respectively. Points 2, 2’, 3 and 3’ are located in the islands so that they are supposed to take into account the flow dynamic involved by the photovoltaic array. Measurement lines are also indicated in the figure; they can be compared with the profile line denoted 1 as they are representative of surface without or low impact of the photovoltaic array. The dynamic profiles show, indeed, that the wind speed in the first island evolves from high to low roughness, the speeds at the top of the domain accelerate along the flow. This results in an almost constant velocity at the ground level, and thus corroborates our hypothesis on the role of the bank in the macroscopic development. The aerodynamic development in the second island is consistent with a braking effect, the velocities at the end of the island are lower than at the entrance. This explains the evolution of the temperature profiles in the power plant for the southern part of the lake.

The temperature profiles show comparable behaviour between the two islands, the first modules of both islands experience low temperatures, while the islands in the flow direction have warmer operating conditions. In the first island, the temperature increase is lower than in the second island, and the flow dynamics in the first island could be one of the causes of this phenomenon. In both cases, the presence of islands heats the air surrounding the lake, which can alter the biophysical phenomena in the vicinity. It is also noted that the measured water temperature may not be suitable for describing the atmospheric profile as a boundary condition on the ground. The measured ambient temperature might be a better measure for this condition (moving the profiles to the ambient temperature measurement range). Furthermore, the increased temperature in the southern island reduces the heat transfer for the modules; therefore, it also explains why the heterogeneity goes from lower module temperatures in the upper part of the southern island to warmer temperatures in the middle of the array.

The mass fraction profiles show identical behaviour for both islands, with very comparable orders of magnitude. The island acts as an agent that prevents evaporation. The hygric measurement obtained is comparable to the profile simulated in the free field. We conclude that the evaporative methodology implemented in the free field is rather coherent, and this confirms the hypotheses also made in the literature of a Dirichlet constraint in saturated vapour at the lake surface to describe the evaporation potential.

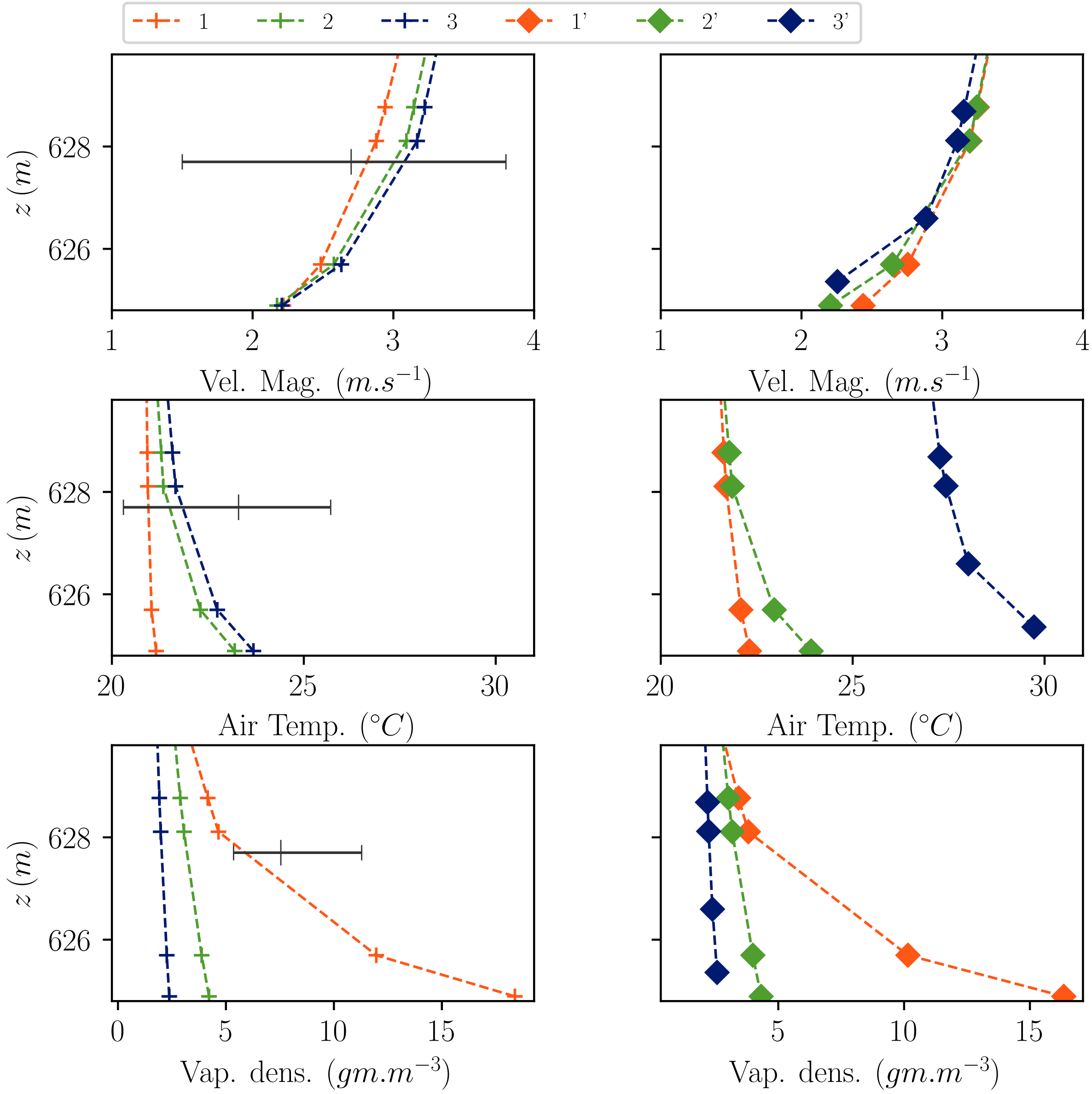

Figure 7.13–*Simulated profiles which are obtained for the six position located on the longitudinal slice A:A shown in Figure 7.10. The profiles are depicted for the first island (front wind) and the second island (leeward) respectively on the left-hand side and the right-hand side. Mediane meteorological value recorded at the test site are indicated as intervals (first quartile, mediane and third quartile).*

7.4.3/ Evaporative Variations at the Reservoir Level

The last paragraph in the previous section has discussed the vapour density profiles and the appropriate accuracy between the water vapour measurements during the FPV2 campaign and the extrapolated vapour level in the southern part of the array. Similarly to Figure 7.10, Figure 7.14 shows the dispersion of evaporation at the reservoir scale. It is observed that the zones where the modules are located have the lowest levels of evaporation and no significant evolution can be observed during plant progress, despite the dependence of evaporation on $u_\star$. The aeraulic blocking is such that even if there is a local evolution of a point in normalised evaporation, the free surface area has an evaporation almost one order of magnitude higher. The numerical methodology appears to overestimate the free surface evaporative rates so that the heterogeneity at the basin level appears quite insignificant. One hypothesis for this inappropriate behaviour is that no retroaction of temperature is involved in the specific humidity of the surface. As evaporative transfer acts as a heat sink for air and water, the temperature at which evaporation takes place should also be reduced because of this effect.

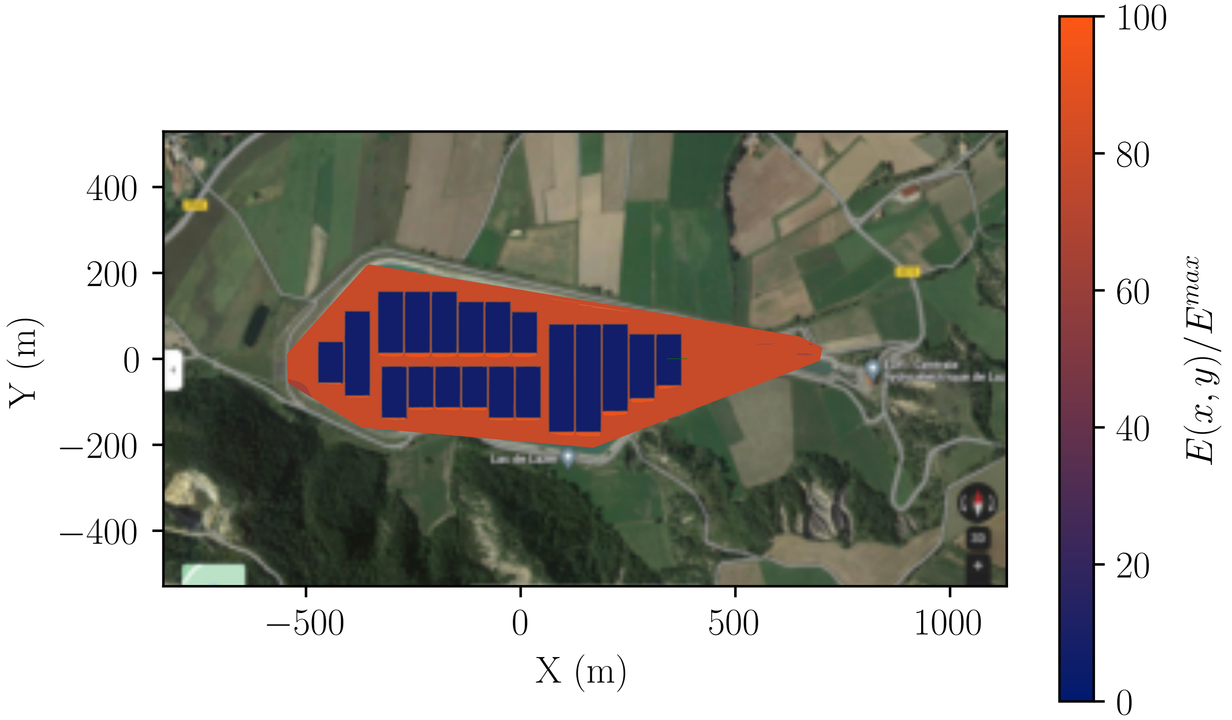

Figure 7.14–*Map of normalised evaporative levels for the simulation case.*

7.5/ Conclusion

In this chapter, the upscaling methodology developed in Chapter 4 has been implemented to simulate thermal and evaporative transfers on the array scale. New geometrically-based correlations have been developed to allow for implicit representation of the modules with conserving their effects on the dynamics of the flow in *full representation*. Then, these correlations have been applied to a case study based on the environmental measurement carried out at the FPV2 site.

Disparity in the temperature of the module surfaces has been predicted, which will ultimately have a significant impact on the yield of the photovoltaic plant. The heterogeneity at the array scale was found to be greater than that found on land. The array configuration for floating set-up was assumed to be responsible for this behaviour. The spread of temperature also appeared to be a complex function of the environment, especially the distance to the embankment, which is seen as an important driver of thermal evolution as the array scale. The focus of the methodology on the evaporative phenomenon also highlighted the aerodynamic blocking effect that compromises most of the evaporation above the covered surfaces.

The correlations are developed as ***wall functions*** and therefore can be deployed in other study cases with respect to the geometry of the power plant. To fulfil the conditions of repeatability and re-usability, they integrate dynamic properties of the atmosphere, and they are constructed as functions of the velocity frictions and wind directions. When running simulation at the array scale was not conceivable due to computational cost, the methodology applied on a single study case has shown its ability to deal with the physical fields for the utility-scaled powerplant.

As a perspective, the case study can be extended to other atmosphere states and waterbody conditions so that the real FPV2 powerplant can be modelled in all meteorological situations. With the deployment of a simple measurement set-up available at industrial power plant site, it would be possible to simulate in real time the behaviour of the floating powerplant. This would improve the thermal management of solar assets, floating or land-based, and potentially be used as a key player in optimising the energy yield. For instance, the observation of topographically based obstacles (embankment here) and their impacts on airflow could be prevented by modifying the physical arrangement of modules.

Furthermore, integrating floating structures in the correlation calculation can be of great interest for the future requirement of evaporative performance on the array scale. Ultimately, the code structure allows to go further in model coupling so that reservoir models, ground models, or even photovoltaic models should be implemented to predict the airflow fields with more precision.

8 CONCLUSIONS & PERSPECTIVES

A sparkling blue-and-white jewel... laced with slowly swirling veils of white... like a small pearl in a thick sea of black mystery.

Edgar Mitchell

8.1/ Conclusions

This work sheds light on the passive cooling effect in floating solar arrays through numerical and experimental contributions. A set of new generalisable methodologies is proposed with the motto of enhancing the construction of numerical boundary conditions for the FPV models.

Indeed, thermal transfer in photovoltaics is one of the most important pet peeves when designing a solar array, it is closely bounded to the performance of the silicon solar cells contained in the modules and suffers from many uncertainties related to outdoor environments. Chapter 1 has introduced existing ways of describing the thermal dynamics of a module, from the simple Ross model with only one explicit equation to solve, to more elaborate multilayer models with ten or so differential equations. In FPV literature, though, the principal model only includes a simple thermal description which fails in quantifying the thermal inertia and the precise effect of each heat mode involved. Therefore, the first interest of the work was to dig deeper in the direction of using a more elaborated model to separate the thermal contributions in the heat budget of PV modules. Outdoor environments and especially atmospheric air flow were also observed to be a key factor in the uncertain thermal behaviour of the photovoltaic array in Chapter 2. Convective transfers are rarely addressed in the literature under the flavour of an array-scale system, mainly because of a lack of available data and methods to couple with the large number of modules. In this regard, the first wind tunnel experiments of photovoltaic array from the literature was used to develop a new simulator system adapted to the solar array scale without soaring the computational effort to simulate such a large spatial scale.

The Chapter 3 has summarised the experimental work carried out under outdoor conditions and especially over waterbodies for two out of three sets of experiments. Each experimental material was dedicated to a precise scientific topic: The first setup showed that microclimate conditions were poorly affected by the waterbody, so the concept of warming effect under a temperate climate and small waterbody dimensions was hypothesised; The second setup showed that a new experimental methodology based on the heat flux sensor was able to catch front-side heat rates and provide better accuracy than the current methodology involved in PV; finally, the last setup showed that a full-scale lake provides a range of conditions that are quite different from the land-based systems. The collected data set was then filtered out to be used in the validation process when evaluating the study cases in the following chapters. Indeed, the next chapter 4 has shown several methods of thermally modelling the FPV setup. An optimised 1-D photovoltaic model was developed by integrating corrective parameters and new data input to represent boundary conditions. When this strategy was ultimately built to be combined with the experimentally collected data, three other numerical models were developed with the aim of simulating solar array systems in different ways. First, the solar array simulator, better called the bi-periodic model, was introduced to be competitive in producing a good level of airflow dynamic and heat transfer for a representative module in the array, with a low computational cost. The second simulator based on the scalability of the preprocessing stages of the first model was then established to better predict the heterogeneous flow located before the fully developed air flow region in the array. Finally, the last model was developed as a high-fidelity 3-D simulation that allows one to evaluate the role of turbulence and developed the flow hypothesis with respect to the previous simulations.

Several proposals related to the first question drawn in the Introduction[1] were addressed in Chapter 5 with the support of the experimental material and the 1-D corrected FPV model. A ranking

---

[1] ***What are the physical fields and the correlations that allows one to describe boundary conditions of Floating PV systems ?***

strategy for thermal prediction with respect to the most likely convective and radiative modes to occur was performed; the results showed that forced convective transfer was improved over waterbodies and that free convective heat rates were degraded with respect to the solid obstacles in the vicinity of modules. Furthermore, the deployment of the new experimental methodology in the second floating experiment revealed that the heat rates on the front surface were increased compared to the conventional land-based correlation. Moreover, the integration of sensor data directly into the photovoltaic simulation greatly increases the accuracy of thermal prediction. It solved the issue of integrating wind-related correlations and thus enhances the integration of the stochastic nature related to forced convective transfer from wind effect.

The second question drawn in introduction[2] was mainly addressed within the two final Chapter 6 and Chapter 7 with the elaboration of a morphometric study for solar arrays and the exploration of the module front-side heat rates for the developed and heterogeneous air flow regions in a FPV array. For the first time, the role of the intermodule spacing, inclination, and height was evaluated, and it appeared that the main impact of the layout of the array is observed on the rear module surface. More importantly, the heat rates in the FPV geometry are found to be lower than those in the typical land-based geometries. These results highlight that thermal management through array-scale layouts is a good candidate to optimise energy yield on the global scale. Furthermore, the evaluation of thermal heterogeneity in the FPV array also showed that considering a constant module temperature (or even an averaged one) is not consistent with the wind-related interaction with the PV systems. The heterogeneous region was found to be as large as the photovoltaic island involved in the assessment, and each island was associated with a specific air flow pattern that results in different thermal performances. The numerical deployment of the study is based on wall functions so that it can be easily generalised to other array configurations. Moreover, the development of the wall function encompasses the integration of the humidity field as a passive scalar in the atmosphere, considering both the evaporative transfer from free and covered waterbody surfaces.

The results obtained in this work are encouraging for the field of floating photovoltaics. Knowledge of the cooling effect is not trivial, and many factors are acting on the performance of the energy yield. The tools developed in the thesis can help project designers choose the best set of correlations for their photovoltaic arrays and ultimately optimise $LCOE$ when conceptualising a new project.

---

[2] ***What are the key geometrical elements that modify the convective transfer at the photovoltaic array scale ?***

8.2/ Perspectives

This thesis opens many perspectives to better understand the effects of passive cooling on floating photovoltaic power plants. Consideration of the microclimate through the effects of evaporation on the sensible temperature above the pond must be taken into account by including a dedicated modelling brick. Two levels of modelling should be used for this phenomenon; the first level would be to integrate a simplified lake model into the photovoltaic models. This technique would allow us to quickly identify the influence of the pond on the photovoltaic system and also to cosimulate the effect of the photovoltaic modules on the lake from a physical (evaporation) and biological/chemical point of view. The second level would be to modify the conservation equations in the CFD models to consider humid air. Under these conditions, the latent to sensible energy transfer would be directly integrated in the energy balance. When homogenisation methods are combined with moist atmosphere modelling, the heterogeneity of all fields would be observed, and it would be possible to estimate passive cooling at the plant scale with higher accuracy. It is also possible to consider soil and lake models (either in co-simulation or in boundary condition with several soil levels) in order to better understand the behaviour of the systems around the plants.

The homogenisation methodology developed is also a tool that could be improved in the future to take into account possible load-bearing structures and especially floats in the case of floating photovoltaics. In this way, the calculation of the wall function would be more accurate for the case of evaporation due to the turbulent effects, which would be modelled in a more realistic way. As the turbulence issue is not addressed in the work, it would also be appropriate to evaluate the various results of the thesis with more realistic (but more expensive) turbulence models. The switch from the methodology to 3-D would be necessary to model real industrial structures, thus the computational cost would be dramatically increased. However, this switch could also allow to work with LES methods and therefore allow to better capture the turbulent fields in the plant.

Finally, the methodology for measuring the convective parameter proved to be very promising for better modelling of the boundary conditions of photovoltaic models. Integration in a minute-time-step model proved to be a very good choice compared to the use of classical correlations; however, it would be useful to lower the time step to be able to reach high-frequency modelling. Although ground-mounted PV systems could benefit from this type of modelling in order to determine dominant transfer modes at specific times of the day (very early in the morning notably with condensation phenomena), floating PV is a priori even more impacted by the evolution of convective boundary conditions due to free surface movements. Therefore, it would be relevant in the future to use this type of experimental setup to study in more detail the operating conditions (for industry) and the complex physical phenomena (for researchers).

8.3/ Scientific Dissemination

The thesis work resulted in the following scientific publications:

Amiot, Baptiste, Matthieu Chiodetti, Rémi Le Berre, Khalid Radouane, David Boublib, Dupeyrat Patrick, Korneel Vermeyen, and Stéphanie Giroux-Julien. Floating Photovoltaics – On-Site Measurements in Temperate Climate and Lake Influence on Module Behavior. In *37th European Photovoltaic Solar Energy Conference and Exhibition Proceedings*, volume 1, 2020

Amiot, Baptiste, Martin Ferrand, Rémi Le Berre, and Stéphanie Giroux-Julien. Hétérogénéité des modes de transferts convectifs au sein des centrales solaires photovoltaïques. In *Actes, Société Française de Thermique*, pages 183–190, 2022.

Amiot, Baptiste, Rémi Le Berre, and Stéphanie Giroux-Julien. Evaluation of thermal boundary conditions in floating photovoltaic systems.*Progress in Photovoltaics: Research and Applications*, pages 1–18, 2022

A General Appendix

A.1/ Physics of radiative fields

Solar resources (SWIR)

The short wavelengths range from 0.290um to 3um; these waves are mostly emitted by the Sun (97% of the top atmosphere irradiation) World Meteorological Organization, 2018. However, the flux density that arrives at the photovoltaic module depends mainly on the position of the Sun in the sky, the absorptivity of the atmosphere, and the inclination of the module with respect to the horizontal and the azimuth. In addition, the radiation incident on the module can also come from a reflection (secular or diffuse) of short wavelengths on surrounding surfaces. Thus, the albedo of these surfaces becomes a parameter to consider (especially in the case of bifacial cells). Finally, shadows can also occur on the modules that make up a powerplant, either because of clouds (we prefer to categorise this situation in the part ”absorptivity of the amtosphere”), or because of near mask and shadowing item (other modules, structure, mountain topology, building, etc.).

Generally, the information about shortwave flux is measured within the horizontal plane, the Global Horizontal Irradiance (GHI) can be defined as follows:

$$GHI_x = \rho \int_0^{2\pi} L(\epsilon, \theta, x) cos\theta \, \mathrm{d}\omega \tag{A.1}$$

Where x is the location of the measurement point in the horizontal plane, ρ is the reflective property of the plane, $L(\epsilon, \theta, x)$ is the associated radiative power integrated in the half-sphere domain, and ω is the elementary solid angle. As the source of radiative power can come from the hemispherical domain, it takes into account Direct Normal Irradiance (DNI or B_n) and Diffuse Horizontal Irradiance (DHI). However, modules are generally inclined (tilt angle) and GHI_x is not adapted to describe the radiative power arriving at the module surfaces ($\phi_{\mathrm{sw,poa}}$ or G_{POA}). Supplementary steps are therefore invoked to transpose the flux in the plane of the modules:

$$\phi_{\mathrm{sw,poa}} = G_{beam} + G_{albedo} + G_{diffuse} \tag{A.2}$$

Whence $\phi_{\mathrm{sw,poa}}$ is the irradiance in the array plane (POA), G_{beam} is the direct flux from the sun, G_{albedo} is the flux reflected from the ground and the near structure, and $G_{diffuse}$ is the flux scattered in the atmosphere. The beam radiation is principally a function of the Direct Normal Irradiance, the solar position, the array inclination, it reads:

$$G_{beam} = B_n \times \left(cos\left(\theta_{z,sun}\right) \times cos\left(\theta_{T,array}\right) + sin\left(\theta_{z,sun}\right) \times sin\left(\theta_{T,array}\right) \times cos\left(\theta_{a,sun} - \theta_{a,array}\right)\right) \tag{A.3}$$

where $\theta_{z,sun}$ and $\theta_{a,sun}$ are the zenith and azimuth angles of the Sun, $\theta_{T,array}$ and $\theta_{a,array}$ are the tilt and azimuth angle of the module/array. B_n represent the direct normal irradiance which is ”the quotient of the radiant flux on a given plane receiver surface received from a small solid angle centred on the Sun’s disk to the area of that surface” as defined in the ISO-9488 standard. A fundamental formula is at follows:

$$B_n = \int_0^{2\pi} \int_0^{\alpha} P(\epsilon, \theta) L(\epsilon, \theta) cos(\epsilon) sin(\epsilon) \, \mathrm{d}\epsilon \, \mathrm{d}\theta \tag{A.4}$$

in which $L(\epsilon,\theta)$ is the short-wave part of the spectrum for an item in the sky, whose angular position is defined by the angular distance ϵ from the centre of the Sun and its corresponding azimuth angle $theta$. $P(\epsilon,\theta)$ stands for the penumbra function that cancels out the function outside of the solid angle where is located the sun.

G_{albedo} principally relies on the surface property reflecting the short-wave flux, the equation reads:

$$G_{albedo} = GHI \times \alpha \times FF^{grd \rightarrow mod} \tag{A.5}$$

Whence GHI in the global horizontal, α is a material characteristic and $FF^{grd \rightarrow mod}$ is a form factor that account for geometry properties.

Finally, the diffuse flux corresponds to the radiation scatter throughout the atmosphere, several sub-models exist and stand on assumption of either: isotropic sky, anisotropic cloudless sky and anistropic clear sky. For instance, the Erbs model Erbs et al., 1982 takes into account the sky coverage to determine the Diffuse Horizontal Irradiance as follows:

$$\begin{cases} f_d = 1 - 0.09 \times K_t, & \text{for } K_t < 0.22 \\ f_d = 1 - 0.9511 - 0.1604 + 4.388 K_t^3 - 16.638 K_t^3 + 12.338 K_t^4, & \text{for } 0.22 < K_t < 0.8 \\ f_d = 0.165, & \text{for } K_t > 0.8 \end{cases} \tag{A.6}$$

The diffuse irradiance being $G_{diffuse} = f_d \times GHI$.

Without direct knowledge / measurement of tilt irradiance in the array plane, two methods pave the way to determine $\phi_{\text{sw,poa}}$ in photovoltaic arrays: Radiosity and Ray-Tracing methods.

Radiosity is based on discretising the power received at one location by the other surfaces, assuming the location of interest i, the observed hemispherical plane is discretised by the N amount of surfaces j, the radiative power received at i is obtained as follows:

$$G_i = \rho_i \sum_{j=1}^{N} FF_{ij} G_j \tag{A.7}$$

Whence, FF is a geometrical form factor that has to be calculated based on the investigated scene. Direct, Reflected and Diffuse fluxes are retrieved through the calculation method. The main drawback lies in the calculation costs necessary to cover a complete scene with precise accuracy

Ray-tracing methods are based on the emission of a photon by a source item in the scene (randomly or deterministic). The observer being interested in the amount of photon reaching the objective, a forward ray tracing method consists in setting the module as the objective item; the photon are therefore emitted by the other components of the scene (sun, sky, ground, and structures). The backward ray tracing does the same job but reversing the source and the objective item. In both cases, the diffuse flux is an obstacle for both settings, taking into account the flux from the whole sky being time consuming. To bypass this problem, a diffuse model is most of the time applied in parallel of the calculation of beam and albedo components.

Heat-losses from thermal radiative transfers (LWIR)

The spectral band known as long wavelength is between $5\mu m$ and $40\mu m+$. The sun participates very little in this spectral band, it is the atmosphere and the surrounding environment (obstacle, structure) that are the main contributors to the density of flux received by the module. Fundamentally, the particles contained within the troposphere emit thermal radiations according to their temperature levels. The media is also participating; therefore, part of the radiations emitted do not come across the module but are transmitted to another layer of the troposphere.

$$L(\nu) = \int_{z_{mod}}^{S_b} B[\nu, T(s)] \frac{\partial \tau(\nu, s)}{\partial s} \mathrm{d}s \tag{A.8}$$

Where ν is the wave-number, s is the distance from the module level, $B_b(\nu)\tau(\nu, s_b)$ is a background source function (troposphere molecules, sun, ...) weighted by the atmosphere transmittance, $B[\nu, T(s)]$ is the monochromatic emission of the source at the equivalent emission height s. $\frac{\partial \tau(\nu,s)}{\partial s}$ stands for the evolution of monochromatic transmittance from the ground to the source of emission. Considering the atmosphere as an horizontal plane:

$$\dot{q}_{IR} = \int_{z_{mod}}^{z_{atm}} \sigma T^4(z_i) \frac{\partial \epsilon(z_i, z)}{\partial z} \mathrm{d}z \tag{A.9}$$

Where $\frac{\partial \epsilon(z_i,z)}{\partial z}$ can be parameterized for an equivalent volume of air or as a mixture of greenhouse gases (H_2O,O_3,CO_2, ...) inducing a ”scaled path” for the influence of each gas on the module. The integral form of equation (A.9) can also be discretised assuming a slab of fluid with homogeneous properties.

The latter approach is challenging as it asks either calculation resources to calculate the contribution of groups of molecules and the meteorological quantities at different levels to characterise the media. Without these pieces of information on the shelves, a lot of effort has been pursued to develop correlations of sky contribution as a ”lumped atmospheric emissivity”,$\bar{\varepsilon}_s$, weighting an affordable ambient temperature.

$$\bar{\varepsilon}_s = \frac{\int \cos\theta \mathrm{d}\Omega \int_0^\infty I_{bb}\left(\lambda, T_{\mathrm{sky}}\right) \varepsilon_s(\Omega, \hat{\lambda}) \mathrm{d}\lambda}{A\sigma T_{\mathrm{sky}}^4} \tag{A.10}$$

Whence T_{sky} is an effective sky temperature. Through the lumped emissivity procedure, many authors have developed either emissivity or sky temperatures adapted to local measurements, most of the time: dew-point temperature, ambient temperature, and clearness index. Repeatability of these correlations is known to be a function of climate conditions and type of sky coverage Zhao et al., 2019. Selecting a non-representative correlation may lead to a mispredict of the influence of the atmosphere and, therefore, the thermal processes at the system level Evangelisti et al., 2019.

A.2/ Velocity profiles in Atmosphere Flow

A.2.1/ Simplification of the momentum equation

The equations of conservation can be written in a convenient form to show the physical phenomena that act on the fluid motion and energy conservation, it reads:

$$\frac{\partial \overline{u_j}}{\partial x_j} = 0 \tag{A.11}$$

$$\begin{aligned}\frac{\partial \overline{u_i}}{\partial t} = &-\underbrace{\frac{\partial \overline{\left(u_j' \times u_i'\right)}}{\partial x_j}}_{\text{Advection}} - \underbrace{\frac{1}{\rho_0} \times \frac{\partial \overline{p}}{\partial x_i}}_{\text{Pressure}} + \underbrace{\beta \times (\overline{\theta} - \theta_0) \times k_i}_{\text{Buoyancy}} \\ &+ \underbrace{\nu \times \frac{\partial^2 \overline{u_i}}{\partial x_j \times \partial x_j}}_{\text{Viscosity}} - \underbrace{2 \times \epsilon_{i,j,\beta} \times \Omega_j \times \overline{u_j}}_{\text{Coriolis}}\end{aligned} \tag{A.12}$$

$$\frac{\partial \overline{\theta}}{\partial t} = -\underbrace{\frac{\partial \overline{\left(u_j' \times \theta'\right)}}{\partial x_j}}_{\text{Advection}} + \underbrace{\nu_\theta \times \frac{\partial^2 \overline{\theta}}{\partial x_j \times \partial x_j}}_{\text{Molecular}} \tag{A.13}$$

Considering a ground surface over which the wind blows with the following characteristics:

- The flow is stationnary and horizontally homogeneous
- The flow is incompressible and there is no effect of the Coriolis force or the density gradient
- The mean velocity sticks to the flow plane $(\mathcal{O}y)$ with a fixed direction

Hypothesis 1

$$\frac{\partial \overline{()}}{\partial x}, \frac{\partial \overline{()}}{\partial y} = 0 \tag{A.14}$$

Hypothesis 2

$$\frac{\partial \overline{w}}{\partial z} = 0 \tag{A.15}$$

Hypothesis 3

$$\frac{\partial \overline{u}_i}{\partial t} = 0 \tag{A.16}$$

Hypothesis 4

$$2 \times \epsilon_{i,j,\beta} \times \Omega_j \times \overline{u_j} = 0 \tag{A.17}$$

Hypothesis 5

$$\beta \times (\overline{\theta} - \theta_0) \times k_i = 0 \tag{A.18}$$

The conservation of momentum is simplified to the following:

$$\begin{gathered}\cancelto{0}{\frac{\partial \overline{u_i}}{\partial t}} = -\underbrace{\frac{\partial \overline{\left(u_j \times u_i\right)}}{\partial x_j}}_{\text{Advection}} - \underbrace{\cancelto{0}{\frac{1}{\rho_0} \times \frac{\partial \overline{p}}{\partial x_i}}}_{\text{Pressure}} + \underbrace{\cancelto{0}{\beta \times (\overline{\theta} - \theta_0) \times k_i}}_{\text{Buoyancy}} \\ + \underbrace{\nu \times \frac{\partial^2 \overline{u_i}}{\partial x_j \times \partial x_j}}_{\text{Viscosity}} \underbrace{\cancelto{0}{- 2 \times \epsilon_{i,j,\beta} \times \Omega_j \times \overline{u_j}}}_{\text{Coriolis}}\end{gathered} \tag{A.19}$$

Adopting the naming convection $x_i = x; u_i = u$ and $x_j = z; u_j = w$, it follows that

$$0 = -\frac{\partial \overline{(w' \times u')}}{\partial z} + \nu \times \frac{\partial^2 \overline{u}}{\partial^2 z} \tag{A.20}$$

— A.2.2/ Vaschy-Buckingham Theorem

Away from the surface and the micro-relief created by the array, the turbulent flux is supposed to dismiss the action of the diffusive flux, therefore:

$$\cancelto{<<}{-\nu \times \frac{\partial \overline{u}}{\partial z}} + \overline{w' \times u'} = -u_\star^2 \tag{A.21}$$

Rewritting $\overline{w' \times u'}$ by inducing that the motion gradient is proportional to the velocity mean such as $K_u \times \frac{\partial u}{\partial z}$, and considering a mixed length of exchange in the form $K_u \simeq L_m^2 \times \frac{\partial u}{\partial z}$ with $L_m = \kappa \times z$, it follows:

$$-(\kappa \times z)^2 \times \frac{\partial \overline{u}}{\partial z} = u_\star^2 \tag{A.22}$$

It follows a functional solution to:

$$\underbrace{\frac{\partial \overline{u}}{\partial z}}_{x} = F\left(\underbrace{u_\star}_{a_1} \underbrace{z}_{a_2} \underbrace{\nu}_{a_3}\right) \tag{A.23}$$

Through a dimensional analysis, it follows that:

$$\left[\underbrace{\frac{\partial \overline{u}}{\partial z}}_{x}\right] = \underbrace{T^{-1}}_{X} \tag{A.24}$$

$$\left[\underbrace{u_\star}_{a_1}\right] = \underbrace{L.T^{-1}}_{A_1} \tag{A.25}$$

$$\left[\underbrace{z}_{a_2}\right] = \underbrace{L}_{A_2} \tag{A.26}$$

$$\left[\underbrace{\nu}_{a_3}\right] = \underbrace{L^2.T^{-1}}_{A_3} \tag{A.27}$$

Only two dimensions are mandatory to describe equation A.23, L and T. The application of the theorem of Vashy-Buckingham gives the number of dimensionless numbers as $4-2=2$ (4 physical variables from equation A.23 minus 2 independent dimensionality). A comfortable choice is to consider $L.T^1 = V$ as a first dimensionally dependant group and L as the second. It follows that:

$$X = A_1^a \times A_2^b \tag{A.28}$$

and

$$A_3 = A_1^c \times A_2^d \tag{A.29}$$

This gives the following couples of parameters in equation A.28:

$$T^{-1} = \left(L.T^{-1}\right)^a \times L^b \rightarrow a = 1; b = -1 \tag{A.30}$$

And the dimensionless group from equation A.29:

$$L^2.T^{-1} = \left(L.T^{-1}\right)^c \times L^d \rightarrow c = 1; d = 1 \tag{A.31}$$

Changing the unity of the dimension dependent groups involved in the problem such as:

$$\widetilde{a_1} = \frac{a_1}{\alpha_1} \tag{A.32}$$

leads to:

$$\widetilde{x} = \frac{x}{\alpha_1^a \times \alpha_2^b} \tag{A.33}$$

With a and b described in equation A.31. Therefore, equation A.23 becomes:

$$\underbrace{\frac{\widetilde{\partial \overline{u}}}{\partial z}}_{\widetilde{x}} = F\left(\underbrace{\widetilde{u_\star}}_{\widetilde{a_1}}, \underbrace{\widetilde{z}}_{\widetilde{a_2}}, \underbrace{\widetilde{\nu}}_{\widetilde{a_3}}\right) \tag{A.34}$$

By inferring that $\alpha_i = a_i$ it leads to:

$$\underbrace{\frac{\frac{\partial \overline{u}}{\partial z}}{u_\star^1 \times z^{-1}}}_{\widetilde{x}} = F\left(\underbrace{1}_{\widetilde{a_1}}, \underbrace{1}_{\widetilde{a_2}}, \underbrace{\frac{\nu}{u_\star \times z}}_{\frac{a_3}{a_1^c \times a_2^d}}\right) \tag{A.35}$$

Which could be rewritten under the form:

$$\frac{\partial \overline{u}}{\partial z} \times \frac{z}{u_\star} = F\left(1, 1, \frac{1}{Re_*}\right) \tag{A.36}$$

With the hypothesis of turbulent regime in the atmosphere, one may raise that Reynolds dependent terms goes to zero. It follows that the velocity profile in the atmosphere is described by:

$$\frac{\partial \overline{u}}{\partial z} = F\left(1, 1, \cancel{\frac{1}{Re_*}}\right) \times \frac{u_\star}{z} \tag{A.37}$$

By integration it follows:

$$\overline{u}(z) = u_\star \times F\left(1, 1, \cancel{\frac{1}{Re_*}}\right) \times (\ln(z) + C) \tag{A.38}$$

The constant C can be rearranged by guessing that the velocity at the ground limit is zero, therefore $\lim_{z \to 0} \overline{u}(z) = -\ln(z_0)$ where z_0 is a fictive height of no mean velocity. Finally the velocity profile is given by:

$$\overline{u}(z) = \frac{u_\star}{\kappa} \ln\left(\frac{z}{z_0}\right) \tag{A.39}$$

A.3/ Code Structure for Thermal-electrical Engine

Running the thermal and electrical model for the 1-D photovoltaic model requires a precise syntax so that the solver can access the data in a proper shape (dimension, unity). When the software is used in standalone mode *(i.e., no radiative calculation are performed)*, the management of files in the study is also modified and follows rules of construction. Two following subsections are dedicated at these numerical details that allows the launch of thermal and electrical calculation and especially multiple-threading calculation.

A.3.1/ Model Inputs

Meteorological conditions

Each timestep of the calculation must be covered by a description of the environmental conditions and assigned in the file *meteo.txt*. A large degree of versatility in data inputs is admitted; for instance, the radiative flux can be integrated whether as a DNI, GHI, DHI. However, the file structure has to be properly followed to ensure that the engine reads the data that was meant by the user. The structure is composed of two aspects: first a file header which describes the file shape as variable type, number of lines, and number of columns; then the meteorological data for each time step separated by tab separators and end of line character. The code snippet contained in Listing A.1 shows the *meteo.txt* syntax. For the local conditions part, the columns are (from left to right): the **timestamp** (expressed in seconds from the yearly 1st of January), the **first radiative component** [GHI, DHI, DNI] (in $\mathrm{W\,m^{-2}}$), the **second radiative component** [GHI, DHI, DNI] (in $\mathrm{W\,m^{-2}}$), the **ambient temperature** (in °C), the **dew point temperature** (in °C), the **sky temperature** (in °C), the **pressure** (in Pa), the **relative humidity** ($]0,1]$), the **wind velocity** (in $\mathrm{m\,s^{-1}}$), its **direction** (between 0 [North] and 360 °), the **Latitude** (decimal degrees), the **Longitude** (decimal degrees), the **precipitable water** (in mm) and the **water temperature** (in °C).

```
#1
double  data(5,14)
11354460    602    0    17.0    0    -1.1    95000    0.54    1.5    88    44.34    5.85    0    15.8
11354520    609    0    16.9    0    -1.1    95000    0.55    1.3    57    44.34    5.85    0    15.8
11354580    630    0    16.8    0    -1.1    95000    0.55    0.9    52    44.34    5.85    0    15.8
11354640    635    0    16.9    0    -1.1    95000    0.55    0.9    41    44.34    5.85    0    15.9
11354700    637    0    16.8    0    -1.0    95000    0.55    0.7    66    44.34    5.85    0    15.9
```

Listing A.1–*Example of meteo.txt file for 5 minutes at FPV2 test-site from 10:00 to 10:05 on the 12 May 2022.*

Several requirements are needed to launch the electrical and thermal engine[1]: The timestamp must be constant throughout the *meteofile.txt* and the relative humidity must be strictly positive.

Module and Inverter files

Electrical parameters are given as separated *.mo* files and consist of two dictionaries with keys and numerical or Boolean values. File shapes correspond to a "record" module from modelica, an illustration is given in Listing A.2 for the *module.mo* file. For the module parameters, the one presented in Table 4.2 are implemented as a function of the investigated study case.

```
record  Module =
    LibraryPV.ModuleName (
        Length = 1.69,
```

---

[1] Ultimately, it would have the final word and abruptly reject the calculation job if these conditions are not met.

```
        Width = 1.00,
        bifacial = false,
        Ns = 60,
        Mp = 2,
        Rs = 0.000446,
        Rsh = 1.596,
        ...
    );
```

Listing A.2–*Example of module.mo file for the module used at the FPV2 test-site.*

A similar record is used for the *inverter.mo* file with the data relying on the maximal DC input and technical specifications (own power consumption, current and voltage admitted).

Sub-module tuning

A last *param.txt* file is required to design the call of appropriated sub-models in the thermal electrical engine and to design the photovoltaic installation. The file shape is similar to a Python assignation of variables, they describe : the type of radiative configuration integrated in the meteofile, the installation losses rates due to ageing and soiling, the number of modules and their electrical connection, the current altitude, the timestep of study, and the starting time. The other variables are Boolean parameters activating sub-modules for such as spectral mismatch calculation, sky temperature calculation is also performed depending on the data inputs.

A.3.2/ File Management

Pre-processing

The preprocessing phase is important in the work, this is at this stage that the weather data is formatted to reflect the boundary conditions to be applied later in the calculation engine. As an input to this phase, a raw dataset is retrieved from a local area network storage on which the data is persisted. The data is retrieved via python and integrated into a dataframe structure. Clipping operations are then performed to match the elements to the format of the *meteo.txt* file. Only the elements necessary for the calculation engine to function are considered. In parallel, a file of experimental results is created in order to propagate the operations performed on the table containing the input data of the calculation engine. This guarantees a coherence to make cross validation tests in post processing.

The data is then cleaned to avoid fatal errors during compilation (removal of NaN, interpretation of inconsistent data). The time-step constant across the table is checked. As the measurement items sometimes encounter latencies, some time steps may be missing in the initial database. The interpolation function of the pandas package is therefore used (timestamp and physical data) when the missing data gap does not exceed 10 minutes in a row.

In standalone mode, two other files must be integrated into the solver, an *irradiance.txt* file that includes only the radiative field (similar to the one in the *meteo.txt* file) and a *mismatch.txt* file which includes the electrical mismatch calculated in the preprocessing phase and accounts for the module and cell shading consequences on the electrical output. The last file is left empty in our work.

Calculation launch

The solver can be run ”on-the-fly” in the Dymola GUI, provided that the working directory is respected. However, this strategy is not practical for repeating a calculation with dynamic parameters and weather files a large number of times. There are therefore two methods to script the calculation without using the graphical interface, either directly using the environment and the scripting functionality, or using an additional library such as *Buildingspy* written in python Wetter et al., 2014. The first method allows to easily use built-in functions in the environment, such as the Sweep Parameters function which offers a calculation optimization for multiparametric exploration. The second method offers greater flexibility in modifying the parameters of the calculations (management of input files, precision of the field of parameters to be explored). Another advantage is to be able to directly integrate the whole stack (preprocessing, calculation engine, postprocessing) in a single language, which facilitates the pure work of cross-validation, as Python has a more suitable tool. It is thus possible to integrate a parametric optimisation step into the calculation stack. The first method is used when the field of parameters to be observed is large (100+ calculations).

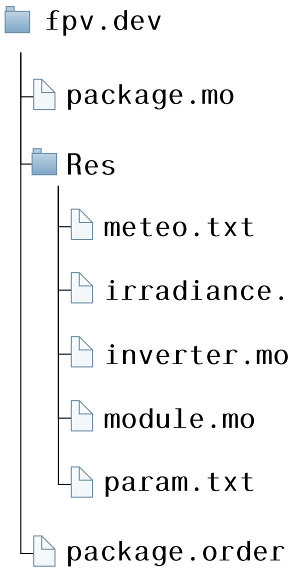

Post-processing

At the end of the calculation, the solver outputs the full set of parameters and variables in a file *output.mat*. The buildingspy library ultimately integrates a reader tool that can convert the file into a Python numpy table. Data treatment can be performed, and cross-validation is later made using the back of module temperature and the electrical production from the output table.

A.4/ code_saturne: Turbulence Models and Wall Functions

A.4.1/ $k-\epsilon LP$ turbulence model

The k–ϵLP (Linear Production) turbulence model is a first-order model in which turbulent kinetic energy k and the rate of dissipation of turbulent energy ϵ are transported variables. The eddy viscosity ν_t reads:

$$\nu_t = C_\mu \frac{k^2}{\epsilon} \tag{A.40}$$

Closure equations read:

$$\begin{cases} \dfrac{\partial k}{\partial t} + U_k \dfrac{\partial k}{\partial x_k} = 2\nu_t S_{ij} Sij - \epsilon + \dfrac{\partial}{\partial x_k}\left[\left(\nu + \dfrac{\nu_t}{\sigma_k}\right)\dfrac{\partial k}{\partial x_k}\right] \\ \dfrac{\partial \epsilon}{\partial t} + U_k \dfrac{\partial \epsilon}{\partial x_k} = C_{\epsilon 1}\dfrac{\epsilon}{k} 2\nu_t S_{ij} Sij - C_{\epsilon 2}\dfrac{\epsilon}{k}\epsilon + \dfrac{\partial}{\partial x_k}\left[\left(\nu + \dfrac{\nu_t}{\sigma_\epsilon}\right)\dfrac{\partial \epsilon}{\partial x_k}\right] \end{cases} \tag{A.41}$$

The set of constants used are summarised in Table A.1.

C_μ	$C_{\epsilon 1}$	$C_{\epsilon 2}$	σ_k	σ_ϵ
0.09	1.44	1.92	1	1.3

Table A.1–*Constants of the $k-\epsilon$ LP model included in code_saturne.*

A.4.2/ $k-\omega SST$ turbulence model

The $k-\omega SST$ (Shear Stress Transport) turbulence model is a first-order model that consists of two transport equations to determine the turbulent viscosity ν_t: one for turbulent kinetic energy k and one for eddy oscillation frequency ω. It was proposed in Menter, 1993 to eliminate the undesirable free stream dependency that occurs in the classical $k-\omega$ model from Wilcox, 1988, it follows:

$$\nu_t = \frac{a_1 k}{\max(a_1 \omega, S F_2)} \tag{A.42}$$

In which the constant a_1 is set to 0.31. Hereafter, the constants used in code_saturne are summarised in Table A.2

The function F_2 is defined as:

$$F_2 = \tanh\left[\Phi_2^2\right] \quad , \Phi_2 = \max\left(\frac{2\sqrt{k}}{\beta^\star \omega y}, \frac{500\nu}{y^2\omega}\right) \tag{A.43}$$

The expression of turbulent kinetic energy is:

$$\frac{\partial k}{\partial t} + U_k \frac{\partial k}{\partial x_k} = P_k - \beta^\star k\omega + \frac{\partial}{\partial x_k}\left[(\nu + \sigma_k \nu_t)\frac{\partial k}{\partial x_k}\right] \tag{A.44}$$

Where P_k is the production term which is expressed as follows:

$$P_k = \min\left(P, 10\beta^\star k\omega\right) \tag{A.45}$$

On the other hand, the eddy oscillation frequency reads:

$$\frac{\partial \omega}{\partial t} + U_k \frac{\partial \omega}{\partial x_k} = \alpha S^2 - \beta^\star \omega^2 + \frac{\partial}{\partial x_k}\left[(\nu + \sigma_\omega \nu_t) \frac{\partial \omega}{\partial x_k} \right] + 2(1-F_1)\sigma_{\omega 2} \frac{1}{\omega} \frac{\partial k}{\partial x_k} \frac{\partial \omega}{\partial x_k} \tag{A.46}$$

With F_1 a function defined as:

$$F_1 = \tanh\left[\Phi_1^4\right], \Phi_1 = \min\left[\max\left(\frac{\sqrt{k}}{\beta^\star \omega y}, \frac{500\nu}{y^2 \omega}\right), \frac{4\sigma}{CD}\right]. \tag{A.47}$$

$$CD_{k\omega} = \max\left(2\rho\sigma_{\omega 2}\frac{1}{\omega}\frac{\partial k}{\partial x_i}\frac{\partial \omega}{\partial x_i}, 10^{-10}\right) \tag{A.48}$$

The constants being:

$\beta^\star$	a_1	α_1	β_1	σ_{k1}	$\sigma_{\omega 1}$	α_2	β_2	σ_{k2}	$\sigma_{\omega 2}$
0.09	0.31	5/9	3/40	0.85	0.5	0.44	0.0828	1	0.856

Table A.2–*Constants of the $k-\omega$ SST model included in code_saturne.*

A final calculation stage is used to blend the behaviour of the turbulence model depending on the closeness to the obstacles in the flow; it reads:

$$\phi = \phi_1 F_1 + \phi_2 (1 - F_1) \tag{A.49}$$

Therefore, with respect to the wall distance y, the function ϕ is simplified to match a classical $k-\omega$ model (low Reynolds model) or to match the $k-\epsilon$ model (high Reynolds).

A.4.3/ Wall functions

From a programming point of view, selection of wall functions is made using the parameters *iwallf* for velocity $\underline{U}$ and *iwalls* for scalar fields Y in the *cs_user_parameters.c* routine.

The initial dimensionless equation for momentum based τ_w at the first cell above the wall is tweaked so that it becomes also non-dimensioned by the turbulent kinetic energy k. a second dimensionless velocity friction is assumed, it is denoted u_k. It fulfils the relation $u_\star = \frac{\tau_w}{\rho u_k}$. Mathematically it reads: $u_k = \sqrt{\sqrt{C_\mu} k}$

Wall function for velocity

For velocity, a law is used that automatically switches from rough to smooth behaviour. Hence u^+ is computed as follows:

$$u^+ = \frac{1}{\kappa}\ln\left(\frac{(z+z_0)u_k}{\nu + \alpha \xi u_k}\right) + Cst_{smooth} \tag{A.50}$$

with:

- $\alpha = \exp\left(-\kappa(Cst_{rough} - Cst_{smooth})\right) \simeq 0.26$

- $z_0 = \alpha\xi \exp\left(-\kappa Cst_{smooth}\right) = \xi \exp\left(-\kappa Cst_{rough}\right) \simeq \frac{\xi}{33}$
- $Cst_{smooth} = 5,2$
- $Cst_{rough} = 8.5$

Wall functions for the scalars

S_f is the joint surface of the cell with the wall. Assuming on the orthogonal cell, eq. (2.26) is simplified such as:

$$(\Phi_Y)_f = S_f h_I^Y \left(Y_I - Y_w\right) \tag{A.51}$$

In which h_I^Y is the rate of transfer. When the flow is turbulent and especially at the first cell level, the velocity profile in the area is of a logarithmic shape. Introducing the scalar friction as $Y_\star$ such as $Y_\star = \frac{\Phi_Y}{\rho u_k}$ [2] and $Y^+ = \frac{Y_I - Y_w}{Y_\star}$ the dimensionless scalar difference at the wall, the exchanged coefficient can be rewritten as:

$$h_I^Y = \frac{\kappa}{d} \times \frac{y^+}{Y^+} \tag{A.52}$$

Whence d is the distance from the cell centre to the wall surface, so $\frac{y^+}{Y^+}$ is the correction factor of the exchange coefficient for molecular diffusion. Introducing the dimensionless distance at the first cell level as $\frac{du_k}{\nu}$ and the dimensionless scalar gradient, eq. (A.52) can be rewritten as:

$$h_I^Y = \frac{\kappa}{\nu} \times \frac{u_k Y_\star}{Y_I - Y_w} \tag{A.53}$$

For the scalars, either temperature or humidity, the Arpaci-Larsen three-layer wall function is used, it reads:

$$\begin{cases} \frac{y^+}{Y^+} = \frac{1}{\sigma} & \text{if } y^+ < y_1^+ \\ \frac{y^+}{Y^+} = \frac{y^+}{a_2 - \frac{\sigma_T}{2a_1 (y^+)^2}} & \text{if } y_1^+ \leqslant y^+ < y_2^+ \\ \frac{y^+}{Y^+} = \frac{y_T^+}{\frac{\sigma_T}{} \ln(y^+) + a_3} & \text{if } y_2^+ \leqslant y^+ \end{cases} \tag{A.54}$$

whence y_1^+ and y_2^+ discriminate the viscous layer and the turbulent layer distances, σ is the Prandtl number (or the Schmidt number), σ_T is the turbulent Prandtl number (or the turbulent Schmidt number) and $a_2 = 15\sigma^{\frac{2}{3}}$ plus $a_3 = 15\sigma^{\frac{2}{3}} - \frac{\sigma_T}{2\kappa}\left(1 + \ln\left(\frac{1000\kappa}{\sigma_T}\right)\right)$ are two functions that make the function continuous.

A.4.4/ code_saturne: Bi-periodic source term

Within the scope of the periodicity condition, the temperature field can be written as a warming contribution between two adjacent periodic motif and a periodic temperature components:

$$T(y,z) = y\alpha_T + \widetilde{T}(y,z) \tag{A.55}$$

With α_T is a constant so that $y\alpha_T$ is not a function of time. The latter reads between two motifs:

$$\widetilde{T}(y,z) = \widetilde{T}(y + \mathcal{S}_\text{m}, z) \tag{A.56}$$

---

[2] When using a single velocity layer, $u_k = u_\star$

The gradient operator is therefore obtained such as:

$$\vec{\mathrm{g}}\mathrm{rad}\,(T(y,z)) = \vec{\mathrm{g}}\mathrm{rad}\left(\widetilde{T}(y,z) + \alpha_T \times y\right) \tag{A.57}$$

Using the linearity property of the gradient operator:

$$\vec{\mathrm{g}}\mathrm{rad}\,(T(y,z)) = \vec{\mathrm{g}}\mathrm{rad}\left(\widetilde{T}(y,z)\right) + \vec{\mathrm{g}}\mathrm{rad}\,(\alpha_T \times y) \tag{A.58}$$

This can be simplified in the streamwise direction as follows:

$$\vec{\mathrm{g}}\mathrm{rad}\,(T(y,z)) = \vec{\mathrm{g}}\mathrm{rad}\left(\widetilde{T}(y,z)\right) + \alpha_T \vec{e}_y \tag{A.59}$$

From the conservation of energy, assuming a heat source (module motif) it reads:

$$C_p\left(\frac{\partial \rho T}{\partial t} + \mathrm{div}\,(\rho\vec{U}T\,(y,z))\right) = -\,\mathrm{div}\,(\vec{\varphi}_T) \tag{A.60}$$

Reinjecting Equation (A.55) in Equation (A.60):

$$C_p\left(\frac{\partial\left[\rho\left(\widetilde{T}(y,z) + \alpha_T y\right)\right]}{\partial t} + \mathrm{div}\left(\rho\vec{u}\widetilde{T}(y,z) + \rho\vec{u}\alpha_T y\right)\right) = -\,\mathrm{div}\left(\vec{\varphi}_{\widetilde{T}}\right) \tag{A.61}$$

Developing the left-hand side of the left term, it reads:

$$C_p\left(\frac{\partial\left(\rho\widetilde{T}(y,z)\right)}{\partial t} + \alpha_T y\frac{\partial\rho}{\partial t} + \underbrace{\mathrm{div}\left(\rho\vec{u}\widetilde{T}(y,z) + \rho\vec{u}\alpha_T y\right)}_{div(A+B)=div(A)+div(B)}\right) = -\,\mathrm{div}\left(\vec{\varphi}_{\widetilde{T}}\right) \tag{A.62}$$

Developing the right-hand side of the left term and using the properties of the divergence operator it leads to:

$$C_p\left(\frac{\partial\left(\rho\widetilde{T}(y,z)\right)}{\partial t} + \mathrm{div}\left(\rho\vec{u}\widetilde{T}(y,z)\right) + \underbrace{\cancelto{0}{\alpha_T y\frac{\partial\rho}{\partial t} + \alpha_T y\,\mathrm{div}\,(\rho\vec{u})}}_{\text{mass conservation}} + \alpha_T\rho\underbrace{\vec{u}\cdot\vec{\mathrm{g}}\mathrm{rad}y}_{u_y}\right) = -\,\mathrm{div}\left(\vec{\varphi}_{\widetilde{T}}\right) \tag{A.63}$$

α_T is then deduced from the global steady-state balance over the periodic domain (Green Gauss Theorem), it reads:

$$\cancelto{0}{\oint_{\partial V}\rho\vec{u}\widetilde{T}(y,z)\cdot\vec{n}\,dS} + \int_V \alpha_T\rho u_y\,dV = \oint_{\partial V} -\vec{\varphi}_{\widetilde{T}}\cdot\vec{n}\,dS \tag{A.64}$$

Finally all calculus performed:

$$\alpha_T = \frac{2\times\Phi(L+e)}{C_p\dot{m}\mathcal{S}_{\mathrm{m}}} \tag{A.65}$$

A.5/ Performance of U_{values} in FPV1 and FPV2 setup

U_{values} method

First, we describe the thermal performance of the floating installations carried out in the course of the work through the spectrum of a single-layer energy balance at the module level. When mathematics reads almost similarly to Equation 1.21, a theoretical capacity term is added to the budget to mimic the real inertia of the floating module. Then the equation reads:

$$mC_p \frac{\partial T_\mathrm{m}}{\partial t} = -\mathrm{P}_\mathrm{m} + \tau\alpha\phi_\mathrm{sw,poa} + \mathrm{U}_{values} \times (T_\mathrm{m} - T_\mathrm{amb}) \tag{A.66}$$

A conservative hypothesis is that the plane of array irradiance $\phi_\mathrm{sw,poa}$ is reduced by an amount of 5% due to glass reflectivity. The calculation is performed using Python; the data inputs are the physical fields measured at the two floating test sites. Specifically in the FPV2 analysis, the power production P_m is set constant to $50\,\mathrm{W\,m^{-2}}$.

The time series of U_{values} obtained are then filtered, selecting the instant for which the incident irradiation is greater than or equal to $500\,\mathrm{W\,m^{-2}}$ (this threshold was applied in Dörenkämper et al., 2021 to describe U_{values} obtained at the two FPV test sites investigated). To reduce the inconsistent U_{values}, very large in front of 10 [3], a filter is applied for values where the temperature difference between the module and the air is greater than 10 °C.

A final filtering step is applied to the FPV2 data to reduce inconsistent values due to the shading of the meteorological mast. Values between 12p.m. and 12a.m. are removed from the data set. Thus, the assumption of constant electrical production of $50\,\mathrm{W\,m^{-2}}$ is rather relevant, the system works a priori in a degraded regime during the afternoon following the charge of the batteries during the morning.

A.5.1/ Global thermal performances of floating systems

The results obtained for the FPV1 experiment and the dependence of the parameter U_{values} on the mean wind speed measured above the water are shown in Figure A.1, the results for the FPV2 experiment are shown in Figure A.2, the dependence of U_{values} is expressed in relation to the mean wind speed measured by the low frequency system. The main statistical results of the study are shown in Table A.3. First, it can be seen that U_{values} increases as the mean wind speed increases, but the level of evidence remains rather low for the FPV1 experiment, as the residuals of the linear law are low (0.1, 0.09, 0.1). The level of relevance is higher for FPV2, but remains low (0.24). Wind levels are quite modest in FPV1 during the filtered period; On average, we observe: $1.2\,\mathrm{m\,s^{-1}}$, $2.1\,\mathrm{m\,s^{-1}}$ and $1.2\,\mathrm{m\,s^{-1}}$, while the average value observed in FPV2 is $2.8\,\mathrm{m\,s^{-1}}$. This character can provide an initial explanation for the low level of proof obtained in FPV1 compared to FPV2.

Interestingly, it can be seen that the level of U_{values} is correlated with seasonal properties in FPV1, with values significantly lower at this time of year compared to warmer periods. As the geometry of the installation has not changed, more than 80% of the distribution of points is below the limit established for the ”Open footprint” class in winter in FPV1. The median is $22.09\,\mathrm{W\,K^{-1}\,m^{-2}}$ while the wind levels are similar to those of the summer period. The median values of U_{values} appear to be consistent with the installation of standalone and free footprint

---

[3] recall that very large means at least $Value > 10 \times Threshold$

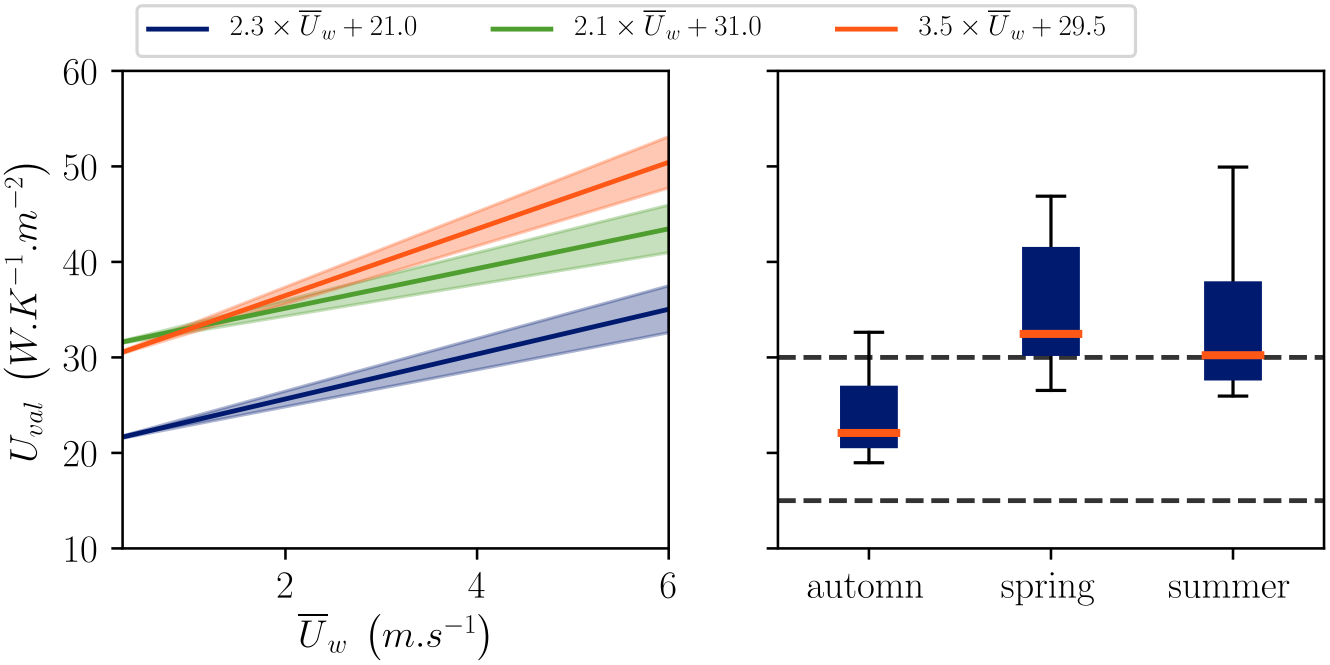

Figure A.1–*Evaluation of* U$_{values}$ *for the FPV1 prototype based on seasonal subsets. Boxplots indicate the data distribution that lead to the linear laws.*

installations experienced (32.46 W K^{-1} m^{-2} and 30.23 W K^{-1} m^{-2} for FPV1, 34.95 W K^{-1} m^{-2} for FPV2).

When we observe the distributions of U$_{values}$, we notice a significant dispersion around the median value, the interquartile spaces which group 50% of the observations range from 6.2 W K^{-1} m^{-2} to 14.8 W K^{-1} m^{-2} at FPV2, and this despite the fact that thermal inertia is taken into account. Furthermore, the values of the third-order moments show a skewness of the whole distribution towards high-value trends. High values occur when the irradiation is very high (at least 800 W m^{-2}) and the difference in module versus atmosphere temperature is modest, so it is a rather transient phenomenon that is at work for these atypical times. The skewness values also provide additional motivation to use the median values, which better represent the real distribution than the mean value, naturally biased by the high transient values and not as representative.

Given the classification thresholds proposed by H. Liu et al., 2018 and the results of the medians of U$_{values}$ obtained experimentally, we can conclude that the classification is quite relevant considering the type of installation investigated. The wind dependence of the cooling is well-modelled, but suffers from inconsistencies despite the integration of an inertial parameter; climatic effects are also notable. Therefore, it is relevant to use the classification to study the cooling performance attributed to the installation geometry when the outdoor conditions are mild, with sufficient sunlight and a significant temperature difference. The method remains biased towards cold climates with less than ideal conditions for PV production. Furthermore, the method requires an estimate of electricity production and the optical reflectance coefficient IAM to be used optimally. A conservative choice of parameters (low power production and low reflectance) leads to an overestimation of U$_{values}$.

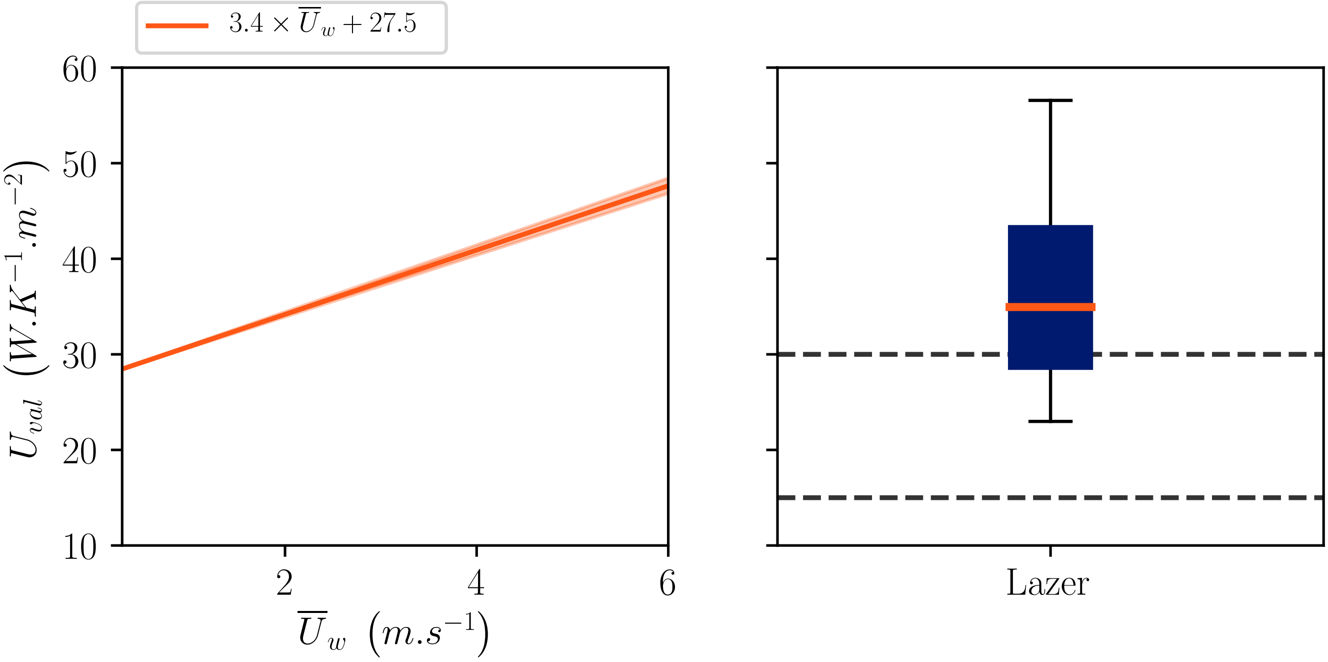

Figure A.2–*Evaluation of the* U$_{values}$ *for the FPV2 experiment. Boxplot indicates the data distribution that lead to the linear law.*

	FPV1			FPV2
Statistical property	Fall	Spring	Summer	-
U_c	21	31	29,5	27,5
U_v	2,3	2,1	3,5	3,4
r^2	0,1	0,09	0,1	0,24
Skewness	1,39	0,89	1,2	1,41
Median	22,09	32,46	30,23	34,95
IQR	6,2	11,1	10	14,82

Table A.3–*Statistical figures describing the distribution of* U$_{values}$ *obtained from empirical heat budgets. Note that U_c and U_v refer to the coefficients of the Fainman model.*

Abdelaziz, O. A. A. (2009). *Development of multi-scake, multi-physics, analysis of capability and its application to novel heat exchangers design and optimization* (Doctoral dissertation). University of Maryland, College Park.

Akhsassi, M., El Fathi, A., Erraissi, N., Aarich, N., Bennouna, A., Raoufi, M., & Outzourhit, A. (2018). Experimental investigation and modeling of the thermal behavior of a solar PV module. *Solar Energy Materials and Solar Cells*, *180*(June 2017), 271–279. https://doi.org/10.1016/j.solmat.2017.06.052

Aly, S. P., Ahzi, S., Barth, N., & Abdallah, A. (2018). Using energy balance method to study the thermal behavior of PV panels under time-varying field conditions. *Energy Conversion and Management*, *175*(July), 246–262. https://doi.org/10.1016/j.enconman.2018.09.007

Amino, H., Flageul, C., Benhamadouche, S., Tiselj, I., Carissimo, B., & Ferrand, M. (n.d.). A time-staggered second order conservative time scheme for variable density flow. *International Journal for Numerical Methods in Fluids*.

Amorocho, J., & DeVried, J. (1981). A new evaluation of the wind stress coefficient over water surfaces. *Journal of Geophysical Research*, *86*(C5), 4307. https://doi.org/10.1029/jc086ic05p04307

Amy de la Breteque, E. (2009). Thermal aspects of c-Si photovoltaic module energy rating. *Solar Energy*, *83*(9), 1425–1433. https://doi.org/10.1016/j.solener.2008.10.013

Anderson, A. M., & Moffat, R. J. (1992). The adiabatic heat transfer coefficient and the superposition kernel function: Part 1—data for arrays of flatpacks for different flow conditions. *Journal of Electronic Packaging, Transactions of the ASME*, *114*(1), 14–21. https://doi.org/10.1115/1.2905435

Archambeau, F., Méchitoua, N., & Sakiz, M. (2004). Code Saturne: A Finite Volume Code for Turbulent flows - Industrial Applications. *International Journal on Finite Volumes*, *1*(1).

Armstrong, S., & Hurley, W. G. (2010). A thermal model for photovoltaic panels under varying atmospheric conditions. *Applied Thermal Engineering*, *30*(11-12), 1488–1495. https://doi.org/10.1016/j.applthermaleng.2010.03.012

Assouline, S., Narkis, K., & Or, D. (2010). Evaporation from partially covered water surfaces. *Water Resources Research*, *46*(10), 1–12. https://doi.org/10.1029/2010WR009121

Assouline, S., Narkis, K., & Or, D. (2011). Evaporation suppression from water reservoirs: Efficiency considerations of partial covers. *Water Resources Research*, *47*(7), 1–8. https://doi.org/10.1029/2010WR009889

Aubinet, M. (1994). Longwave sky radiation. *Solar Energy*, *53*(2), 147–154.

Aubinet, M., Vesala, T., & Papale, D. (2012). *Eddy Covariance: A pratical Guide To Measurement and Data Analysis*. https://doi.org/10.1007/978-94-007-2351-1

A.W. Blakers, A. Wang, A.M. Milne, J. Zhao, & M.A. Green. (1989). 22.8% Efficient SiliconSolar Cell, Appl. Phys. Lett. 55 (1989) 1363–1365. *Appl. Phys. Lett*, *55*(13), 363–365.

Babuška, I. (1976). Homogenization Approach In Engineering, 137–153. https://doi.org/10.1007/978-3-642-85972-4_8

Baumeister, H., Nordrhein-westfalen, L. G., & Hornberg, C. (2013). Evidence for the temperature-mitigating capacity of urban blue space - A health geographic perspective BLUE SPACE – A HEALTH GEOGRAPHIC PERSPECTIVE. (December). https://doi.org/10.3112/erdkunde.2013.04.05

Beljaars, A. C. M. (1987). The Influence of Sampling and Filtering on Measured Wind Gusts. *Journal of Atmospheric and Oceanic Technology*, *4*(4), 613–626. https://doi.org/10.1175/1520-0426(1987)004⟨0613:TIOSAF⟩2.0.CO;2

Berdahl, P., & Fromberg, R. (1982). The thermal radiance of clear skies. *Solar Energy*, *29*(4), 299–314. https://doi.org/10.1016/0038-092X(82)90245-6

Blair, M. F. (1983). Influence of free-stream turbulence on turbulent boundary layer heat transfer and mean profile development, part II—analysis of results. *Journal of Heat Transfer*, *105*(1), 41–47. https://doi.org/10.1115/1.3245557

Blanken, P. D., Rouse, W. R., Culf, A. D., Spence, C., Boudreau, L. D., Jasper, J. N., Kochtubajda, B., Schertzer, W. M., Marsh, P., & Verseghy, D. (2000). Eddy covariance measurements of evaporation from Great Slave Lake, Northwest Territories, Canada. *Water Resources Research*, *36*(4), 1069–1077. https://doi.org/10.1029/1999WR900338

Blas, M. A. D., Torres, J. L., & Prieto, E. (2002). Selecting a suitable model for characterizing photovoltaic devices. *25*, 371–380.

Blasius, H. (1908). *Grenzschichten in Flüssigkeiten mit kleiner Reibung* (tech. rep.). Zeitschrift für Mathematik und Physik.

Bliss, R. W. (1961). Atmospheric radiation near the surface of the ground: A summary for engineers. *Solar Energy*, *5*(3), 103–120. https://doi.org/https://doi.org/10.1016/0038-092X(61)90053-6

Blocken, B., Stathopoulos, T., & Carmeliet, J. (2007). CFD simulation of the atmospheric boundary layer : wall function problems. *41*, 238–252. https://doi.org/10.1016/j.atmosenv.2006.08.019

Bontempo Scavo, F., Tina, G. M., Gagliano, A., & Nižetić, S. (2021). An assessment study of evaporation rate models on a water basin with floating photovoltaic plants. *International Journal of Energy Research*, *45*(1), 167–188. https://doi.org/10.1002/er.5170

Bottaro, A. (2019). Flow over natural or engineered surfaces: An adjoint homogenization perspective. *Journal of Fluid Mechanics*, *877*, P1. https://doi.org/10.1017/jfm.2019.607

Bowen, I. S. (1926). The Ratio of Heat Losses by Conduction and by Evaporation from any Water Surface. *Physical Review*, *27*(6), 779–787. https://doi.org/10.1103/PhysRev.27.779

Braisaz, B., Dupeyrat, P., Lindsay, A., & Radouane, K. (2011). AN ADVANCED MODEL OF PV POWER PLANTS BASED ON MODELICA®, 3644–3648.

Broadbent, A., Coutts, A., Tapper, N., Demuzere, M., & Beringer, J. (2018). The microscale cooling effects of water sensitive urban design and irrigation in a suburban environment. *Theoretical and Applied Climatology*, *134*. https://doi.org/10.1007/s00704-017-2241-3

Brutsart, W. (1982). *Evaporation into the Atmosphere*. https://doi.org/10.1017/978-94-017-1497-6

Burt, W. V. (1954). Albedo Over Wind-Roughened Water. https://doi.org/10.1175/1520-0469(1954)011⟨0283:aowrw⟩2.0.co;2

Chahine, A., Matharan, P., Wendum, D., Musson-Genon, L., Bresson, R., & Carissimo, B. (2015). Modelling atmospheric effects on performance and plume dispersal from natural draft wet cooling towers. *Journal of Wind Engineering and Industrial Aerodynamics*, *136*, 151–164. https://doi.org/10.1016/j.jweia.2014.11.007

Charnock, H. (1955). Wind stress on water. *Quarterly Journal of the Royal Meteorological Society*, *81*(350), 639–639. https://doi.org/10.1002/qj.49708135026

Chatterjee, A., Keyhani, A., & Kapoor, D. (2011). Identification of photovoltaic source models. *IEEE Transactions on Energy Conversion*, *26*(3), 883–889. https://doi.org/10.1109/TEC.2011.2159268

Chen, B., Maloney, J., Clark, D., & Mei, W. N. (1995). Measurement of night sky emissivity in determining radiant cooling from cool storage roofs and roof ponds. *Proceedings of the National Passive Solar Conference*, *20*(1), 1–6.

Chenni, R. Ã., Makhlouf, M., Kerbache, T., & Bouzid, A. (2007). A detailed modeling method for photovoltaic cells. *32*, 1724–1730. https://doi.org/10.1016/j.energy.2006.12.006

Choi, S. M., Park, C.-d., Cho, S.-h., & Lim, B.-j. (2022). Effects of wind loads on the solar panel array of a fl oating photovoltaic system e Experimental study and economic analysis. *Energy*, *256*, 124649. https://doi.org/10.1016/j.energy.2022.124649

Chowdhury, M. G., Goossens, D., Goverde, H., & Catthoor, F. (2018). Experimentally validated CFD simulations predicting wind effects on photovoltaic modules mounted on inclined surfaces. *Sustainable Energy Technologies and Assessments*, *30*(March 2017), 201–208. https://doi.org/10.1016/j.seta.2018.10.005

Chowdhury, M. G., Goverde, H., Manganiello, P., Voroshazi, E., Poortmans, J., & Catthoor, F. (2019). Sensitivity analysis of the effect of forced convection on photovoltaic module temperature and energy yield. *Conference Record of the IEEE Photovoltaic Specialists Conference*, 1237–1241. https://doi.org/10.1109/PVSC40753.2019.8980517

Churchill, S. W., & Chu, H. H. (1975). Correlating equations for laminar and turbulent free convection from a vertical plate. *International Journal of Heat and Mass Transfer*, *18*(11), 1323–1329. https://doi.org/10.1016/0017-9310(75)90243-4

Condie, S. A., & Webster, I. T. (1997). The influence of wind stress, temperature, and humidity gradients on evaporation from reservoirs. *33*(12), 2813–2822.

Cooley, K. R. (1970). Energy Relationships in the Design of Floating Covers for Evaporation Reduction. *Water Resources Research*, *6*(3), 717–727. https://doi.org/10.1029/WR006i003p00717

Coskun, C., Toygar, U., Sarpdag, O., & Oktay, Z. (2017). Sensitivity analysis of implicit correlations for photovoltaic module temperature: A review. *Journal of Cleaner Production*, *164*, 1474–1485. https://doi.org/10.1016/j.jclepro.2017.07.080

Dabaghzadeh, N., & Eslami, M. (2019). Temperature distribution in a photovoltaic module at various mounting and wind conditions: A complete CFD modeling. *Journal of Renewable and Sustainable Energy*, *11*(5). https://doi.org/10.1063/1.5114895

Dalton, J. (1802). Experimental essays on the constitution of mixed gases ; on the force of steam or vapour from water and other liquids in different temperatures, both in a Torricellian vacuum and in air ; on evaporation ; and on the expansion of gases. *Manchester Literary and Philosophical Society*, 535–602.

Dammeier, F., Happle, G., & Rohrer, J. (2017). The contribution of water surface Fresnel reflection to BIPV yield. *Solar Energy*, *155*, 951–962. https://doi.org/10.1016/j.solener.2017.07.041

Dauxois, T., Peacock, T., Bauer, P., Caulfield, C. P., Cenedese, C., Gorlé, C., Haller, G., Ivey, G. N., Linden, P. F., Meiburg, E., Pinardi, N., Vriend, N. M., & Woods, A. W. (2021). Confronting Grand Challenges in environmental fluid mechanics. *020501*(6), 1–40. https://doi.org/10.1103/PhysRevFluids.6.020501

Davenport, A. G. (1960). Rationale for determining design wind velocities. *ASCE Journal of the Structural Division*, *86*(5), 39–68.

Daviau, N. (2016). *Études fines des échanges énergétiques entre les bâtiments et l ' atmosphère urbaine* (Doctoral dissertation).

De Moor, G. (2006). *Couche limite atmosphérique et turbulence - Les bases de la micrométéorologie dynamique* (M. France, Ed.).

Dhaundiyal, A., & Atsu, D. (2020). The effect of wind on the temperature distribution of photovoltaic modules. *Solar Energy*, *201*(October 2019), 259–267. https://doi.org/10.1016/j.solener.2020.03.012

Dolara, A., Leva, S., & Manzolini, G. (2015). ScienceDirect Comparison of different physical models for PV power output prediction. *Solar Energy*, *119*, 83–99. https://doi.org/10.1016/j.solener.2015.06.017

Domínguez, S. A., & de la Flor, F. J. S. (2016). The effect of evaporative cooling techniques on reducing urban heat. *Urban Climate Mitigation Techniques*, 113–130. https://doi.org/10.4324/9781315765839

Doormaal, J. P. V., & Raithby, G. D. (1984). Enhancements of the simple method for predicting incompressible fluid flows. *Numerical Heat Transfer*, *7*(2), 147–163. https://doi.org/10.1080/01495728408961817

Dörenkämper, M., Wahed, A., Kumar, A., de Jong, M., Kroon, J., & Reindl, T. (2021). The cooling effect of floating PV in two different climate zones: A comparison of field test data from the Netherlands and Singapore. *Solar Energy*, *214*(December 2020), 239–247. https://doi.org/10.1016/j.solener.2020.11.029

Driesse, A., Stein, J. S., & Theristis, M. (2022). Improving Common PV Module Temperature Models by Incorporating Radiative Losses to the Sky. (August).

Dubois, A. M., Badosa, J., Bourdin, V., Torres Aguilar, M. I., & Bonnassieux, Y. (2021). Estimation of the Uncertainty due to Each Step of Simulating the Photovoltaic Conversion under Real Operating Conditions. *International Journal of Photoenergy*, *2021*. https://doi.org/10.1155/2021/4228658

Dupré, O., Vaillon, R., & Green, M. (2015a). Physics of the temperature coefficients of solar cells. *Solar Energy Materials and Solar Cells*, *140*, 92–100. https://doi.org/10.1016/j.solmat.2015.03.025

Dupré, O. (2016). *Physics of the thermal behavior of photovoltaic devices* (Doctoral dissertation).

Dupré, O., Vaillon, R., & Green, M. (2015b). Physics of the temperature coefficients of solar cells. *Solar Energy Materials and Solar Cells*, *140*, pp. 92–100. https://hal.archives-ouvertes.fr/hal-01281189

Erbs, D. G., Klein, S. A., & Duffie, J. A. (1982). Estimation of the diffuse radiation fraction for hourly, daily and monthly-average global radiation. *Solar Energy*, *28*(4), 293–302. https://doi.org/10.1016/0038-092X(82)90302-4

Evangelisti, L., Guattari, C., & Asdrubali, F. (2019). On the sky temperature models and their influence on buildings energy performance: A critical review. *Energy and Buildings*, *183*, 607–625. https://doi.org/10.1016/j.enbuild.2018.11.037

Faiman, D. (2008). Assessing the outdoor operating temperature of photovoltaic modules. *Progress in Photovoltaics: Research and Applications*, *16*(4), 307–315. https://doi.org/10.1002/pip.813

From, E., & Kinneret, L. (1993). Eddy Correlation System Measurements and Energy Budget Estimates. *Water Resources*, *29*(4), 901–910.

Gao, W. (1993). Thermal effects of open space with a green area on urban environment Part I: A theoretical analysis and its application. *Journal of Architecture, Planning, Environment*, *448*.

Garratt, J. R. (1978). Transfer characteristics for a heterogeneous surface of large aerodynamic roughness. *Quarterly Journal of the Royal Meteorological Society*, *104*(440), 491–502. https://doi.org/10.1002/qj.49710444019

Gerasimov, D. N., & Yurin, E. I. (2018). *Kinetics of Evaporation* (Vol. 68). https://doi.org/10.1007/978-3-319-96304-4

Giuseppe Marco Tina, L. M., Fausto Bontempo Scavo. (2021). Analysis of water environment on the production of floating photovoltaic plants. *Renewable Energy*, *175*(In Press), 281–295. https://doi.org/10.1016/j.renene.2021.04.082

Glanz, D. J. G. T. O. (1973). Lincoln Lake ecologic study. *Water Resource Engineering*.

Gleick, P. (1996). *Water Resources* (Encycloped). Oxford University Press.

Glick, A., Ali, N., Bossuyt, J., Calaf, M., & Cal, R. B. (2020). Utility-scale solar PV performance enhancements through system-level modifications. *Scientific Reports*, *10*(1), 1–9. https://doi.org/10.1038/s41598-020-66347-5

Glick, A., Ali, N., Bossuyt, J., Recktenwald, G., Calaf, M., & Cal, R. B. (2020). Infinite photovoltaic solar arrays: Considering flux of momentum and heat transfer. *Renewable Energy*, *156*, 791–803. https://doi.org/10.1016/j.renene.2020.03.183

Glick, A., Smith, S. E., Ali, N., Bossuyt, J., Recktenwald, G., Calaf, M., & Cal, R. B. (2020). Influence of flow direction and turbulence intensity on heat transfer of utility-scale photovoltaic solar farms. *Solar Energy*, *207*(November 2019), 173–182. https://doi.org/10.1016/j.solener.2020.05.061

Gnielinski, V. (1975). Neue Gleichungen für den Wärme- und den Stoffübergang in turbulent durchströmten Rohren und Kanälen. *Forschung im Ingenieurwesen*, *41*(1), 8–16. https://doi.org/10.1007/BF02559682

Gökmen, N., Hu, W., Hou, P., Chen, Z., Sera, D., & Spataru, S. (2016). Investigation of wind speed cooling effect on PV panels in windy locations. *Renewable Energy*, *90*, 283–290. https://doi.org/10.1016/j.renene.2016.01.017

Golroodbari, S. Z., & van Sark, W. (2020). Simulation of performance differences between offshore and land-based photovoltaic systems. *Progress in Photovoltaics: Research and Applications*, (February), 1–14. https://doi.org/10.1002/pip.3276

Green, M. A., Blakers, A. W., Shi, J., Keller, E. M., & Wenham, S. R. (1984). 19.1% Efficient Silicon Solar Cell. *Applied Physics Letters*, *44*(12), 1163–1164. https://doi.org/10.1063/1.94678

Green, M., Emery, K., & Blakers, A. (1982). Silicon solar cells with reduced temperature sensitivity. *Electronics Letters*, *18*(2), 97. https://doi.org/10.1049/el:19820066

Green, M. A. (2003). General temperature dependence of solar cell performance and implications for device modelling. *Progress in Photovoltaics: Research and Applications*, *11*(5), 333–340. https://doi.org/10.1002/pip.496

Green, M. A. (1982). *Solar cells : operating principles, technology, and system applications*. Prentice-Hall Englewood Cliffs, N.J.

Green, M. A. (2001). Third generation photovoltaics: Ultra-high conversion efficiency at low cost. *Progress in Photovoltaics: Research and Applications*, *9*(2), 123–135. https://doi.org/10.1002/pip.360

Grimmond, C. S. B., & Oke, T. R. (1999). Aerodynamic Properties of Urban Areas Derived from Analysis of Surface Form. *Journal of Applied Meteorology*, *38*(9), 1262–1292. https://doi.org/10.1175/1520-0450(1999)038⟨1262:APOUAD⟩2.0.CO;2

Gross, G. (2017). Some effects of water bodies on the n environment – numerical experiments. *12*, 1–11.

Gu, W., Ma, T., Shen, L., Li, M., Zhang, Y., & Zhang, W. (2019). Coupled electrical-thermal modelling of photovoltaic modules under dynamic conditions. *Energy*, *188*, 116043. https://doi.org/10.1016/j.energy.2019.116043

Guen, V. L. (2022). *Deep learning for spatio-temporal forecasting – application to solar energy* (Doctoral dissertation). http://arxiv.org/abs/2205.03571

Guillemoles, J.-F., Kirchartz, T., Cahen, D., & Rau, U. (2018). *S-Q Guide for the Perplexed Solar Energy Conversion and the Shockley-Queisser Model, a Guide for the Perplexed* (tech. rep.).

Guimet, V., & Laurence, D. (2002). A linearised turbulent production in the k-ε model for engineering applications. *Engineering turbulence modelling and experiments 5* (pp. 157–166). Elsevier.

Haegel, B. N. M., Jr, H. A., Barnes, T., Breyer, C., Chiang, Y.-m., Wolf, S. D., Dimmler, B., Feldman, D., Goldschmidt, J. C., Hochschild, D., Inzunza, R., Kaizuka, I., Kroposki, B., Kurtz, S., Leu, S., Margolis, R., Matsubara, K., Metz, A., Metzger, W. K., … Bett, A. W. (2019). Terawatt-scale photovoltaics: Transform global energy. *Science*, 836. https://doi.org/10.1126/science.aaw1845

Hamilton, C. (2010). The ethical foundations of climate engineering. *Climate Change Geoengineering: Philosophical Perspectives, Legal Issues, and Governance Frameworks*, (July 2011), 39–58. https://doi.org/10.1017/CBO9781139161824.004

Hasan, K., Yousuf, S. B., Tushar, M. S. H. K., Das, B. K., Das, P., & Islam, M. S. (2022). Effects of different environmental and operational factors on the PV performance: A comprehensive review. *Energy Science and Engineering*, *10*(2), 656–675. https://doi.org/10.1002/ese3.1043

Helfer, F., Zhang, H., & Lemckert, C. (2009). Evaporation Reduction by Suspended and Floating Covers: Overview, Modelling and Efficienc. *Urban Water*, (16).

Hemmati, F., & Tariku, F. (2019). Review of the sky temperature and solar decomposition and their impact on thermal modeling. *Science and Technology for the Built Environment*, *25*(9), 1237–1243. https://doi.org/10.1080/23744731.2019.1629242

Henderson-Sellers, B. (1986). Calculating the surface energy balance for lake and reservoir modeling: A review. *Reviews of Geophysics*, *24*(3), 625–649. https://doi.org/10.1029/RG024i003p00625

Hindmarsh, A. C., Brown, P. N., Grant, K. E., Lee, S. L., Serban, R., Shumaker, D. E., & Woodward, C. S. (2005). SUNDIALS. *ACM Transactions on Mathematical Software*, *31*(3), 363–396. https://doi.org/10.1145/1089014.1089020

Hipsey, M. R., Bruce, L. C., Boon, C., Busch, B., Carey, C. C., Hamilton, D. P., Hanson, P. C., Read, J. S., De Sousa, E., Weber, M., & Winslow, L. A. (2019). A General Lake Model (GLM 3.0) for linking with high-frequency sensor data from the Global Lake Ecological Observatory Network (GLEON). *Geoscientific Model Development*, *12*(1), 473–523. https://doi.org/10.5194/gmd-12-473-2019

Hipsey, M. R., & Sivapalan, M. (2003). Parameterizing the effect of a wind shelter on evaporation from small water bodies. *Water Resources Research*, *39*(12), 1–9. https://doi.org/10.1029/2002WR001784

Hirst, L. C., & Ekins-Daukes, N. J. (2011). Fundamental losses in solar cells. *Progress in Photovoltaics: Research and Applications*, *19*(3), 286–293. https://doi.org/10.1002/pip.1024

Hollemann, C., Haase, F., Rienäcker, M., Barnscheidt, V., Krügener, J., Folchert, N., Brendel, R., Richter, S., Großer, S., Sauter, E., Hübner, J., Oestreich, M., & Peibst, R. (2020). Separating the two polarities of the POLO contacts of an 26.1%-efficient IBC solar cell. *Scientific Reports*, *10*(1), 1–15. https://doi.org/10.1038/s41598-019-57310-0

Horton, R. E. (1915). A New Evaporation Formula Developed. *78-4*, 196–200.

Huttner, S. (2012). Further development and application of the 3D microclimate simulation ENVI-met. *Mainz: Johannes Gutenberg-Universitat in Mainz*, 147. http://ubm.opus.hbz-nrw.de/volltexte/2012/3112/

J. F. Turner, J. (1966). Evaporation Study in a Humid Region, Lake Michie North Carolina. *Geological Survey Professinonal Paper*.

Jacobs, C., Klok, L., Bruse, M., Cortesão, J., Lenzholzer, S., & Kluck, J. (2020). Are urban water bodies really cooling? *Urban Climate*, *32*(January), 100607. https://doi.org/10.1016/j.uclim.2020.100607

Jaszczur, M., Hassan, Q., Szubel, M., & Majewska, E. (2018). Fluid flow and heat transfer analysis of a photovoltaic module under varying environmental conditions. *Journal of Physics: Conference Series*, *1101*(1). https://doi.org/10.1088/1742-6596/1101/1/012009

Jeong, H. S., Choi, J., Lee, H. H., & Jo, H. S. (2020). A study on the power generation prediction model considering environmental characteristics of floating photovoltaic system. *Applied Sciences (Switzerland)*, *10*(13). https://doi.org/10.3390/app10134526

JOHN FITZGERALD, W. (2022). Humans have installed 1 terawatt of solar capacity, generated over 1 petawatt of solar electricity in 2021. *PV Magazine USA*. https://pv-magazine-usa.com/2022/03/14/humans-install-1-terawatt-of-solar-capacity-generate-over-1-petawatt-of-solar-electricity-in-2021/

Jones, A. D., & Underwood, C. P. (2002). A thermal model for photovoltaic systems. *Fuel and Energy Abstracts*, *43*(3), 199. https://doi.org/10.1016/s0140-6701(02)85831-3

Jubayer, C. M., & Hangan, H. (2016). A numerical approach to the investigation of wind loading on an array of ground mounted solar photovoltaic (PV) panels. *Journal of Wind Engineering and Industrial Aerodynamics*, *153*, 60–70. https://doi.org/10.1016/j.jweia.2016.03.009

Jubayer, C. M., & Hangan, H. (2015). Numerical simulation of wind effects on a stand-alone ground mounted Photovoltaic (PV) system. *Journal of Wind Engineering and Industrial Aerodynamics*, *134*, 1–37. https://doi.org/10.1016/j.jweia.2014.08.008

Jubayer, C. M., & Hangan, H. (2014). Numerical simulation of wind effects on a stand-alone ground mounted photovoltaic (pv) system. *Journal of Wind Engineering and Industrial Aerodynamics*, *134*, 56–64. https://doi.org/https://doi.org/10.1016/j.jweia.2014.08.008

Jubayer, C. M., Siddiqui, K., & Hangan, H. (2016). CFD analysis of convective heat transfer from ground mounted solar panels. *Solar Energy*, *133*, 556–566. https://doi.org/10.1016/j.solener.2016.04.027

Kaplani, E., & Kaplanis, S. (2014). Thermal modelling and experimental assessment of the dependence of PV module temperature on wind velocity and direction, module orientation and inclination. *Solar Energy*, *107*, 443–460. https://doi.org/10.1016/j.solener.2014.05.037

Karatas, Y., & Yilmaz, D. (2021). Experimental investigation of the microclimate effects on floating solar power plant energy efficiency. *Clean Technologies and Environmental Policy*, (0123456789). https://doi.org/10.1007/s10098-021-02122-y

Kayri, M., Kayri, I., & Gencoglu, M. T. (2017). The performance comparison of Multiple Linear Regression, Random Forest and Artificial Neural Network by using photovoltaic and atmospheric data. *2017 14th International Conference on Engineering of Modern Electric Systems, EMES 2017*, 1–4. https://doi.org/10.1109/EMES.2017.7980368

Kim, J., & Verma, S. B. (1990). Components of surface energy balance in a temperate grassland ecosystem. *Boundary-Layer Meteorology*, *51*(4), 401–417. https://doi.org/10.1007/BF00119676

King, D. L., Boyson, W. E., & Kratochvil, J. A. (2004). Photovoltaic array performance model, SANDIA Report SAND2004-3535. *Sandia Report No. 2004-3535*, *8*(December), 1–19.

King, D. L., Gonzalez, S., Galbraith, M., & Boyson, W. E. (2007). *Performance Model for Grid-Connected Photovoltaic Inverters* (tech. rep.).

Kjeldstad, T., Lindholm, D., Marstein, E., & Selj, J. (2021). Cooling of floating photovoltaics and the importance of water temperature. *Solar Energy*, *218*(February), 544–551. https://doi.org/10.1016/j.solener.2021.03.022

Klasen, N., Lux, F., Weber, J., Roessler, T., & Kraft, A. (2022). A Comprehensive Study of Module Layouts for Silicon Solar Cells under Partial Shading. *IEEE Journal of Photovoltaics*, *12*(2), 546–556. https://doi.org/10.1109/JPHOTOV.2022.3144635

Kondo, J. (1975). Air-sea bulk transfer coefficients in diabatic conditions. *Boundary-Layer Meteorology*, *9*(1), 91–112. https://doi.org/10.1007/BF00232256

Kuchler, T. M. (1979). Evaluation of models to predict insolation on tilted surfaces. *Solar Energy*, *23*, 111–114.

Kumar, M. (2022). Impact of Water Waves on the Output Power of Floating PV Systems on Water Bodies.

Lalwani, M., Kothari, D., & Singh, M. (2010). Investigation of Solar Photovoltaic Simulation Softwares. *International Journal of Applied Engineering Research*, *1*(3), 585–601.

Launder, B. E., & Spalding, D. B. (1974). The numerical computation of turbulent flows. *Computer Methods in Applied Mechanics and Engineering*, *3*(2), 269–289. https://doi.org/https://doi.org/10.1016/0045-7825(74)90029-2

Lee, M., & Moser, R. D. (2015). Direct numerical simulation of turbulent channel flow up to {*re*}_{{τ}} ≈ *5200*. *Journal of Fluid Mechanics*, *774*, 395–415.

Li, P., Gao, X., Li, Z., & Zhou, X. (2022). Effect of the temperature difference between land and lake on photovoltaic power generation. *Renewable Energy*, *185*, 86–95. https://doi.org/10.1016/j.renene.2021.12.011

Lindholm, D., Kjeldstad, T., Selj, J., Marstein, E. S., & Fjær, H. G. (2021). Heat loss coefficients computed for floating PV modules. *Progress in Photovoltaics: Research and Applications*, (April), 1–12. https://doi.org/10.1002/pip.3451

Lindholm, D., Selj, J., Kjeldstad, T., Fjær, H., & Nysted, V. (2022). CFD modelling to derive U-values for floating PV technologies with large water footprint. *Solar Energy*, *238*(April), 238–247. https://doi.org/10.1016/j.solener.2022.04.028

Liu, H., Krishna, V., Lun Leung, J., Reindl, T., & Zhao, L. (2018). Field experience and performance analysis of floating PV technologies in the tropics. *Progress in Photovoltaics: Research and Applications*, *26*(12), 957–967. https://doi.org/10.1002/pip.3039

Liu, L., Wang, Q., Lin, H., Li, H., Sun, Q., & Wennersten, R. (2017). Power Generation Efficiency and Prospects of Floating Photovoltaic Systems. *Energy Procedia*, *105*, 1136–1142. https://doi.org/10.1016/j.egypro.2017.03.483

Lo, V., Orioli, A., Ciulla, G., & Gangi, A. D. (2010). An improved five-parameter model for photovoltaic modules Solar Energy Materials & Solar Cells An improved five-parameter model for photovoltaic modules. *Solar Energy Materials and Solar Cells*, *94*(8), 1358–1370. https://doi.org/10.1016/j.solmat.2010.04.003

Luo, M., Khayyer, A., & Lin, P. (2021). Particle methods in ocean and coastal engineering. *Applied Ocean Research*, *114*, 102734. https://doi.org/10.1016/j.apor.2021.102734

Maeda, M., Nagaoka, A., Araki, K., & Nishioka, K. (2022). Practical and simplified measurements for representative photovoltaic array temperatures robust to climate variations. *Solar Energy*, *231*(October 2020), 243–251. https://doi.org/10.1016/j.solener.2021.11.035

Magare, D., Sastry, O., Gupta, R., Bora, B., Singh, Y., & Mohammed, H. (2018). Wind Effect Modeling and Analysis for Estimation of Photovoltaic Module Temperature. *Journal of Solar Energy Engineering, Transactions of the ASME*, *140*(1). https://doi.org/10.1115/1.4038590

Manteghi, G., Bin Limit, H., & Remaz, D. (2015). Water bodies an urban microclimate: A review. *Modern Applied Science*, *9*(6), 1–12. https://doi.org/10.5539/mas.v9n6p1

Marco, G., Bontempo, F., Merlo, L., & Bizzarri, F. (2021). Comparative analysis of monofacial and bifacial photovoltaic modules for floating power plants. *Applied Energy*, *281*(October 2020), 116084. https://doi.org/10.1016/j.apenergy.2020.116084

Marinić-Kragić, I., Nižetić, S., Grubišić-Čabo, F., & Papadopoulos, A. M. (2018). Analysis of flow separation effect in the case of the free-standing photovoltaic panel exposed to various operating conditions. *Journal of Cleaner Production*, *174*, 53–64. https://doi.org/https://doi.org/10.1016/j.jclepro.2017.10.310

Martin, M., & Berdahl, P. (1984). Characteristics of infrared sky radiation in the united states. *Solar Energy*, *33*(3), 321–336. https://doi.org/https://doi.org/10.1016/0038-092X(84)90162-2

Mastrippolito, F. (2018). Optimisation de forme numérique de problèmes multiphysiques et multiéchelles : Application aux échangeurs de chaleur.

Matsukawa, H., & Kurokawa, K. (2005). Temperature fluctuation analysis of photovoltaic modules at short time interval. *Conference Record of the IEEE Photovoltaic Specialists Conference*, (February 2005), 1816–1819. https://doi.org/10.1109/PVSC.2005.1488505

Matthieu Chiodetti. (2019). Predicting Yields of Bifacial Pv Power Plants – What Accuracy Is Possible?, 991–996.

May Tzuc, O., Bassam, A., Mendez-Monroy, P. E., & Dominguez, I. S. (2018). Estimation of the operating temperature of photovoltaic modules using artificial intelligence techniques and global sensitivity analysis: A comparative approach. *Journal of Renewable and Sustainable Energy*, *10*(3). https://doi.org/10.1063/1.5017520

McGloin, R., McGowan, H., McJannet, D., & Burn, S. (2014). Modelling sub-daily latent heat fluxes from a small reservoir. *Journal of Hydrology*, *519*(PB), 2301–2311. https://doi.org/10.1016/j.jhydrol.2014.10.032

Melchor, V., Centeno. (1982). New formula for the equivalent night sky emissivity. *Solar Energy*, *28*(6), 489–498.

Menter, F. R. (1993). Zonal two equation k-w turbulence models for aerodynamic flows.

Merlier, L. (2016). On the interactions between urban structures and air flows : A numerical study of the effects of urban morphology on the building wind environment and the related building energy loads To cite this version : HAL Id : tel-01368556.

Micheli, L. (2022). The Temperature of Floating Photovoltaics: Case Studies, Models and Recent Findings. *Solar Energy*, *242*(May), 234–245. https://doi.org/10.1016/j.solener.2022.06.039

Migan-Dubois, A., Badosa, J., Bourdin, V., Torres Aguilar, M. I., & Bonnassieux, y. (2021). Conversion photoélectrique : quelles sont les étapes de simulation les plus incertaines ? *Journées Nationales sur l'Énergie Solaire (JNES)*. https://hal.archives-ouvertes.fr/hal-03312390

Miguet, F., & Groleau, D. (2002). A daylight simulation tool for urban and architectural spaces-application to transmitted direct and diffuse light through glazing. *Building and Environment*, *37*(8-9), 833–843. https://doi.org/10.1016/S0360-1323(02)00049-5

Mittag, M., Vogt, L., Herzog, C., Pfreundt, A., Shahid, J., Neuhaus, D. H., & Wirth, H. (2019). Thermal Modelling of Photovoltaic Modules in Operation and Production. *PV Solar Energy*, (September), 9–13.

Monin, A. S., & Obukhov, A. M. (1954). Basic laws of turbulent mixing in the surface layer of the atmosphere. *Tr. Akad. Nauk SSSR Geophiz. Inst*, *24*(151), 163–187.

Muresan, C., Vaillon, R., Menezo, C., & Morlot, R. (2004). Discrete ordinates solution of coupled conductive radiative heat transfer in a two-layer slab with fresnel interfaces subject to diffuse and obliquely collimated irradiation [Eurotherm Seminar 73 - Computational Thermal Radiation in Participating Media]. *Journal of Quantitative Spectroscopy and Radiative Transfer*, *84*(4), 551–562. https://doi.org/https://doi.org/10.1016/S0022-4073(03)00271-1

Nazari, S., & Eslami, M. (2021). Impact of frame perforations on passive cooling of photovoltaic modules: Cfd analysis of various patterns. *Energy Conversion and Management*, *239*, 114228. https://doi.org/https://doi.org/10.1016/j.enconman.2021.114228

Neau, H., Pigou, M., Fede, P., Ansart, R., Baudry, C., Mérigoux, N., Laviéville, J., Fournier, Y., Renon, N., & Simonin, O. (2020). Massively parallel numerical simulation using up to 36,000 CPU cores of an industrial-scale polydispersed reactive pressurized fluidized bed with a mesh of one billion cells. *Powder Technology*, *366*(March), 906–924. https://doi.org/10.1016/j.powtec.2020.03.010

Nguyen, X. H., & Nguyen, M. P. (2015). Mathematical modeling of photovoltaic cell/module/arrays with tags in Matlab/Simulink. *Environmental Systems Research*, *4*(1). https://doi.org/10.1186/s40068-015-0047-9

Notton, G., Cristofari, C., Mattei, M., & Poggi, P. (2005). Modelling of a double-glass photovoltaic module using finite differences. *Applied Thermal Engineering*, *25*(17-18), 2854–2877. https://doi.org/10.1016/j.applthermaleng.2005.02.008

Oke, T. (1987). Boundary layer climates, methuen london and new york.

Oliveira-Pinto, S., & Stokkermans, J. (2020). Assessment of the potential of different floating solar technologies – Overview and analysis of different case studies. *Energy Conversion and Management*, *211*(November 2019), 112747. https://doi.org/10.1016/j.enconman.2020.112747

Osborne, D. G., & Incropera, F. P. (1985). Experimental study of mixed convection heat transfer for transitional and turbulent flow between horizontal, parallel plates. *International Journal of Heat and Mass Transfer*, *28*(7), 1337–1344. https://doi.org/10.1016/0017-9310(85)90164-4

Pandey, D. K., Lee, R. B., & Paden, J. (1995). Effects of atmospheric emissivity on clear sky temperatures [International Conference on Sustainable Development Strategies and Global/Regional/Local Impacts on Atmospheric Composition and Climate]. *Atmospheric Environment*, *29*(16), 2201–2204. https://doi.org/https://doi.org/10.1016/1352-2310(94)00243-E

Pascal, R. (2022). Effects of Wind Load on the Mechanics of a PV Power Plant. *WCPEC2022 Conf.*

Peters, I., & Nobre, A. (2022). Deciphering the thermal behavior of floating photovoltaic installations. *Solar Energy Advances*, *2*(November 2021), 100007. https://doi.org/10.1016/j.seja.2021.100007

Pivovarov, A. (1973). *Thermal conditions in Freezing lakes and rivers.*

Plessis, G., Kaemmerlen, A., & Lindsay, A. (2014). BuildSysPro: a Modelica library for modelling buildings and energy systems. *Proceedings of the 10th International Modelica Conference, March 10-12, 2014, Lund, Sweden*, *96*, 1161–1169. https://doi.org/10.3384/ecp140961161

Pohlhausen, E., & Angrew, Z. (1921). -. *Math. Mech.*, *1*, 115.

Pörtner, H., & Roberts, D. (2022). *Ipcc, 2022: Climate change 2022: Impacts, adaptation, and vulnerability. contribution of working group ii to the sixth assessment report of the intergovernmental panel on climate change*. Cambridge University.

Pouyaud, B. (1987). L ’ évaporation des nappes d ’ eau libre L ’ exemple du Lac de Bam au Burkina Faso Évaporation. *Hydrology Continental*, *2*(2), 127–149.

Ranjbaran, P., Yousefi, H., Gharehpetian, G. B., & Astaraei, F. R. (2019). A review on floating photovoltaic (FPV)power generation units. *Renewable and Sustainable Energy Reviews*, *110*(April 2018), 332–347. https://doi.org/10.1016/j.rser.2019.05.015

Raupach, M. R. (1992). Drag and drag partition on rough surfaces. *Boundary-Layer Meteorology*, *60*(4), 375–395. https://doi.org/10.1007/BF00155203

Rekioua, D., & Matagne, E. (2012). *Optimization of Photovoltaic Power Systems*. https://doi.org/10.2174/97816080528511120101

Reza Reisi, A., Hassan Moradi, M., & Jamasb, S. (2013). Classification and comparison of maximum power point tracking techniques for photovoltaic system: A review. *Renewable and Sustainable Energy Reviews*, *19*, 433–443. https://doi.org/10.1016/j.rser.2012.11.052

Richter, A., Hermle, M., & Glunz, S. W. (2013). Reassessment of the limiting efficiency for crystalline silicon solar cells. *IEEE Journal of Photovoltaics*, *3*(4), 1184–1191. https://doi.org/10.1109/JPHOTOV.2013.2270351

Ritchie, H., & Roser, M. (2017). Water use and stress [https://ourworldindata.org/water-use-stress]. *Our World in Data.*

Ross, R. (1976). INTERFACE DESIGN CONSIDERATIONS FOR TERRESTRIAL SOLAR CELL MODULES, 801–806.

Ruschel, S. C., Gasparin, F. P., Costa, R. E., & Krenziger, A. (2016). Assessment of PV modules shunt resistance dependence on solar irradiance. *Solar Energy*, *133*, 35–43. https://doi.org/10.1016/j.solener.2016.03.047

Sah, C.-T., Noyce, R. N., & Shockley, W. (1956). Carrier Generation and Recombination in P-NV Junctions and P-N Junction Characteristics. *1*, 1228–1243. https://doi.org/10.1109/jrproc.1957.278528

Sahu, A., Yadav, N., & Sudhakar, K. (2016). Floating photovoltaic power plant: A review. *Renewable and Sustainable Energy Reviews*, *66*, 815–824. https://doi.org/10.1016/j.rser.2016.08.051

Sainju, A., & Regmi, A. (2014). A Collision Model to Improve Stability of Explicit Moving Particle Simulation Method. (January 2016).

Santiago, I., Trillo-Montero, D., Moreno-Garcia, I. M., Pallarés-López, V., & Luna-Rodríguez, J. J. (2018). Modeling of photovoltaic cell temperature losses: A review and a practice case in South Spain. *Renewable and Sustainable Energy Reviews*, *90*(March), 70–89. https://doi.org/10.1016/j.rser.2018.03.054

Sartori, E. (2006). Convection coefficient equations for forced air flow over flat surfaces. *Solar Energy*, *80*(9), 1063–1071. https://doi.org/10.1016/j.solener.2005.11.001

Schiro, F., Benato, A., Stoppato, A., & Destro, N. (2017). Improving photovoltaics efficiency by water cooling: Modelling and experimental approach. *Energy*, *137*, 798–810. https://doi.org/10.1016/j.energy.2017.04.164

Schuss, C., Eichberger, B., & Rahkonen, T. (2016). Impact of sampling interval on the accuracy of estimating the amount of solar energy. *Conference Record - IEEE Instrumentation and Measurement Technology Conference*, *2016-July*. https://doi.org/10.1109/I2MTC.2016.7520566

Schuss, C., & Fabritius, T. (2022). Impact of Environmental Conditions on the Degree of Efficiency and Operating Range of PV-Powered Electric Vehicles. *Applied Sciences (Switzerland)*, *12*(3). https://doi.org/10.3390/app12031232

Schwingshackl, C., Petitta, M., Wagner, J. E., Belluardo, G., Moser, D., Castelli, M., Zebisch, M., & Tetzlaff, A. (2013). Wind effect on PV module temperature: Analysis of different techniques for an accurate estimation. *Energy Procedia*, *40*, 77–86. https://doi.org/10.1016/j.egypro.2013.08.010

Sciffert, C. (2022). Mechanical Stress in PV panels in floating PV systems. *WCPEC2022 Conf.*

Shademan, M., Barron, R., Balachandar, R., & Hangan, H. (2014). Numerical simulation of wind loading on ground-mounted solar panels at different flow configurations. *Canadian Journal of Civil Engineering*, *41*(8), 728–738. https://doi.org/10.1139/cjce-2013-0537

Sharples, S., & Charlesworth, P. S. (1998). Full-scale measurements of wind-induced: Convective heat transfer from a roof mounted flat plate solar collector. *Solar Energy*, *62*(2), 69–77. https://doi.org/10.1016/S0038-092X(97)00119-9

Shockley, W. (1950). *Electrons and holes in semiconductors: With applications to transistor electronics*. van Nostrand.

Shockley, W., & Queisser, H. J. (1961). Detailed balance limit of efficiency of p-n junction solar cells. *Journal of Applied Physics*, *32*(3), 510–519. https://doi.org/10.1063/1.1736034

Shongwe, S., & Hanif, M. (2015). Comparative Analysis of Different Single-Diode PV Modeling Methods, 1–9.

Shuttleworth, W. J. (2007). Putting the 'vap' into evaporation. *Hydrology and Earth System Sciences*, *11*(1), 210–244. https://doi.org/10.5194/hess-11-210-2007

Silvestre, S. (2018). *Strategies for Fault Detection and Diagnosis of PV Systems*. Elsevier Inc. https://doi.org/10.1016/B978-0-12-812959-3.00007-1

Skoplaki, E., & Palyvos, J. A. (2009). Operating temperature of photovoltaic modules: A survey of pertinent correlations. *Renewable Energy*, *34*(1), 23–29. https://doi.org/10.1016/j.renene.2008.04.009

Smith, S. E., Glick, A., Ali, N., Bossuyt, J., McNeal, J., Recktenwald, G., Calaf, M., & Cal, R. B. (2020). Configuration Effects on Flow Dynamics and Convective Behavior in Large-Scale Solar Arrays. *Conference Record of the IEEE Photovoltaic Specialists Conference*, *2020-June*, 2195–2196. https://doi.org/10.1109/PVSC45281.2020.9300740

Sparrow, E. M., Niethammer, J. E., & Chaboki, A. (1982). Heat transfer and pressure drop characteristics of arrays of rectangular modules encountered in electronic equipment. *International Journal of Heat and Mass Transfer*, *25*(7), 961–973. https://doi.org/10.1016/0017-9310(82)90071-0

Steadman, R., & Steadman, R. (1994). Norms of apparent temperature in australia. *Aust. Met. Mag*, *43*.

Stefan, H. G., Dhamotharan, S., & Schiebe, F. R. (1982). Temperature/Sediment Model for a Shallow Lake. *Journal of the Environmental Engineering Division*, *108*(4), 750–765. https://doi.org/10.1061/JEEGAV.0001324

Suh, J., Jang, Y., & Choi, Y. (2019). Comparison of Electric Power Output Observed and Estimated from Floating Photovoltaic Systems: A Case Study on the Hapcheon Dam, Korea. *Sustainability*, *12*(1), 276. https://doi.org/10.3390/su12010276

Test, F. L., Lessmann, R. C., & Johary, A. (1981). Heat transfer during wind flow ower rectangular bodies in the natural environment. *Journal of Heat Transfer*, *103*(2), 262–267. https://doi.org/10.1115/1.3244451

Theristis, M. (2022). International Photovoltaic Modeling Intercomparison.

Theristis, M., Venizelou, V., Makrides, G., & Georghiou, G. E. (2018). Energy Yield in Photovoltaic Systems. *Mcevoy's handbook of photovoltaics* (pp. 671–713). Elsevier. https://doi.org/10.1016/B978-0-12-809921-6.00017-3

Tian, H., Mancilla-david, F., Ellis, K., Jenkins, P., & Muljadi, E. (2012). A Detailed Performance Model for Photovoltaic Systems Preprint. *Solar Energy Journal*, (July).

Tian, W., Wang, Y., Ren, J., & Zhu, L. (2007). Effect of urban climate on building integrated photovoltaics performance. *Energy Conversion and Management*, *48*(1), 1–8. https://doi.org/10.1016/j.enconman.2006.05.015

Tim Umoette, A. (2016). Design of Stand Alone Floating PV System for Ibeno Health Centre. *Science Journal of Energy Engineering*, *4*(6), 56. https://doi.org/10.11648/j.sjee.20160406.12

Tina, G. M., Marletta, G., & Sardella, S. (2012). Multi-layer thermal models of pv modules for monitoring applications. *2012 38th IEEE Photovoltaic Specialists Conference*, 002947–002952.

Tina, G. M., & Gagliano, A. (2016). An improved multi-layer thermal model for photovoltaic modules. *2016 International Multidisciplinary Conference on Computer and Energy Science, SpliTech 2016*. https://doi.org/10.1109/SpliTech.2016.7555927

Tobler, W. (1970). A COMPUTER MOVIE SIMULATING URBAN GROWTH IN THE DETROIT REGION. *Economic Geography*, *46*, 234–240. https://doi.org/10.1126/science.ns-13.332.462

Tominaga, Y., Sato, Y., & Sadohara, S. (2015). CFD simulations of the effect of evaporative cooling from water bodies in a micro-scale urban environment : Validation and application studies. *Sustainable Cities and Society*, *19*, 259–270. https://doi.org/10.1016/j.scs.2015.03.011

Toparlar, Y., Blocken, B., Maiheu, B., & van Heijst, G. J. (2017). A review on the CFD analysis of urban microclimate. *Renewable and Sustainable Energy Reviews*, *80*(June), 1613–1640. https://doi.org/10.1016/j.rser.2017.05.248

Trapani, K., & Redón Santafé, M. (2015). A review of floating photovoltaic installations: 2007-2013. *Progress in Photovoltaics: Research and Applications*, *23*(4), 524–532. https://doi.org/10.1002/pip.2466

Vaillon, R., Robin, L., Muresan, C., & Ménézo, C. (2006). Modeling of coupled spectral radiation, thermal and carrier transport in a silicon photovoltaic cell. *International Journal of Heat and Mass Transfer*, *49*(23), 4454–4468. https://doi.org/https://doi.org/10.1016/j.ijheatmasstransfer.2006.05.014

Vasel, A., & Iakovidis, F. (2017). The e ff ect of wind direction on the performance of solar PV plants. *Energy Conversion and Management*, *153*(October), 455–461. https://doi.org/10.1016/j.enconman.2017.09.077

Veldhuis, A. J., Nobre, A., Reindl, T., Ruther, R., & Reinders, A. H. (2013). The influence of wind on the temperature of PV modules in tropical environments, evaluated on an hourly basis. *Conference Record of the IEEE Photovoltaic Specialists Conference*, *31*(0), 824–829. https://doi.org/10.1109/PVSC.2013.6744273

Veldhuis, A. J., Nobre, A. M., Peters, I. M., Reindl, T., Ruther, R., & Reinders, A. H. M. E. (2015). An Empirical Model for Rack-Mounted PV Module Temperatures for Southeast Asian Locations Evaluated for Minute Time Scales. *IEEE Journal of Photovoltaics*, *5*(3), 774–782. https://doi.org/10.1109/JPHOTOV.2015.2405762

Verburg, P., & Antenucci, J. P. (2010). Persistent unstable atmospheric boundary layer enhances sensible and latent heat loss in a tropical great lake: Lake Tanganyika. *Journal of Geophysical Research Atmospheres*, *115*(11), 1–13. https://doi.org/10.1029/2009JD012839

Verkaik, J. W. (2000). Evaluation of two gustiness models for exposure correction calculations. *Journal of Applied Meteorology*, *39*(9), 1613–1626. https://doi.org/10.1175/1520-0450(2000)039⟨1613:EOTGMF⟩2.0.CO;2

Vidal-López, P. (2012a). Determination of synthetic wind functions for estimating open water evaporation with Computational Fluid Dynamics. *3952*(July), 3945–3952. https://doi.org/10.1002/hyp.9503

Vidal-López, P. (2012b). Determination of synthetic wind functions for estimating open water evaporation with Computational Fluid Dynamics. *3952*(July), 3945–3952. https://doi.org/10.1002/hyp.9503

Vimal, S., & Singh, V. (2021). Re-discovering Robert E. Horton's Lake Evaporation Formulae: New Directions for Evaporation Physics. *Hydrology and Earth System Sciences Discussions*, (July), 1–37. https://doi.org/10.5194/hess-2021-234

Volz, F. (1965). The dependence of albedo on solar elevation. *Pure and Applied Geophysics PAGEOPH*, *60*(1), 197–200. https://doi.org/10.1007/BF00874823

Wah, W. P., Shimoda, Y., Nonaka, M., Inoue, M., & Mizuno, M. (2005). Field Study and Modeling of Semi-Transparent PV in Power, Thermal and Optical Aspects. *Journal of Asian Architecture and Building Engineering*, *4*(2), 549–556. https://doi.org/10.3130/jaabe.4.549

Waithiru, C. L., Jong Rok, L., Chang Sub, W., & Ahn, H. K. (2018). Prediction Model of Photovoltaic Module Temperature for Power Performance of Floating PVs. https://doi.org/10.3390/en11020447

Wang, K., & Dickinson, R. (2012). a Review of Global Terrestrial Evapotranspiration : Observation. *Reviews of Geophysics*, *50*(2011), 1–54. https://doi.org/10.1029/2011RG000373.1.INTRODUCTION

Waterworth, D., & Armstrong, A. (2020). Southerly winds increase the electricity generated by solar photovoltaic systems. *Solar Energy*, *202*(April), 123–135. https://doi.org/10.1016/j.solener.2020.03.085

Webster, I. T., & Sherman, B. S. (1995). Evaporation from fetch-limited water bodies. *Irrigation Sciences*, (September 1994), 53–64.

Weiss, L. (2015). Modeling of a photovoltaic module under environmental conditions and optimisation of its performance.

Weiss, L., Amara, M., & Ménézo, C. (2016). Impact of radiative-heat transfer on photovoltaic module temperature. *Progress in Photovoltaics: Research and Applications*, *24*(1), 12–27. https://doi.org/10.1002/pip.2633

Wenbo, G., Tao, M., Meng, L., Lu, S., & Yijie, Z. (2020). A coupled optical-electrical-thermal model of the bifacial photovoltaic module. *Applied Energy*, *258*, 114075. https://doi.org/https://doi.org/10.1016/j.apenergy.2019.114075

Wetter, M., Zuo, W., Nouidui, T. S., & Pang, X. (2014). Modelica Buildings library. *Journal of Building Performance Simulation*, *7*(4), 253–270. https://doi.org/10.1080/19401493.2013.765506

Where Sun Meets Water: Floating Solar Market Report (tech. rep.). (2019). World Bank Group, ESMAP an SERIS. Washington DC. https://doi.org/10.1596/32804

Wieringa, J. (1976). An objective exposure correction method for average wind speeds measured at a sheltered location. *Quarterly Journal of the Royal Meteorological Society*, *102*(431), 241–253. https://doi.org/https://doi.org/10.1002/qj.49710243119

Wieringa, J. (1996). Does representative wind information exist? *Journal of Wind Engineering and Industrial Aerodynamics*, *65*(1-3), 1–12. https://doi.org/10.1016/S0167-6105(97)00017-2

Wieringa, J. (1973). Gust factors over open water and built-up country. *Boundary-Layer Meteorology*, *3*, 424–441.

Wieringa, J. (1992). Updating the Davenport roughness classification. *Journal of Wind Engineering and Industrial Aerodynamics*, *41*(1-3), 357–368. https://doi.org/10.1016/0167-6105(92)90434-C

Wilcox, D. C. (1988). Reassessment of the scale-determining equation for advanced turbulence models. *AIAA Journal*, *26*, 1299–1310.

World Meteorological Organization. (2018). *Volume I – Measurement of meteorological variables* (Vol. 1). https://library.wmo.int/index.php?lvl=notice_display&id=12407%0Ahttps://library.wmo.int/index.php?lvl=notice_display&id=12407#.YkdSz3XMLio

Wossenu, A., & Assefa, M. (2012). *Evaporation and Evapotranspiration - Measurements and Estimations.*

Wu, Y.-Y., Wu, S.-Y., & Xiao, L. (2017). Numerical study on convection heat transfer from inclined pv panel under windy environment. *Solar Energy*, *149*, 1–12. https://doi.org/https://doi.org/10.1016/j.solener.2017.03.084

Yang, P., Chua, L. H., Irvine, K. N., & Imberger, J. (2021). Radiation and energy budget dynamics associated with a floating photovoltaic system. *Water Research*, *206*(September), 117745. https://doi.org/10.1016/j.watres.2021.117745

Zhang, Q., Zeng, J., & Yao, T. (2012). Interaction of aerodynamic roughness length and wind-flow conditions and its parameterization over vegetation surface. *Chinese Science Bulletin*, *57*(13), 1559–1567. https://doi.org/10.1007/s11434-012-5000-y

Zhang, S., Morita, K., Fukuda, K., & Shirakawa, N. (2006). An improved MPS method for numerical simulations of convective heat transfer problems. *International Journal for Numerical Methods in Fluids*, *51*(1), 31–47. https://doi.org/10.1002/fld.1106

Zhao, D., Aili, A., Zhai, Y., Xu, S., Tan, G., Yin, X., & Yang, R. (2019). Radiative sky cooling: Fundamental principles, materials, and applications. *Applied Physics Reviews*, *6*(2). https://doi.org/10.1063/1.5087281